



**One-dimensional inversion of airborne time-domain
electromagnetic data from Taylor Brook, western Newfoundland,
and 3D finite-element time-domain forward modeling using
unstructured grids**

by

© Cevdet Anil Kilic

A thesis submitted to the School of Graduate Studies in partial fulfilment of
the requirements for the degree of

Master of Science

Department of Earth Sciences

Memorial University of Newfoundland

December 2020

St. John's

Newfoundland and Labrador

Abstract

In this thesis, geophysical inversion and numerical modeling are carried out on a dataset collected using the Airborne Time-Domain Electromagnetic (ATEM) survey method over an area called Taylor Brook, western Newfoundland, which potentially hosts massive sulfide mineralization. ATEM profiles are interpreted using a 1D inversion code (EM1DTM). The inversion results indicate that the majority of the dataset collected in the part of the area which does not show any anomaly is highly noise-contaminated. In contrast, several observation points near the sulfide mineralization have reasonable anomalies. For a better understanding of the sulfide-bearing zone's dip, thickness and depth in the survey area, 2D cross-sections along each profile are created by combining 1D models for each observation point. Also, 3D forward modeling is applied to several Earth models that are created using the information of boreholes and the results of 1D inversions. For 3D modeling of time-domain EM problems, the finite-element time-domain (FETD) method using unstructured tetrahedral meshes is used. The dataset for two different survey profiles that have boreholes nearby were chosen to guide the building of the 3D models. A trial-and-error method, in which the physical properties and thicknesses of the geological structures were varied, resulted in a reasonable match between the vertical component (z-component) of the calculated responses from the FETD forward modeling and the measured data. This reasonable match would mean that the final Earth model is reasonable representation of the subsurface in the survey area.

General Summary

To interpret what is beneath the Earth is like guessing about something that cannot be seen. To interpret it reliably, many methods and devices based on physics and engineering are used. The methods were only used on the ground before about 1950, but there have been many developments in geophysical methods and computers since then, so we are now able to use methods in the air. This makes the exploration process over an area faster. In this thesis, a couple of geophysical interpretation methods are applied to data acquired in the air at an area called Taylor Brook, which is a prospective mining area. One of these interpretation methods is to estimate the real physical properties of the Earth by inverse modeling the dataset that is collected from the survey area. Another is to create artificial 3D Earth models, calculate a dataset from them, and compare the similarity between the calculated dataset and the real dataset. The artificial model is adjusted to make the calculated dataset closer to the real dataset. In this way, we are able to infer one realistic model of what geological structure might be beneath the survey area.

Acknowledgements

I would like to thank my supervisor, Dr. Colin Farquharson, for his inversion code (EM1DTM), precious advice, help, and continuous support during my MSc program, and to thank Alison Leitch for being my other supervisory committee member, her help and valuable advice. Also, many thanks to Dr. Xushan Lu for his code for 3D forward modeling that makes this thesis more valuable, and his never-ending support anytime I needed. I am thankful to Dr. Peter Lelièvre for developing the software FacetModeller, which makes creating complex 3D Earth models so easy.

I am grateful to the Ministry of National Education of the Republic of Turkey for the financial support that made this wonderful opportunity possible. I would like to thank the Geological Survey of Newfoundland and Labrador for providing the dataset, and Gerry Kilfoil for helping with this.

Finally, I would like to thank my family and my friends for their never-ending support in every way and their encouragement, and special thanks to my fiancé, Emine Sebnem Dokumaci who made the stressful time that I had during my program bearable with her invaluable support and companionship.

Table of Contents

Abstract	i
General Summary.....	ii
Acknowledgements	iii
Table of Contents	iv
List of Figures	vi
List of Tables	xiii
1. Introduction.....	1
2. The Geology of Taylor Brook	4
2.1 Regional Geological Surveys	4
2.2 The Application of Boreholes.....	10
2.3 Geophysical Surveys	16
3. The Airborne Time-Domain Electromagnetic Method.....	19
3.1 Introduction.....	19
3.2 Background Theory of Electromagnetic Methods.....	20
3.3 The Measured Data of ATEM	22
3.4 The Taylor Brook AeroTEM Survey.....	31
4. Inversion	36

4.1 Introduction to Inversion (and program “EM1DTM”).....	36
4.2 The Inversion Result of the Taylor Brook ATEM Data	44
5. Finite-Element Time-domain Electromagnetic Forward Modeling (3D)....	56
5.1 Governing Equations	58
5.1.1 Vector FE method	59
5.2 Time Discretization	61
5.3 The Applications of FETD Forward Modeling to the Taylor Brook Survey	64
5.3.1 Trial-and-Error Modeling.....	65
6. Summary and Conclusions	91
Bibliography	93
Appendix.....	99
A. Inversion (EM1DTM) Results	99
B. The FETD Responses of 3D Earth Models.....	234

List of Figures

Figure 1.1: Regional location map of the project area (O'Reilly et. al., 2012). The black star represents the survey area.	3
Figure 2.1: A generalized interpretive geology map of Newfoundland (Williams, 2004). The white star represents the survey area.....	5
Figure 2.2: The Geology of the Long-Range Inlier, Newfoundland. The labelled dots represent the collected rock samples (Heaman et al., 2002). The blue star represents the Taylor Brook area.	6
Figure 2.3: SiO ₂ vs MgO – Taylor Brook Gabbro and Mafic Dikes (Fitzpatrick, 2000).	8
Figure 2.4: Regional geology prospecting of the survey area (Fitzpatrick, 2000). The rightmost red star represents the Layden showing.	9
Figure 2. 5: The trench geology at the Layden showing (Fitzpatrick, 2000).....	10
Figure 2.6: Taylor Brook drill hole location map (Ebert, 2008).....	12
Figure 2. 7: The z-component of secondary magnetic field (dB/dt) responses from the AeroTEM-II system, and the locations of the drill holes, in the part of the survey area with the conductors (Ebert, 2008).	13
Figure 2.8: A cross section showing holes 08TB-09 and 10 and the centre of the airborne EM anomaly (Ebert,2008).....	14
Figure 2.9: A cross-section showing drill hole 08TB-17 at the Layden showing (Ebert,2008)... ..	15
Figure 2.10: In-phase Fraser-filtered profiles of the VLF-EM data (the black lines) and colored contours for the Layden showing area (right bottom) and to the northwest of the Layden	

showing (top left). The white star represents the location of the Layden showing (Fitzpatrick, 2000). The black dots on the black lines are the observation points.....	16
Figure 2.11: Total magnetic intensity (TMI) profiles (the black lines) and colored contours for the Layden showing area (right bottom) and to the northwest of the Layden showing (top left). The white star represents the location of the Layden showing (Fitzpatrick, 2000).	17
Figure 2.12: Typical ranges of conductivities/resistivities of materials (Palacky, 1987).	18
Figure 3.1: The principles of airborne transient electromagnetic surveying (Korus, 2018).	22
Figure 3.2: The AeroTEM-II EM bird. The large outer ring is the transmitter whereas the red circle in the centre of the transmitter shows the receiver. The arrow at the right-hand side of the figure shows the second caesium magnetometer sensor (Churchill, 2008).	23
Figure 3.3: Schematic of the transmitter waveform and typical receiver responses of the AeroTEM system (Churchill, 2008).	23
Figure 3.4: a) A generated noisy response over a 2-layered earth model. Logarithmically increasing time windows are created and displayed at the bottom of the plot. b) The decay curve of log-gated data in figure a) are marked as a “x”. c) The stacked response of the ten log-gated responses from b). “◇” represents the data points (Munkholm and Auken, 1996).	24
Figure 3.5: The variation of voltage measured at the receiver with respect to the resistivity of the homogeneous half-space (Turkoglu, 2003).	25
Figure 3.6: The apparent resistivity (y-axis) for the in-loop TEM configuration, which has the receiver located in the centre of the transmitter, for a 10 Ωm homogeneous half-space. The solid line indicates the true resistivity and the dashed curves are the early-time and late-time asymptotic apparent resistivities (Spies et. al, 1986).	27

Figure 3.7: a) The responses (dB/dt) for a half-space with respect to varying resistivities of the homogeneous half-space (black lines). The apparent resistivity curves (ρ_a) in b) are converted from the same curves. The grey line represents the response of a two-layer earth model with 100 Ωm in layer-1 and 10 Ωm in layer-2. Layer-1 is 40 m thick (Christiansen et. al., 2006).	28
Figure 3.8: The response of AeroTEM to a ‘thin’ vertical conductor. The black lines represent the response of the z-component whereas the red lines indicate the response of the x-component (Churchill, 2008). The yellow loop on the top left represents the transmitter configuration.	29
Figure 3.9: The response of AeroTEM to a ‘thick’ vertical conductor (Churchill, 2008).	29
Figure 3.10: The response of AeroTEM to a ‘thin’ dipping conductor (Churchill, 2008).	30
Figure 3.11: The survey block (the red solid lines) and flight paths for the Taylor Brook AeroTEM survey (Churchill, 2008).	32
Figure 3.12: The off-time channel responses plotted as colour lines aligned along each profile, zoomed-in to the area around the Layden showing (Churchill, 2008).	33
Figure 3.13: The contour map of the z-component off-time channel response ($Z_{\text{off1}}=1.1848\text{ ms}$) over the Layden showing in Taylor Brook area (Churchill, 2008).	34
Figure 3.14: Total magnetic intensity (TMI) map of the Taylor Brook survey area. The white rectangle represents the area of interest for EM inversion and modeling later in this thesis (Churchill, 2008).	35
Figure 4.1: The Earth model settings used in the program EM1DTM. Z_j is the depth to the bottom of the j th layer, σ_j and l_j are the conductivity and thickness of the j th layer, respectively. S is the source, and h is the height of the source above the surface. R is the location of an observation point (Farquharson and Oldenburg, 1993).	38

Figure 4.2: (a) TEM responses acquired with a 60x60m sized loop. The inversion models of the curves in panel (a) are shown in panel (b), which are two versions of the flattest model (Farquharson et. al., 1993; two curves are indistinguishable from one to another in panel (b)).	42
Figure 4.3: The results of inverting the line of frequency-domain EM observations from Heath Steele Stratmat closest to the mineralized zone. (a) The observations (shown with the error bars) and the lines for predicted data of the model generated by the inversion (solid-in-phase; dashed-quadrature) are shown (edited; Farquharson et al., 2003). (b) The final values of the misfit (solid circles and model-structure term (open circles) are presented. (c) The conductivity model of the inversion in which the mineralized zone is shown with the gray outline.	43
Figure 4.4: The map of the survey area showing the z-component of the second off-time channel (on the left). The map on the right indicates the main area of interest (Churchill, 2008).	45
Figure 4.5: The maps on the top and bottom left show the second off-time channel. The dashed arrows represent flight-line directions. The graphs on the right indicate all the measured off-time channels along the two profiles that are highlighted with dashed lines on the maps on the left.	46
Figure 4.6: The maps on the top and bottom left show the second off-time channel. The dashed arrows represent flight-line directions. The graphs on the right indicate all the measured off-time channels along the two profiles that are highlighted on the maps on the left.	47
Figure 4.7: The map shows the second off-time channel over the area of interest (on the left). All time channels over the area of interest (on the right; Churchill, 2008).	48

Figure 4.8: The 2-D conductivity section of line L10140 (top panel). The numbers on the top of the cross-section indicate the index of the observation points. The lower panels show the smooth 1D models of the Earth produced by the inversion for 4 different observation points.....	49
Figure 4.9: The comparison of the measured and the predicted data for the 4 observation points shown in the lower panel of Figure 4.8.....	50
Figure 4.10: The 2-D conductivity section for line L10150 (upper). The numbers on the top of the cross-section indicate the index of the observation points. In the lower panels, the models constructed by inversion for 4 different observation points.....	51
Figure 4.11: The comparison of the measured and the predicted data for the 4 observation points shown in Figure 4.10.....	51
Figure 4.12: The 2-D conductivity section for L10170 (top). The numbers on the top of the cross-section indicate the index of the observation points. In the lower panels, the smooth models after inversion for 4 different observation points are shown.	52
Figure 4.13: The comparison of the measured and the predicted data for the 4 observation points shown in Figure 4.12.....	53
Figure 4.14: The 2-D conductivity section for line L10180 (top). The numbers on the top of the cross-section indicate the index of the observation points. In the lower panels, the models constructed by inversion for 4 different observation points are shown.	54
Figure 4.15: The comparison of the measured and the predicted data for the 4 observation points shown in Figure 4.14.....	54
Figure 4.16: The 3D conductivity volume combined from all the 1D conductivity models from the 1D inversions (on the top left and right). A cross-section through the 3-D visualisation crossing the survey lines at the main conductor zone (on the bottom).	55

Figure 5.1: The workflow of the FETD method (Li et al., 2018).....	63
Figure 5.2: A screenshot from the FacetModeller software that shows a 3D Earth model (which is just the central volume of interest, not the entire volume of the 3D model that is used for forward-modeling) built for the survey area. On the left side, 2D view of the model is shown, while the 3D view of the model is shown on the right side of the screenshot.	66
Figure 5.3: The unstructured tetrahedral mesh generated by TetGen for the model in Figure 5.2.	67
Figure 5.4: The locations of the dikes, of Line L10170 (upper line), and of Line L10180 (bottom line). The blue block is Dike-1, whereas the red one is Dike-2.	68
Figure 5.5: The z-component of the measured dB/dt data from Line L10170 at the observation points used for comparison with the numerical modeling. (Note the different scales in each panel.).....	73
Figure 5.6: The locations of the dikes, of Line L10170 (upper line) and of Line L10180 (bottom line) for Model 5. The blue dike is Dike-1, whereas the red one is Dike-2.	75
Figure 5.7: The 3D Earth model generated in FacetModeller and meshed by Tetgen for Model 5.	76
Figure 5.8: The EM response of Model 5 calculated using a conductivity of 10 S/m (on the left) and 100 S/m (on the right) for Dike-1. The solid lines show the real data and the dashed lines and crosses indicate the calculated data.	77
Figure 5.9: The z-component of the measured dB/dt data from Line L10180 at the observation points used for comparison with the numerical modeling.	78

Figure 5.10: The EM response of Model 5 calculated using a conductivity of 10 S/m (on the left) and 100 S/m (on the right) for Dike-2. The solid lines show the real data and the dashed lines and crosses indicate the calculated data.	79
Figure 5.11: The locations of the dikes, and of Line L10170 (upper line) and of Line L10180 (bottom line) for Model 8. The blue dike is Dike-1, whereas the red one is Dike-2.	81
Figure 5.12: The 3D Earth model generated in FacetModeller and meshed by Tetgen for Model 8.	82
Figure 5.13: The EM response of Model 8 calculated using a conductivity of 10 S/m (on the left) and 100 S/m (on the right) for the Dike-1.	83
Figure 5.14: The EM response of Model 8 calculated using a conductivity of 10 S/m (on the left) and 100 S/m (on the right) for the Dike-2.	84
Figure 5.15: The locations of the dikes, and of Line L10170 (upper line) and of Line L10180 (bottom line) for Model 10. The blue dike is Dike-1, whereas the red one is Dike-2.	86
Figure 5.16: The 3D Earth model generated in FacetModeller and meshed by Tetgen for Model 10.	87
Figure 5.17: The EM responses of Model 10 calculated using a conductivity of 10 S/m (on the left) and 100 S/m (on the right) for the Dike-1.	88
Figure 5.18: The EM responses of Model 10 calculated using a conductivity of 10 S/m (on the left) and 100 S/m (on the right) for Dike-2 being a 120 m vertical extent.	89
Figure 5.19: The EM response (on the left panel) calculated for the dike having a conductivity of 100 S/m and a 90 m vertical extent (Model 5). The EM response (on the right panel) calculated for the dike having a conductivity of 100 S/m and 120 m a vertical extent (Model 10).	90

List of Tables

Table 2.1: Taylor Brook drill holes.....	11
Table 5.1: The computational times of each time-stepping scheme chosen for a homogeneous half-space (0.001 S/m). The initial time-step is 10^{-7} s (from Li et al., 2018).....	62
Table 5.2: Conductivities of each region in the 3D Earth models.	66
Table 5.3: The 3D Earth models and, in particular, the locations and sizes of the dikes, for which 3D numerical modeling was carried out.	69

Chapter 1

1. Introduction

There have been considerable improvements in the methods of geophysical exploration with developments in technology over time. Data acquisition by electromagnetic methods generally takes time. For ground-based time-domain electromagnetic (TEM) methods, for instance, setting up the survey configuration and moving it to another observation point is quite time-consuming. However, airborne data acquisition, which has been used since 1950, has been a common method after survey systems became more portable and easily assembled on an aircraft. This saves considerable time during data acquisition by enabling users to collect data over a large-scale survey area (e.g. Smith et al., 1996).

Also, data processing of these datasets takes much less time than in the past because of the development of modern computers. Hence, airborne methods, whether using a fixed-wing plane or helicopter, make the data acquisition process faster and easier than ground-based methods. Conveniently, in terms of its physical and mathematical background, airborne time-domain electromagnetic (ATEM) methods use a similar type of measurement system to the classical ground-based TEM methods. ATEM has become one of the main methods for mineral exploration in the past two decades, mostly because of significant improvements in equipment (Fountain et al, 2005). In addition to this, geological mapping and exploration for groundwater are also carried out using ATEM. Traditionally, the data are presented as conductivity-depth pseudo-sections (Macnae

et. al., 1991) or sections derived from inversion (Yang and Oldenburg, 2012), or trial-and-error numerical modeling of the measured data (Li et al., 2018).

One of the aims of this M.Sc. research is to demonstrate the contribution of ATEM methods to surveying for metallic mineral deposits. Therefore, a dataset, from the Taylor Brook property located in the White Bay region of western Newfoundland (Figure 1.1), is analyzed and modeled in order to show how effective ATEM is for exploring for metallic minerals by identifying zones of increased conductivity in the subsurface. It is known that an inversion requires forward modeling starting from initial models that are defined by users. To get a reliable inversion result, having a fast and accurate forward solver is a must for a researcher, especially in 3D cases (Lu, 2020). This leads us to the other goal of this thesis, which is to emphasize how helpful trial-and-error numerical modeling of the measured data for candidate 3D Earth models based on geology, boreholes, and any available geophysical data is for having a better understanding of the geological structure of the subsurface in the survey area.

This thesis has four main chapters, which are ‘The Geology of Taylor Brook’ (Chapter 2), ‘Airborne Time-Domain Method’ (Chapter 3), ‘Inversion’ (Chapter 4), and ‘Finite-Element Time-Domain Forward Modeling’ (Chapter 5). Chapter 2 includes a description of the background geology of Newfoundland and of the geological and geophysical surveys that have been done in the survey area before. Chapter 3 provides the theory of ATEM, the measured ATEM data and the magnetic data over the survey area, and information from the boreholes that were drilled based on ATEM anomalies. Chapter 4 covers the theory of the 1D inversion method used in this thesis and its results. Chapter 5 provides the theory of the finite-element time-domain (FETD) forward modeling approach that was used and the results of its applications to the candidate 3D Earth models.

Chapter 2

2. The Geology of Taylor Brook

2.1 Regional Geological Surveys

The Taylor Brook property is located within the Long-Range Inlier of western Newfoundland. The Long-Range Inlier is the largest basement massif in the Appalachian Orogen, comprising crystalline rocks of Proterozoic age (Owen et al., 1989; Figure 2.1 and Figure 2.2). In the mid 1980's, the Geological Survey of Canada (GSC) surveyed the Long-Range Inlier area with numerous mapping projects. The following information on regional geology is based on the research of Victor Owen, who carried out one of the mapping projects for the GSC during the mid to late eighties (Owen, 1986). Taylor Brook and its surroundings are predominantly underlain by middle to upper Proterozoic gneisses and mafic to felsic plutonic rocks. The majority of gneisses are quartzofeldspathic rocks including quartz dioritic, tonalitic, granodioritic and granitic compositional variants. The protolith of the quartzofeldspathic gneisses in the Long Range are a subject of ongoing scientific debate. Owen (1986) suggests that an abundance of quartz and feldspar present within these rocks suggests an igneous (granitoid) origin. Based on uranium-lead age dating, the quartzofeldspathic gneisses have been assigned a minimum age of 1.5 Ga.

In the late 1990's, the survey area saw a number of exploration projects. The majority of exploration in the region has either been gold- or uranium-focused and located generally north or south of Taylor Group claim (O'Reilly et al., 2012). The Taylor Brook area has also been covered

by the province-wide lake sediment geochemical survey by the Newfoundland Department of Mines (Ebert, 2008). In the lake sediments, up to 51 ppm of nickel was discovered.

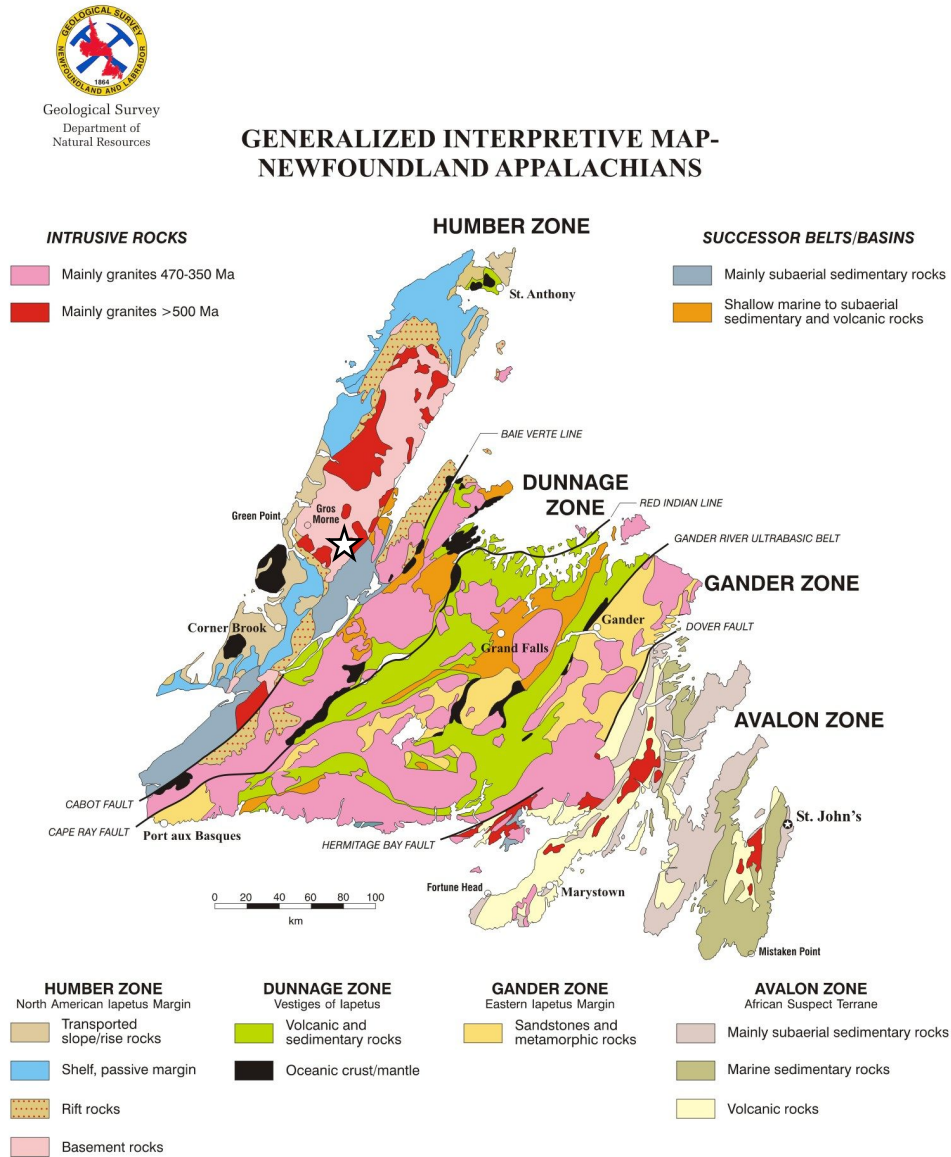


Figure 2.1: A generalized interpretive geology map of Newfoundland (Williams, 2004). The white star represents the survey area.

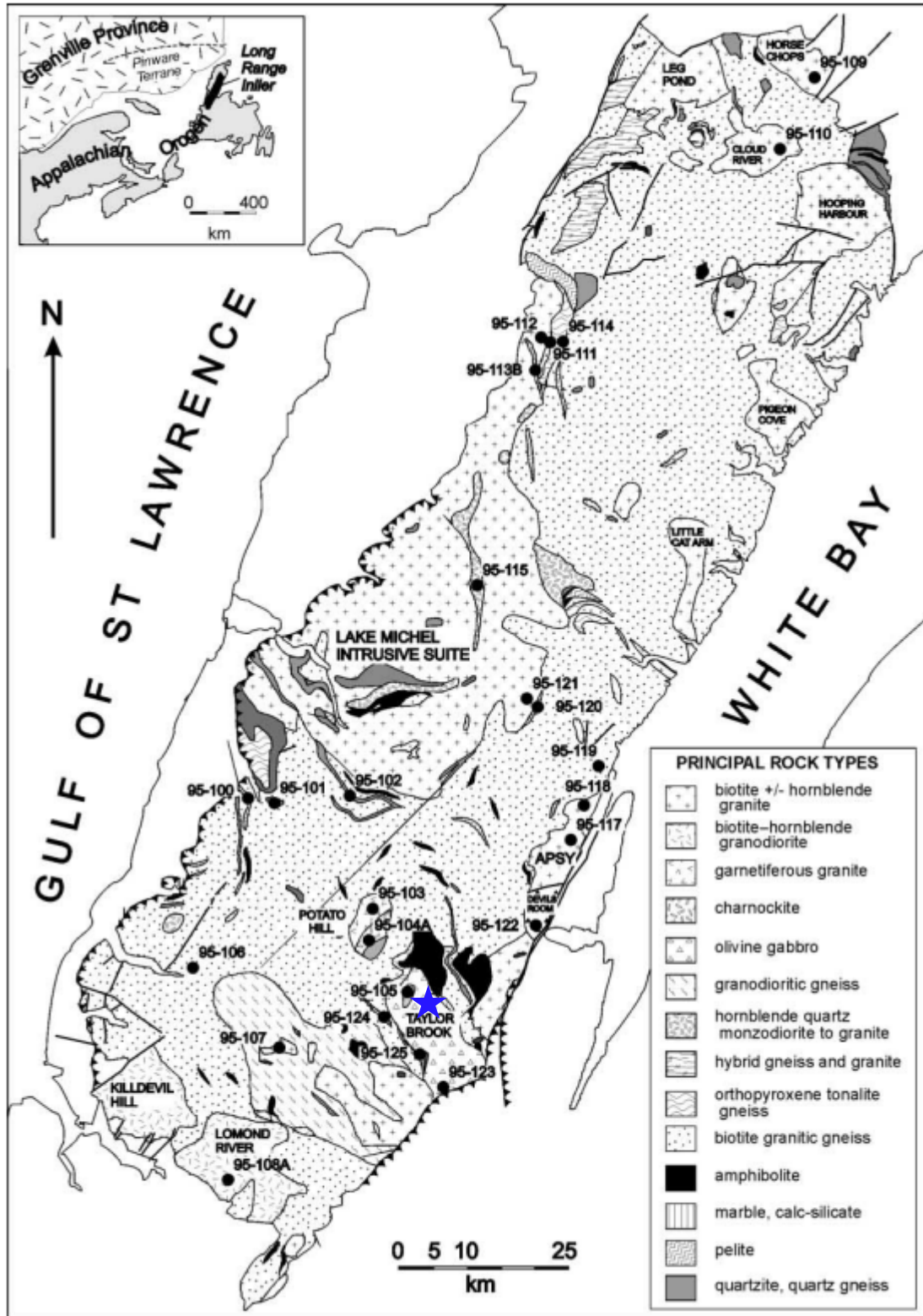


Figure 2.2: The Geology of the Long-Range Inlier, Newfoundland. The labelled dots represent the collected rock samples (Heaman et al., 2002). The blue star represents the Taylor Brook area.

In 1998, Jerry Layden, a geologist, found sulfide occurrences, with nickel and copper (weakly anomalous) during the initial construction of roads in the area. This discovery led him to the high-grade nickel mineralization, which has been called the Layden showing since then, a few hundred metres south of the Upper Humber River. After this discovery, in 1999 and 2000, Altius Minerals Corporation visited and sampled the area, and confirmed the high nickel tenor with copper, cobalt and precious metals. Eleven grab samples taken from the Layden showing returned averages of 5.38% Ni, 1.05 Cu, 0.1 Co, 112 ppb Pt, 232 ppb Pd and 416 ppb Au, and 32 rock samples were collected during the survey to submit to laboratory examination. The company also conducted reconnaissance mapping and prospecting, grid mapping, magnetic, and very low frequency electromagnetic surveys (VLF–EM) and trenching.

The rock samples that were sent to the laboratory for analyzing were taken from different rock units (i.e. amphibolite, Taylor Brook gabbro, mafic dike, gneiss, biotitic amphibolite). Two of the rock samples from the mafic dike units were from dikes hosted by gneisses while a third was from a dike that cuts the Taylor Brook gabbro (Fitzpatrick, 2000). The result of analyzing samples also suggests that the mafic dikes might be related to the Taylor Brook gabbro in that they have similar abundances of SiO₂ and MgO (Figure 2.3), and that they are not related to mineralization, and the amphibolites have a composition which is close to gabbroic (Fitzpatrick, 2000).

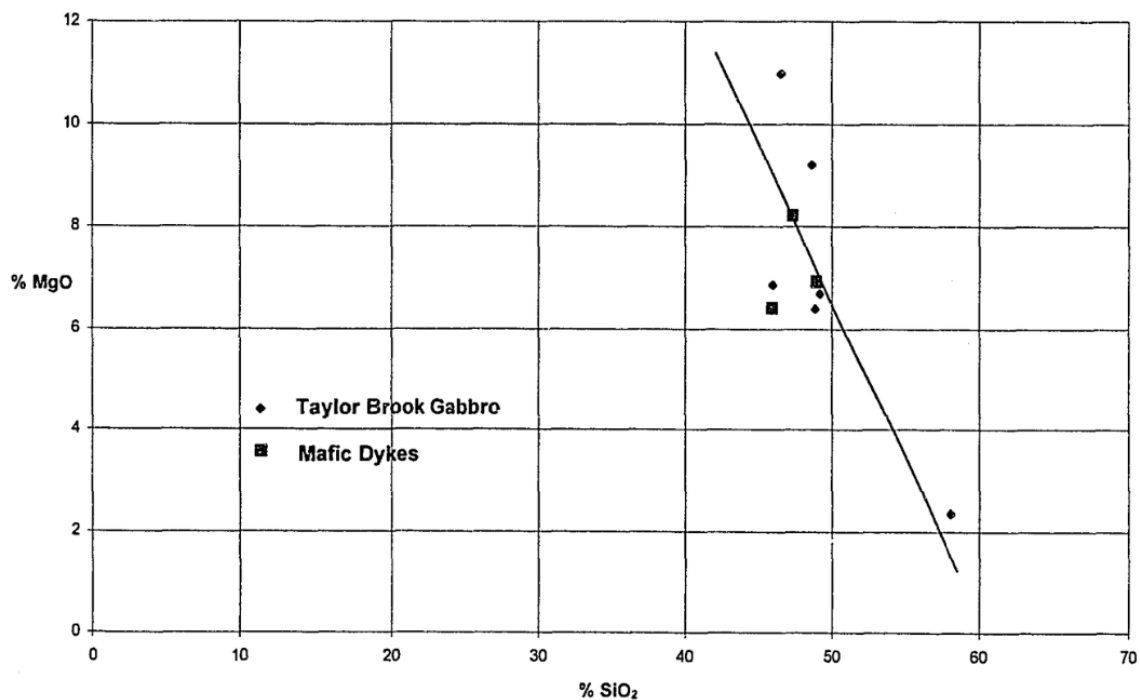
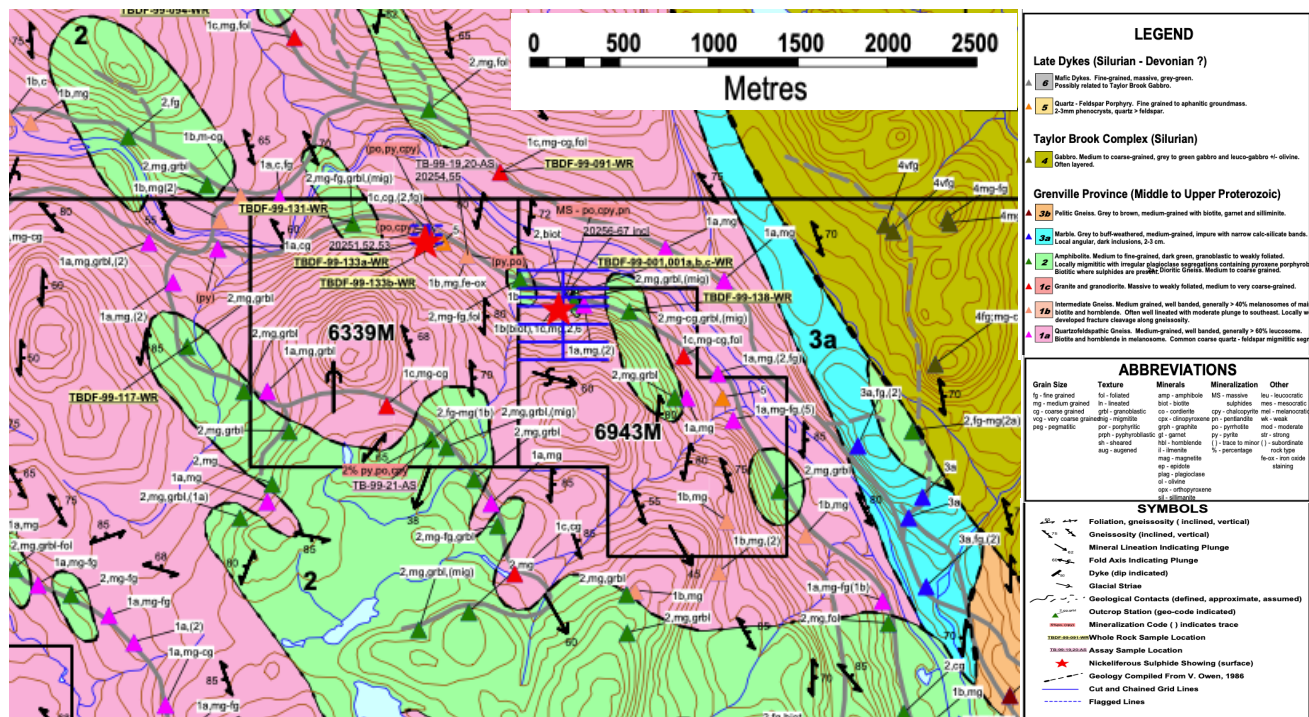


Figure 2.3: SiO₂ vs MgO – Taylor Brook Gabbro and Mafic Dykes (Fitzpatrick, 2000).

Trenching was applied to the part of the survey area at the Layden showing in order to observe the geological context of the high-grade nickel mineralization. The trench is approximately 12 metres long by 4 metres wide and its depth is almost 1 metre. Trenching and detailed mapping of the survey area have indicated that sulfide mineralization at the Layden showing is hosted in highly deformed and metamorphosed mafic to ultramafic structures within strongly biotitic amphibolite (Fitzpatrick, 2000; Figure 2.4 and Figure 2.5).



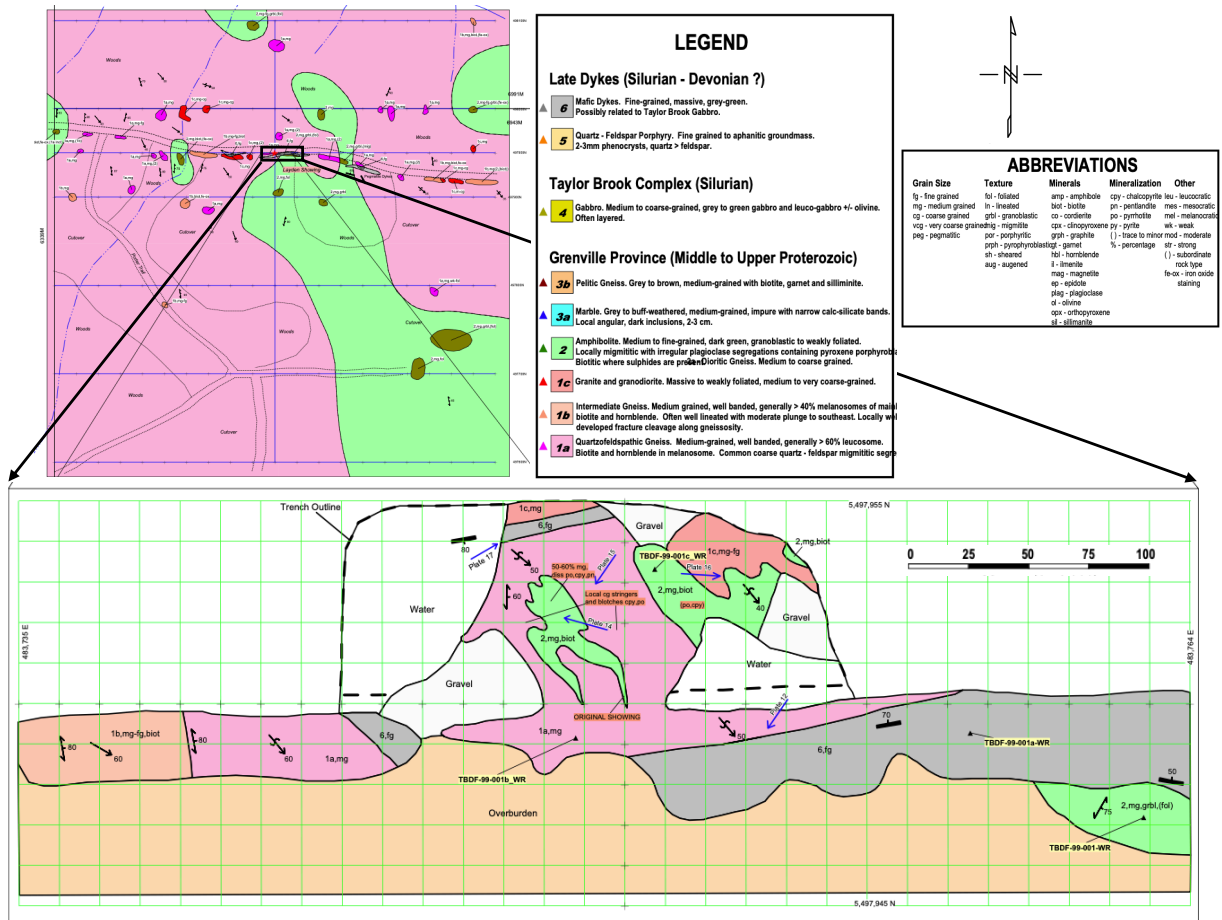


Figure 2. 5: The trench geology at the Layden showing (Fitzpatrick, 2000).

2.2 Boreholes Information

The data from the ATEM survey provided essential information about where conductive bodies might be found (see Chapter 3). Using geological information from previous investigations and the ATEM responses, 17 boreholes were drilled over the survey area (Table 2.1). The following geological information, including information about mineralization, is summarized from Ebert (2008), the knowledge obtained from the boreholes and from Owen (1986). Figure 2.6 indicates the locations of the boreholes that were analysed to determine the amount of sulfide mineralization in the study area, while Figure 2.7 shows the relation between the z-component (vertical

component) of the secondary magnetic field responses (dB/dt) measured using the AeroTEM ATEM system over the area and the locations of the boreholes. Also, two detailed cross-sections that were created by using the cores from the boreholes are shown in Figures 2.8 and 2.9. This knowledge provides us with initial information about the subsurface that can be used to create the 3D model of the survey area, in addition to the results of 1D inversion.

Table 2.1: Taylor Brook drill holes.

HOLE	Easting	Northing	Elevation	Azimuth	Dip	Depth
07TB-01	483767	5497956	240	275	-51	102.72
07TB-02	483767	5497956	240	265	-51	47.85
07TB-03	483781	5497957	240	335	-58	171.3
07TB-04	483781	5497957	240	335	-75	172.82
07TB-05	483781	5497957	240	310	-51	135
07TB-06	483803	5497975	235	335	-51	178.92
07TB-07	483803	5497975	235	335	-70	114.33
07TB-08	483803	5497975	235	305	-60	282.55
08TB-09	483754	5497769	273	50	-50	197
08TB-10	483754	5497769	273	50	-70	149
08TB-11	483716	5497874	260	50	-51	185
08TB-12	483807	5497847	265	240	-60	160
08TB-13	483783	5497957	240	0	-90	203.5
08TB-14	483753	5498102	213	40	-50	213.7
08TB-15	483552	5498132	219	70	-50	179
08TB-16	483093	5498243	261	235	-47	133
08TB-17	483759	5497956	239	0	-90	10.6

The Taylor Brook property has varying amounts of felsic gneisses and amphibolites that show strong metamorphic foliation. Lesser amounts of granite-pegmatite dikes and late fine-grained mafic dikes are also present. Sulfide mineralization seems to be associated with a deformed mafic to ultramafic metabasite unit. The Layden showing is a high-grade massive sulfide lens that

outcrops at the surface within a small metabasite body about 2 to 3 metres wide by 9 metres long. The sulfide lens is interpreted to be deformed, forming a rod-shaped body dipping to the southeast.

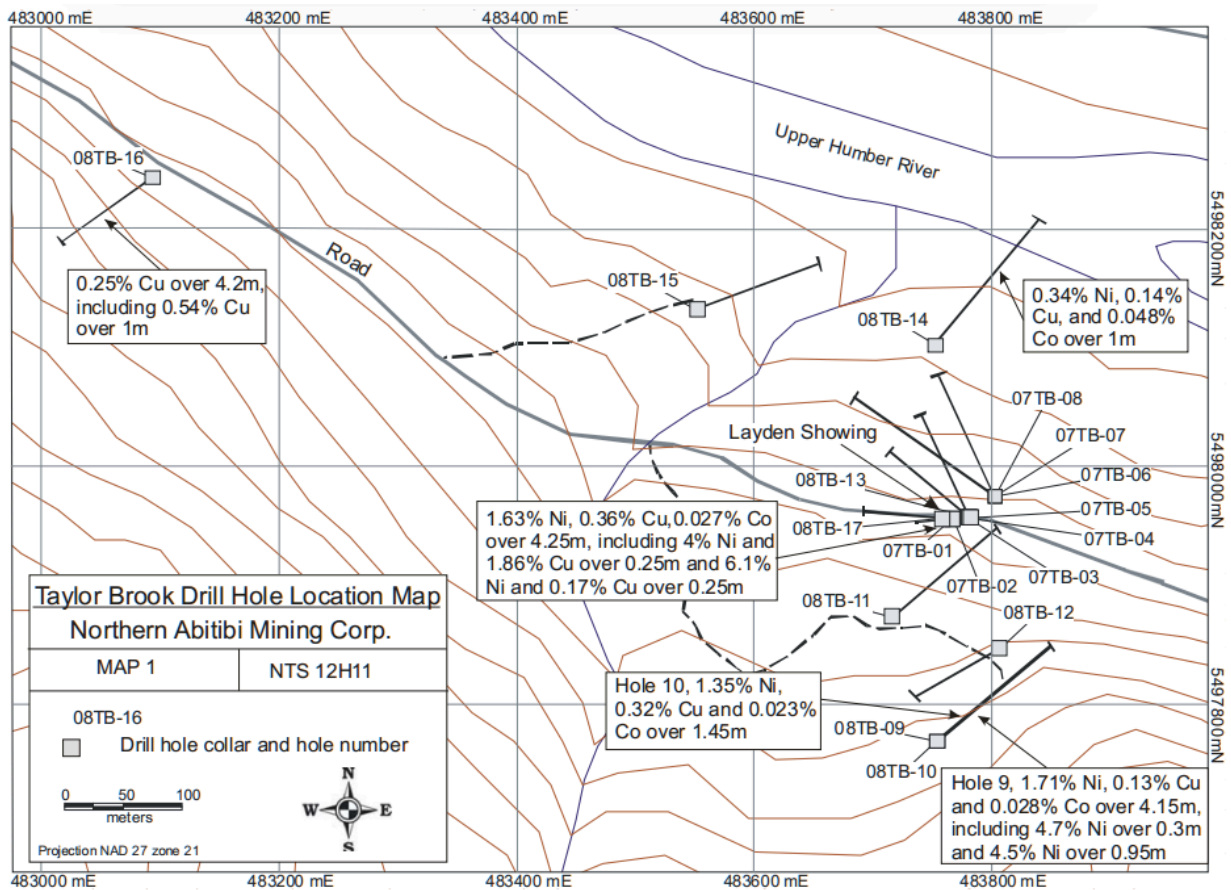


Figure 2.6: Taylor Brook drill hole location map (Ebert, 2008).

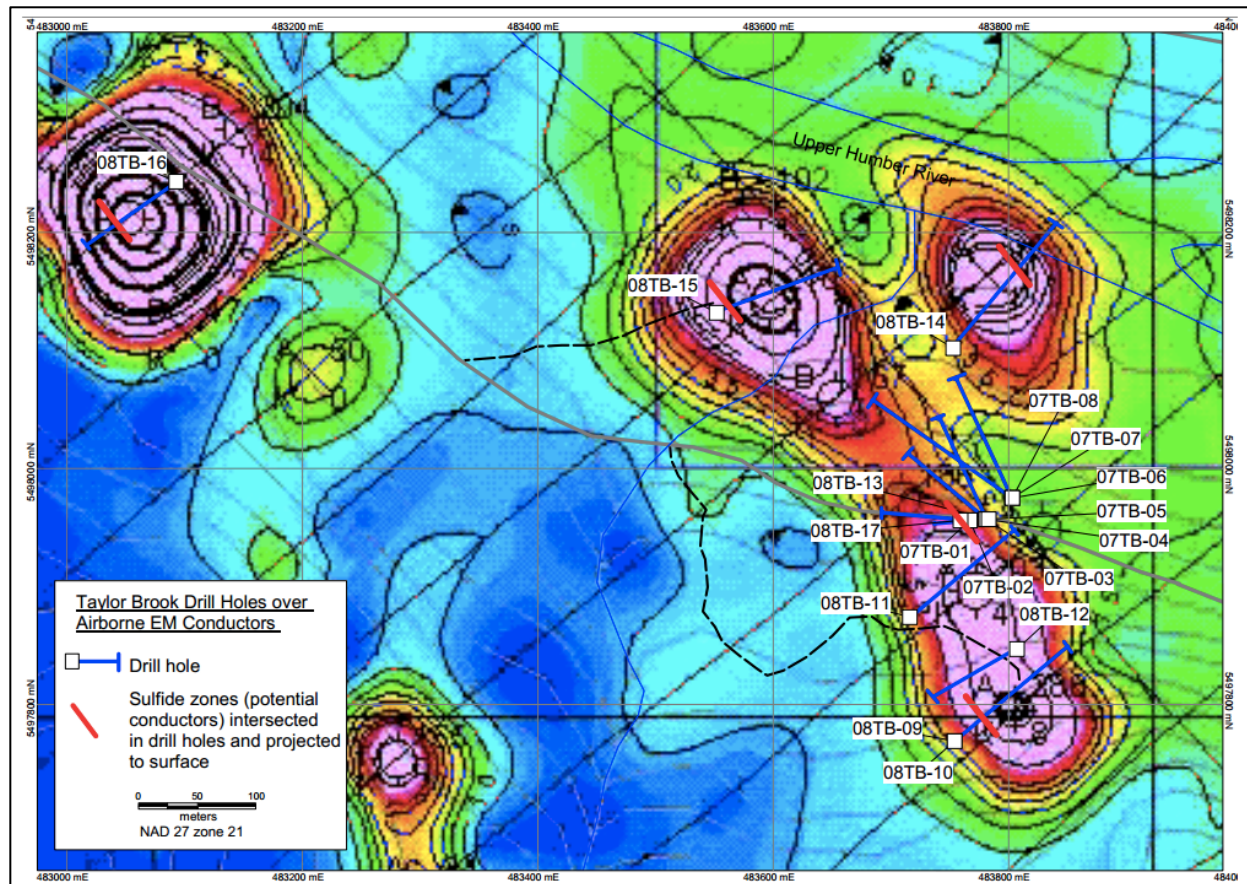


Figure 2. 7: The z-component of secondary magnetic field (dB/dt) responses from the AeroTEM-II system, and the locations of the drill holes, in the part of the survey area with the conductors (Ebert, 2008).

Eleven samples that were taken by Altius from the Layden showing averaged 5.38% Ni, 1.05% Cu, 0.10% Co, 112 ppb Pt, 232 ppb Pd and 416 ppb Au. A 125-metre-long by up to 90-metre-wide body of metabasite occurs 40 metres north of the Layden showing. This body includes a zone of disseminated to semi-massive sulfides 15 metres wide and up to 50 metres long along its southern margin. This sulfide-bearing zone includes nickel values up to 0.15% and copper values up to 0.47%.

The boreholes 08TB-09 and 10 (Figure 2.8) intersected a mineralized sulfide zone largely hosted in felsic gneiss but closely associated with thin zones of metabasite. Hole 08TB-09 intersected 1.71% nickel, 0.13% copper, and 0.028% cobalt over a core length of 4.15 metres, from

42 to 46.15 metres depth in the hole. Within this interval are two massive sulfide zones containing 4.5% nickel, 0.16% copper, and 0.073% cobalt over a core length of 0.95 metres, and 4.7% nickel, 0.17% copper, and 0.071% cobalt over a core length of 0.3 metres. The true width of the sulfide zone is interpreted to be approximately 70% of the drill core intercept. Hole 08TB-10 hit a less developed sulfide zone with similar mineralogy and textures as that in 08TB-09, approximately 60 metres deeper (vertically). Hole 08TB-10 returned 1.35% Ni, 0.32% Cu, and 0.023% Co over a core length of 1.45 metres from 95.95 to 97.4 metres depth in the hole. The sulfide zone in hole 08TB-10 was intersected at a low angle to the core axis (10 to 30 degrees to core axis) and has an interpreted true width of about 0.7 metres (Ebert, 2008).

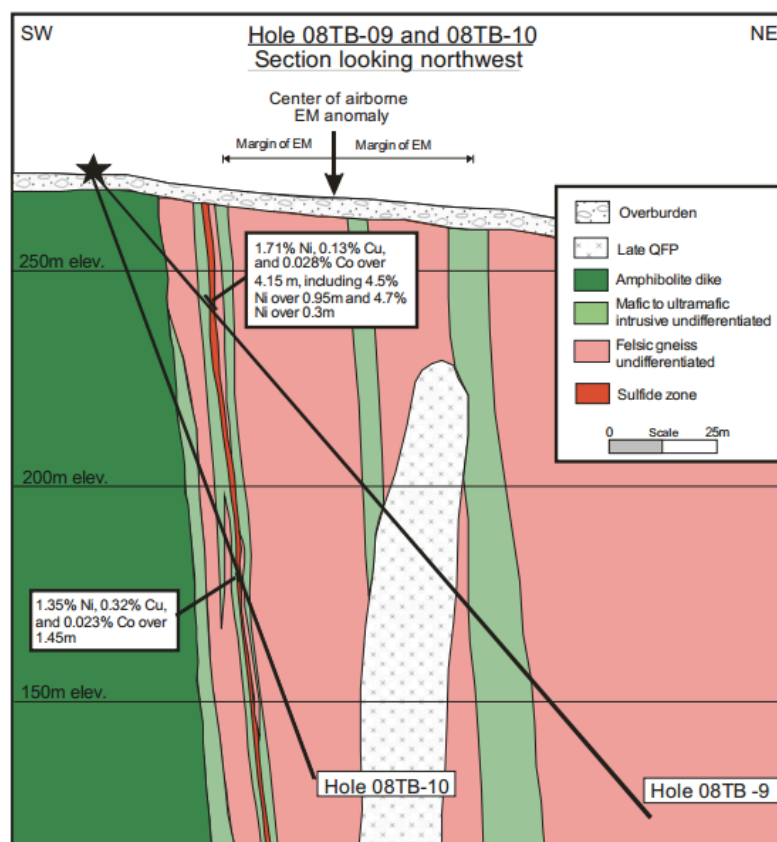


Figure 2.8: A cross section showing holes 08TB-09 and 10 and the centre of the airborne EM anomaly (Ebert,2008).

As shown in Figure 2.9, Hole 08TB-17 is a short vertical hole that directly tested the Layden showing. The hole intersected 3.5 metres of metabasite before passing into felsic gneiss. The metabasite is well mineralized with small semi-massive sulfide zones developed on the upper and lower contacts of the metabasite and felsic gneiss, and with disseminated sulfides occurring throughout the metabasite itself. The metabasite at the Layden showing is thought to be a rod or dike surrounded by felsic gneiss. A zone from 0 to 4.25 metres depth in hole 08TB-17 averages 1.63% Ni, 0.36% Cu, and 0.027% Co. Included within this zone is 0.25 metres with 4.0% Ni, 1.86% Cu, and 0.051% Co, and another 0.25 metres with 6.1% Ni, 0.17% Cu, and 0.111% Co (Ebert, 2008).

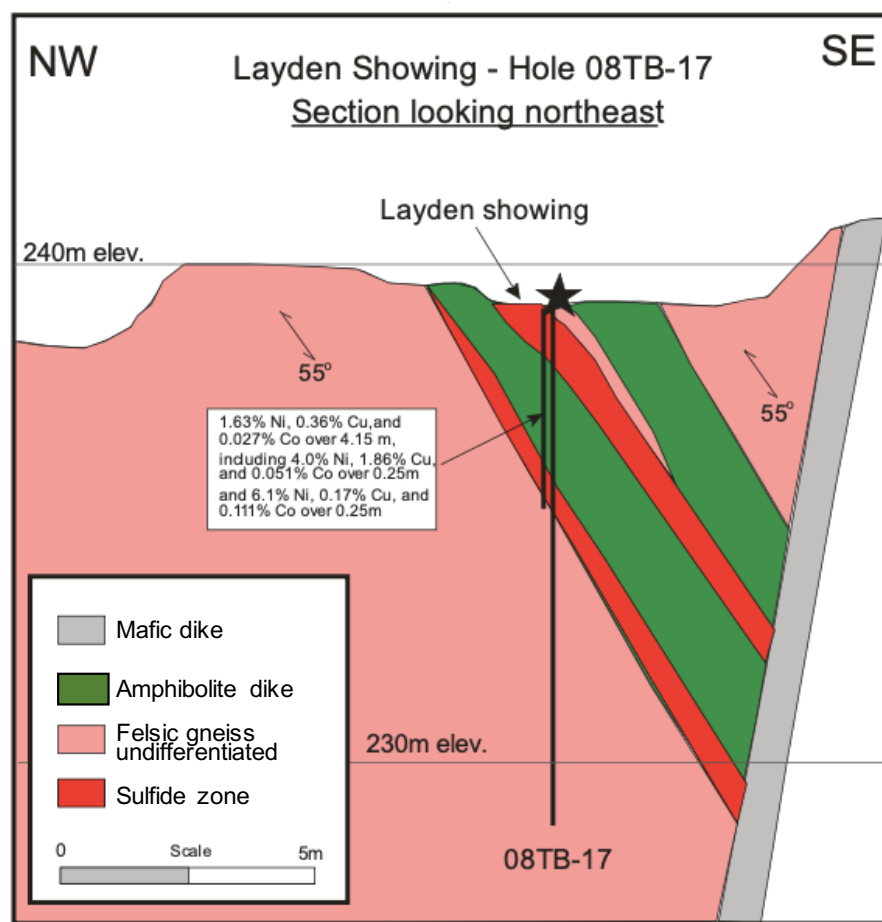


Figure 2.9: A cross-section showing drill hole 08TB-17 at the Layden showing (Ebert,2008).

2.3 Geophysical Surveys

A VLF-EM and magnetometer (Omni Plus Mag/VLF-EM system) survey has also been applied to the area. A small grid was created over the Layden showing in the local UTM coordinate system with a 5 km baseline, which was orientated North-South. The VLF-EM responses and total magnetic intensity were measured every 12.5 metres. The Fraser-filtered VLF-EM data shows no obvious response for interpretation about the survey area. (Figure 2.10). Fraser filter is applied to a dataset to make it smooth, and to obtain maximum values over the conductor from it for contouring (Fraser, 1969). A VLF-EM total-field anomaly roughly coincides with a strong magnetic response in this area. Another strong magnetic anomaly is measured roughly 50 metres to the north of the Layden showing (Figure 2.11), 100 metres wide by 150 metres long. However, no explanation for this anomaly has been proposed (Fitzpatrick et al., 2000).

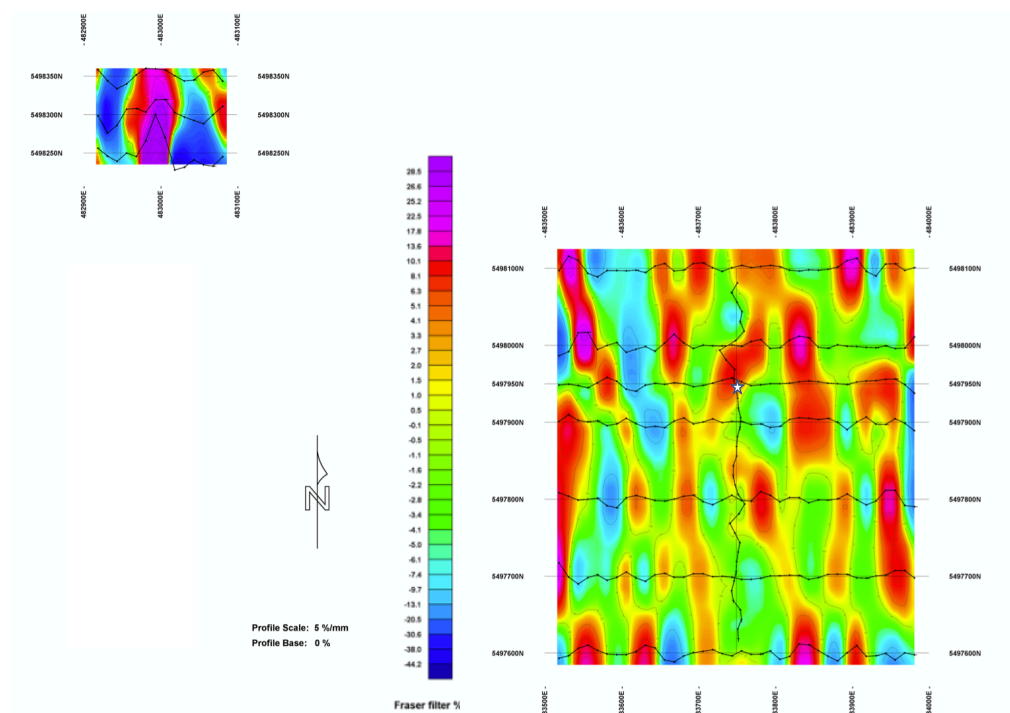


Figure 2.10: In-phase Fraser-filtered profiles of the VLF-EM data (the black lines) and colored images for the Layden showing area (right bottom) and an area to the northwest of the Layden

showing (top left). The white star represents the location of the Layden showing (Fitzpatrick, 2000). The black dots on the black lines are the observation points.

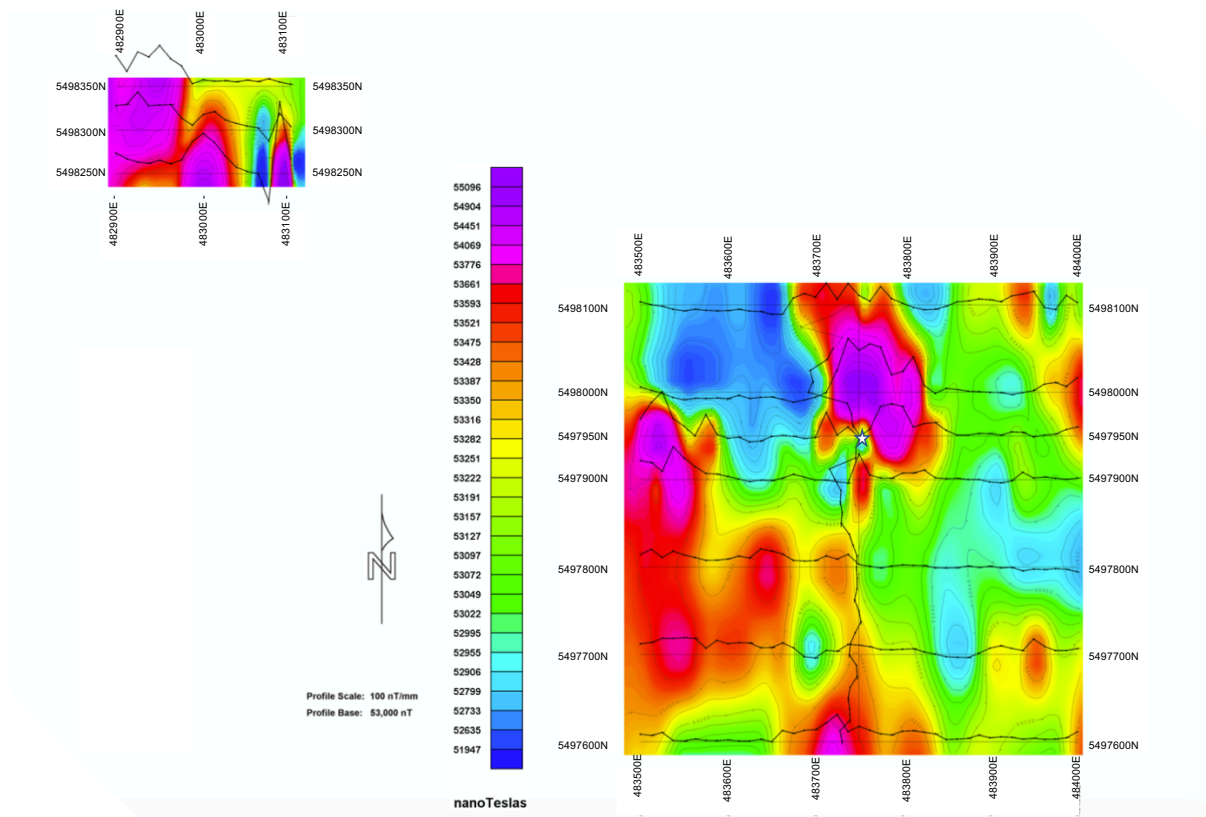


Figure 2.11: Total magnetic intensity (TMI) profiles (the black lines) and colored image for the Layden showing area (right bottom) and another area to the northwest of the Layden showing (top left). The white star represents the location of the Layden showing (Fitzpatrick, 2000).

The regional geological survey indicated that lithologies throughout the survey area are expected to be resistive (generally gneiss). However, in some parts of the survey area, minor existence of sulphide in otherwise resistive structures results in what are expected to be conductive features. The high-grade nickel mineralization at the Layden showing, for instance, is hosted in a mafic unit (Fitzpatrick, 2000). From Figure 2.12, it can be seen that the target mineralization (sulphides) occurring in the survey area would be highly conductive (between 1 S/m and 100 S/m) whereas the surrounding rock (generally gneiss) would be very resistive (roughly 10000 Ω m).

Therefore, application of airborne TEM survey methods should be beneficial for detecting the sulphide zones in these resistive structures.

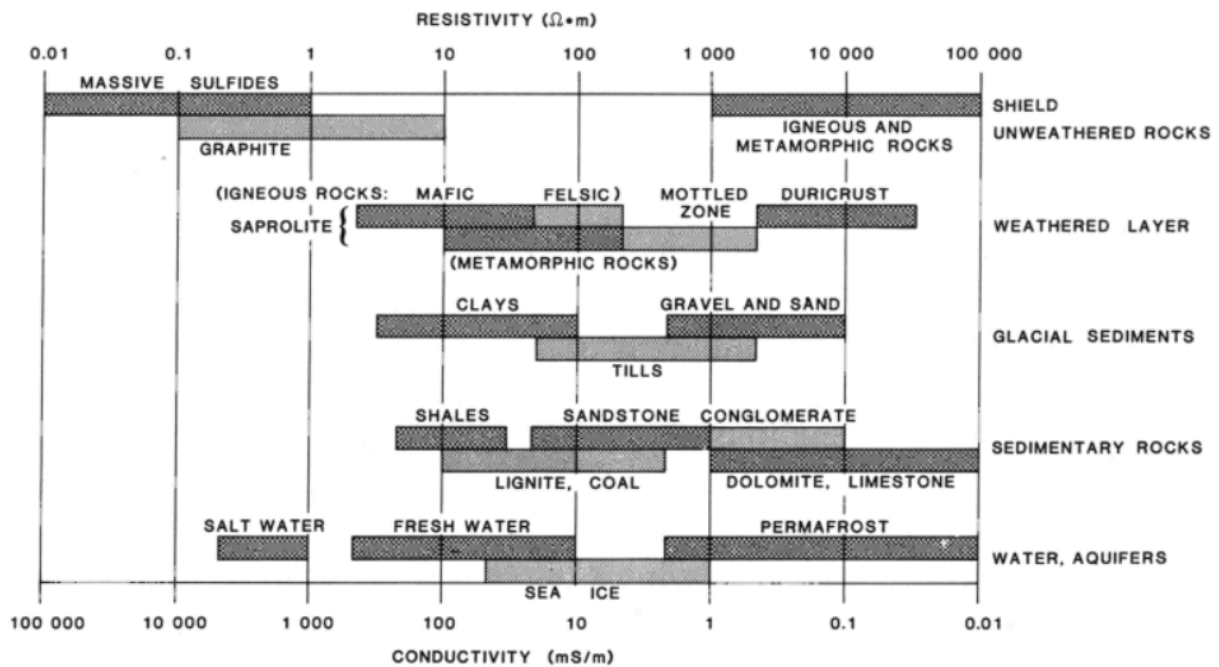


Figure 2.12: Typical ranges of conductivities/resistivities of materials (Palacky, 1988).

Chapter 3

3. The Airborne Time-Domain Electromagnetic Method

3.1 Introduction

Airborne electromagnetics (AEM) is one of the most popular geophysical methods used in mineral exploration and for surveying shallow crust. These systems are separated into two different groups, namely time-domain and frequency-domain systems. In this chapter, some history and the theory of the airborne time-domain system are given.

The test flights of the Stanmac-McPhar fixed-wing airborne EM system in Canada in 1948 can be called the birth of this method of geophysical surveying. The discovery of the Heath Steel deposit in New Brunswick, Canada, in 1954 showed this method to be a reliable application for geophysical exploration, and prompted additional developments of AEM systems worldwide (Fountain, 1998). This was accompanied by expositions of the theory and principles of the method by various researchers (which were later summarized by Kaufman and Keller, 1983; Ward and Hoffman, 1988).

3.2 Background Theory of Electromagnetic Methods

Maxwell's Equations

The behaviour of electromagnetic fields in linear media is described by Maxwell's equations, which consist of four fundamental physical laws: Gauss's law, Gauss's law for magnetism, Faraday's law, and Ampère's law. The time-domain Maxwell's equations can be written in differential form as (Ward and Hohmann, 1988)

$$\nabla \times \mathbf{e} = -\frac{\partial \mathbf{b}}{\partial t}, \quad (3.1)$$

$$\nabla \times \mathbf{h} = \mathbf{j} + \frac{\partial \mathbf{d}}{\partial t}, \quad (3.2)$$

$$\nabla \cdot \mathbf{b} = 0, \quad (3.3)$$

$$\nabla \cdot \mathbf{d} = q, \quad (3.4)$$

where \mathbf{e} is electric field intensity (V/m), \mathbf{h} is the magnetic field intensity (A/m), \mathbf{j} is the current density (A/m²), \mathbf{d} is the electric displacement vector (C/m²), \mathbf{b} is magnetic flux density (Wb/m²), and q is the free charge density (C/m³). The relationships between \mathbf{e} , \mathbf{h} , \mathbf{d} and \mathbf{b} for linear media are given by the constitutive relations

$$\mathbf{b} = \mu_0 \mathbf{h}, \quad (3.5)$$

$$\mathbf{d} = \epsilon_0 \mathbf{e}, \quad (3.6)$$

$$\mathbf{j} = \sigma \mathbf{e}, \quad (3.7)$$

where μ_0 is the magnetic permeability of free space (H/m), ϵ_0 is the electric permittivity of free space (F/m), and σ (S/m) is the electrical conductivity. Equation 3.7 is Ohm's law.

Equations 3.1 and 3.2 can be re-written using equations 3.5, 3.6, 3.7 as:

$$\nabla \times \mathbf{e} = -\mu_0 \frac{\partial \mathbf{h}}{\partial t}, \quad (3.8)$$

$$\nabla \times \mathbf{h} = \sigma \mathbf{e} + \epsilon_0 \frac{\partial \mathbf{e}}{\partial t}. \quad (3.9)$$

With the assumption that magnetic permeability does not vary with position, taking the curl of both sides of equation 3.8 and then substituting equation 3.9 gives:

$$\nabla \times \nabla \times \mathbf{e} = -\mu_0 \frac{\partial}{\partial t} (\nabla \times \mathbf{h}) = -\mu_0 \sigma \frac{\partial \mathbf{e}}{\partial t} - \epsilon_0 \mu_0 \frac{\partial^2 \mathbf{e}}{\partial t^2}. \quad (3.10)$$

Time variations of EM fields used in geophysical surveys are relatively slow (frequencies $< 10^5$ Hz) and frequencies higher than 10^5 Hz are negligible in the time-domain method. This means that the quasi-static approximation holds and hence the part of equation 3.10 including the electric permittivity (ϵ_0) can be neglected (Spies and Frischknecht, 1991), giving:

$$\nabla \times \nabla \times \mathbf{e} = -\mu \sigma \frac{\partial \mathbf{e}}{\partial t}. \quad (3.11)$$

Equation 3.11 is essentially a diffusion equation since it has only a first-order derivative with respect to time, as opposed to equation 3.10, which describes both wave behaviour and damping.

The diffusion equation is the equation that is relevant to geophysical EM methods.

3.3 The Measured Data of ATEM

The primary magnetic field in the ATEM method is created by sending a current through a transmitter loop as shown Figure 3.1. The primary magnetic field decreases rapidly as the current is switched off (Ampere's law). This time-varying primary magnetic field induces an electric field in the subsurface (Faraday's law), which result in currents (eddy currents) in the ground (Ohm's law), and these induced currents create a secondary magnetic field (Palacky and West, 1973), a consequence of Ampere's law.

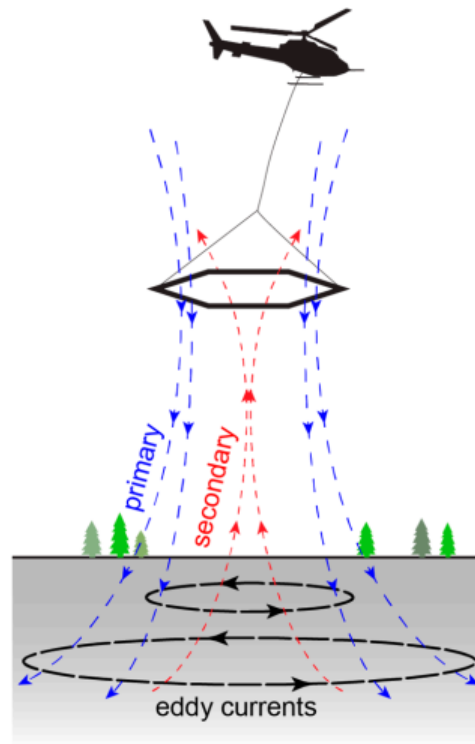


Figure 3.1: The principles of airborne transient electromagnetic surveying (Korus, 2018).

This process is repeatedly applied by switching on and off the transmitter current. Figure 3.2 shows the EM bird of the AeroTEM-II system that was used for data acquisition in the Taylor Brook survey area. The entire system, called a sling load, is carried by the helicopter.



Figure 3.2: The AeroTEM-II EM bird. The large outer horizontal white ring is the transmitter whereas the red circle in the centre of the transmitter shows the receiver. The arrow at the right-hand side of the figure shows the second caesium magnetometer sensor (Churchill, 2007).

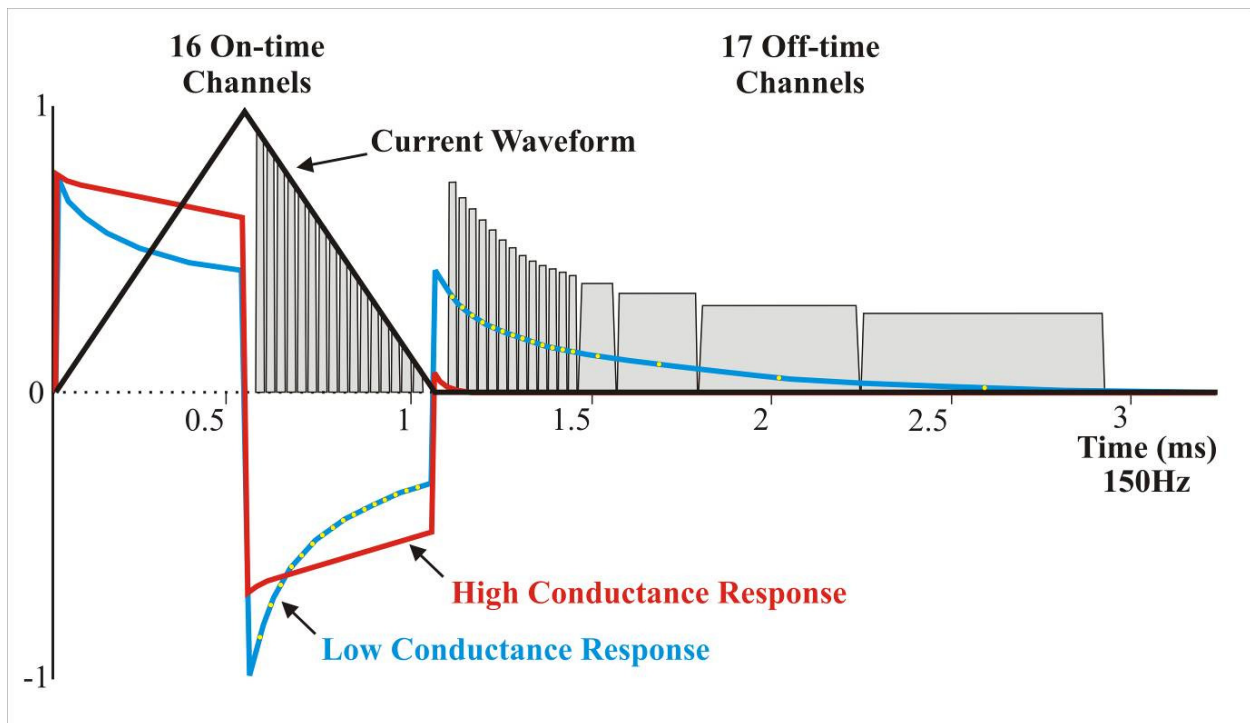


Figure 3.3: Schematic of the transmitter waveform and typical receiver responses of the AeroTEM system (Churchill, 2007).

The time-decay of the secondary magnetic field, or its time derivative, is measured by averaging over windows/gates/channels (Figure 3.3). The widths of the gates (grey boxes in Figure 3.3) increase logarithmically in order to improve the signal-to-noise ratio (S/N), especially for the late-time data as illustrated in Figure 3.4. This is necessary because the secondary magnetic field gets weaker at late-times and is easily swamped by noise. This recording type is called log-gating, and 8-10 gates for each decade in decay time are generally used (Christiansen, et. al., 2006).

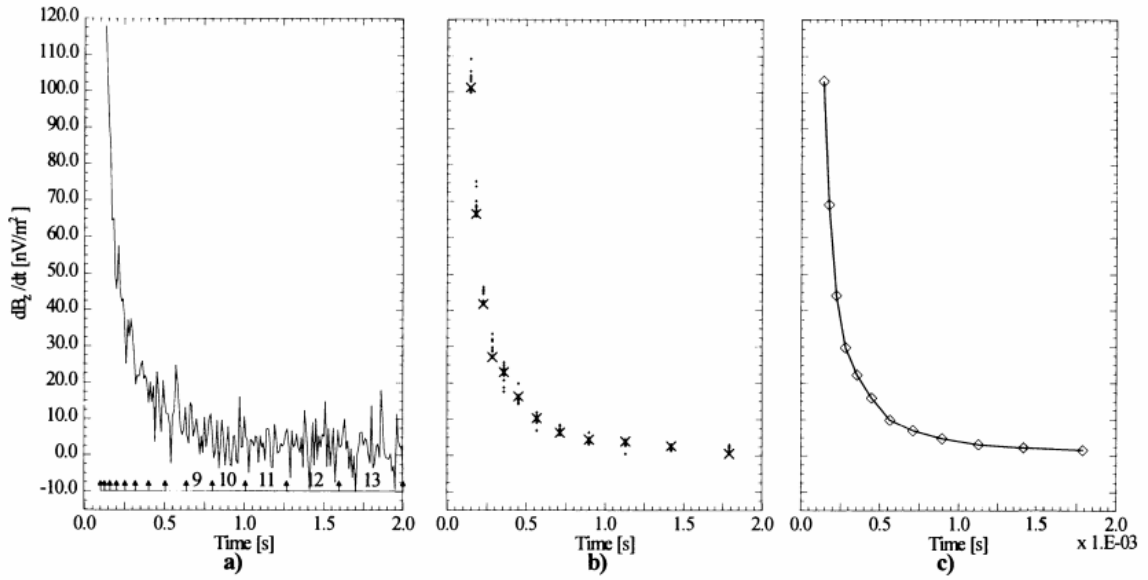


Figure 3.4: a) A generated noisy response over a 2-layered earth model. Logarithmically increasing time windows are created and displayed at the bottom of the plot. b) The decay curve of log-gated data in figure a) are marked as a “x”. c) The stacked response of the ten log-gated responses from b). “◇” represents the data points (Munkholm and Auken, 1996).

Spies and Frischknecht (1991) have shown that the vertical component (z-component) of the secondary magnetic field and its time derivate generated on a homogenous half space of resistivity, ρ , excited by a dipole source and measured by a coincident receiver are given by

$$h_z = \frac{Ipt}{\mu_0 a^3} \left[\left(\frac{1}{2\tau} - 3 \right) \text{erf} \left(\frac{1}{2\sqrt{\tau}} \right) + \frac{3}{\sqrt{\pi\tau}} e^{-\frac{1}{4\tau}} \right], \quad (3.12)$$

and

$$\frac{\partial h_z}{\partial t} = -\frac{I\rho}{\mu_0 a^3} \left[3\text{erf}\left(\frac{1}{2\sqrt{\tau}}\right) - \frac{1}{\sqrt{\pi\tau}} \left(3 + \frac{1}{2\tau}\right) e^{-\frac{1}{4\tau}} \right], \quad (3.13)$$

where erf is the error function, and τ is a scaled time variable (Abramowitz and Stegun, 1965):

$$\tau = \frac{t\rho}{\mu_0 a^2}, \quad (3.14)$$

where a is the radius of the transmitter loop. The speed of decay of the secondary magnetic field as a function of time depends on the resistivity of the subsurface. This means that the less resistive the half-space we have, the larger the amplitude and the slower the rate of decay we get (see Figure 3.5).

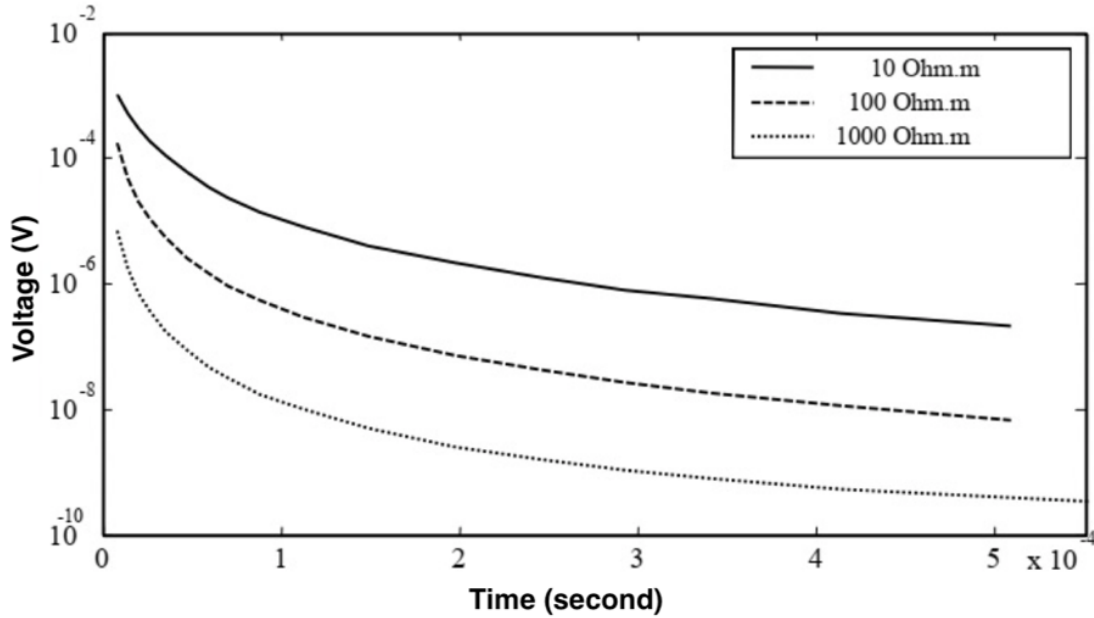


Figure 3.5: The variation of voltage measured at the receiver with respect to the resistivity of the homogeneous half-space (Turkoglu, 2003).

In the TEM method, it is not quite as easy to generate a single apparent resistivity curve as a function of proxy depth as it is for the DC resistivity method (Spies et. al, 1986). Figure 3.6 displays the curves of early time and late time apparent resistivities as being asymptotic to the true resistivity of the half-space. However, Kaufman and Keller (1983), Sheng (1986), and Denghai and Meju (2000) have derived single all-time apparent resistivities. The all-time apparent resistivity of Kaufman and Keller (1983) is:

$$\rho_a = \frac{\mu_0}{4\pi t} \left(\frac{2 I_0 a^2 \mu_0}{5t \frac{dB_z}{dt}} \right)^{2/3} . \quad (3.15)$$

The impulse response, dB/dt (proportional to dh_z/dt ; eq. 3.13) of the magnetic induction is presented in Figure 3.7a for various half-space resistivities. The response curves shown in Figure 3.7a are shown as ρ_a -converted curves in Figure 3.7b. It is important to note that oscillations of an apparent resistivity curve are not necessarily reflections of variations in geology and cannot be interpreted as such. For instance, over a layered earth, a ρ_a -curve always goes up before it goes down and vice versa (see the overshoot in Figure 3.7b at 2×10^{-5} s). Even keeping in mind that the apparent resistivity is not equal to the true resistivity for a layered earth, it does provide a valuable normalization of data with respect to source and the measuring configuration (Christiansen et. al., 2006).

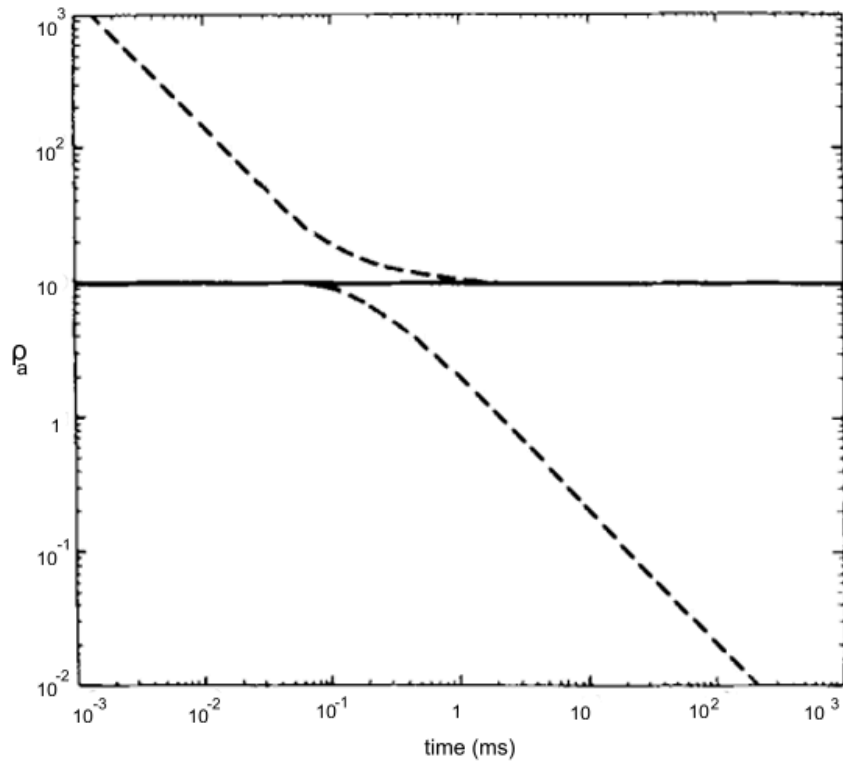


Figure 3.6: The apparent resistivity (y-axis) for the in-loop TEM configuration, which has the receiver located in the centre of the transmitter, for a $10 \, \Omega\text{m}$ homogeneous half-space. The solid line indicates the true resistivity and the dashed curves are the early-time and late-time asymptotic apparent resistivities (Spies et. al, 1986).

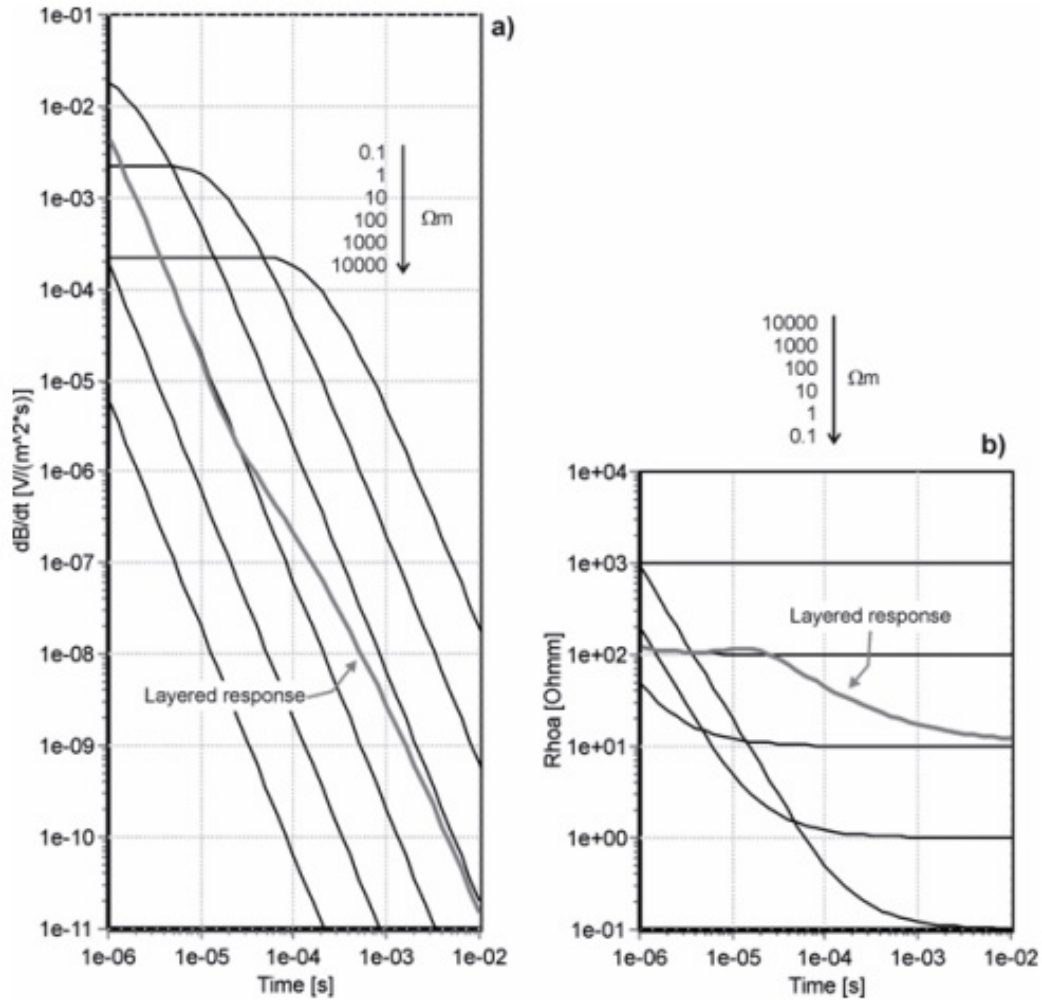


Figure 3.7: a) The responses ($\frac{dB}{dt}$) for a half-space with respect to varying resistivities of the homogeneous half-space (black lines). The late-time apparent resistivity curves (ρ_a) in b) are converted from the same curves. The grey line represents the response of a two-layer earth model with 100 Ωm in layer-1 and 10 Ωm in layer-2. Layer-1 is 40 m thick (Christiansen et. al., 2006).

However, the geological structure of the underground is not always horizontally layered. In the case of our project, where surveying is over localized conductors (mineralization), the response of the airborne time-domain method will be different. Typical EM anomalies are determined by the conductivity, size and shape of the deposit. Also, the dip of a localized conductor makes a difference in the response (see Figure 3.10). A thin target (see Figure 3.8) that is orientated

vertically produces a double-peak anomaly in the z-component response and a positive-to-negative crossover in the x-component response (Churchill, 2007).

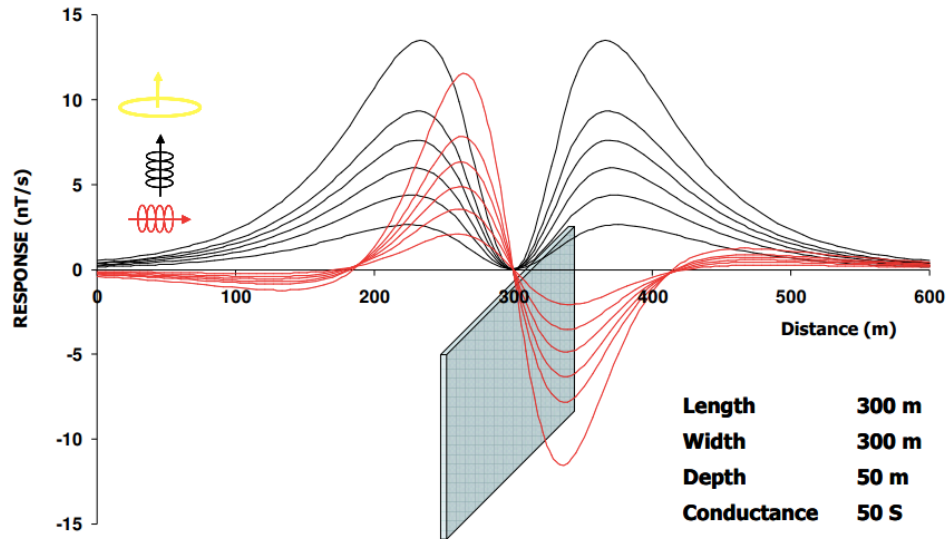


Figure 3.8: The response of AeroTEM to a 'thin' vertical conductor. The black lines represent the response of the z-component whereas the red lines indicate the response of the x-component (Churchill, 2007). The yellow loop on the top left represents the transmitter configuration.

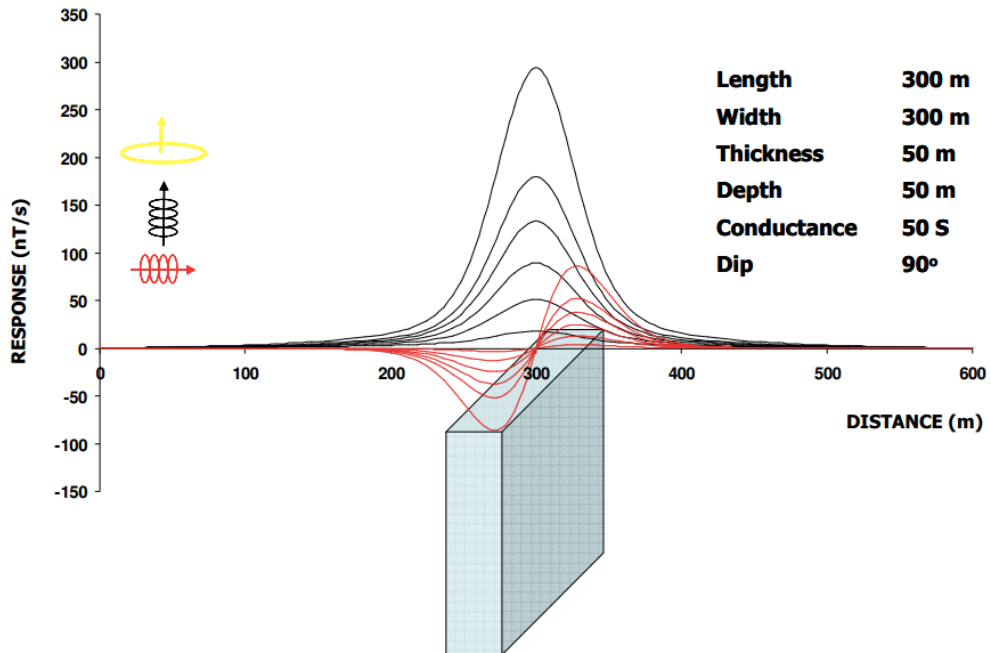


Figure 3.9: The response of AeroTEM to a 'thick' vertical conductor (Churchill, 2007).

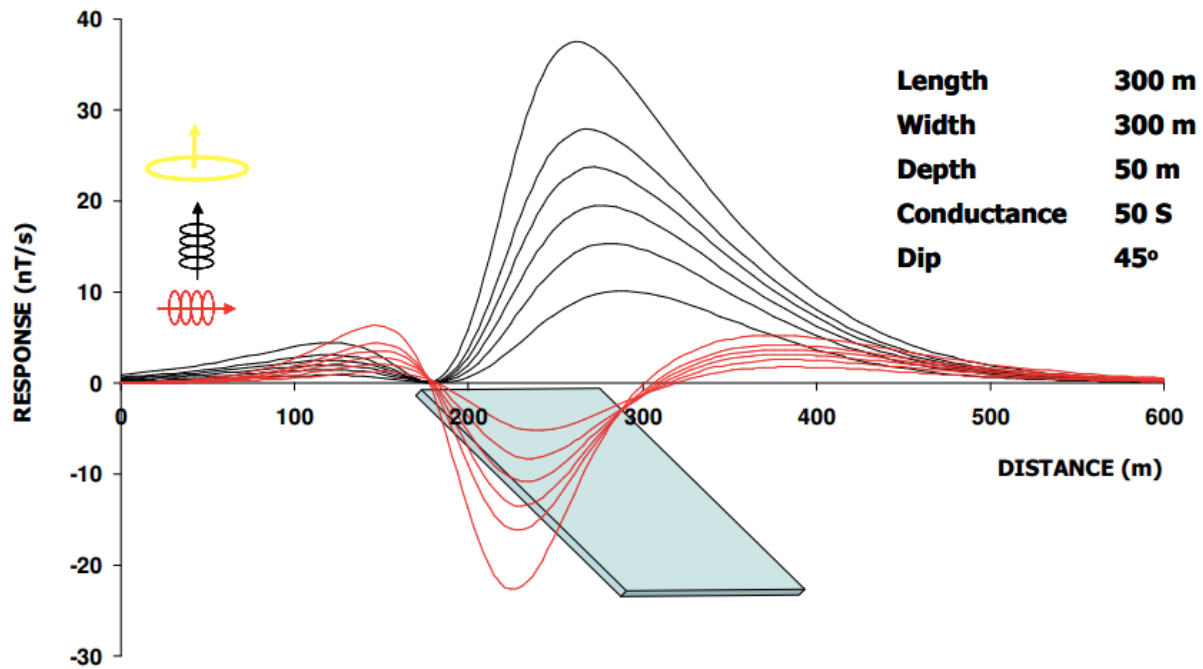


Figure 3.10: The response of AeroTEM to a 'thin' dipping conductor (Churchill, 2007).

For a vertically orientated thick conductor (say, with a thickness greater than 10 m), the response is a single peak in the z-component response and a negative-to-positive crossover in the x-component response (Figure 3.9). Where multiple, closely spaced conductors occur, or where the conductor has a shallow dip, it can be difficult to uniquely determine the type (thick vs. thin) of the target (Figure 3.10; Churchill, 2007).

3.4 The Taylor Brook AeroTEM Survey

The survey system used in the survey area is an Aeroquest AeroTEM-II time-domain towed-bird system. The AeroTEM transmitter dipole moment is 38.8 kAm^2 . The AeroTEM bird is towed 38 m below the helicopter. The waveform is triangular with a symmetric transmitter on-time pulse of 1.10 ms and a base frequency of 150 Hz (see Figure 3.3).

The survey was flown with a line spacing of 100 m, and the total length of all survey lines was equal to 148.2 km (Figure 3.11). The nominal EM bird terrain clearance was 30 m, and the nominal survey speed was 75 km/hr. The EM data were acquired as a data stream at a sampling rate of 38,400 samples per second and were processed by stacking to generate final windowed data at 10 samples per second. The 10 samples per second, at each observation, translates to a geophysical reading in 16 on-time channels and 17 different off-time channels about every 2-3 metres along the flight path.

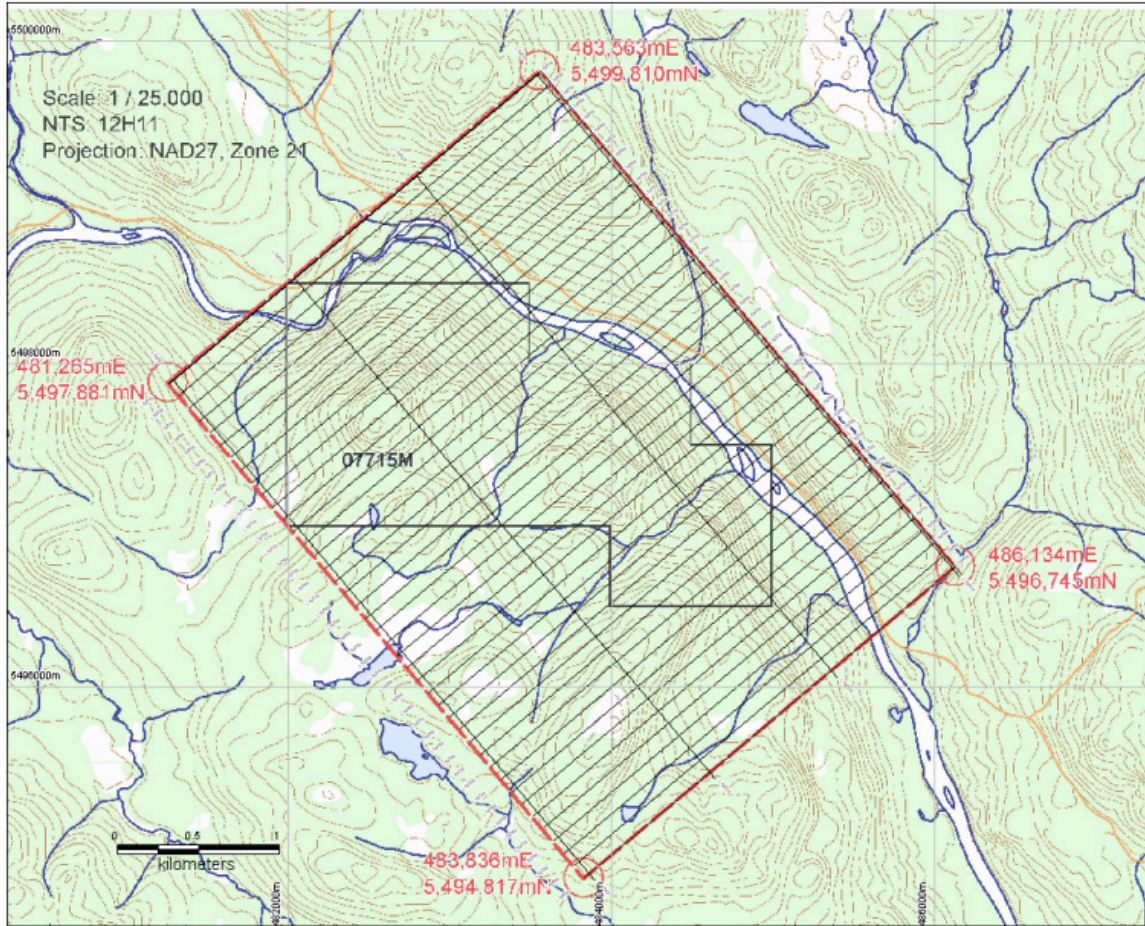


Figure 3.11: The survey block (the red solid lines) and flight paths for the Taylor Brook AeroTEM survey (Churchill, 2007).

Figure 3.12 shows the profiles of multiple channels of EM responses that were measured. Although this is a common way of representing TEM data over a survey area, the responses at each off-time channel can be mapped separately as shown in Figure 3.13 where the responses for the second off-time channel (Zoff1), where the first channel is called Zoff0, are plotted as a map. The pinkish-red areas in Figure 3.13 are where one should be focusing for detailed work (i.e., application of small-scale geophysical surveys and boreholes), and where conductive bodies might exist.

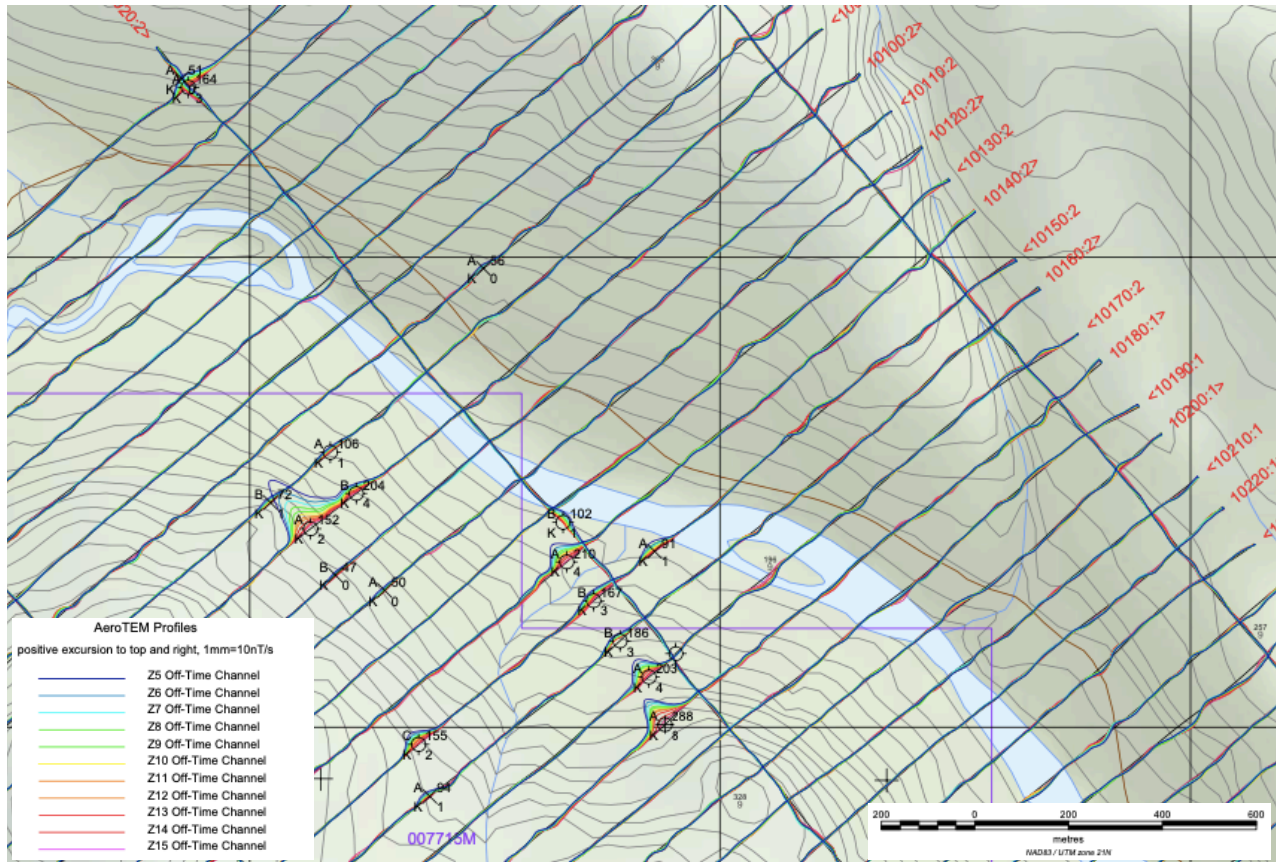


Figure 3.12: The off-time channel responses plotted as colour lines aligned along each profile, zoomed-in to the area around the Layden showing (Churchill, 2007).

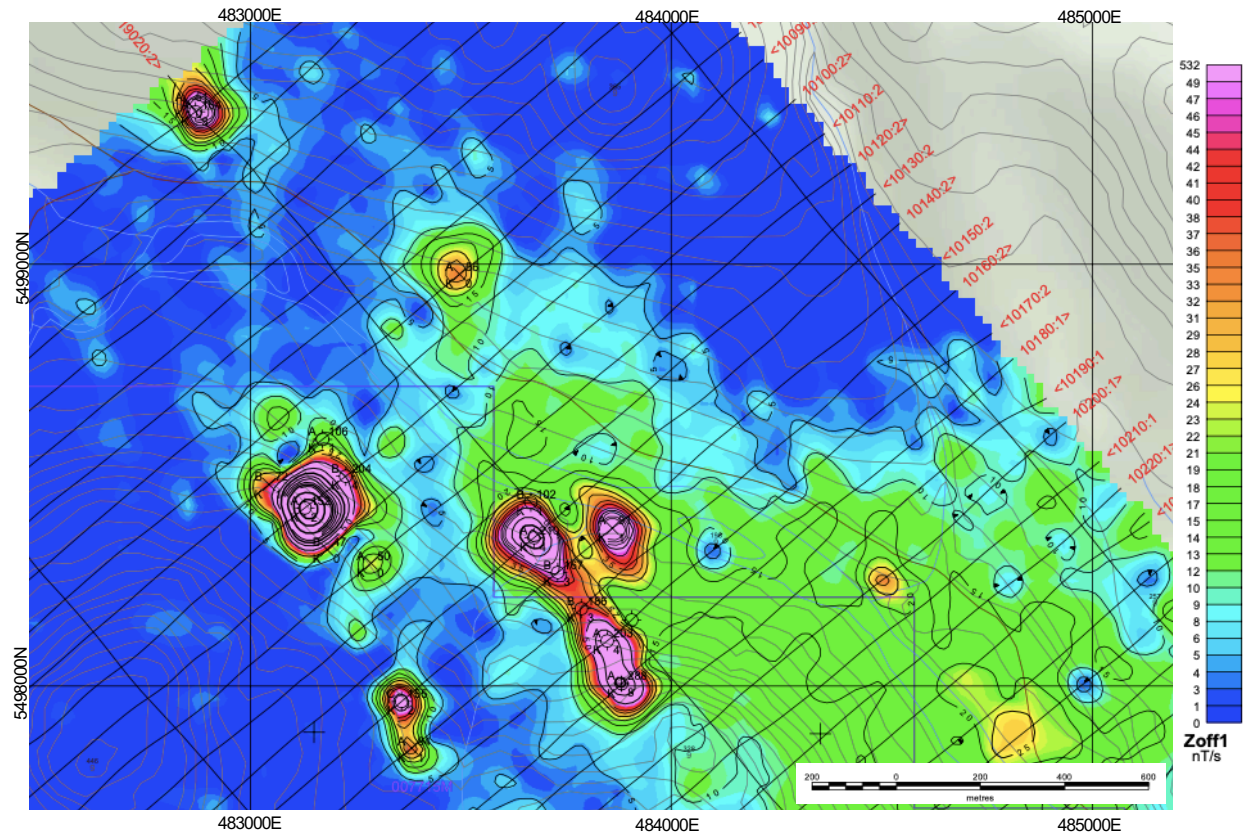


Figure 3.13: The contour map of the z-component off-time channel response ($Z_{off1}=1.1848$ ms) over the Layden showing in Taylor Brook area (Churchill, 2007).

In addition to the time-domain EM data, a magnetometer was carried by the helicopter that collected magnetic data while the EM responses were measured. As is well known, magnetic data are good at indicating regional trends in terms of rock units. By looking at Figure 3.14, it can be seen that the sulfide mineralization sits at a magnetic low in the survey area (the white rectangle). The reason for this might be because massive sulfide minerals typically do not have high magnetic susceptibilities even though they are conductive, or that there has been a loss of magnetism in the host geology caused by the mineralization process.

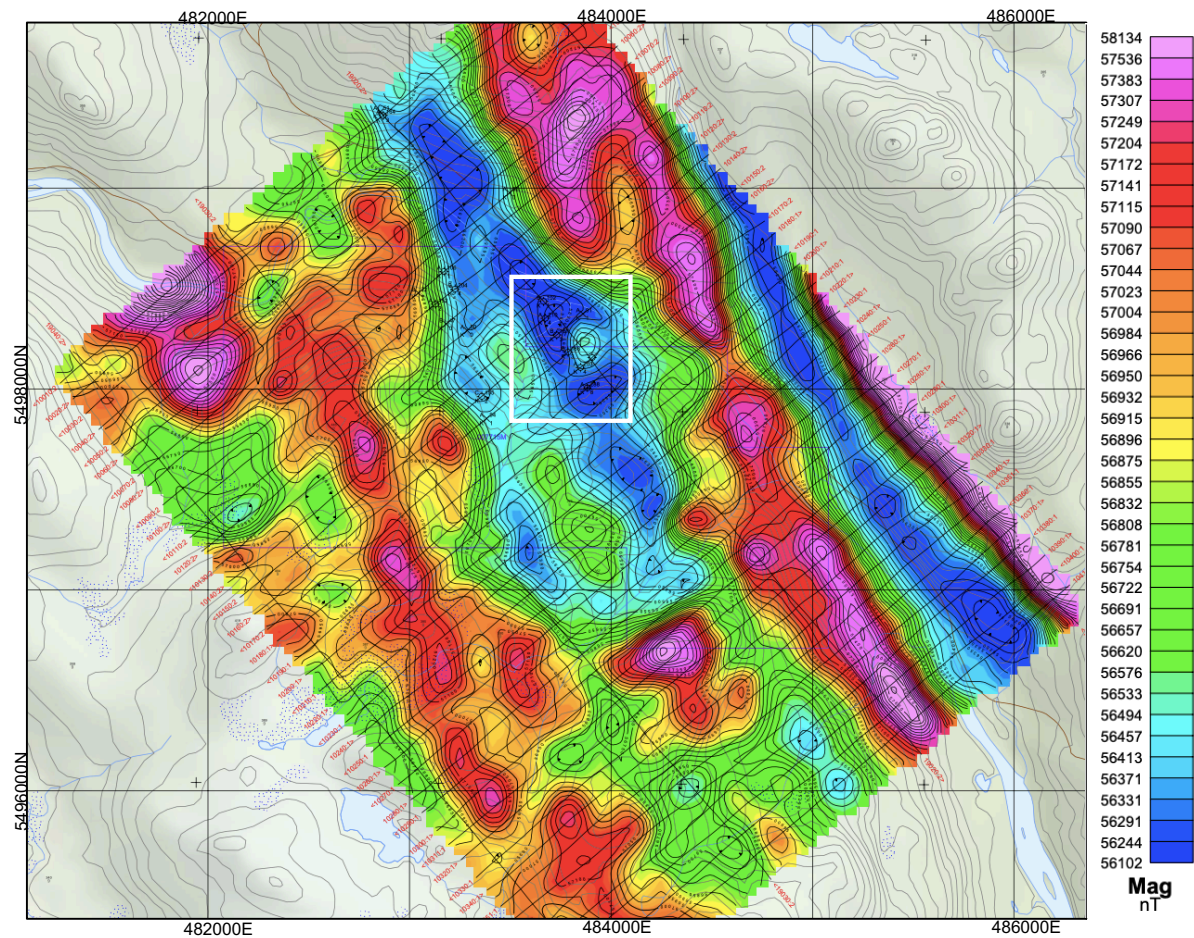


Figure 3.14: Total magnetic intensity (TMI) map of the Taylor Brook survey area (Churchill, 2007). The white rectangle represents the area of interest for the EM inversion and modeling undertaken later in this thesis.

Chapter 4

4. Inversion

4.1 Introduction to Inversion (and program “EM1DTM”)

Inversion in 1D, 2D, and 3D is applied to determine the subsurface model of a study area surveyed with the time-domain EM method as for other geophysical methods. However, the data of Airborne EM methods are generally interpreted using an approximate conductivity-depth transform or 1D inversion since the AEM surveys being done around the world measure thousands of line-kilometres of data every year, and the process of non-linear 3D inversion can be expensive computationally (Viezzoli et al., 2008).

There are two common interpretation approaches for Airborne TEM data: imaging and inversion. Furthermore, there are two different approaches to inversion: parametric inversion and underdetermined, minimum-structure inversion. In parametric inversion, an over-determined least-squares problem is solved to find layer properties (thicknesses and conductivities) that can reproduce the observed data. However, though it is an acceptable approach, a drawback for this method is that the results are dependent on the assumed number of layers (Farquharson et al., 1993).

1D inversion is applied to the AeroTEM data using a 1D inversion code called EM1DTM, which was developed by the University of British Columbia–Geophysical Inversion Facility (2005). EM1DTM uses an underdetermined, minimum-structure inversion method. An

undetermined inverse problem is solved because the number of layers in the Earth model (initial model) used in the code typically has more layers than in the true Earth. That is, rather than an initial model having a limited number of layers, we use a model having a large set of horizontal layers that have fixed thicknesses and uniform conductivities (see Figure 4.1; Farquharson and Oldenburg, 1993). The model corresponds to the spatial distribution of the physical property in the Earth, m , and is discretized as

$$m(\mathbf{r}) = \sum_{j=1}^N m_j \psi_j(\mathbf{r}), \quad (4.1)$$

where \mathbf{r} is the position vector and ψ_j are basis functions.

We would like to have a solution that is less affected by outliers in the data and other non-Gaussian noise, so that our solution is more robust than when we use the standard measure of data misfit (sum-of-squares). Also, we would like to be able to create models that are constant or blocky using a different measure of model structure (Farquharson and Oldenburg, 1998). The method used here is based on a linearized and iterative approach (e.g., Constable, 1987). At each iteration, the solution to the system of equations arising from the use of the non-standard measures is obtained using an iteratively reweighted least-squares method.

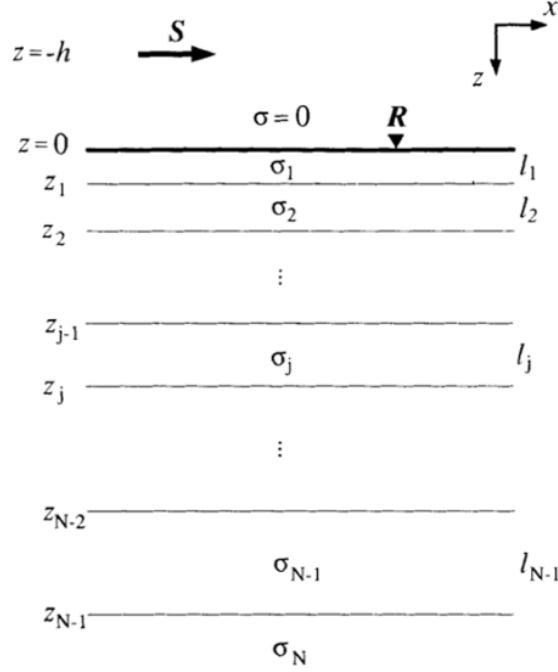


Figure 4.1: The Earth model settings used in the program EM1DTM. Z_j is the depth to the bottom of the j th layer, σ_j and l_j are the conductivity and thickness of the j th layer, respectively. S is the source, and h is the height of the source above the surface. R is the location of an observation point (Farquharson and Oldenburg, 1993).

Many functions can be used for obtaining a measure of the size of a vector, where the elements of the vector correspond to the misfit between predicted and observed data, or the parameters representing the model. Consider a vector \mathbf{x} and its elements x_j , $j = 1, \dots, N$. A general measure of its size is given by:

$$\phi(\mathbf{x}) = \sum_{j=1}^N \rho(x_j). \quad (4.2)$$

When $\rho(\mathbf{x}) = x^2$ this expression gives the l_2 norm of the vector, which is typically sum-of-squares:

$$\|\mathbf{x}\|_2^2 = \sum_{j=1}^N x_j^2. \quad (4.3)$$

Equation 4.2 also allows for the more general l_p norm:

$$\|\mathbf{x}\|_p^p = \sum_{j=1}^N |x_j|^p, \quad (4.4)$$

where $1 \leq p < \infty$. Other measures are the so called M-estimator of Huber (1964) and a measure given by Eklblom (1973, 1987). The first of these is equivalent to

$$\rho(x) = \begin{cases} x^2 & |x| \leq c, \\ 2c|x| - c^2 & |x| > c, \end{cases} \quad (4.5)$$

where c is a positive constant, which splits the elements of the vector \mathbf{x} into two parts that are considered small and large, with the l_2 norm applied to the small values and an l_1 -type measure applied to the large values.

The measure of Eklblom (1973, 1987) is

$$\rho(x) = (x^2 + \varepsilon^2)^{p/2}, \quad (4.6)$$

where ε is any positive number, provides something that is useful from a numerical point of view, and avoids something that is bothersome with the l_p norm. This measure reduces to the l_p norm with $p=1$ (Eq. 4.4) as ε gets small, and acts as a scaled sum-of-squares measure when ε is a larger number. This can be shown by expanding Eq. 4.6 as the first terms in its infinite series, which is valid for large values of ε (Eklblom,1973):

$$\rho(x) = \varepsilon^p \left[1 + \frac{p}{2} \frac{x^2}{\varepsilon^2} + O \frac{x^4}{\varepsilon^3} \right]. \quad (4.7)$$

Forward modeling is a way of computing predicted data for a model, which can be expressed as

$$\mathbf{d}^{prd} = \mathbf{G}(\mathbf{m}), \quad (4.8)$$

where the parameters of the model are $\mathbf{m} = (m_1, \dots, m_N)^T$, \mathbf{d}^{prd} is the set of predicted data for this model, and \mathbf{G} is the forward-modeling operator. The solution of the inverse problem consists

of finding a model that can reproduce the observations within an acceptable level of data misfit. Therefore, an objective function is designed whose minimum will give the solution to the inverse problem:

$$\Phi = \alpha_s \phi_s(\mathbf{W}_s(\mathbf{m} - \mathbf{m}^{ref})) + \alpha_x \phi_x(\mathbf{W}_x \mathbf{m}) + \beta [\phi_d(\mathbf{W}_d(\mathbf{d}^{prd} - \mathbf{d}^{obs})) - \phi_d^{tar}], \quad (4.9)$$

where ϕ_s provides a measure of how close the constructed model, \mathbf{m} , is to the reference model, \mathbf{m}^{ref} , and ϕ_x and ϕ_d provide, respectively, measures of the amount of structure in the model and the misfit between the predicted data (\mathbf{d}^{prd}) and the observed data (\mathbf{d}^{obs}). The desired data misfit, ϕ_d^{tar} , is appropriate for the amount of noise in the observations. Also, α_s , α_x and β are dependent constant values that are used to obtain a certain symmetry to the objective function.

\mathbf{W}_s , \mathbf{W}_x , \mathbf{W}_d are weighting matrices:

$$\mathbf{W}_x = \begin{bmatrix} 0 & & & & \\ -1 & 1 & & 0 & \\ & -1 & 1 & & \\ & & \cdots & & \\ & 0 & & -1 & 1 \end{bmatrix}, \quad (4.10)$$

\mathbf{W}_s is the identity matrix, and \mathbf{W}_d is the data-weighting matrix, which is diagonal under the assumption that the noise in the observations is not correlated between observations.

The final linear system inversion equations to be solved at each iteration obtained by minimizing the objective function, Φ , is:

$$[\alpha_s \mathbf{W}_s^T \mathbf{R}_s \mathbf{W}_s + \alpha_x \mathbf{W}_x^T \mathbf{R}_x \mathbf{W}_x + \beta \mathbf{J}^T \mathbf{W}_d^T \mathbf{R}_d \mathbf{W}_d] \mathbf{m} = \beta \mathbf{J}^T \mathbf{W}_d^T \mathbf{R}_d \mathbf{W}_d \mathbf{d}^{obs} + \alpha_s \mathbf{W}_s^T \mathbf{R}_s \mathbf{W}_s \mathbf{m}^{ref}, \quad (4.11)$$

where \mathbf{J} is the Jacobian matrix containing the partial derivatives of the calculated data with respect to the model parameters, \mathbf{J}^T is the transpose of the \mathbf{J} matrix, and \mathbf{R}_x , \mathbf{R}_s , \mathbf{R}_d are diagonal matrices

resulting from the iteratively reweighted least squares solution for non- l_2 measures. By applying an iterative process, therefore, the inverse problem can be solved:

$$\mathbf{m}^{k+1} = \mathbf{M}_k^{-1} \mathbf{y}^k \quad (4.12)$$

where, from Eq. 4.11, \mathbf{M}_k equals:

$$\mathbf{M}_k = [\alpha_s \mathbf{W}_s^T \mathbf{R}_s^k \mathbf{W}_s + \alpha_x \mathbf{W}_x^T \mathbf{R}_x^k \mathbf{W}_x + \beta \mathbf{J}^T \mathbf{W}_d^T \mathbf{R}_d^k \mathbf{W}_d] \quad (4.13)$$

and

$$\mathbf{y}^k = \beta \mathbf{J}^T \mathbf{W}_d^T \mathbf{R}_d^k \mathbf{W}_d \mathbf{d}^{obs} + \alpha_s \mathbf{W}_s^T \mathbf{R}_s^k \mathbf{W}_s \mathbf{m}^{ref} \quad (4.14)$$

where $\mathbf{R}_s^k = \mathbf{R}_s(\mathbf{m}^k)$. To start this procedure, \mathbf{m}^1 , which is the starting model, is a homogeneous half-space of some guessed-at value of conductivity with $\mathbf{R}_s = \mathbf{R}_x = \mathbf{R}_d = \mathbf{I}$, where \mathbf{I} is the identity matrix. Then, at every iteration, these matrices, and the Jacobian matrix, are re-calculated and the system of equations (4.12-4.14) solved to give the new model. This iterative process stops when the model does not change by a significant amount between iterations (Farquharson and Oldenburg, 1998).

The theory described above is the methodology used by the program EM1DTM, which is used for 1D inversion in this thesis. The l_1 -type measure ($p=1$ in Eq. 4.4) is used for the measure of model structure, and the approach used in this thesis is to use a prescribed, constant value of the trade-off parameter throughout any one inversion since it is consistent; that is, it makes the 2D section (or 3D model) the most consistent-looking along a line (volume) with the minimum amount of artefacts. The data might be a little under-fit in some parts and over-fit in others, but it is

reasonable to accept this in order to get this consistency. The values that are used for the parameters of α_s and α_x are 0.001 and 1, respectively.

Figures from a study of Farquharson et al. (1993) are presented in which the program EM1DTM is used (see Figure 4.2 and 4.3). Basically, the program produces 1D conductivities of the subsurface (Figure 4.2b) by inverting the response of the time-domain EM method (Figure 4.2a). Figure 4.3 indicates that 1D inversion can give a satisfying result over 3D structures. The conductivity model obtained from the inversion of the data in Figure 4.3a are shown in Figures 4.3c. The application of the inversion in Figure 4.2 is applied to the data obtained by a ground-based TEM survey (i.e., Farquharson et al., 1993)

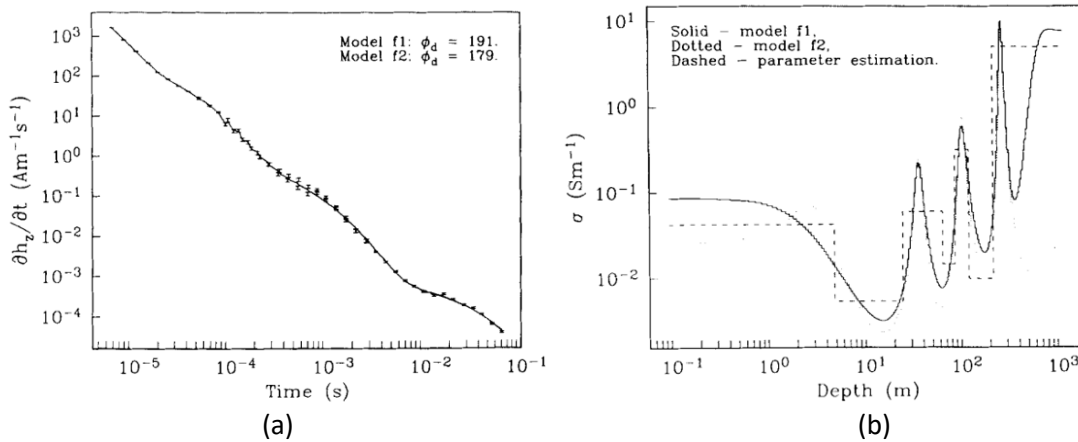


Figure 4.2: (a) TEM responses acquired with a 60x60m sized loop. The inversion models of the curves in panel (a) are shown in panel (b), which are two versions of the flattest model (Farquharson et. al., 1993; two curves are indistinguishable from one to another in panel (b)).

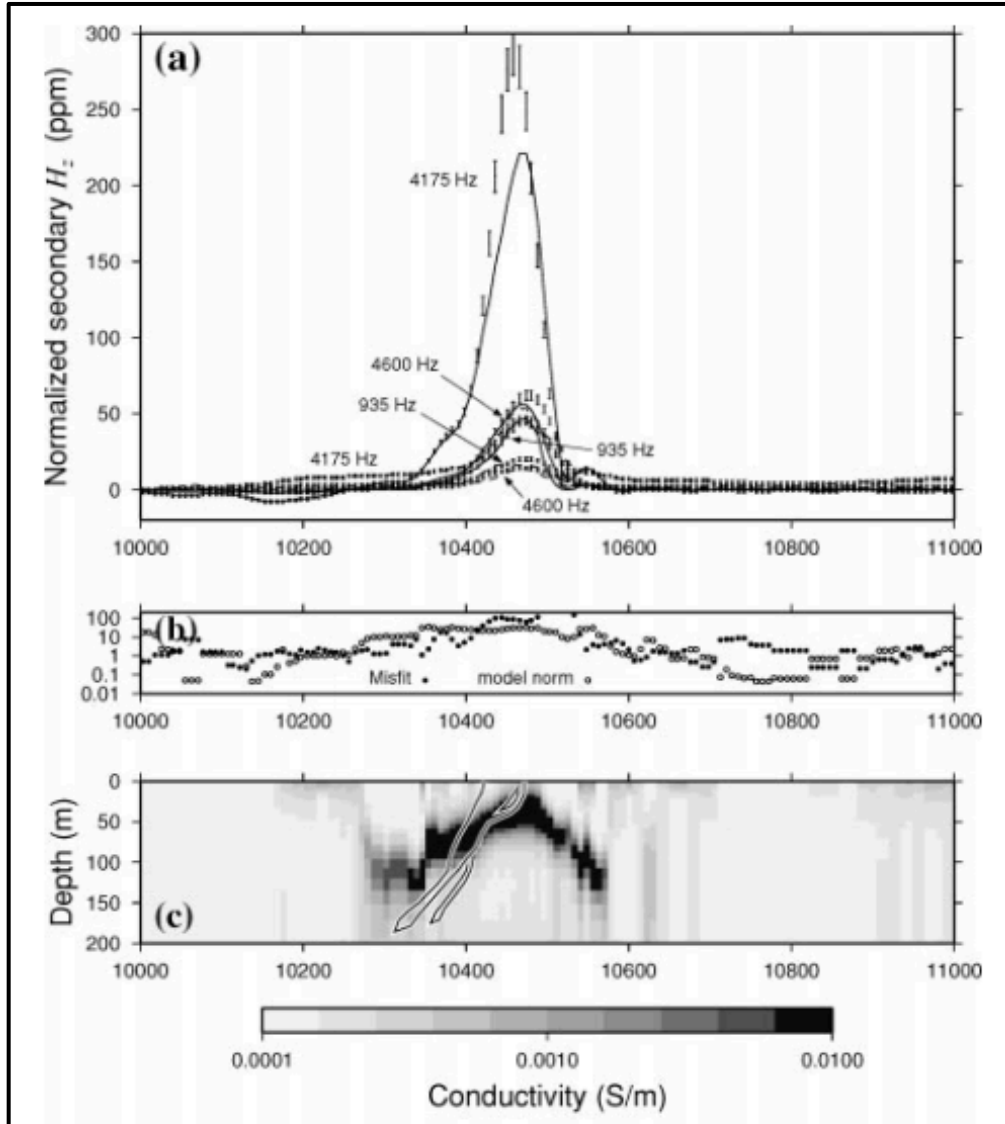


Figure 4.3: The results of inverting the line of frequency-domain EM observations from Heath Steele Stratmat closest to the mineralized zone. (a) The observations (shown with the error bars) and the lines for predicted data of the model generated by the inversion (solid-in-phase; dashed-quadrature) are shown (edited; Farquharson et al., 2003). (b) The final values of the misfit (solid circles and model-structure term (open circles) are presented. (c) The conductivity model of the inversion in which the mineralized zone is shown with the gray outline.

4.2 The Inversion Result of the Taylor Brook ATEM Data

In this section, the result of inverting the Taylor Brook airborne TEM dataset is shown. Before describing the 1D inversion results, I would like to reiterate the context of these 1D inversions. The aim of the thesis is to make a quantitative interpretation about the survey area. To do so, 1D inversion is applied to the data by using the code EM1DTM. The result of 1D inversions and the borehole information are then used to create a 3D geological model. Finally, 3D finite-element forward modeling is applied to the model (see Chapter 5). The data from the 3D modeling can then be compared with the real data to assess the chances of the model being a good representation of the subsurface. I focused on a part of the survey area containing clear anomalies in the ATEM data.

Let us take a more detailed look at the measured data first. The left-hand map in Figure 4.4 shows the second off-time channel measured by the AeroTEM system. The right-hand map shows the part of the survey area being focused on.

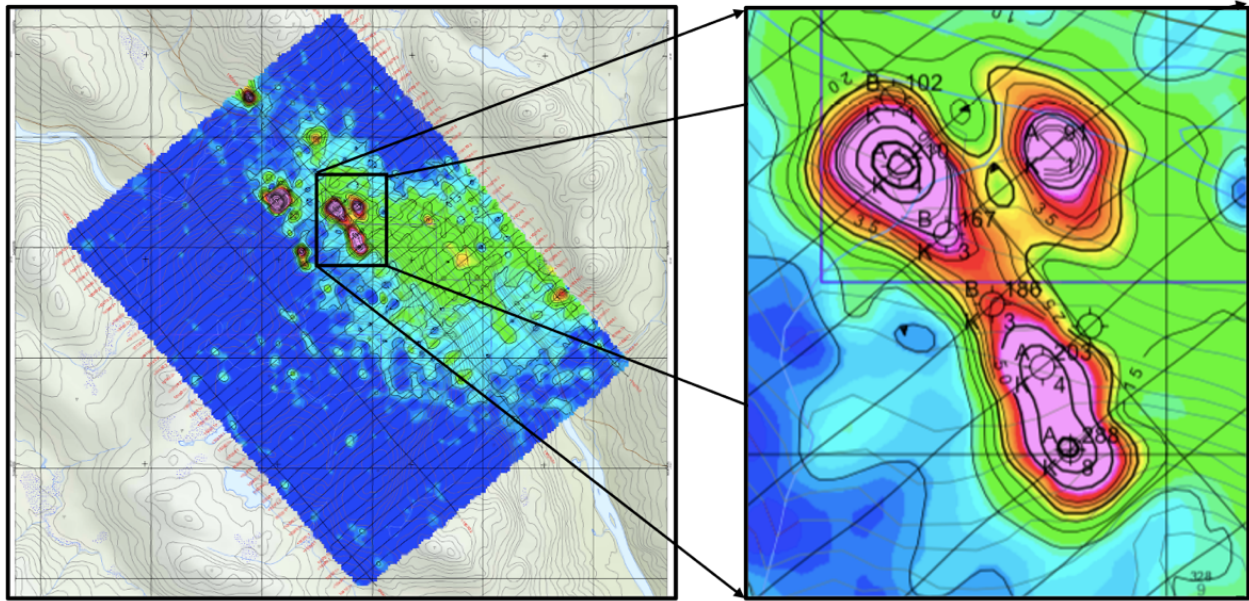


Figure 4.4: The map of the survey area showing the z-component of the second off-time channel (on the left). The map on the right indicates the main area of interest (Churchill, 2007).

In Section 3.2, in Figures 3.8 to 3.10, it is shown that there are common anomaly patterns in ATEM that can be used to give an indication of the shape and orientation of an underground target. Comparing these patterns with the main anomalies in the Taylor Brook dataset, which are shown in Figures 4.5 to 4.7, allows for an initial interpretation of the subsurface features. Accordingly, it can be seen that line L10140 in Figure 4.5 has a thin dipping conductor, and line L1050 in Figure 4.5 has either two thick vertical conductors at each anomaly showing a peak or a thin vertical conductor in between two peaks while line L10170 and line L10180 in Figure 4.6 have a thin dipping conductor and a thick vertical conductor, respectively.

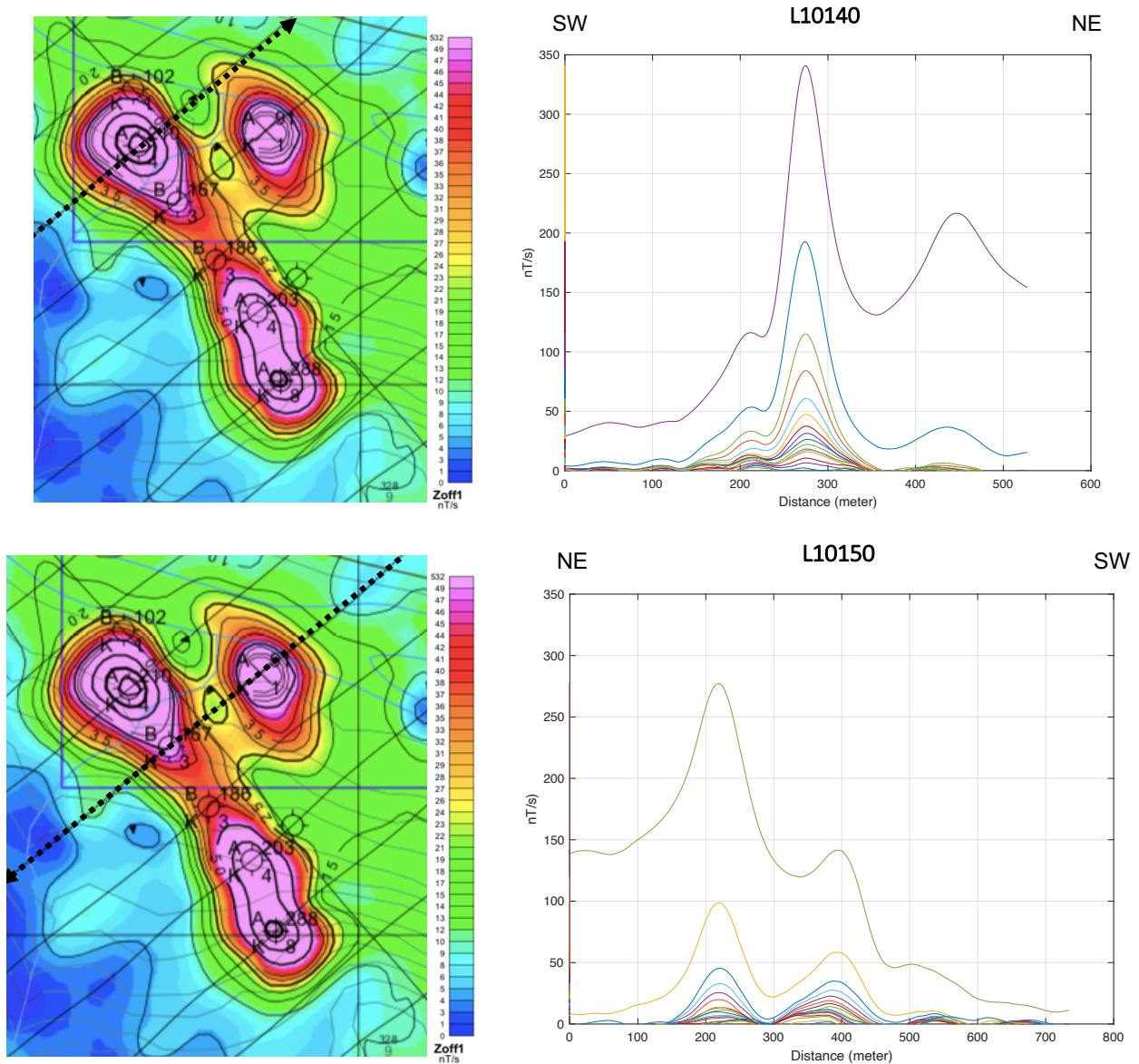


Figure 4.5: The maps on the top and bottom left show the second off-time channel. The dashed arrows represent flight-line directions. The graphs on the right indicate all the measured off-time channels along the two profiles that are highlighted with dashed lines on the maps on the left.

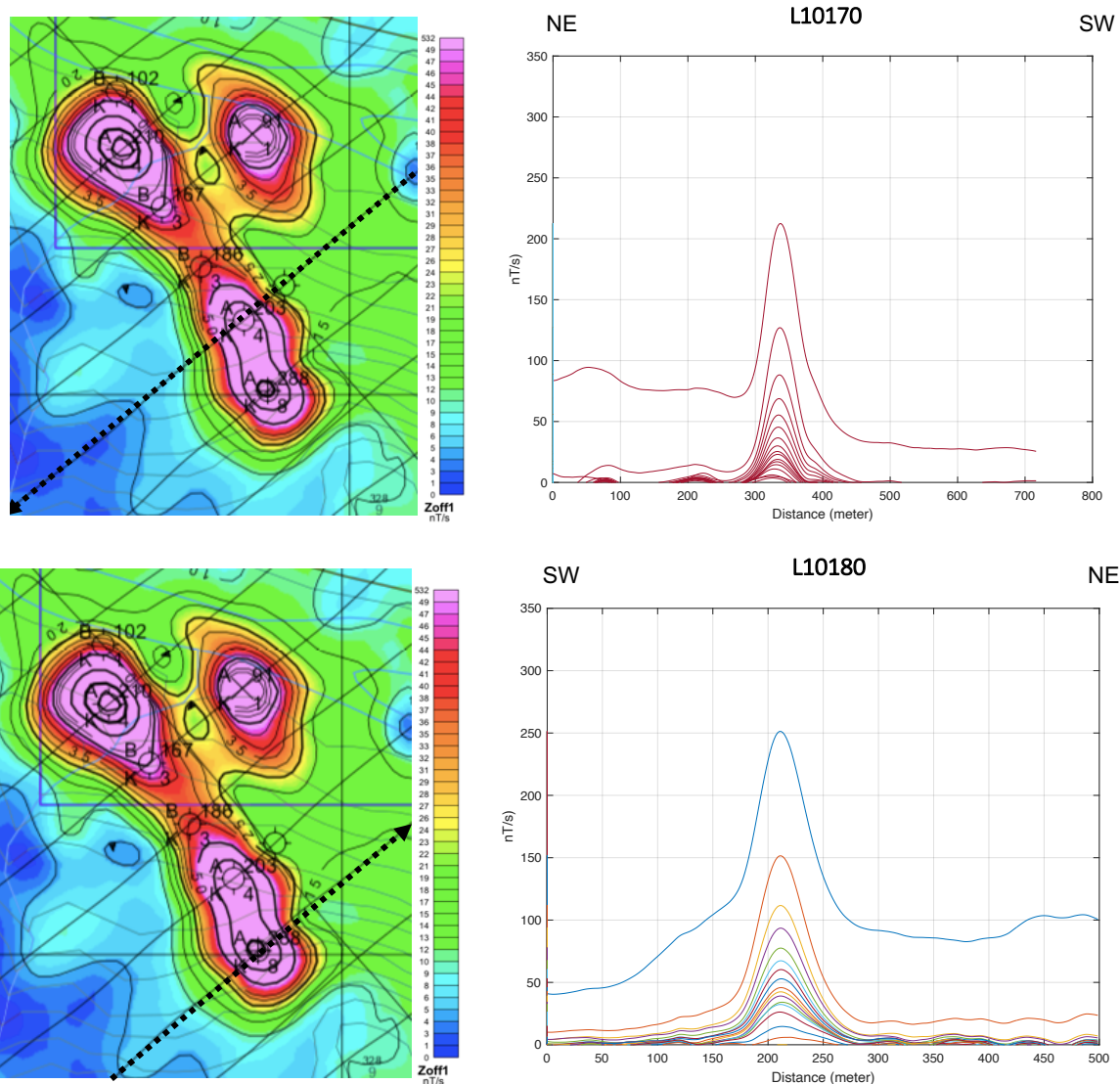


Figure 4.6: The maps on the top and bottom left show the second off-time channel. The dashed arrows represent flight-line directions. The graphs on the right indicate all the measured off-time channels along the two profiles that are highlighted on the maps on the left.

Recall from Section 3.2 how the magnetic field response with time is visualized (i.e., decay curves). Figures 4.8 to 4.14 show the comparison between the decay curves of the measured data and predicted data for the model produced by 1D inversion, as well as the 2-D conductivity section for some of the profiles and the smooth model of the subsurface generated by 1-D inversion results. The inversion results for all lines considered can be found in Appendix A.

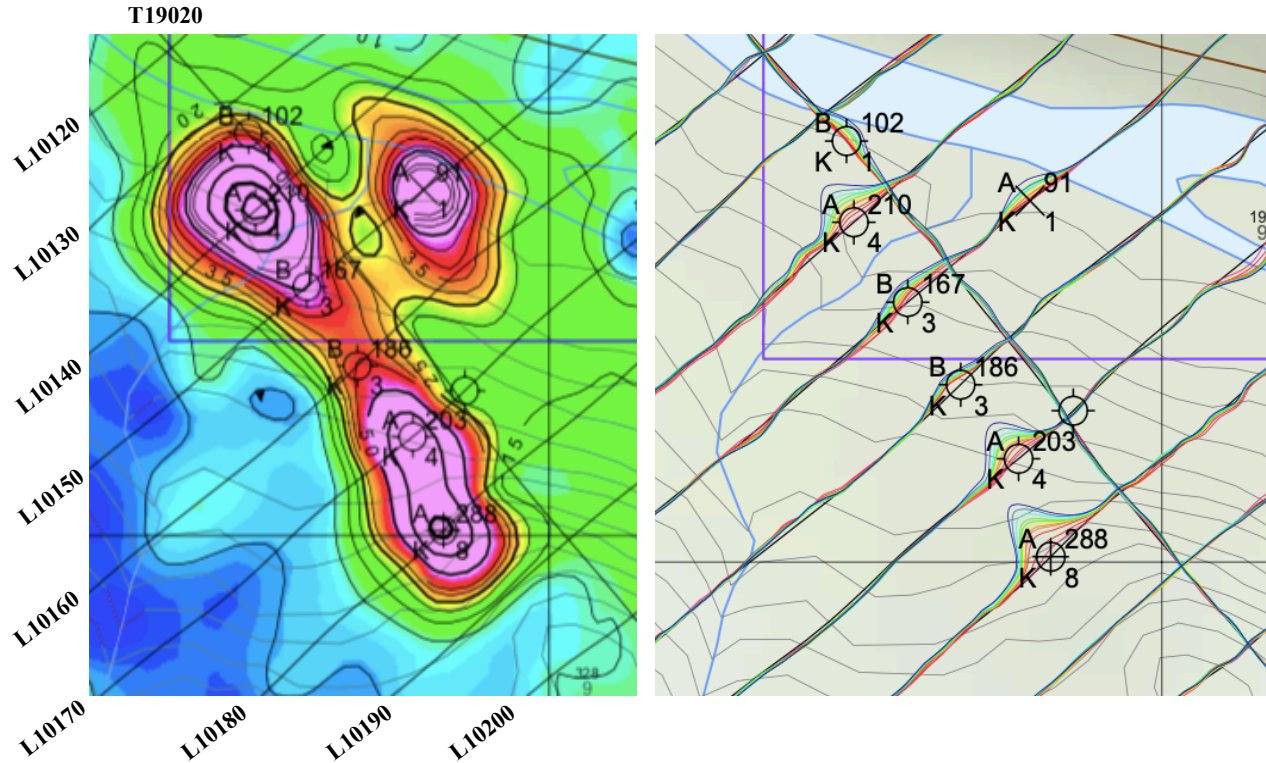


Figure 4.7: The map shows the second off-time channel over the area of interest (on the left). Profiles of all time channels over the area of interest (on the right; Churchill, 2007).

Even though the existence of a conductive deposit beneath the surface might be deduced just by looking at the profiles of the measured data in Figure 4.7, it cannot be known how deep, or thick or long the conductive deposit is. At this point, the results of the inversion give an interpreter an estimate of the physical properties of the subsurface and of the deposit. In general, it is known from the geology that the area has a resistive basement, which is dominantly gneiss. This makes it easier to locate a conductive deposit in the survey area.

Figure 4.8 shows the conductivity cross-section for the L10140 profile created by pasting together all the 1D inversion models. As can be seen, there exists a conductive feature in the middle of the profile. What can be said from this cross-section is that the conductive feature could be at a depth of between 30 m and 50 m. Also, it can be said that the data are quite noisy from considering the decay curves in Figure 4.9. The measured data and the predicted data at those locations do not

have a good match, except observation point #21 and the ones really close to the conductive feature (i.e., #20, #22). As one can see from Figure 4.9, the measured data away from the conductor level off after decaying to roughly 1 mV in the third or the fourth time channel. This levelling off is characteristic of the data reaching the noise level of the instrumentation. The decay curve from over the conductor has values above 1 mV for essentially all time channels.

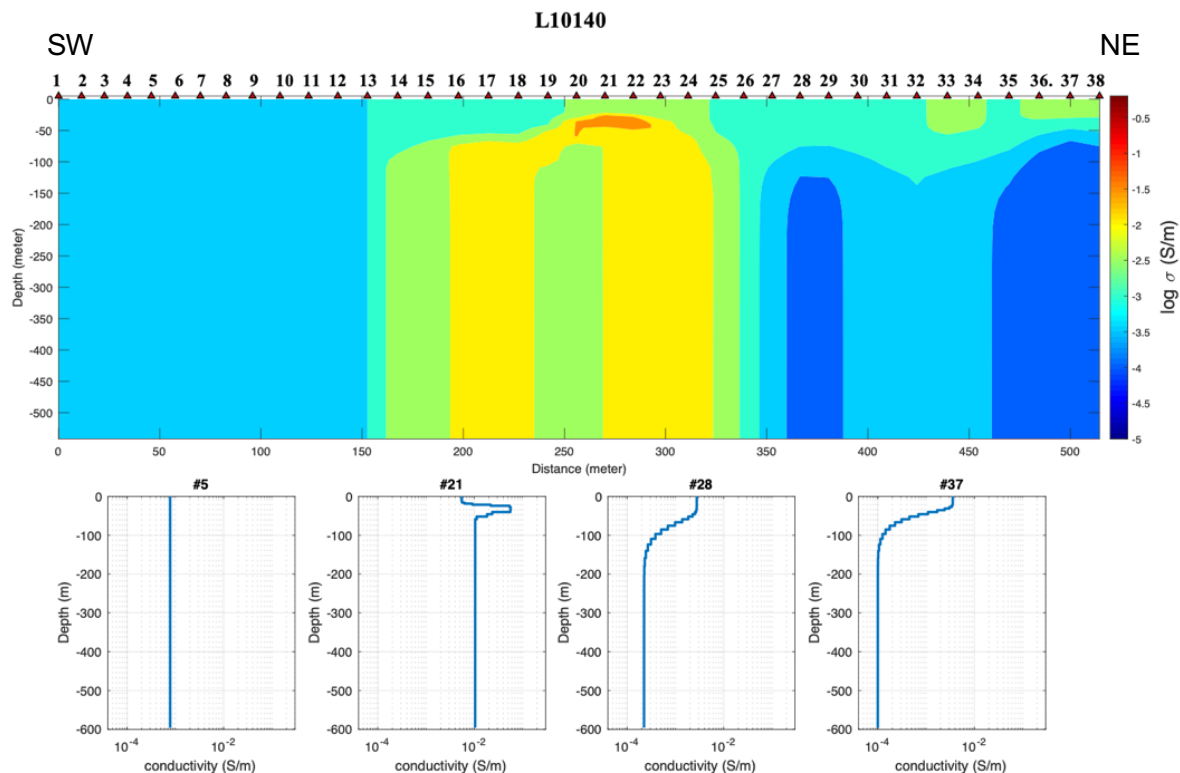


Figure 4.8: The 2-D conductivity section of line L10140 (top panel). The numbers on the top of the cross-section indicate the index of the observation points. The lower panels show the smooth 1D models of the Earth produced by the inversion for 4 different observation points.

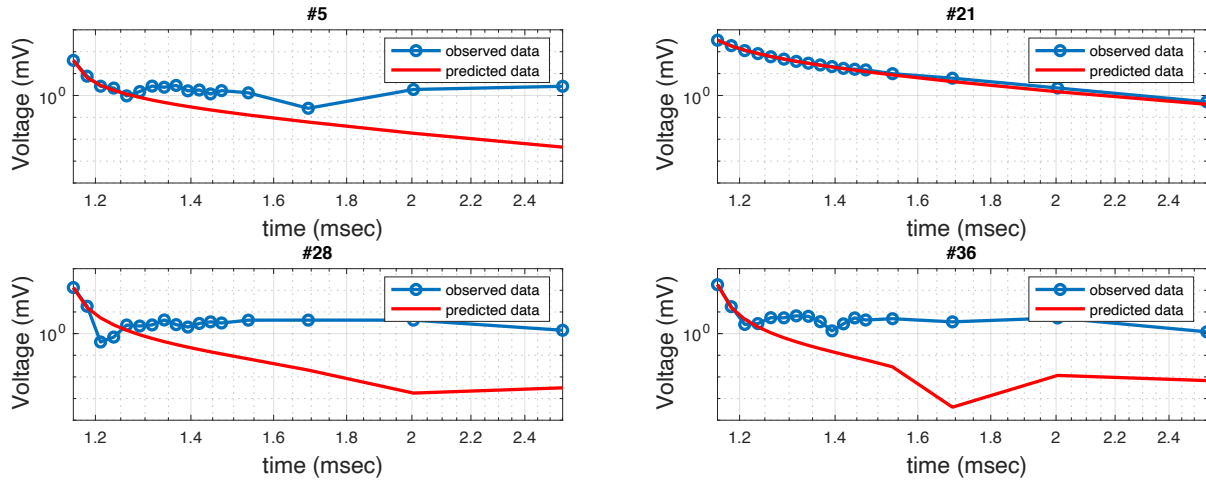


Figure 4.9: The comparison of the measured and the predicted data for the 4 observation points shown in the lower panel of Figure 4.8.

The statements for profile L10140 also apply to profile L10150, which is shown in Figure 4.10. Since the measured data are not of great quality, I am not able to say much about the physical properties of the subsurface after the first 50-60 m at the beginning of the profile (approximately from observation locations #1 to #9), except that the subsurface must be resistive without any conductive targets. By using the information from the boreholes, it might be said that the anomaly between observation points #12 and #13 and at the depth of 50 m correspond to the sulfide mineralization. The borehole that is drilled into this anomaly is 213.7 metres long with a 50° degree dip. It intercepted the sulfide zone at 133 metres, which is at around 100 metres vertical depth from the surface. In the middle of the profile, there is an anomaly that might correspond to a conductive body. However, the existence of the sulfide mineralization there cannot be confirmed unless a borehole is drilled in that part of the survey area.

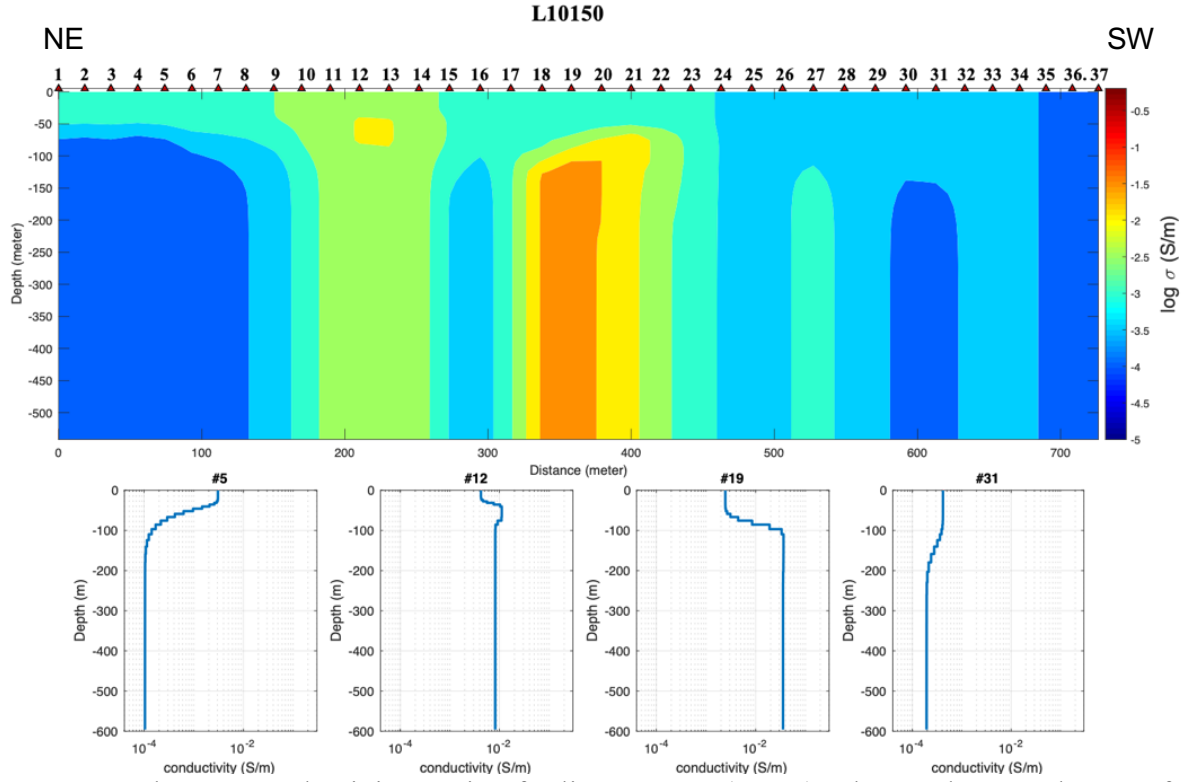


Figure 4.10: The 2-D conductivity section for line L10150 (upper). The numbers on the top of the cross-section indicate the index of the observation points. In the lower panels, the models constructed by inversion for 4 different observation points.

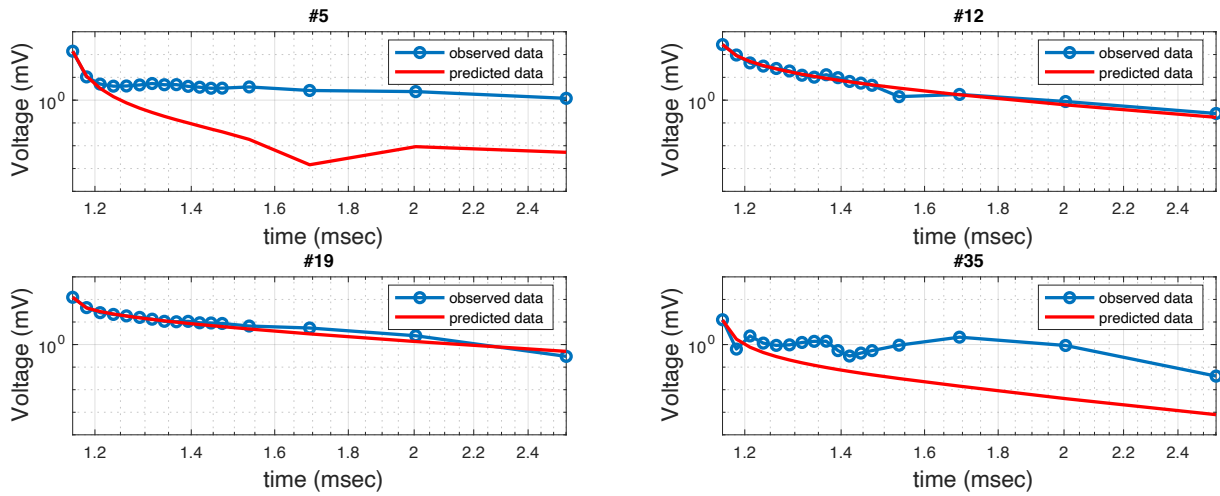


Figure 4.11: The comparison of the measured and the predicted data for the 4 observation points shown in Figure 4.10.

The inversion results for profile L10170 are shown in Figure 4.12 and 4.13, and those for profile L10180 are shown in Figure 4.14 and 4.15. In these figures, the samples of observed data are chosen close to the conductive feature. As can be seen, the match between the measured data and the predicted data for these observation points is better than others that are far from the conductive body, and almost all of the off-time channels are matched just above the noise level. The decay curves of those observation points that are close to the conductive body decay more slowly than those where there is no conductive feature, thus staying above the noise level for longer.

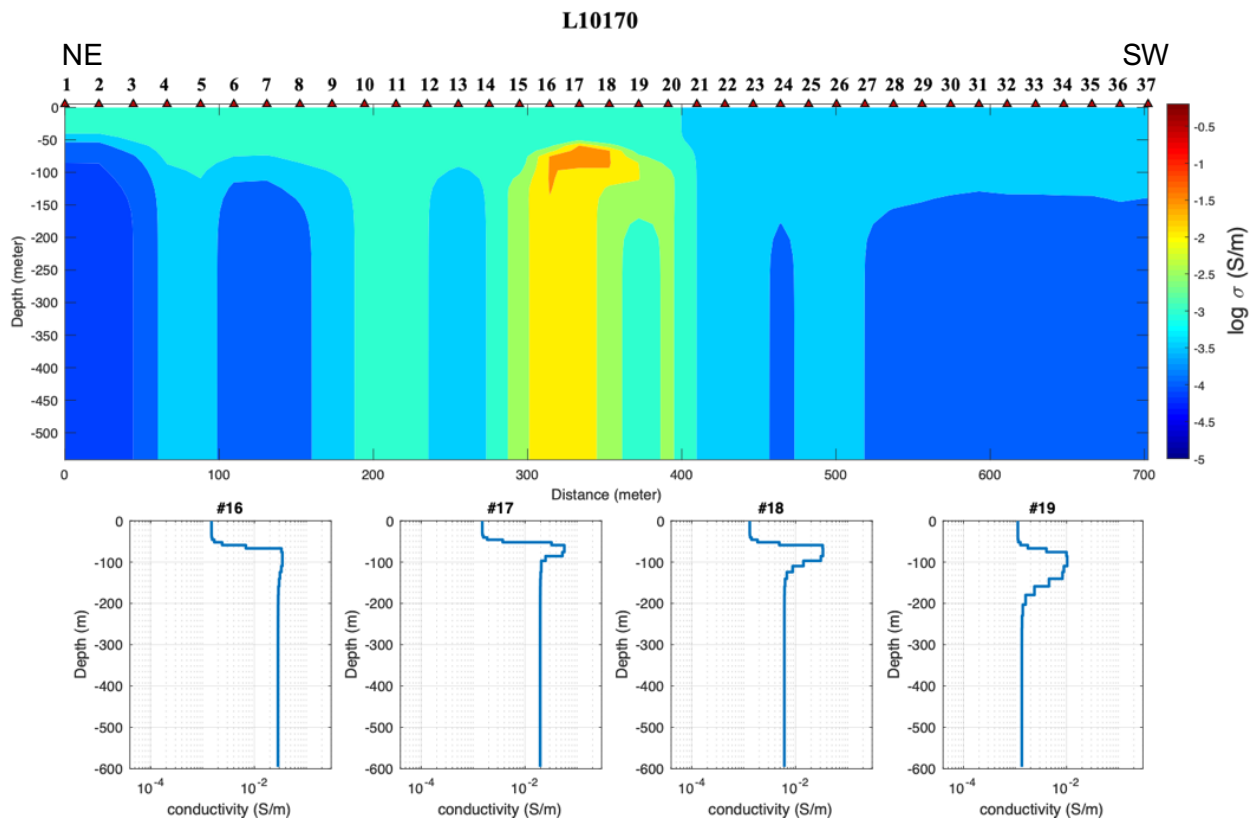


Figure 4.12: The 2-D conductivity section for L10170 (top). The numbers on the top of the cross-section indicate the index of the observation points. In the lower panels, the smooth models after inversion for 4 different observation points are shown.

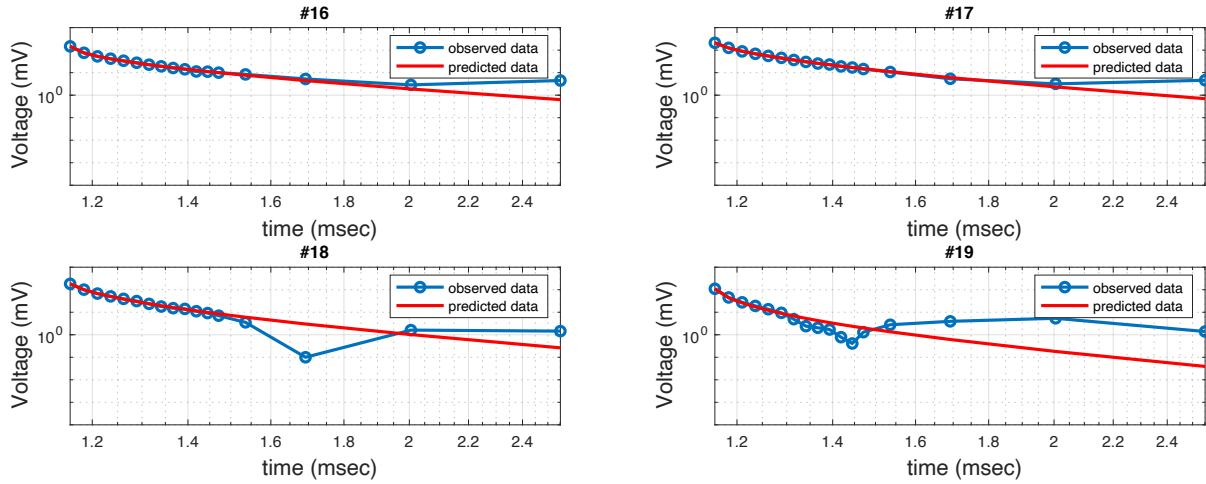


Figure 4.13: The comparison of the measured and the predicted data for the 4 observation points shown in Figure 4.12.

One important point to realize from the 2-D conductivity sections in Figures 4.8, 4.10, 4.12 & 4.14 is that the red and orange shades in these cross-sections do not mean that there is the existence of a conductive deposit all the way down to the bottom of the section. The TEM data are really just sensitive to the top of the conductive feature, with the currents induced by the measurement process sitting on the top of the conductor. The data are therefore not really sensitive to how deep the conductor might reach.

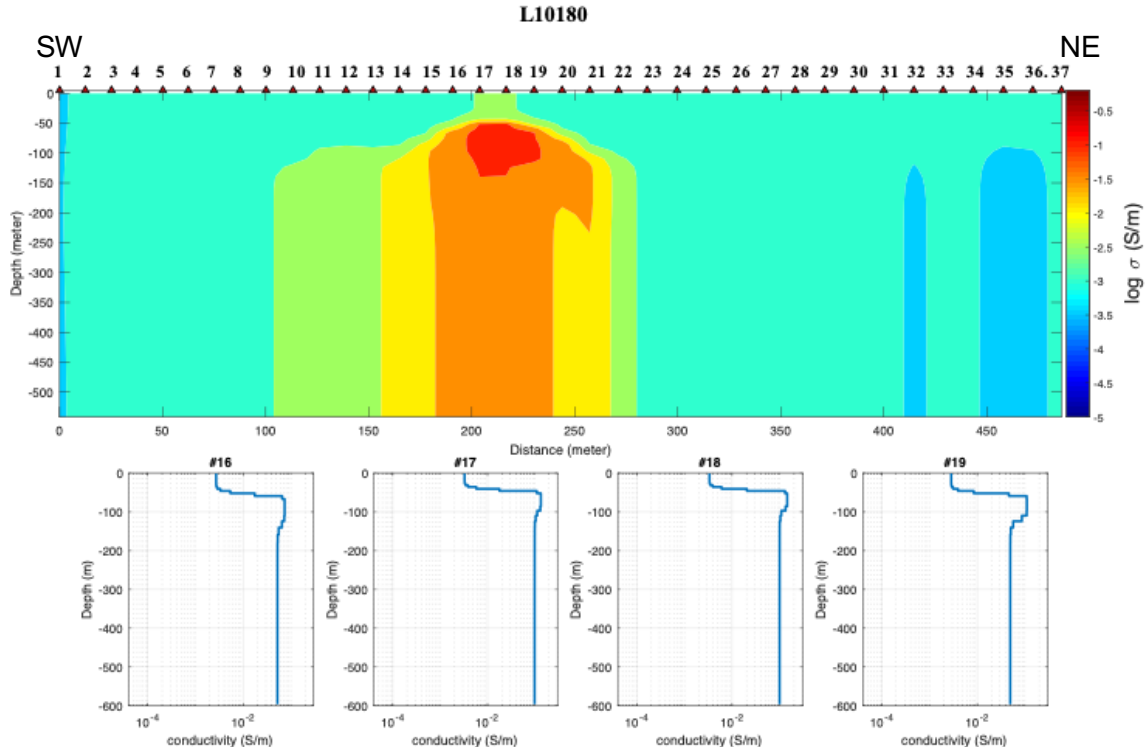


Figure 4.14: The 2-D conductivity section for line L10180 (top). The numbers on the top of the cross-section indicate the index of the observation points. In the lower panels, the models constructed by inversion for 4 different observation points are shown.

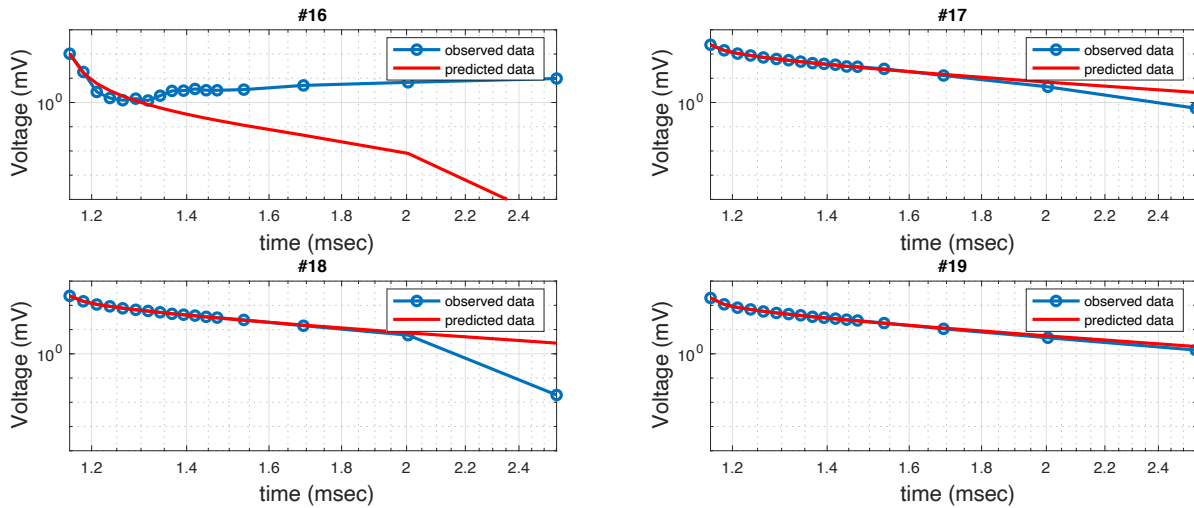


Figure 4.15: The comparison of the measured and the predicted data for the 4 observation points shown in Figure 4.14.

To better represent the results of the 1D inversions in 3D under the survey area, all 1D conductivity models were gathered together and combined into a 3D volume (Figure 4.16). Once again, the existence of the conductive deposit in the bottom of Figure 4.16 looks like it starts from the surface and goes deep down in the model, but it does not. Those anomalies are just artefacts. It cannot be said how deep the conductive body extends. To be able to say more about this, 3D forward modeling was applied, so that we can have a chance to compare the z-component of the result of 3D forward modeling with the measured data, and hence to decide the shape, the length and the orientation of the conductive body in the subsurface.

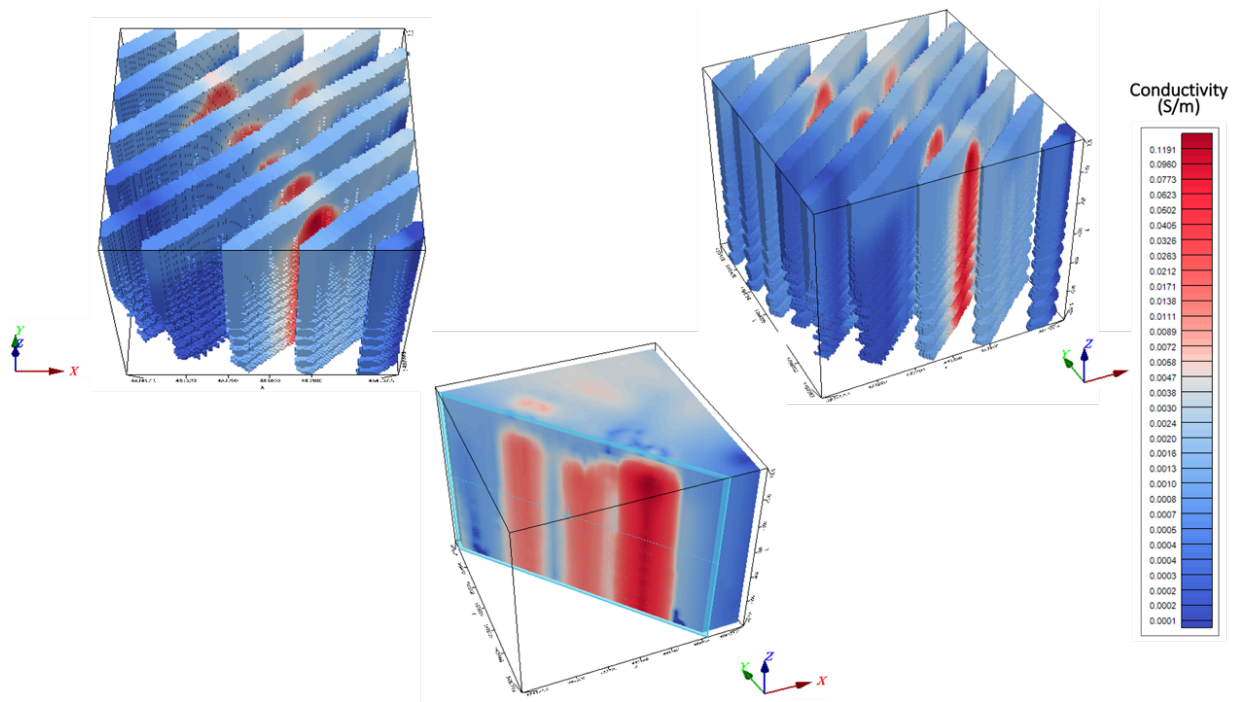


Figure 4.16: The 3D conductivity volume combined from all the 1D conductivity models from the 1D inversions (on the top left and right). A cross-section through the 3-D visualisation crossing the survey lines at the main conductor zone (on the bottom).

Chapter 5

5. Finite-Element Time-domain Electromagnetic Forward Modeling (3D)

Since the time-domain electromagnetic (TEM) method is widely used in applied geophysics, and inverse and forward modeling are a necessary tool for interpretation of TEM data in geologically complex areas, forward-modeling numerical solutions for TEM applications have drawn considerable attention (e.g., Um et al., 2010). The finite-element time-domain (FETD) approach, like other numerical methods (e.g., finite-difference), converts the partial differential equations describing the behaviour of EM fields in the ground into a set of linear equations. Since the finite-element method was first published in the literature of applied mathematics by Courant (1943), this method has been developed for and applied to many fields (Jin, 2011).

The use of numerical schemes that can accurately handle geological structures and interfaces are beneficial for modeling geophysical EM (e.g., Jahandari and Farquharson, 2014). It is well-known that structured rectilinear grids are commonly used for modeling geophysical electromagnetic datasets (e.g., Jahandari et al., 2017), but the models can be blocky and poor approximations to the geology. In comparison with structured meshes, the use of so-called unstructured tetrahedral meshes allows a geophysical model which is closer to a complex geological model to be constructed (Lelièvre et al., 2012). Furthermore, rectilinear grids have difficulty adding local refinement of the mesh, as this refinement often also extends in multiple directions. Finite-element time-domain (FETD) and finite-volume time-domain (FVTD) methods

can use unstructured grids and thus accurately represent complicated interfaces. In unstructured grids, the facets of the elements can more easily conform to the irregular interfaces that are being approximated, which can prevent the use of further refinements at these interfaces (Jahandari et al., 2017).

In this thesis, I used computer program that works based on the FETD method using unstructured grids (Li et al., 2018). The program was developed by Lu (2020). The reader is referred to his doctoral thesis (i.e. Lu, 2020) for more detailed information about the program.

Li et al. (2018) stated that the methods of modeling 3D time-domain EM fields can be divided into three main categories. The first category includes direct calculation of the numerical solutions in the time domain. This category includes two different methods, which are explicit and implicit time-stepping methods. One of the implicit methods is used in this thesis: this is the backward Euler method, which avoids a stability constraint on the time step although it requires the solution, at each time step, of a large linear system of equations (Börner, 2010). The second category is spectral methods, which involve transforming the EM responses from the frequency or Laplace domain into the time domain by using a Fourier or Laplace transform. The third category refers to Krylov subspace projection methods. For detailed information about how to use these methods, the reader is referred to Druskin and Knizhnerman (1988, 1994).

The FETD method used in this thesis can provide three component TEM responses from early time to late time, and it uses unstructured tetrahedral meshes. These meshes are generated by the software called Tetgen (Si, 2015). In order to get a 3D earth model which gives a good visual match between the measured data and the calculated data generated by the FETD forward-modeling, a trial-and-error forward modeling approach is implemented.

5.1 Governing Equations

Recall from Section 3.2 how the EM fields are described using Maxwell's equations. The FETD method also works using these equations. Let us reiterate them here briefly. Faraday's law and Ampere's law in the time domain can be written in a quasi-static regime as

$$\nabla \times \mathbf{e}(t) + \mu_0 \frac{\partial \mathbf{h}(t)}{\partial t} = 0, \quad (5.1)$$

$$\nabla \times \mathbf{h}(t) - \sigma \mathbf{e}(t) = \mathbf{j}_e^s(t), \quad (5.2)$$

where \mathbf{e} is the electric field, \mathbf{h} is the magnetic field, μ_0 is the magnetic permeability of free space, σ is the conductivity, \mathbf{j}_e^s is the electric current density of the source, and t is time. Taking the curl of Eq. 5.1 and substituting into Eq. 5.2 gives an equation for the total electric field:

$$\nabla \times \left(\frac{1}{\mu_0} \nabla \times \mathbf{e}(t) \right) + \sigma \frac{\partial \mathbf{e}(t)}{\partial t} + \frac{\partial \mathbf{j}_e^s(t)}{\partial t} = 0. \quad (5.3)$$

The partial differential equation, Equation 5.3, is the equation that is discretized in the FE method.

5.1.1 Vector FE method

Li et al. (2018) state that Eq. 5.3 can be discretized in space by using the vector FE method based on Whitney elements (see Li et al., 2011) and using the FETD approach of Um et al. (2010) for simulating 3D electromagnetic diffusion phenomena. In this approach, the Galerkin method is used, which is a type of weighted residual method, to create vector FE equations (Jin, 2014):

$$\mathbf{r} = \nabla \times \left(\frac{1}{\mu_0} \nabla \times \tilde{\mathbf{e}}(t) \right) + \sigma \frac{\partial \tilde{\mathbf{e}}(t)}{\partial t} + \frac{\partial \mathbf{j}_e^s(t)}{\partial t}, \quad (5.4)$$

where $\tilde{\mathbf{e}}$ is the approximated electric field. A set of vector basis functions \mathbf{N}_i with i that has a range from 1 to 6 for tetrahedral cells are used for the weighting functions in the Galerkin method. Equation 5.5 below can be obtained by multiplying the residual \mathbf{r} by \mathbf{N}_i , integrating over the computational domain, and setting the residual to zero:

$$\int_{\Omega} \mathbf{N}_i \cdot \mathbf{r} d\Omega = 0. \quad (5.5)$$

The approximate electric field $\tilde{\mathbf{e}}$ in each cell for tetrahedral grids can be written as

$$\tilde{\mathbf{e}} = \sum_{j=1}^6 N_j e_j, \quad (5.6)$$

where e_j is the value of the approximated electric field that corresponds to the j th edge, and \mathbf{N}_j is the first-order vector basis function (the same as the weight functions, which is the defining characteristic of the Galerkin method), which can be expressed as

$$\mathbf{N}_j = l_j (N_{j1} \nabla N_{j2} - N_{j2} \nabla N_{j1}), \quad (5.7)$$

where l_j is the length of the j th edge in a tetrahedral element, N_{j1} and N_{j2} are the scalar nodal basis functions for the two nodes linked by the j th edge. Jin (2014) has given the formulas for these scalar functions.

The FE formulation is obtained by substituting Eq. 5.4 and Eq. 5.6 into Eq. 5.5:

$$\mathbf{A} \frac{\partial \mathbf{u}(t)}{\partial t} + \mathbf{B} \mathbf{u}(t) + \mathbf{S} = 0, \quad (5.8)$$

where \mathbf{u} is a vector of size N , \mathbf{A} and \mathbf{B} are $N \times N$ sized matrices and N represents the number of edges in the mesh (which is the number of degrees of freedom). For tetrahedral cell te , for example, the elements of \mathbf{u} are $[e_1^{te} e_2^{te} e_3^{te} e_4^{te} e_5^{te} e_6^{te}]^T$, and the elements of \mathbf{A} and \mathbf{B} are (Li et al., 2018)

$$\mathbf{A}_{te} = \sigma \int_{\Omega_{te}} N_i \cdot N_j d\Omega_{te}, \quad \text{and} \quad (5.9)$$

$$\mathbf{B}_{te} = \frac{1}{\mu_0} \int_{\Omega_{te}} (\nabla \times N_i) \cdot (\nabla \times N_j) d\Omega_{te} \quad (5.10)$$

For elements including a segment of the transmitter, the term \mathbf{S} in Eq. 5.8 is nonzero and can be given by

$$\mathbf{S} = \int_{\Omega_{te}} N_i \cdot \frac{\partial j_e^s(t)}{\partial t} d\Omega_{te}. \quad (5.11)$$

Eq 5.11 amounts to integrating the basis function N_i around the wire of the transmitter loop (which is where the current density of the source is concentrated and exists).

5.2 Time Discretization

Li et al. (2018) state that one of the main methods for time-domain modeling is the time-stepping method. Time-stepping is one of the significant parameters of the FETD methods in terms of defining the number of iterations that the code needs to do, and the amount of memory that the code uses, during the computations. The first-order backward Euler method is implemented to discretize Eq 5.8 in time. By doing so, Eq 5.8 can be rewritten as

$$(\mathbf{A} + \Delta t \mathbf{B})\mathbf{u}^{k+1}(t) = \mathbf{A}\mathbf{u}^k(t) - \Delta t \mathbf{S}^{k+1}, \quad (5.12)$$

where k , which is equal to or greater than zero, is the time-stepping index. The way Eq. 5.12 is solved plays an important role in getting a precise solution.

Here, a direct solver, called MUMPS (Amestoy et al., 2006), is used to solve the linear system of equations (Li et al., 2018). This method has three steps for solving the linear system of equations: analysis, factorization and solution. Since the process of factorization is expensive computationally, a strategy is used to minimize the number of times this step has to be done. Therefore, the size of time step is generally kept the same for a specific number of iterations before it is changed (Lu, 2020). The workflow for the FETD method is shown in Figure 5.1.

In a time-stepping method, a small time step is used at early times in order to accurately compute the rapidly changing E-field at early times, whereas a larger time step is generally used at later times when the field is not changing as quickly (Lu,2020). Table 5.1 shows the importance of choosing the size of the time step in the computations. In Table 5.1, seven different schemes are considered and their computational times are shown. Schemes 1 and 5, for example, although they have the same number of iterations, which is 100, have a difference in computational times of almost three times because of the different time-stepping multiplier.

Table 5.1: The computational times of each time-stepping scheme chosen for a homogeneous half-space (0.001 S/m). The initial time-step is 10^{-7} s (from Li et al., 2018).

Scheme	The time-stepping multiplier	The number of iterations for a same-sized time step	The number of iterations of reaching 50 ms	Computational time	
				96,701 edges	1,046,588 edges
Scheme 1	2	100	1223	≈ 7 min	≈ 218 min
Scheme 2	5	100	608	≈ 4 min	≈ 112 min
Scheme 3	5	200	1111	≈ 4.5 min	≈ 129 min
Scheme 4	5	500	2536	≈ 8.5 min	≈ 182 min
Scheme 5	10	100	439	≈ 2.5 min	≈ 88 min
Scheme 6	10	200	828	≈ 5.5 min	≈ 102 min
Scheme 7	10	500	1945	≈ 6.5 min	≈ 132 min

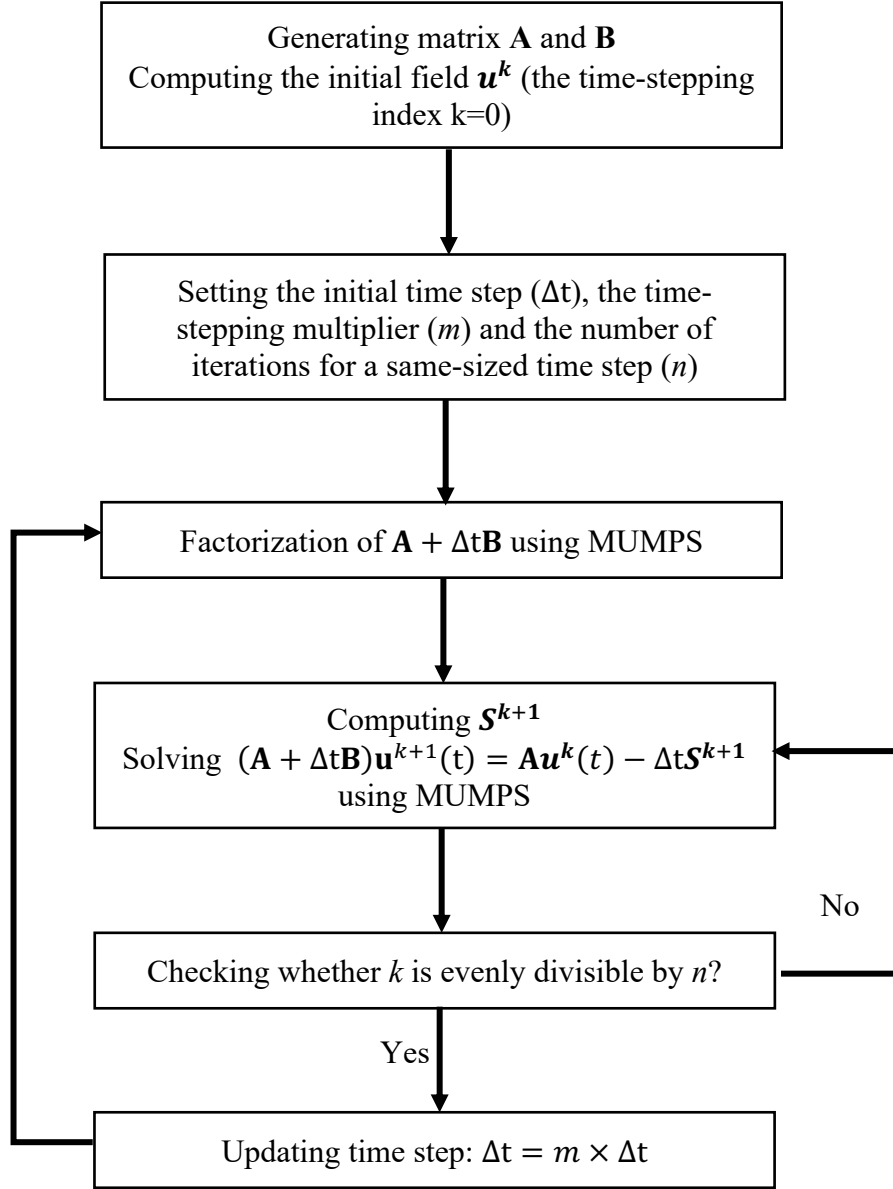


Figure 5.1: The workflow of the FETD method (Li et al., 2018).

In the next section, the 3D FETD code developed by Lu (2020) for modeling three-dimensional electromagnetic problems using unstructured grids is applied to the airborne time-domain dataset of the Taylor Brook area.

5.3 The Applications of FETD Forward Modeling to the Taylor

Brook Survey

In this section, several 3D geological Earth models that are used in the process of 3D forward modeling using unstructured tetrahedral grids will be presented, and the results of the 3D forward modeling applied to those models are compared with the real data in order to decide which model might be an appropriate representation the geology at Taylor Brook. During the creation of these models, the information from the boreholes (the dip and direction of the mineralization) that were drilled in the survey area was used as well as the results of the 1D inversions. The software called FacetModeller (Lelièvre et al., 2018), which allows the creation of models in a graphical user interface (GUI) environment, was used to build the models.

Recall that the survey is located in western Newfoundland where the geology is mainly igneous and metamorphic rocks. This is beneficial for detecting a conductor in the area, and it also makes the creation of a 3D Earth model easier. The model building was guided by geological information of the survey area and the 2D cross-sections of the geology (see Figures 2.8 and 2.9) that are close to the ATEM anomaly. Also, note that the majority of the boreholes have been applied mainly around Line L10170 and Line L10180 (Figures 2.6 and 2.7) since the samples that were collected there have high-grade mineralization and the samples near the other lines did not. Therefore, this part of the survey area is suitable for a test of the trial-and-error method to see the effectiveness of 3D forward modeling in interpreting the measured data. Creating a 3D Earth model which can provide an EM response that reasonably matches the measured data was an objective of this thesis.

5.3.1 Trial-and-Error Modeling

In this section, various pairs of mineralized dikes having different physical properties (i.e., thickness, length, conductivity) are created for use in the 3D Earth models that are to be used for the 3D forward modeling process. One of the dikes, called Dike-1 from now on, is nearby Line L10170 while the other one, called Dike-2, is close to Line L10180. These dikes are created based on two of the 2D cross-sections created by Altius, which have been derived from the borehole information. The physical properties of these dikes were then customized to get a good visual match between the real data and the results of the 3D forward modeling.

Figure 5.2 is a screenshot from the FacetModeller software which indicates the general overview of the 3D Earth model created for the survey area. According to the topography information obtained from the Government of Canada, the surface of the area is quite uneven, hence the topography is considered during the forward modeling. Since the geology of the survey area is not horizontally layered but is a ground that consists of metamorphic and igneous rocks, which are highly resistive (see Section 2; see Fig. 2.12), the model dikes are located in a highly resistive homogeneous background. Table 5.2 gives the conductivities of the units in the initial 3D Earth model. Note that the conductivities for air and the basement in Table 5.2 are the same in all subsequent 3D models. As for the two dikes, the various conductivity values investigated are between 1 S/m and 100 S/m, but generally the results of forward modeling for the values 10 S/m and 100 S/m for the dikes are shown in the following, since they have distinguishable results to compare with the real data.

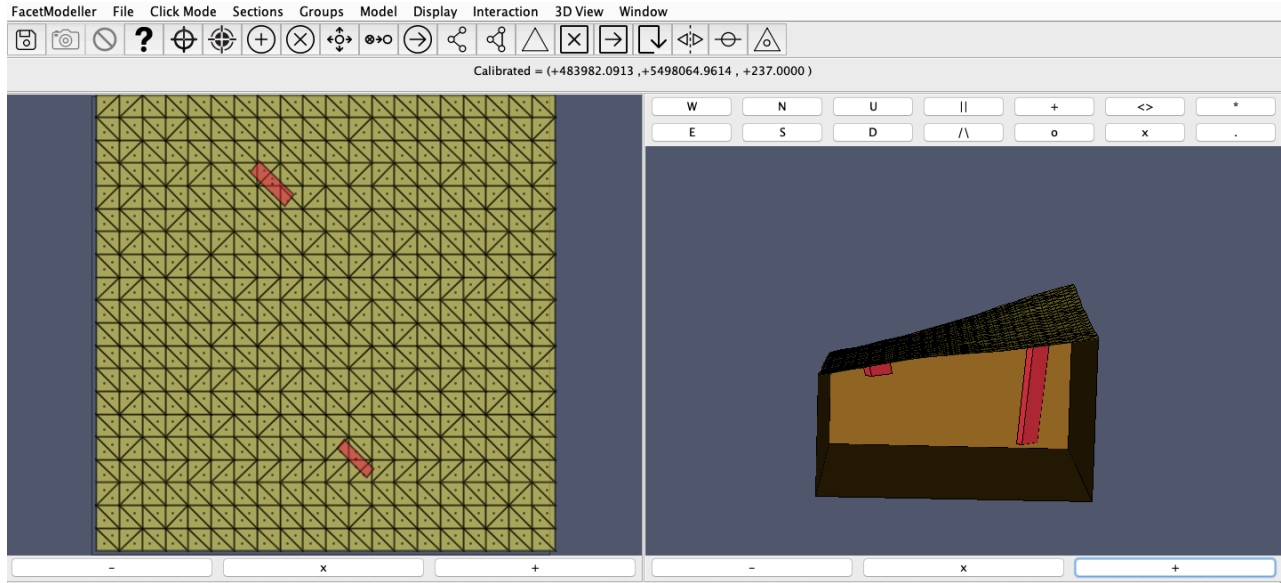


Figure 5.2: A screenshot from the FacetModeller software that shows a 3D Earth model (which is just the central volume of interest, not the entire volume of the 3D model that is used for forward-modeling) built for the survey area. On the left side, 2D plan view of the model is shown, while the 3D view of the model is shown on the right side of the screenshot, with the view being from the west.

Table 5.2: Conductivities of each region in the 3D Earth models.

Unit	Conductivity (S/m)
Air	10^{-8}
Basement	10^{-4}
Dikes	$1 - 10^2$

Figure 5.3 shows the tetrahedral mesh for one of the 3D Earth models that was built by FacetModeller and TetGen. TetGen (Si, 2015) is the software used here for generating unstructured tetrahedral meshes from the wireframe model created by FacetModeller. From now on, in each 3D Earth model, the blue coloured volume represents Dike-1 (which is close to Line L10170), whereas the red one indicates Dike-2 (which is close to Line L10180). Figure 5.4 shows the locations of the dikes and the profiles for one of the models. The white dots represent the observation points along the profiles.

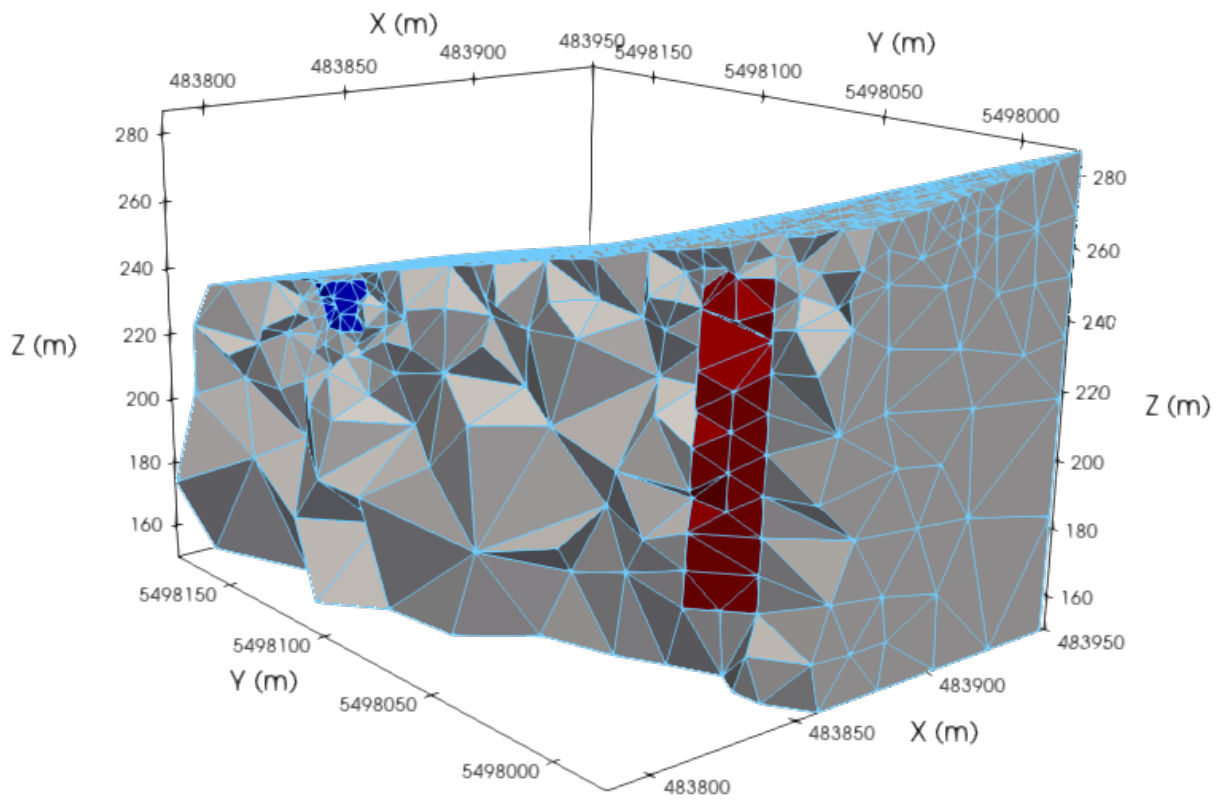


Figure 5.3: The unstructured tetrahedral mesh generated by TetGen for the model in Figure 5.2.

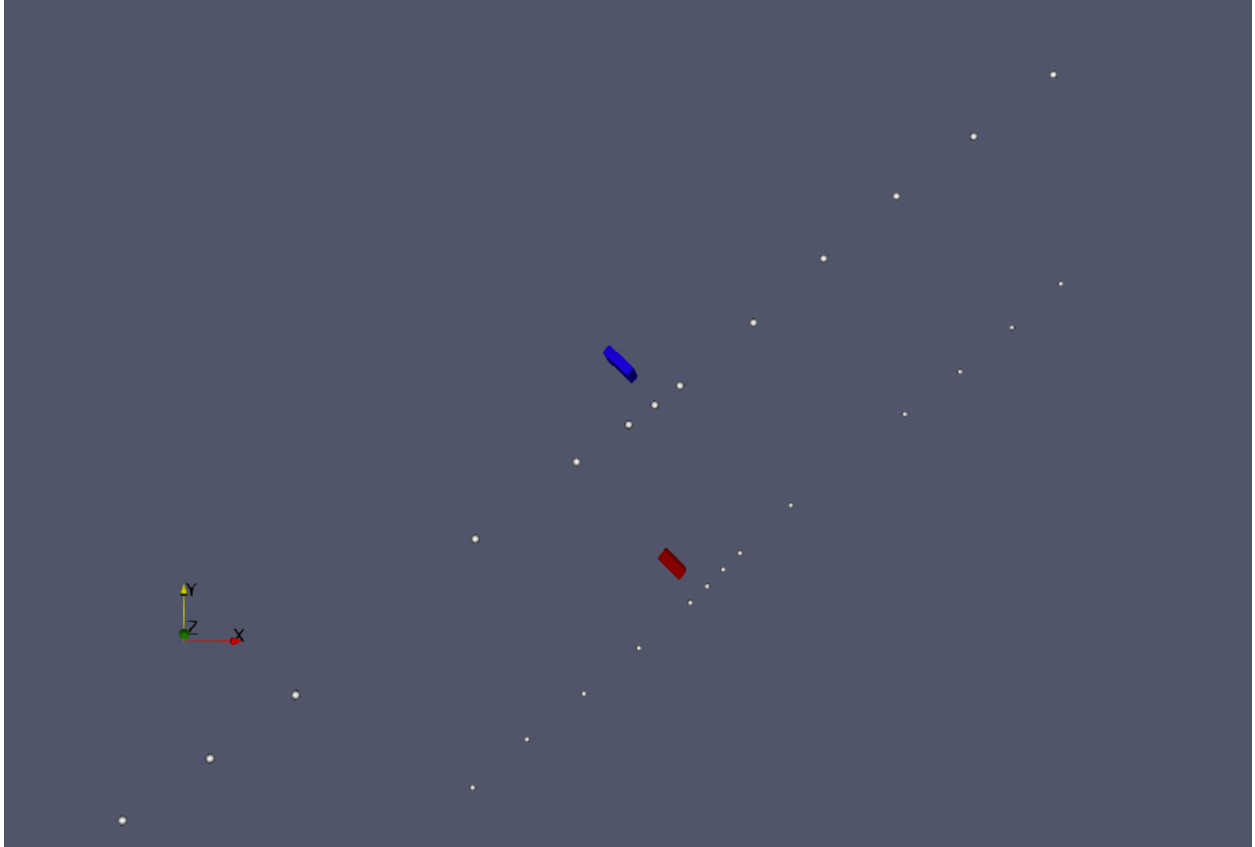


Figure 5.4: The locations of the dikes, of Line L10170 (upper line), and of Line L10180 (bottom line). The blue block is Dike-1, whereas the red one is Dike-2.

Many 3D Earth models were constructed and used for 3D FETD forward modeling and the match between the calculated data and the real data investigated. Table 5.3 shows all of the Earth models that were used for the 3D forward modeling process, including the locations of the dikes. In this section, the results shown and discussed belong to two of these Earth models. The reader is referred to Appendix B to see the 3D forward modeling results for the rest of the Earth models in Table 5.3.

Table 5.3: The 3D Earth models and, in particular, the locations and sizes of the dikes, for which 3D numerical modeling was carried out.

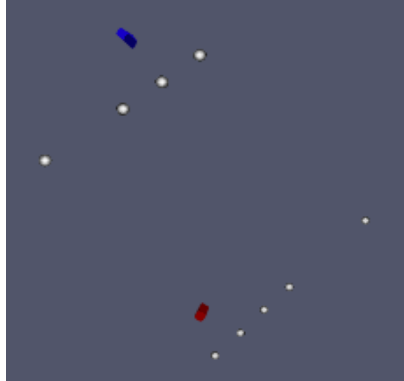
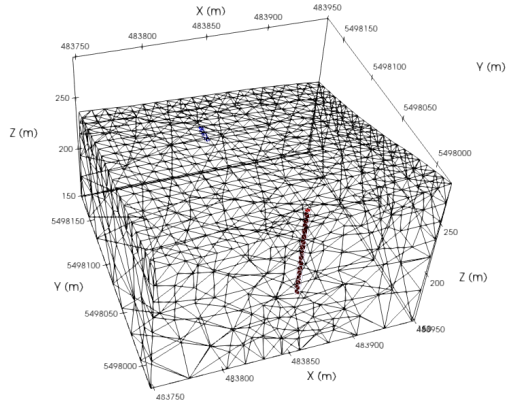
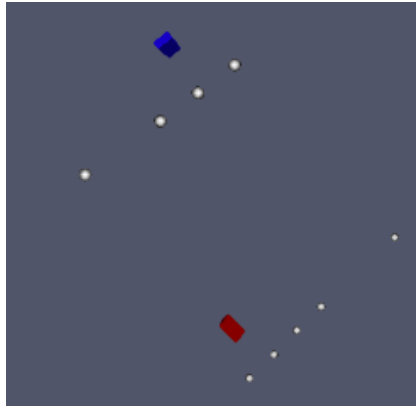
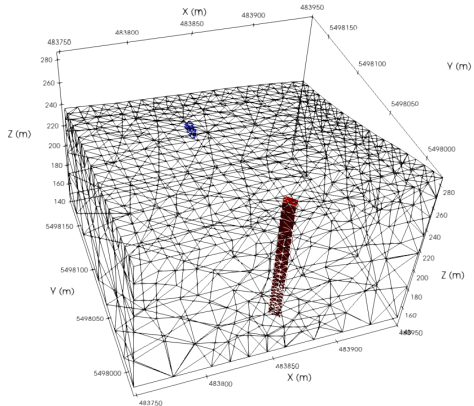
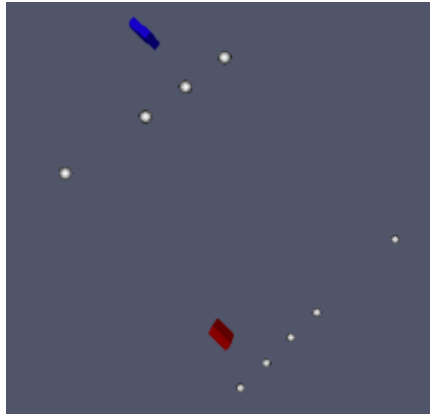
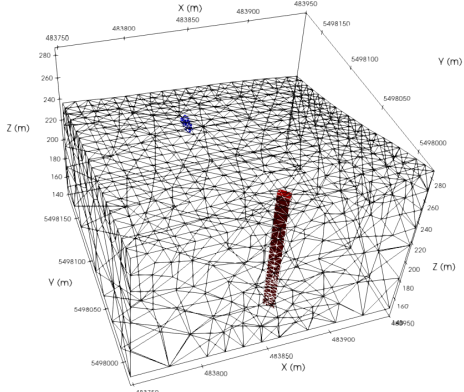
Model number	2D view (bird's eye)	Size (m) (thickness x length x depth)	3D view
Model 1		Dike-1 3x4x10m Dike-2 3x4x90m	
Model 2		Dike-1 8x3x10m Dike-2 6x10x120 m	
Model 3		Dike-1 3x9x10m Dike-2 3x9x90m	

Table 5.3: The 3D Earth models and, in particular, the locations and sizes of the dikes, for which 3D numerical modeling was carried out (continued).

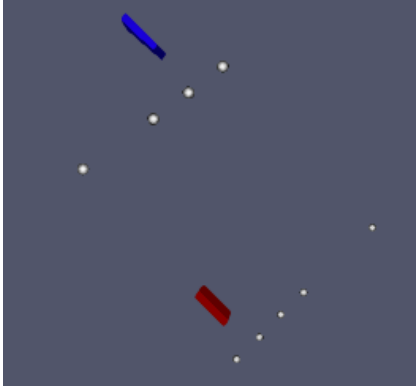
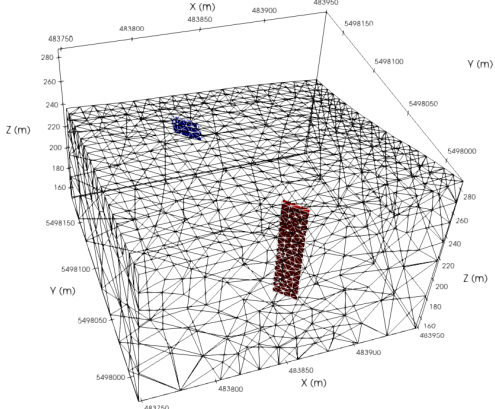
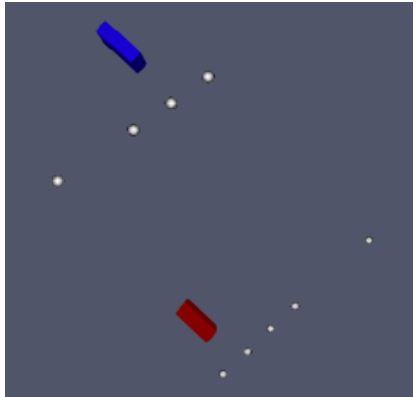
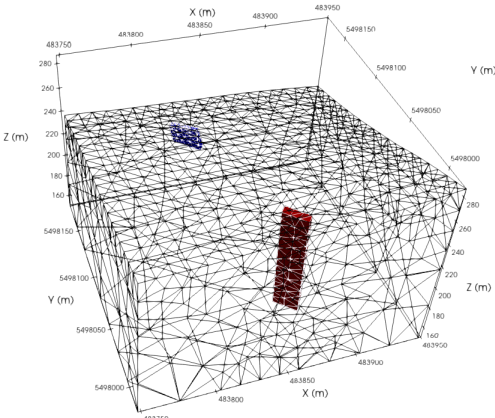
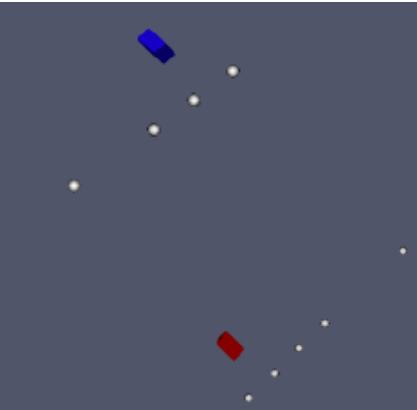
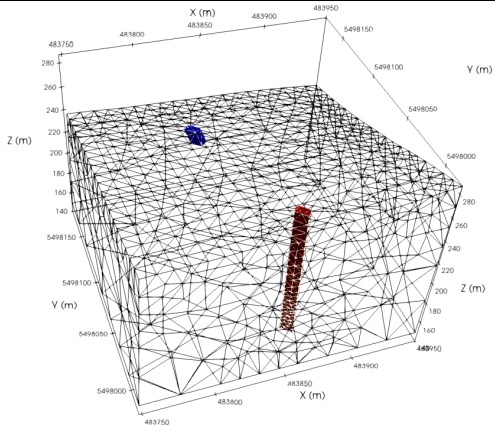
Model number	2D view (bird's eye)	Size (m) (thickness x length x depth)	3D view
Model 4		Dike-1 3x20x10m Dike-2 3x18x90m	
Model 5		Dike-1 6x20x10m Dike-2 6x18x90m	
Model 6		Dike-1 6x9x10m Dike-2 6x9x120m	

Table 5.3: The 3D Earth models and, in particular, the locations and sizes of the dikes, for which 3D numerical modeling was carried out (continued).

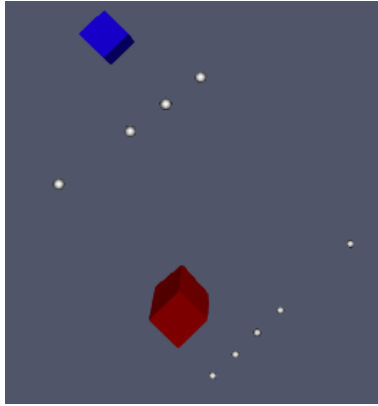
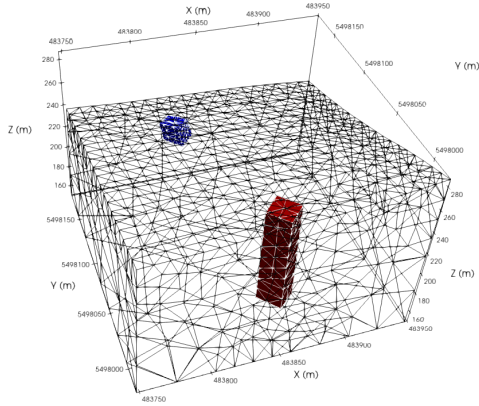
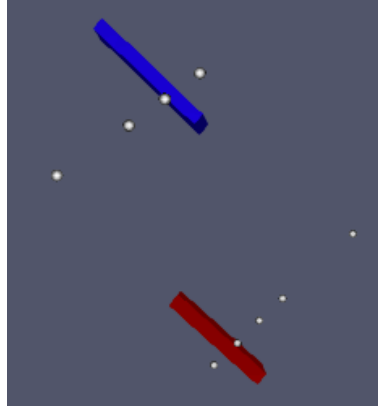
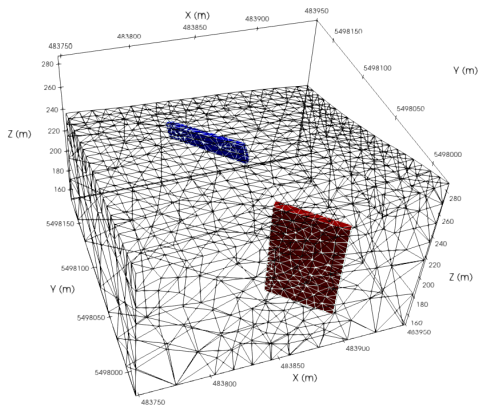
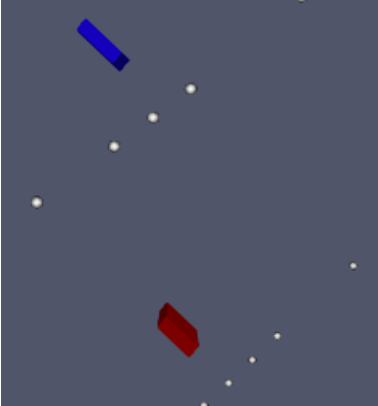
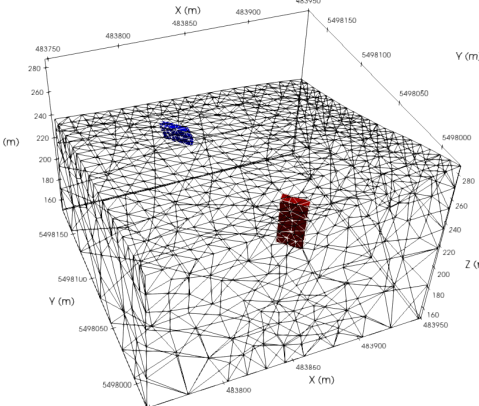
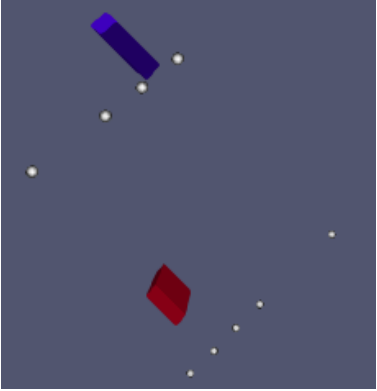
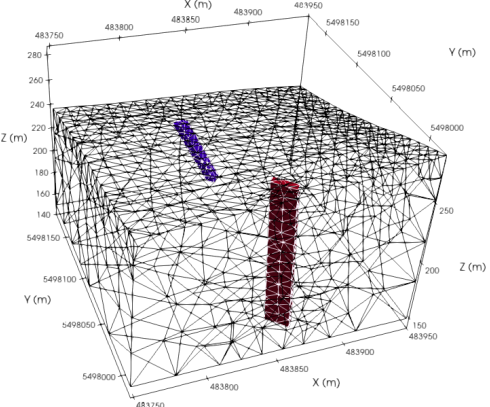
Model number	2D view (bird's eye)	Size (m) (thickness x length x depth)	3D view
Model 7		Dike-1 15x15x10m Dike-2 18x18x90m	
Model 8		Dike-1 6x70x10m Dike-2 6x60x90m	
Model 9		Dike-1 6x20x10m Dike-2 6x18x40m	

Table 5.3: The 3D Earth models and, in particular, the locations and sizes of the dikes, for which 3D numerical modeling was carried out (continued).

Model number	2D view (bird's eye)	Size (m) (thickness x length x depth)	3D view
Model 10		Dike-1 9x6x40m Dike-2 6x18x120m	

As can be seen from Table 5.3, many different 3D Earth models that might represent the structure of mineralization in the survey area were tested. The 3D forward modeling result of Model 5 is considered, in comparison with the others, as having the best visual match between the real data and the calculated data, as detailed below.

Model 5

The top right figure in Figure 4.6 shows the measured EM response along Line L10170 over the area containing the mineralization. This part of the line includes more than a thousand measurement points (observation locations). This gives the EM response high resolution. However, the 3D EM forward modeling code that is used takes a long time to run, with the computational time increasing with the number of transmitters. Therefore, only 13 observation points were used along this part of the survey line. I compared the calculated data and the real data at the same observation points. Figure 5.5 shows the measured data at the same observation points

that are used for the calculated data along Line L10170. On the right side of Figure 5.5, the legends indicates that there are 17 different times (off-time channels) at which the measurements occurred.

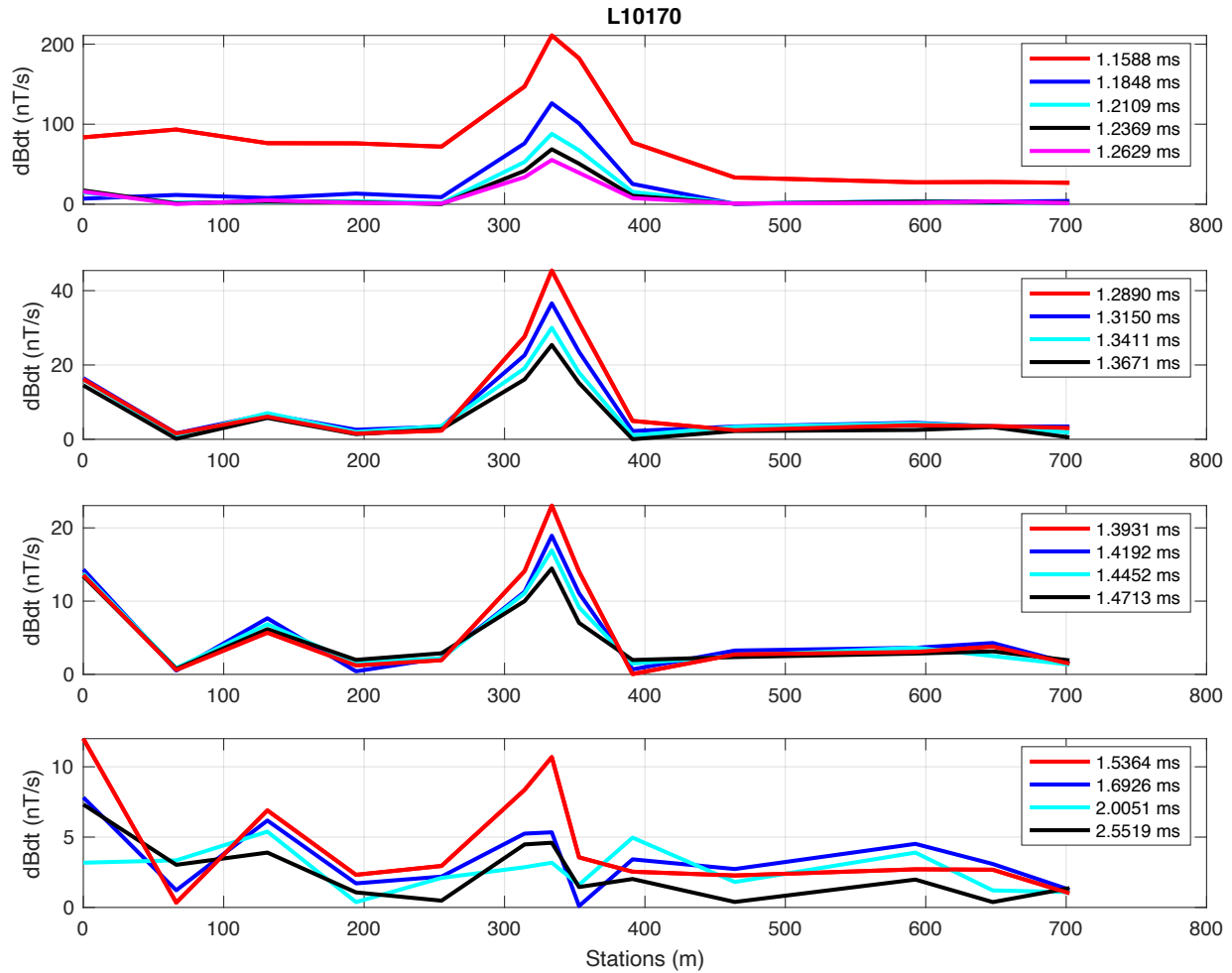


Figure 5.5: The z-component of the measured dB/dt data from Line L10170 at the observation points used for comparison with the numerical modeling. (Note the different scales in each panel.)

The background subsurface of the project area can be considered electrically uniform since the geology of the area is mainly metamorphic and igneous rocks with low conductivities. Since there are no actual conductivity measurements for the rock samples collected from the survey area, the background of the project area is assigned a conductivity of 10^{-4} S/m, which is typical of unweathered metamorphic and igneous shield rocks (Figure 2.12). During the creation of the dikes

for 3D forward modeling, the 2D geological cross-sections (see Figures 2.8 and 2.9) were used to guide the initial model. However, since the 2D cross-section relevant for Dike-1 only indicates two definite places where mineralization exists, and the west-southwest part of the Layden showing is largely unknown because of the limited extent of the drilling and trenching in this area, there is not much guidance for building the initial model. After many forward-modeling trials, it was decided that Model 5 produces good enough (good visual match) EM responses matching the real data. The specifications of Model 5 are given in Table 5.3.

Another parameter is to decide the value of the conductivity of the dikes. Determining the physical properties of a geological structure can be tricky in geophysical applications because of non-uniqueness (i.e., many different Earth models can give equivalent data). Therefore, different Earth models were generated and the responses for them calculated by the forward modeling process, and the model giving the best responses taken as the one that is the most possible representation of the survey area. After a couple of trials, it was understood that using 10 S/m and 100 S/m for the dikes gave the best responses for comparison. Hence, for this model, the results for conductivities of 10 S/m and 100 S/m are presented for the dikes. Figure 5.8 shows the EM responses of forward modeling for Dike-1 in Model 5 for different conductivities. Dike-1 has a dip of 55 degrees towards Line L10170 and also is touching the surface. As seen, the case of using 10 S/m for Dike-1 did not produce a strong enough secondary magnetic field to match the real data. However, the EM response calculated for 100 S/m is a reasonable match for the real data for most of the time channels. Figure 5.6 shows the locations of the dikes and the observation points while Figure 5.7 indicates the 3D Earth model generated in FacetModeller and meshed using an unstructured tetrahedral mesh by Tetgen.

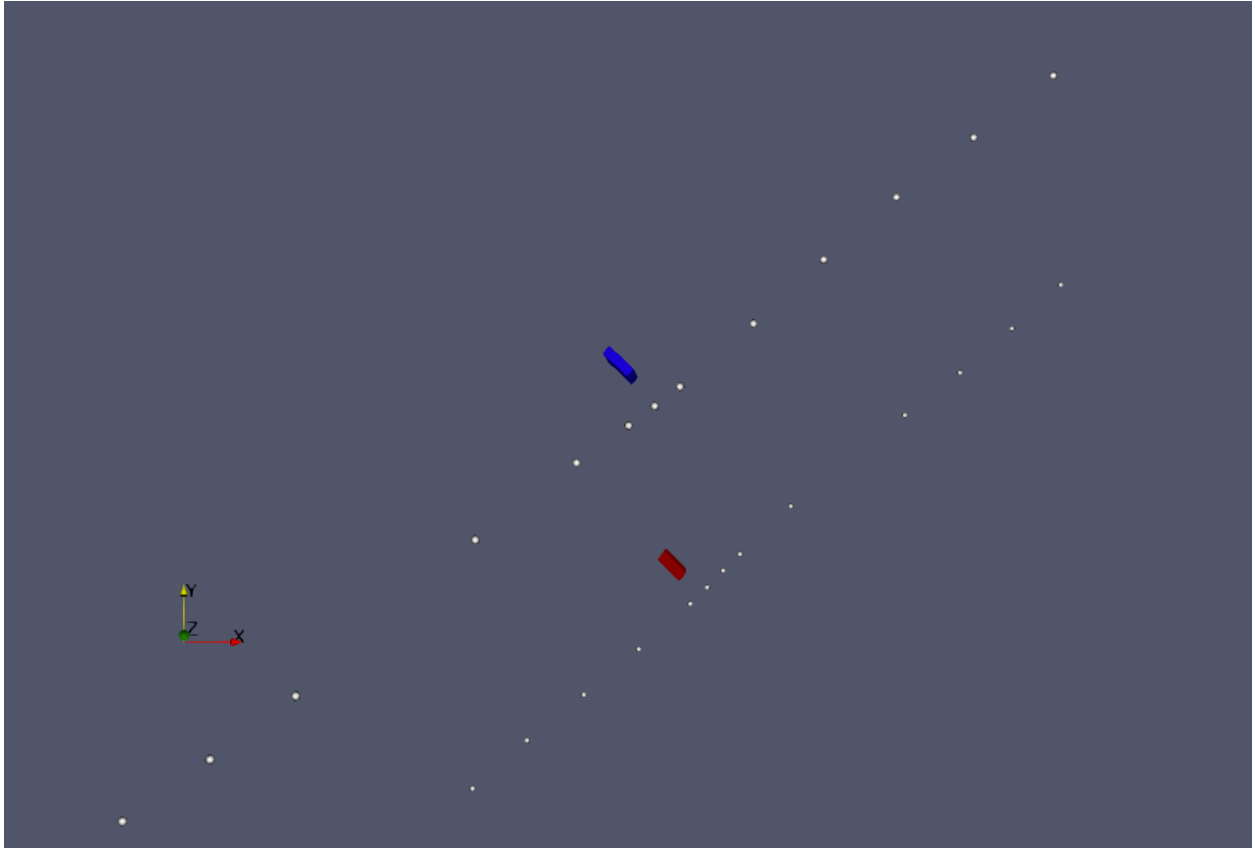


Figure 5.6: The locations of the dikes, of Line L10170 (upper line) and of Line L10180 (bottom line) for Model 5. The blue dike is Dike-1, whereas the red one is Dike-2.

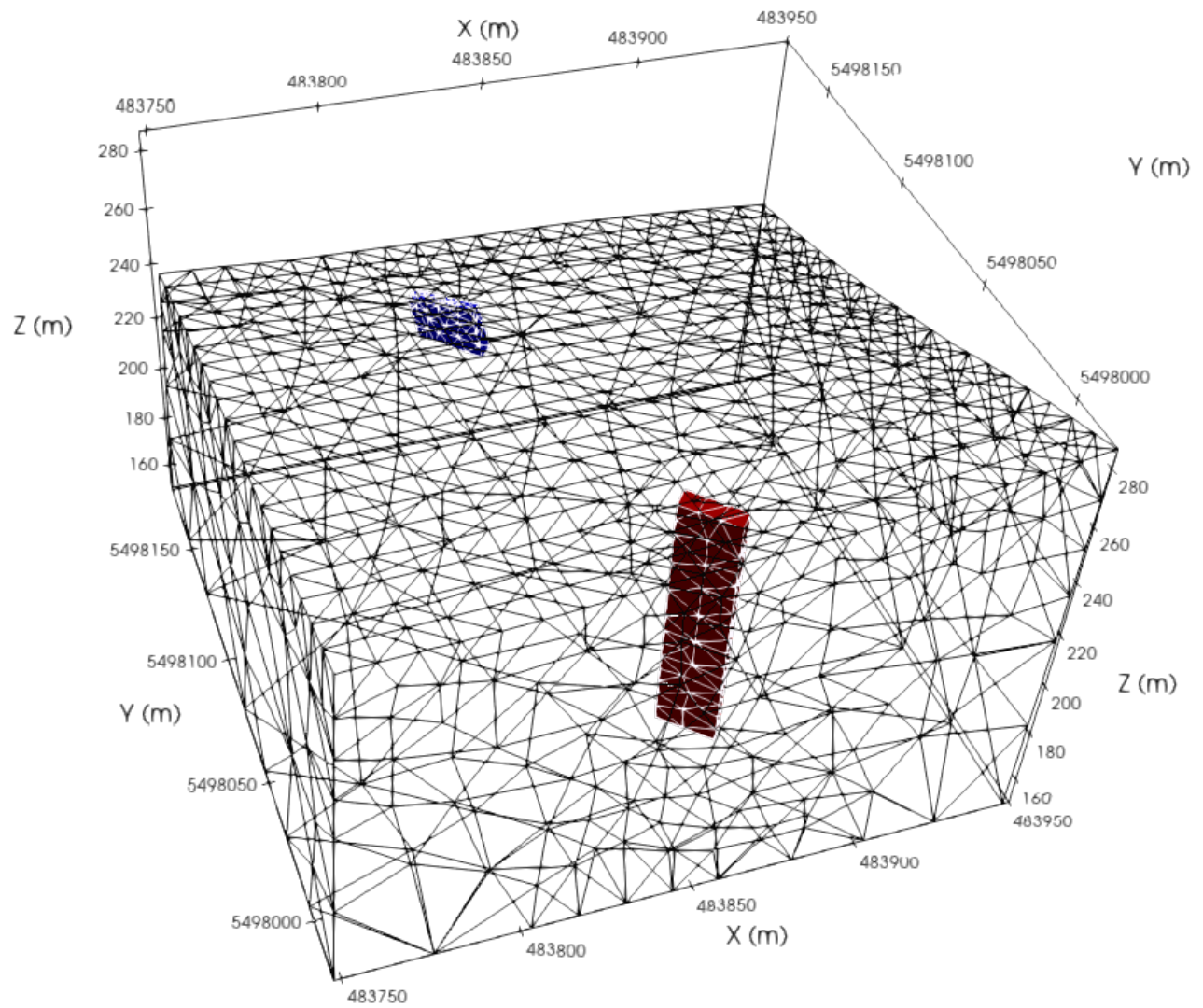


Figure 5.7: The 3D Earth model generated in FacetModeller and meshed by Tetgen for Model 5.

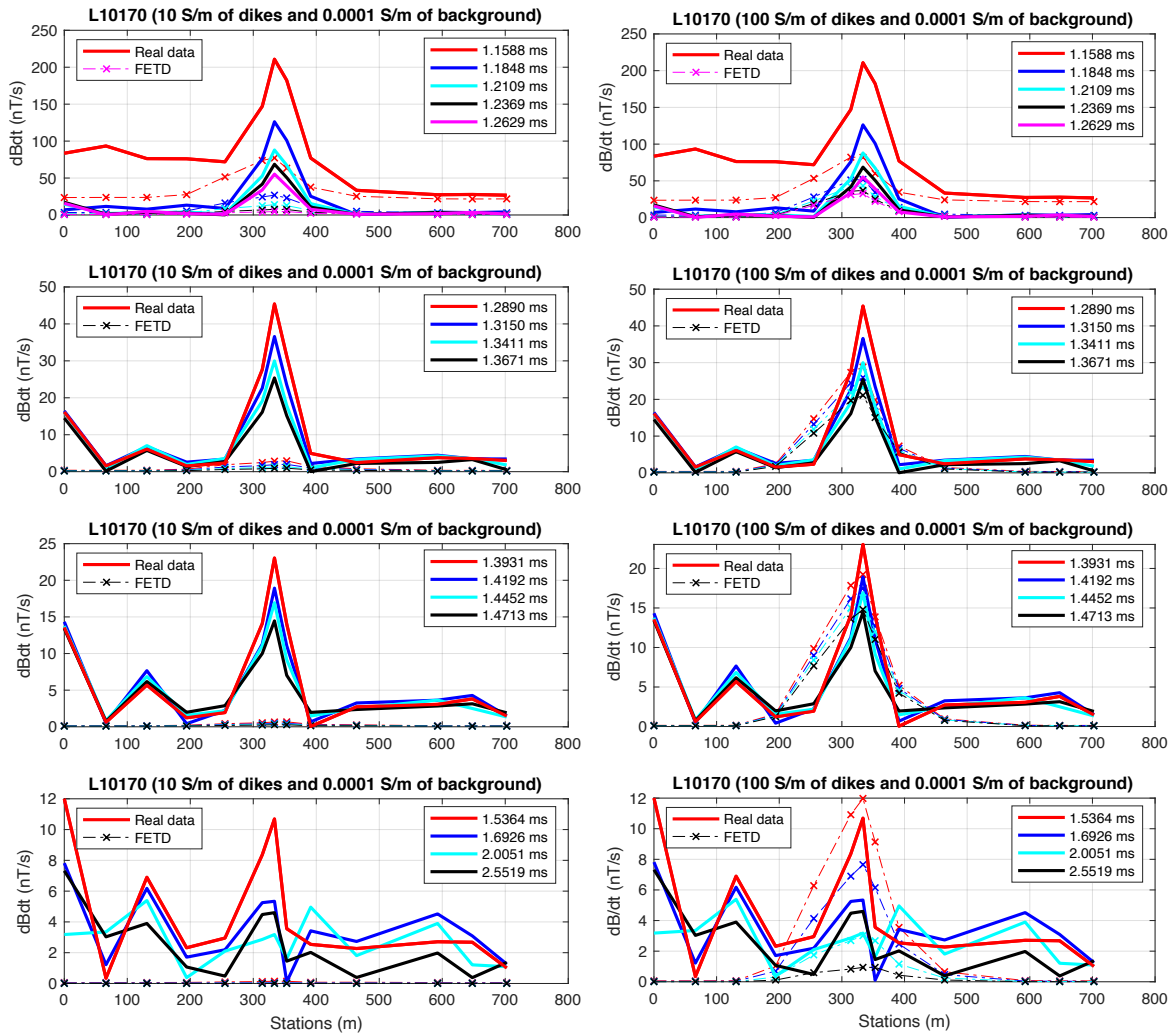


Figure 5.8: The EM response of Model 5 calculated using a conductivity of 10 S/m (on the left) and 100 S/m (on the right) for Dike-1. The solid lines show the real data and the dashed lines and crosses indicate the calculated data.

Figure 5.9 shows the EM response for the part of Line L10180 over the mineralized zone, showing only the same observation points that are used for the calculated data. The dike (Dike-2) created in this part of the survey area is dipping towards the northwest at 85 degrees and starting from 5 m below the surface.

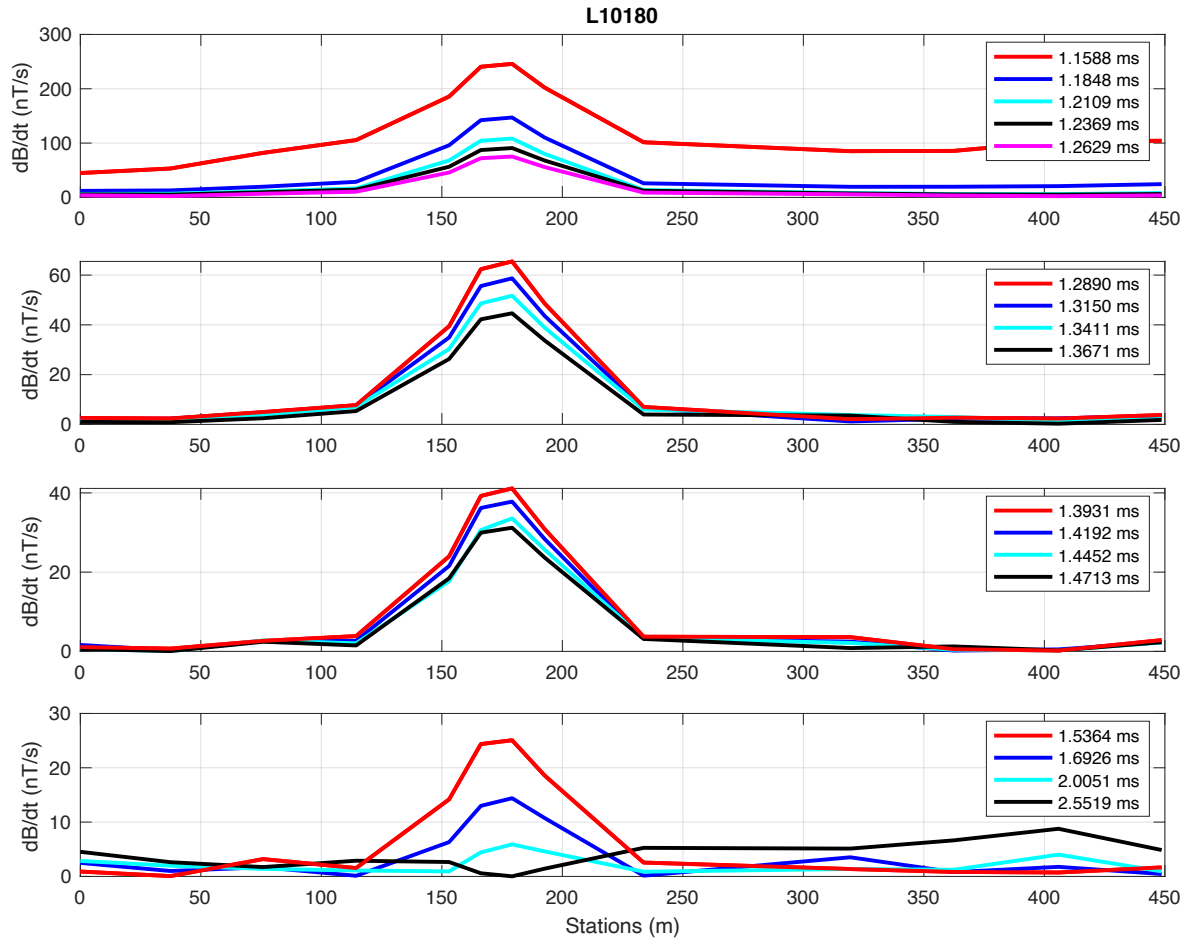


Figure 5.9: The z-component of the measured dB/dt data from Line L10180 at the observation points used for comparison with the numerical modeling.

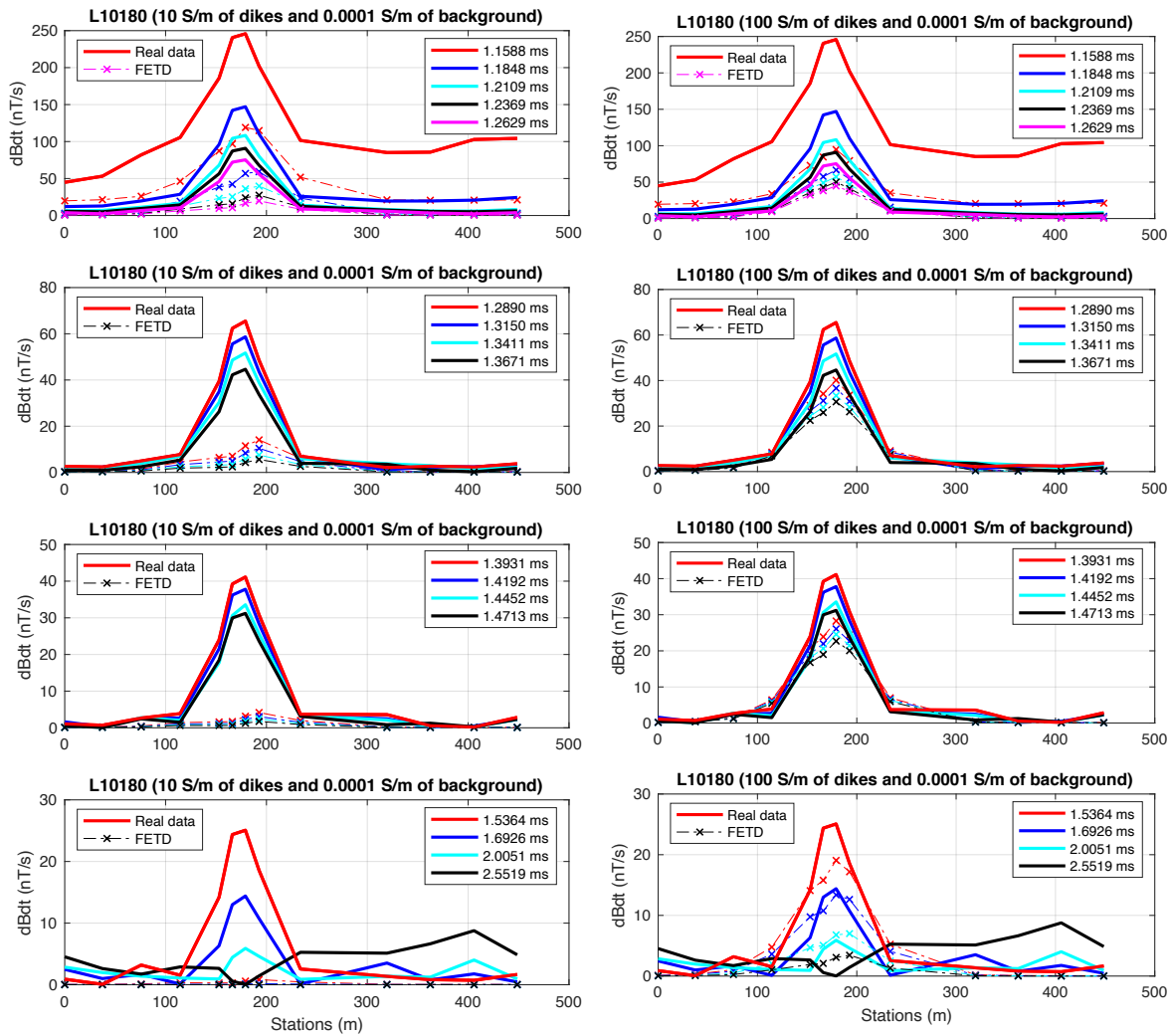


Figure 5.10: The EM response of Model 5 calculated using a conductivity of 10 S/m (on the left) and 100 S/m (on the right) for Dike-2. The solid lines show the real data and the dashed lines and crosses indicate the calculated data.

For Line L10180, as for Line 10170, the EM response for the dike with conductivity of 10 S/m did not generate a strong enough secondary magnetic field to match the real data, especially at the middle and late times. However, there is a reasonable match between the real data and the calculated data when a conductivity of 100 S/m is used for Dike-2. It should be noted that there are only three boreholes near the mineralization. Two of them (08TB-09 and 10, see Figure 2.8), which have different dips, intersect the sulfide zone, and thus give us information about the

minimum depth of Dike-2. The other borehole (08TB-12) passes into the subsurface roughly 40-50 m away from the sulfide mineralization. This means that it is not known how far the mineralization extends. Hence, it is of interest to test the length of mineralization in the area by using different Earth models.

Model 8

This model is created to see the result of extending the dikes in horizontal direction, passing beneath the survey lines L10170 and L10180. Figure 5.11 shows the location of the dikes and observation points while Figure 5.12 indicates the 3D Earth model generated in FacetModeller and meshed using an unstructured tetrahedral mesh by Tetgen. Dike-1 is extended to 70 m towards lines L10170 while Dike-2 is extended to 60 m towards line L10180. Figure 5.13 and Figure 5.14 show the calculated EM response in comparison with the real data for lines L10170 and L10180, respectively.

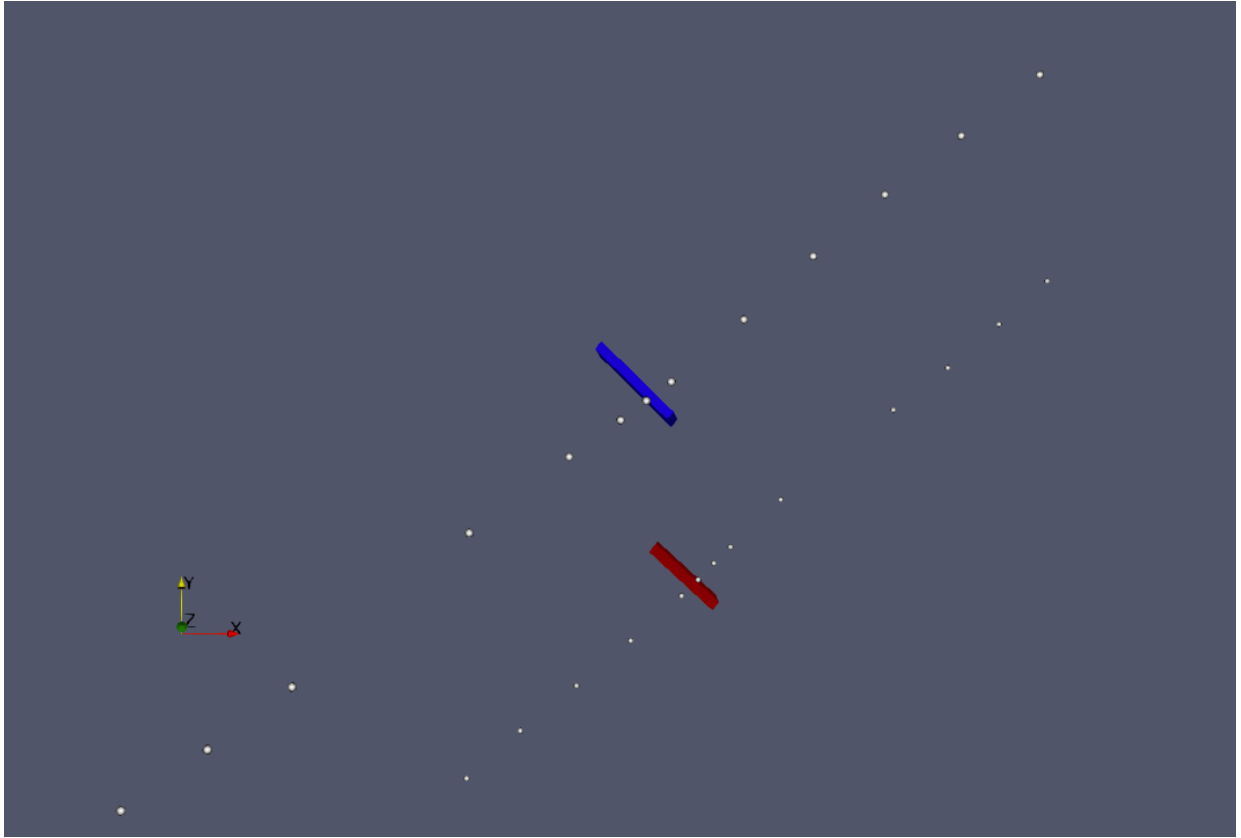


Figure 5.11: The locations of the dikes, and of Line L10170 (upper line) and of Line L10180 (bottom line) for Model 8. The blue dike is Dike-1, whereas the red one is Dike-2.

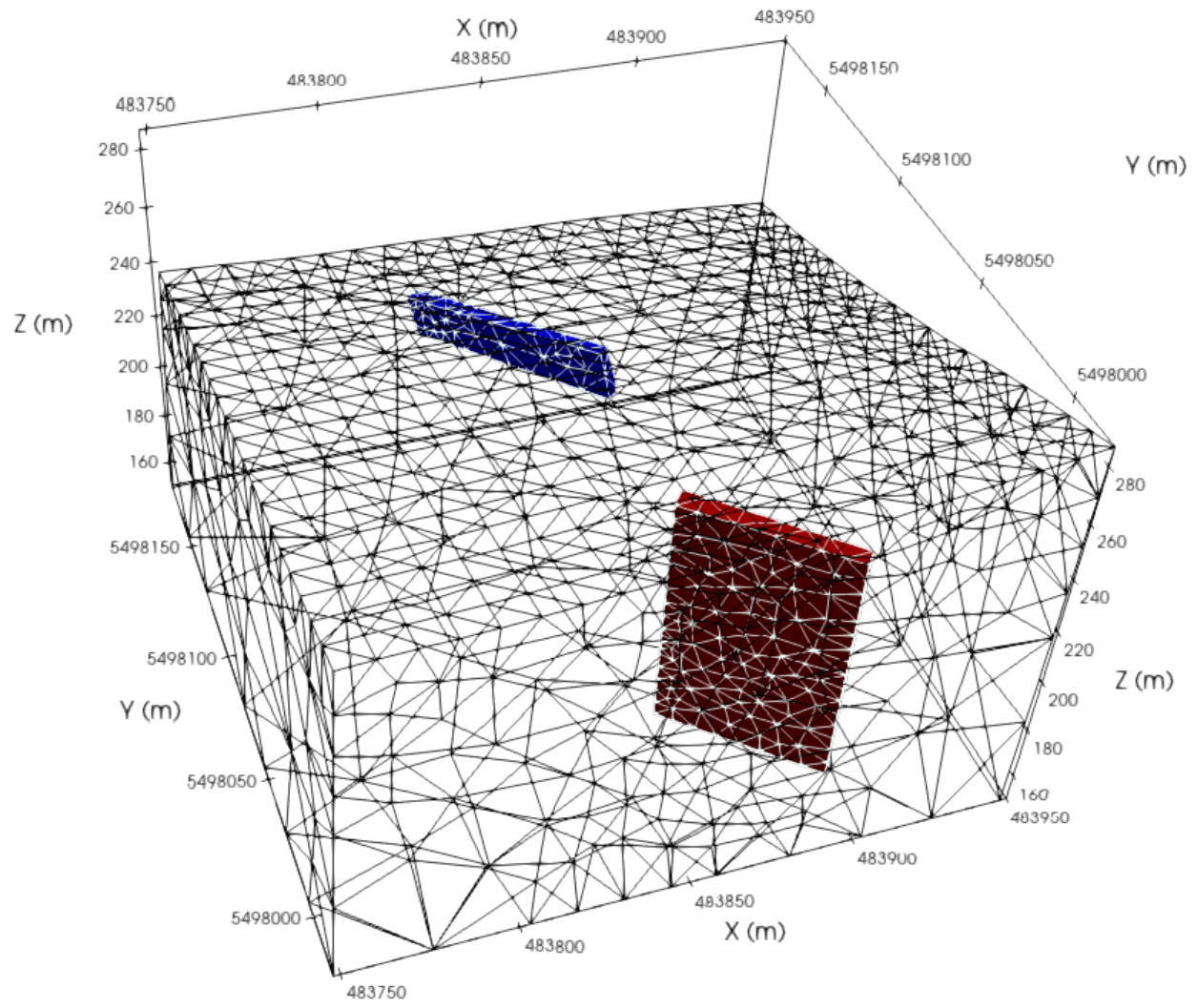


Figure 5.12: The 3D Earth model generated in FacetModeller and meshed by Tetgen for Model 8.

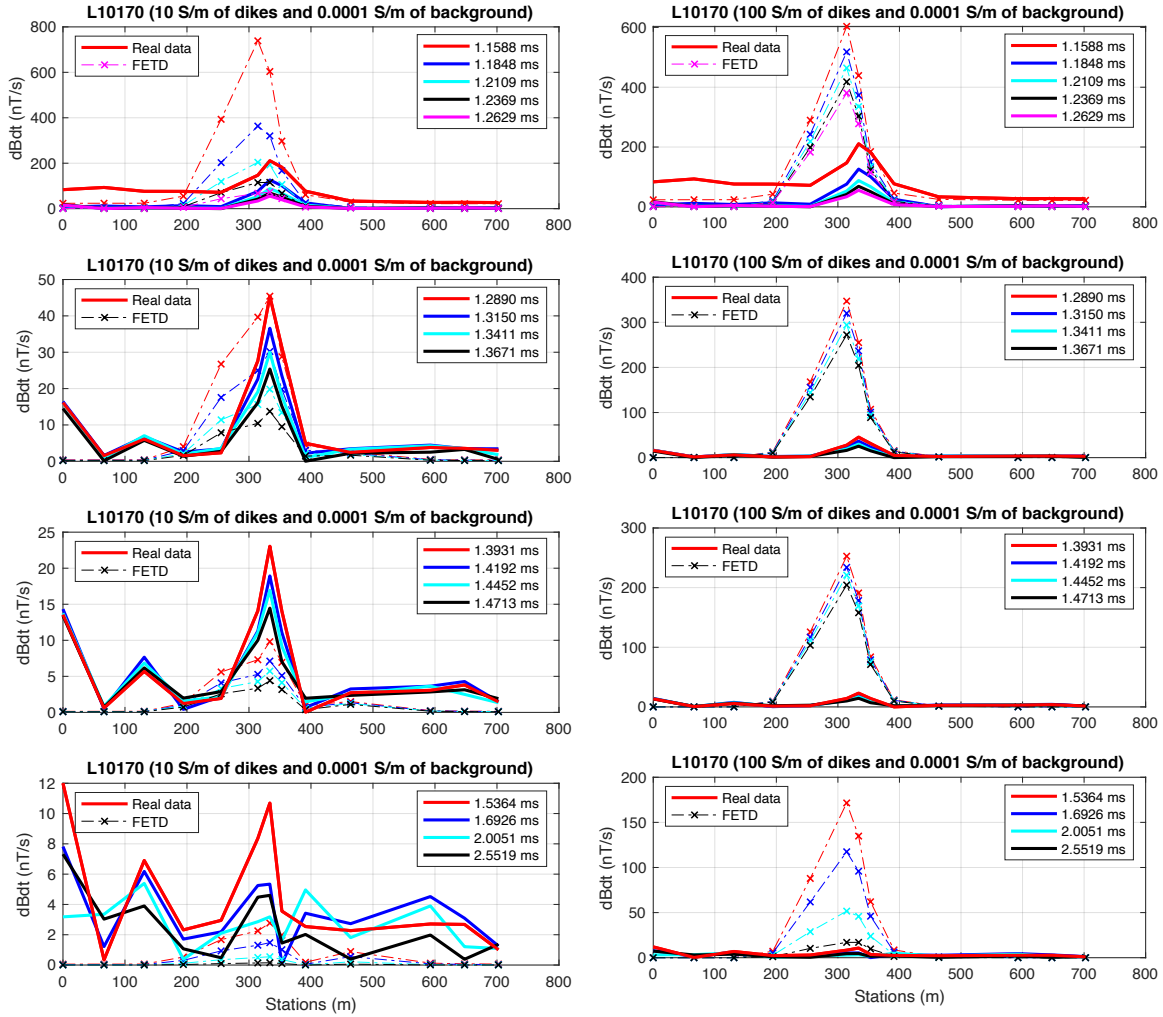


Figure 5.13: The EM response of Model 8 calculated using a conductivity of 10 S/m (on the left) and 100 S/m (on the right) for the Dike-1.

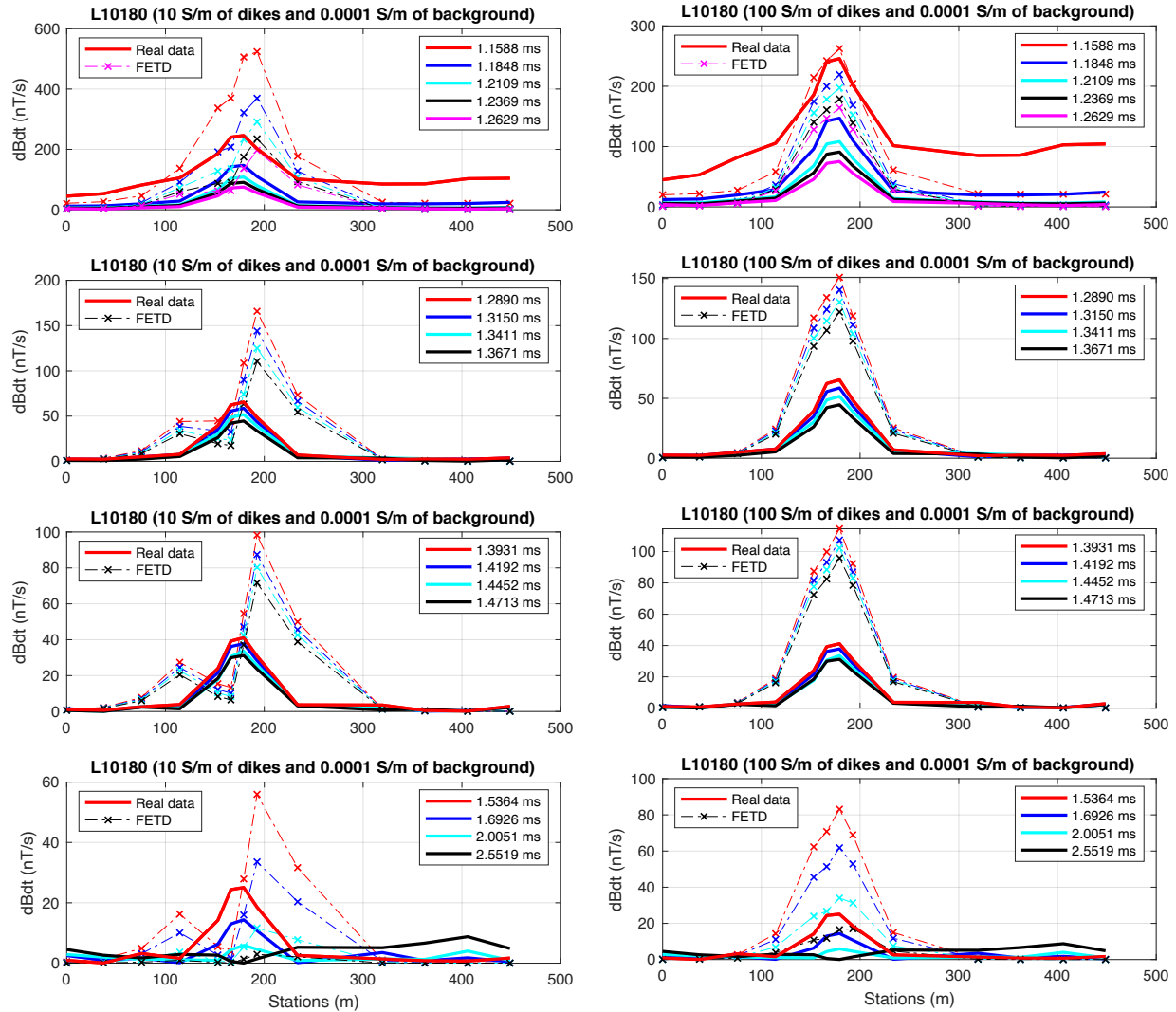


Figure 5.14: The EM response of Model 8 calculated using a conductivity of 10 S/m (on the left) and 100 S/m (on the right) for the Dike-2.

Recall that Dike-1 has a dip of 55 degrees towards Line L10170. Since the vertical extent of Dike-1 is relatively short and its horizontal extent is relatively long, for the ATEM system finds it hard to detect the dip of the conductive body. That is why the response in Figure 5.13 does not resemble the double peak response of a thin dipping sheet as shown in Figure 3.10; instead it looks

more like the single peak response of a thick vertical conductor as illustrated in Figure 3.9. Hence, this calculated EM response for Dike-1 does not match the real data for either conductivity value in Figure 5.13.

For the 3D forward modeling result of Dike-2 in Figure 5.14, an EM response that is similar to that of a dipping sheet is calculated when the dike has lower conductivity. However, when using a conductivity of 100 S/m for Dike-2, the EM response looks like the response of a thick vertical dike. The reason for this might be that for the time-domain method at higher conductivity, induced currents do not penetrate to the depths of the conductor but remain within the top of the dike. Note that the eddy currents spend more time in the shallow part of conductors, and decay slower in regions of high conductivity than in regions of lower conductivity.

To sum up, we are able to see the EM response of a dipping conductor beneath Line L10180 when 10 S/m is used for the dike since the conductivity of Dike-2 is small enough to enable the induced currents to move to greater depths in the conductor. This could be the explanation for the difference between the responses of Dike-2 when conductivities of 10 S/m and 100 S/m are used.

Model 10

This model is designed to show what response might be observed if Dike-1 extended to greater depths. As illustrated in Figure 2.9, there is a mafic dike where the sulfide zone ends, and there is no drill information to show whether the sulfide zone continues to depth or not. It is possible that the mafic dike cuts the sulfide in two. To investigate this, Dike-1 is extended by 30 m towards Line L10170. Figure 5.15 shows the location of the dikes and the observation points while Figure 5.16 indicates the 3D Earth model generated in FacetModeller and meshed using unstructured tetrahedral meshes by Tetgen. Furthermore, Figure 5.17 and Figure 5.18 show the calculated EM

response in comparison with the real data for Lines L10170 and L10180, respectively. Once again, the EM response of this model did not match the real data for both conductivities used for Dike-1 (Figure 5.17). It can therefore be said that the sulfide does not extend towards Line L10170, which is towards the southeast of the area.

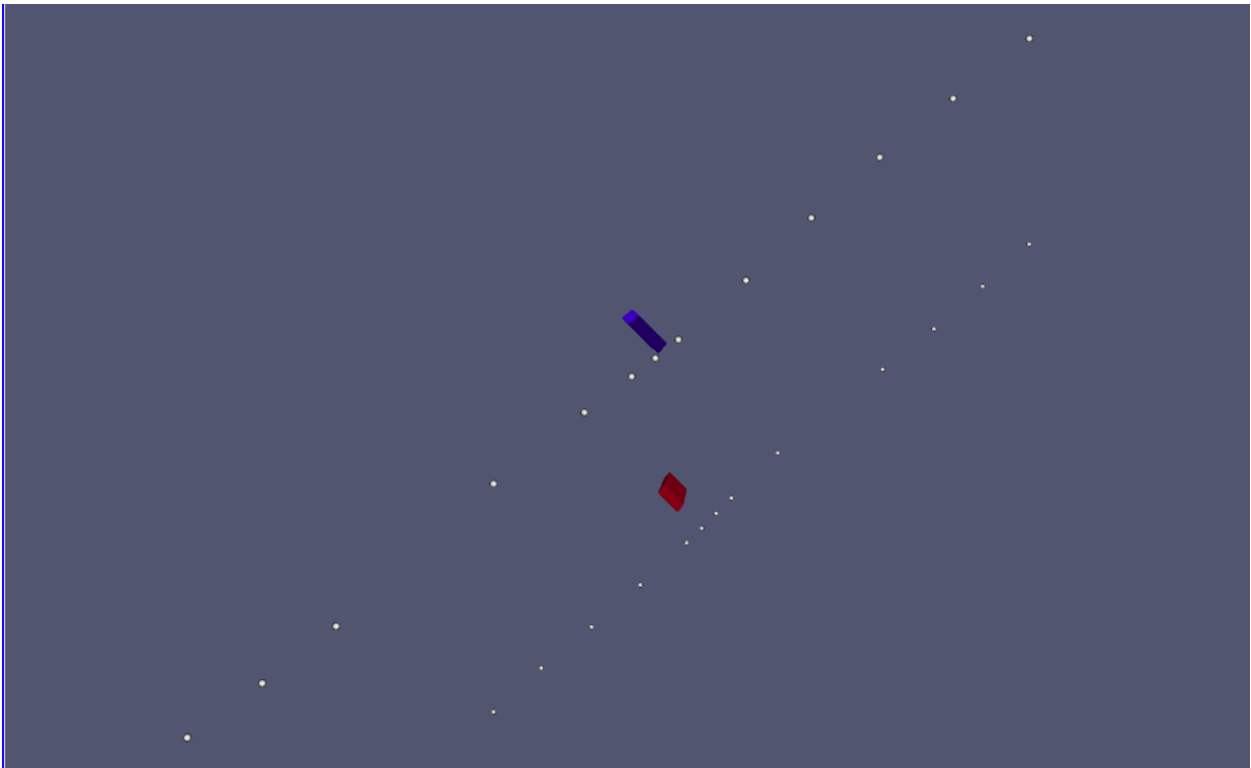


Figure 5.15: The locations of the dikes, and of Line L10170 (upper line) and of Line L10180 (bottom line) for Model 10. The blue dike is Dike-1, whereas the red one is Dike-2.

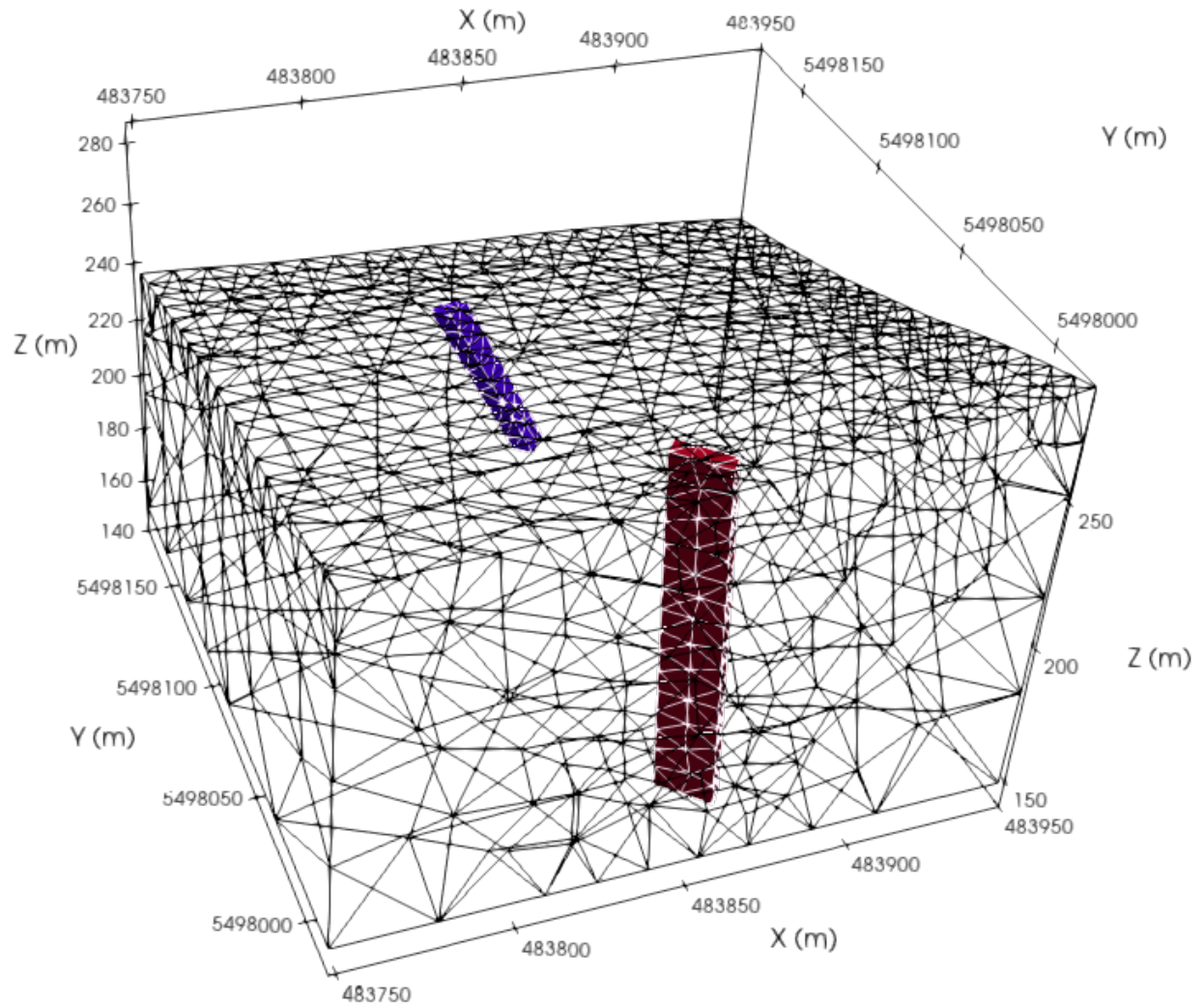


Figure 5.16: The 3D Earth model generated in FacetModeller and meshed by Tetgen for Model 10.

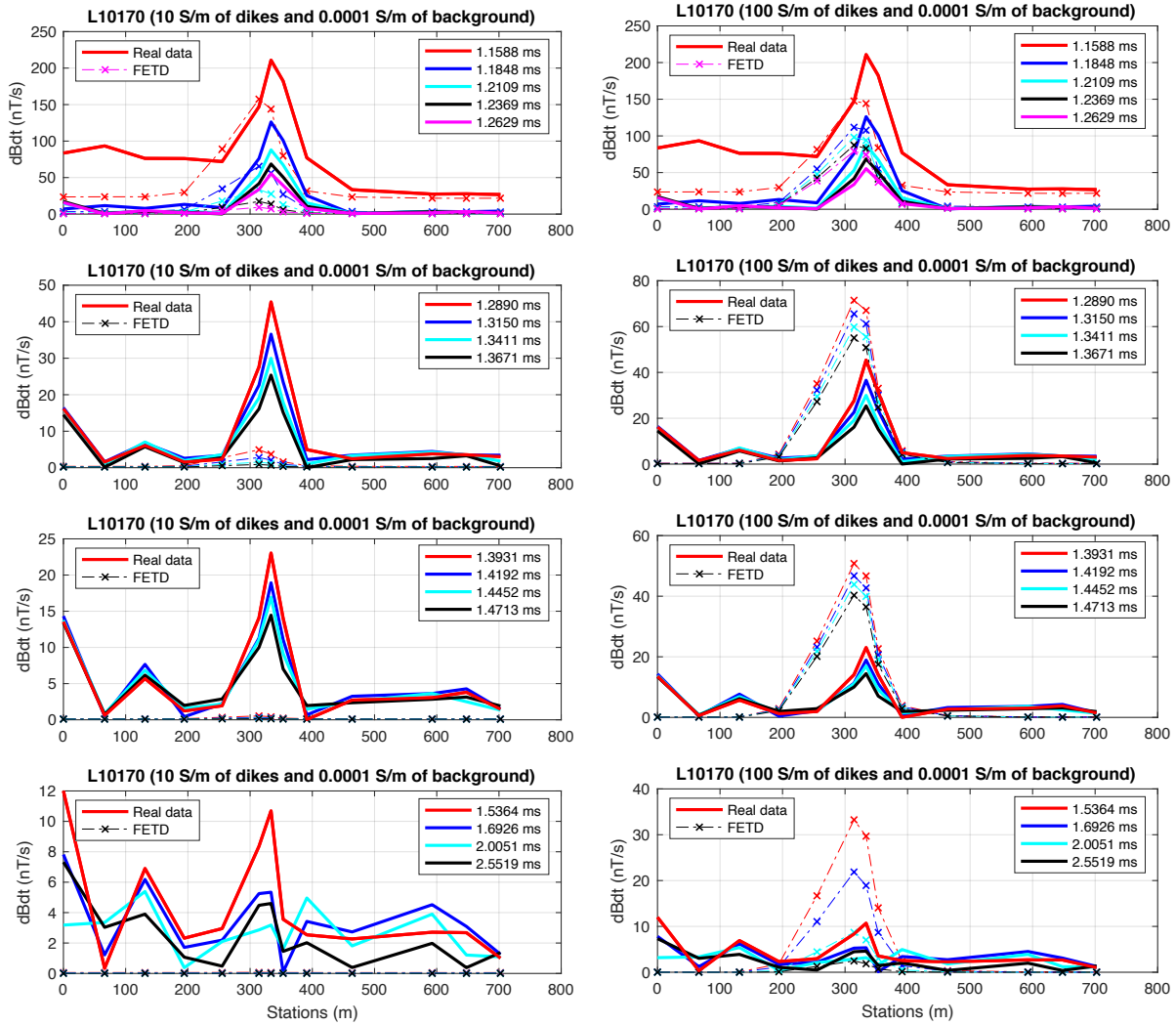


Figure 5.17: The EM responses of Model 10 calculated using a conductivity of 10 S/m (on the left) and 100 S/m (on the right) for the Dike-1.

As for the previous example, Dike-2 is extended in depth by 30 m in order to see whether the result could match the real data or not, and also to check if there is any difference between the calculated data for both the 90-m-deep dike and the 120-m-deep one (see Figure 5.19).

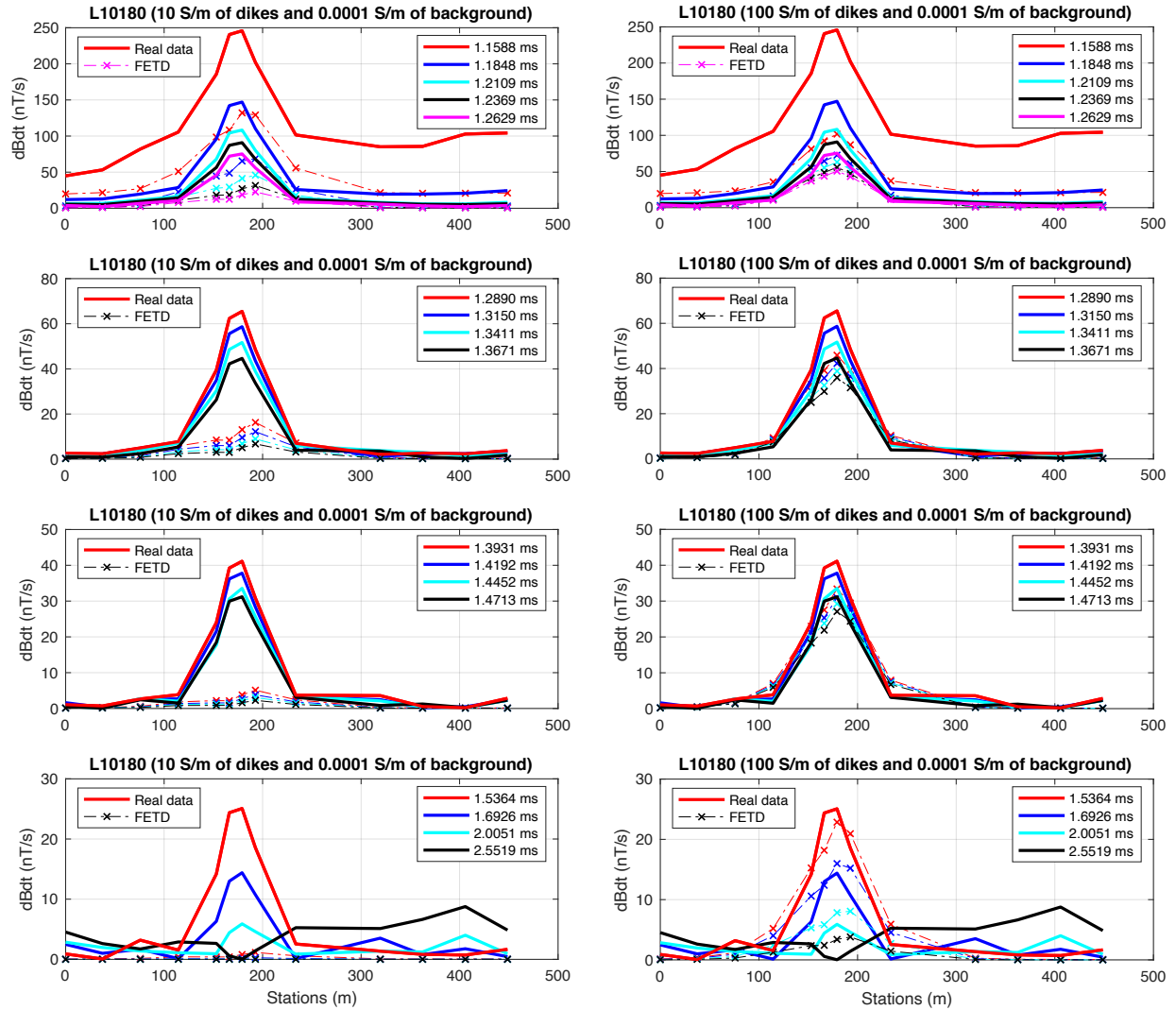


Figure 5.18: The EM responses of Model 10 calculated using a conductivity of 10 S/m (on the left) and 100 S/m (on the right) for Dike-2 being a 120 m vertical extent.

For comparison, the EM responses for Dike-2 having a 90 m vertical extent and having a 120 m vertical extent are presented in Figure 5.19. It seems that the larger vertical extent produces a slightly better response, which can match the real data, than the shorter dike, especially from middle times to late times. This suggests that Dike-2 might extend deeper than detected from the boreholes.

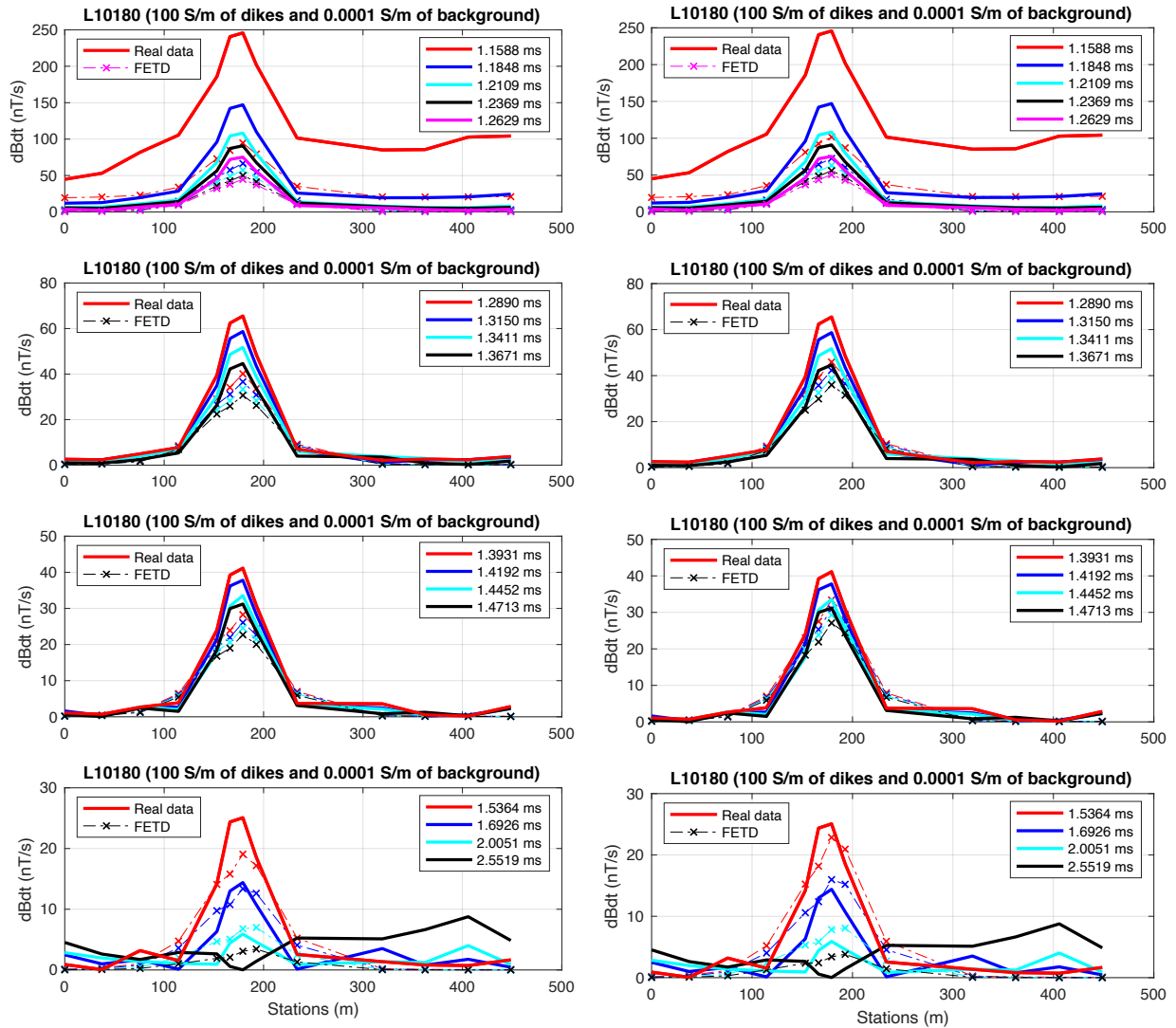


Figure 5.19: The EM response (on the left panel) calculated for the dike having a conductivity of 100 S/m and a 90 m vertical extent (Model 5). The EM response (on the right panel) calculated for the dike having a conductivity of 100 S/m and 120 m a vertical extent (Model 10).

The quality of the match between the real data and the measured data can be improved by trying more different models having different thickness, dip and length of the dikes besides it takes a considerable time and costs. However, the results of the models used for the forward modeling can provide noteworthy information about the length, dip, and depth of the dikes given visually matching the real data and the measured data. This information could have saved costs in the drilling program.

Chapter 6

6. Summary and Conclusions

The Taylor Brook area is situated within the Long-Range Gneiss Complex of western Newfoundland. The project area is underlain by mid-Proterozoic gneisses that are intruded by mafic and ultramafic intrusive rocks. After sulfide mineralization was discovered by a geologist, Jerry Layden, in the Taylor Brook area, the area became a prospective mining area, with geological and geophysical surveys being carried out.

An airborne TEM and magnetic survey was conducted over the survey area in 2006. Forty-five profiles were flown with a spacing of 100 m and for a total line-kilometres of 148.2 km. Seventeen boreholes were drilled based on the responses measured by the airborne TEM survey.

In this thesis, 1D inversion was applied to part of the dataset over an area of interest where a significant EM response was measured, and it was seen that the inversion results of the observation points on the profiles close to the conductive bodies have better fits than the ones that are far from the target. Also, it was seen that the bedrock within the area of interest is highly resistive and this is consistent with the regional geological setting. The 1D inversion results and information from the boreholes were used to guide the building of candidate 3D Earth models that were then used for 3D FETD forward modeling. Based on the result of inversion and the borehole information, the measured EM anomalies were associated with two dikes, and modeling was carried out to

constrain the properties of these dikes. This was done by trial-and-error models of the dikes with different dimensions and conductivities. During the forward modeling process, a machine of Intel Xeon E5 2650 v4 processors running at 2.2 GHz and with 256 GB RAM is used and a run for a profile having 13 observations take about 7-8 hours.

For Dike-1, the results of the FETD forward modeling obtained from candidate 3D Earth models shows that there might be a thicker and longer sulfide zone having a conductivity of 100 S/m (Model 5) than is sampled by the boreholes. This is because boreholes are drilled only on the northeast side of the mineralization area (the Layden showing) and the results of forward modeling for a thinner and shorter dike (Model 1) do not match the observations.

For Dike-2, the EM responses that were obtained from Model 5 can match the measured data with a conductivity of 100 S/m and, from Model 10, which has the same conductivity and a greater vertical extent for the conductor (30 metres longer).

From the application of 1D inversion and FETD forward-modeling, it can be said that the conductor targets in the survey area may be thicker and longer than indicated by the limited information from the boreholes around the targets. However, the shapes of the conductor are still not completely understood. For further geophysical and geological work, ground-based time-domain method can be applied with a small-scale over mineralization to have better resolution, and applied additional drill holes to the west part of the mineralization can be applied.

Bibliography

- Abramowitz, M., & Stegun, I. A. (1965). Handbook of mathematical functions: with formulas, graphs, and mathematical tables (Vol. 55)., 1046 p. Courier Corporation.
- Börner, R. U. (2010). Numerical modelling in geo-electromagnetics: advances and challenges. *Surveys in Geophysics*, 31(2), 225-245.
- Christiansen, A. V., Auken, E., & Sørensen, K. (2006). The transient electromagnetic method. In *Groundwater geophysics* (pp. 179-225). Springer, Berlin, Heidelberg.
- Churchill, R. (2007). Eighth year assessment report on an airborne geophysical survey covering mineral licence 7715m, Hampden Area, western Newfoundland, NTS Sheet 12H11.
- Churchill, R. (2011). First, fourth & twelfth year assessment report documenting airborne geophysical surveys over Taylor Brook property comprised of map-staked licenses 007715M, 013125M, 0167741M, 016742M, 016744M, 016977M, 016978M, 016979M, 016980M & 017925M, Hampden Area, Newfoundland, NTS Sheet 12H/11.
- Denghai, B. A. I., & Meju, M. A. (2000). All-time apparent resistivity for transient electromagnetic method. In *Proceedings of the 15th Workshop on Electromagnetic Induction in the Earth*, Cabo Frio, Brazil (Vol. 33).

- Ebert, S. (2008). 10th year assessment report on diamond drilling and downhole geophysics covering mineral licences 7715m, and 13125m Hampden area, western Newfoundland, nts 12h11. Altius Resources Inc. (2008).
- Ekblom, H. (1973). Calculation of linear best L_p -approximations. BIT Numerical Mathematics, 13(3), 292-300.
- Ekblom, H. (1987). The L_1 -estimate as limiting case of an L_p - or Huber- estimate, in Statistical Data Analysis Based on the L_1 -Norm and Related Methods, pp. 109–116, ed. Dodge, Y., Elsevier, Amsterdam.
- Farquharson, C. G., & Oldenburg, D. W. (1993). Inversion of time-domain electromagnetic data for a horizontally layered Earth. Geophysical Journal International, 114(3), 433-442.
- Farquharson, C. G., Oldenburg, D. W., & Routh, P. S. (2003). Simultaneous 1D inversion of loop–loop electromagnetic data for magnetic susceptibility and electrical conductivity. Geophysics, 68(6), 1857-1869.
- Fitzpatrick, D. (2000). First year assessment report on prospecting, geology, linecutting, geophysics & trenching conducted on map staked licences 6339M, 6943M, 6992M, 6993M, 6994M, 6995M, 6996M & 6997M, Taylor Brook Property, White Bay Area, Northcentral Newfoundland, NTS Sheet 12H/11.
- Fountain, D. (1998). Airborne electromagnetic systems-50 years of development. Exploration Geophysics, 29(2), 1-11.
- Fountain, D., Smith, R., Payne, T., & Limieux, J. (2005). A helicopter time-domain EM system applied to mineral exploration: System and data. First Break, 23(11).
- Fraser, D. C. (1969). Contouring of VLF-EM data. Geophysics, 34(6), 958-967.

- Heaman, L. M., Erdmer, P., & Owen, J. V. (2002). U–Pb geochronologic constraints on the crustal evolution of the Long Range Inlier, Newfoundland. *Canadian Journal of Earth Sciences*, 39(5), 845-865.
- Jahandari, H., & Farquharson, C. G. (2014). A finite-volume solution to the geophysical electromagnetic forward problem using unstructured grids. *Geophysics*, 79(6), E287-E302.
- Jefferson, C. W., D. J. Thomas, S. S. Gandhi, P. Ramaekers, G. Delaney, D. Brisbin, C. Cutts, D. Quirt, P. Portella, and R. A. Olson, (2007). Unconformity-associated uranium deposits of the Athabasca Basin, Saskatchewan and Alberta, Mineral deposits of Canada: A synthesis of major deposit- types, district metallogeny, the evolution of geological provinces, and exploration methods: Geological Association of Canada, Mineral Deposits Division, Special publication no. 5, 273–305.
- Jin, J. M. (2011), *Theory and computation of electromagnetic fields*. John Wiley & Sons
- Jin, J. M. (2014), *The finite element method in electromagnetics*, 3rd ed.: Wiley-IEEE Press.
- Kaufman, A. A., & Keller, G. V. (1983), *The magnetotelluric sounding method*, Elsevier, pp 595.
- Korus, J. (2018). Combining hydraulic head analysis with airborne electromagnetics to detect and map impermeable aquifer boundaries. *Water*, 10(8), 975.
- Lelièvre, P., Carter-McAuslan, A., Farquharson, C., & Hurich, C. (2012). Unified geophysical and geological 3D Earth models. *The Leading Edge*, 31(3), 322-328.

- Li, J., Lu, X., Farquharson, C. G., & Hu, X. (2018). A finite-element time-domain forward solver for electromagnetic methods with complex-shaped loop sources. *Geophysics*, 83(3), E117-E132.
- Lu, X., & Farquharson, C. G. (2020). 3D finite-volume time-domain modeling of geophysical electromagnetic data on unstructured grids using potentials. *Geophysics*, 85(6), 1-69.
- Munkholm, M. S., & Auken, E. (1996). Electromagnetic noise contamination on transient electromagnetic soundings in culturally disturbed environments. *Journal of Environmental and Engineering Geophysics*, 1(2), 119-127.
- Macnae, J. C., Smith, R., Polzer, B. D., Lamontagne, Y., & Klinkert, P. S. (1991). Conductivity-depth imaging of airborne electromagnetic step-response data. *Geophysics*, 56(1), 102-114.
- O'Reilly, D., & Hill K., & Churchill, R. (2012) The 2nd & 5th year assessment report on prospecting, rock sampling and soil sampling on the Taylor Brook project, map-staked licenses 013125m, 019351m & 019356m, western newfoundland, NTS sheet 12H/11. Altius Resources Inc.
- Owen, J. V. (1986). Precambrian and Paleozoic Metamorphism in the Long Range Inlier: western Newfoundland. Geological Survey of Canada.
- Owen, J. V., & Erdmer, P. (1989). Metamorphic geology and regional geothermobarometry of a Grenvillian massif: the Long Range Inlier, Newfoundland. *Precambrian Research*, 43(1-2), 79-100.

- Palacky, G. J., & West, G. F. (1973). Quantitative interpretation of INPUT AEM measurements. *Geophysics*, 38(6), 1145-1158.
- Palacky, G. J. (1988). Resistivity characteristics of geologic targets. *Electromagnetic methods in applied geophysics*, 1, 53-129.
- Si, H., 2015, TetGen, a quality tetrahedral mesh generator: *AMC Transactions on Mathematical Software*, 41, 11.
- Smith, R. S., Annan, A. P., Lemieux, J., & Pedersen, R. N. (1996). Application of a modified GEOTEM® system to reconnaissance exploration for kimberlites in the Point Lake area, NWT, Canada. *Geophysics*, 61(1), 82-92.
- Spies, B. R., & Eggers, D. E. (1986). The use and misuse of apparent resistivity in electromagnetic methods. *Geophysics*, 51(7), 1462-1471.
- Spies, B. R., & Frischknecht, F. C. (1991). Electromagnetic sounding. *Electromagnetic Methods in Applied Geophysics*, vol 2 (Part A), 285-426, Society of Exploration Geophysicists.
- Sheng, Y. (1986). A single apparent resistivity expression for long-offset transient electromagnetics. *Geophysics*, 51(6), 1291-1297.
- Türkoğlu, E., 2003, Joint inversion of time-domain EM data and direct current resistivity data: Thesis of Master, Istanbul Technical University, Faculty of Science, İstanbul.
- Viezzoli, A., Christiansen, A. V., Auken, E., & Sørensen, K. (2008). Quasi-3D modeling of airborne TEM data by spatially constrained inversion. *Geophysics*, 73(3), F105-F113.

Wait, J. R. (1951). The magnetic dipole over the horizontally stratified earth. *Canadian Journal of Physics*, 29(6), 577-592.

Ward, S. H., & Hohmann, G. W. (1988). Electromagnetic theory for geophysical applications. In *Electromagnetic Methods in Applied Geophysics*, vol 1, Theory, 130-311, Society of Exploration Geophysicists.

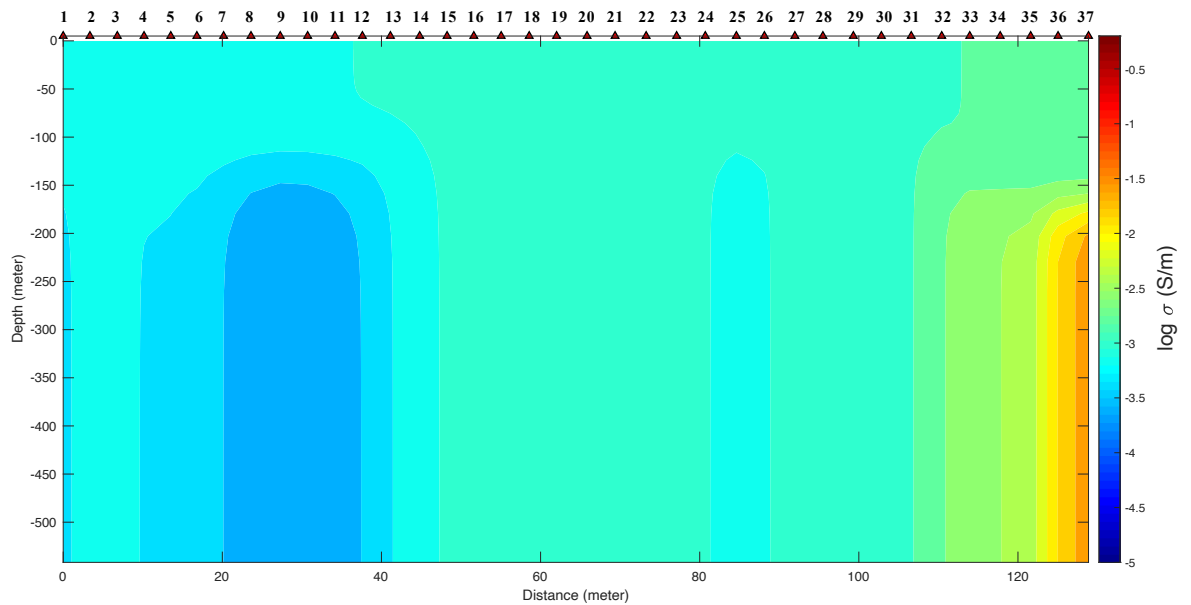
Yang, D., & Oldenburg, D. W. (2012). Three-dimensional inversion of airborne time-domain electromagnetic data with applications to a porphyry deposit. *Geophysics*, 77(2), B23-B34.

University of British Columbia, 2005, EM1DTM: A program library for forward modeling and inversion of time domain electromagnetic data over 1D structures, version 1.0: University of British Columbia, Geophysical Inversion Facility.

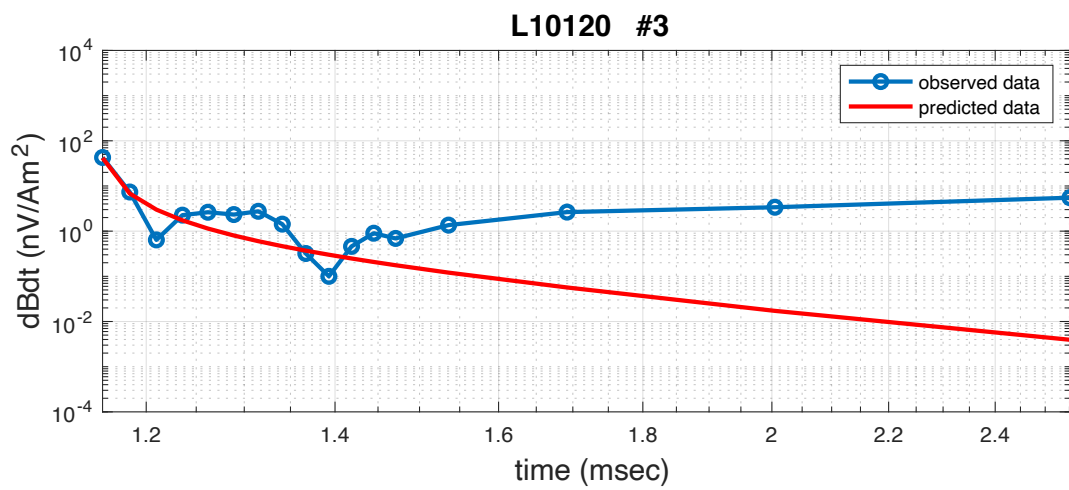
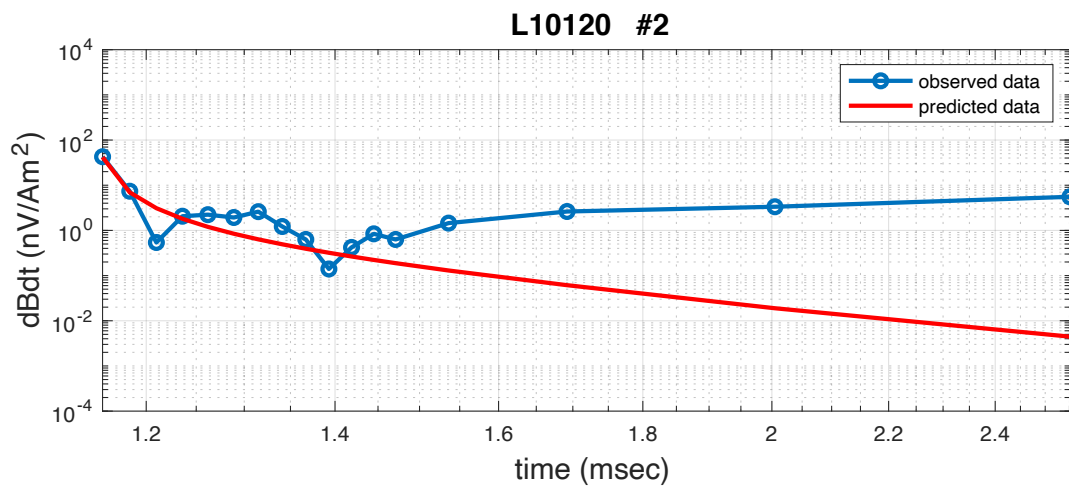
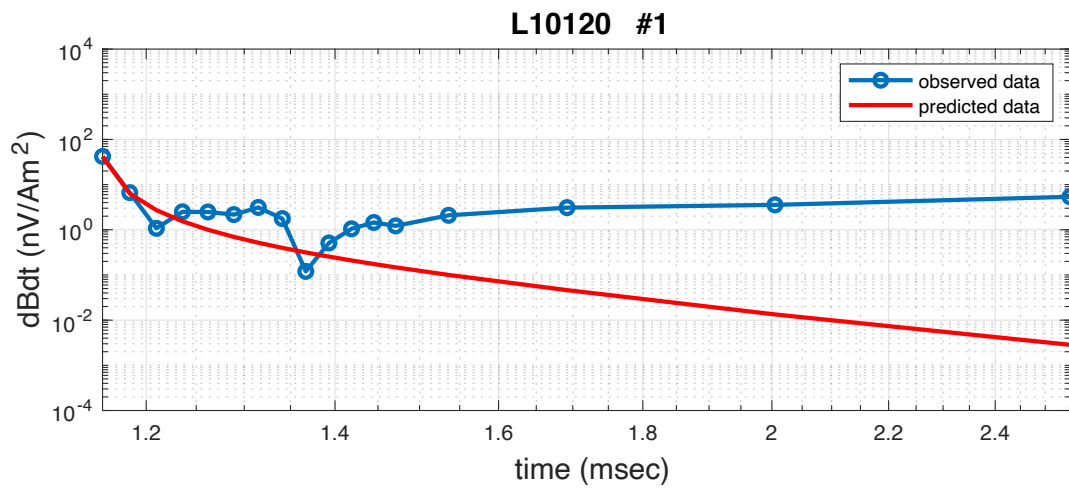
Appendix

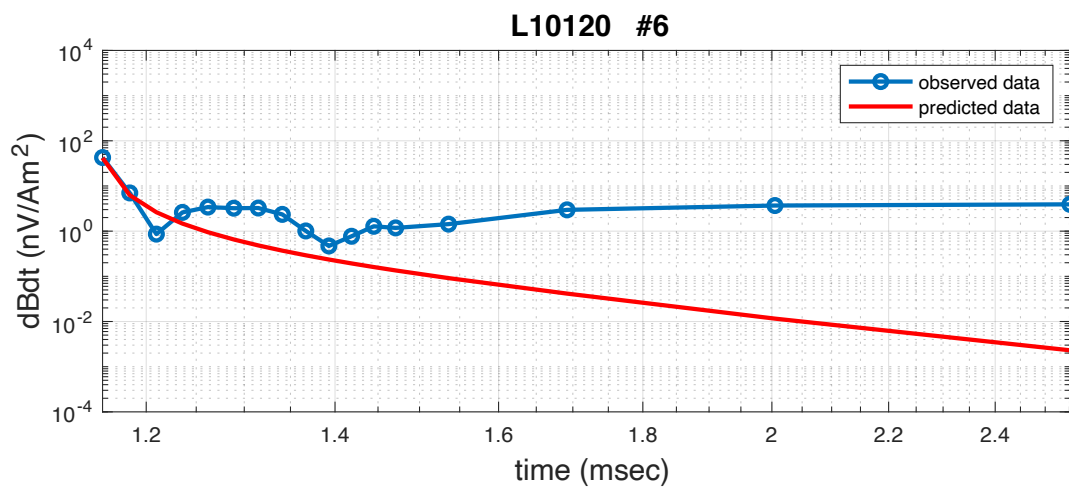
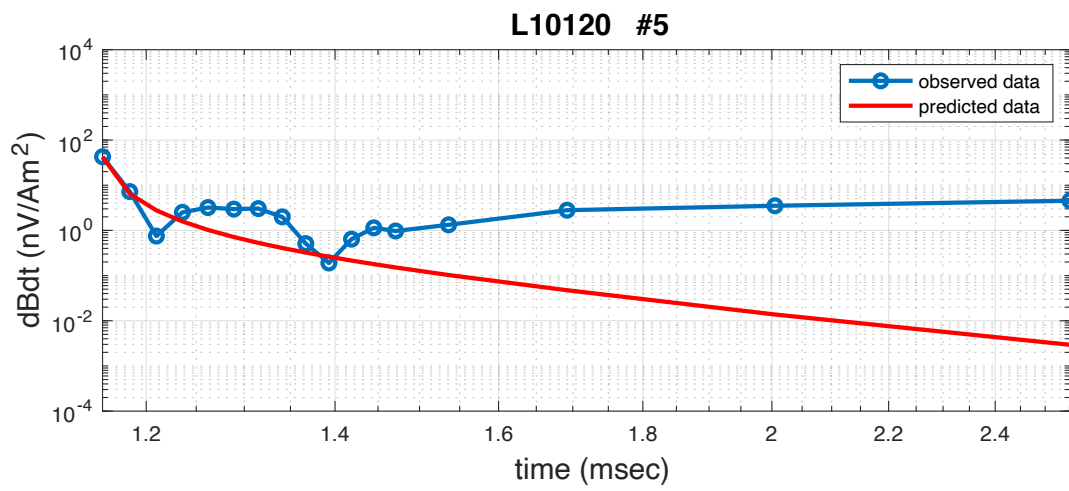
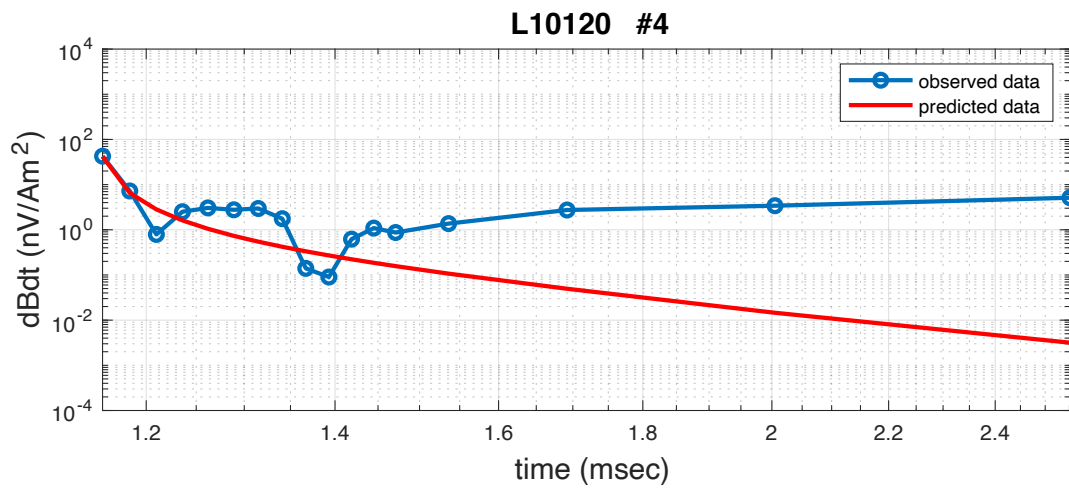
A. Inversion (EM1DTM) Results

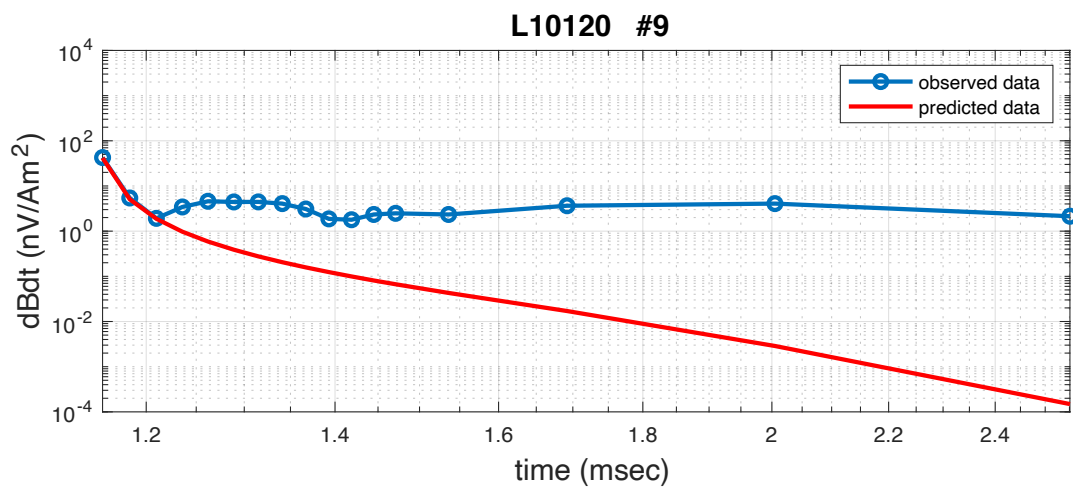
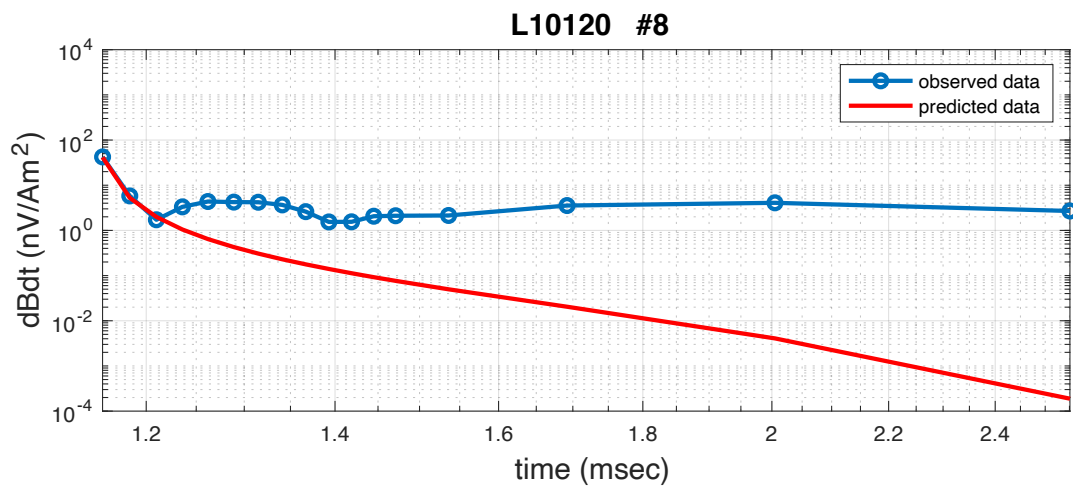
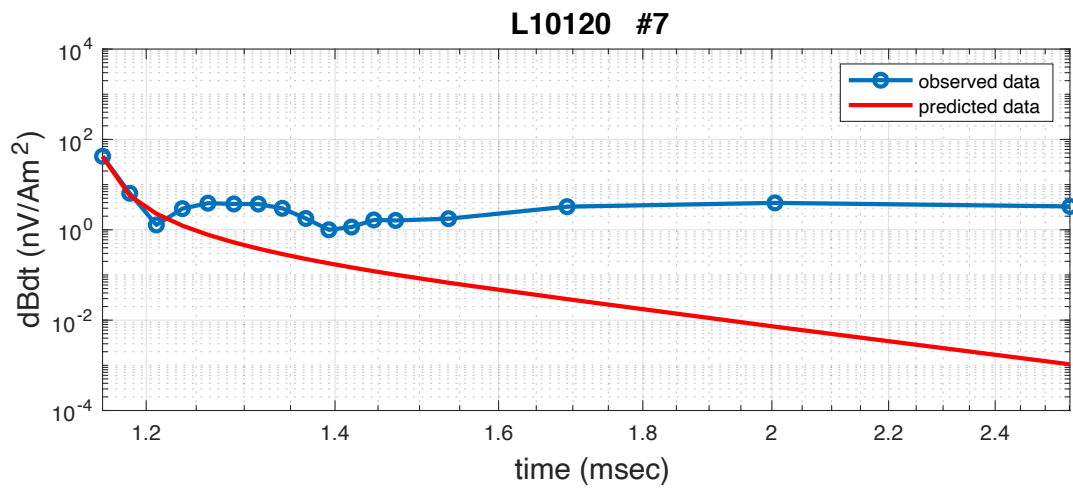
L10120

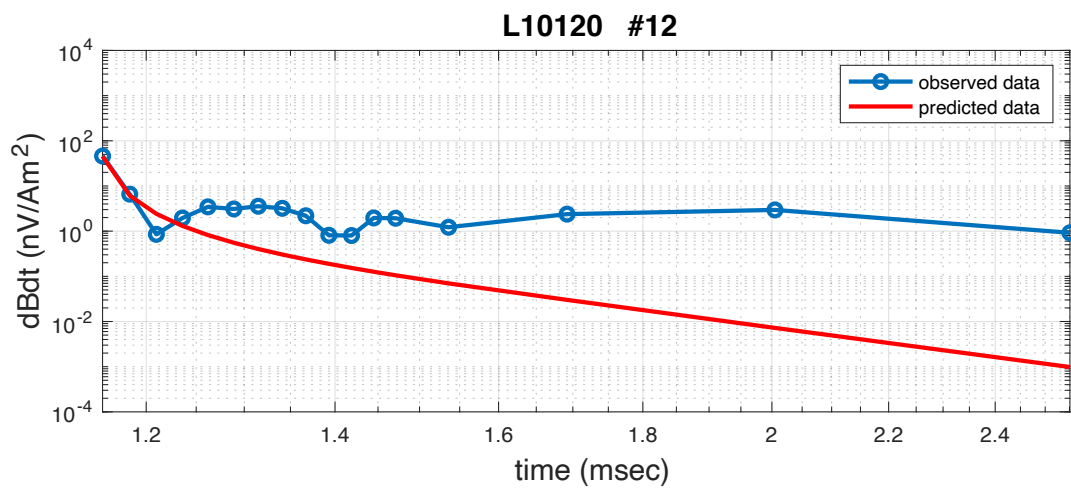
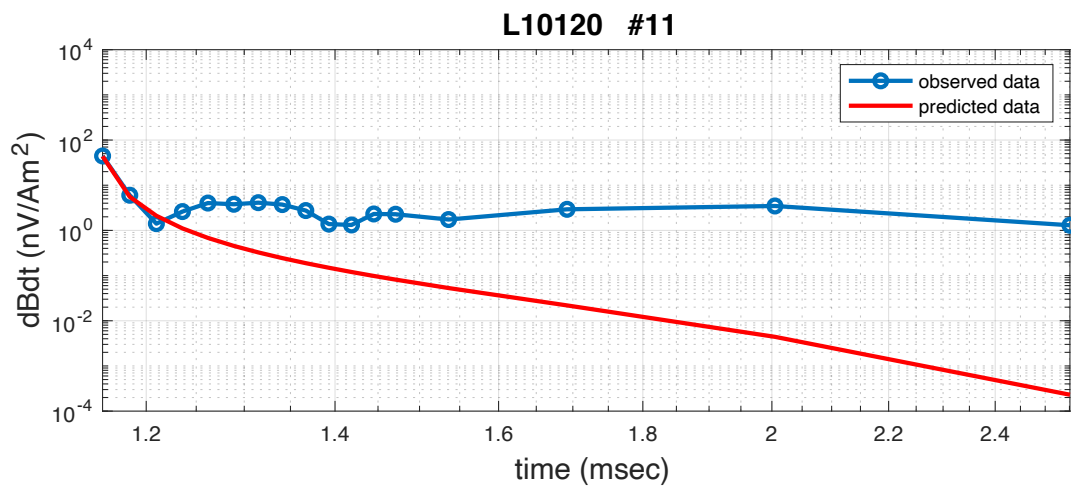
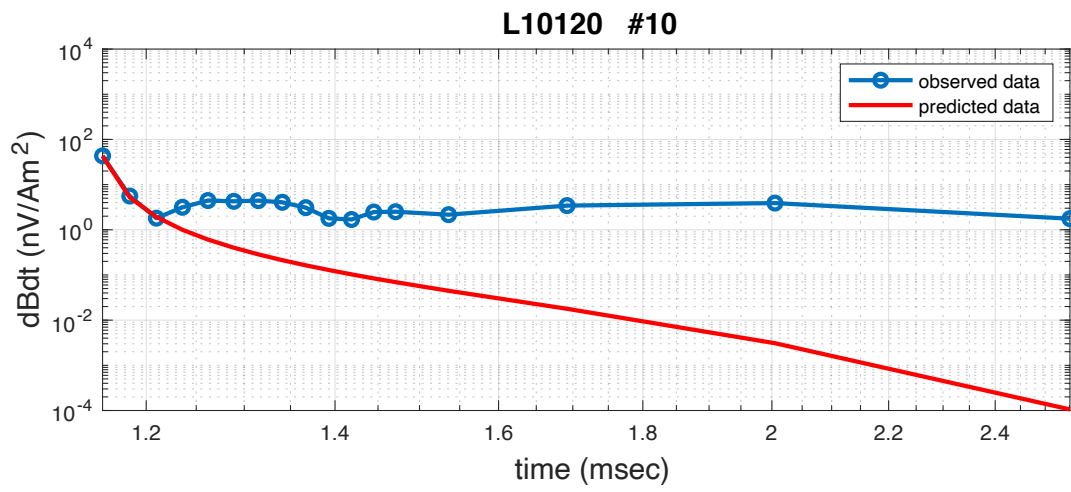


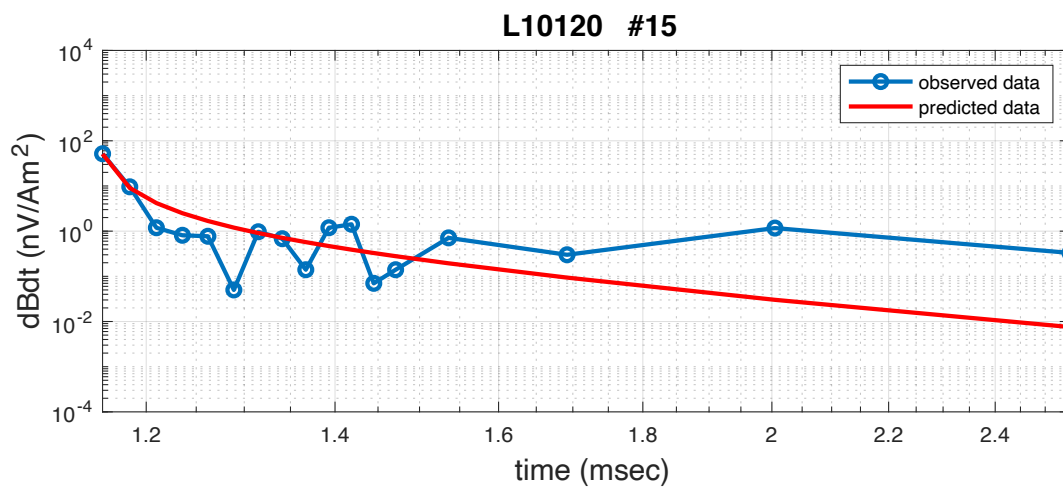
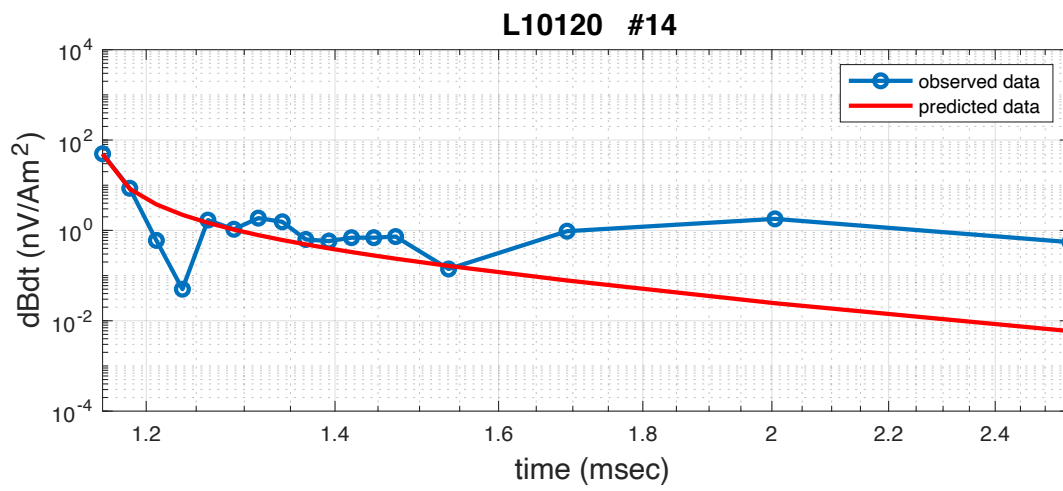
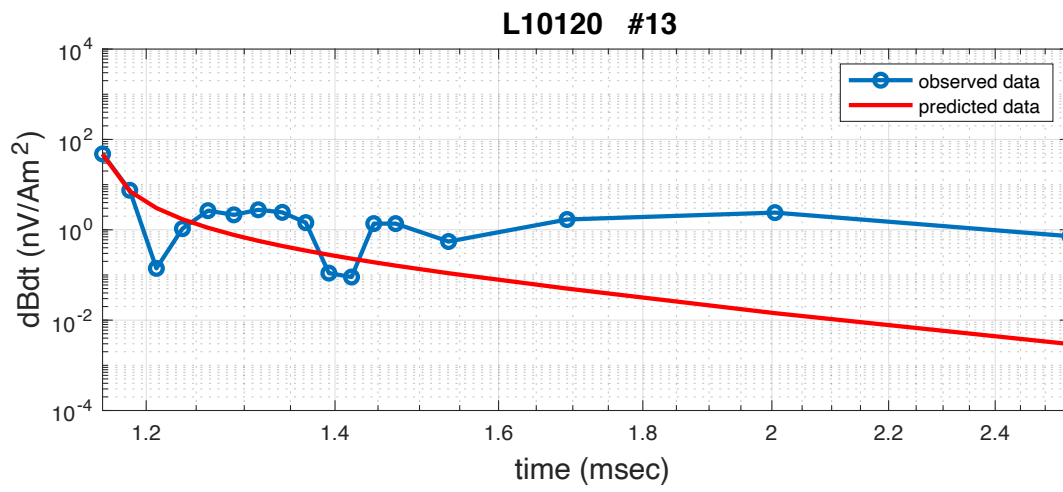
The observation points on L10120

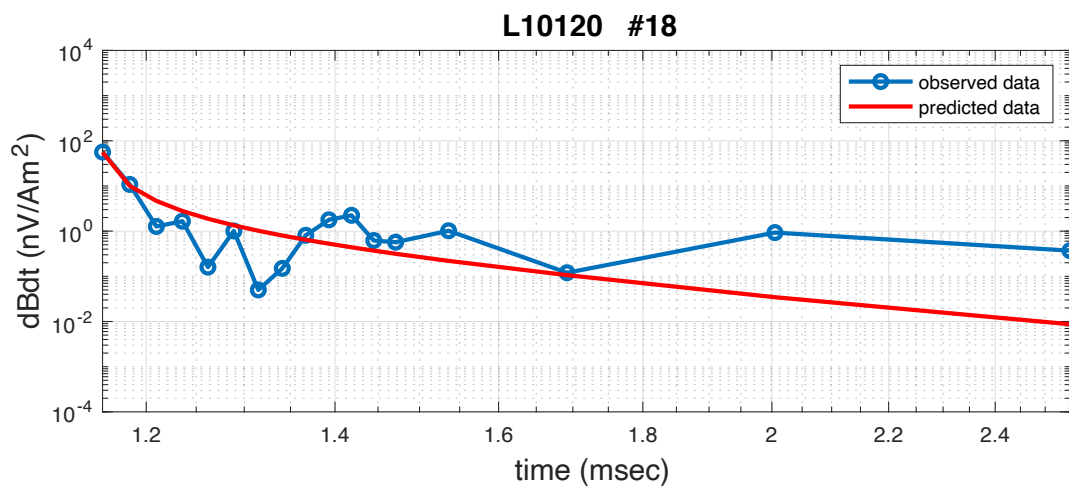
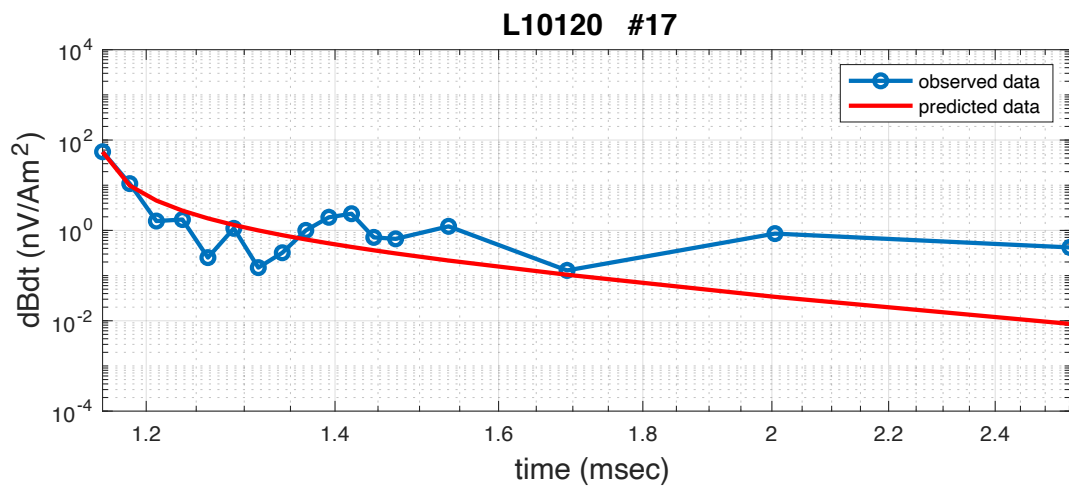
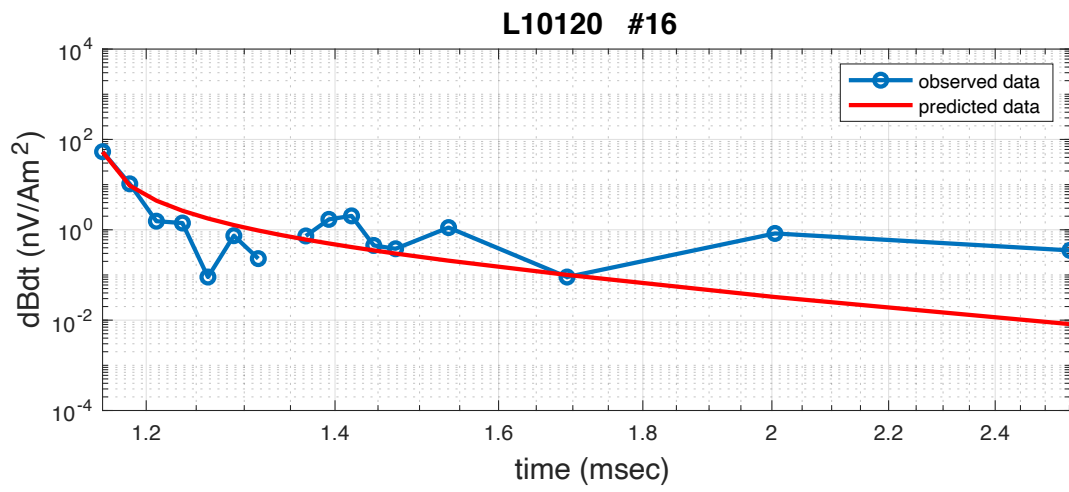


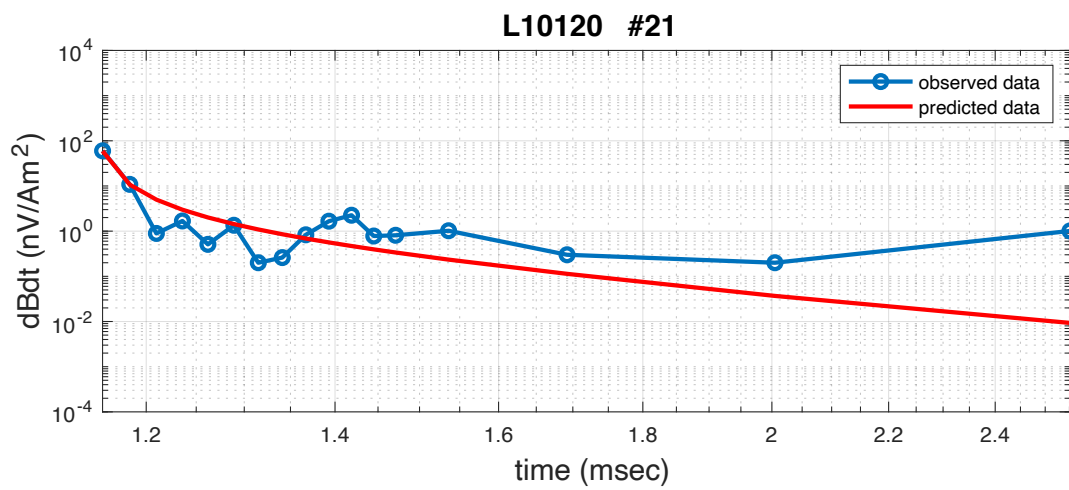
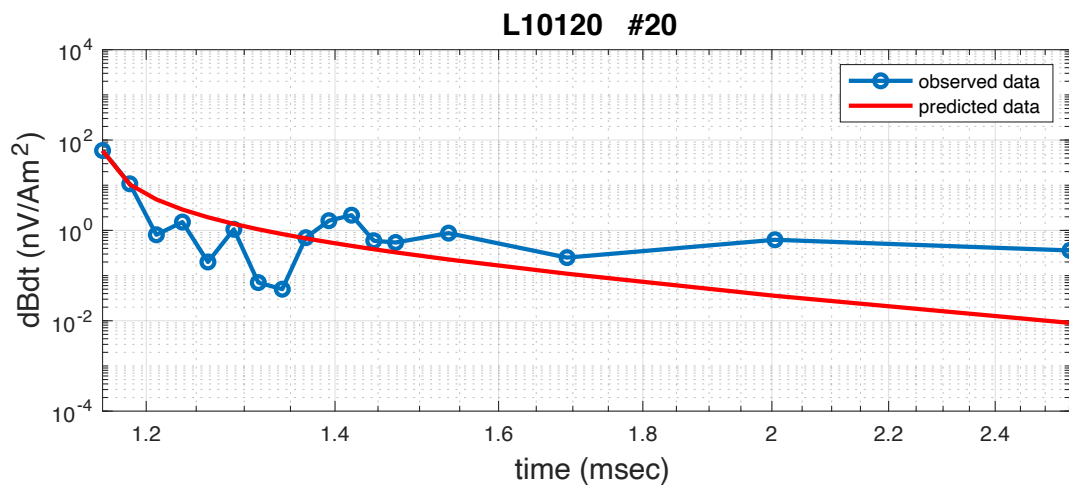
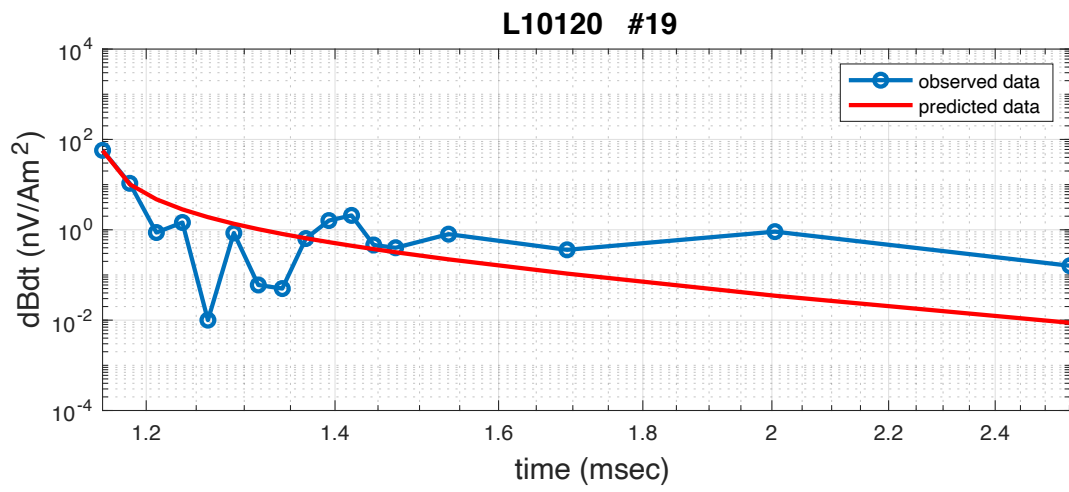


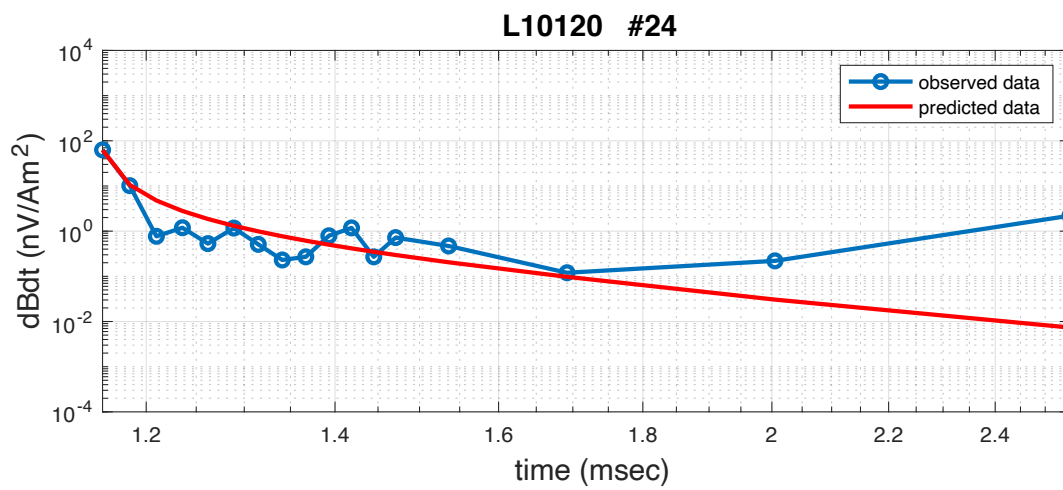
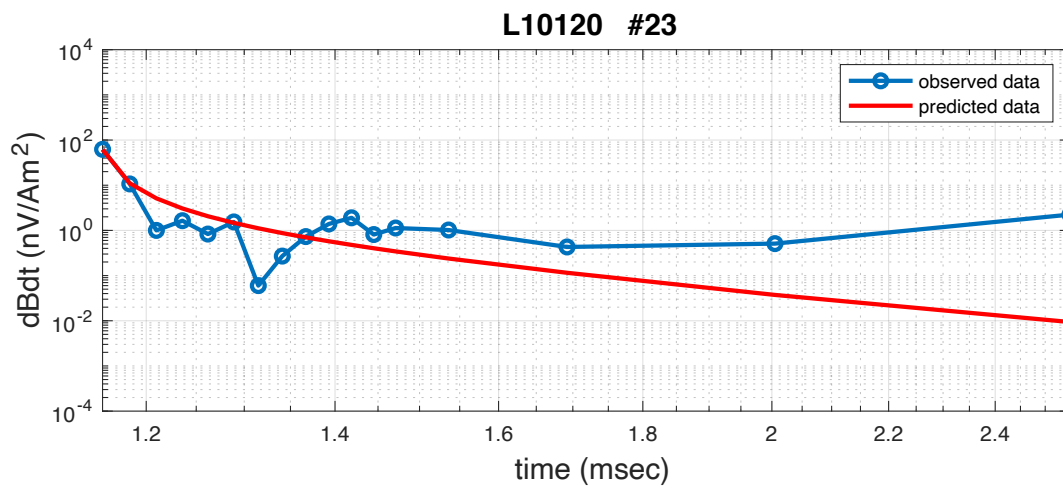
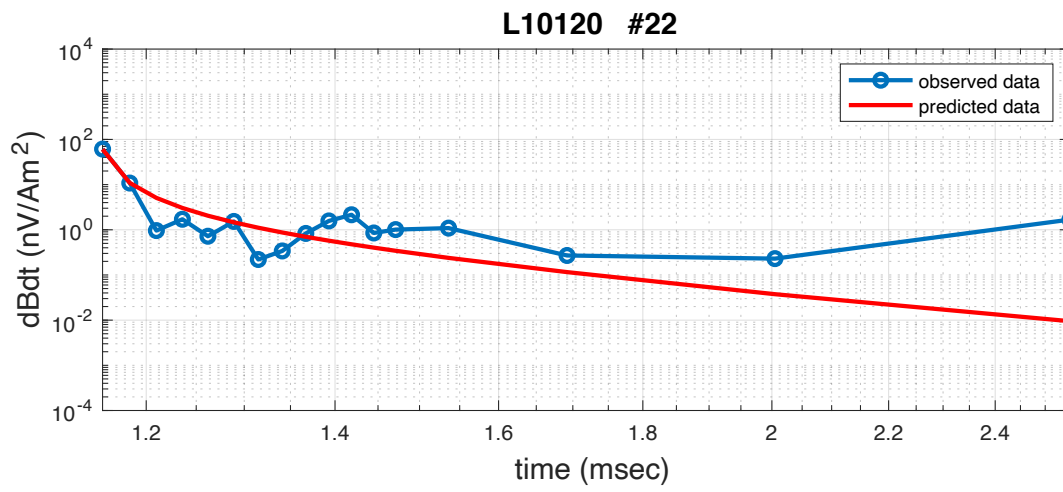


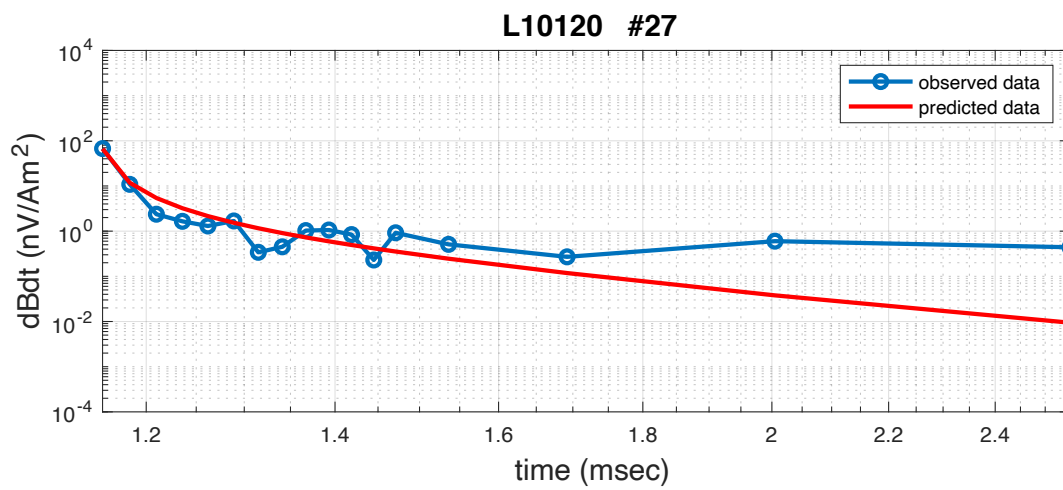
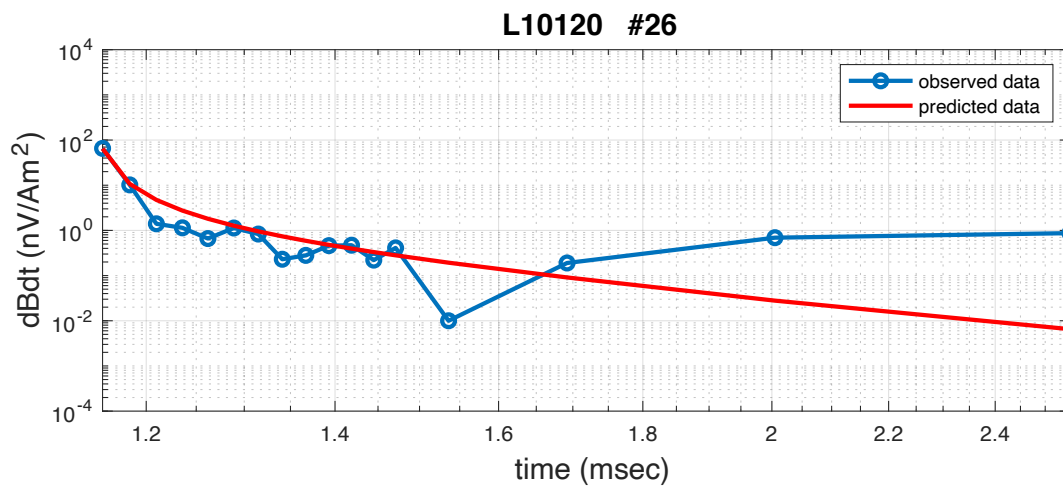
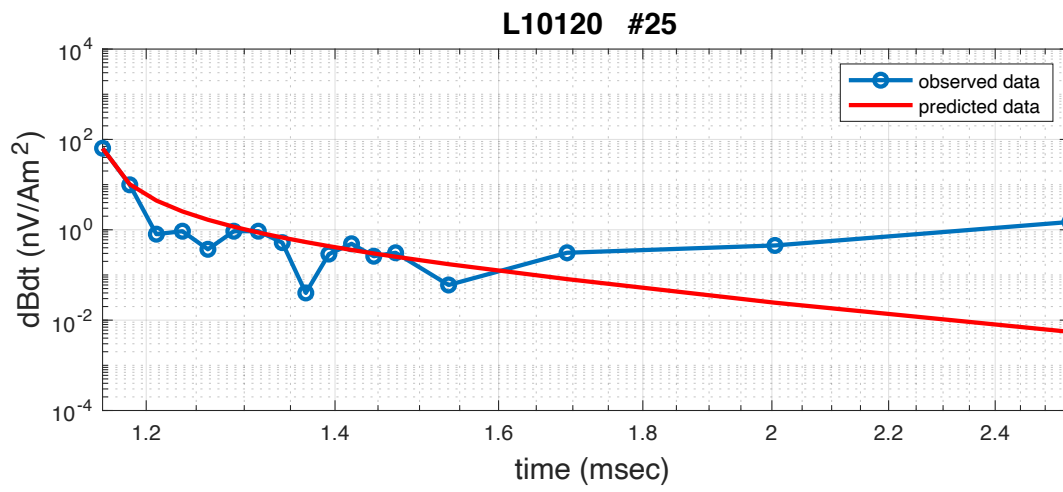


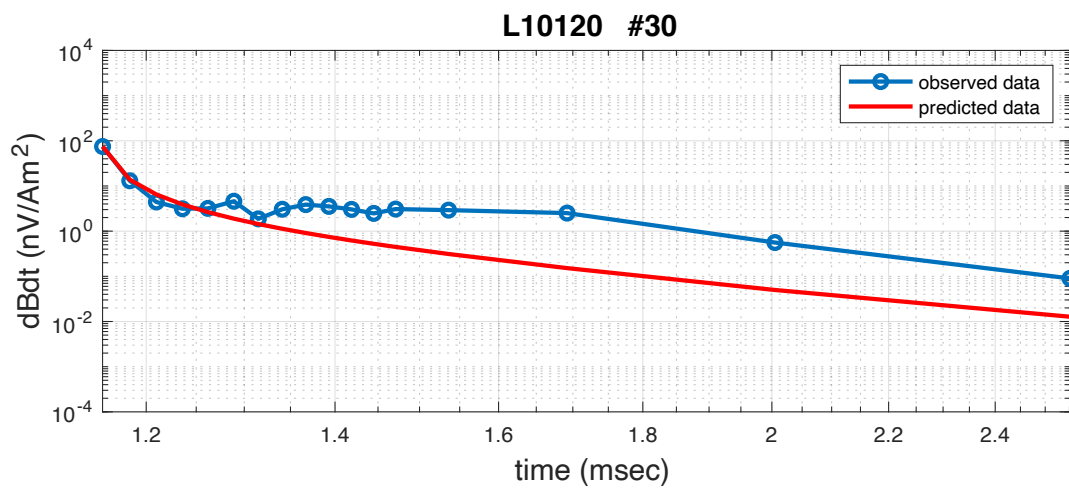
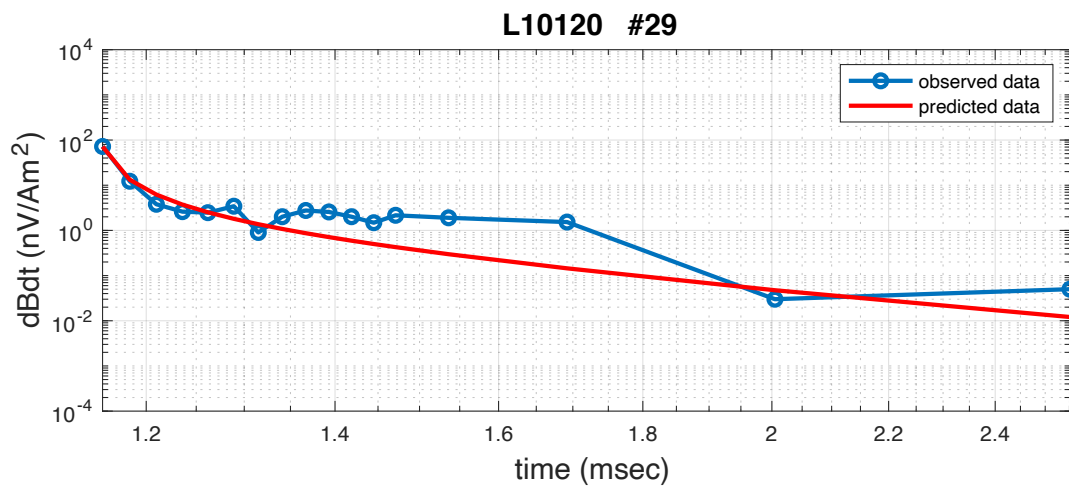
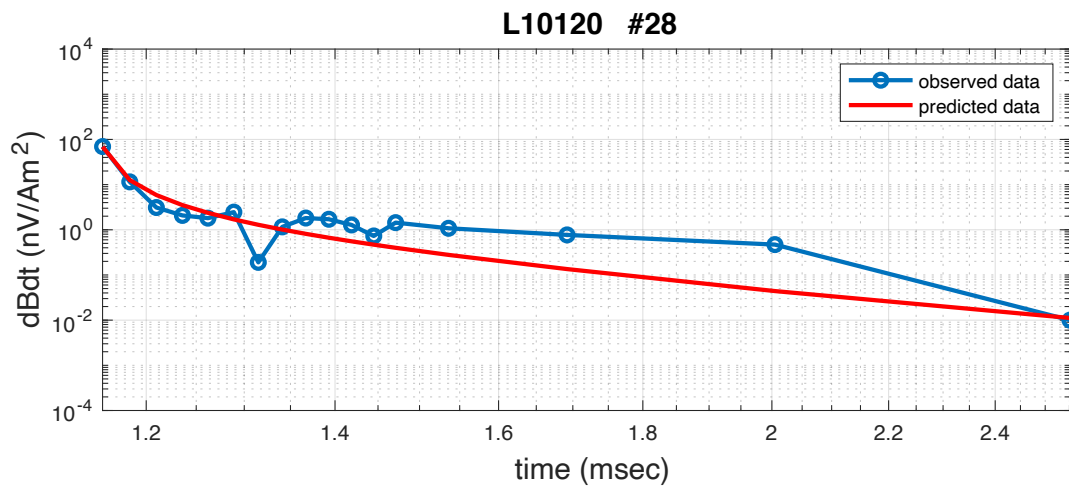


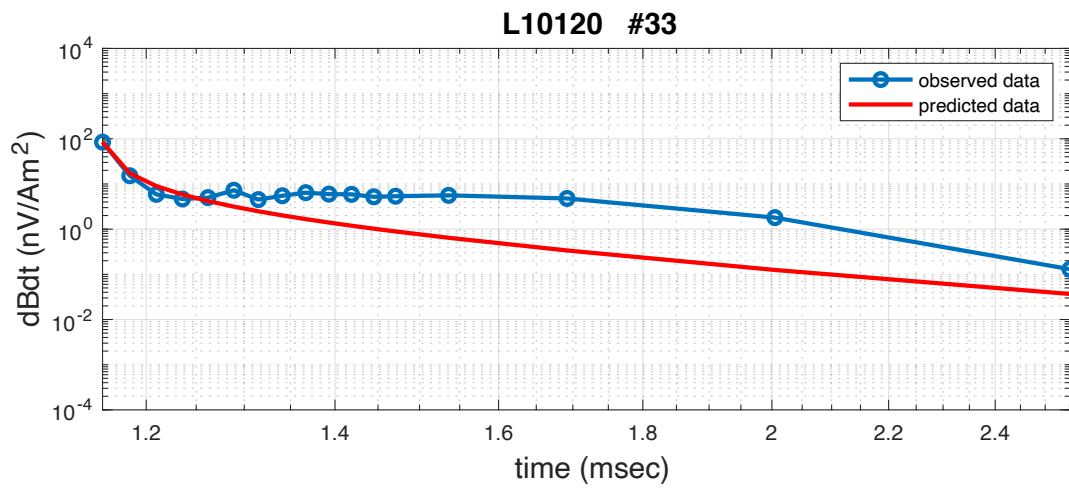
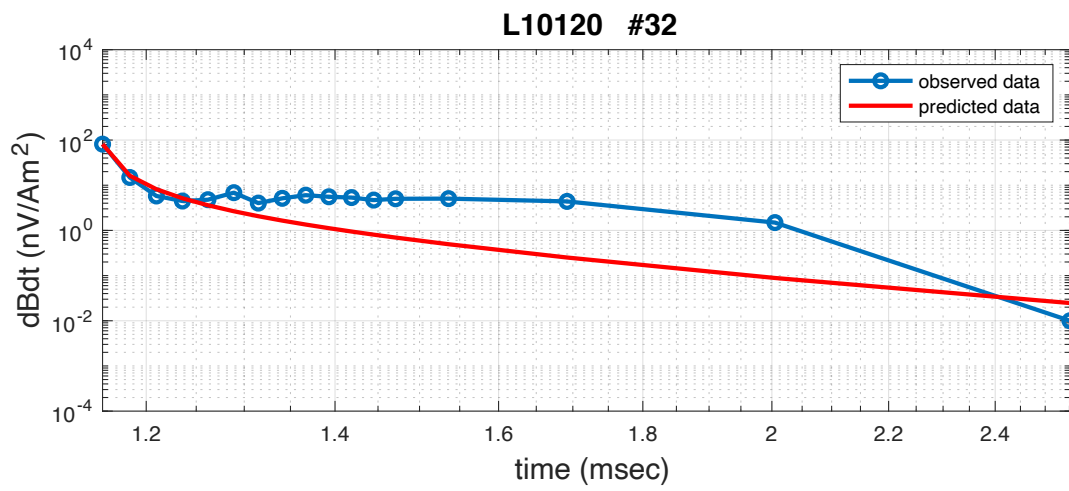
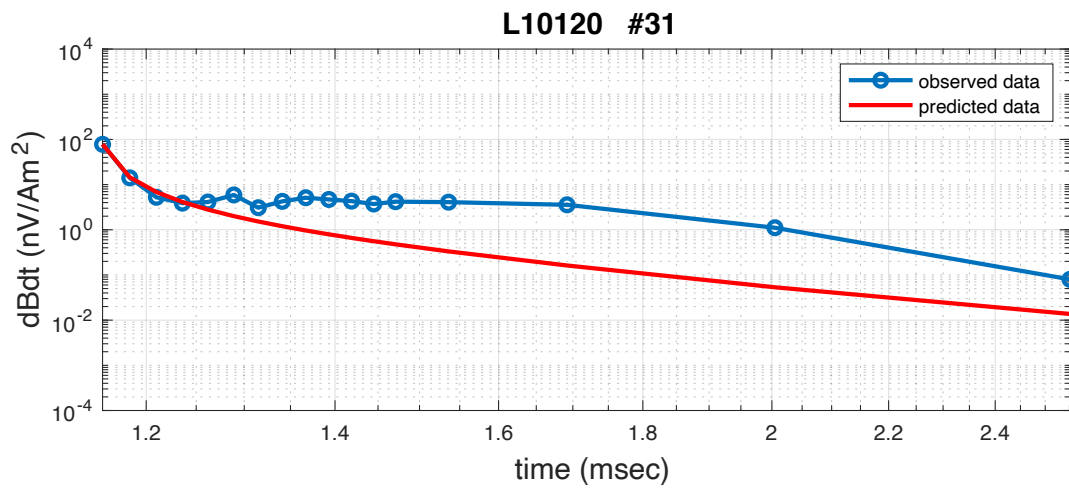


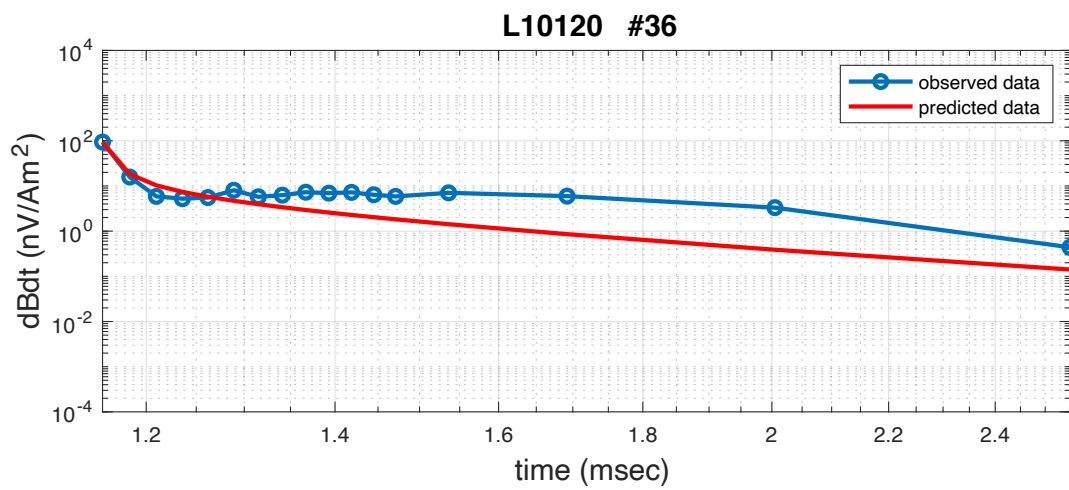
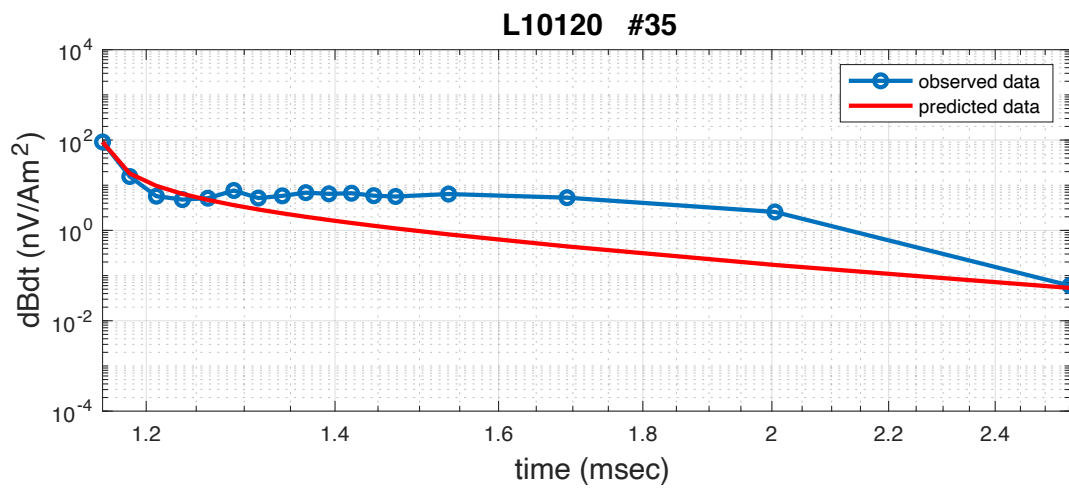
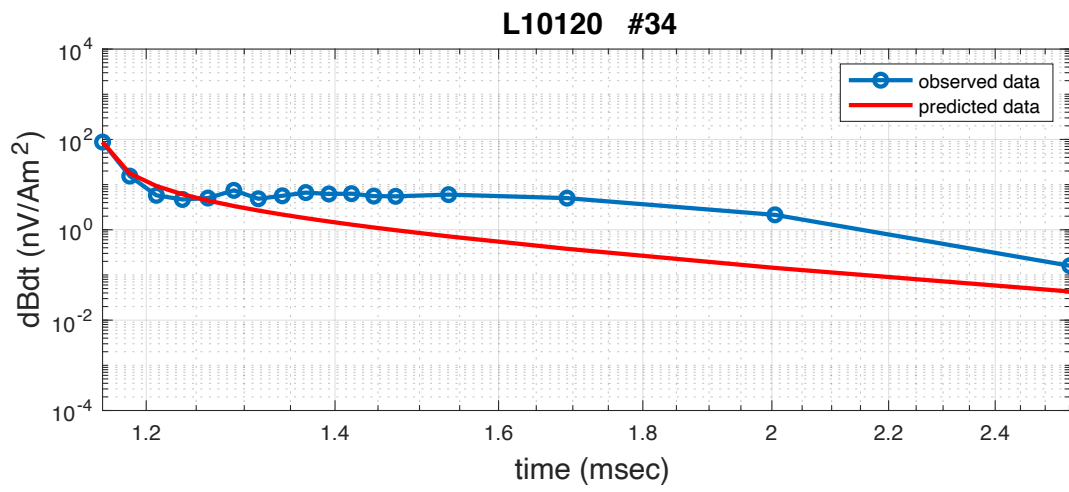


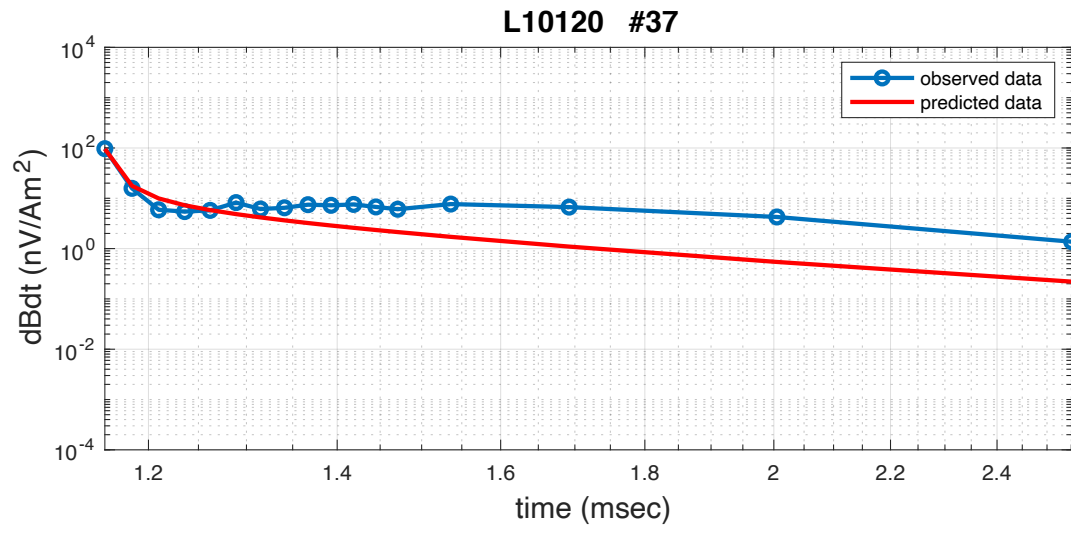




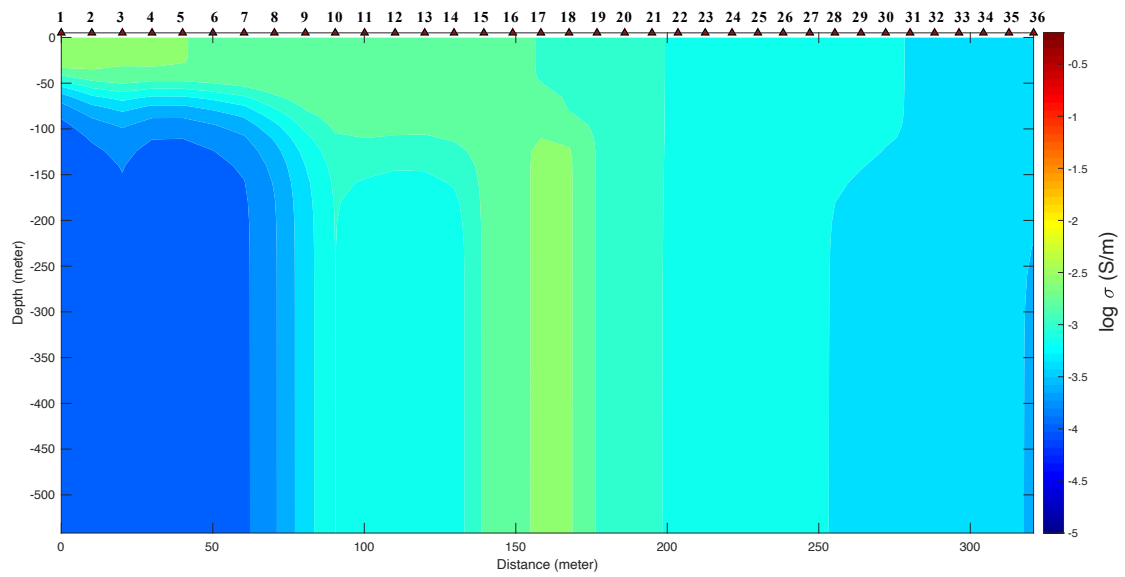




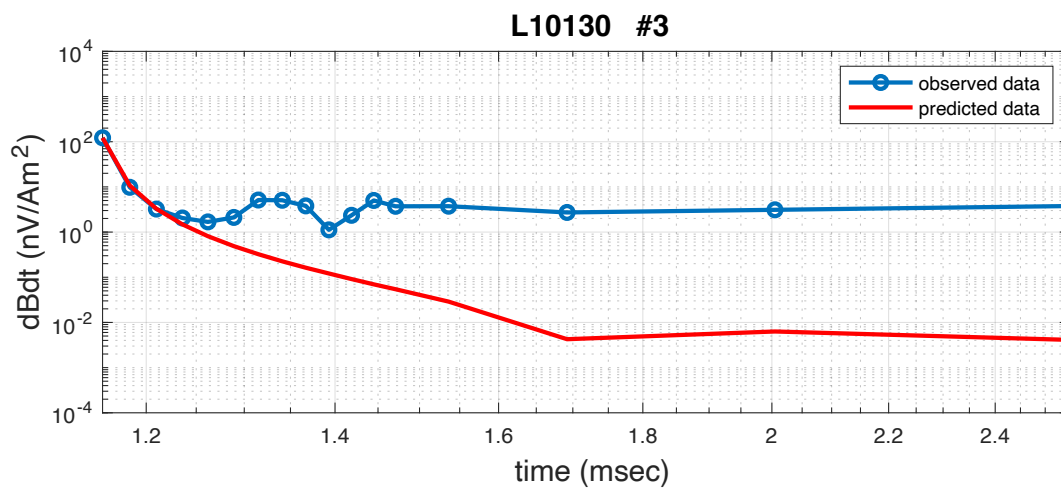
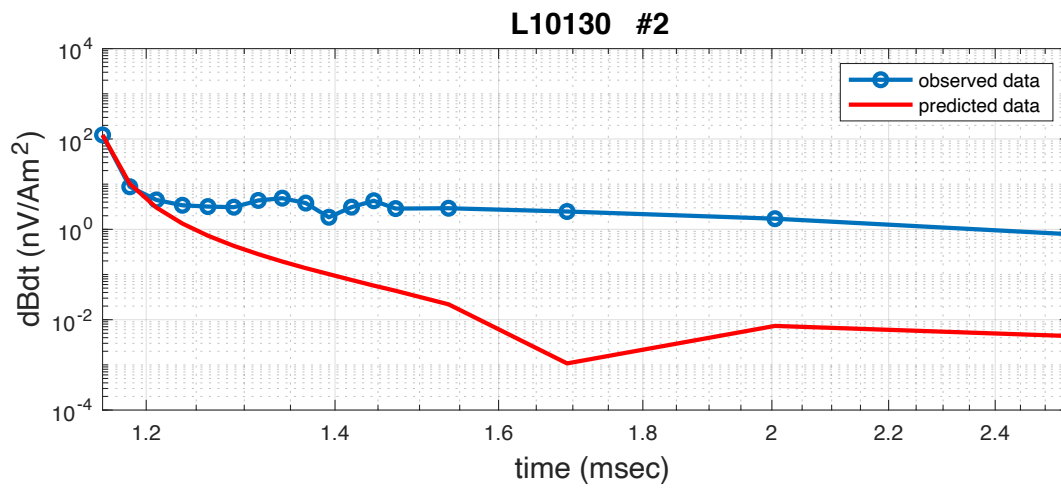
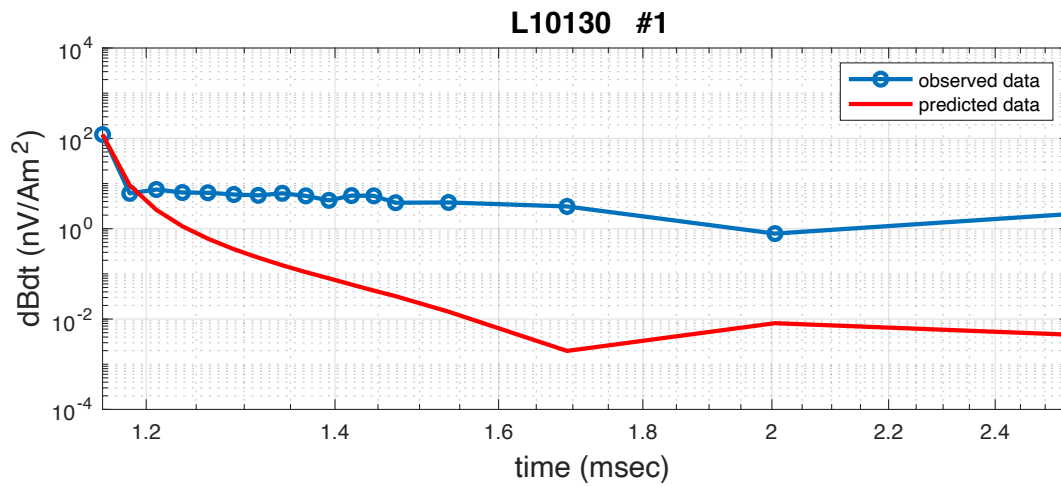


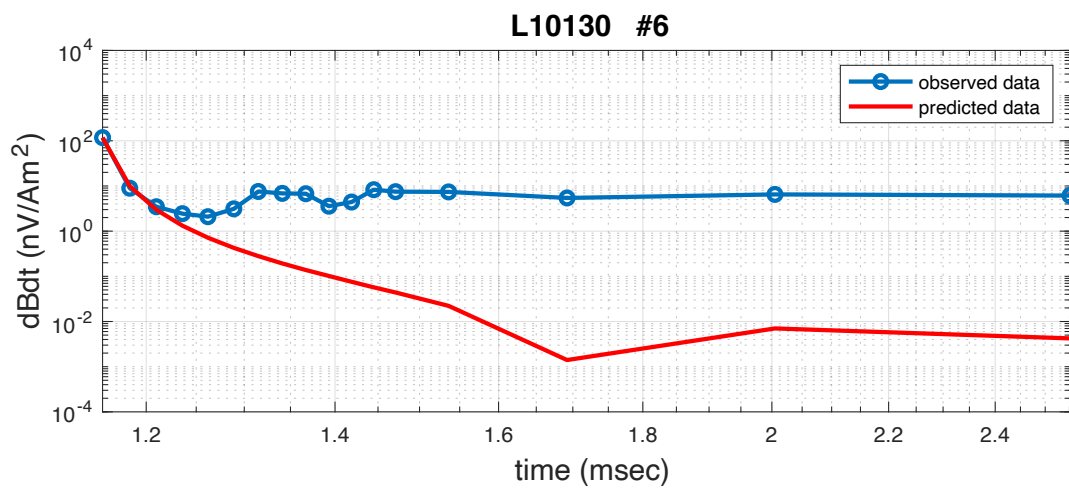
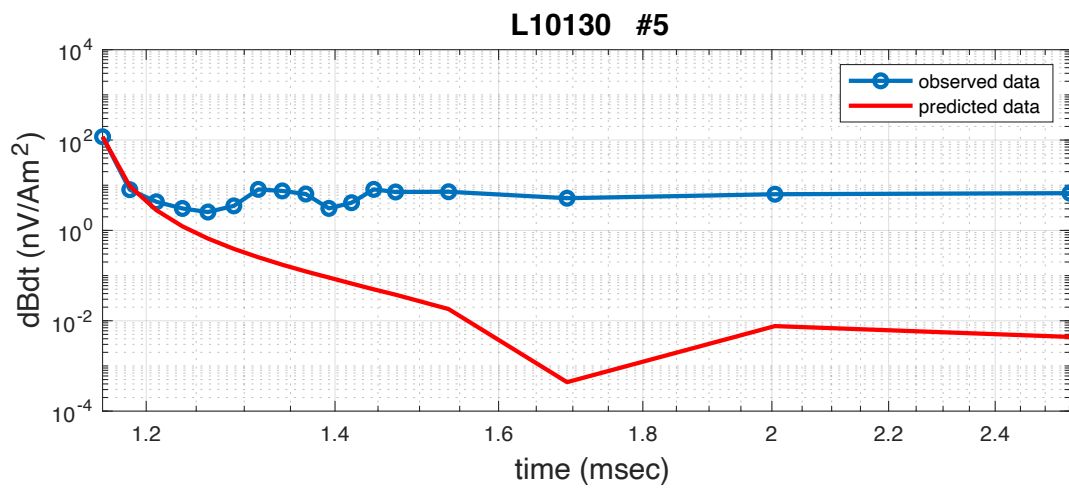
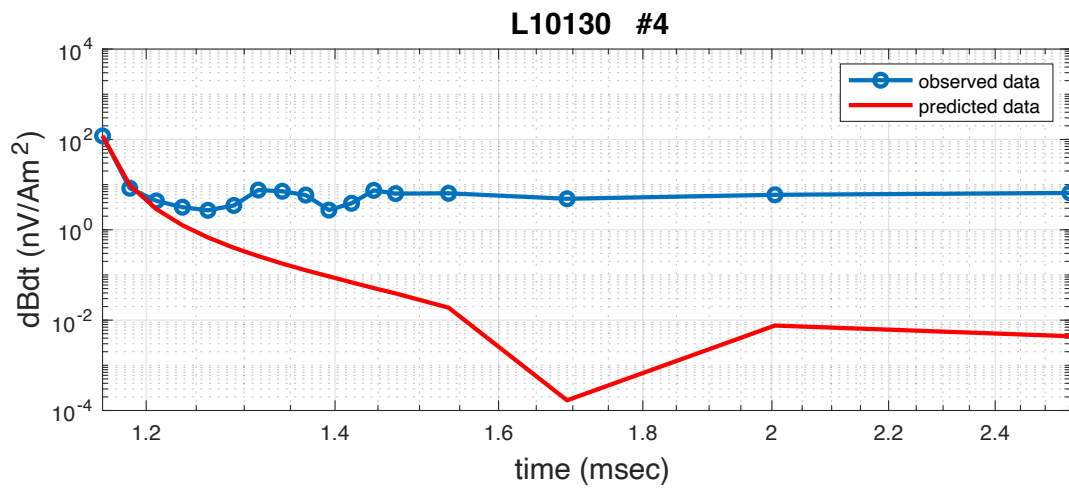


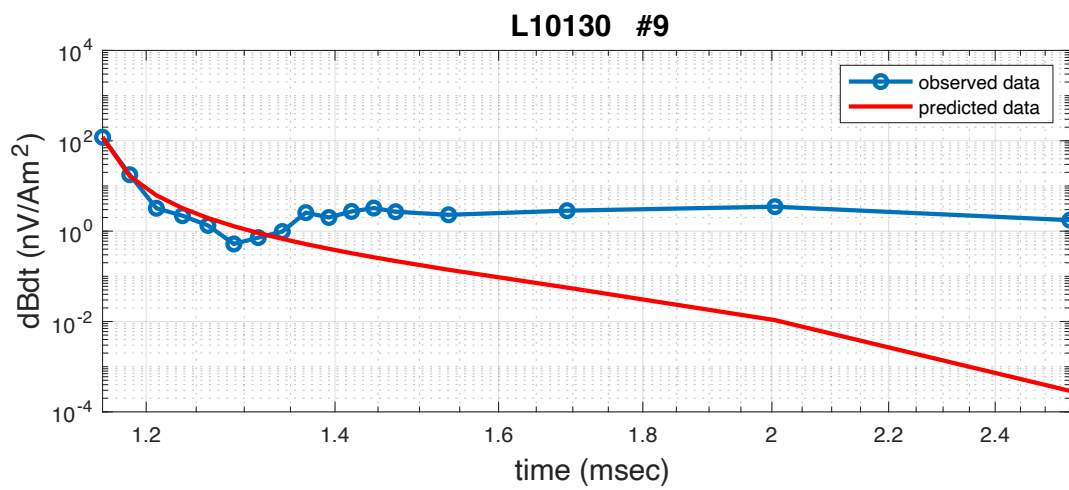
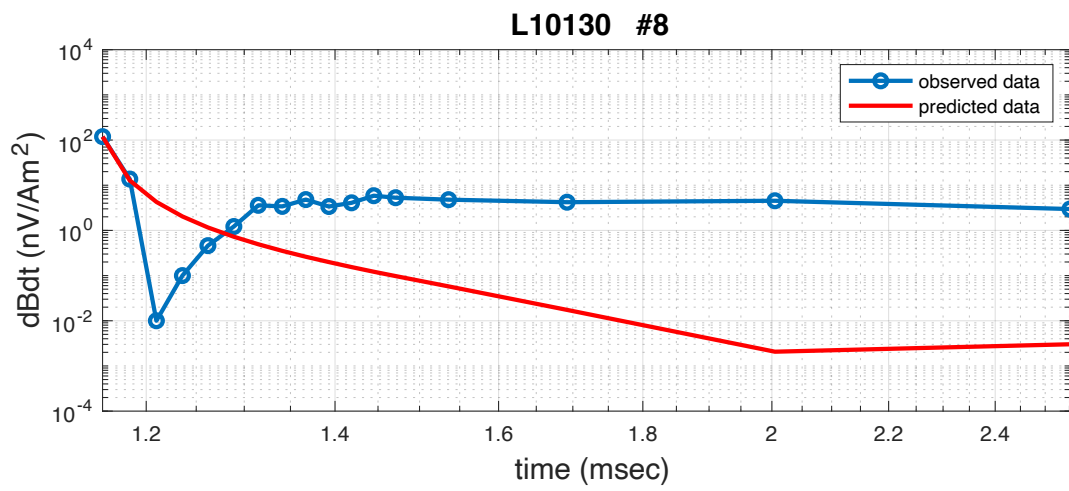
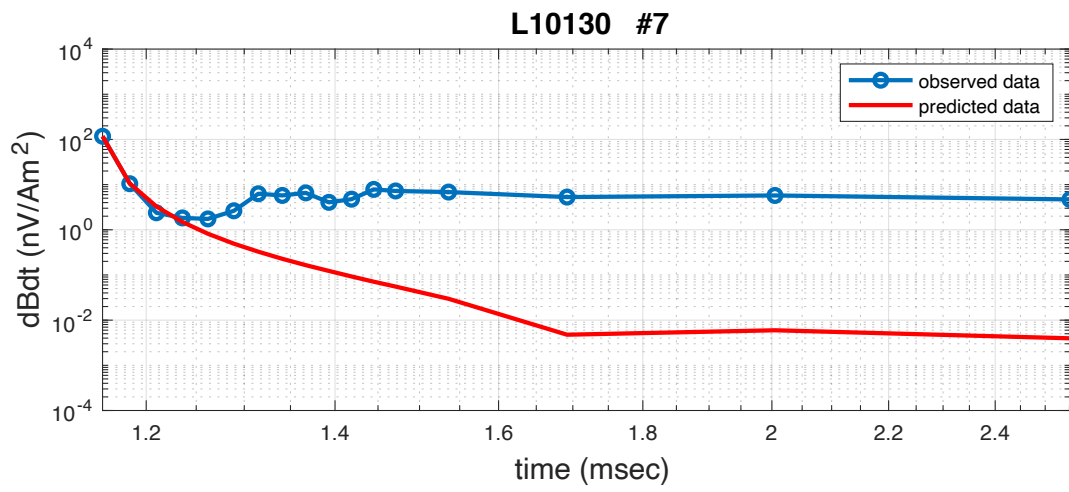
L10130

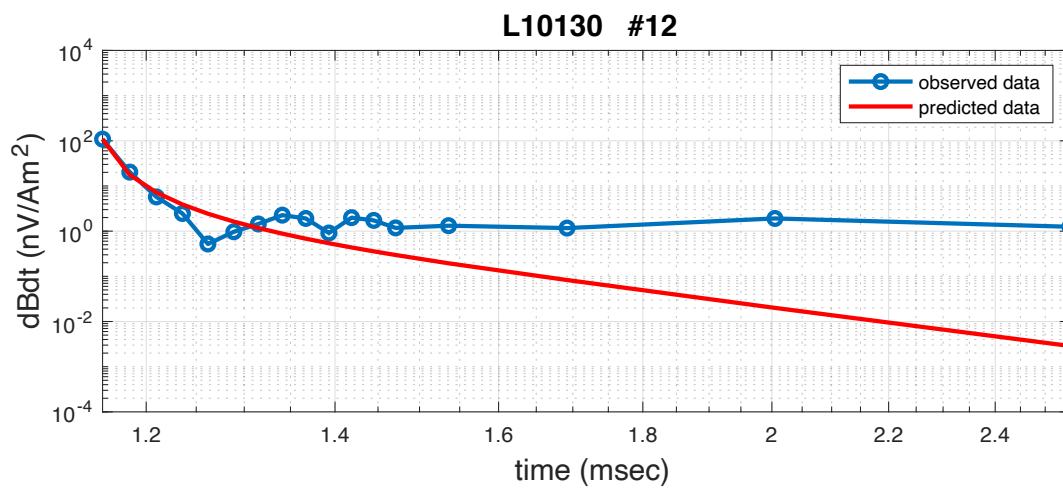
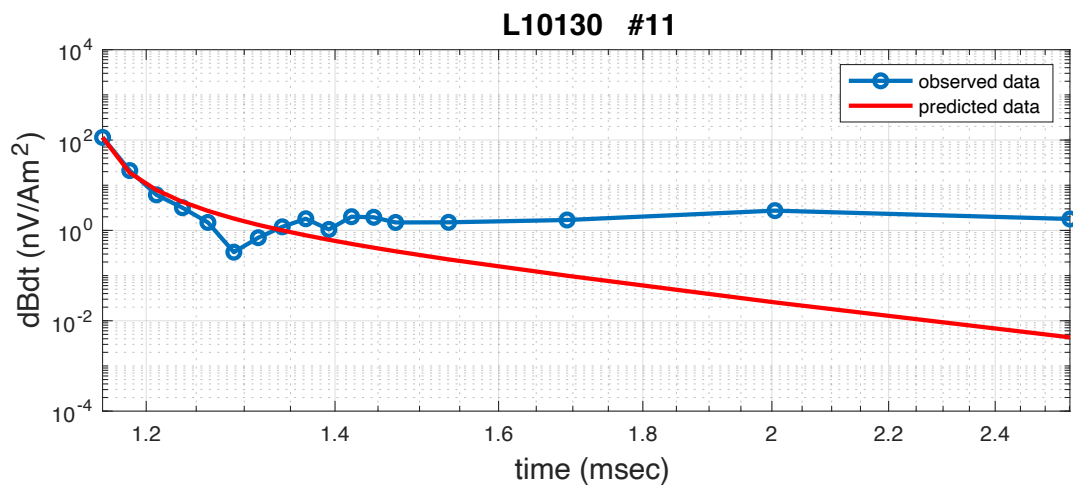
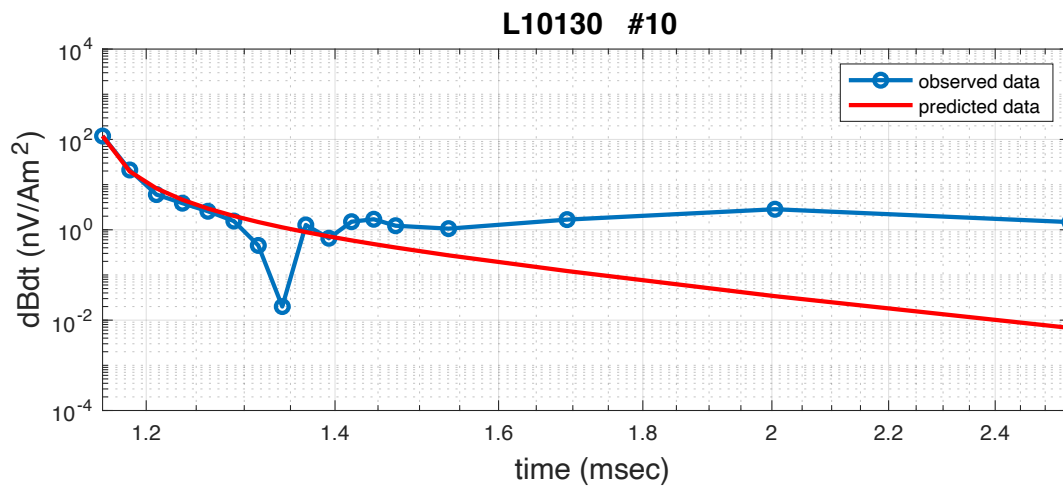


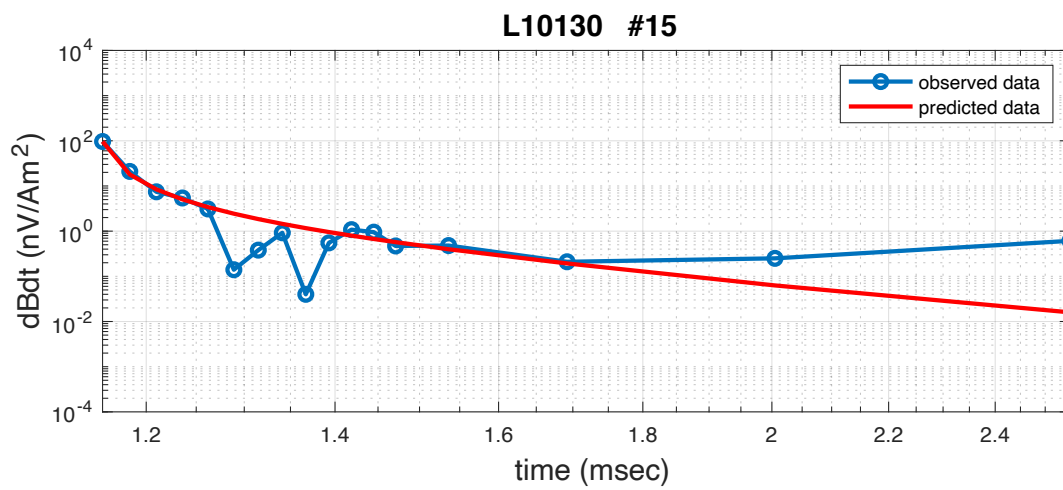
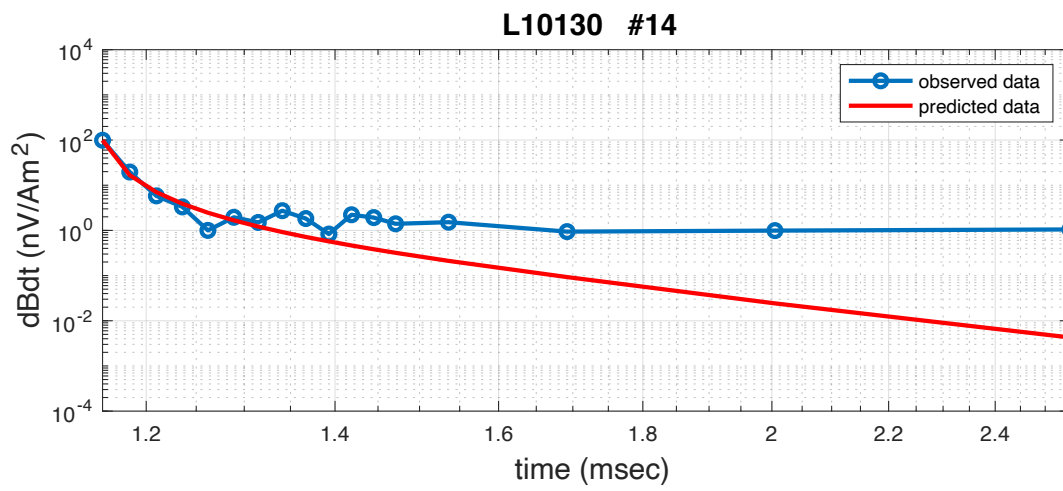
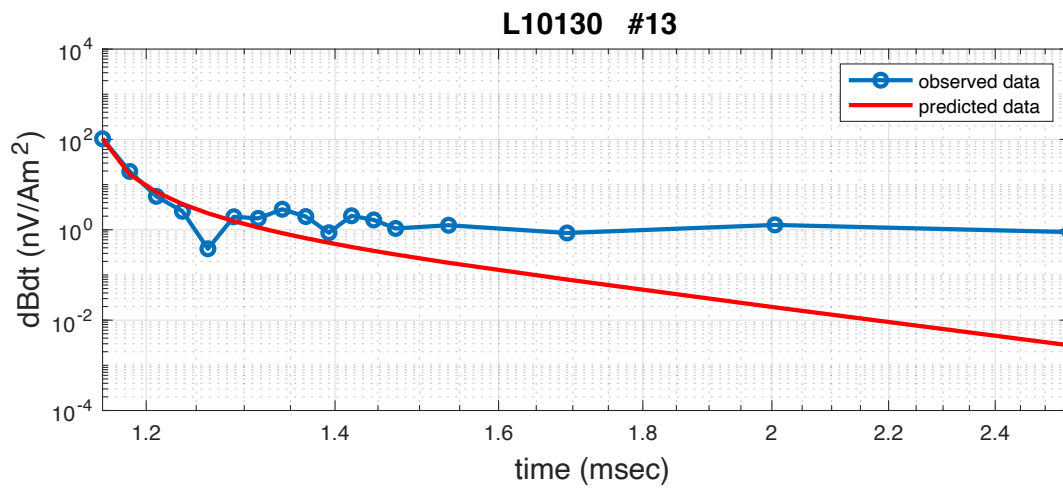
The observation points on L10130

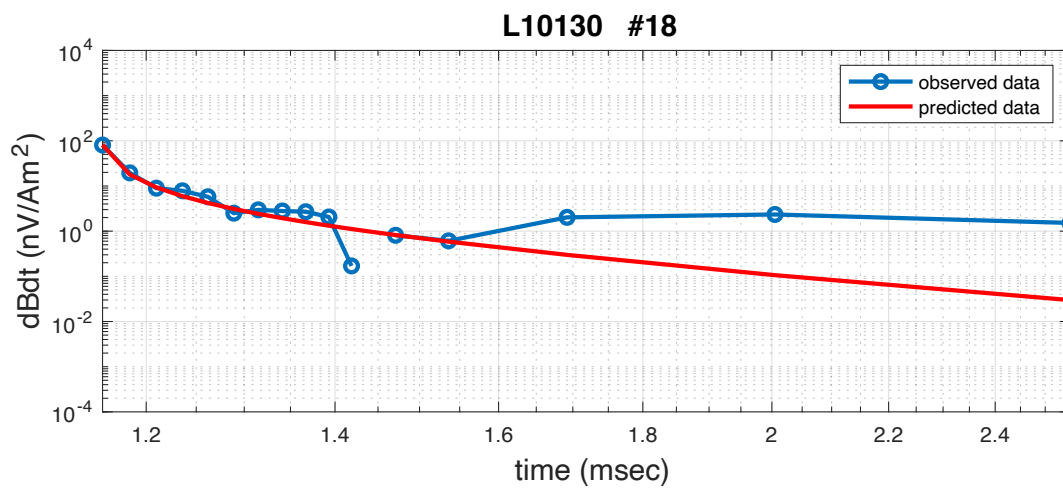
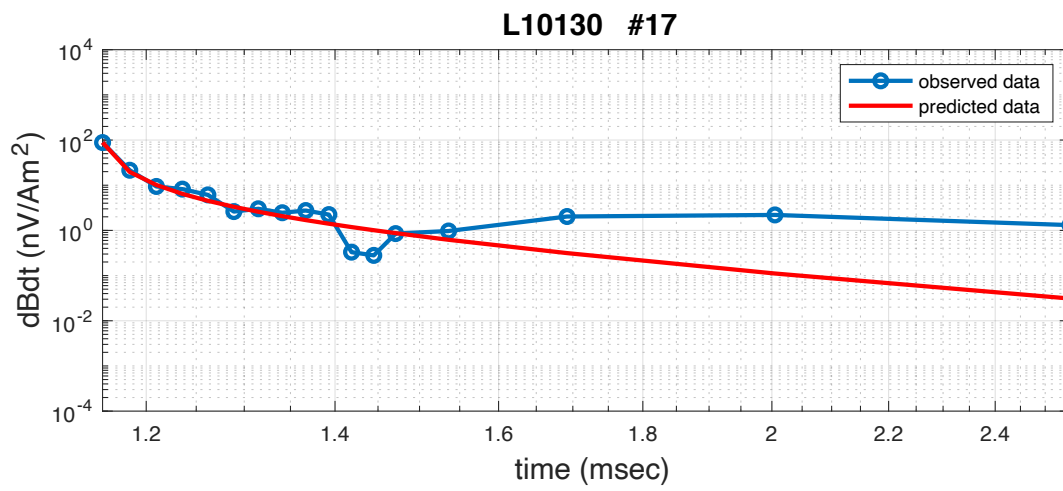
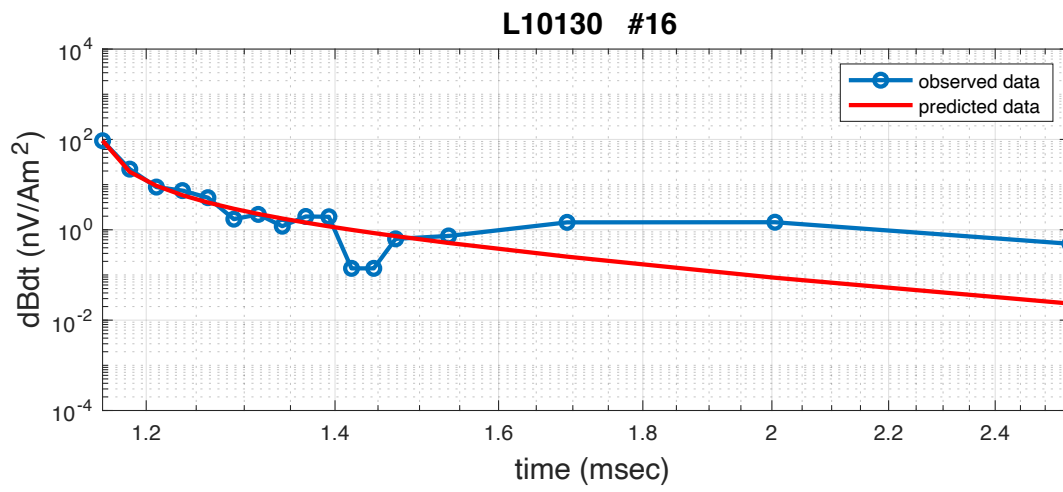


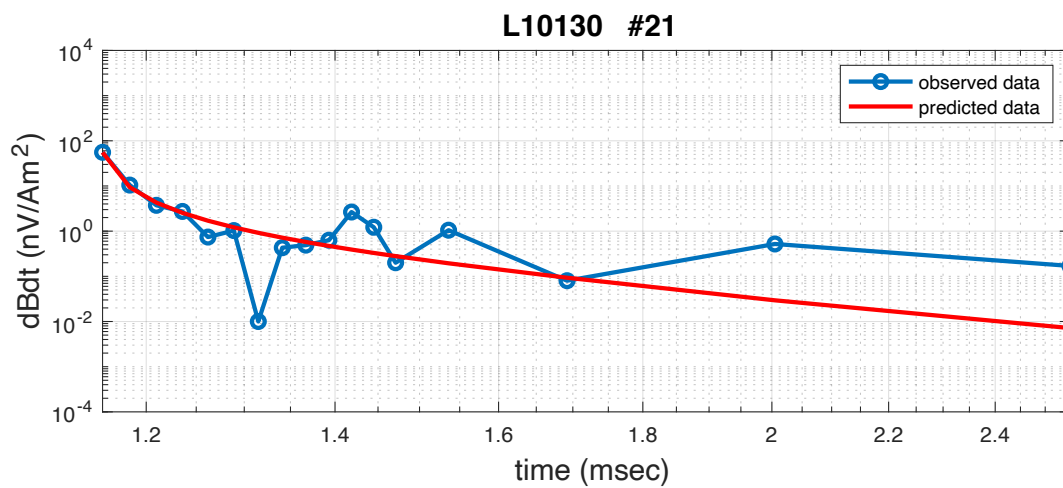
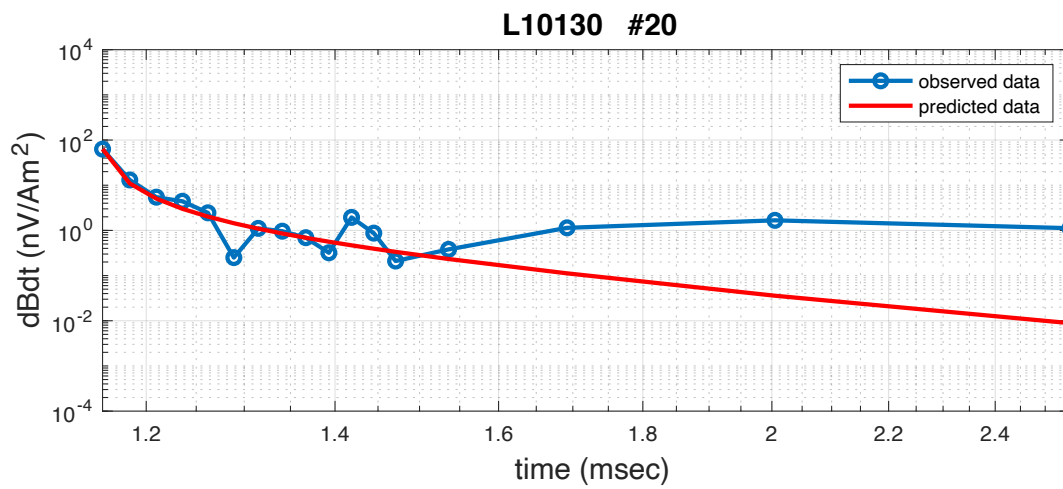
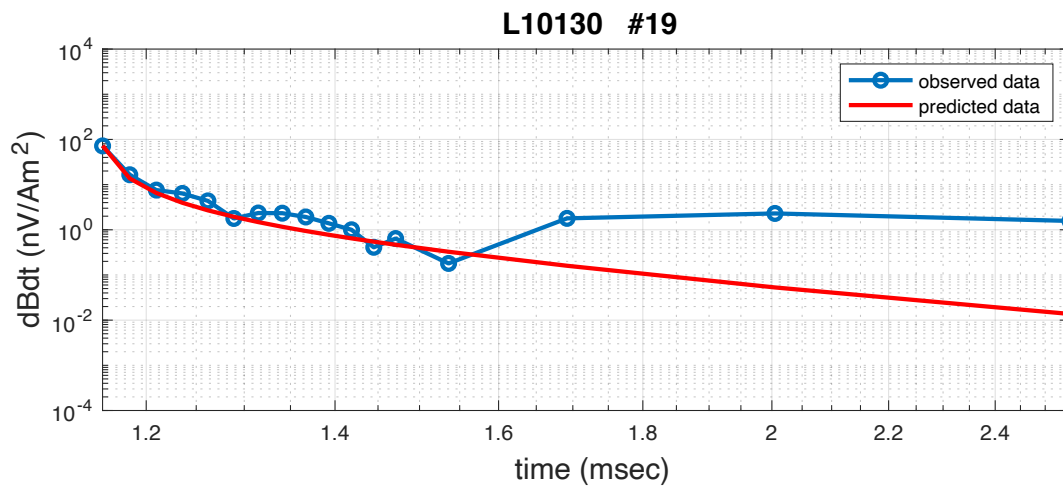


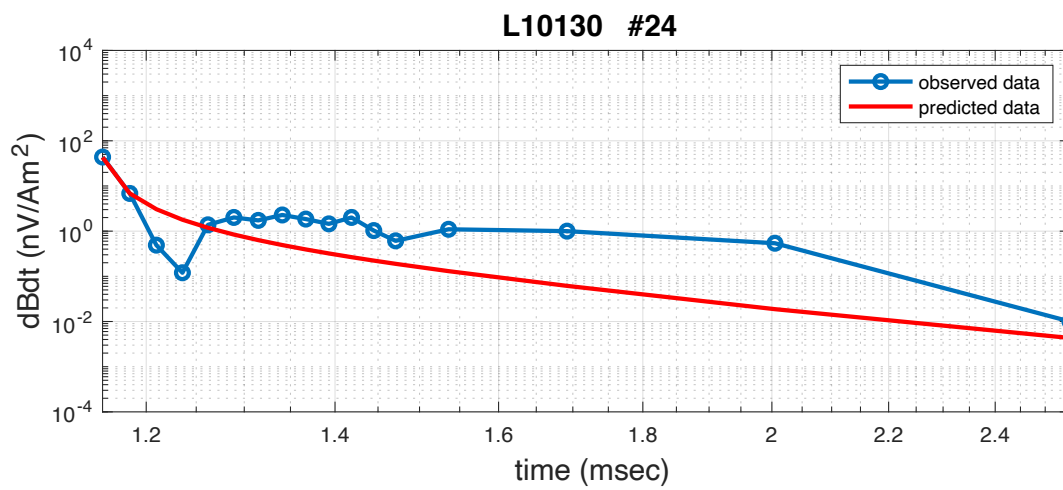
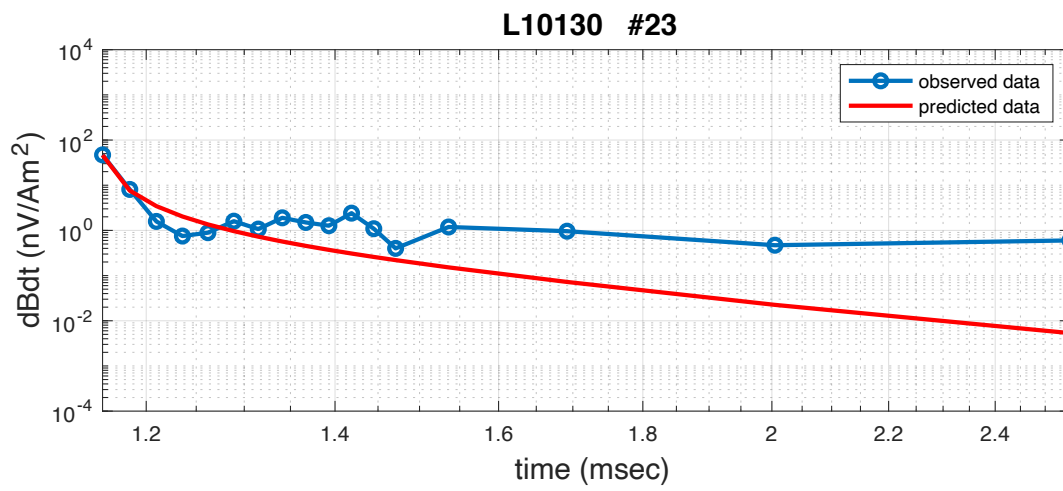
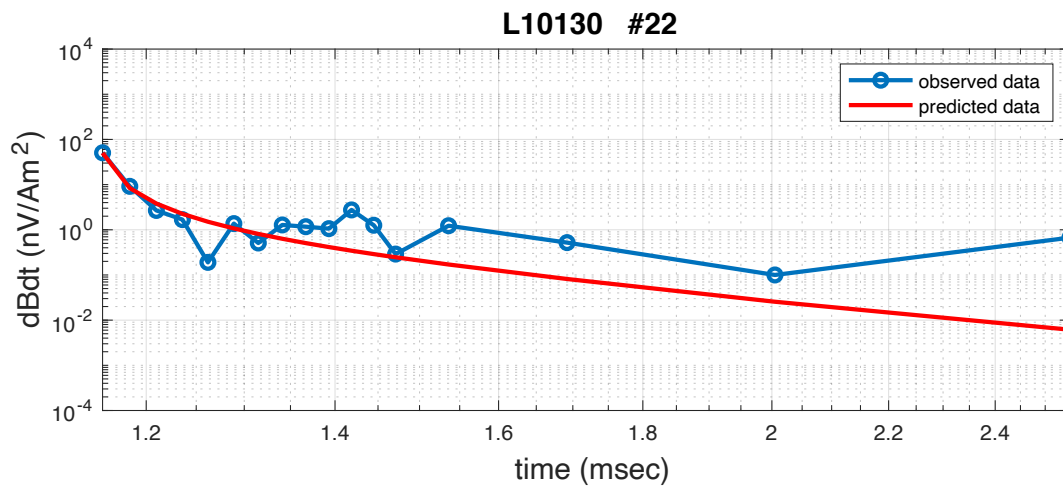


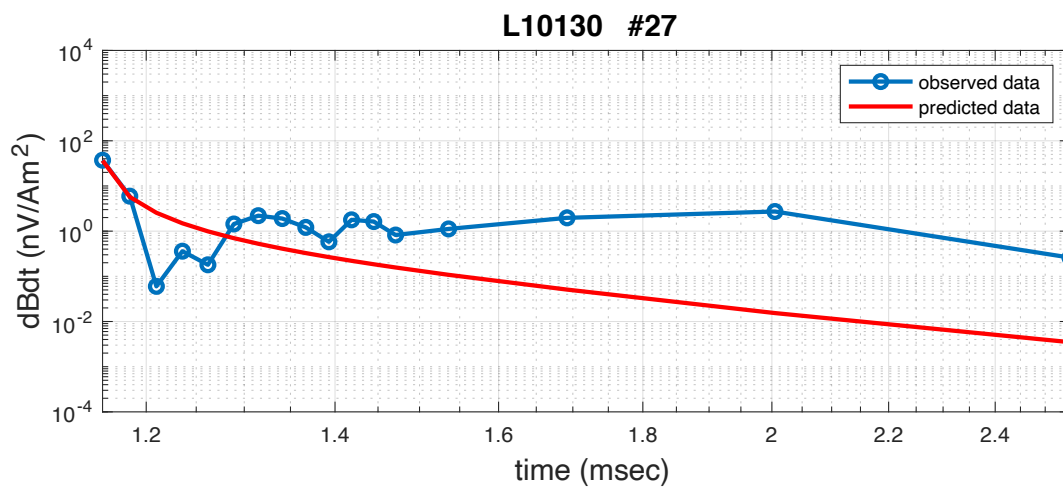
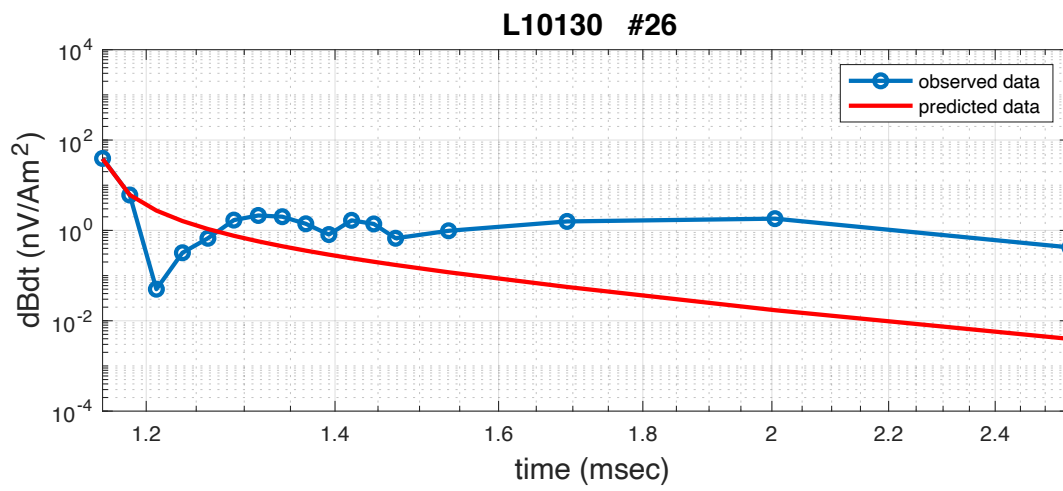
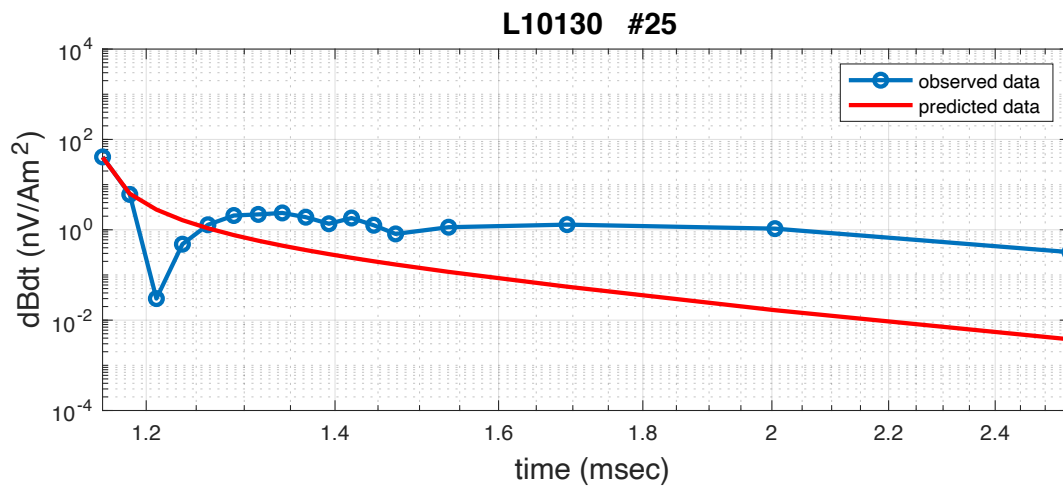


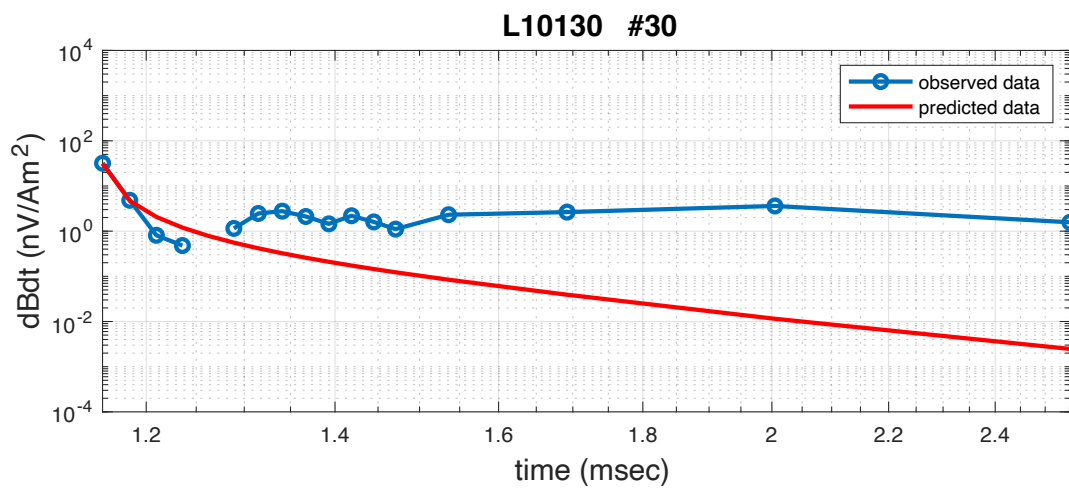
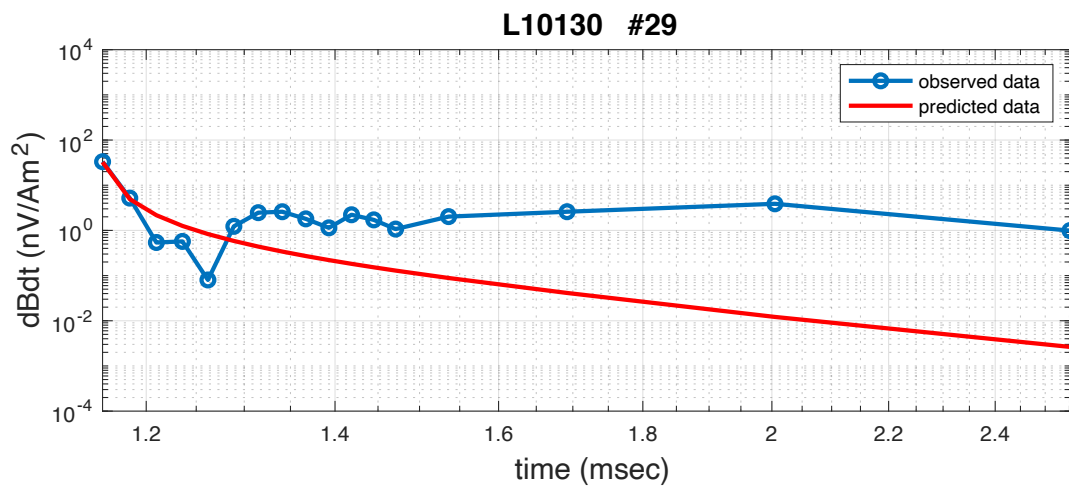
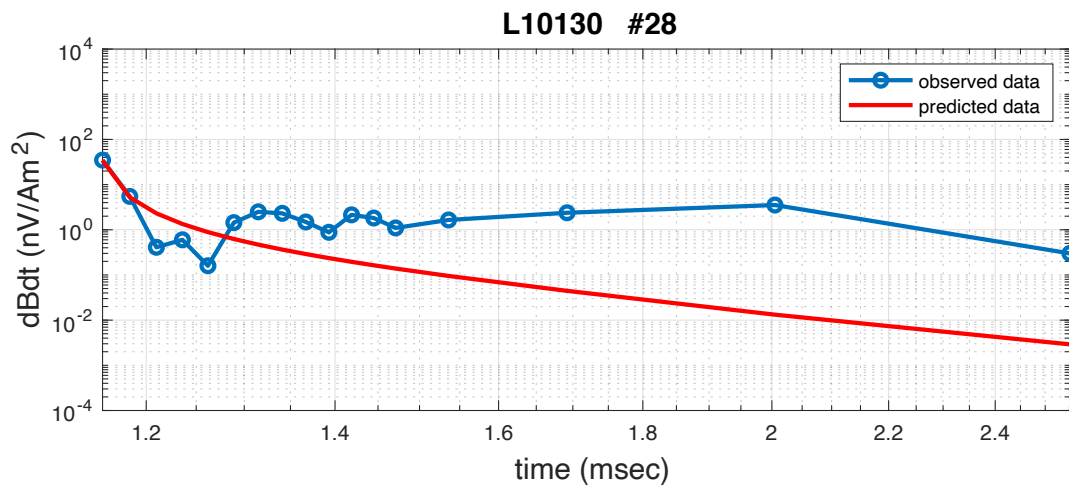


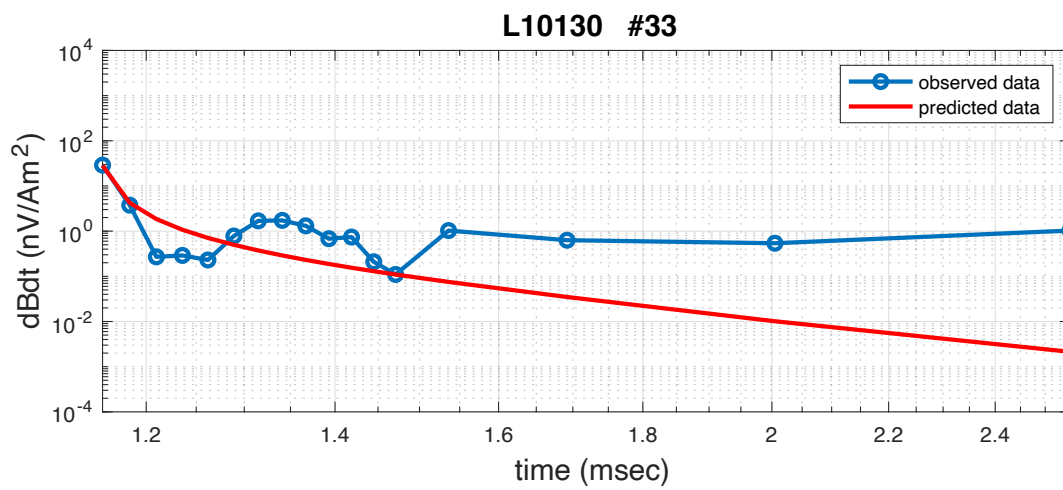
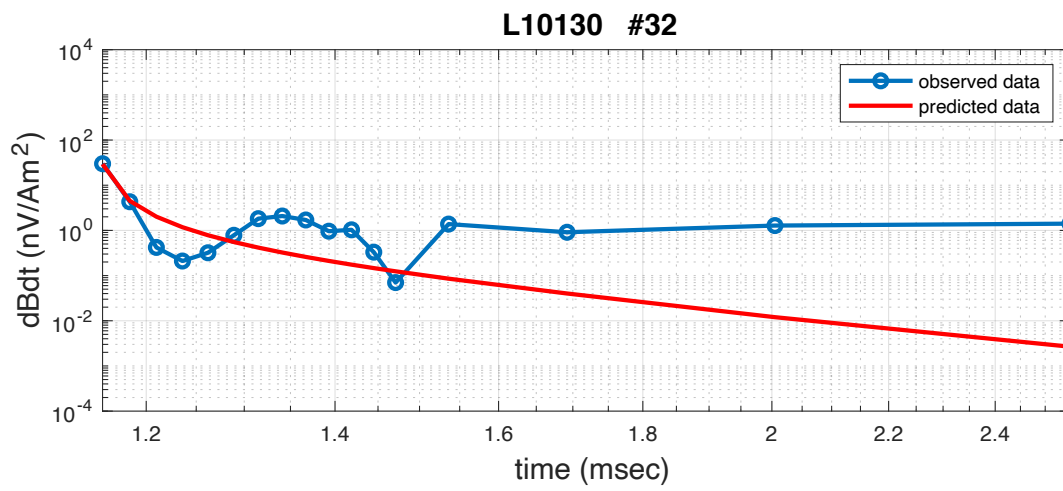
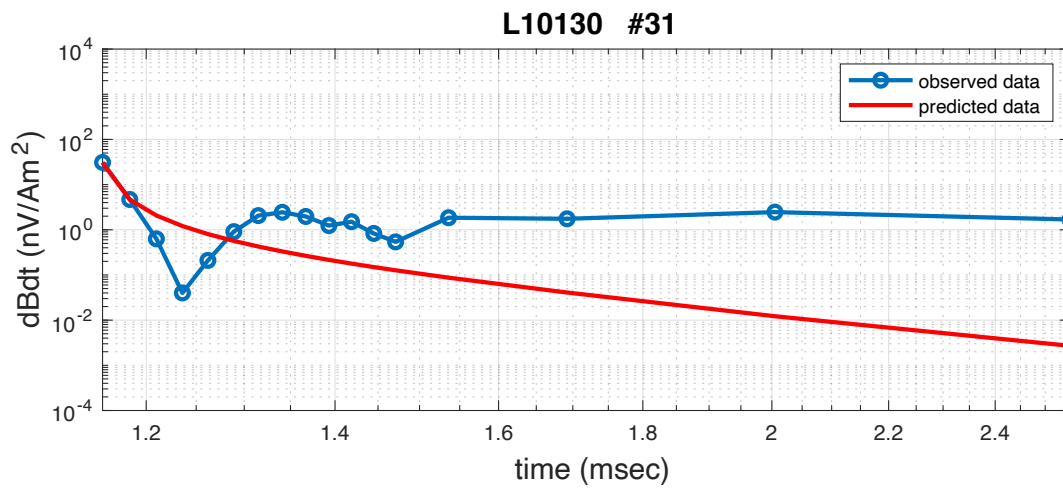


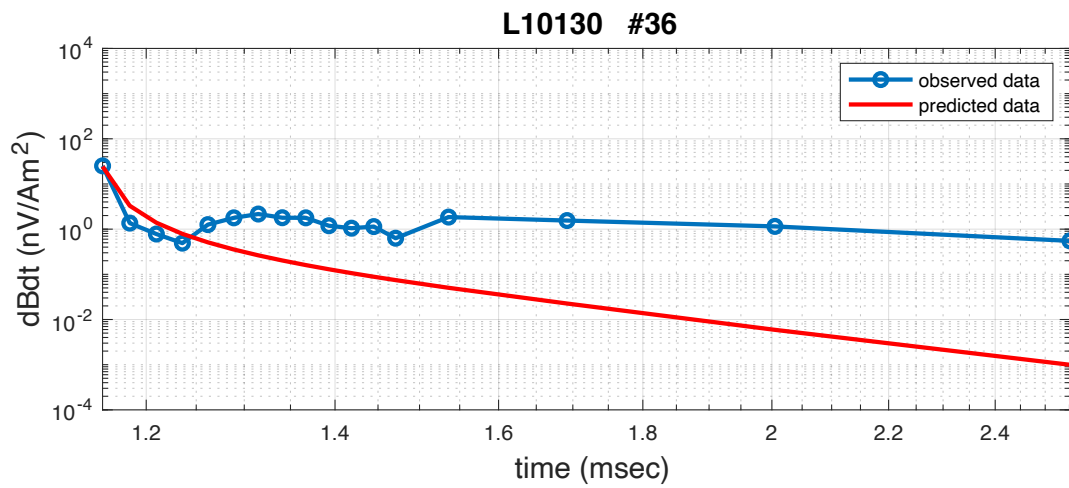
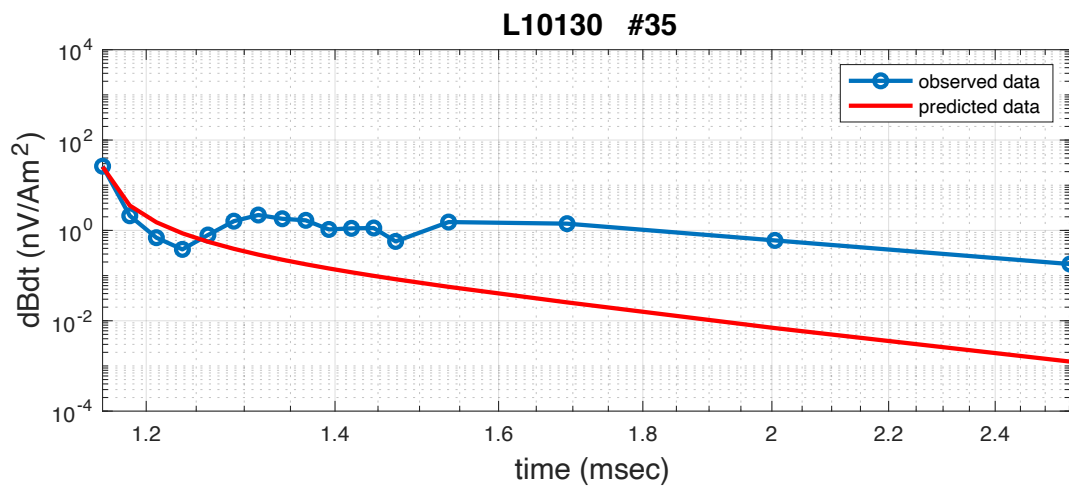
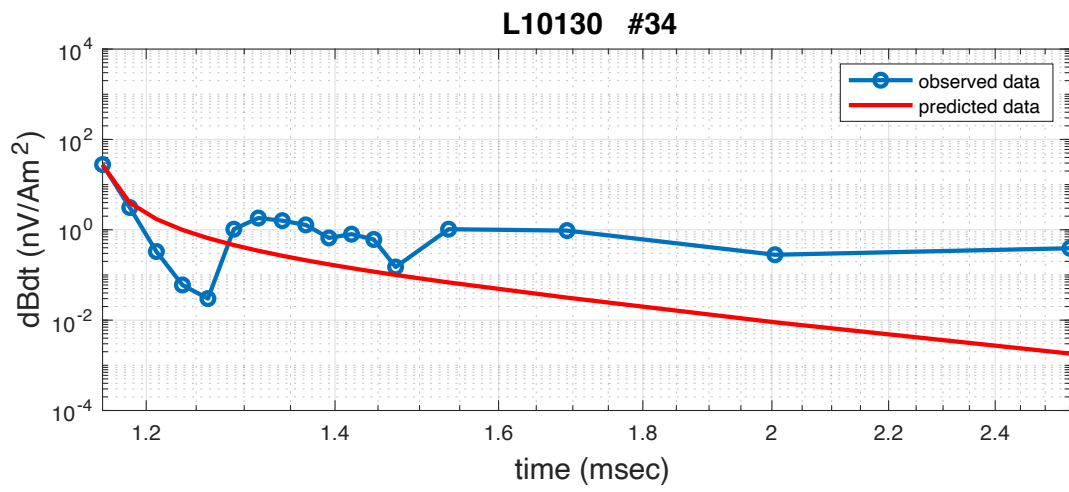




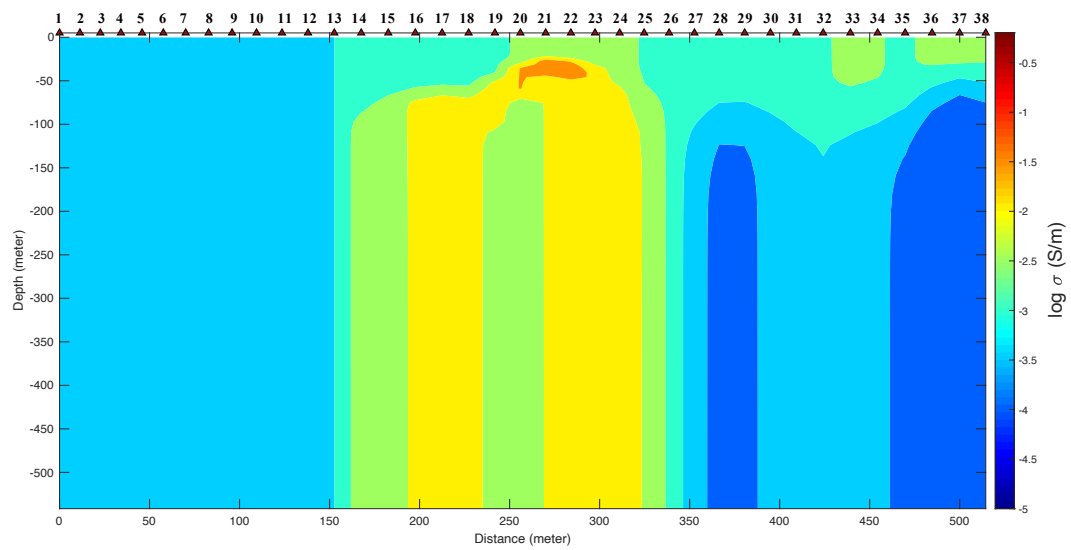




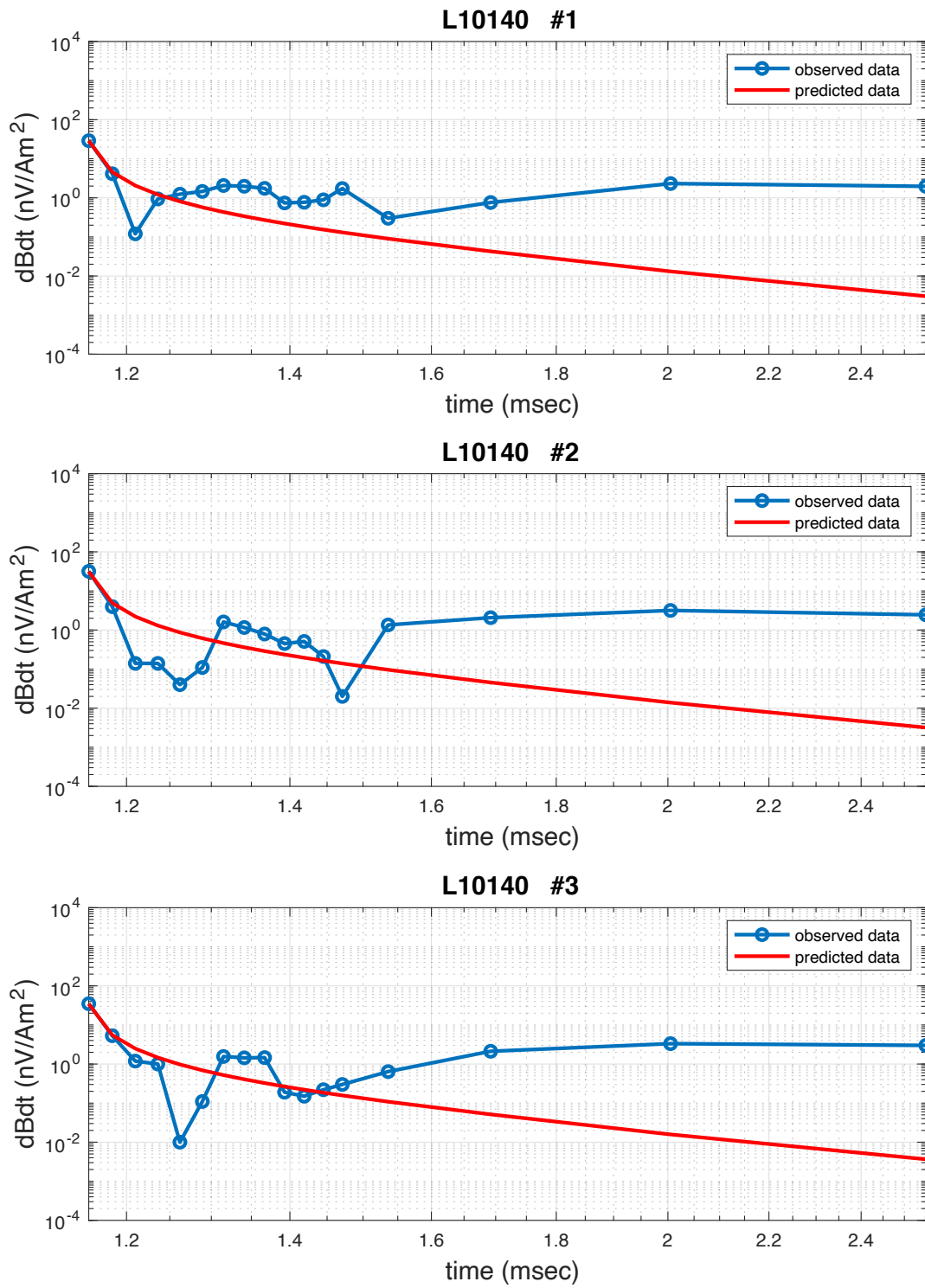


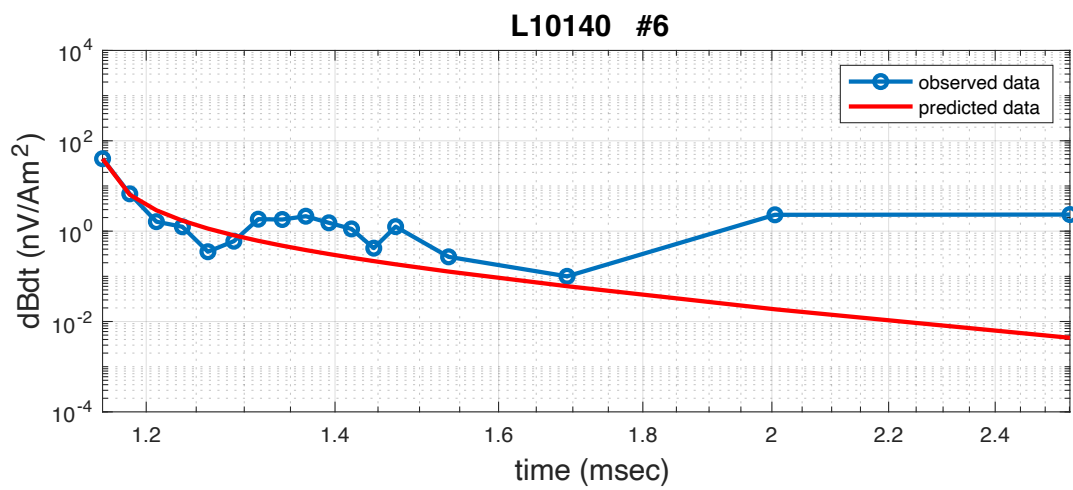
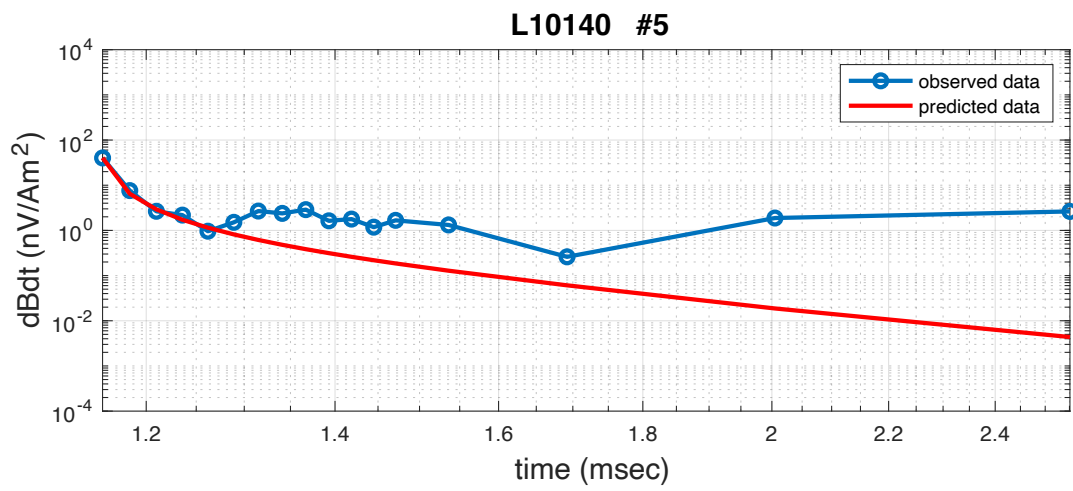
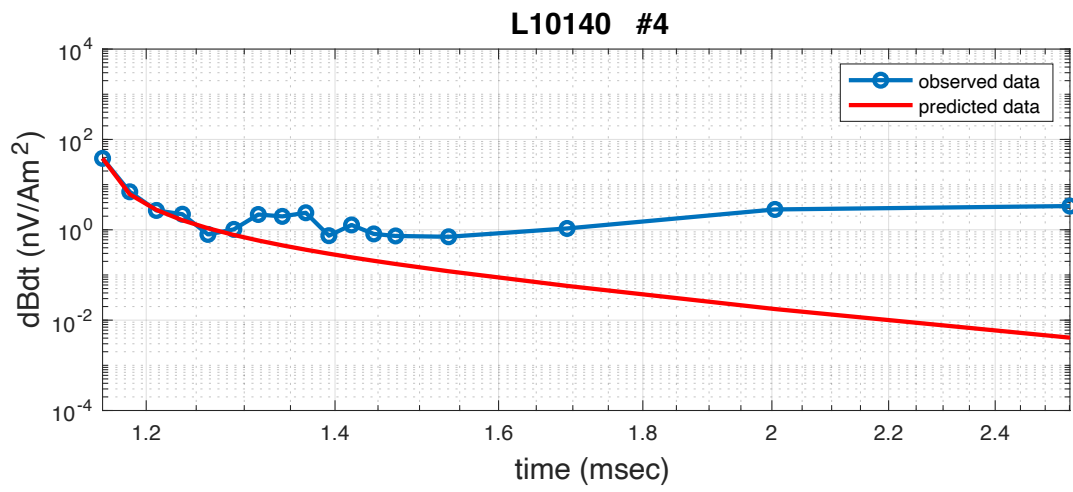


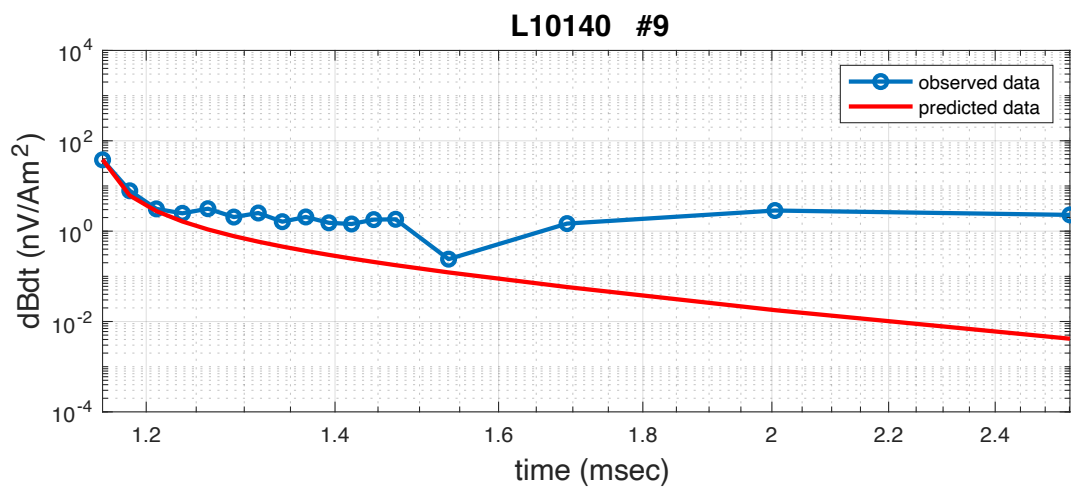
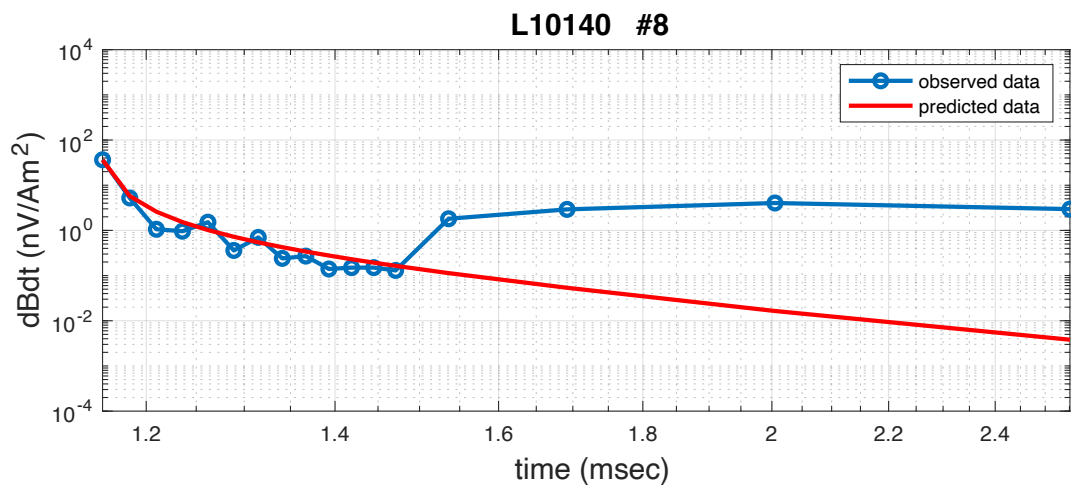
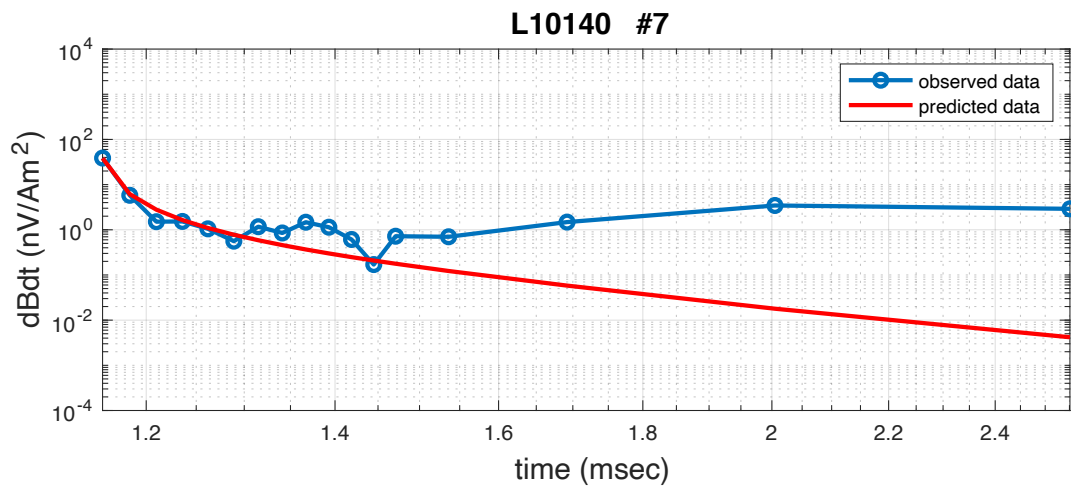
L10140

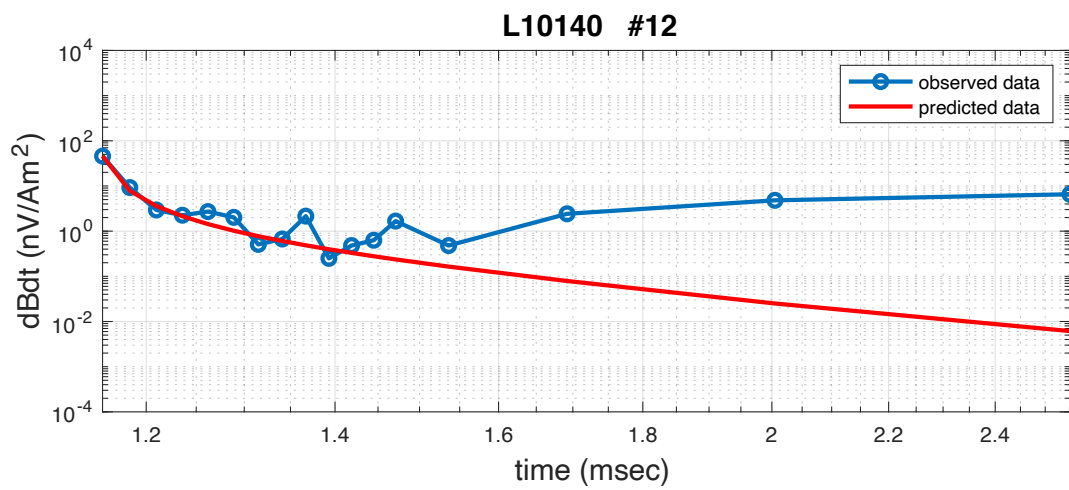
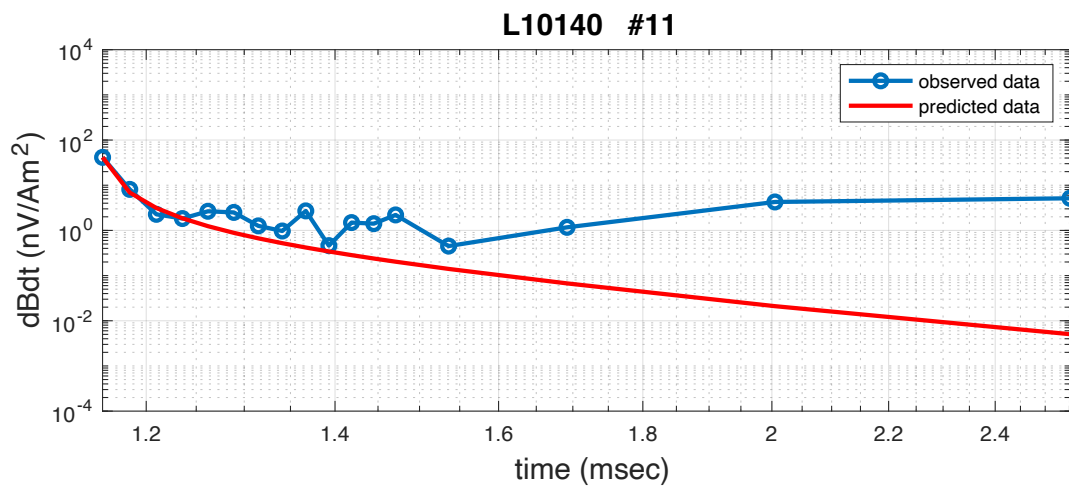
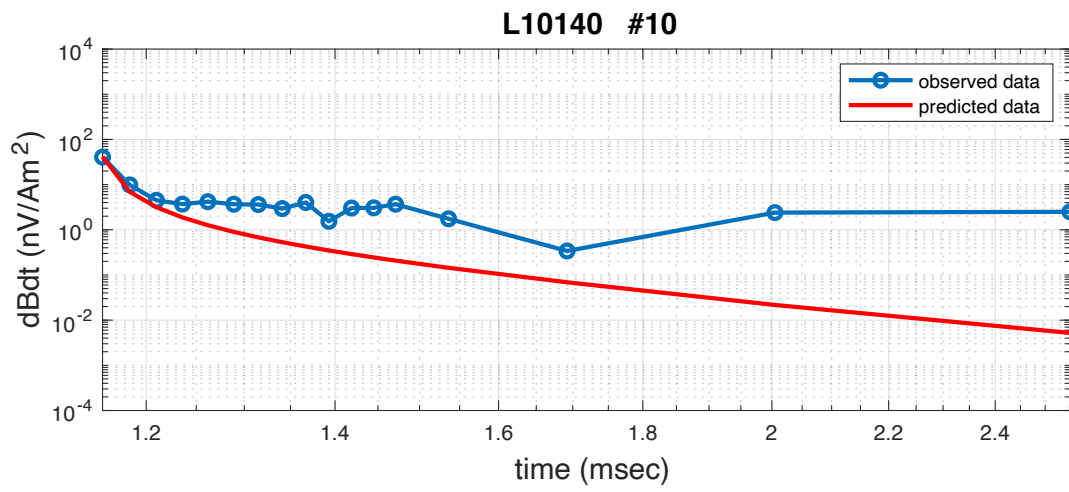


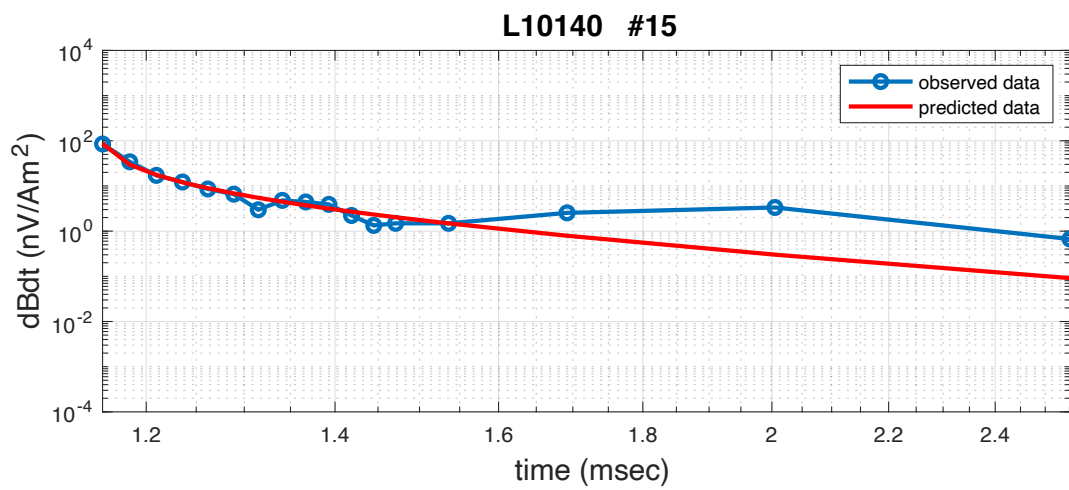
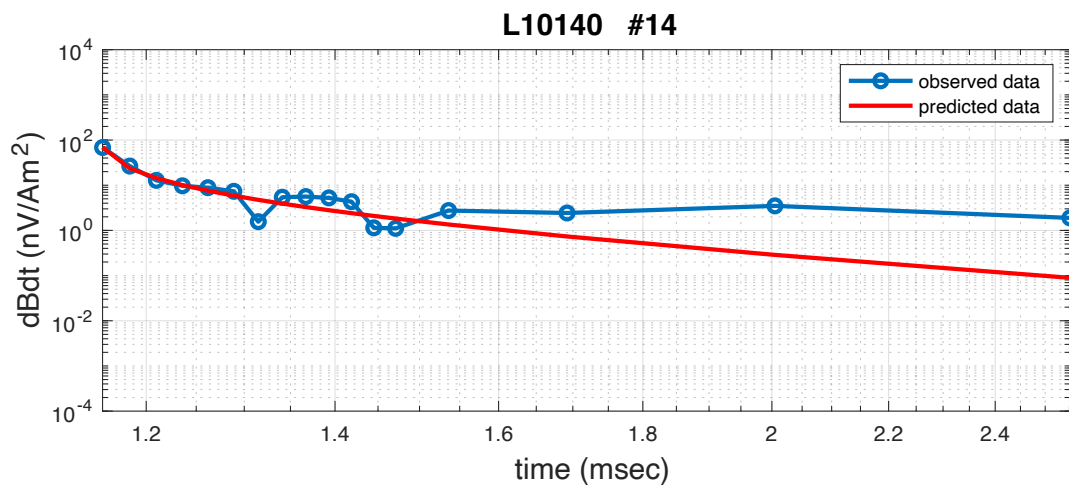
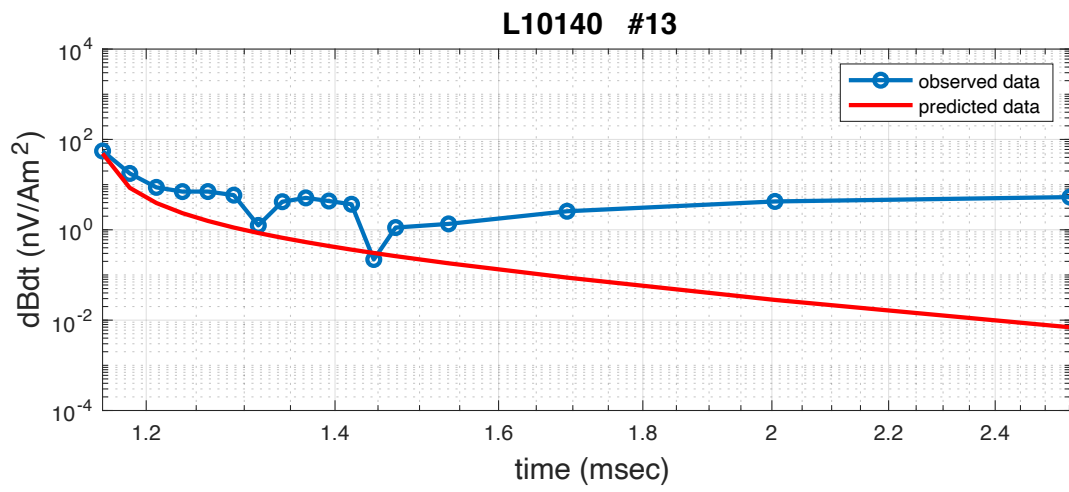
The observation points on L10140

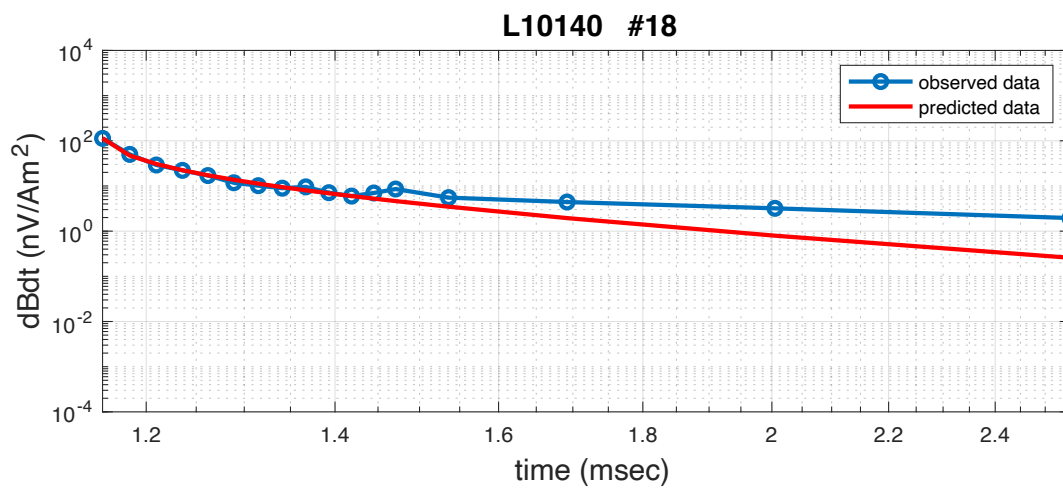
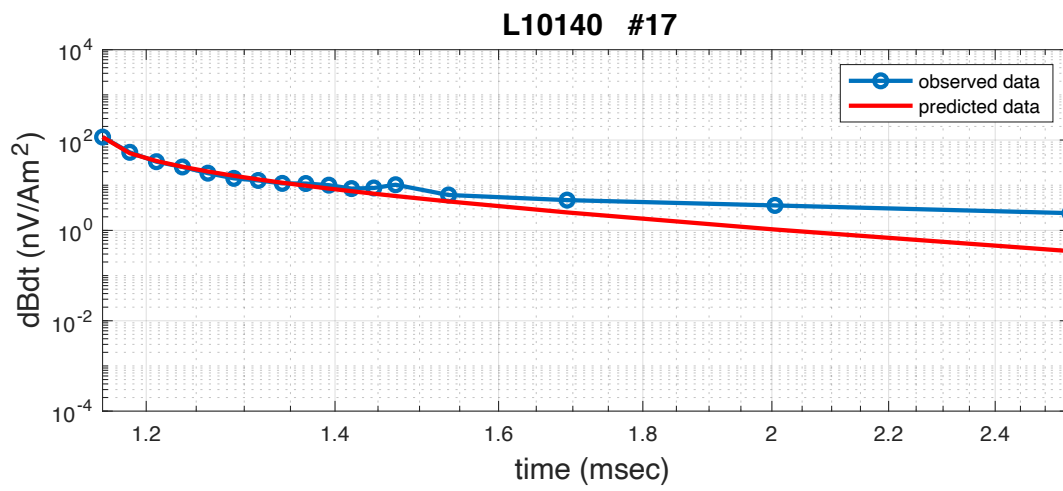
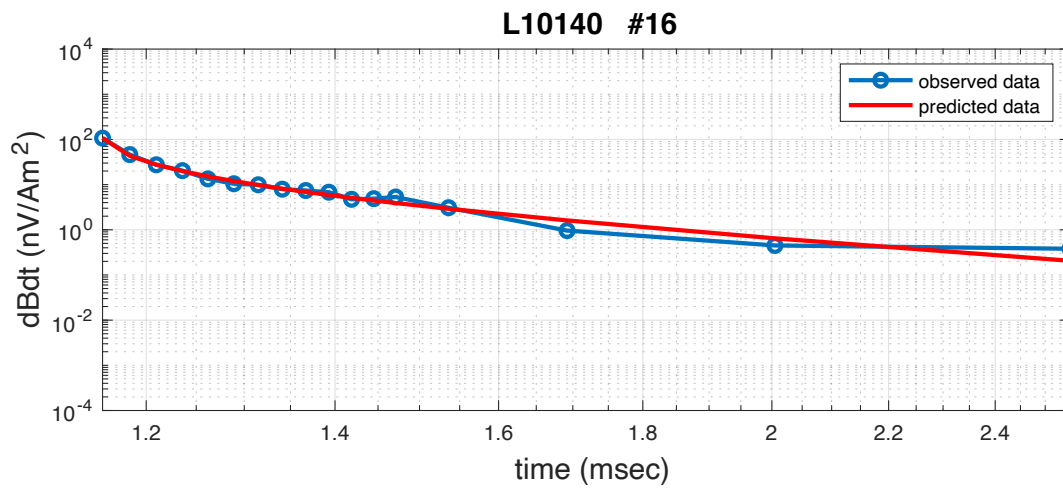


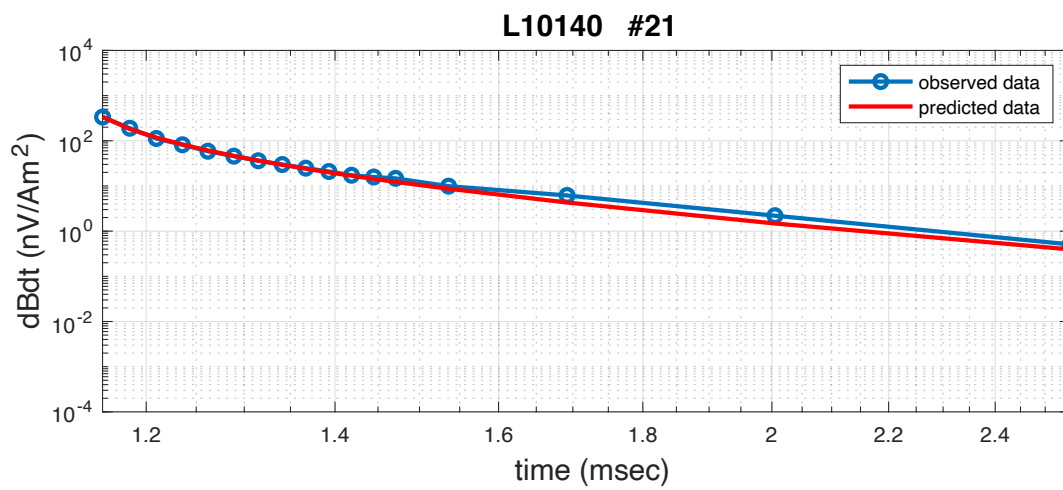
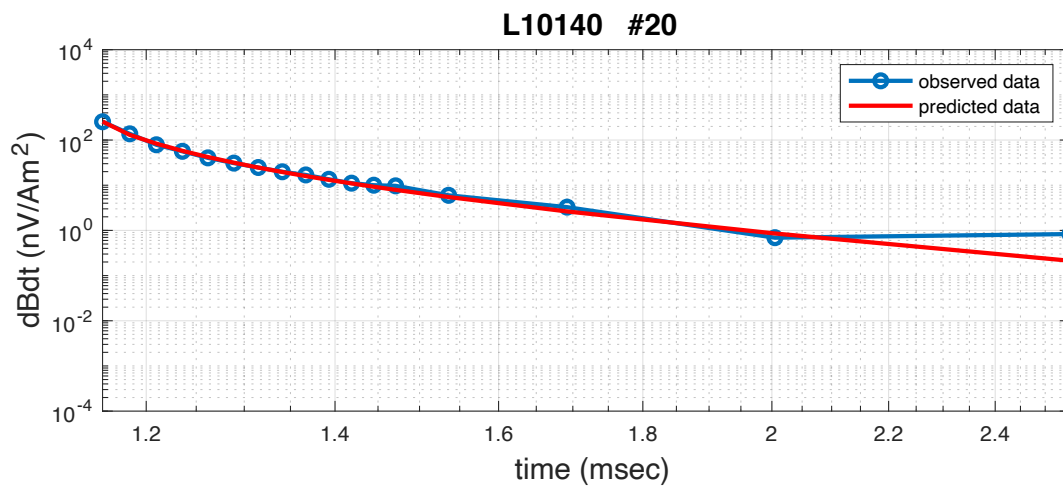
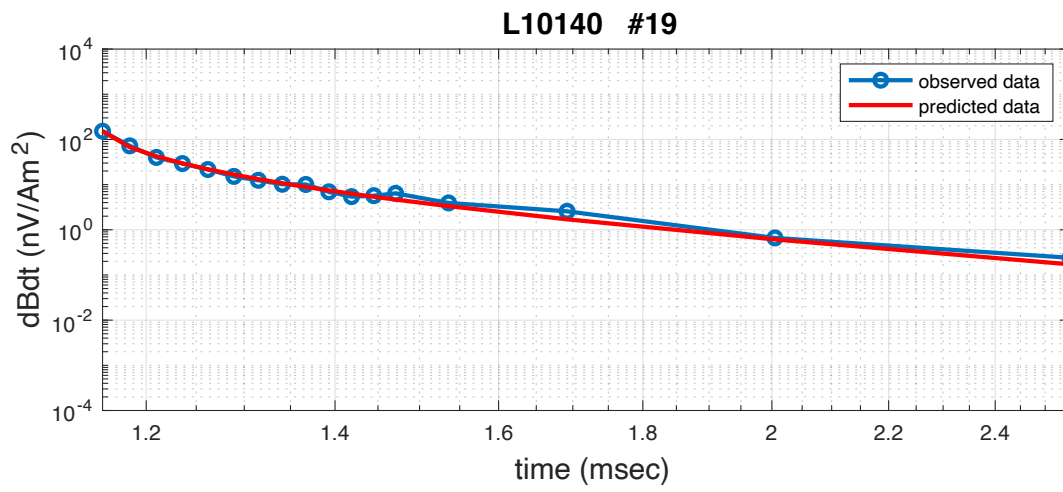


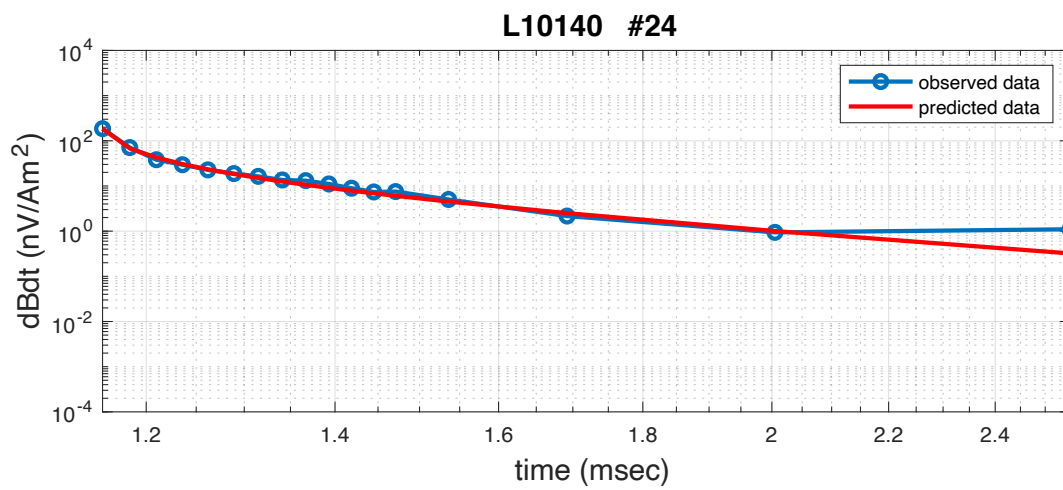
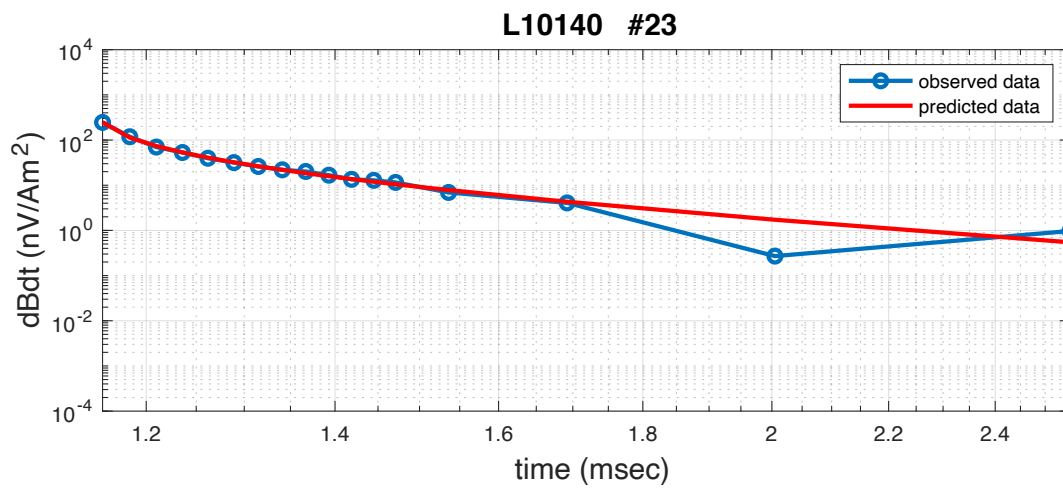
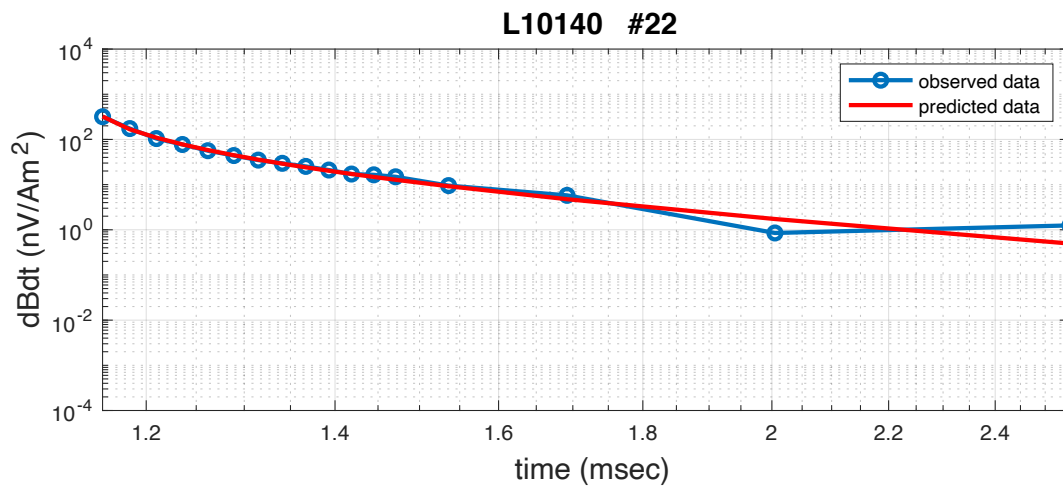


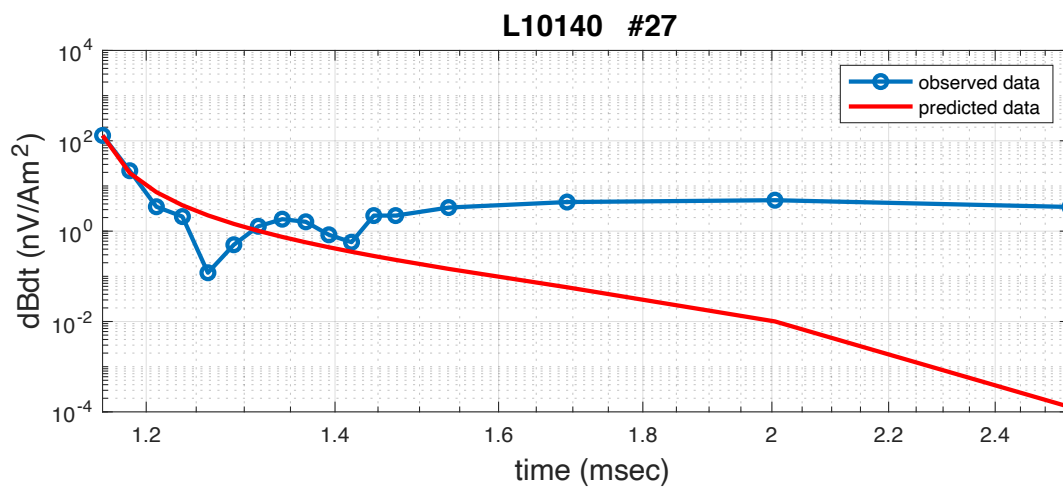
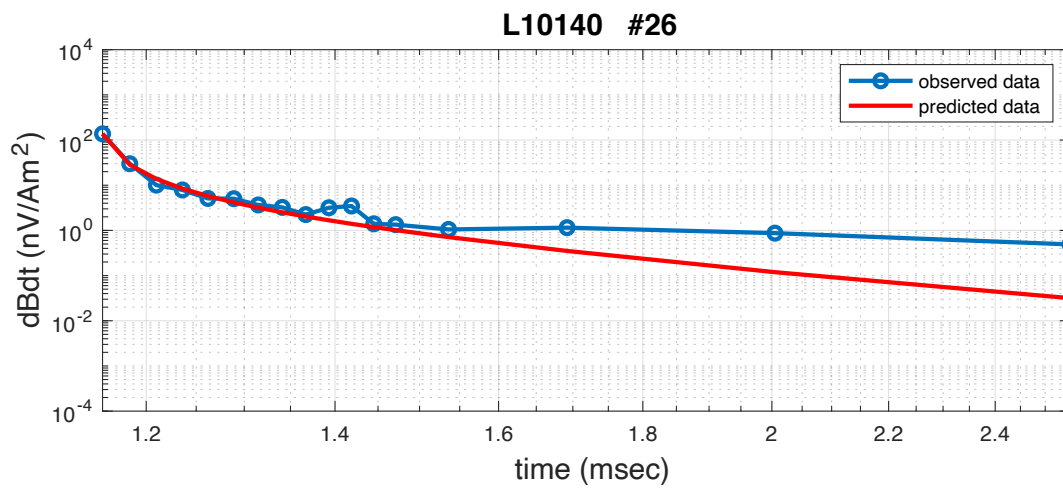
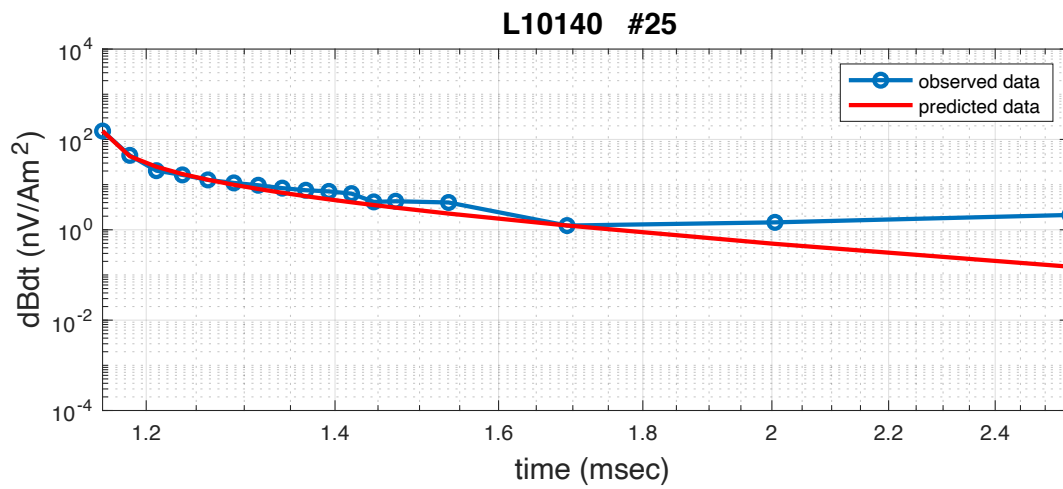


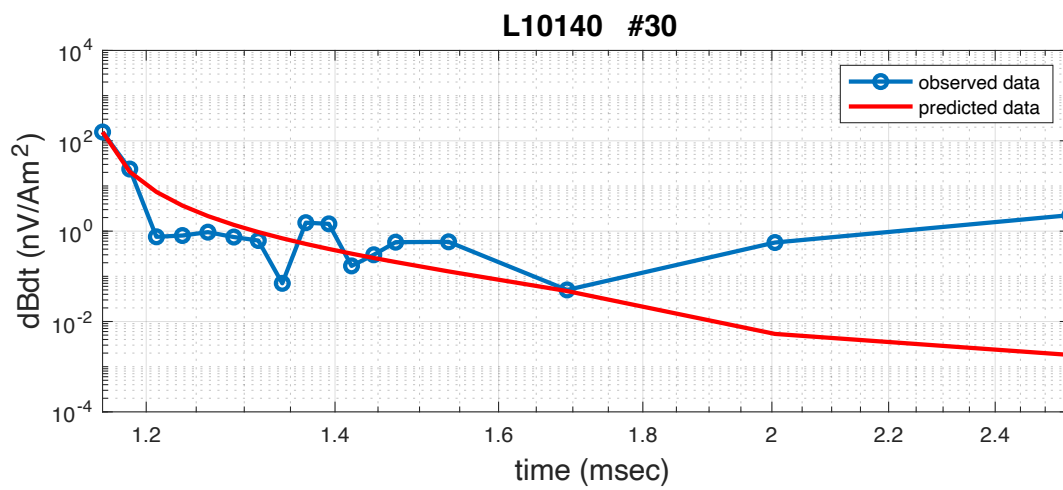
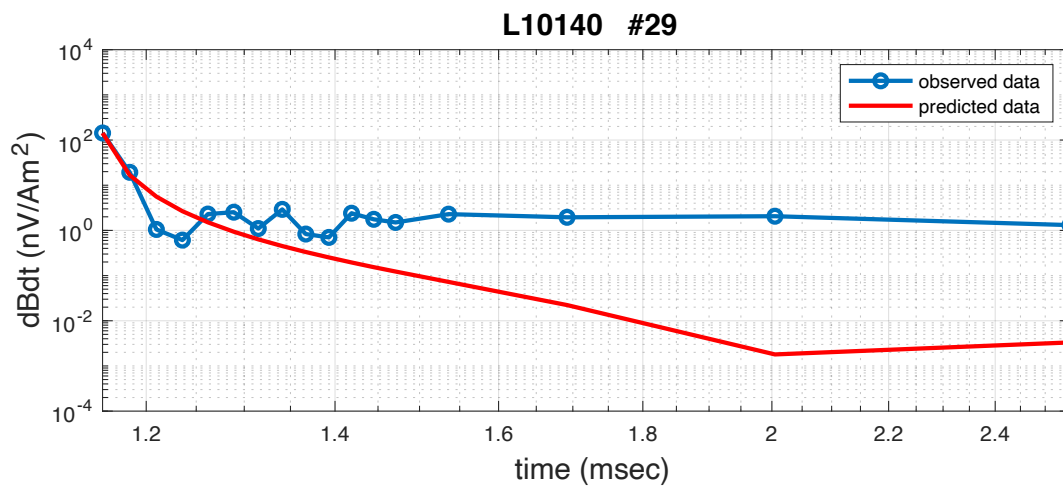
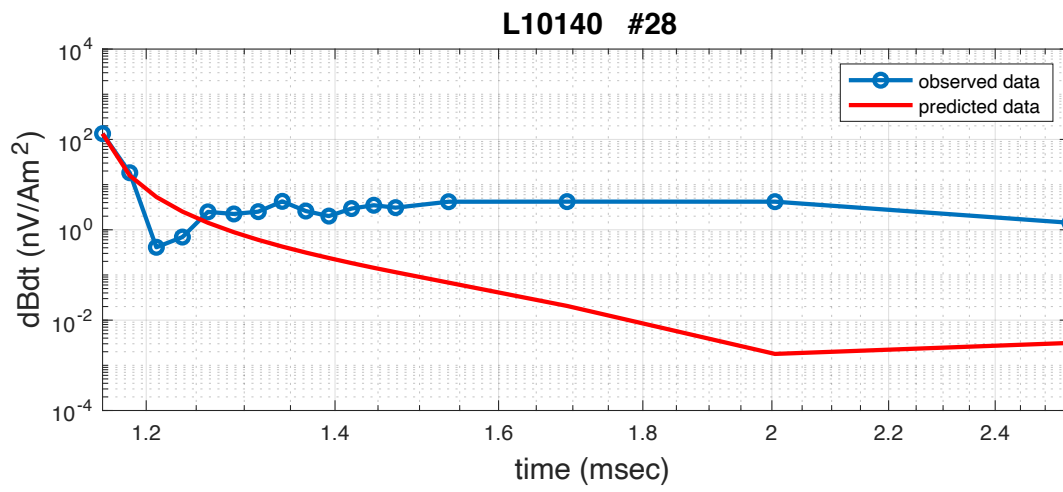


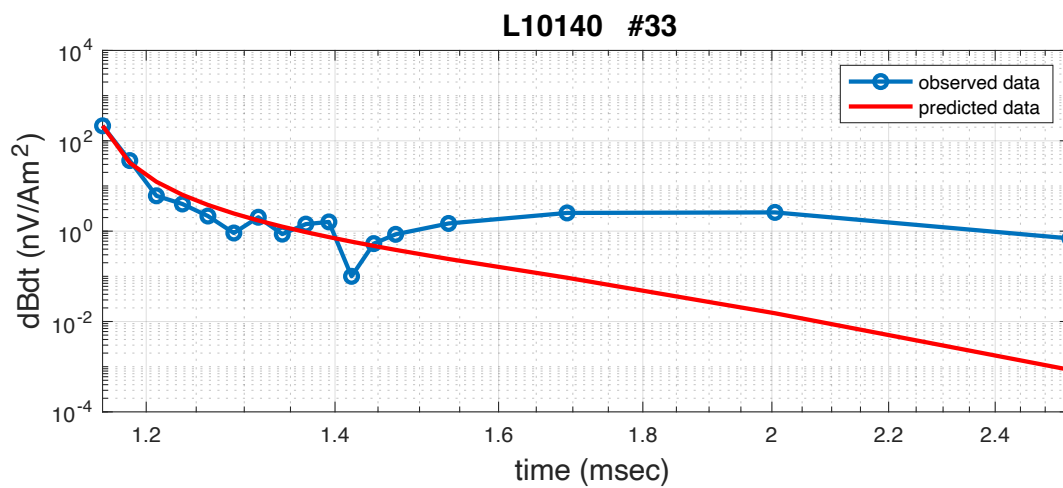
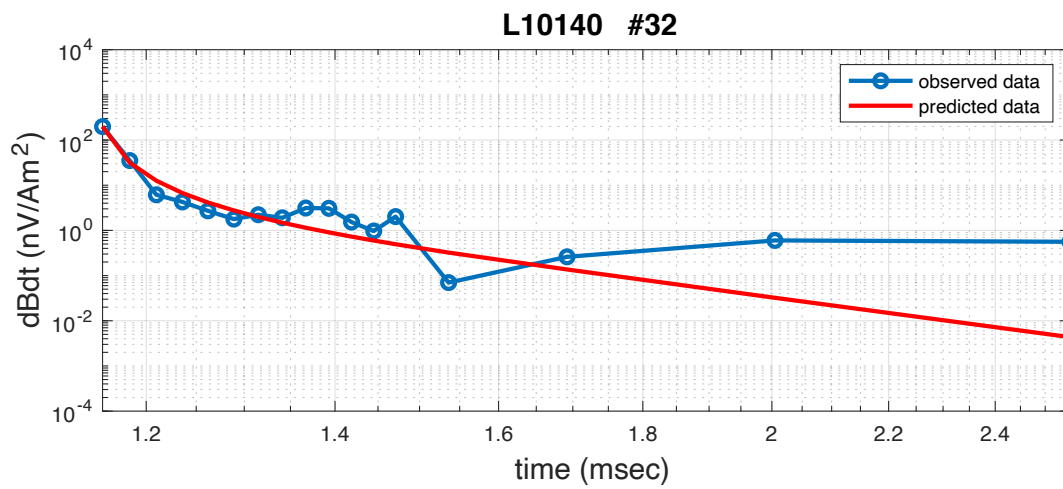
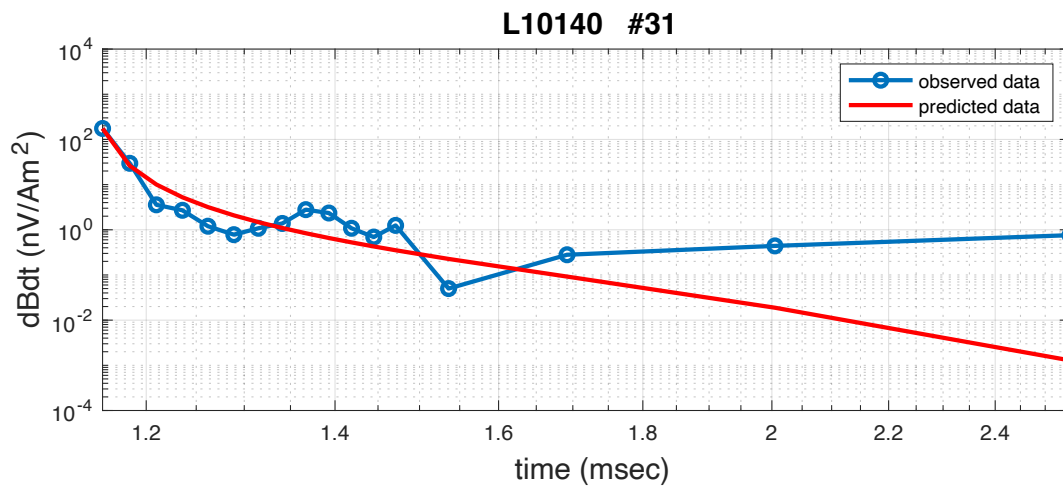


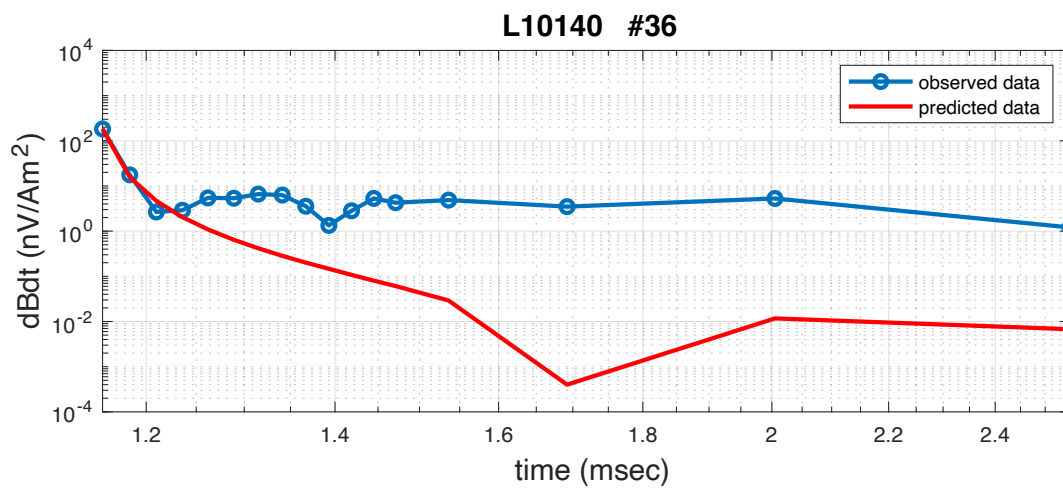
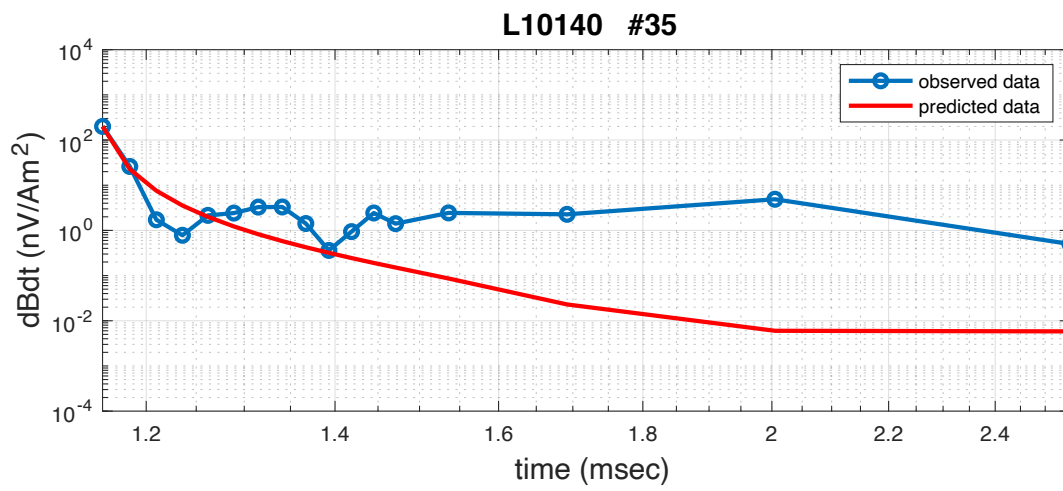
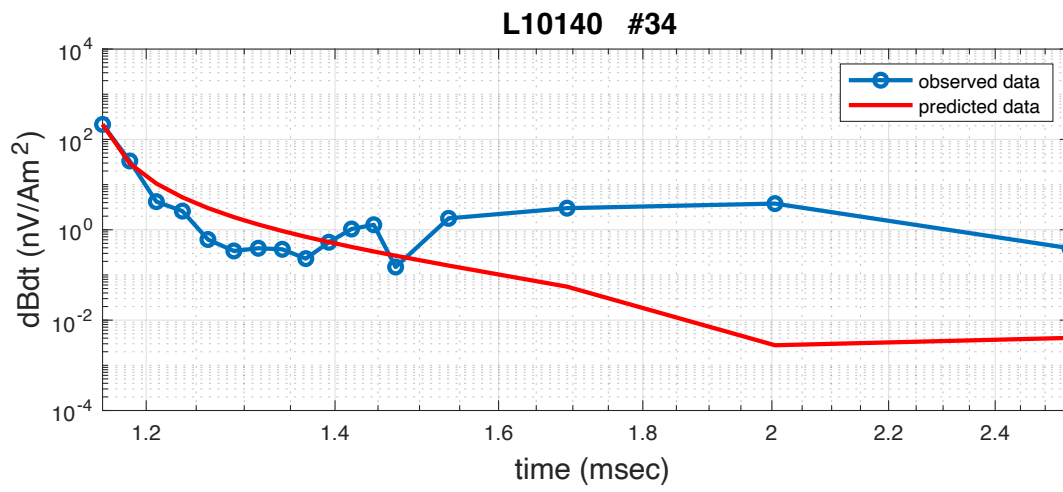


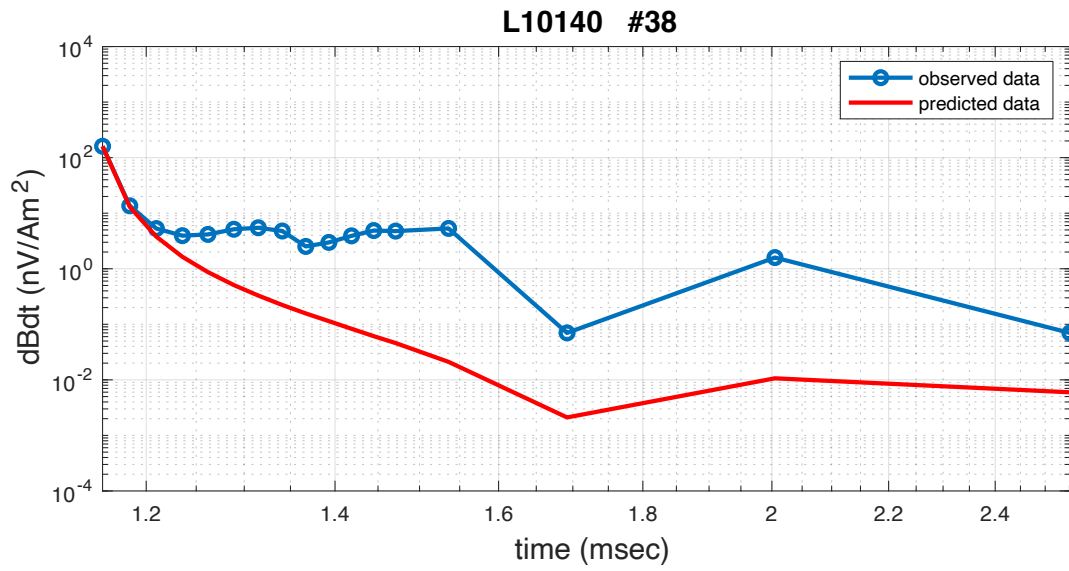
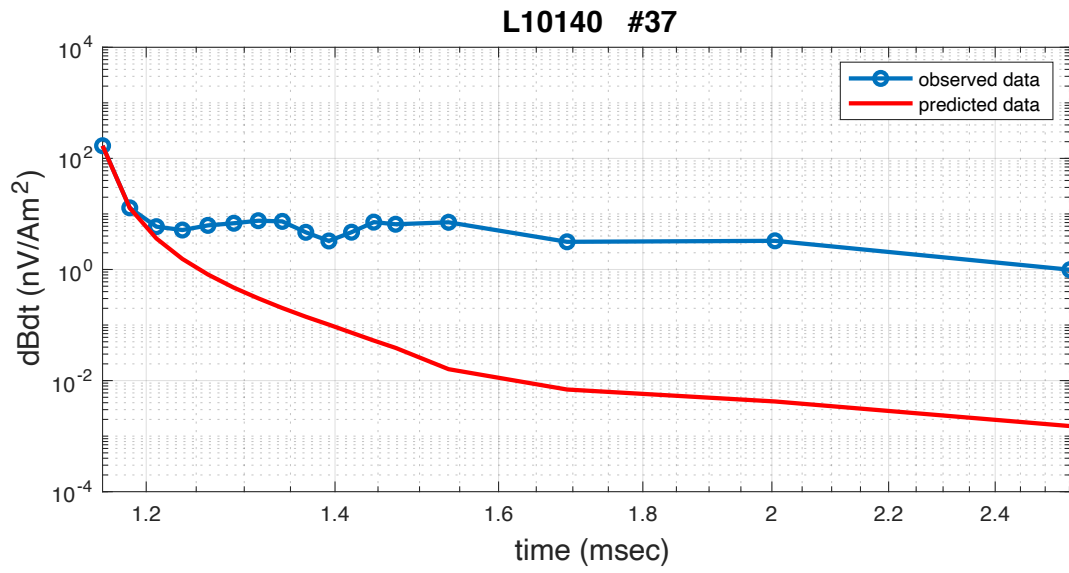




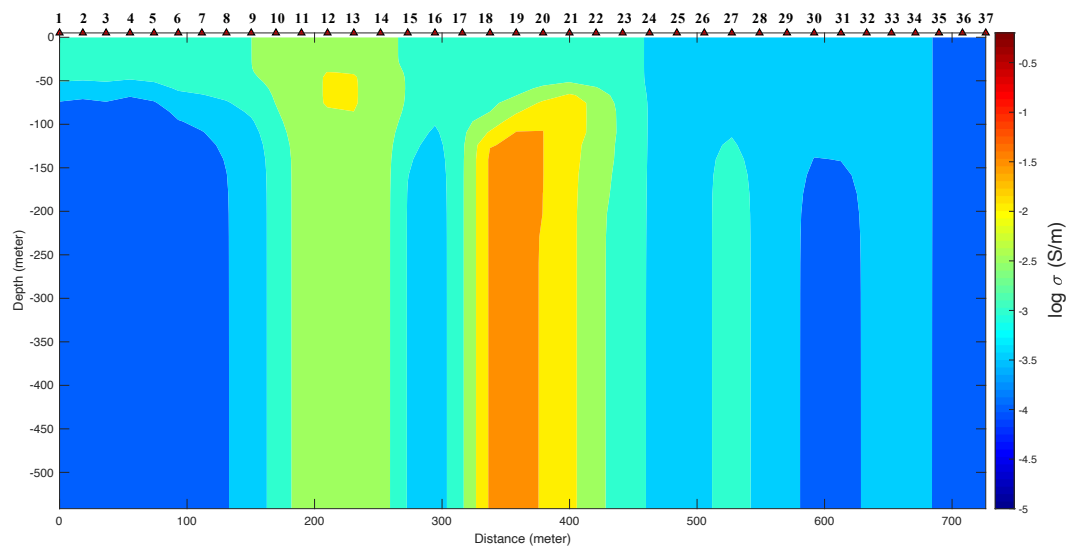




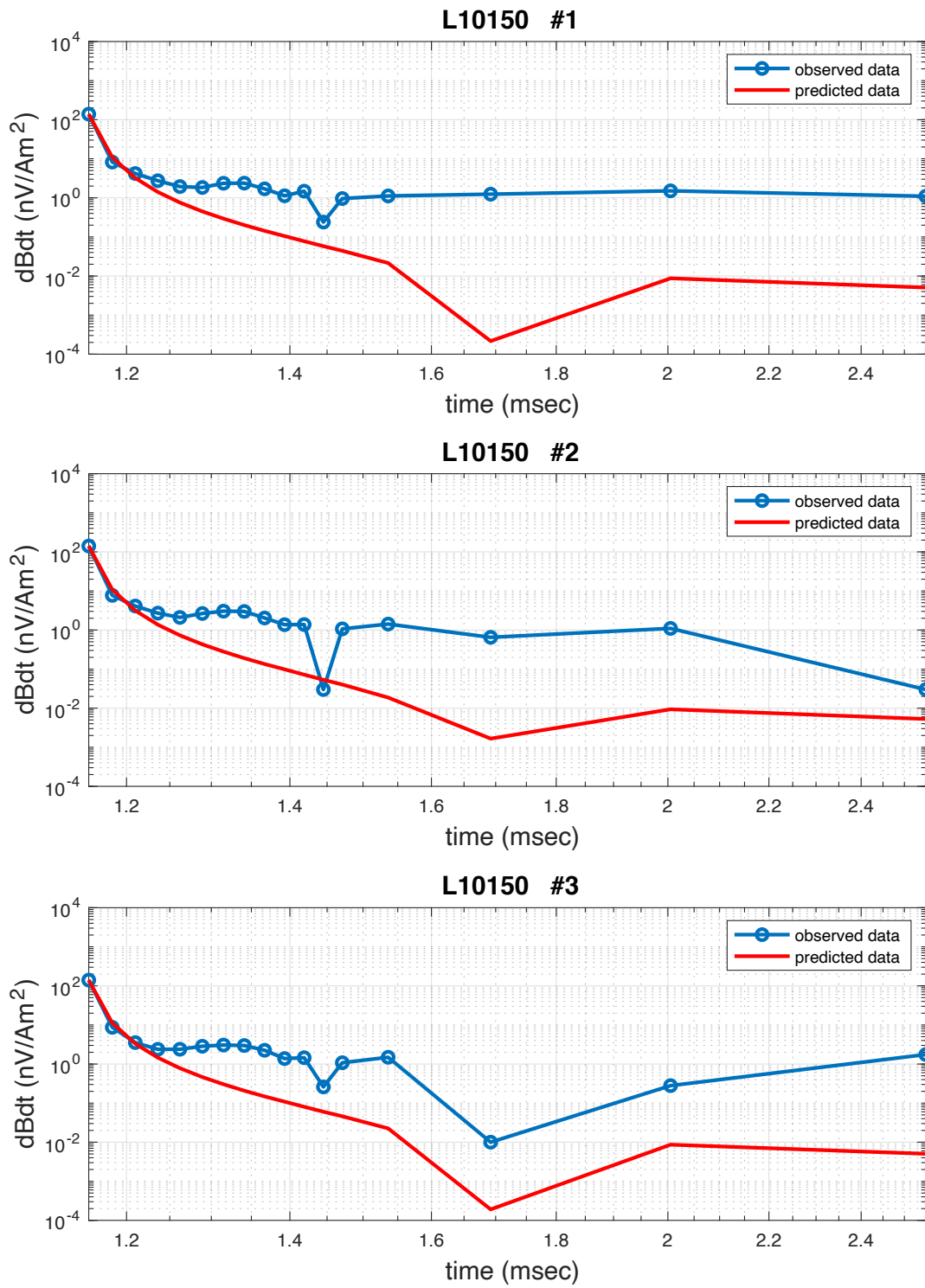


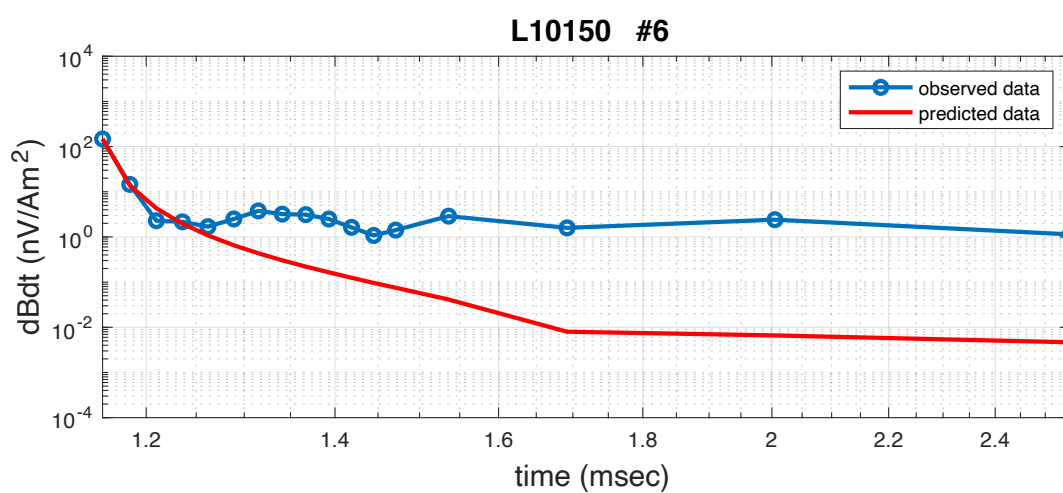
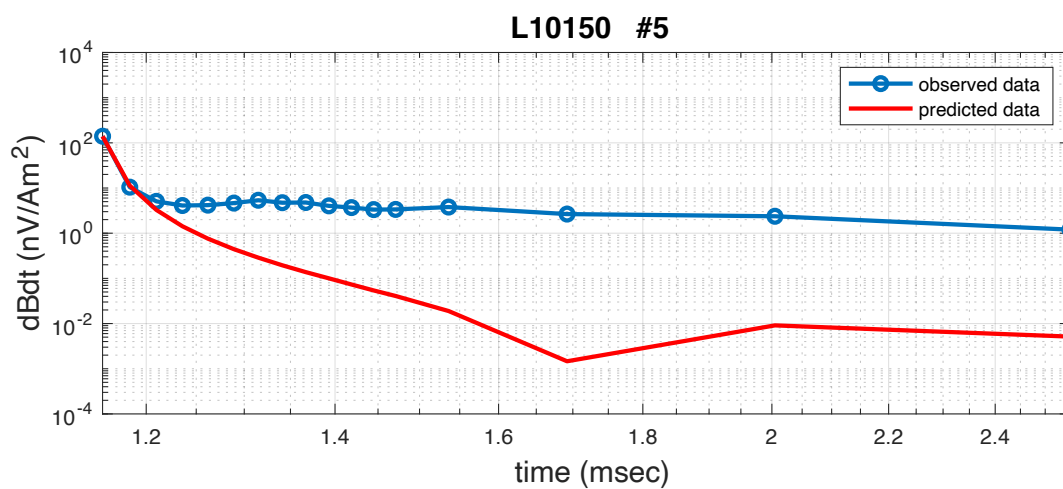
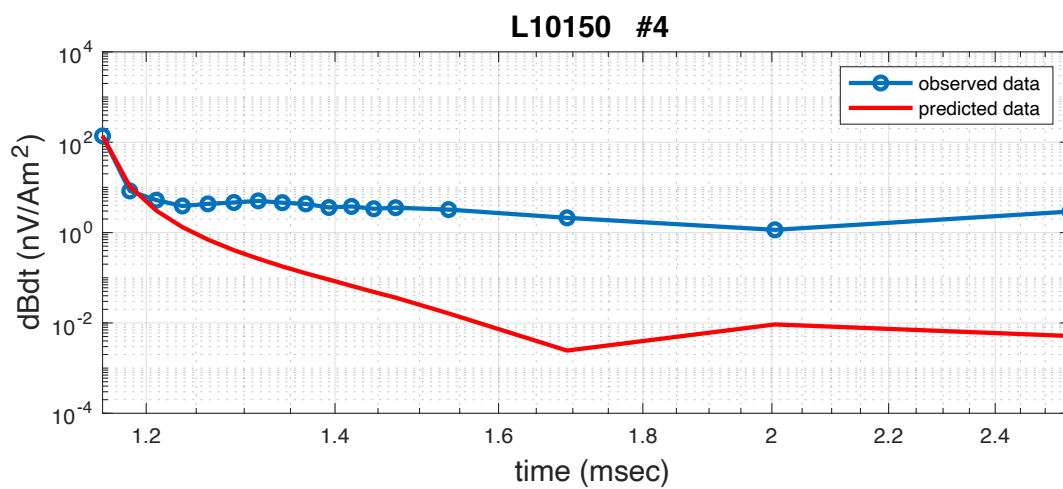


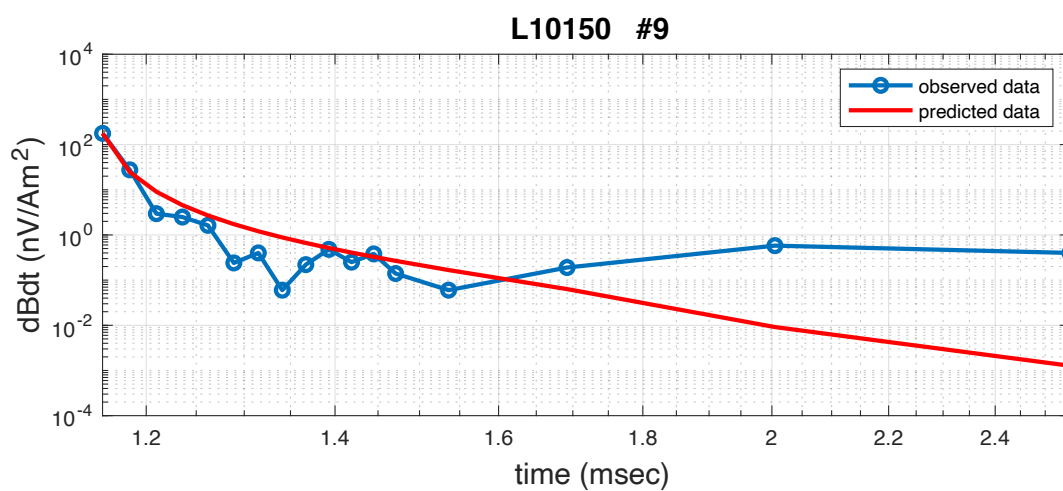
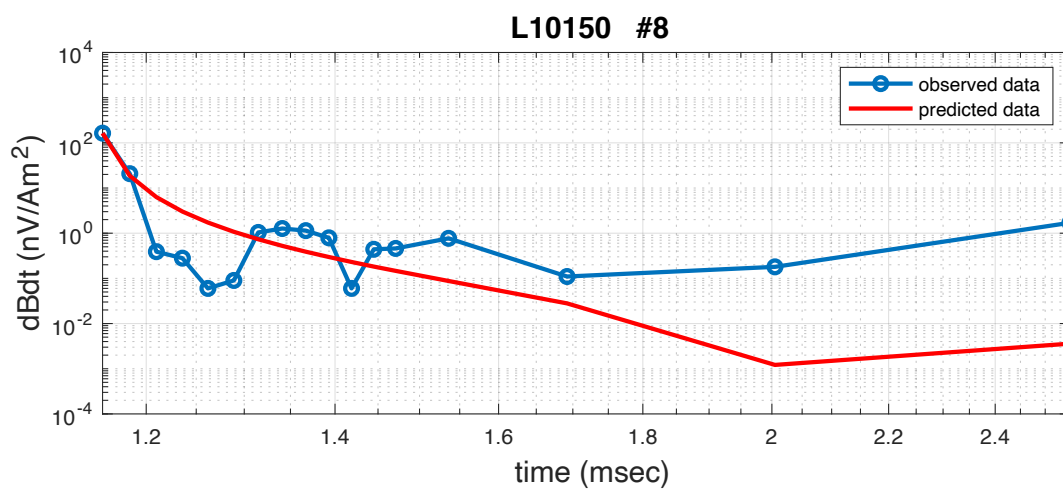
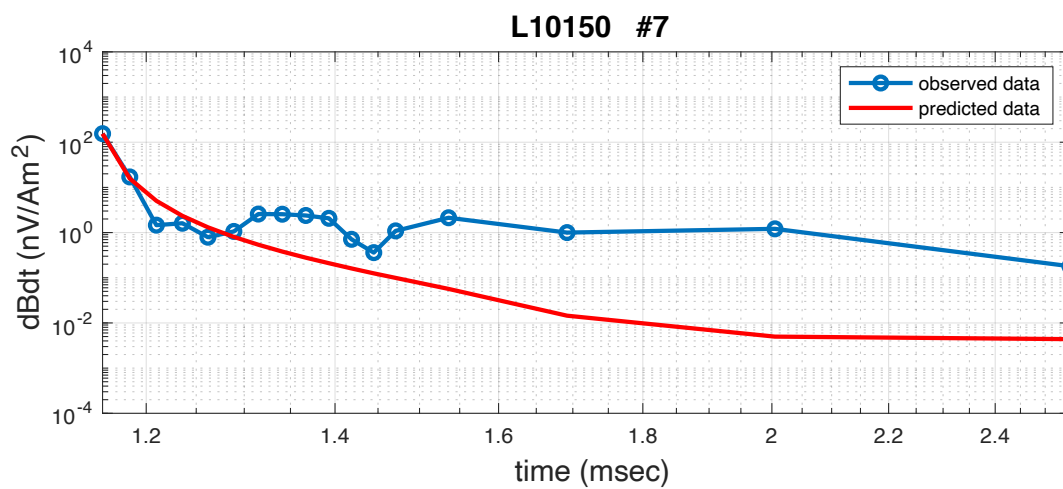
L10150

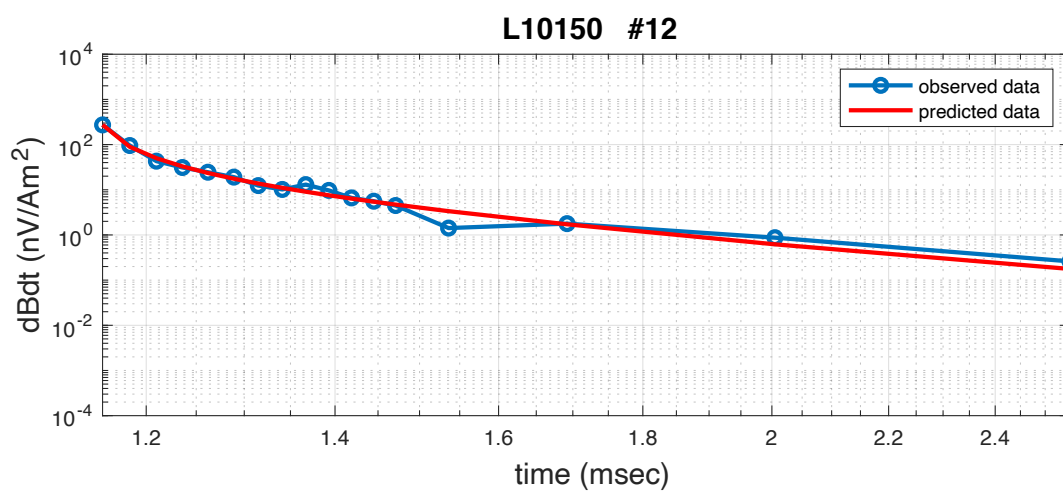
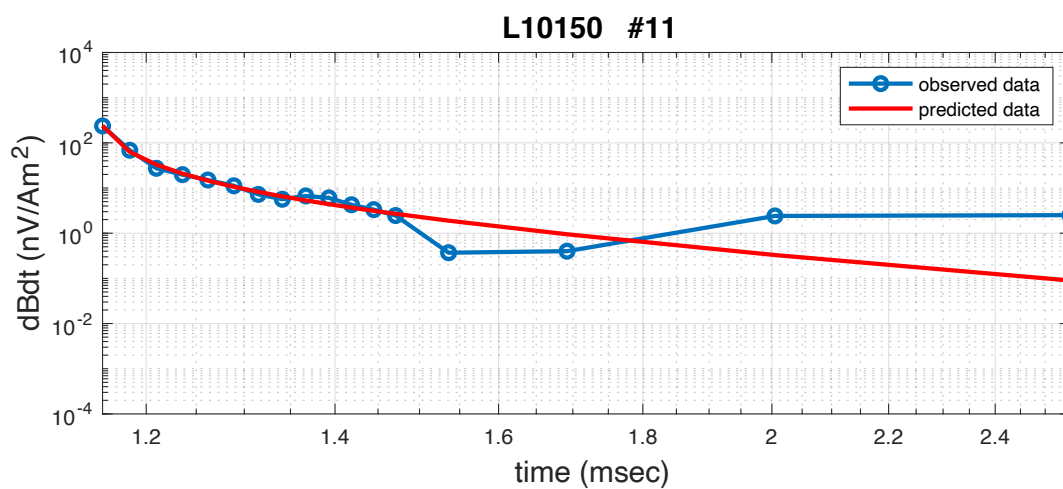
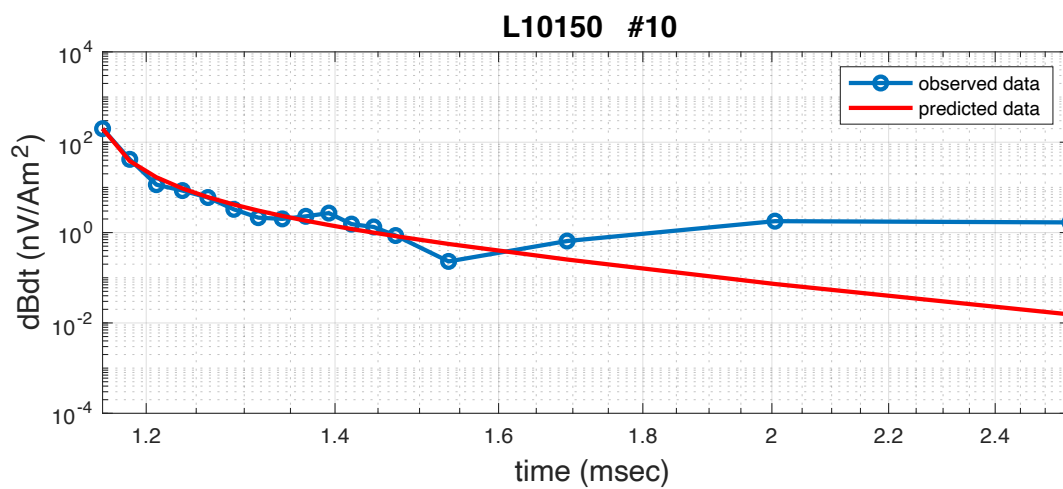


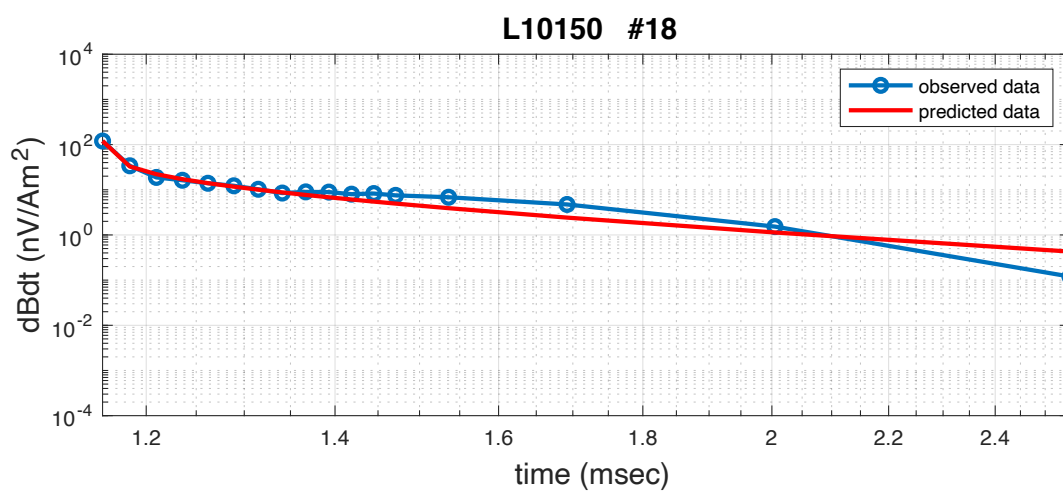
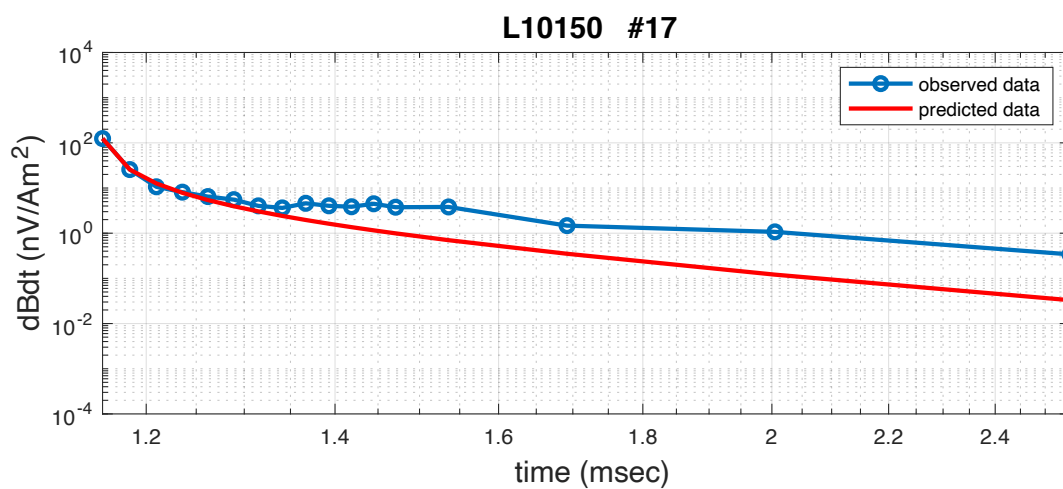
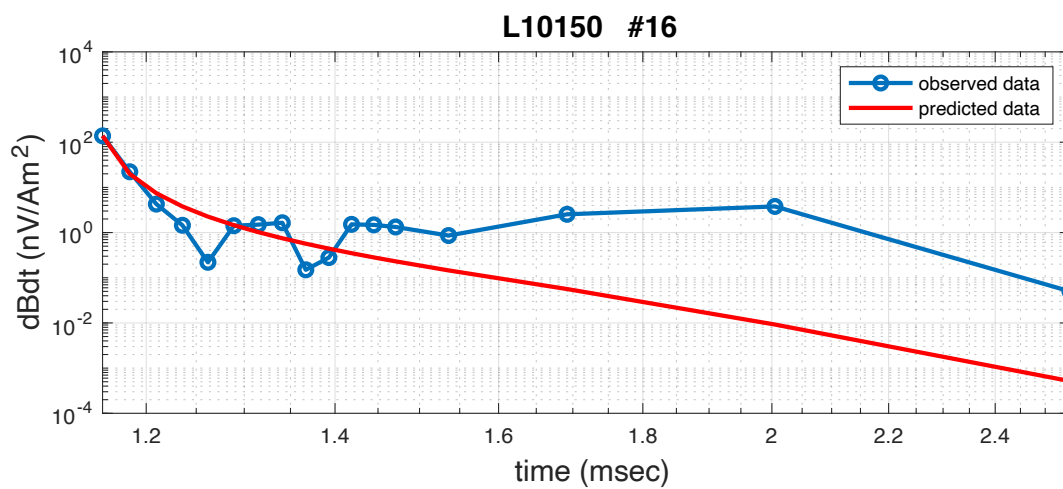
The observation points on L10150

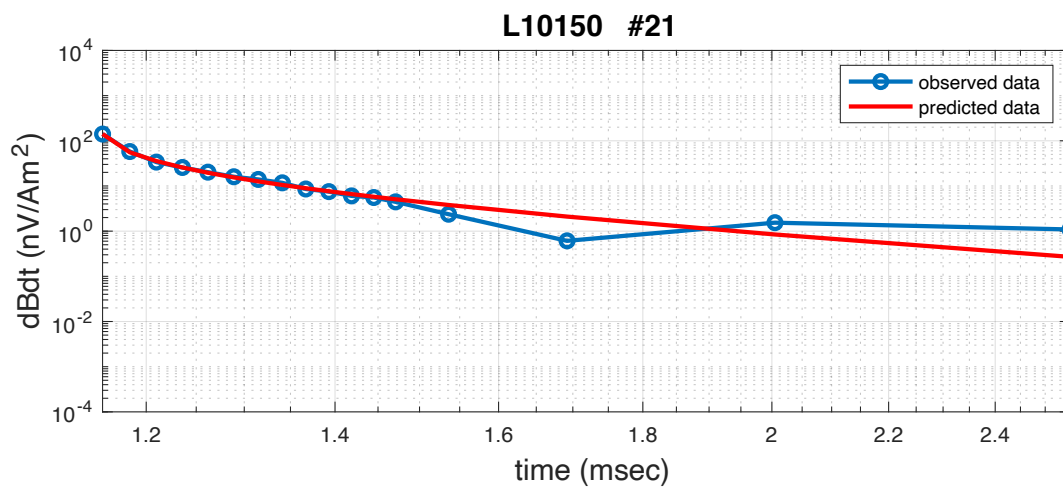
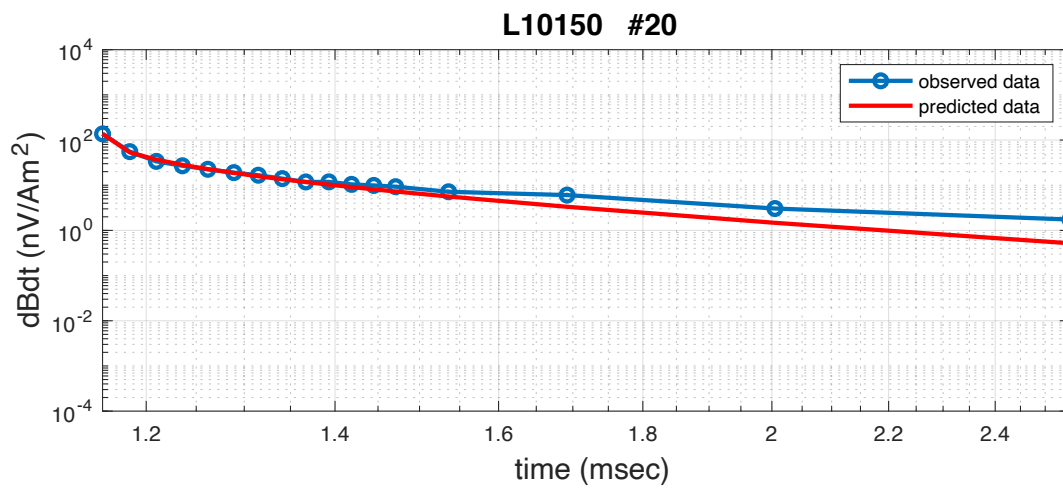
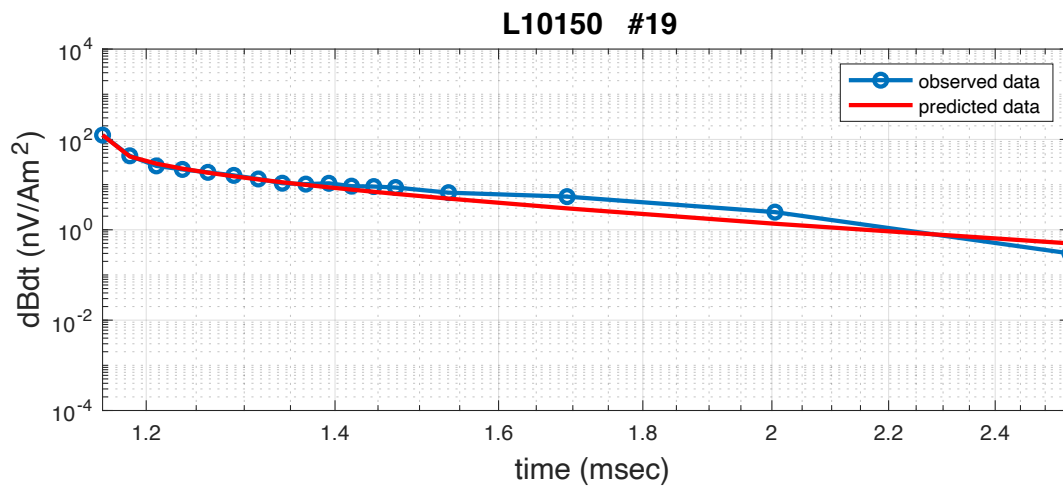


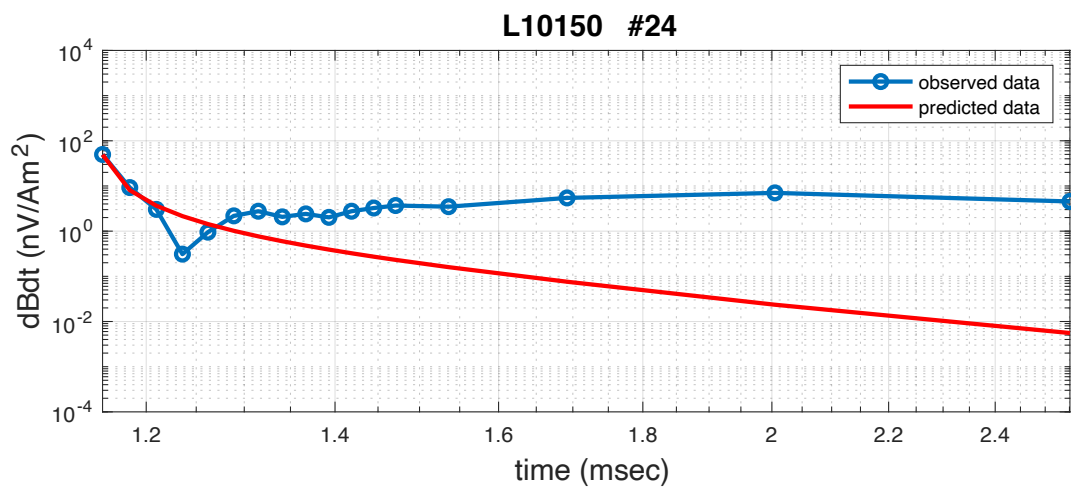
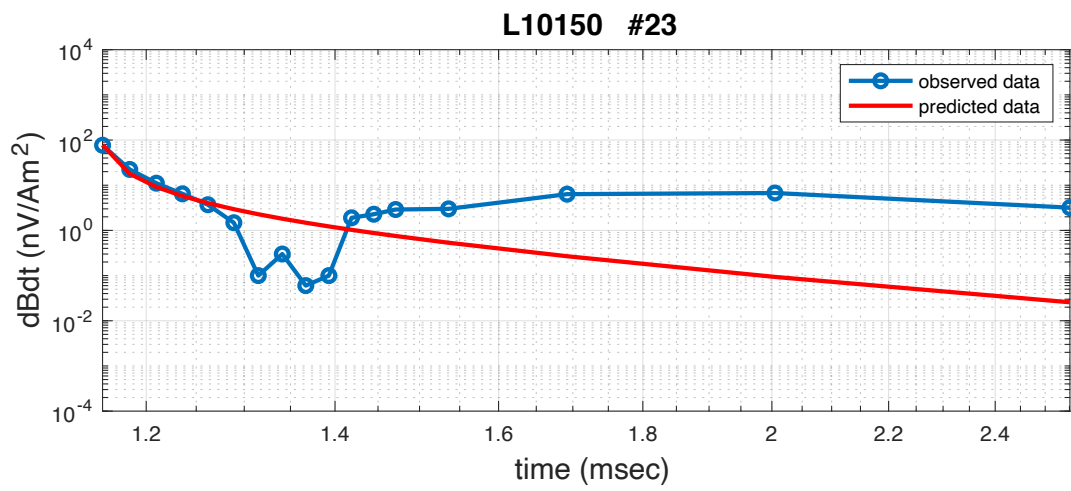
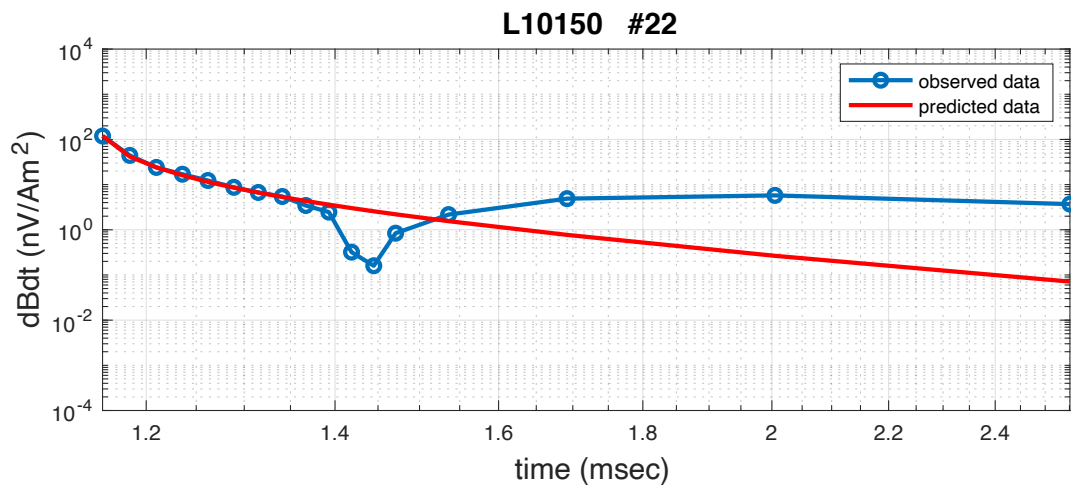


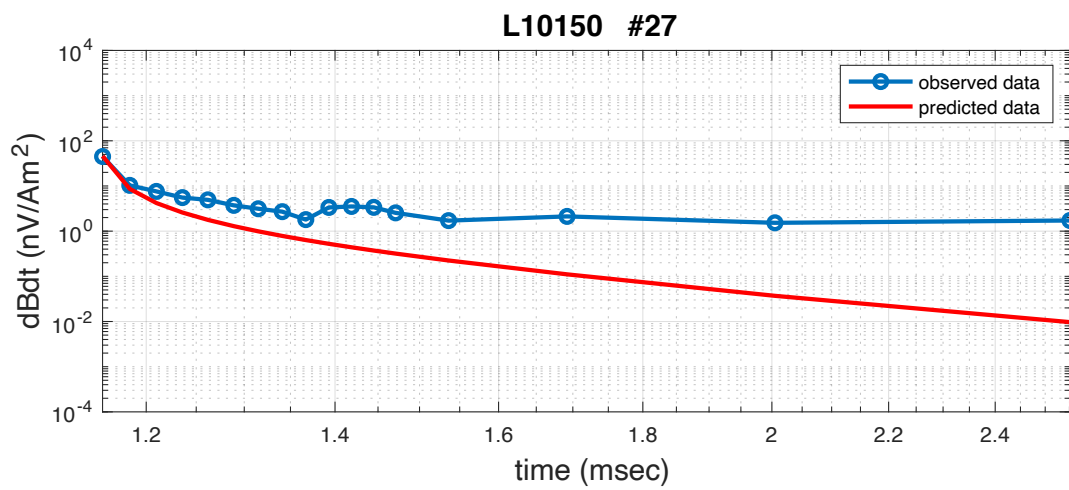
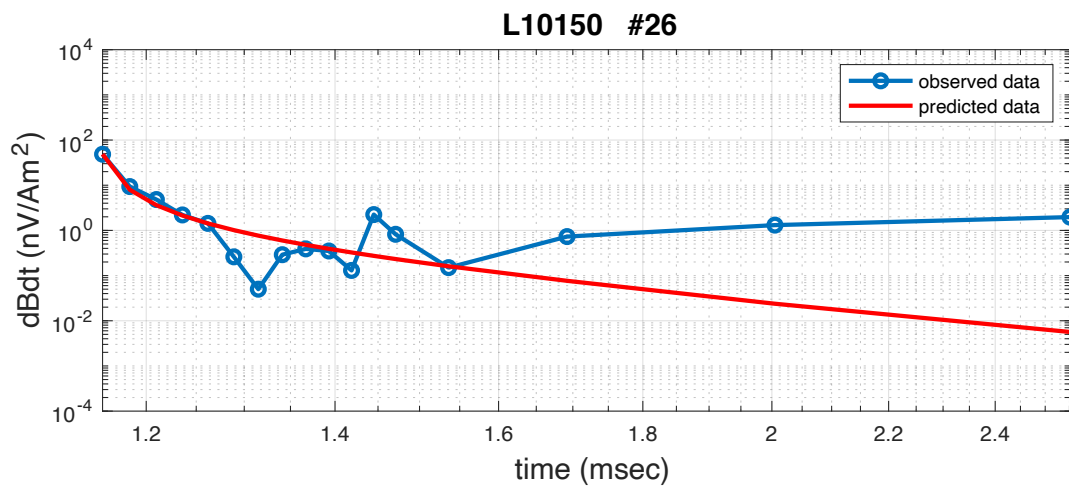
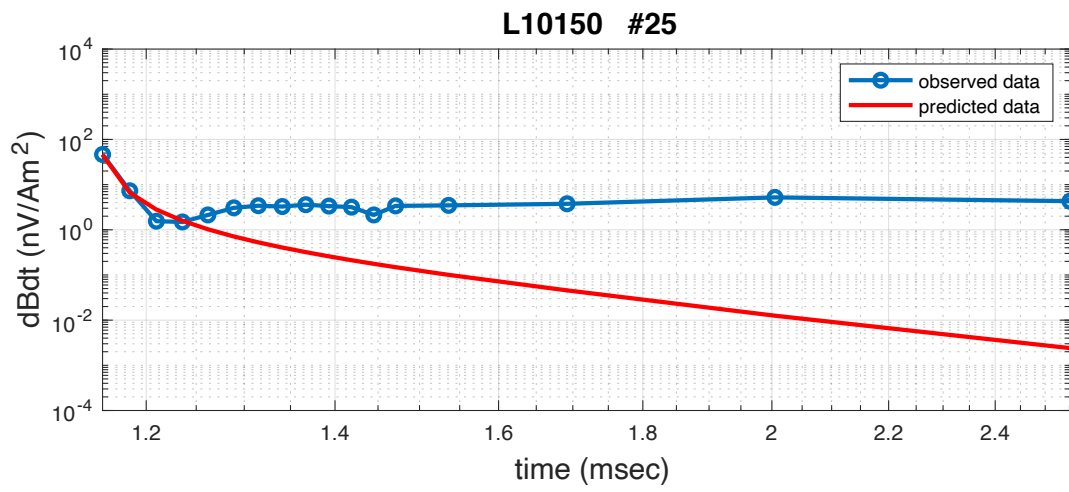


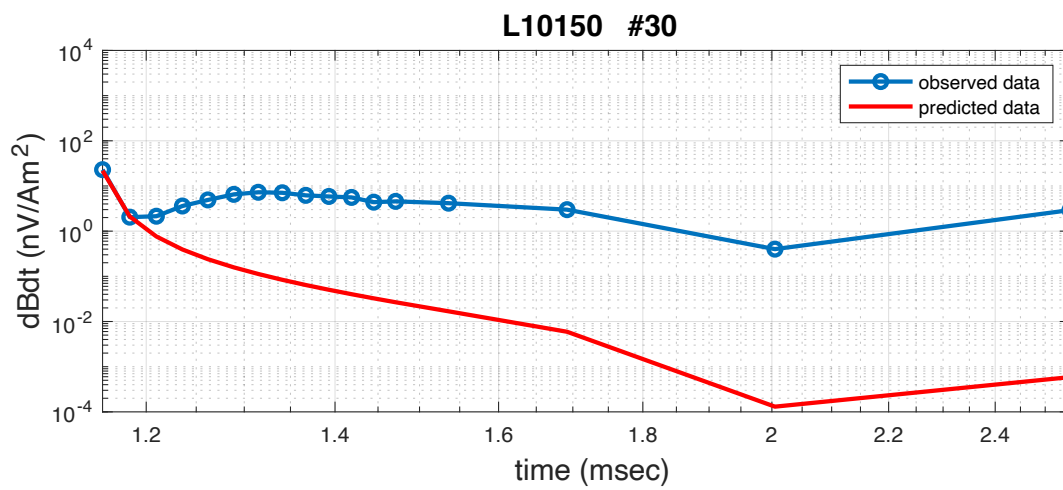
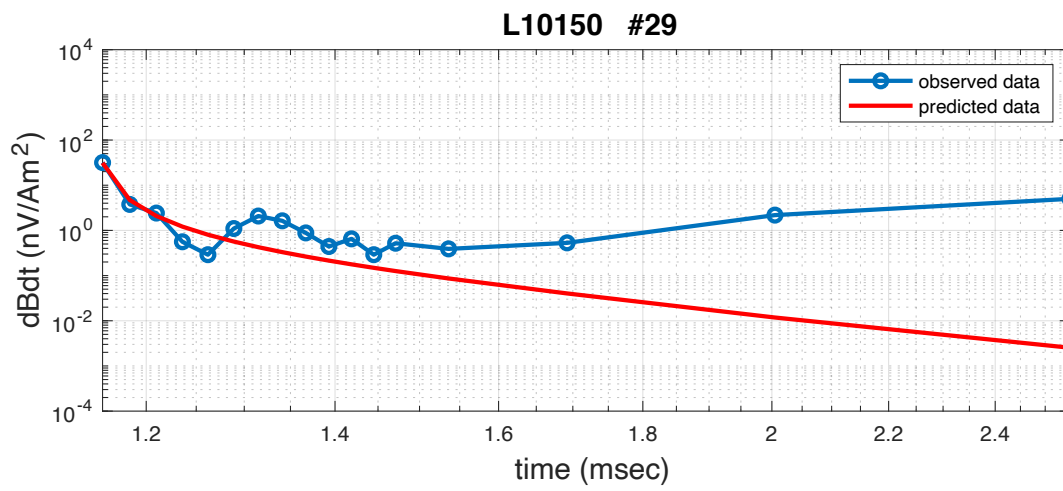
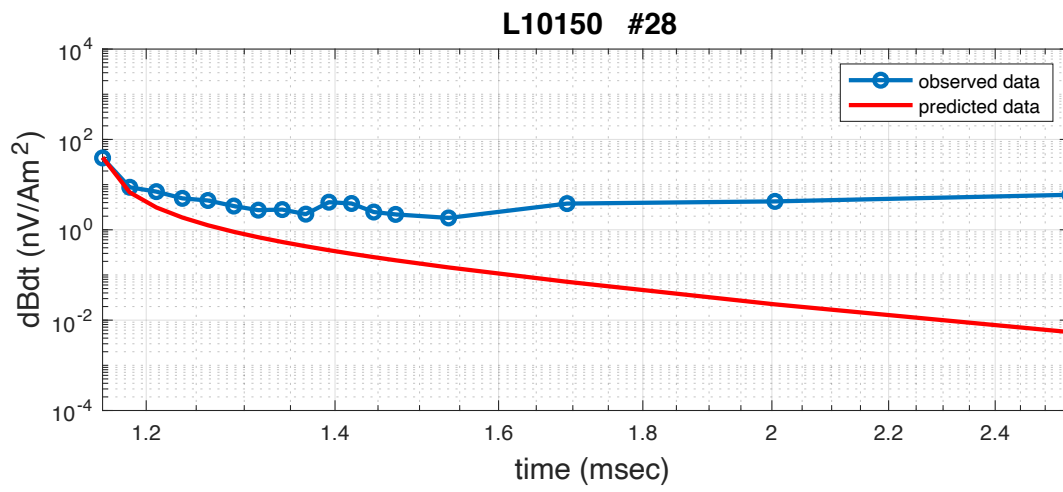


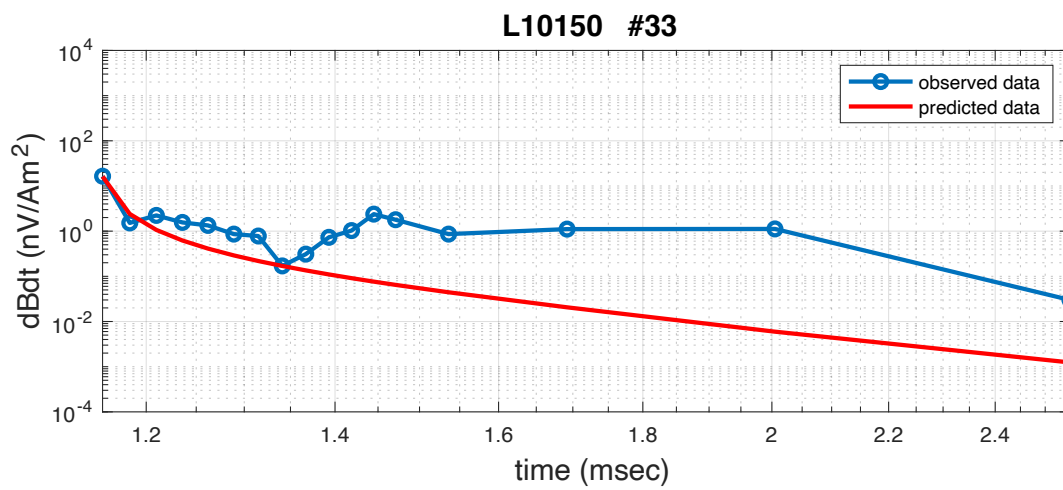
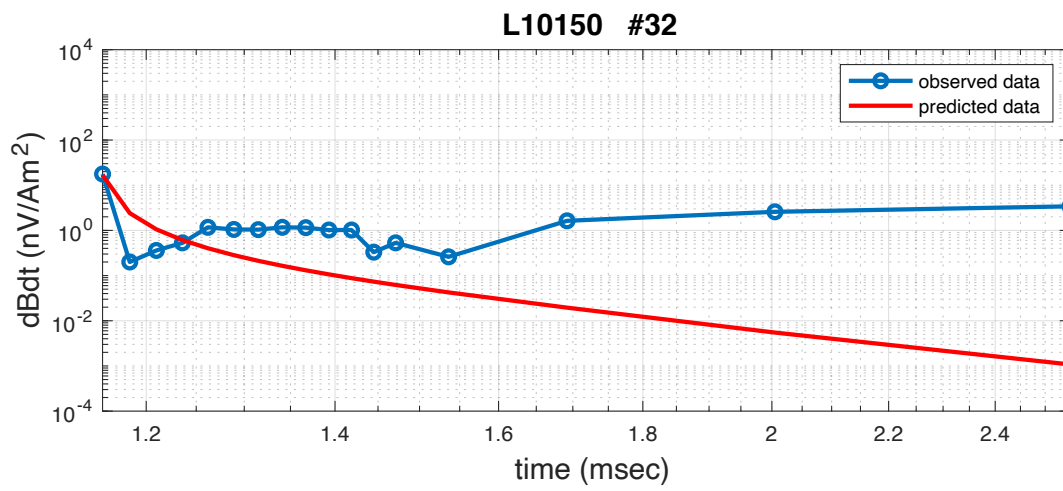
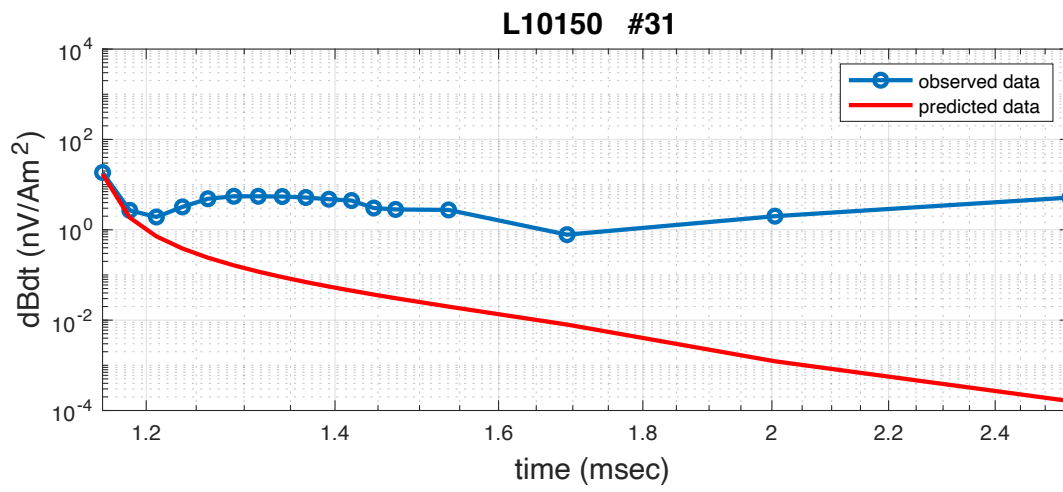


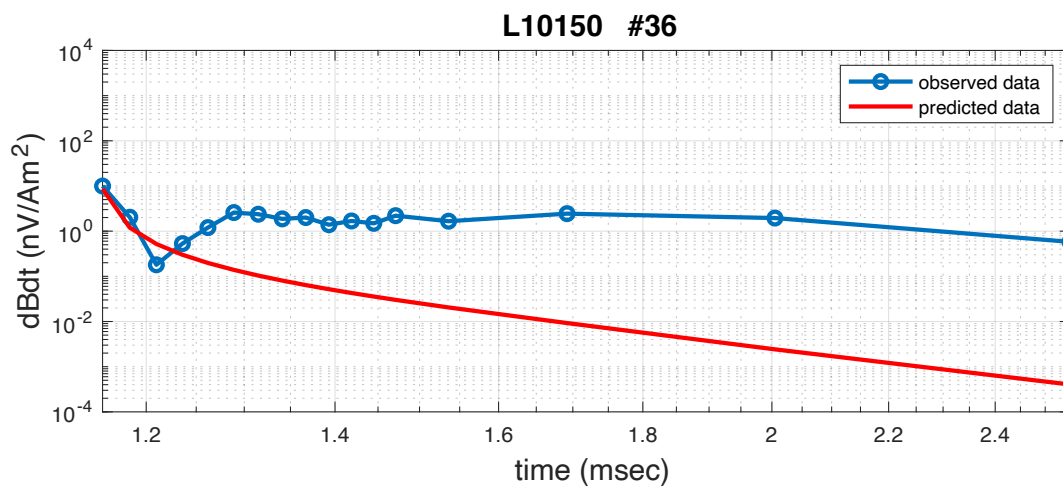
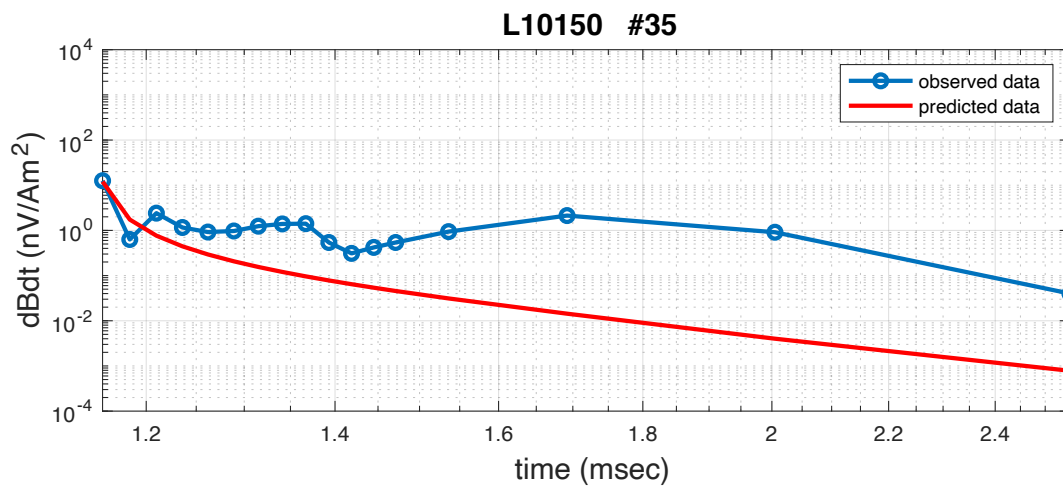
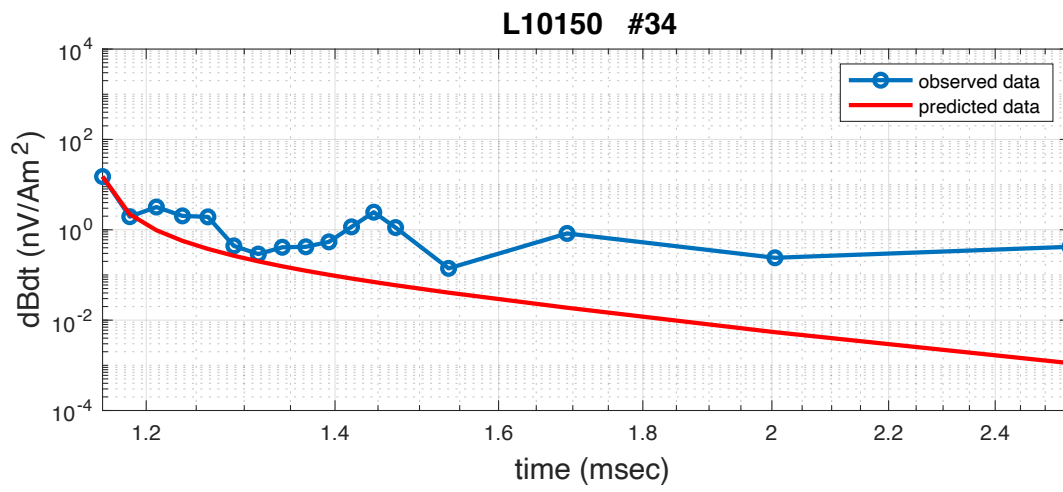


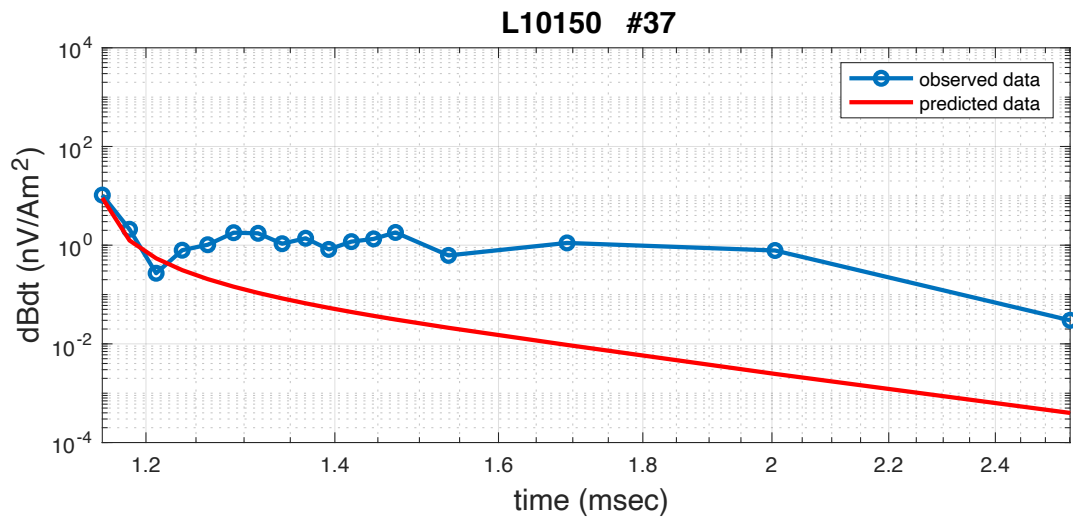




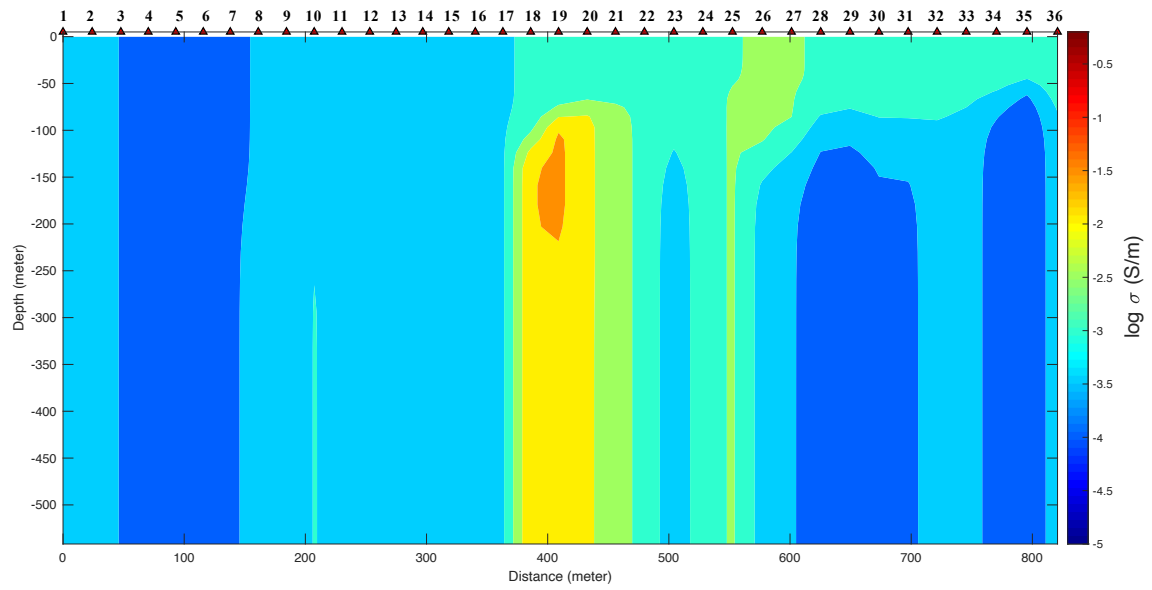




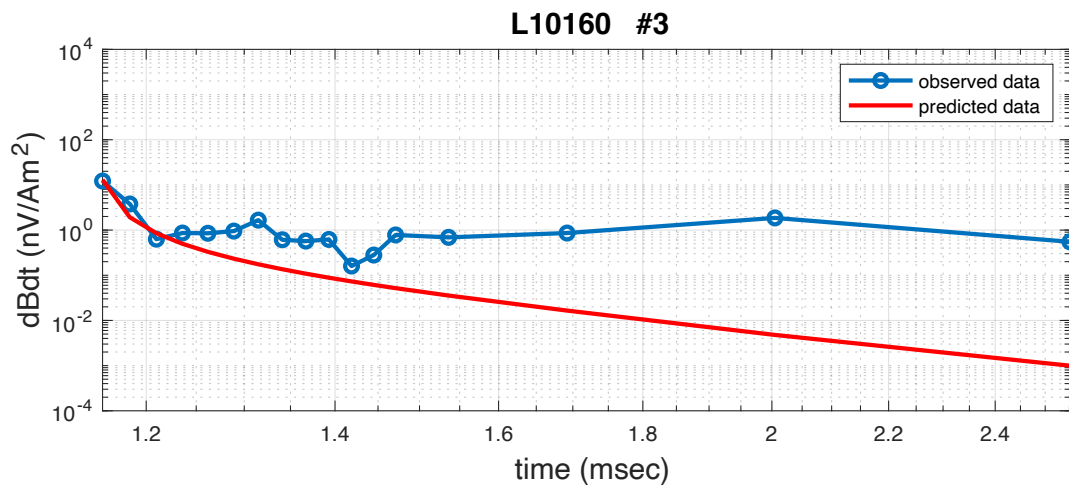
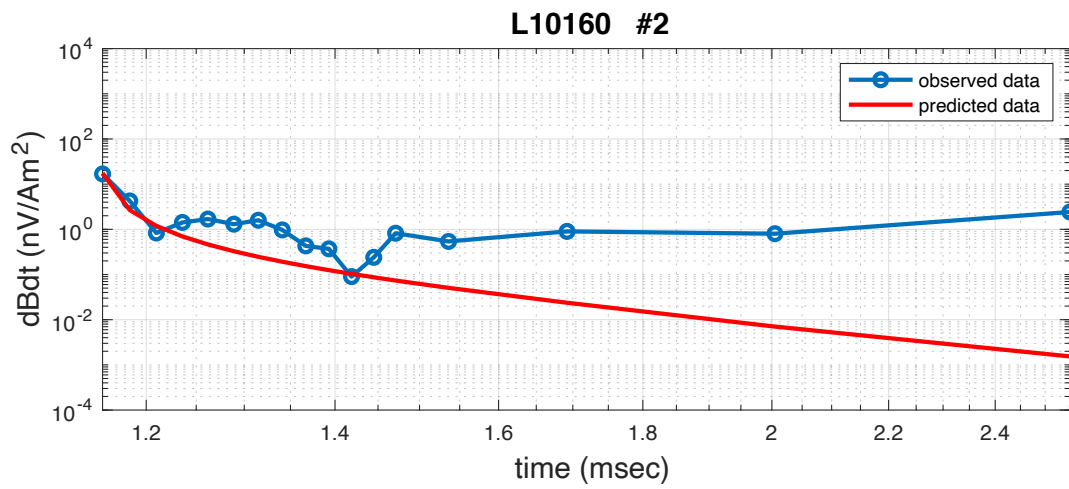
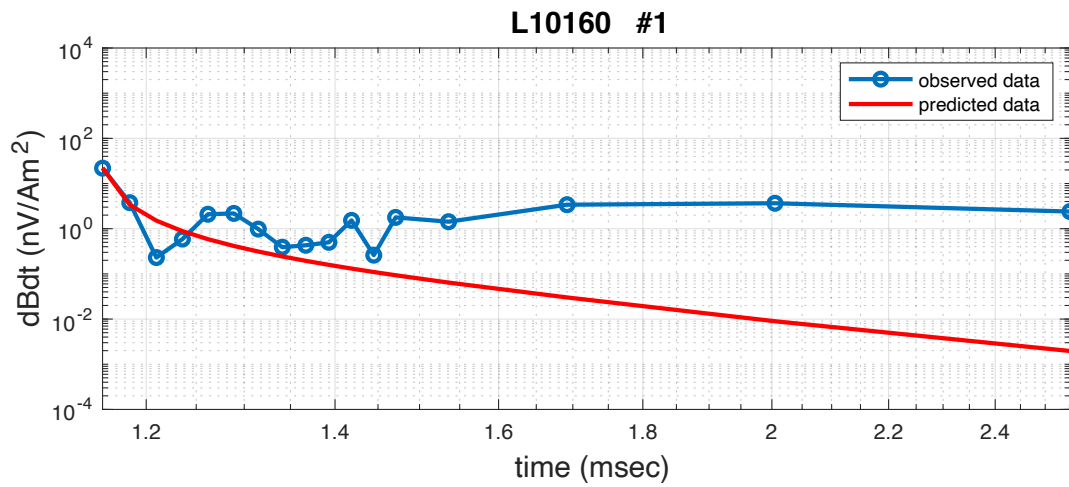


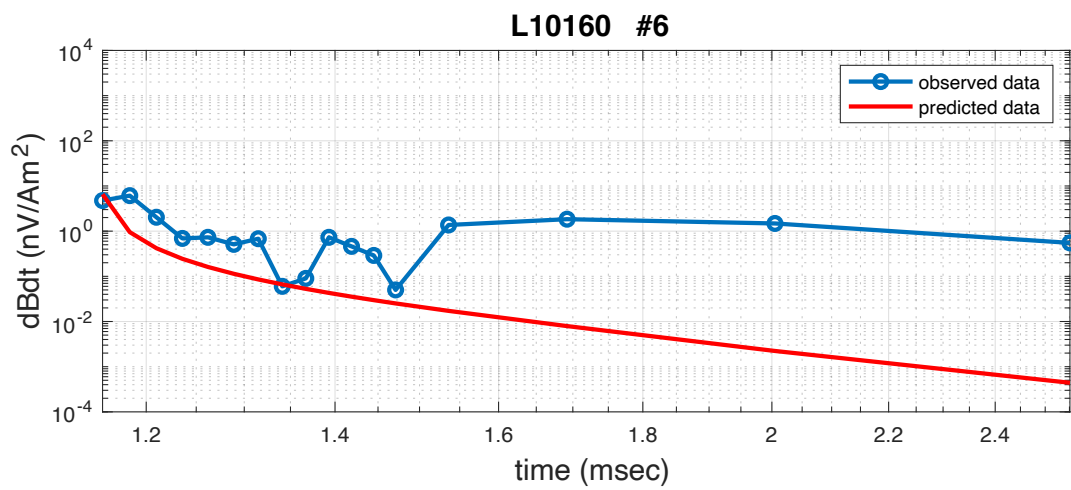
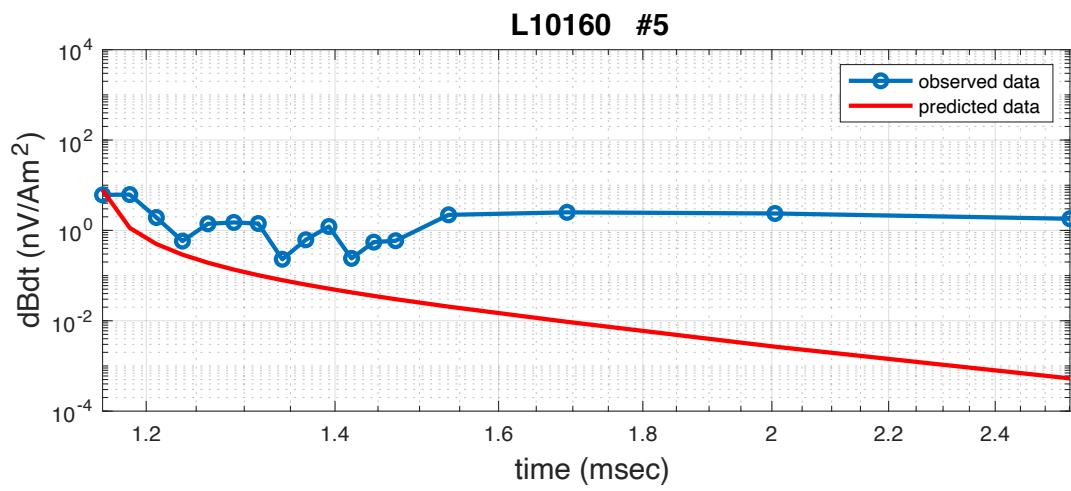
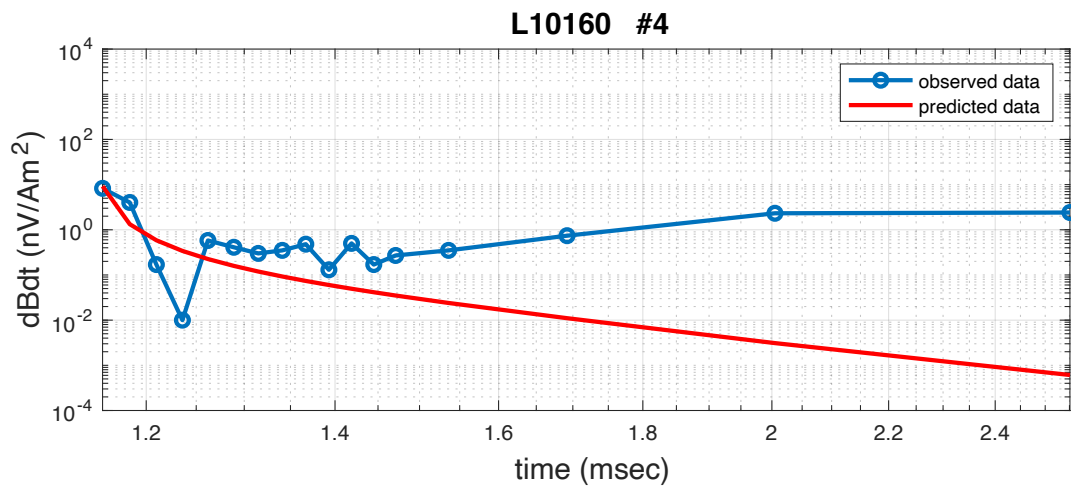


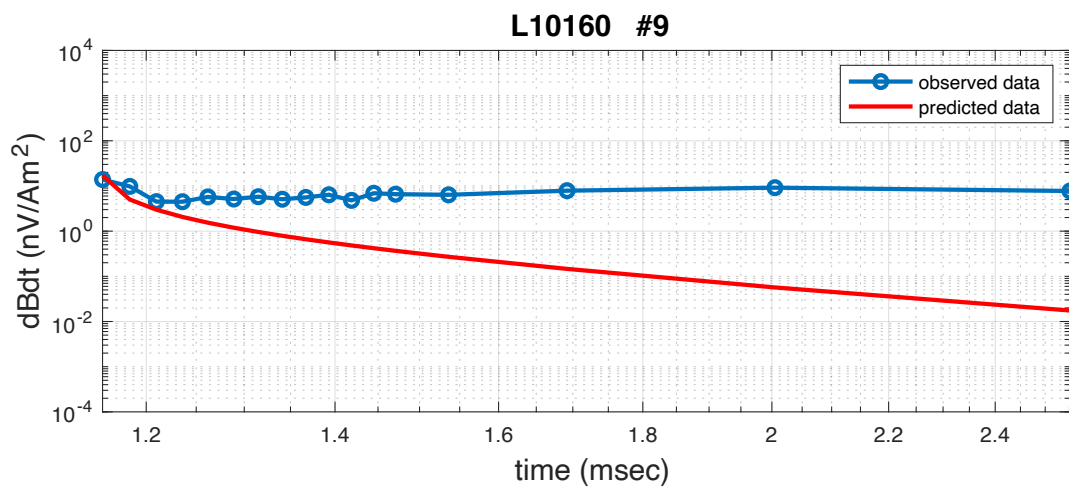
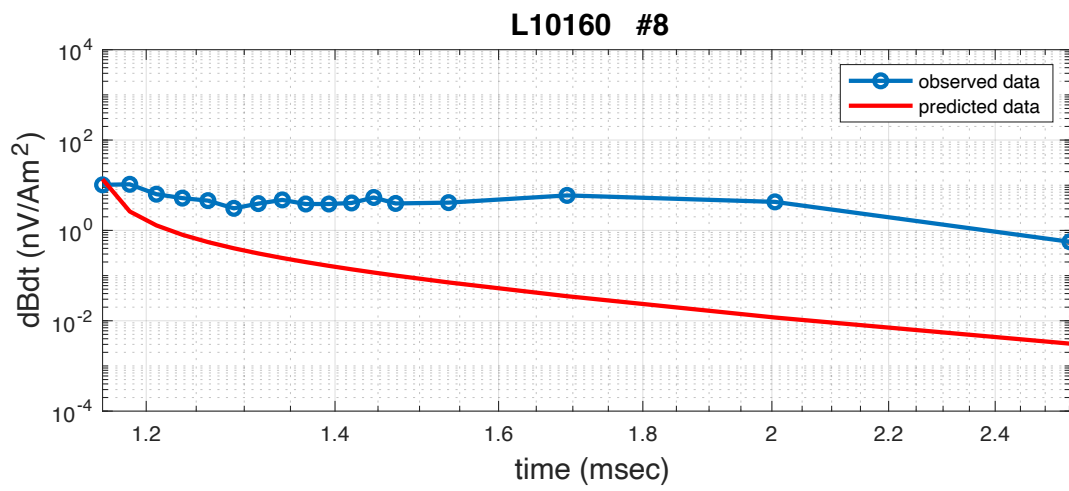
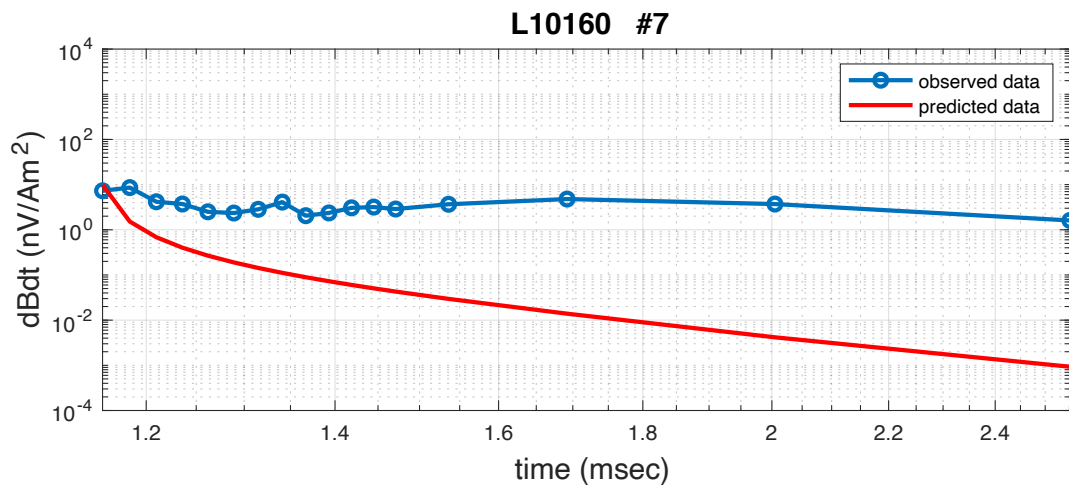
L10160

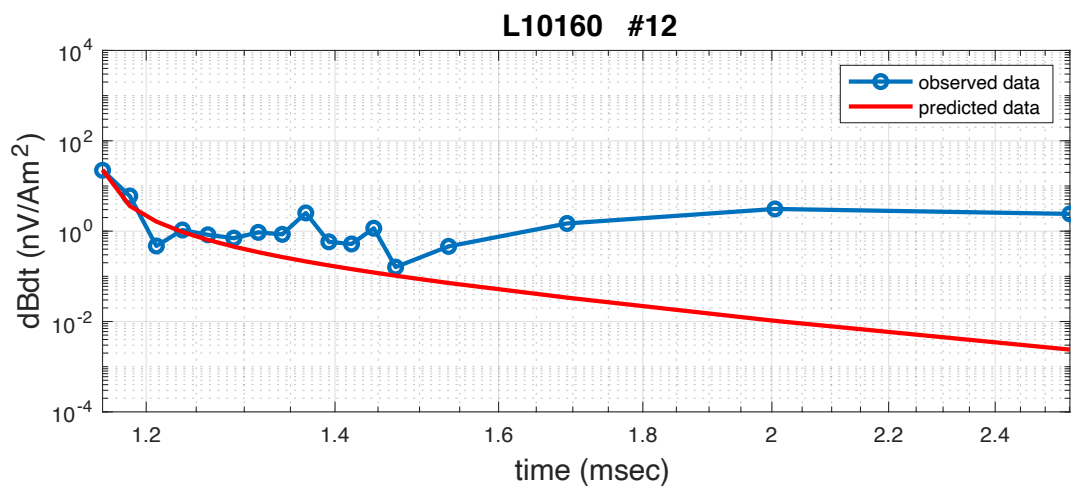
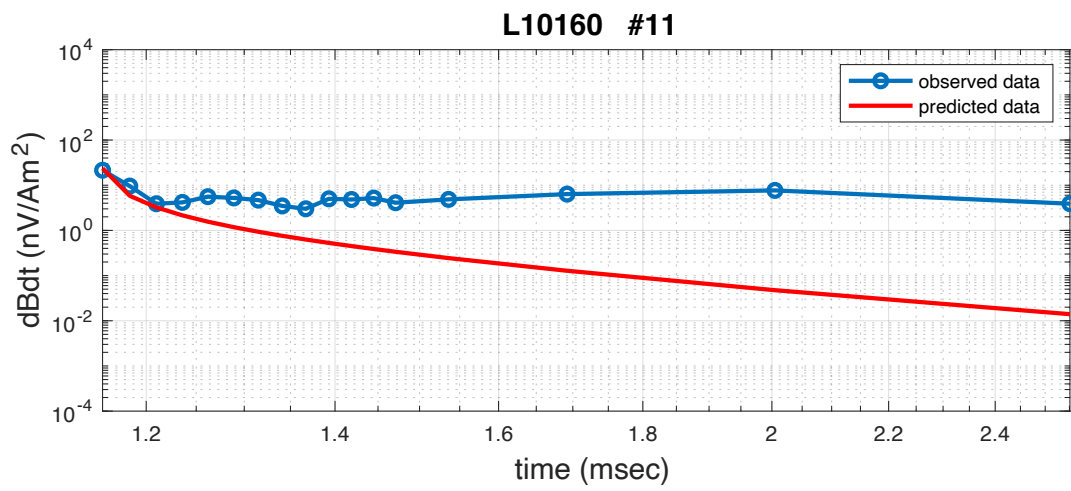
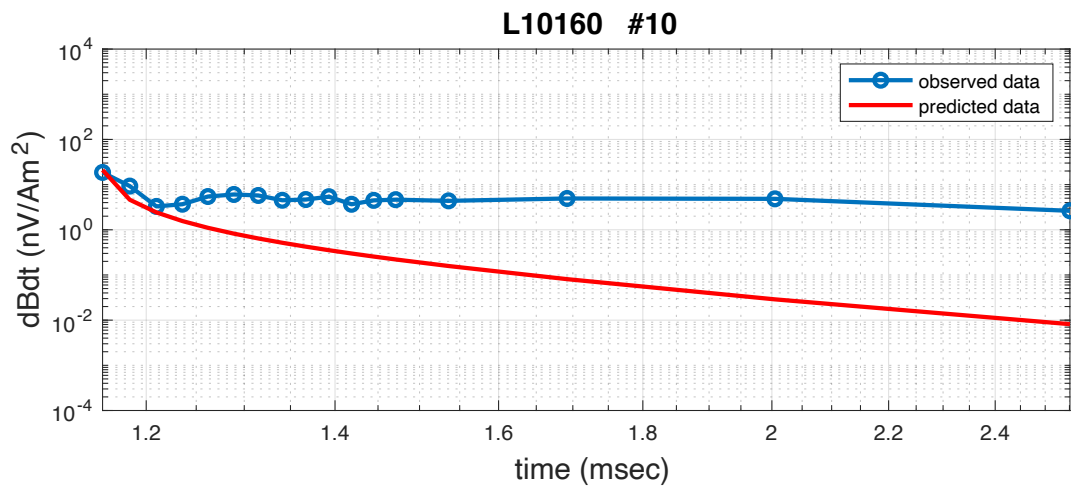


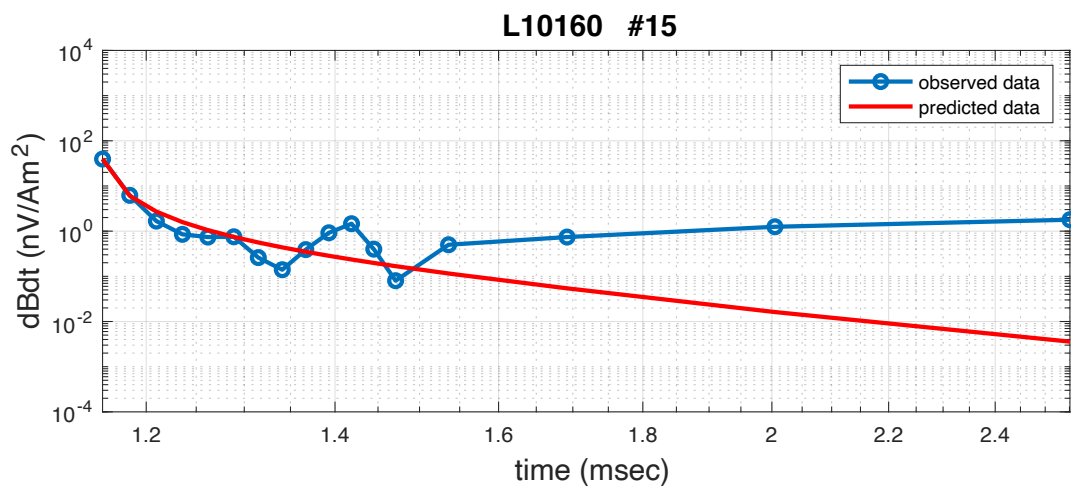
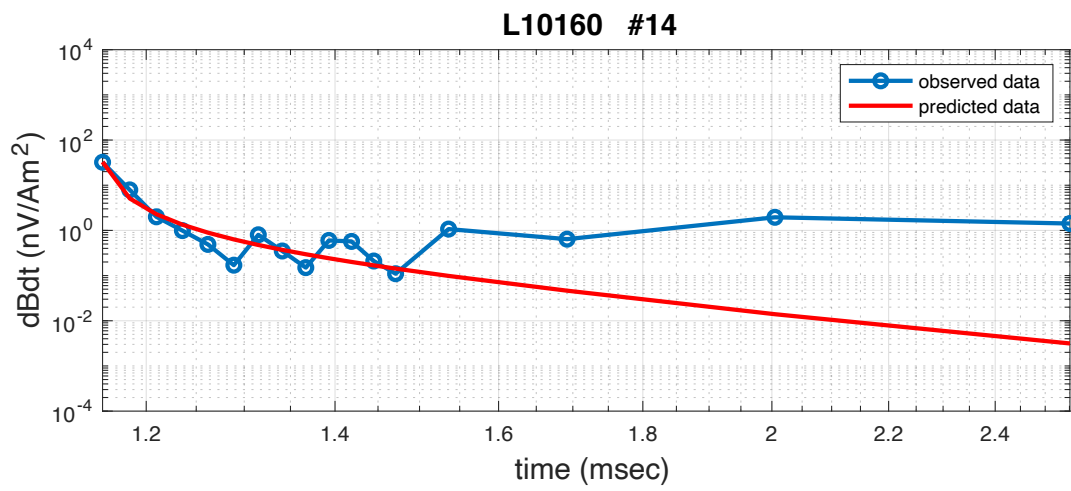
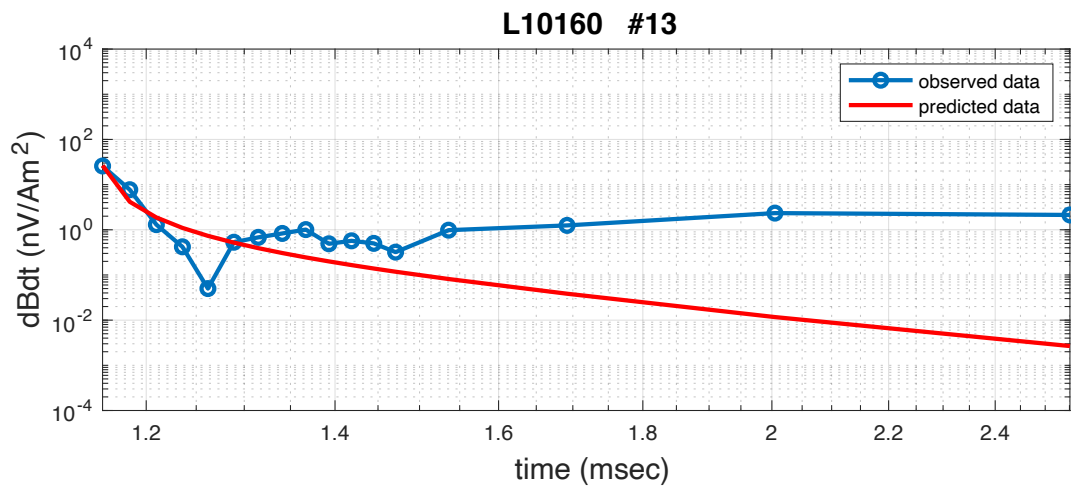
The observation points on L10160

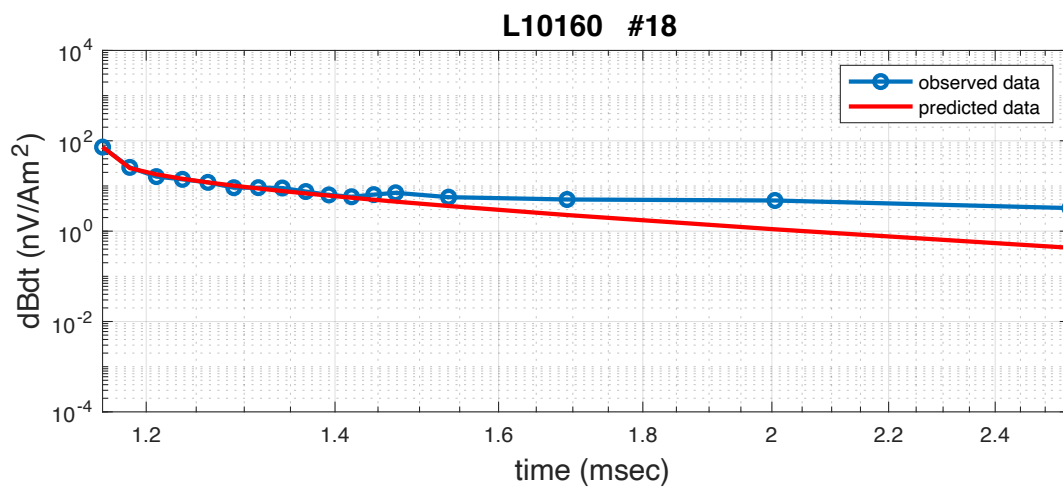
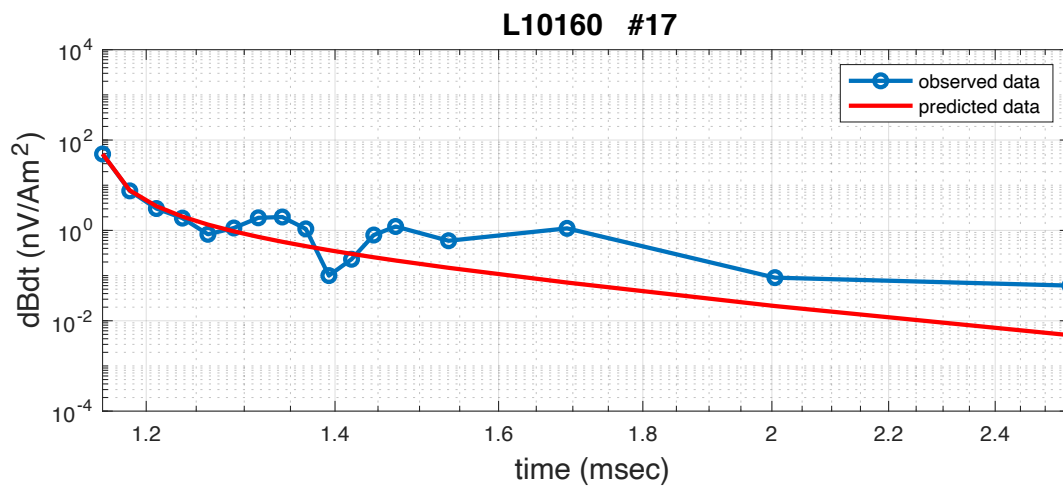
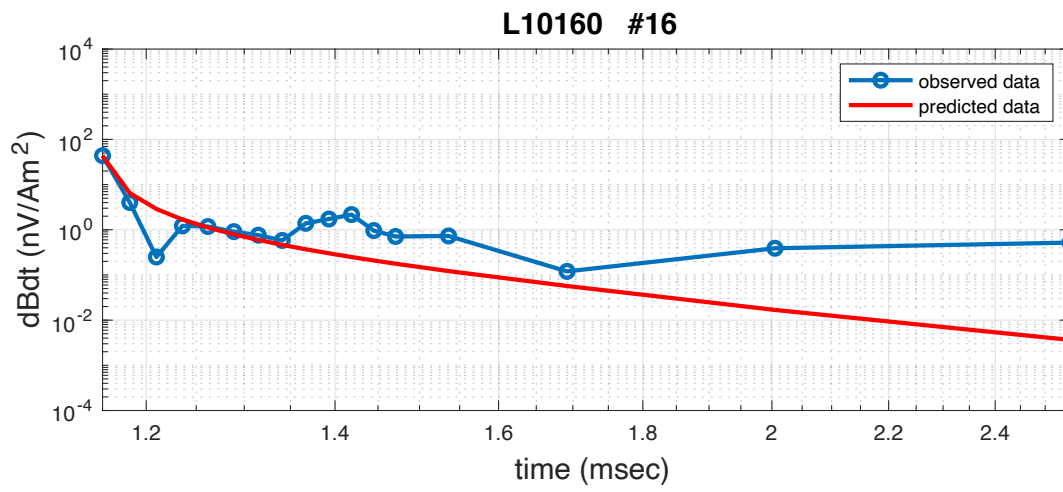


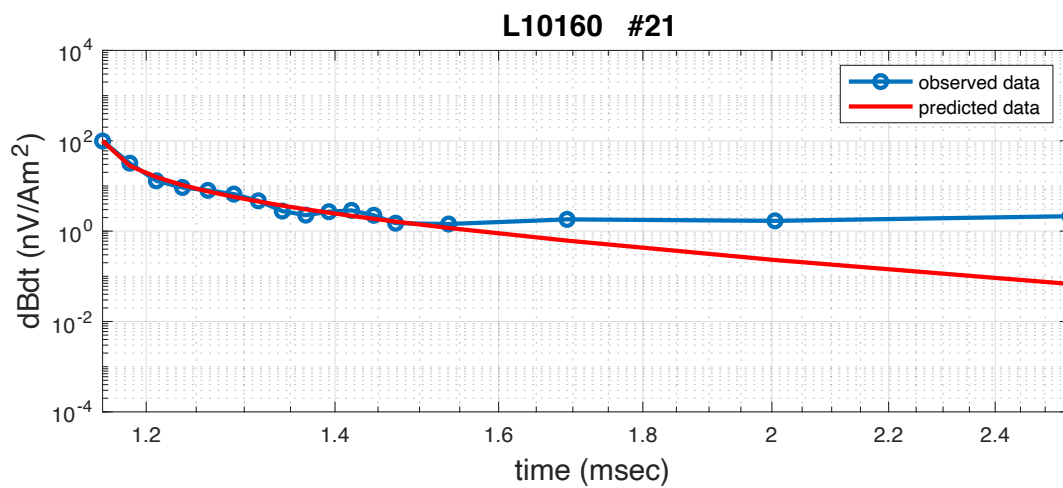
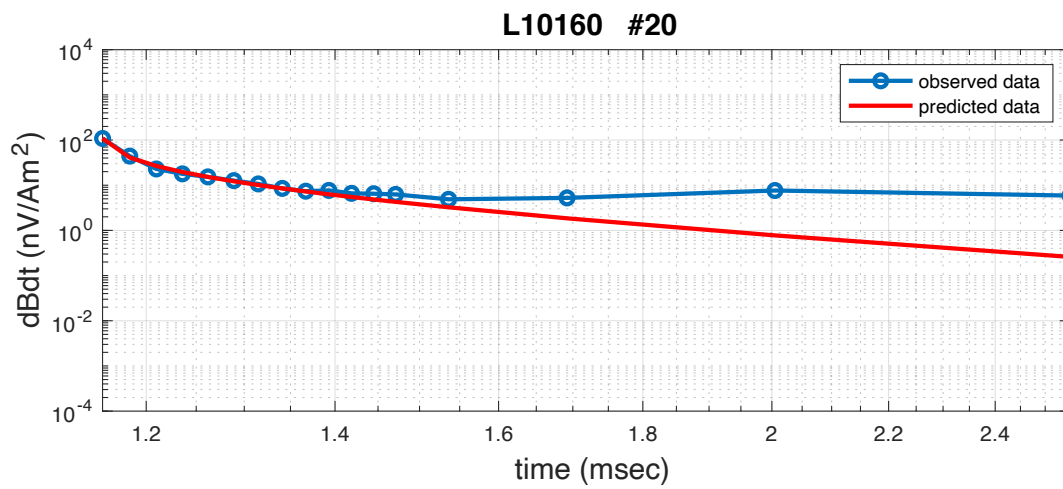
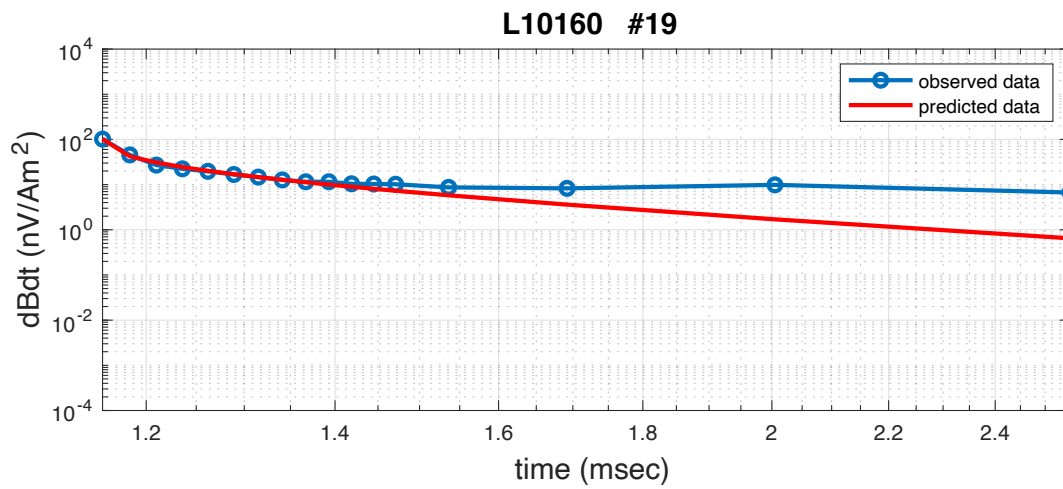


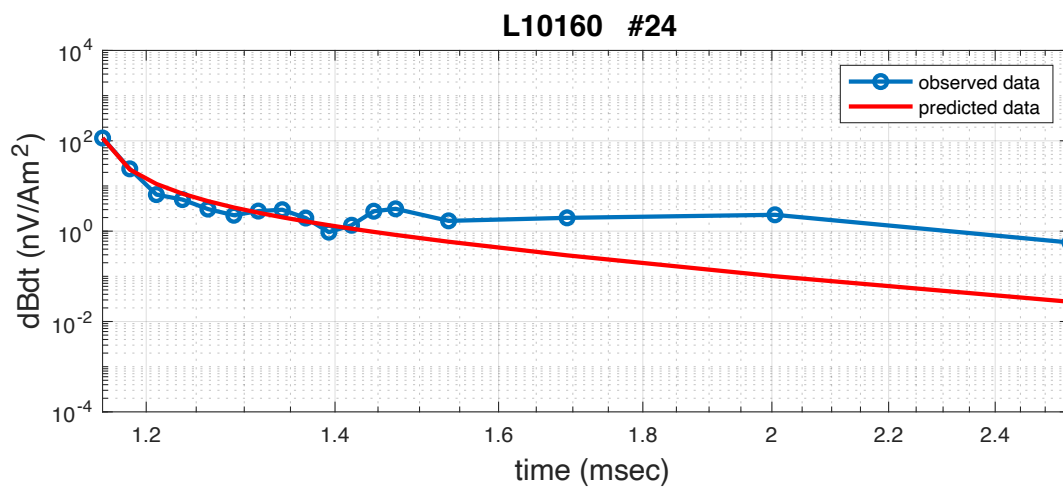
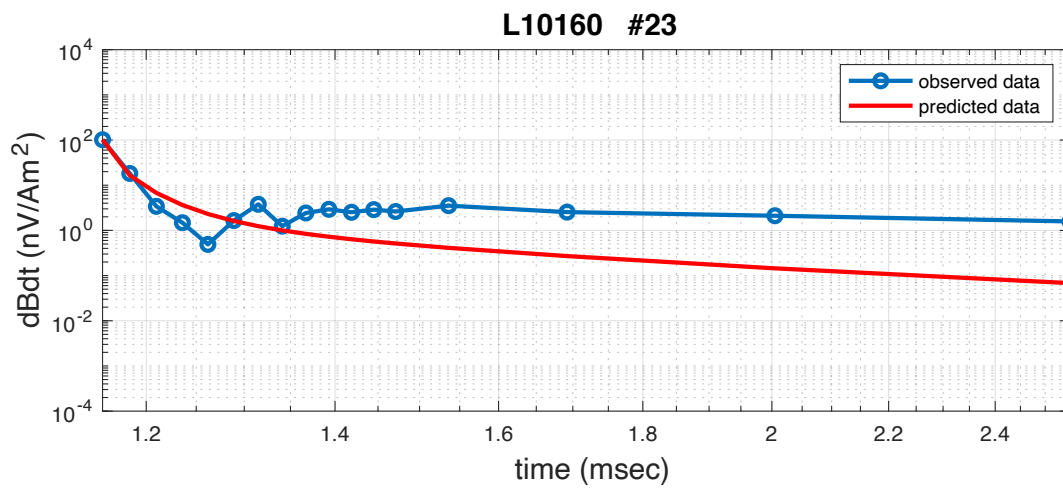
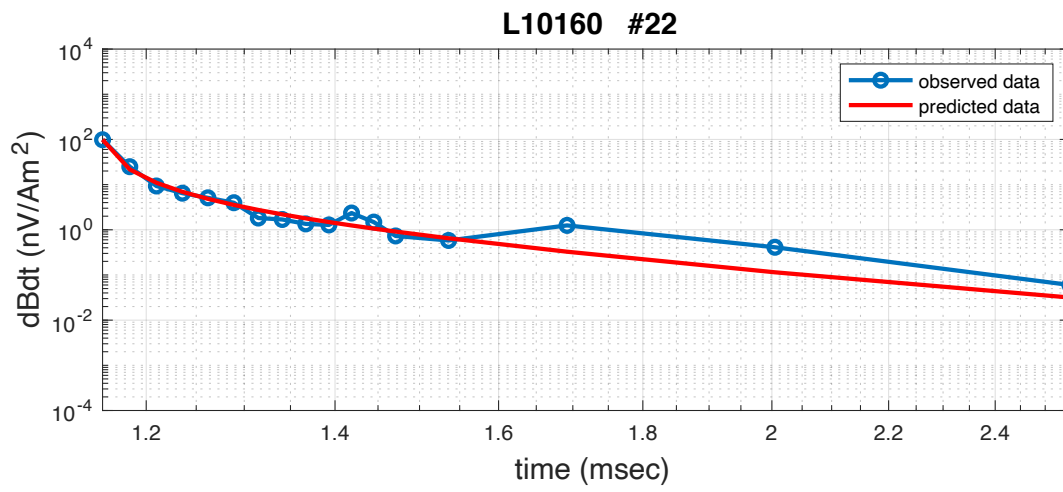


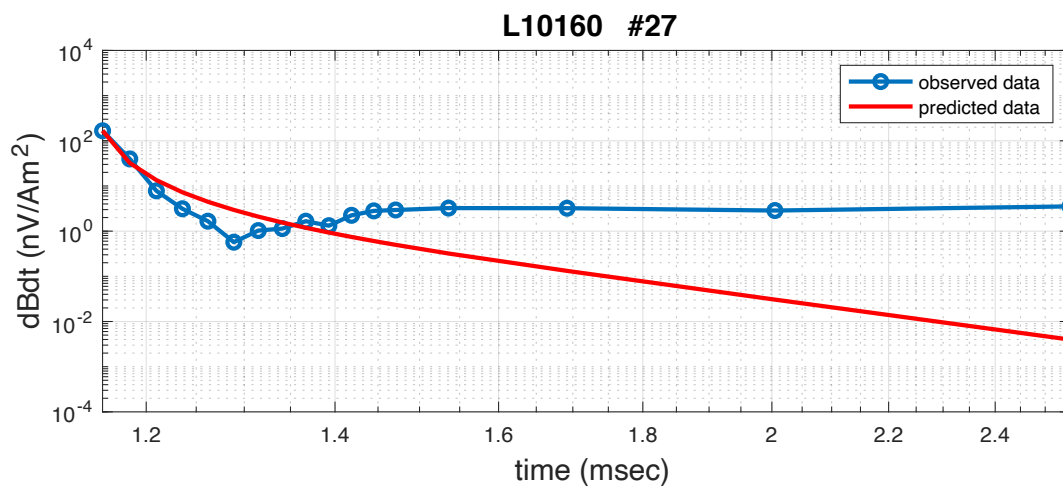
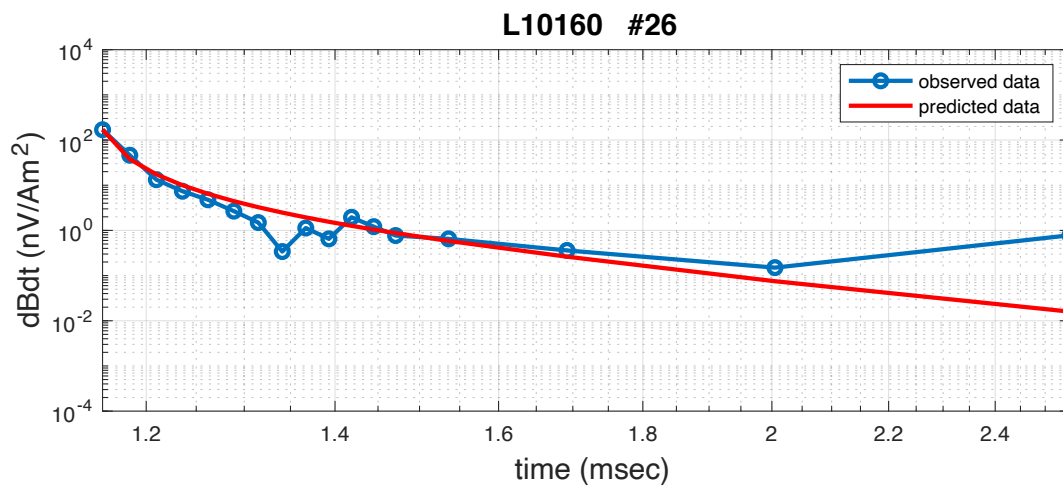
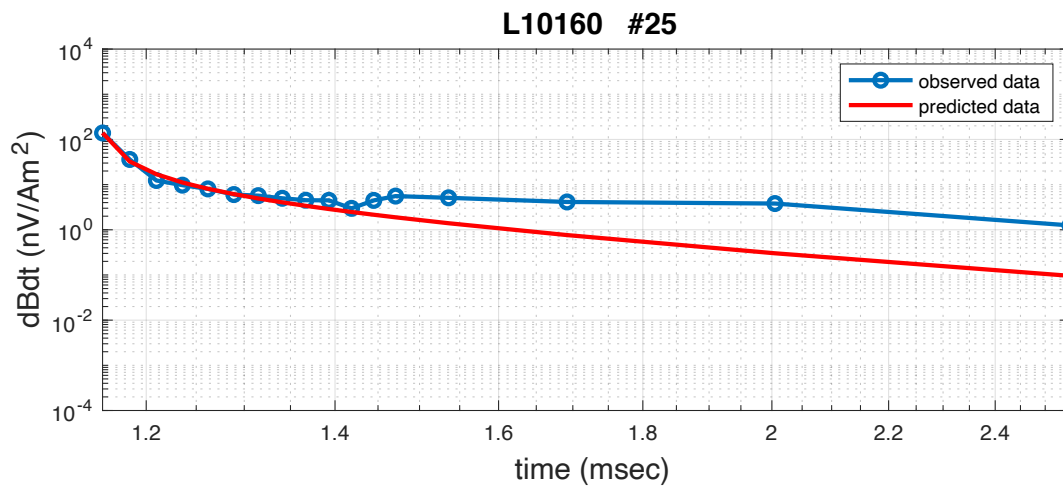


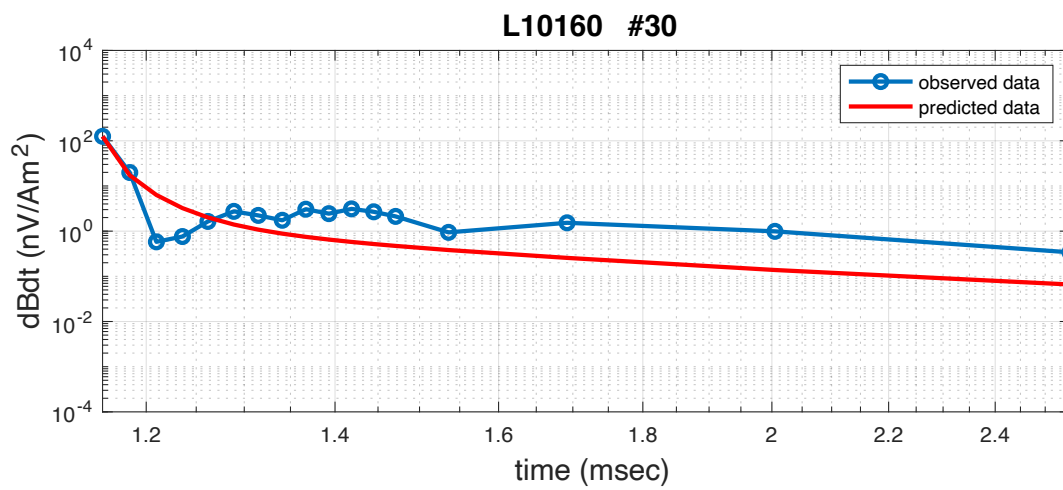
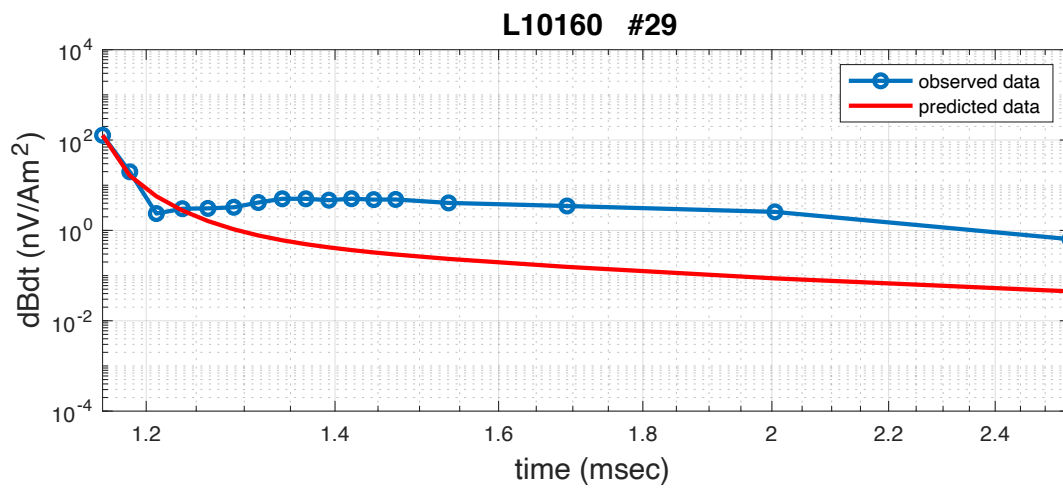
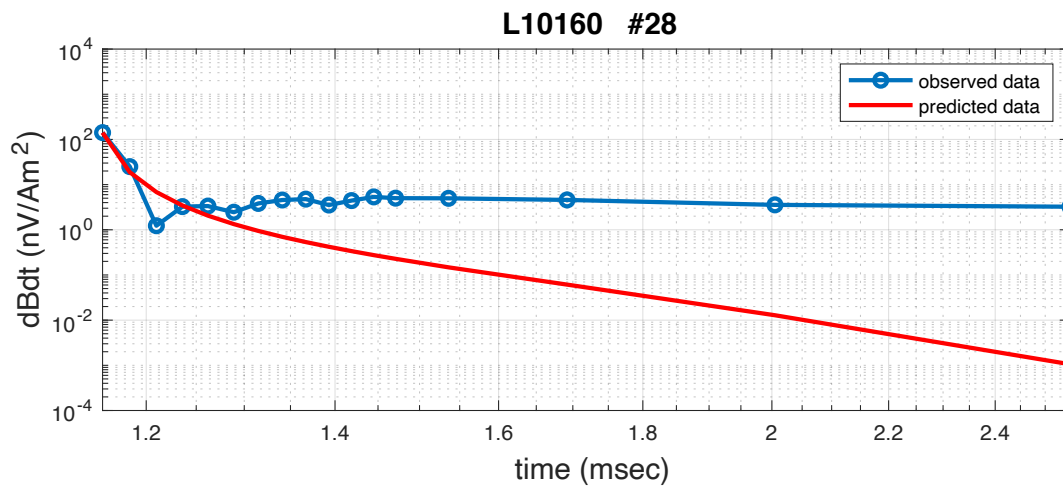


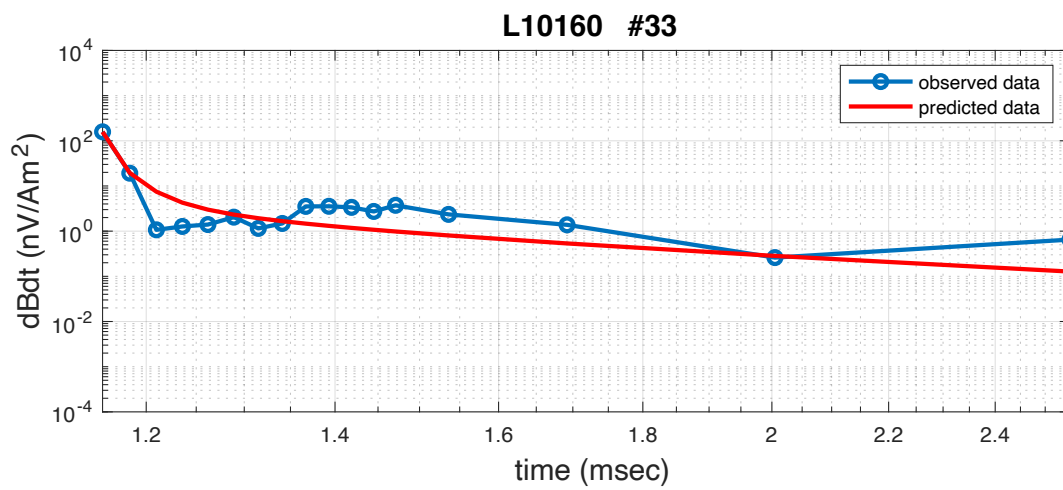
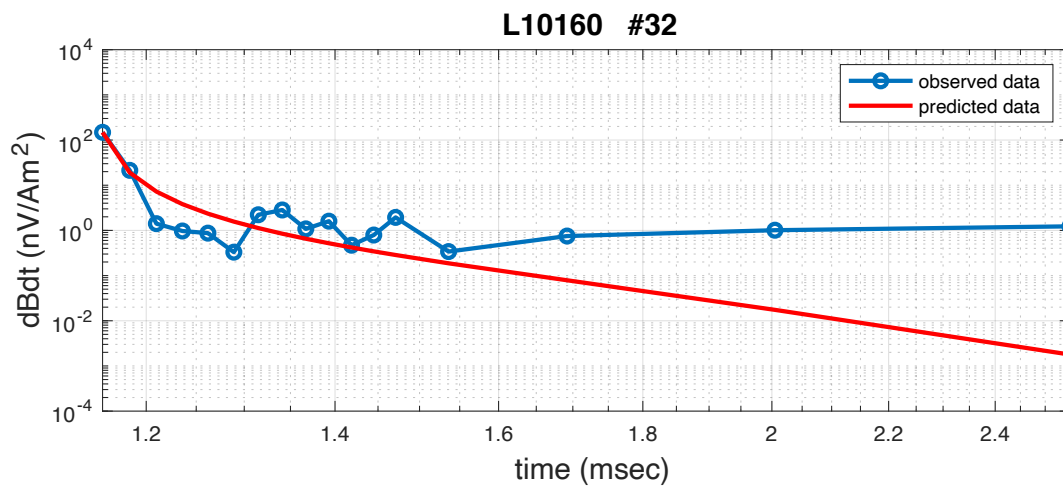
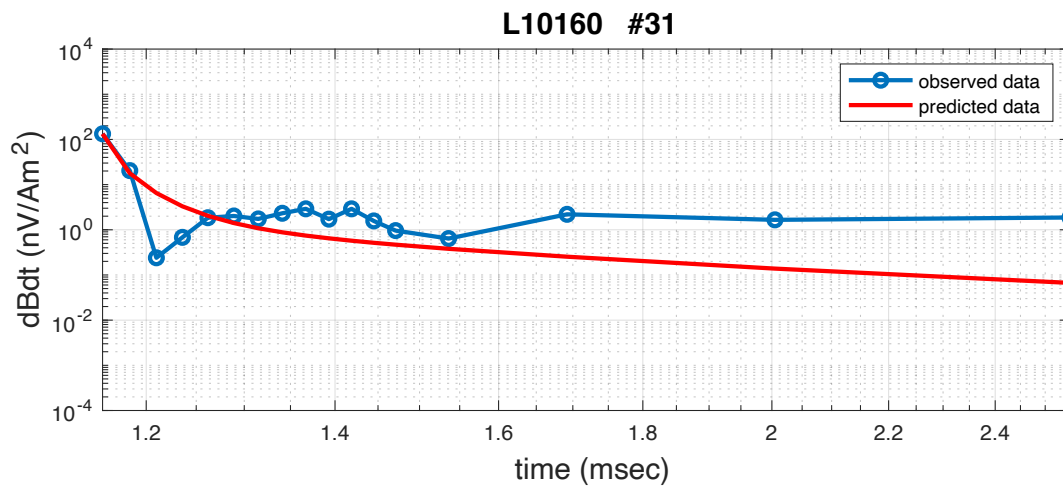


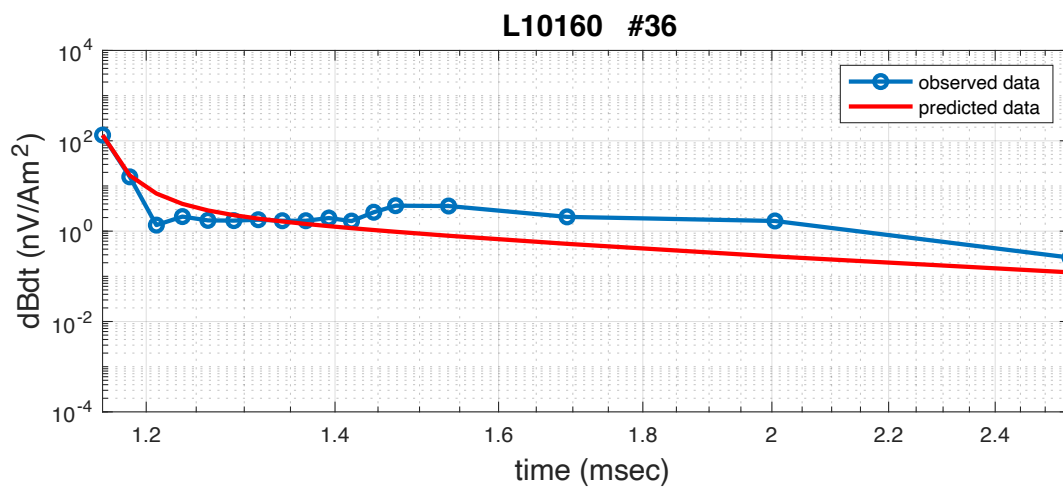
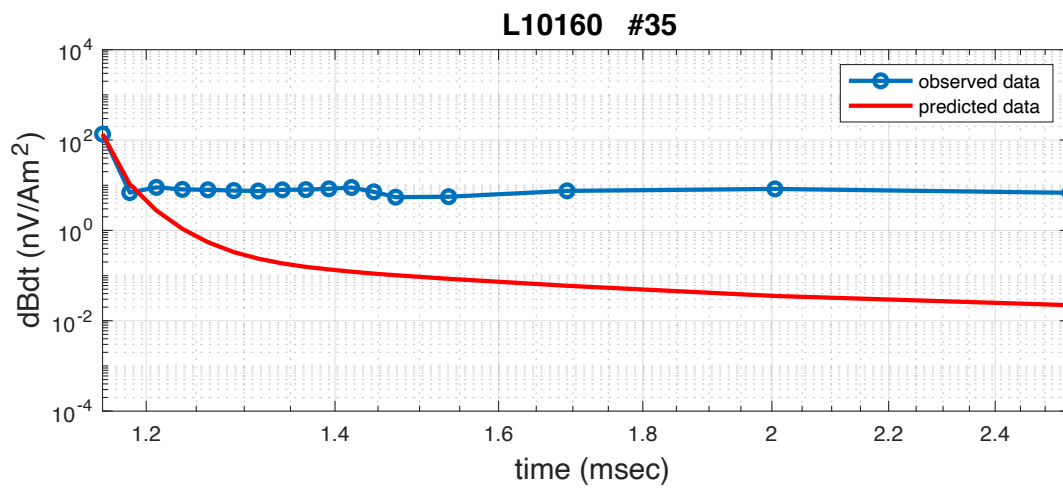
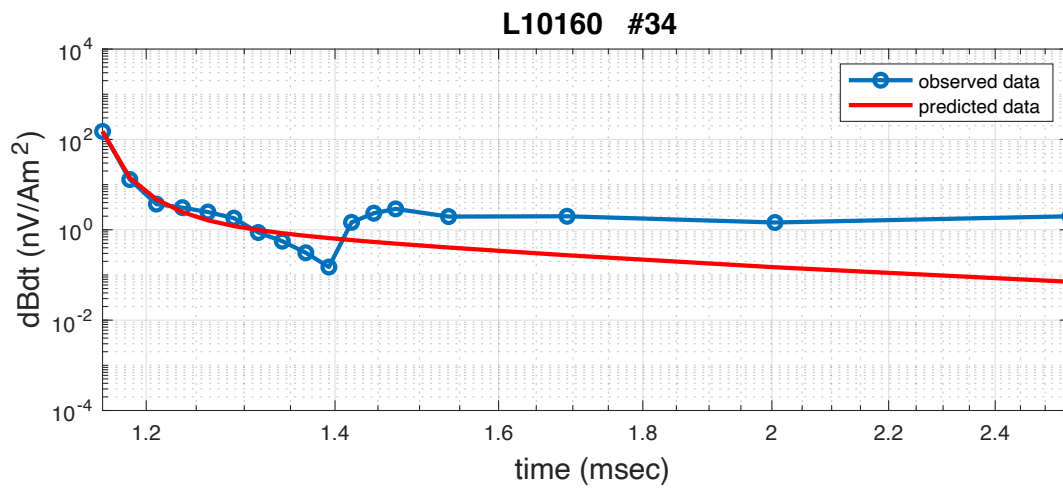




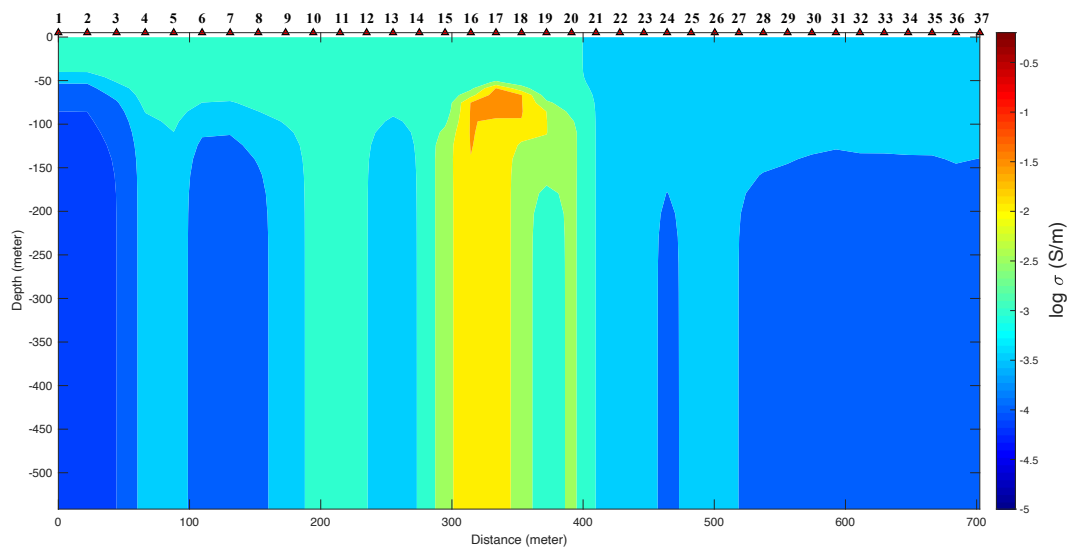




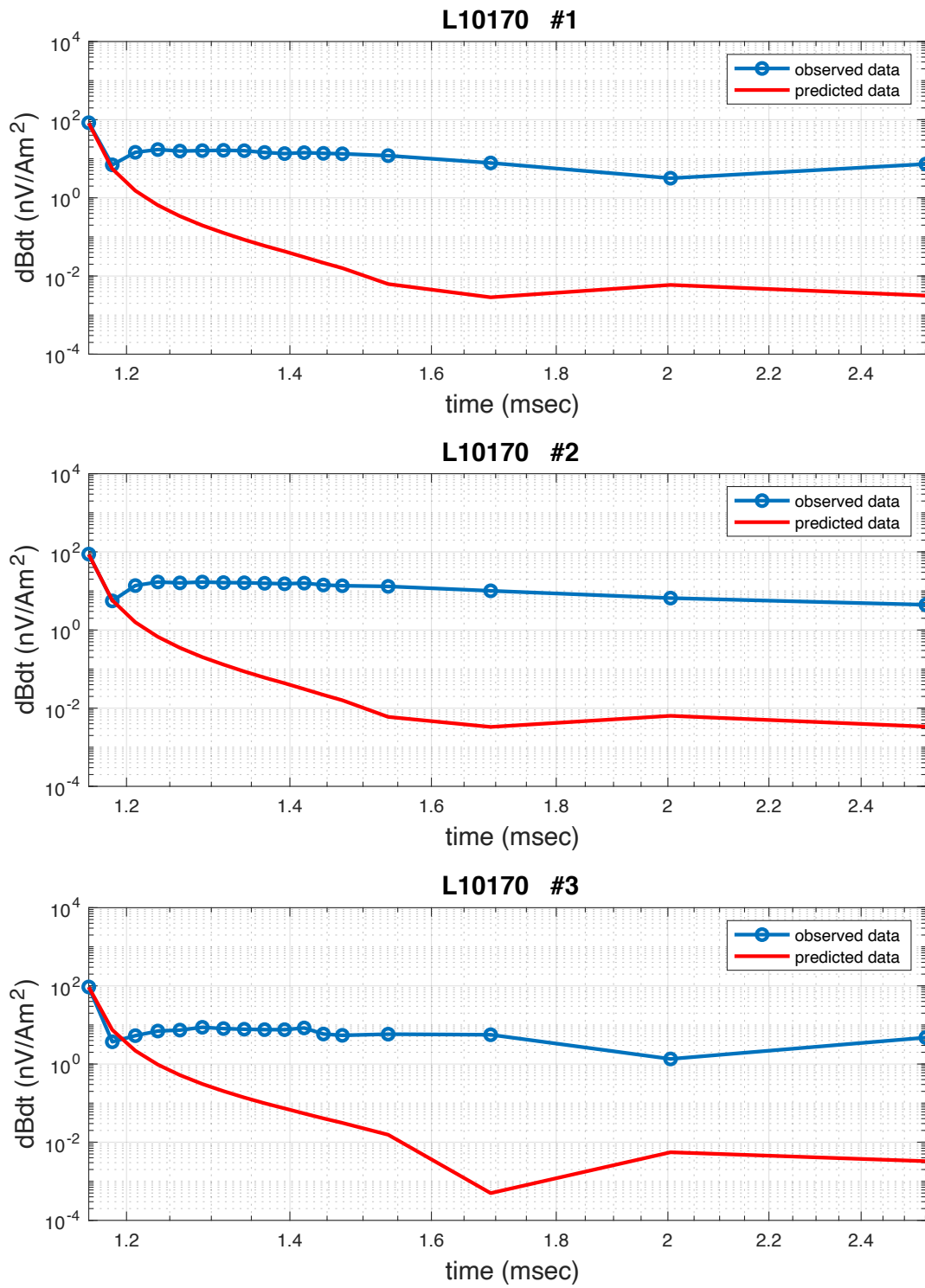


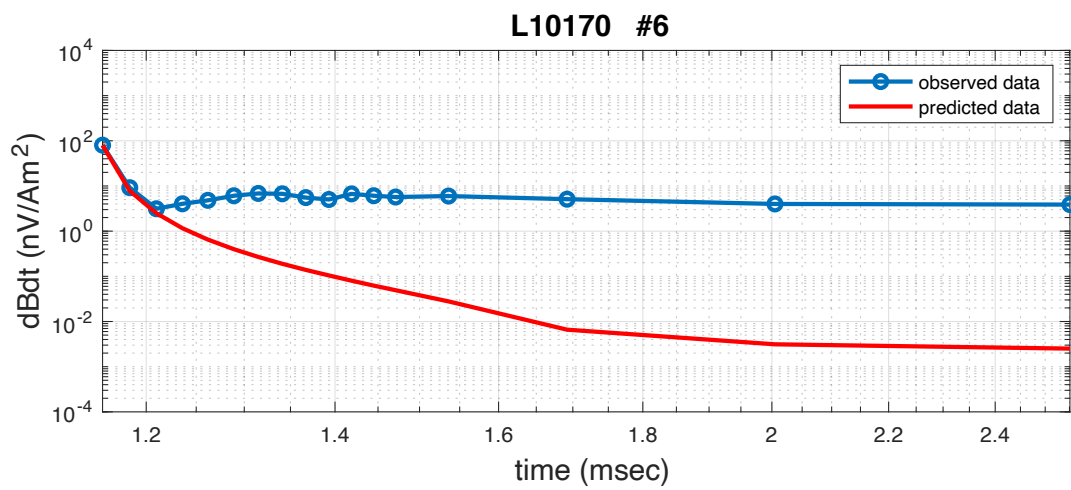
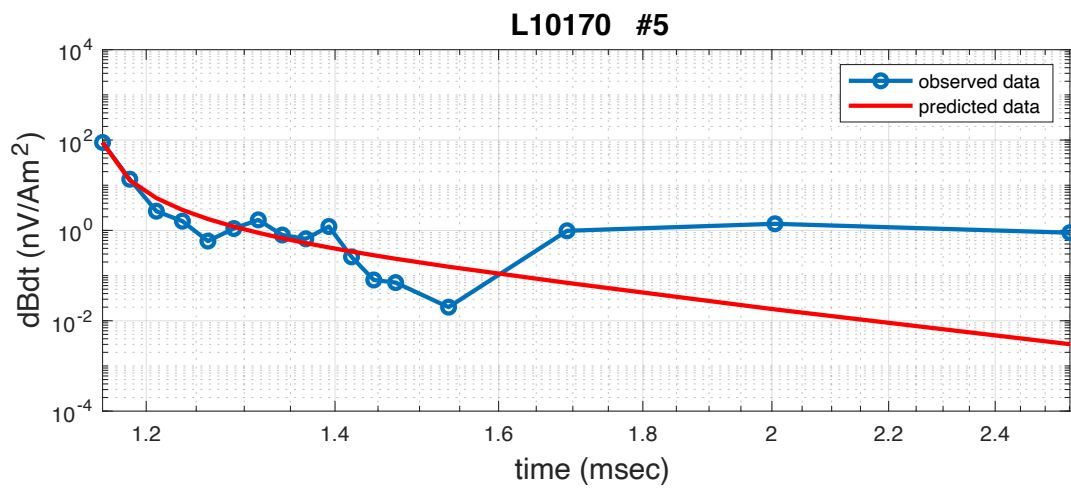
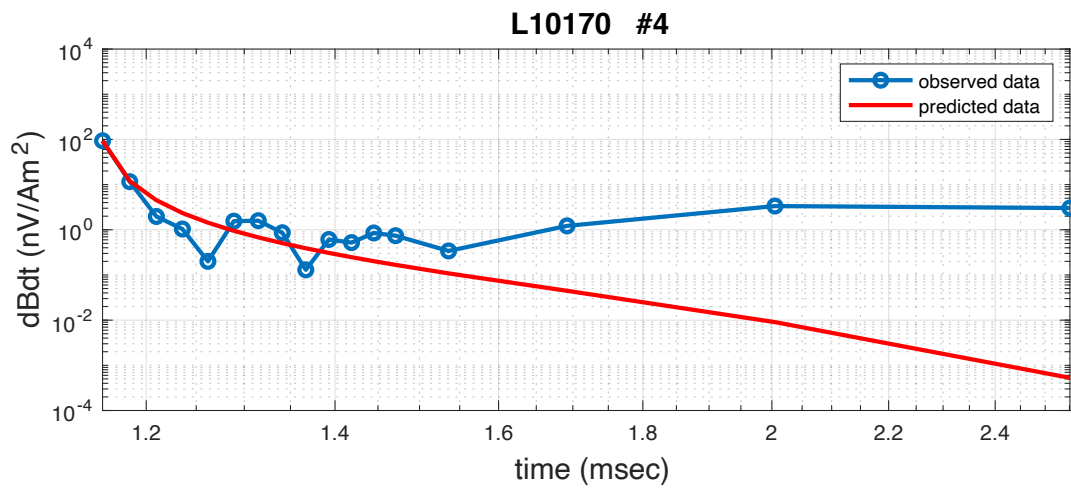


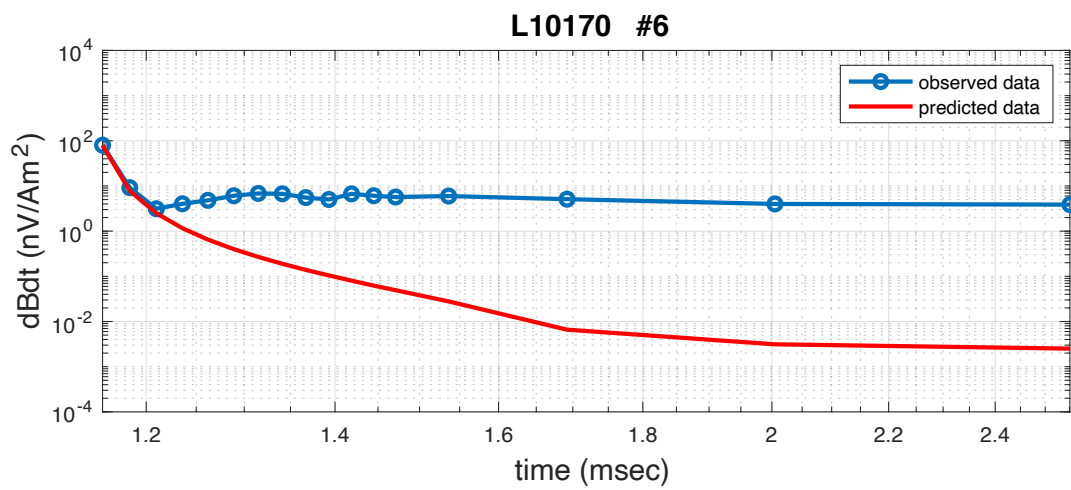
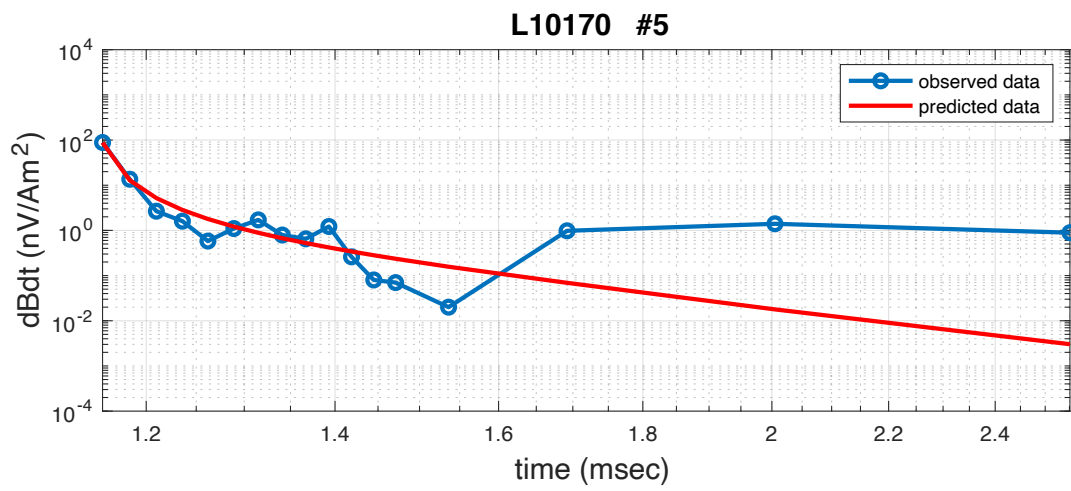
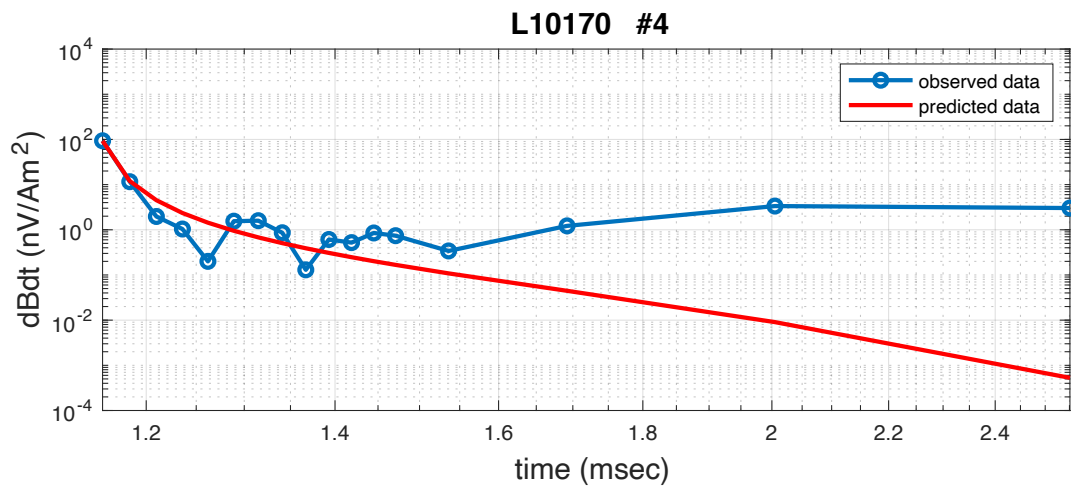
L10170

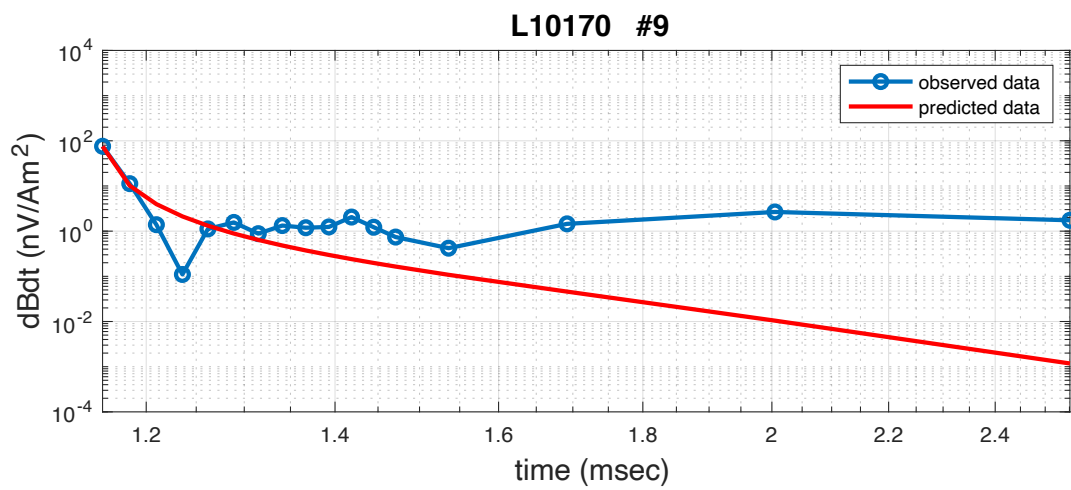
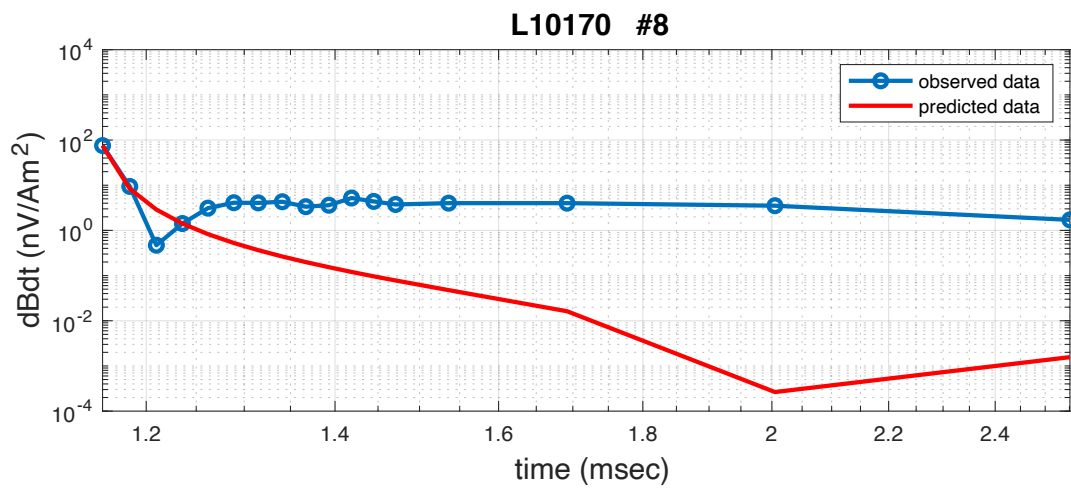
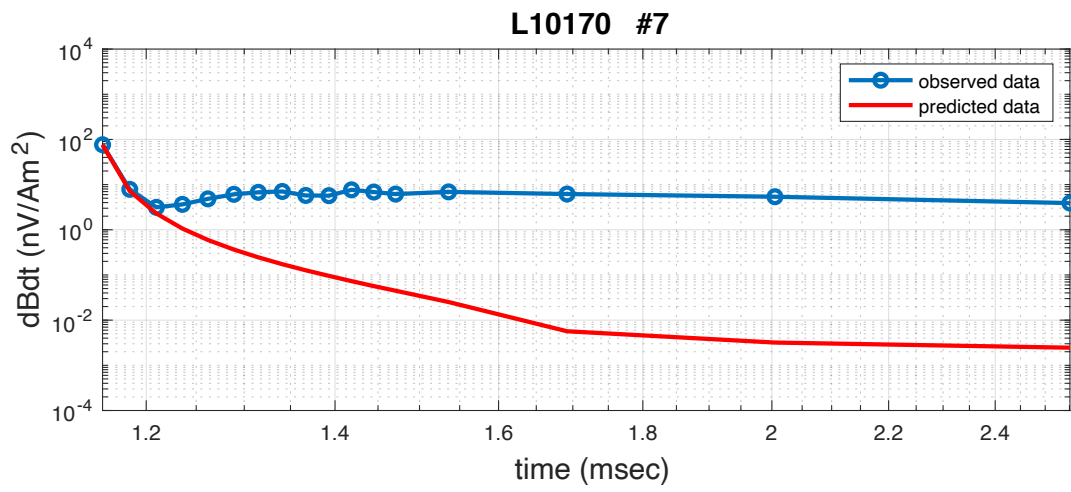


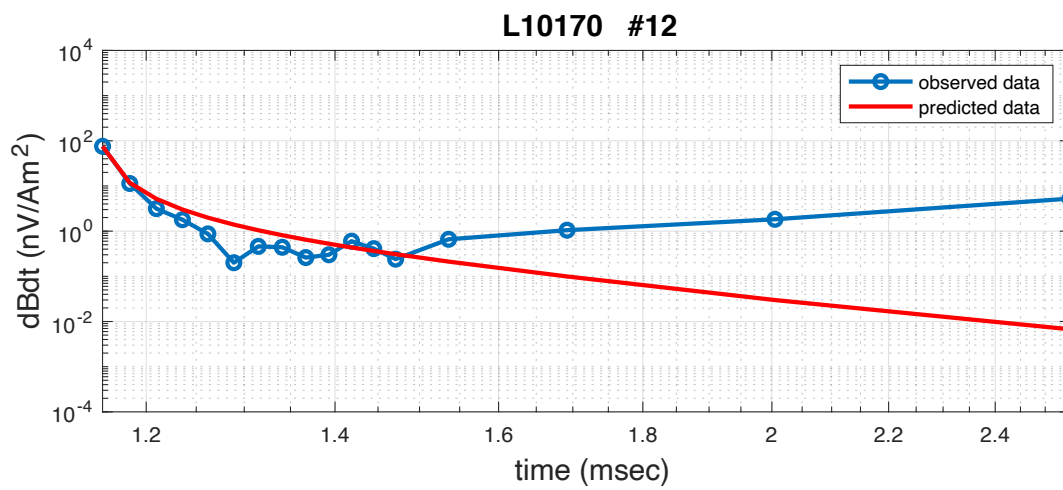
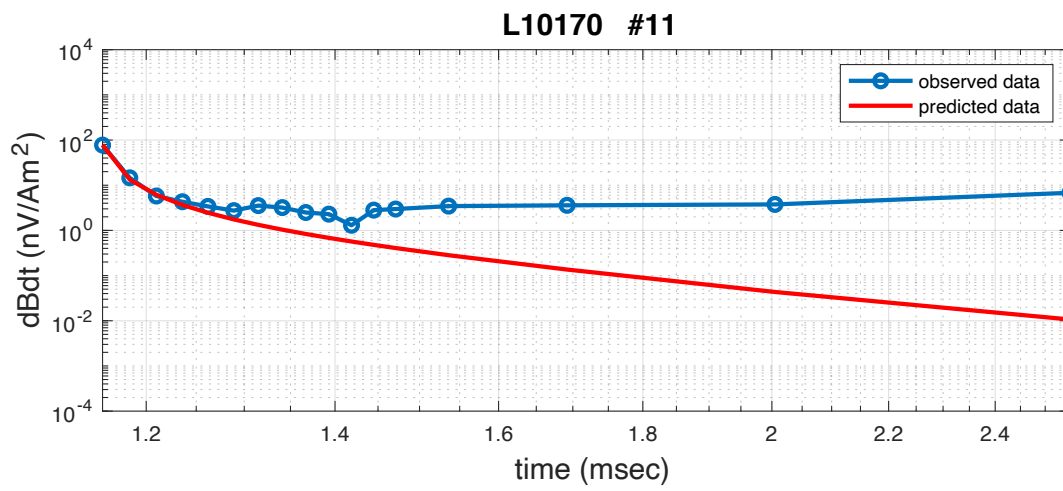
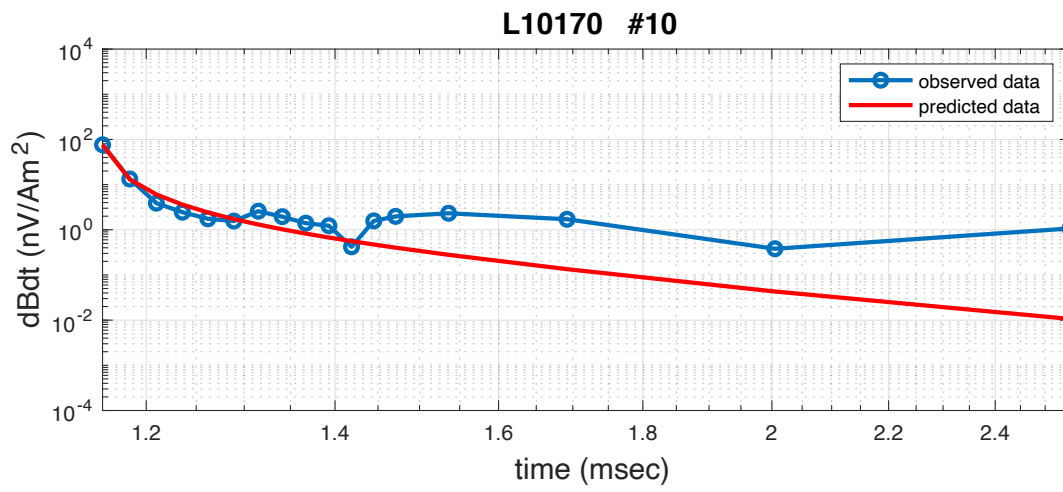
The observation points on L10170

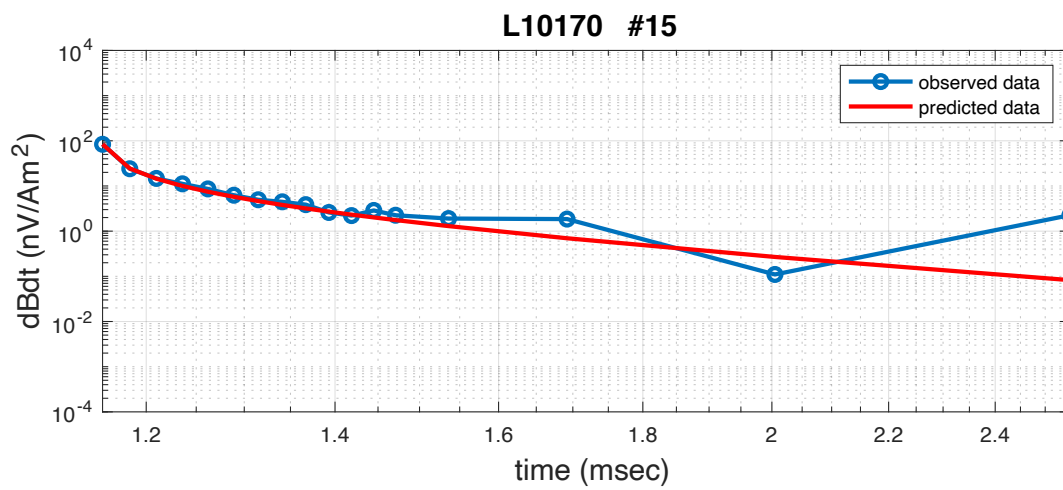
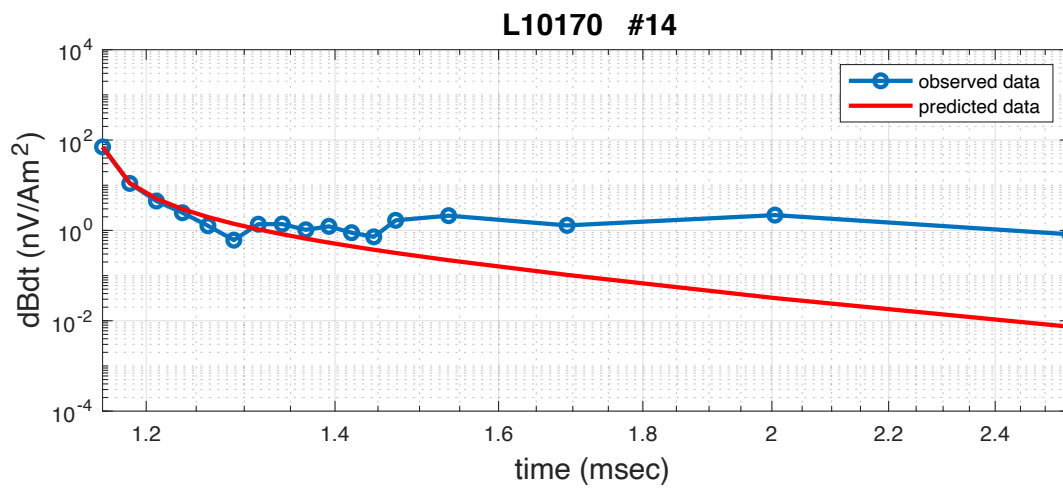
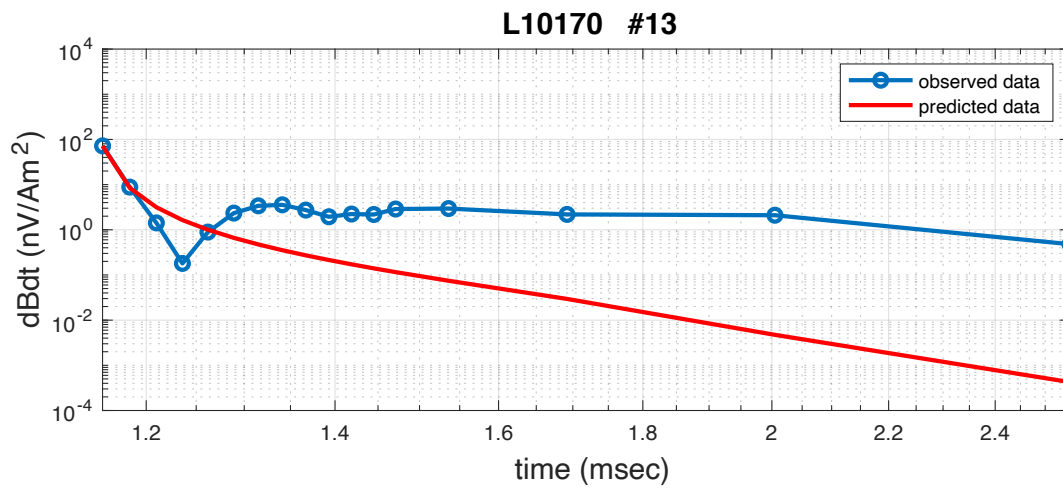


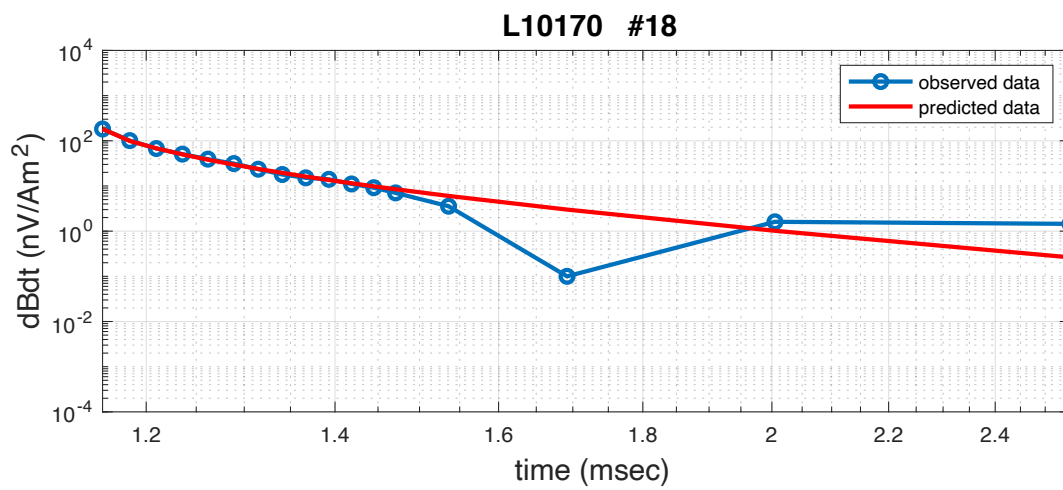
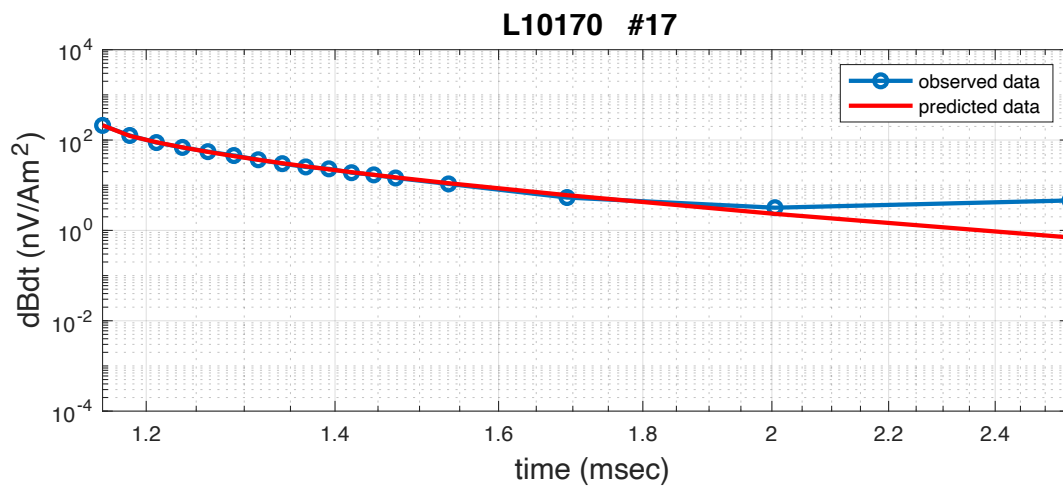
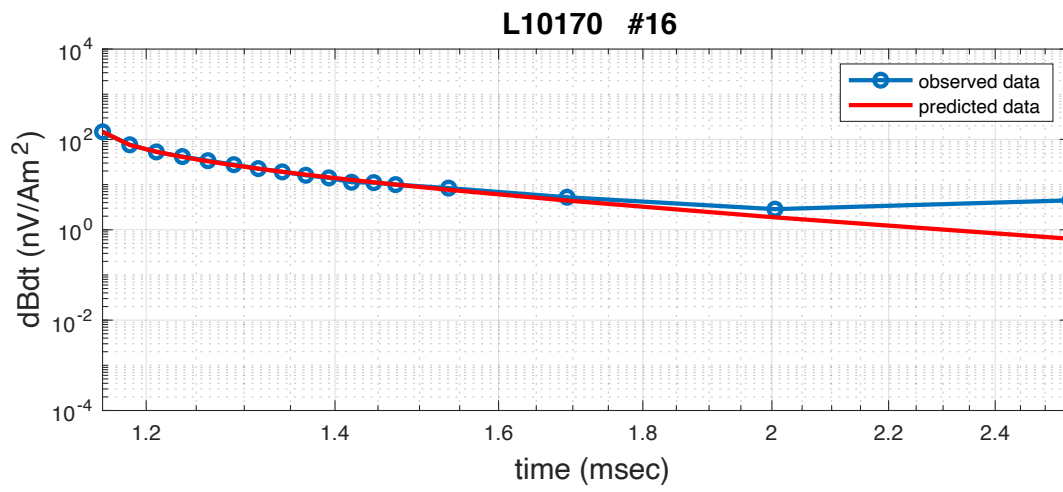


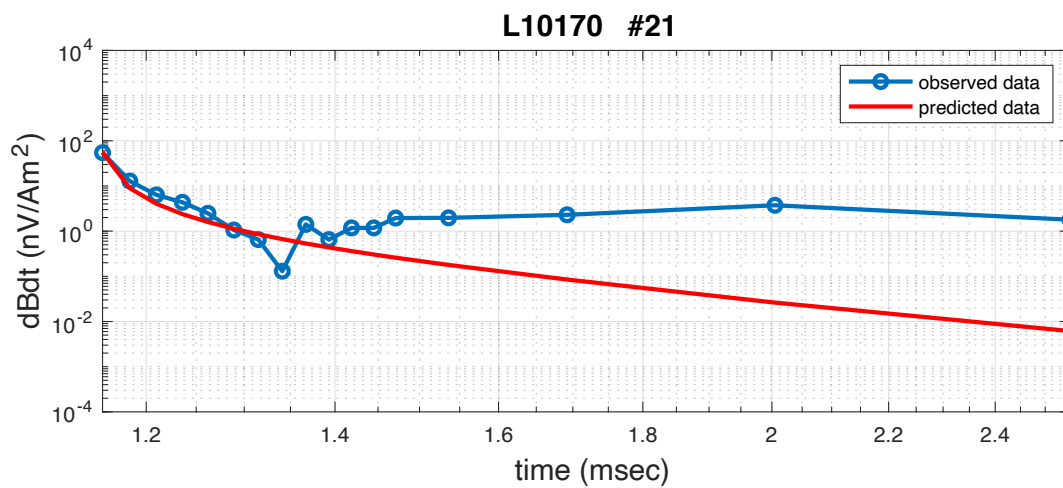
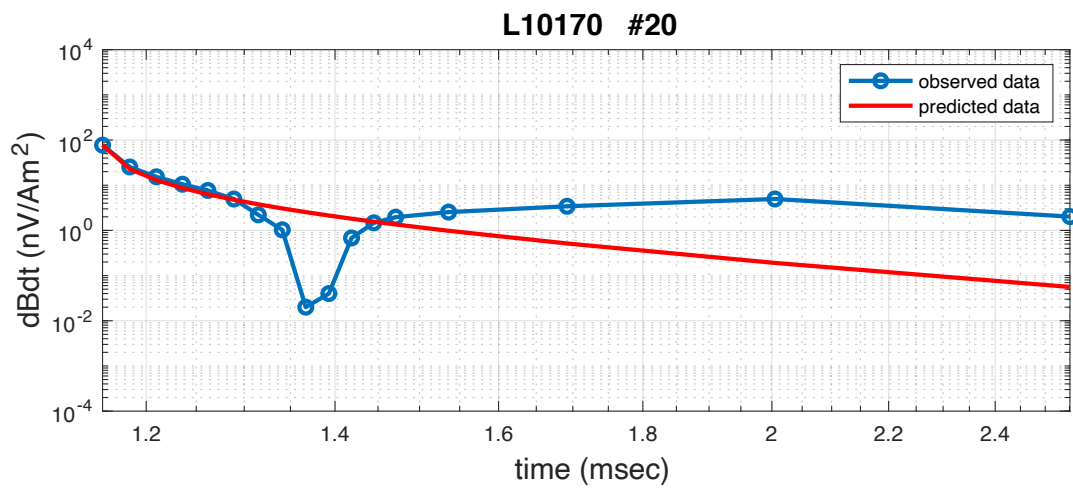
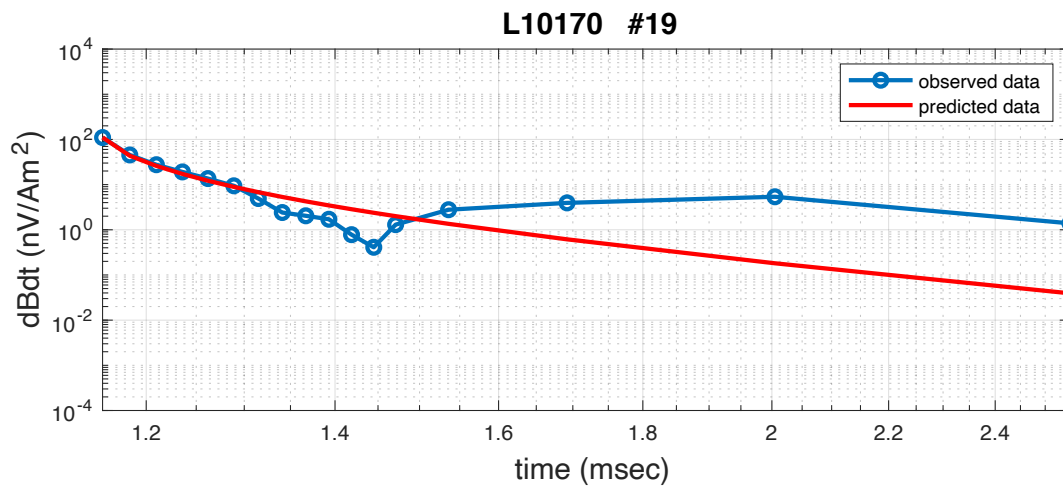


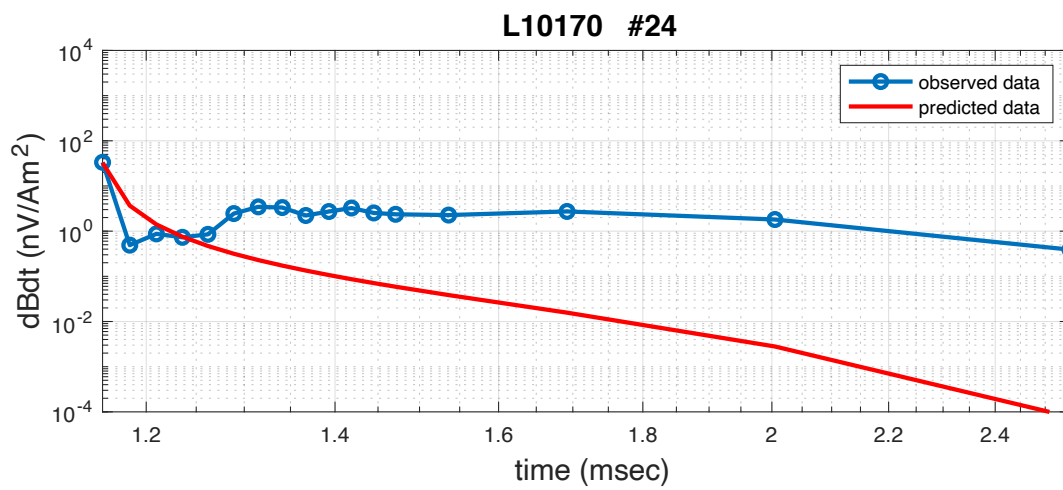
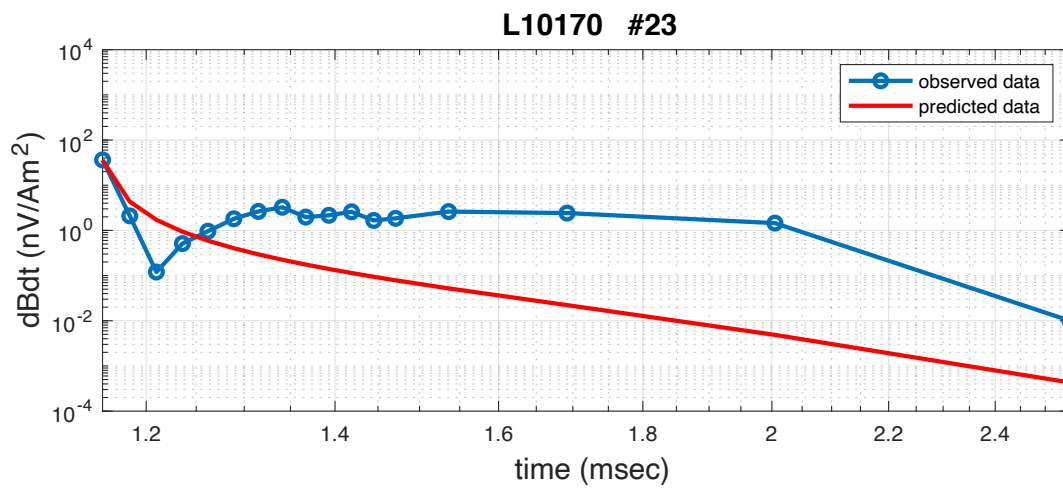
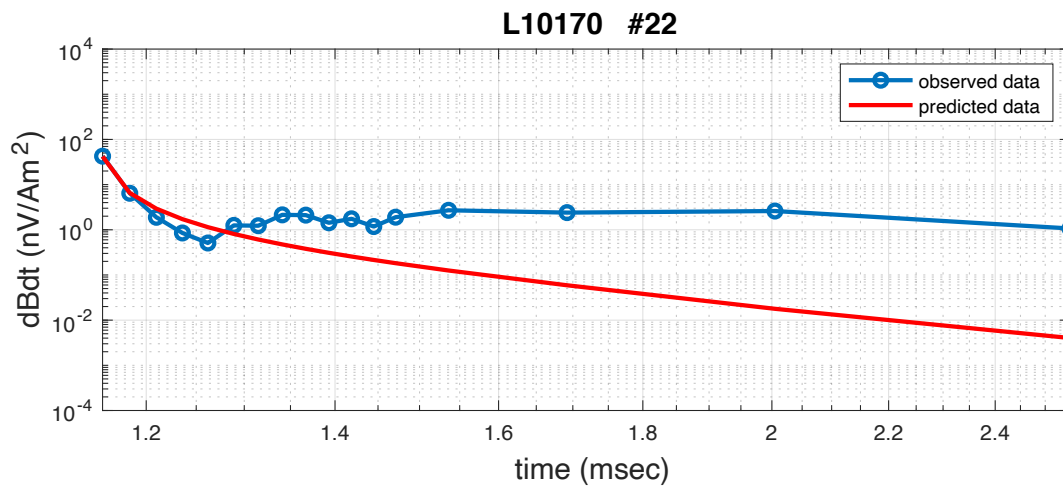


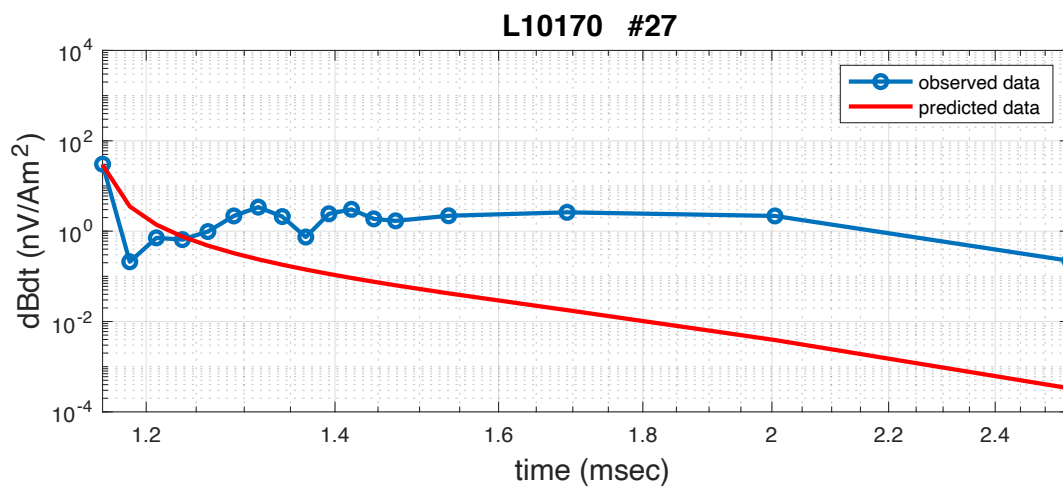
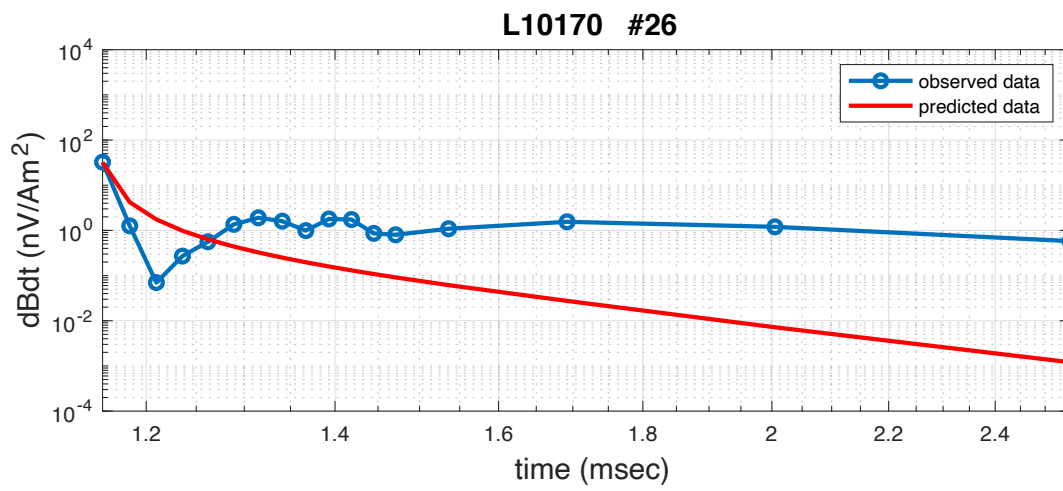
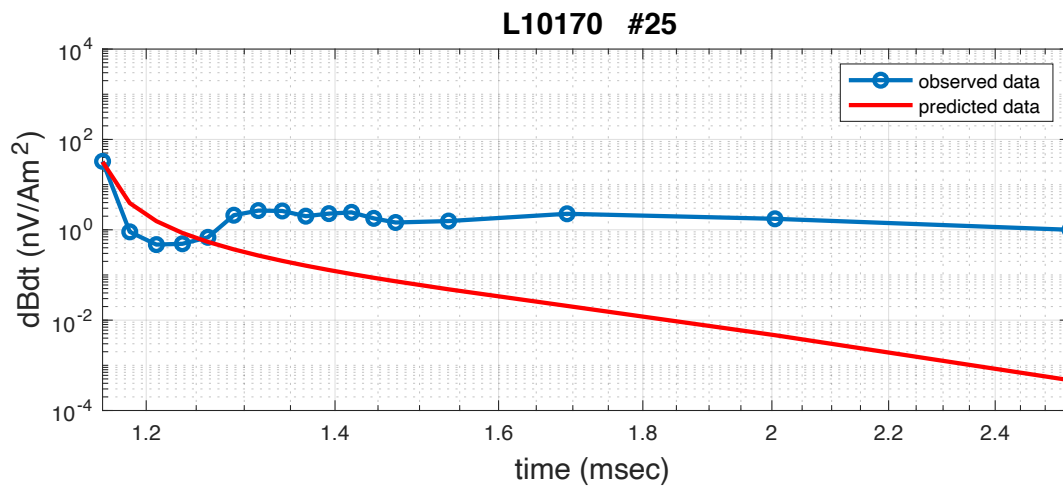


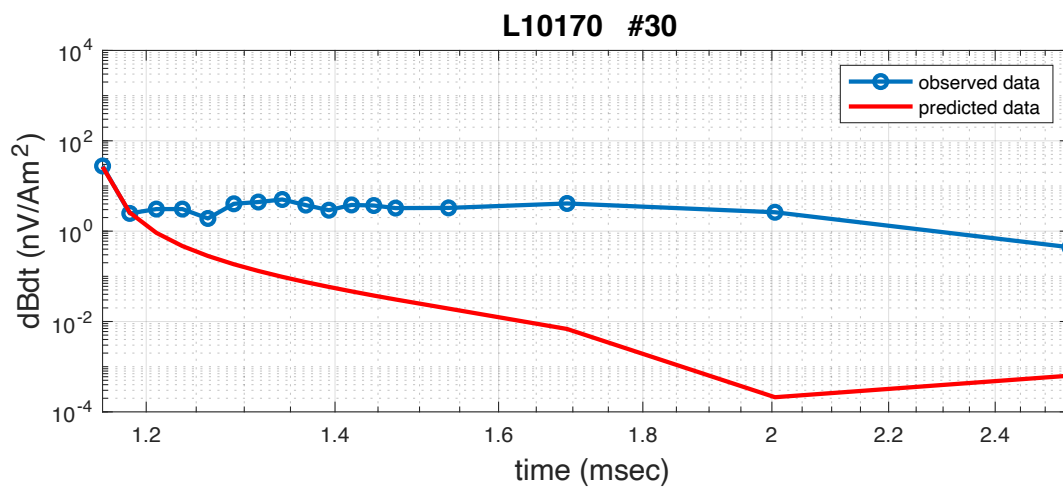
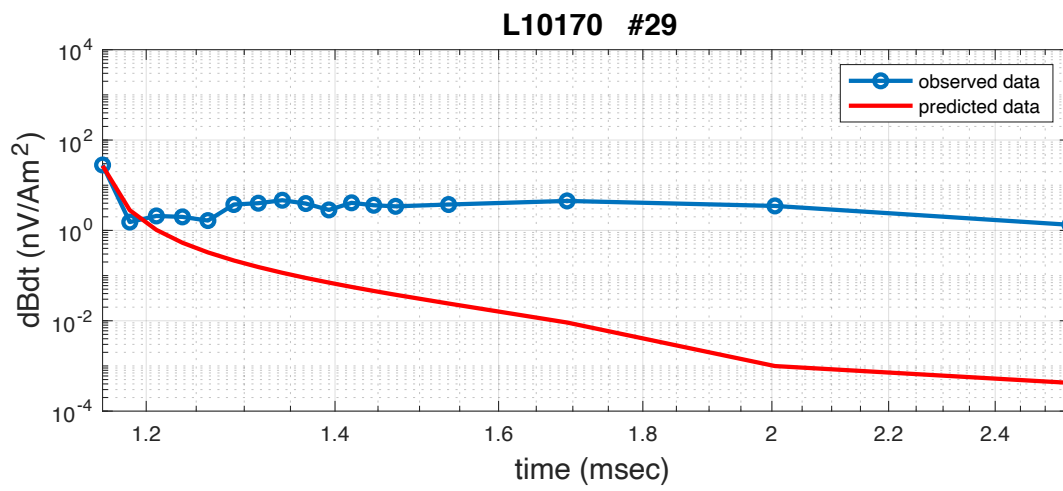
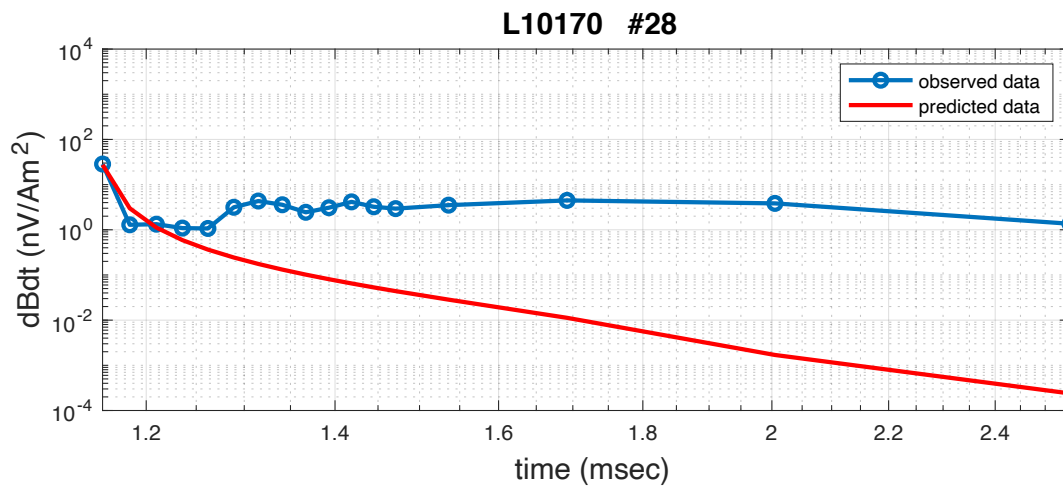


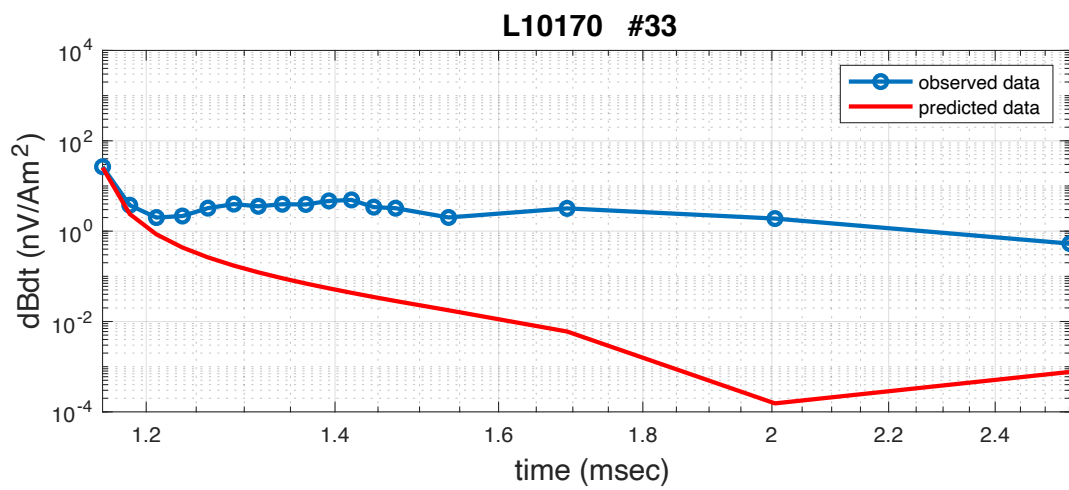
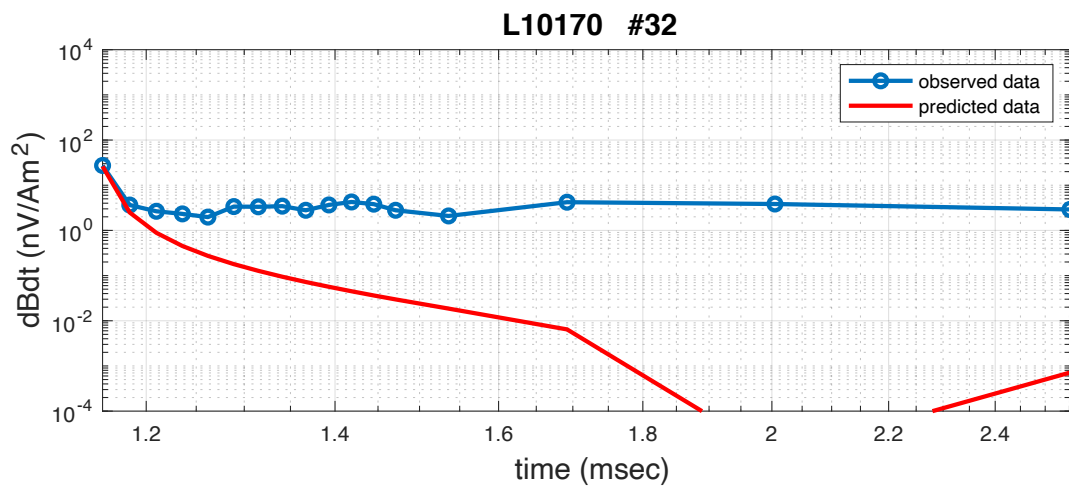
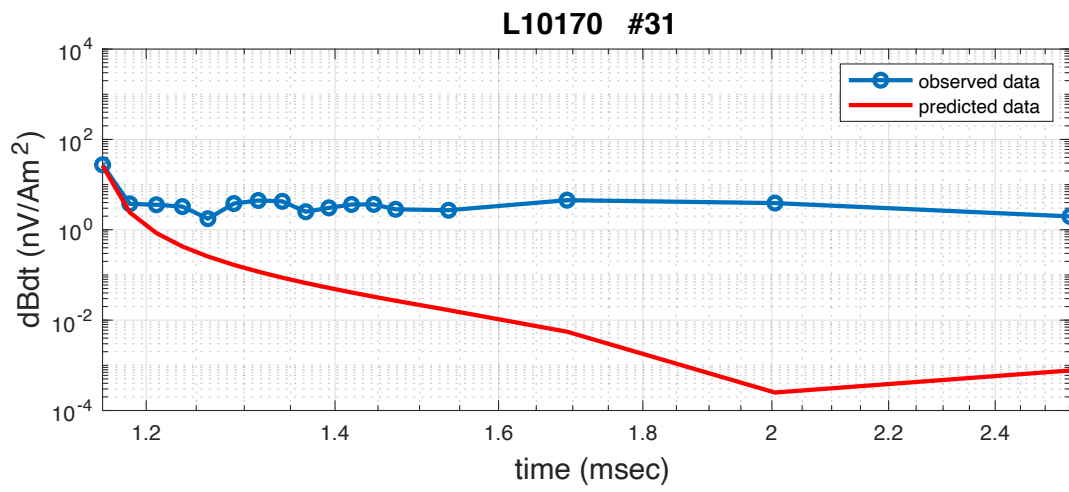


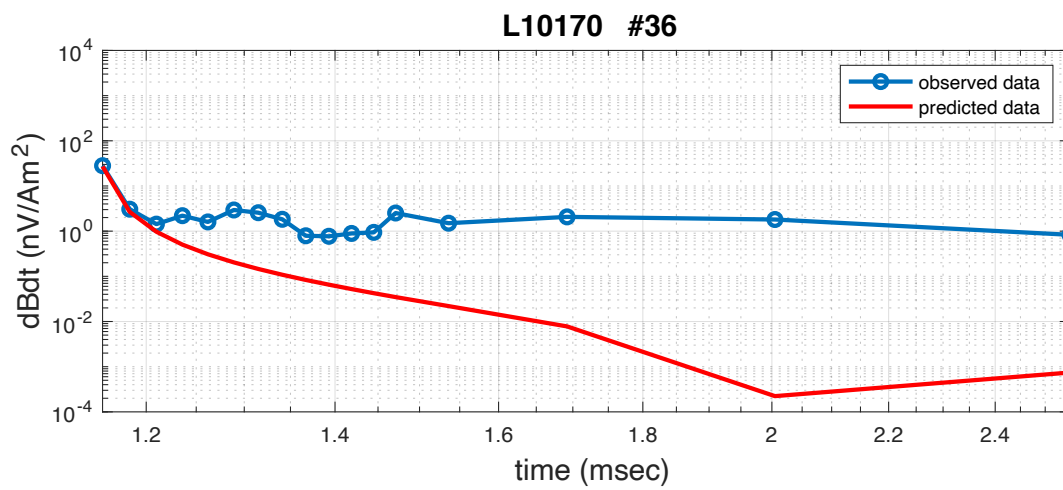
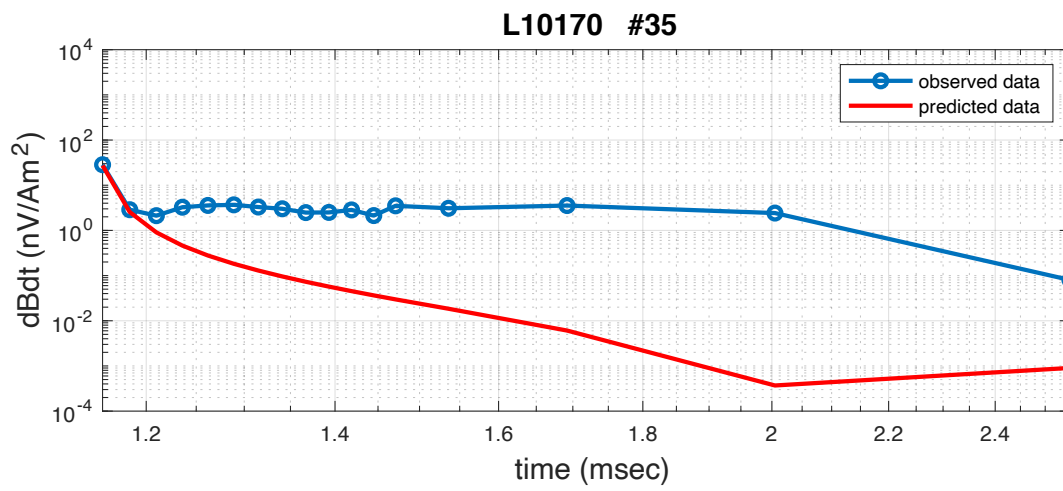
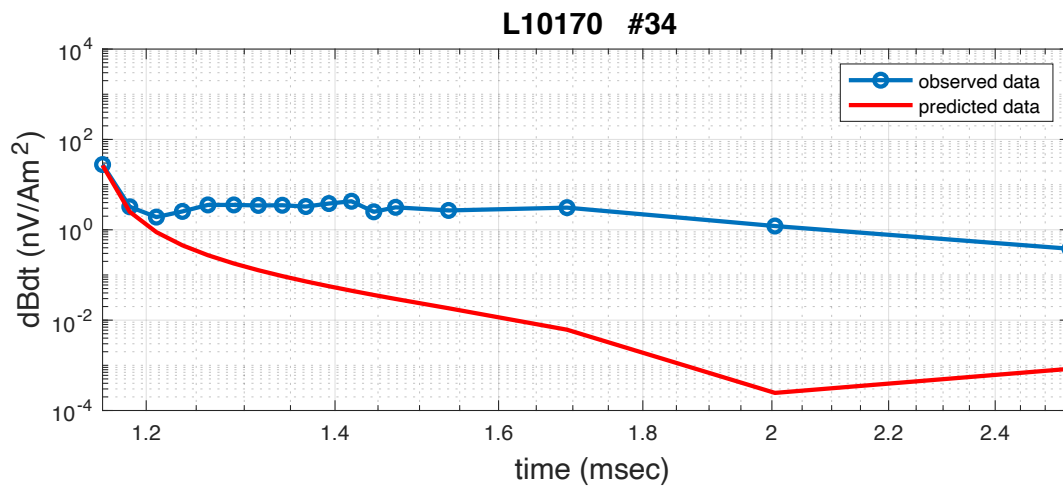


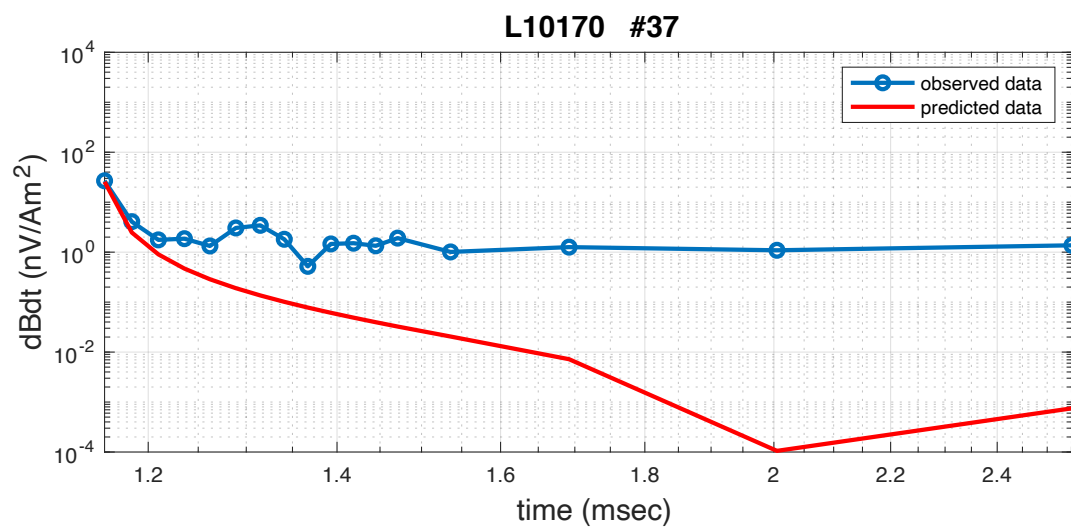




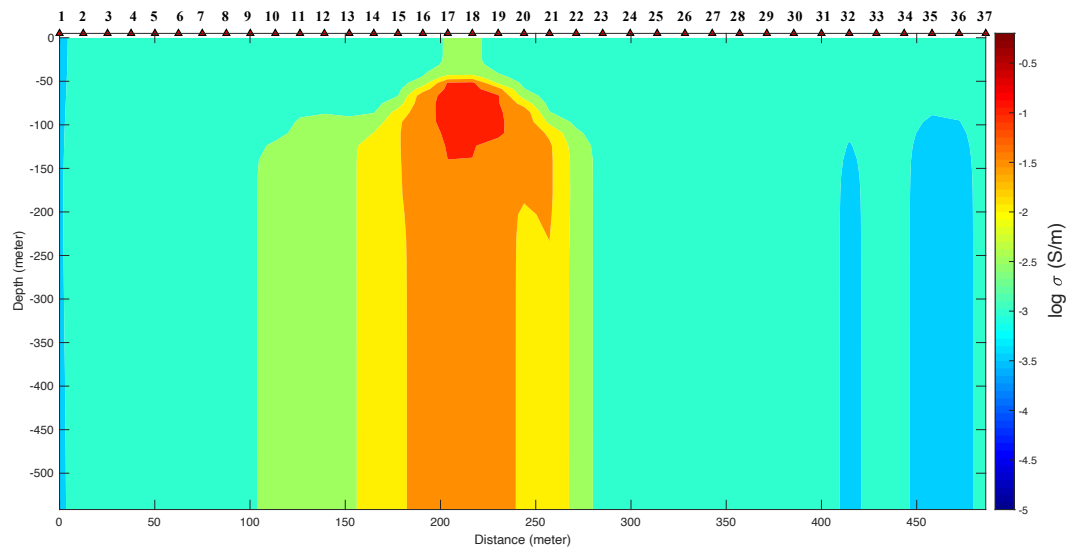




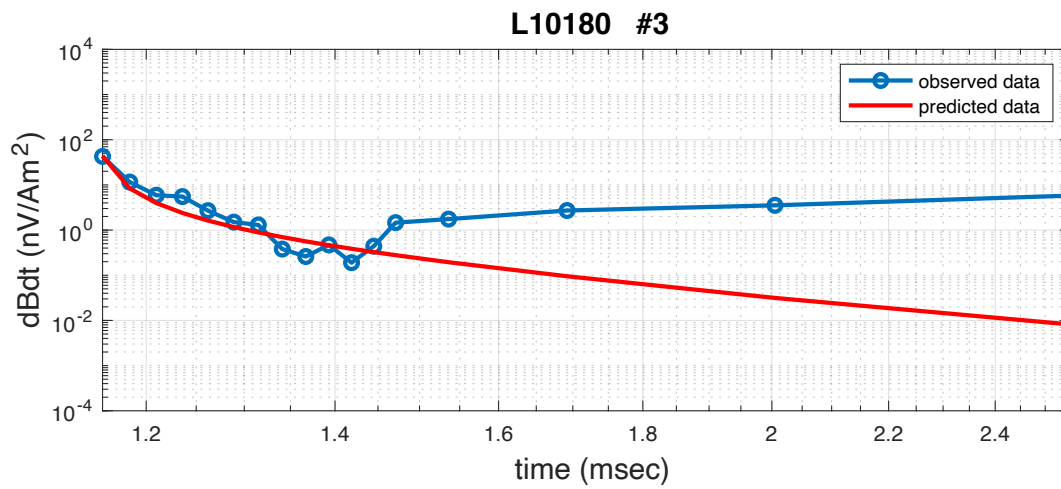
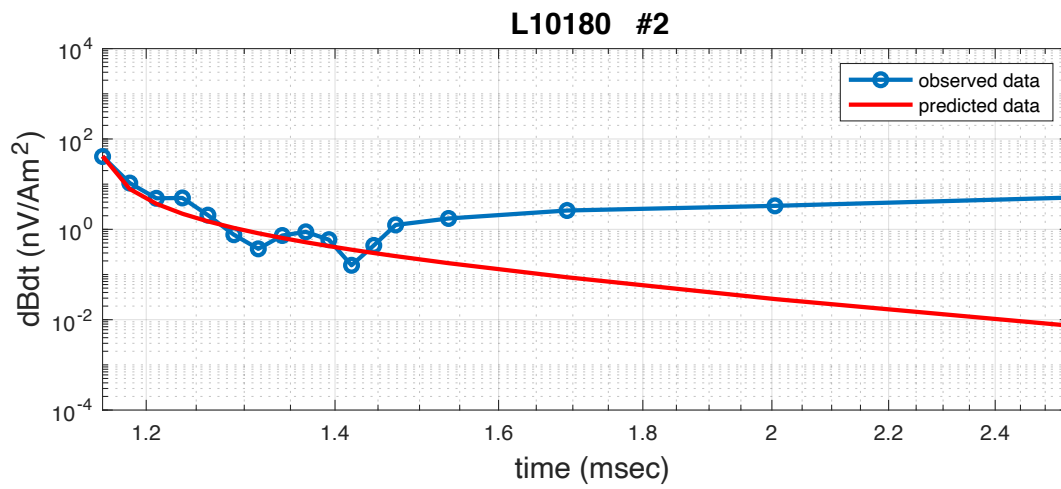
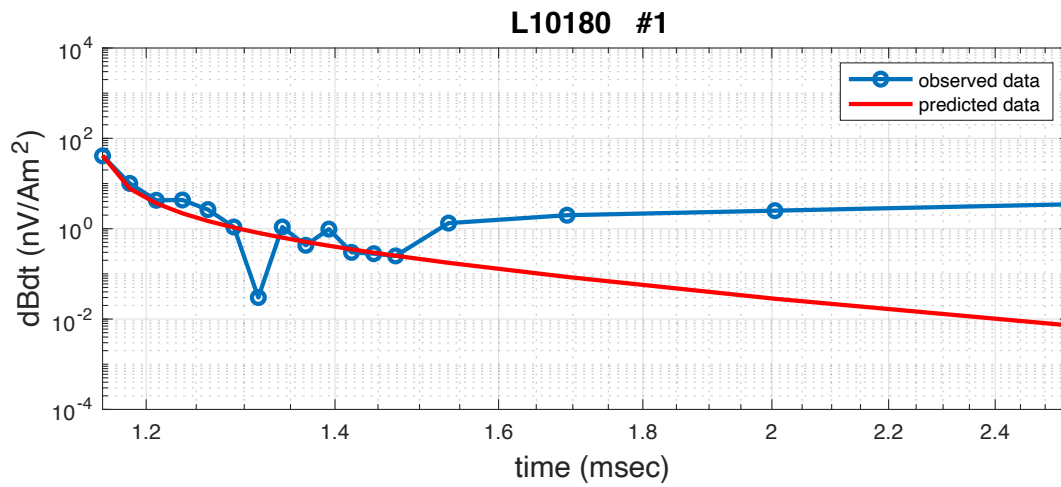


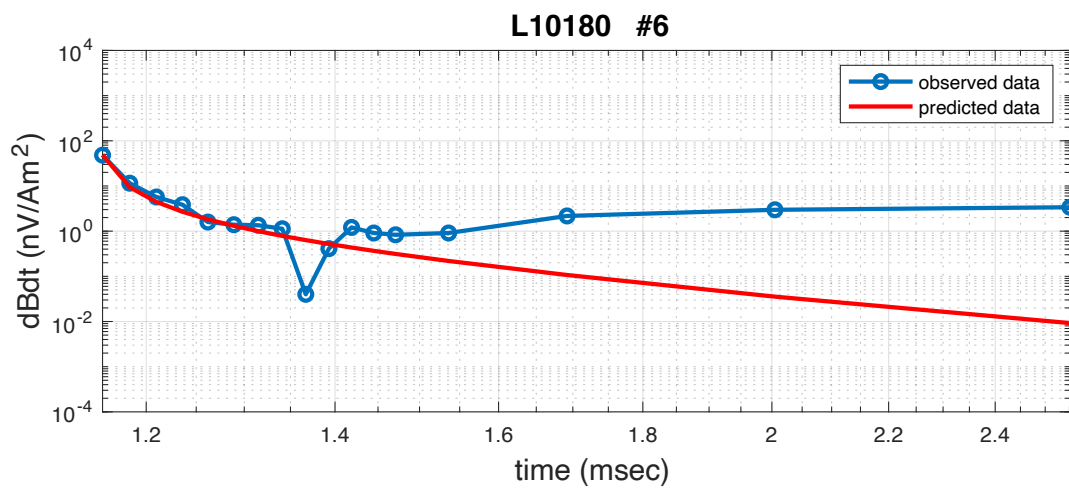
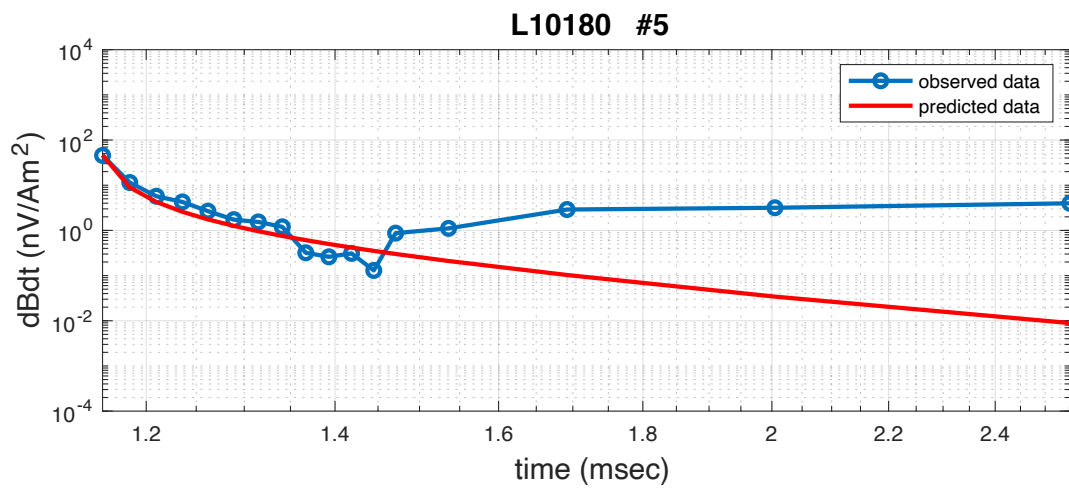
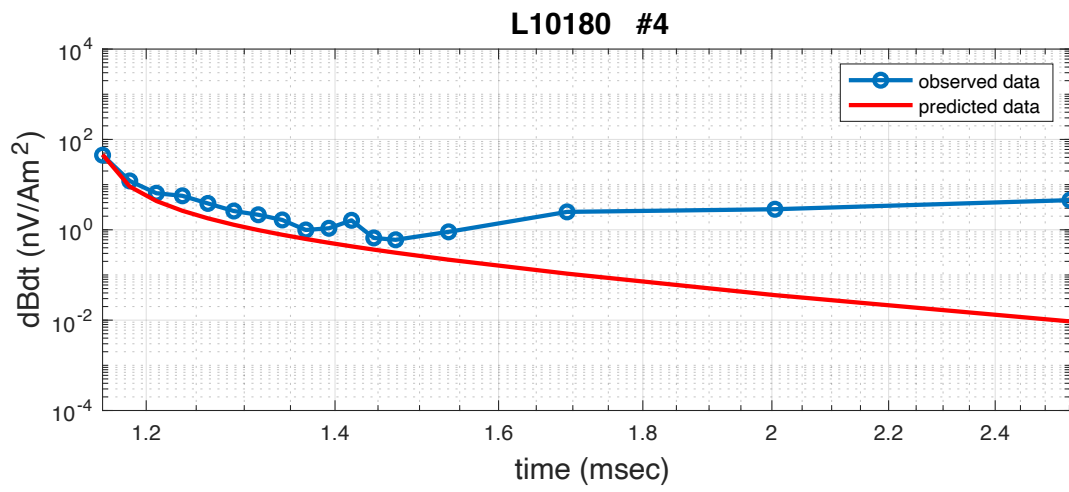


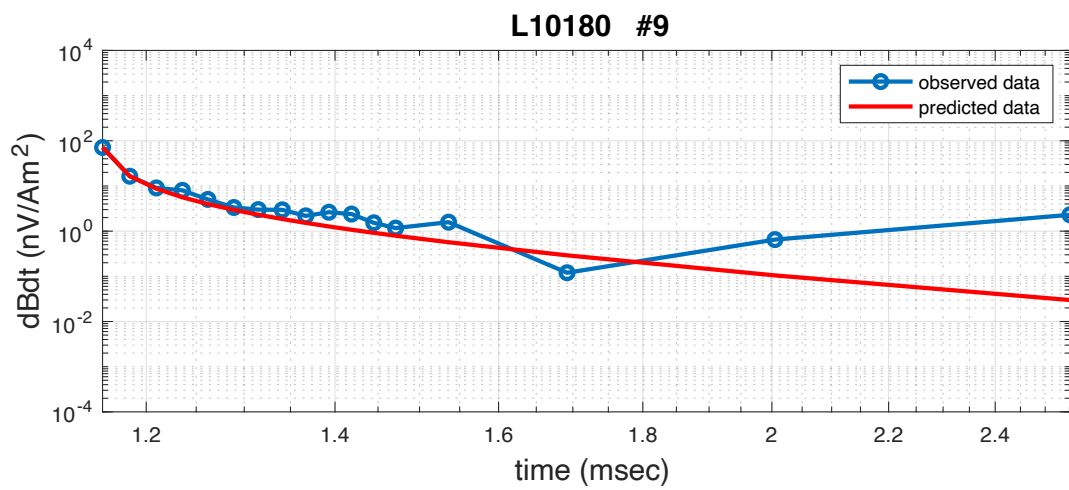
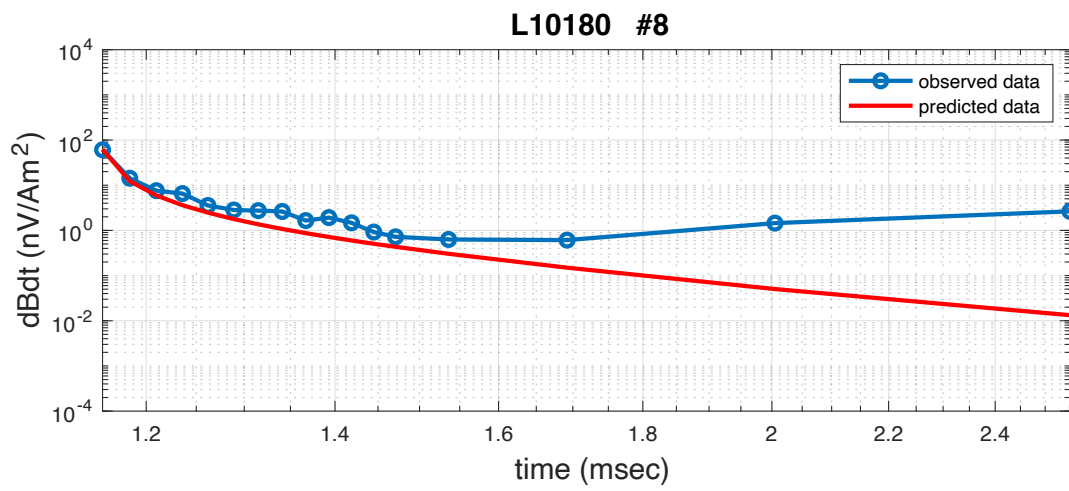
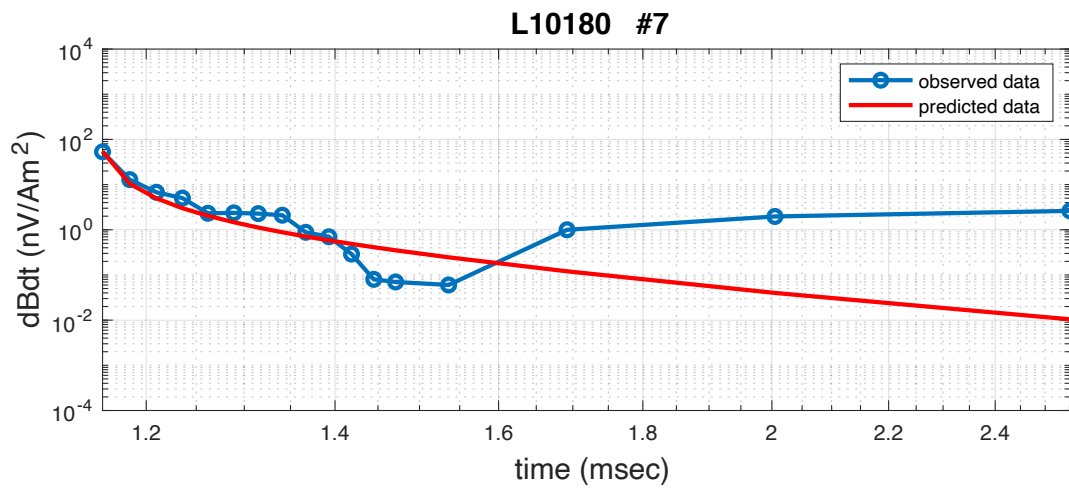
L10180

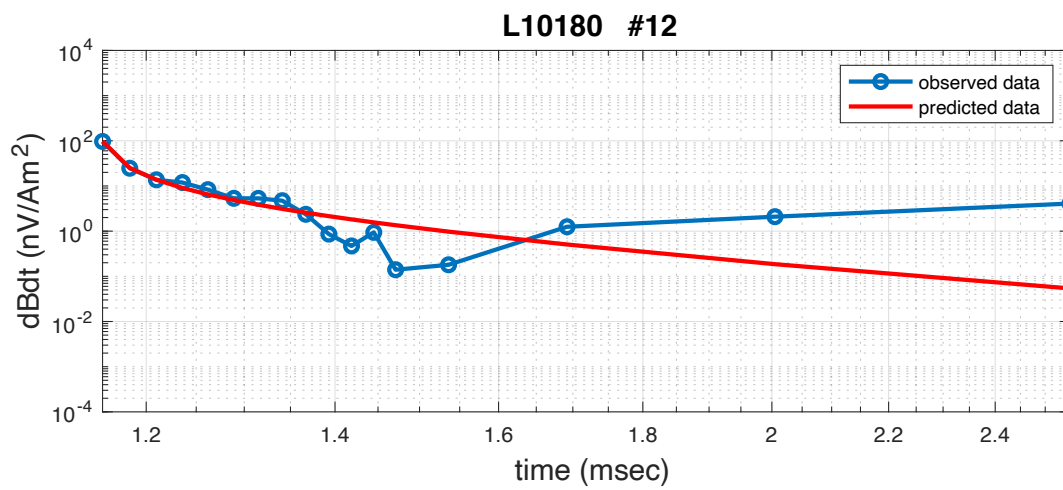
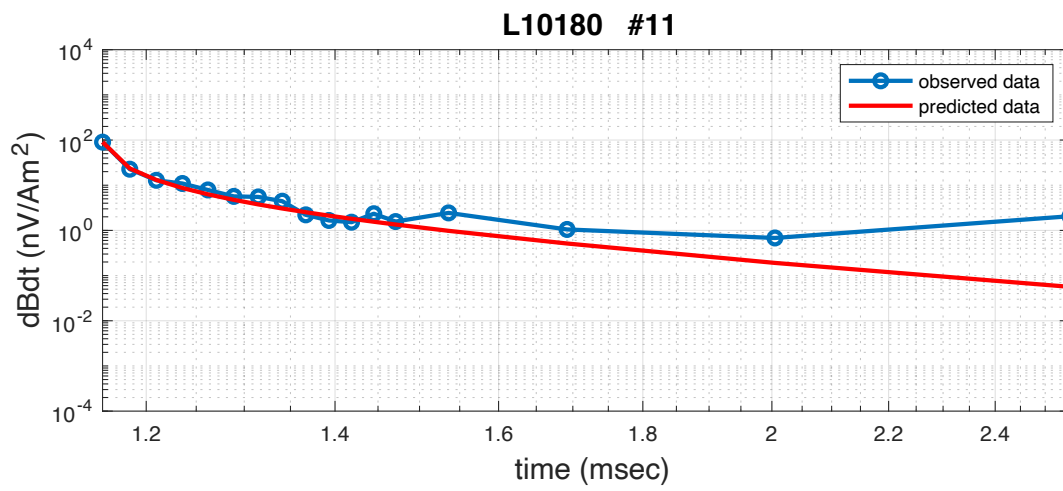
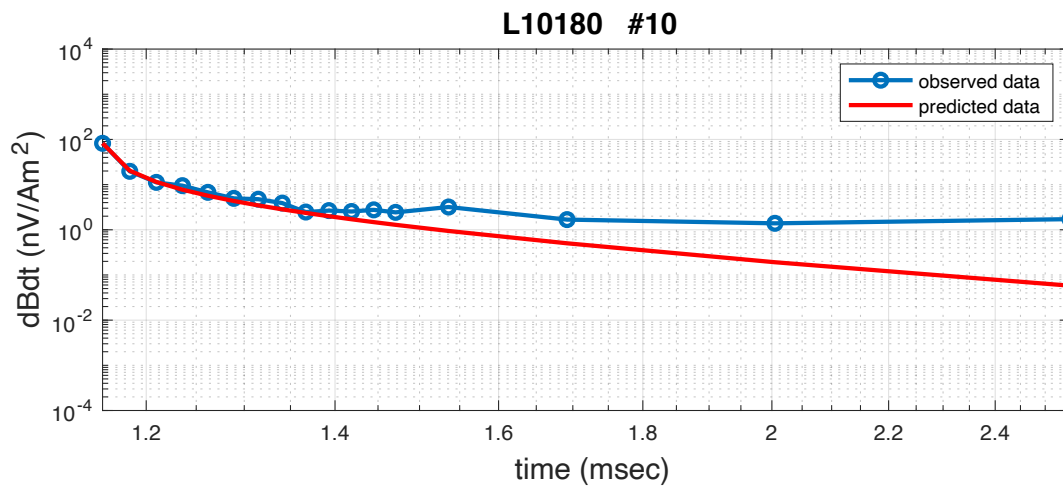


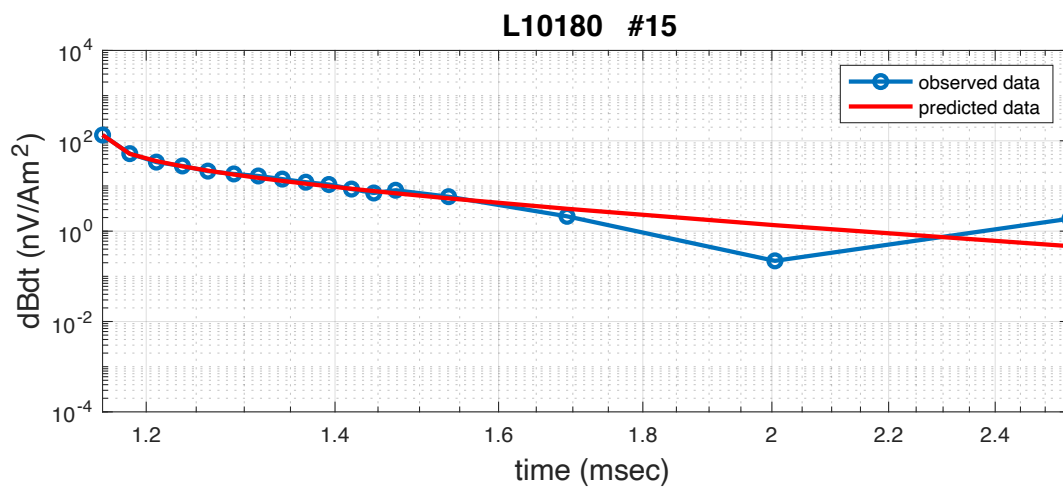
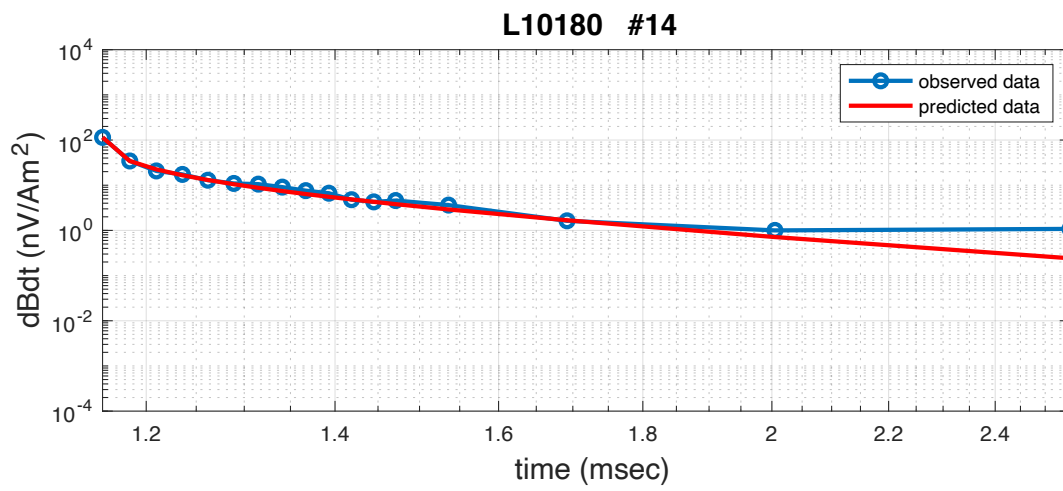
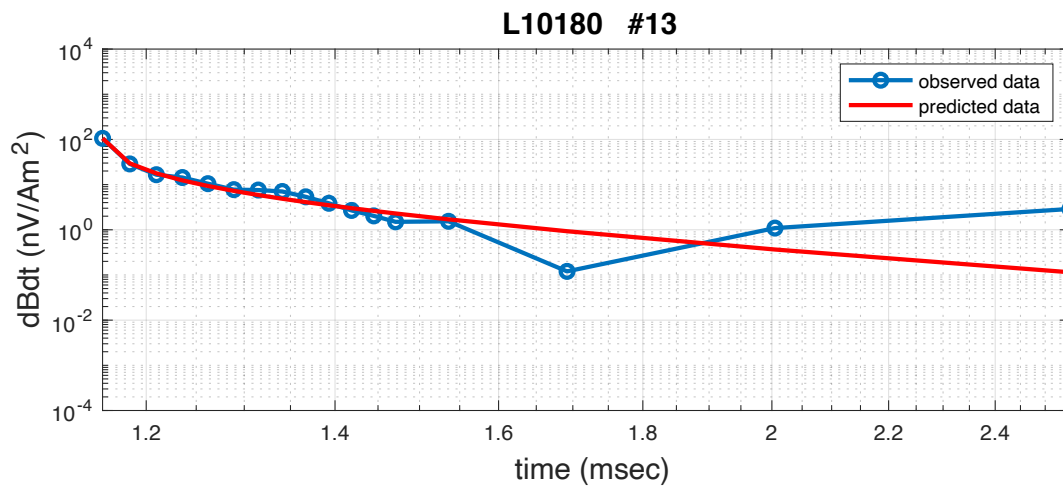
The observation points on L10180

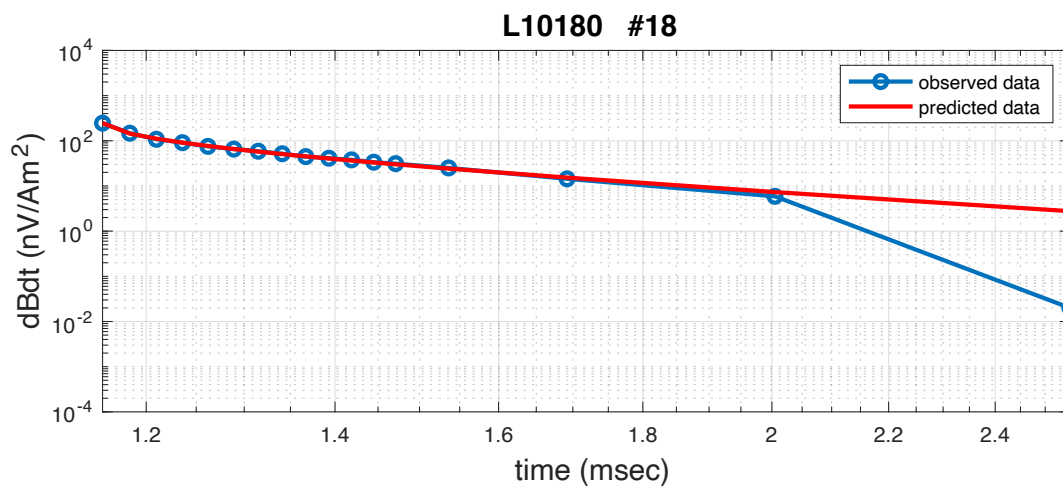
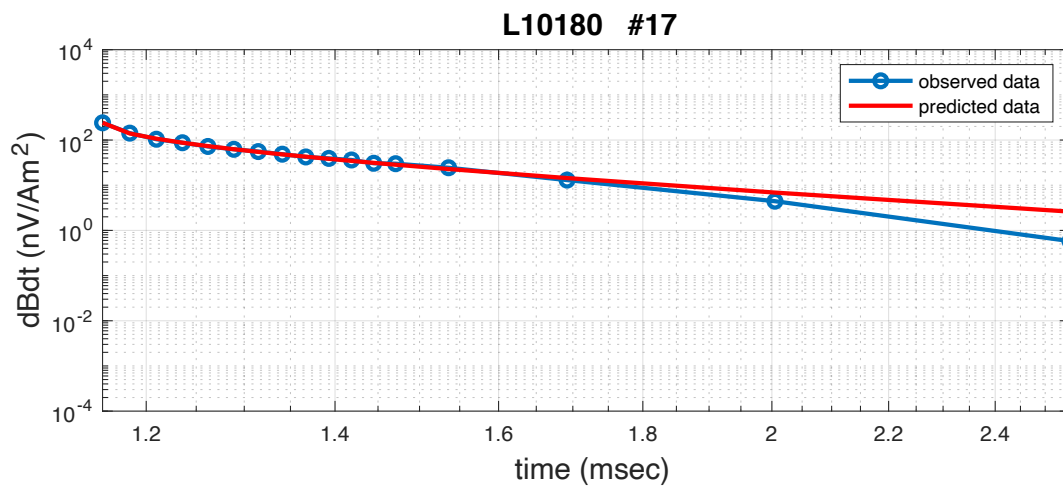
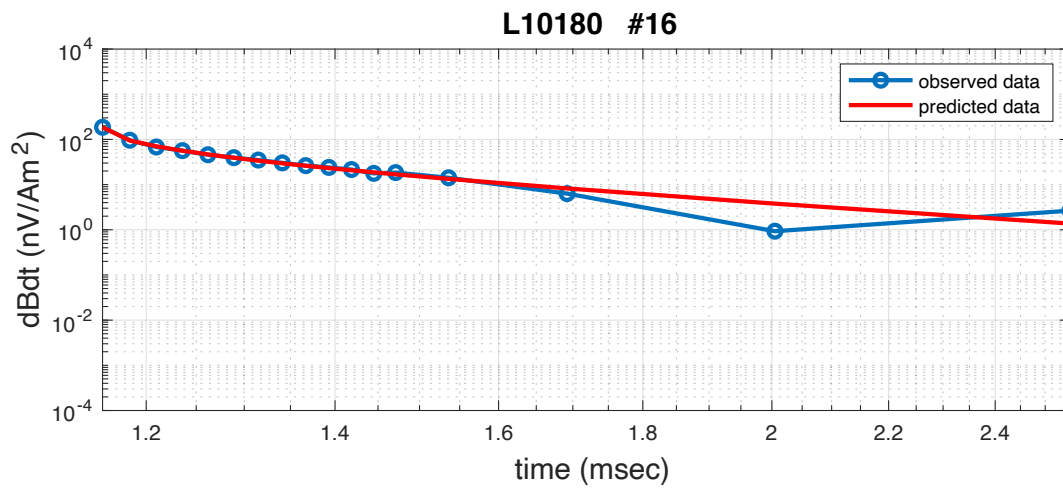


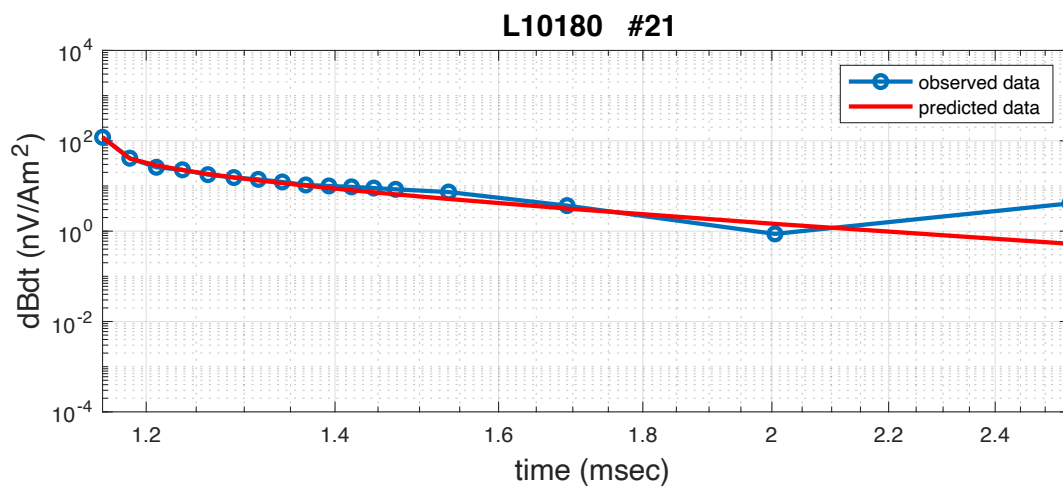
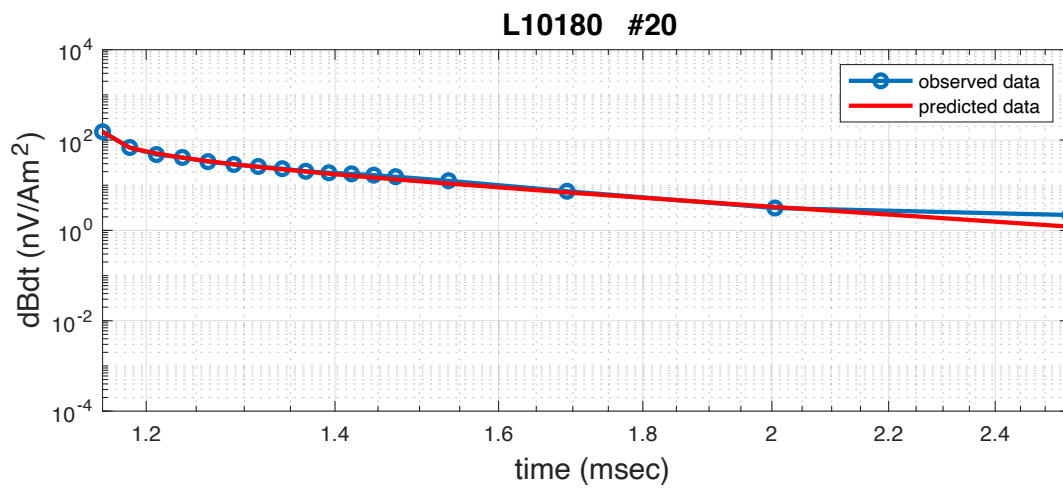
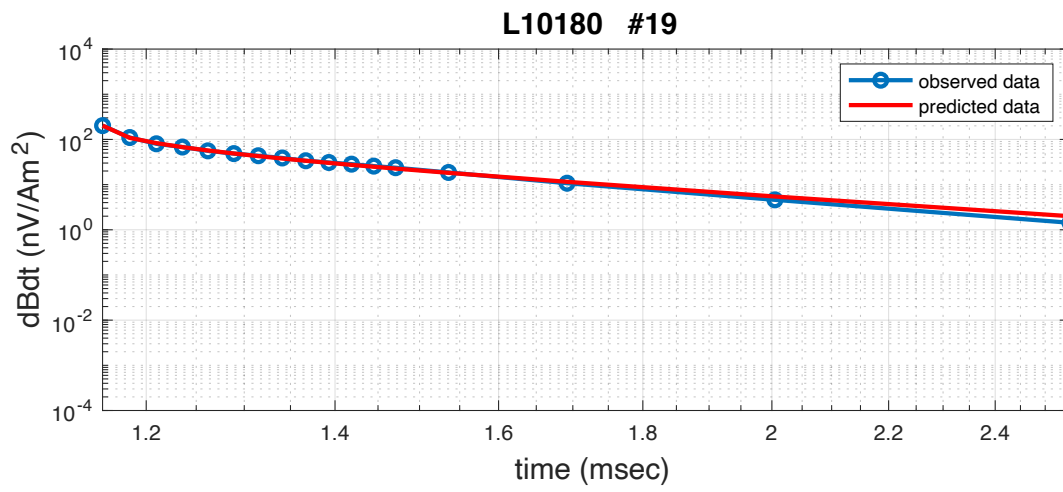


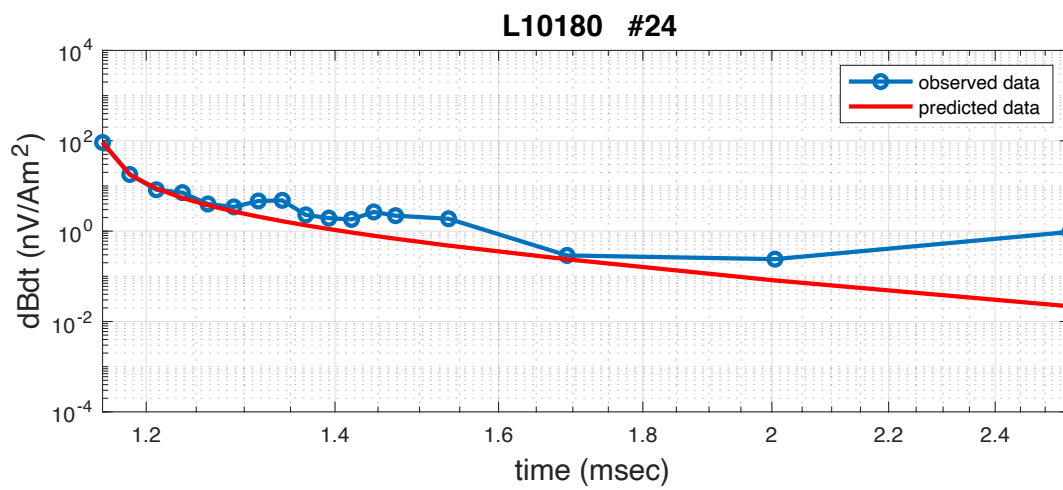
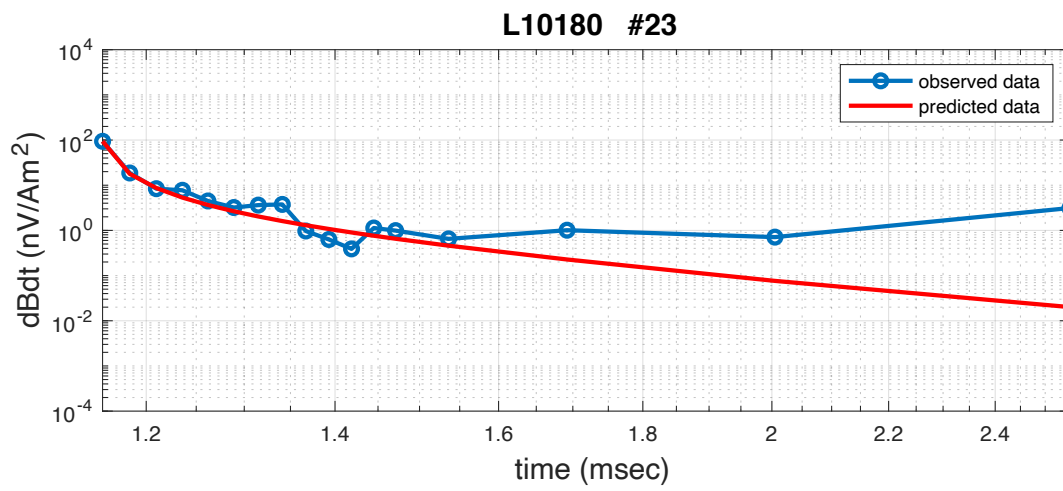
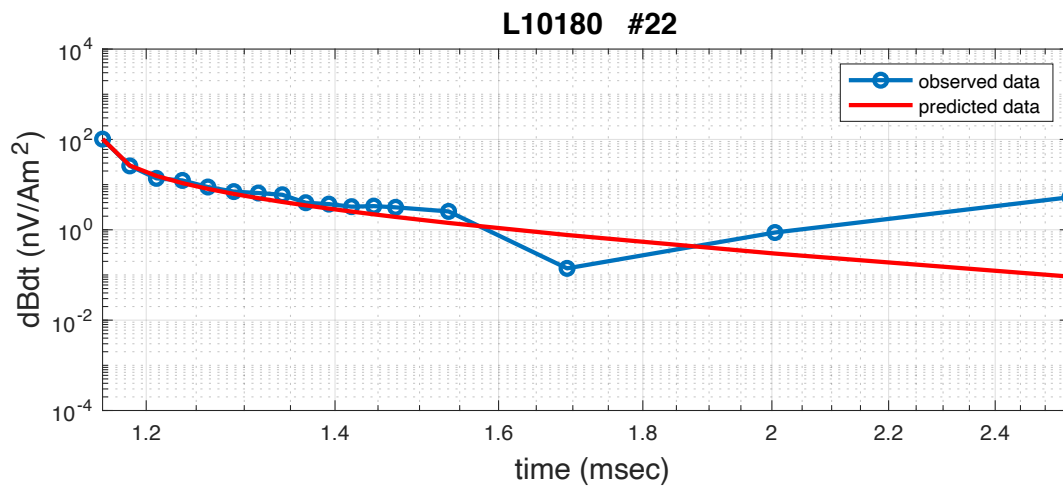


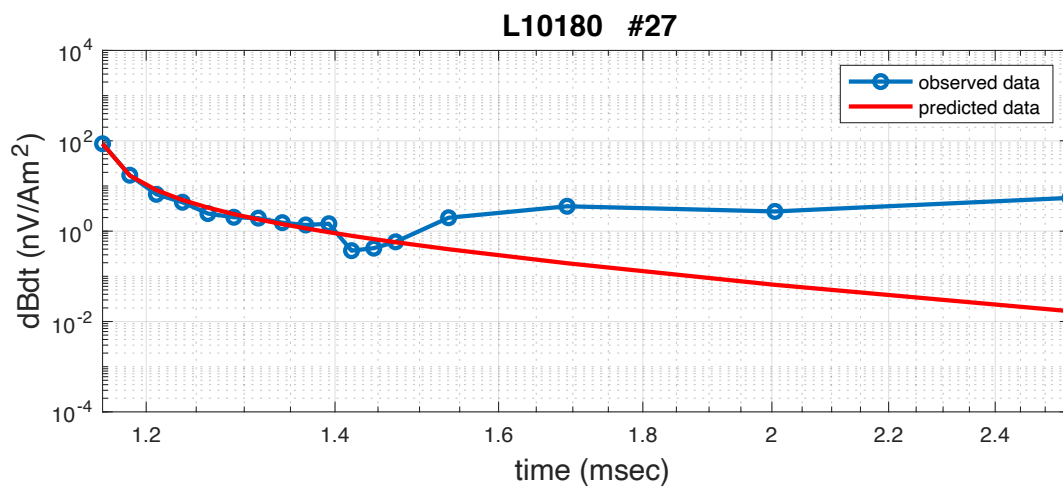
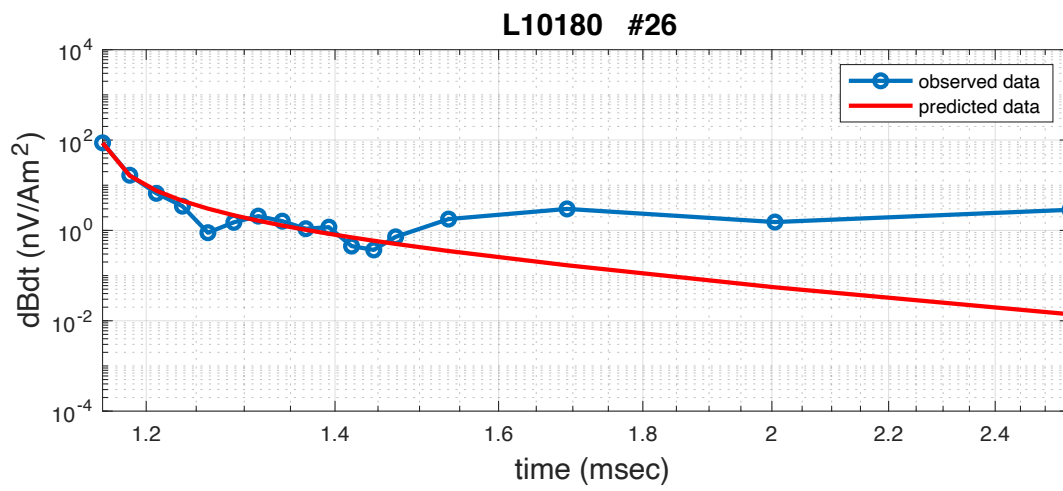
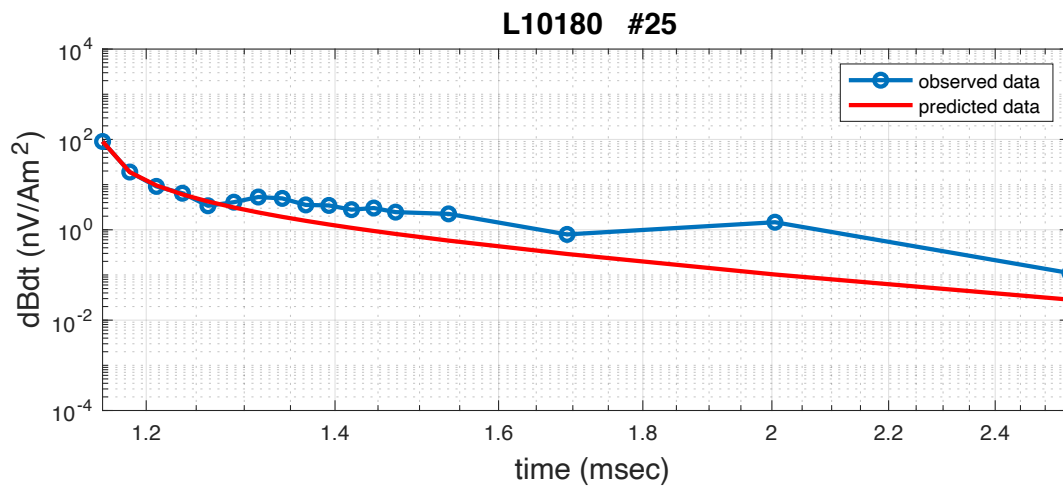


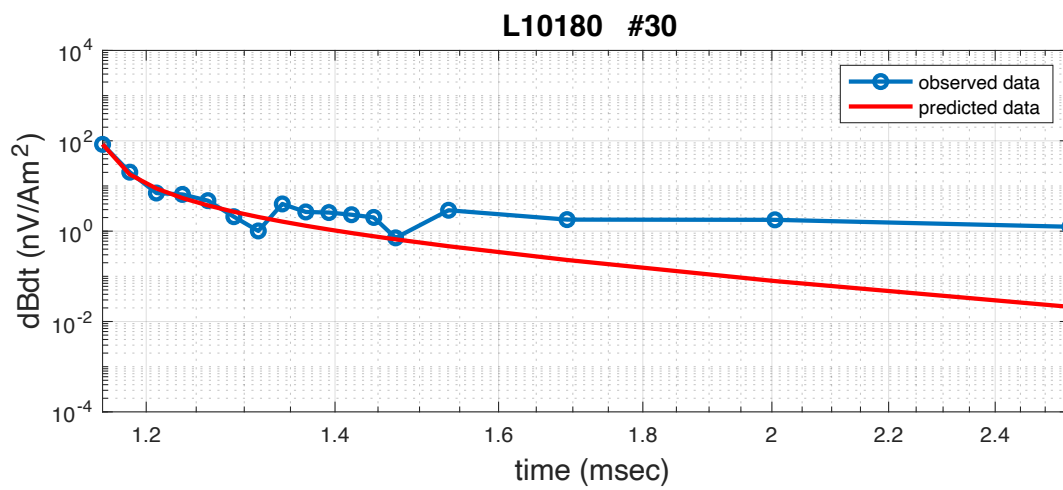
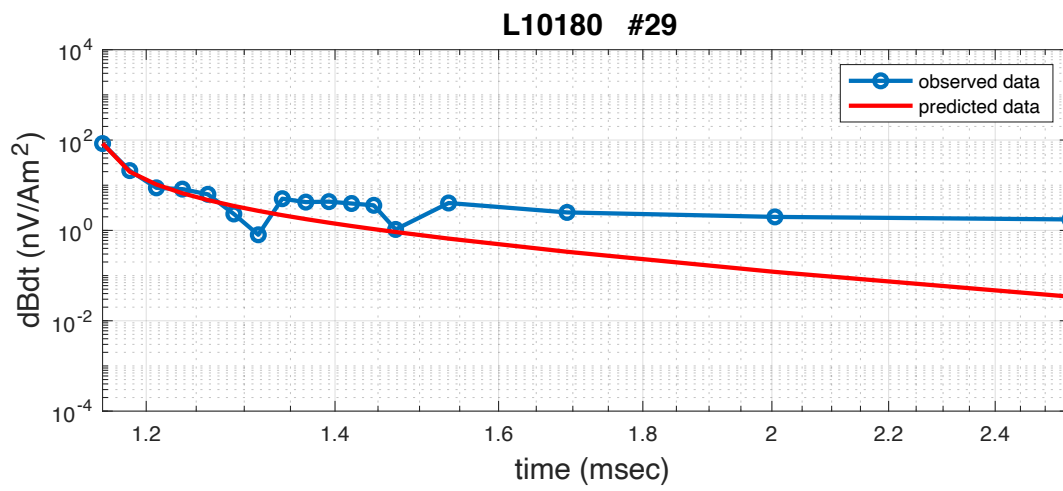
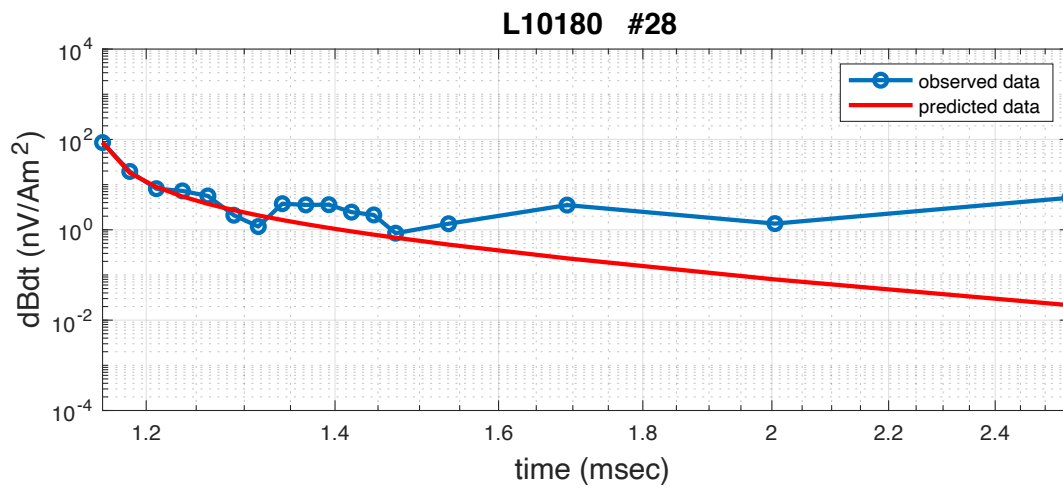


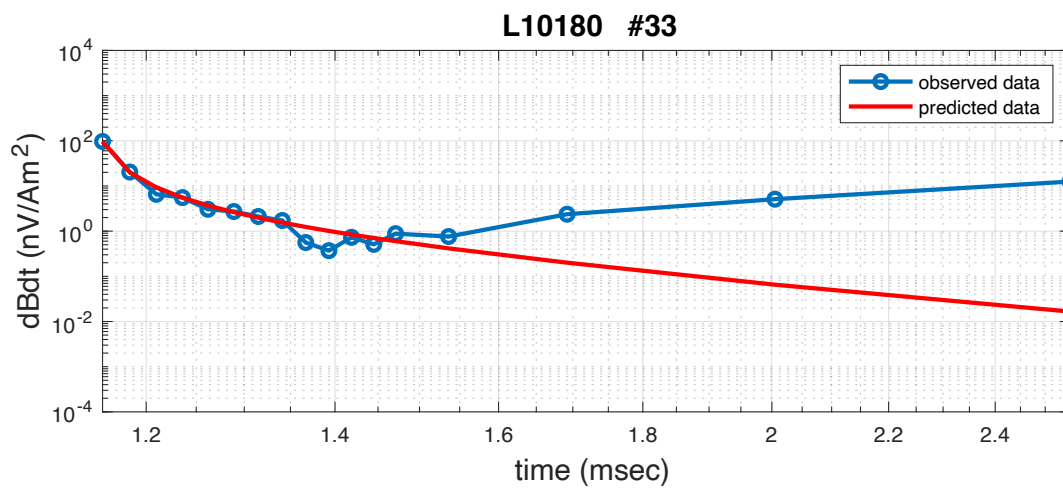
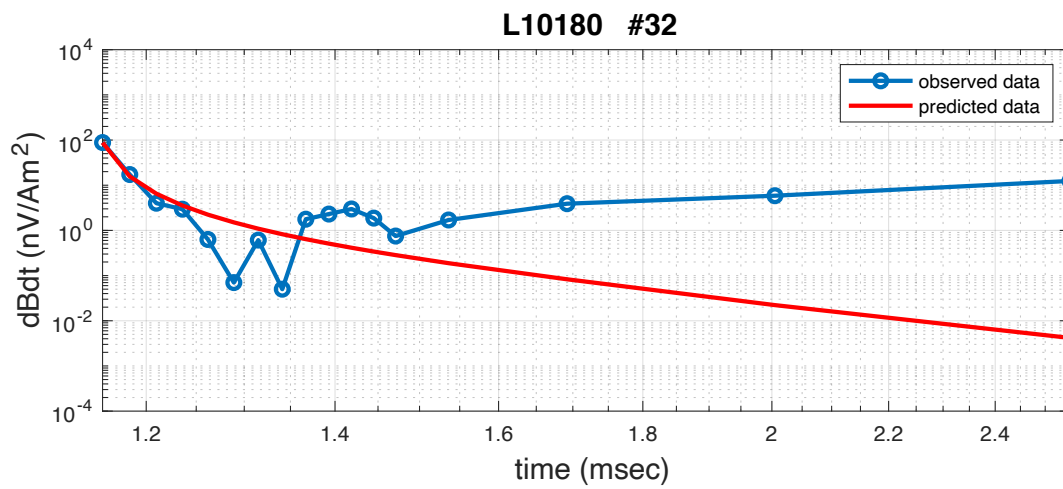
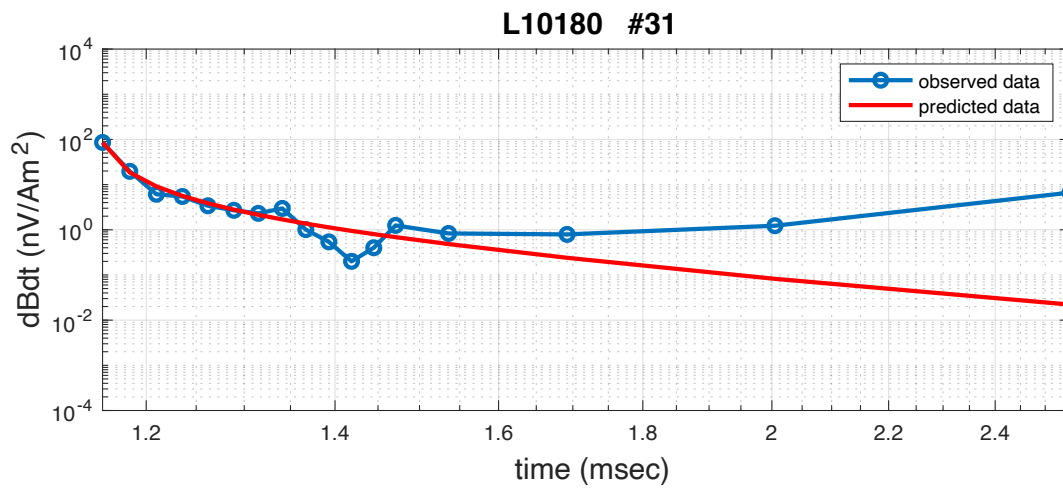


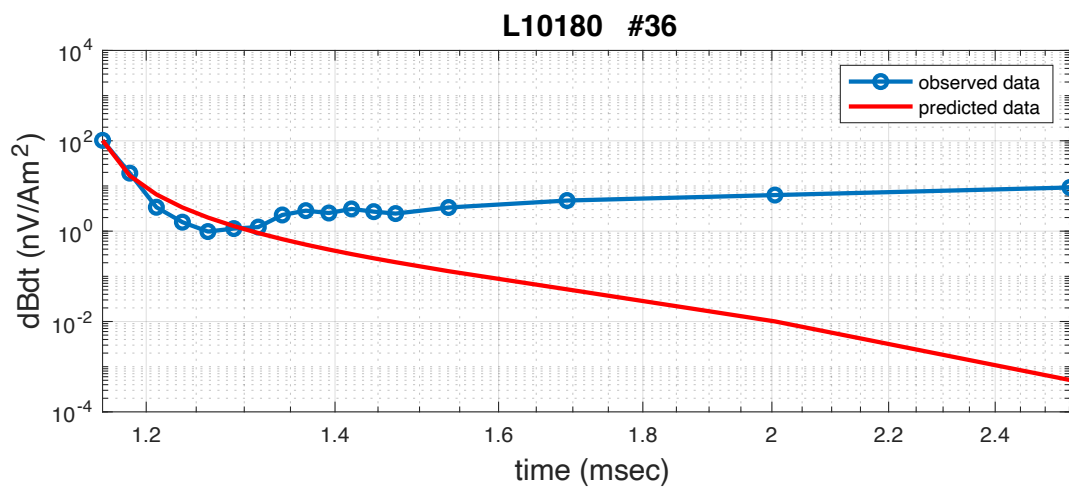
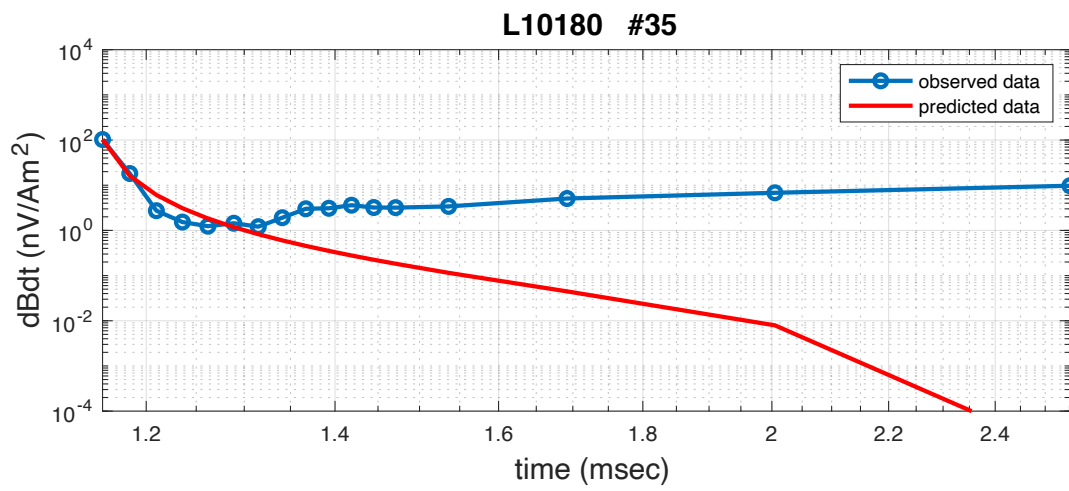
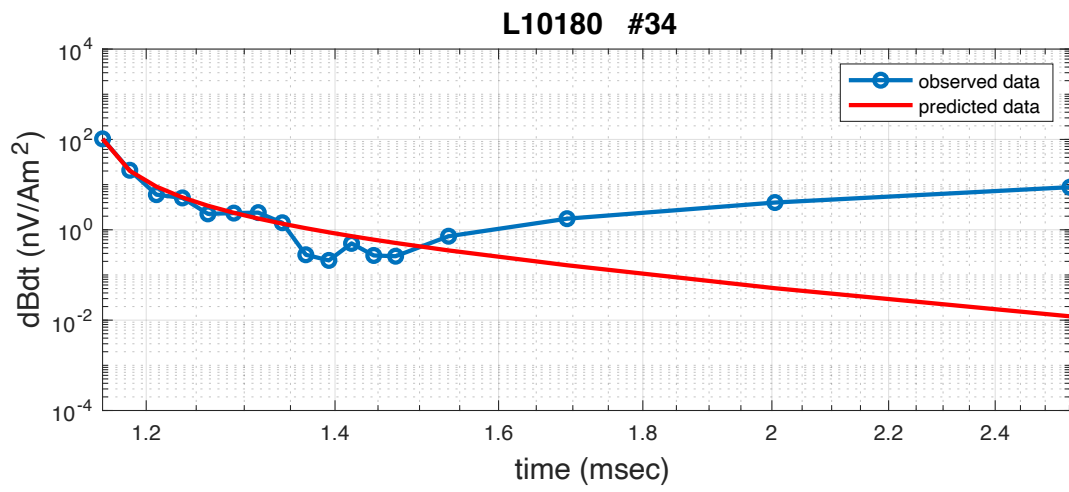


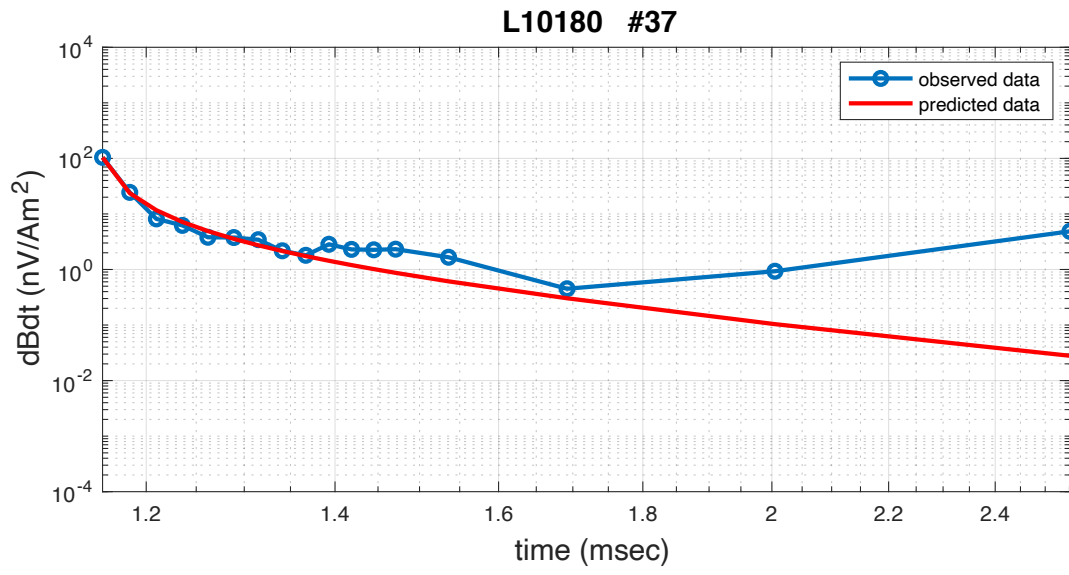




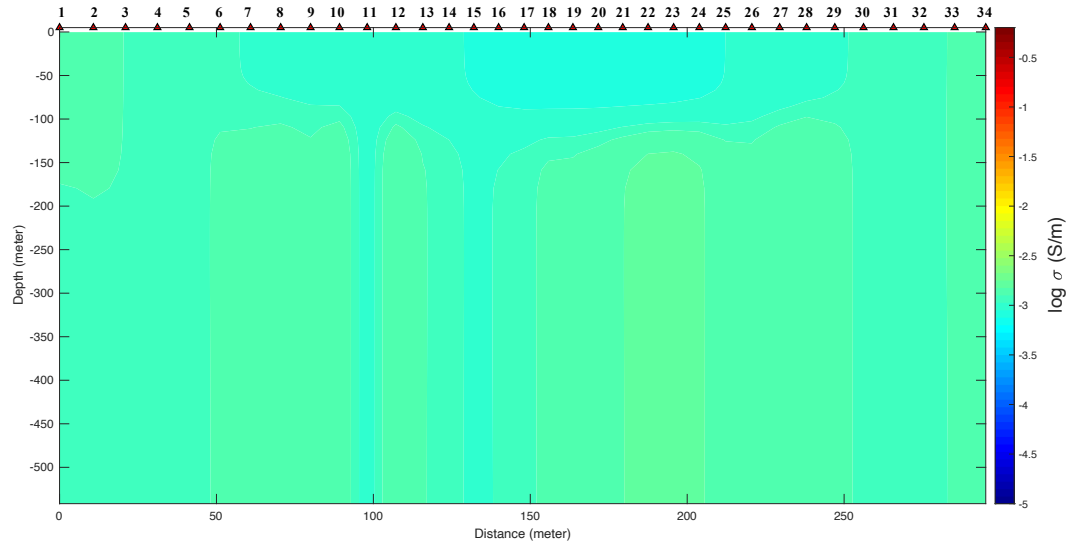




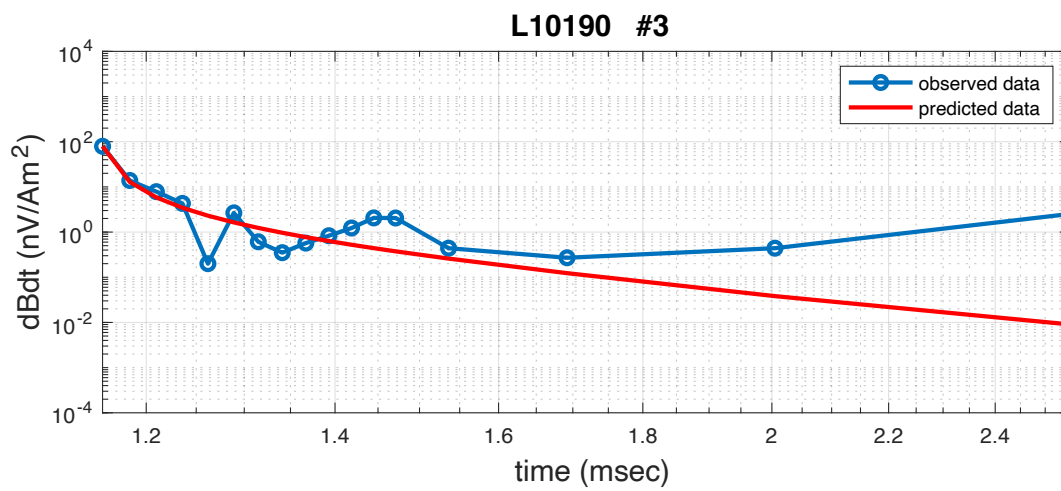
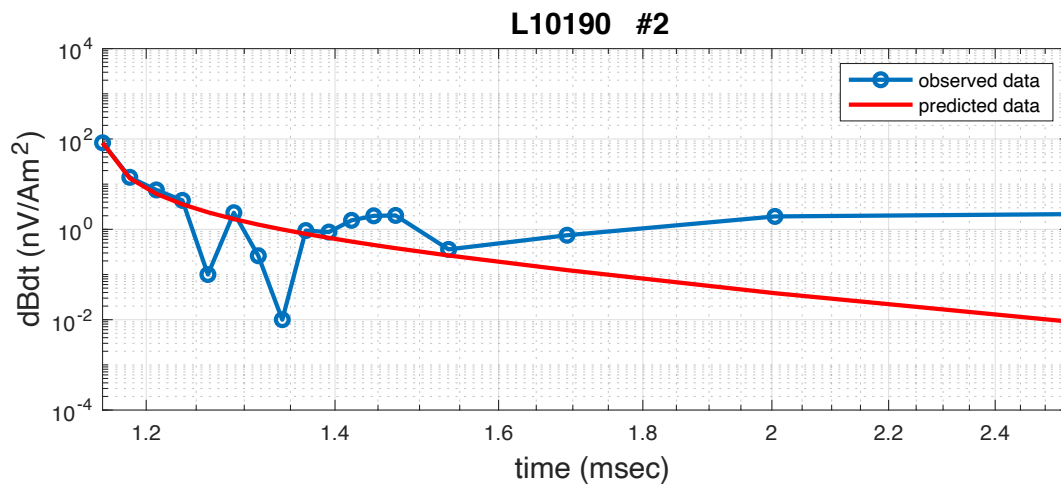
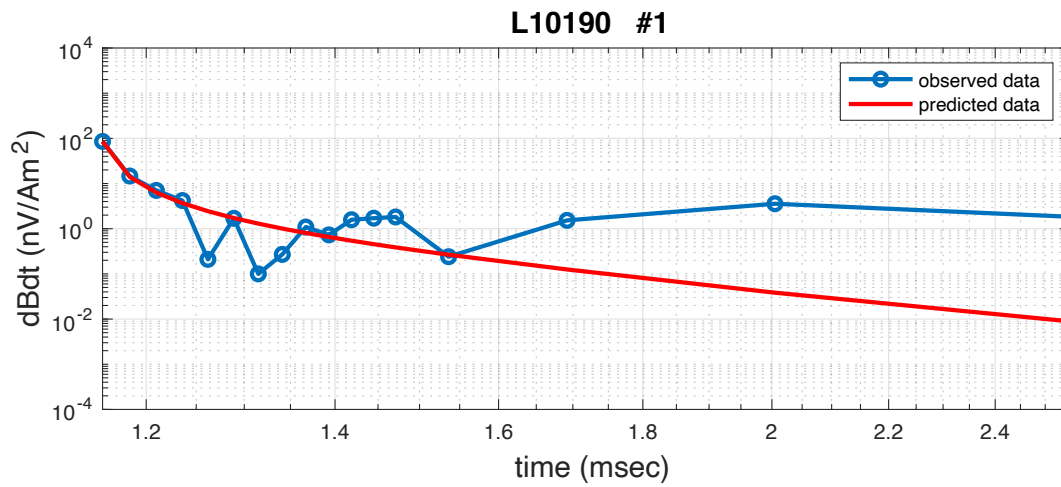


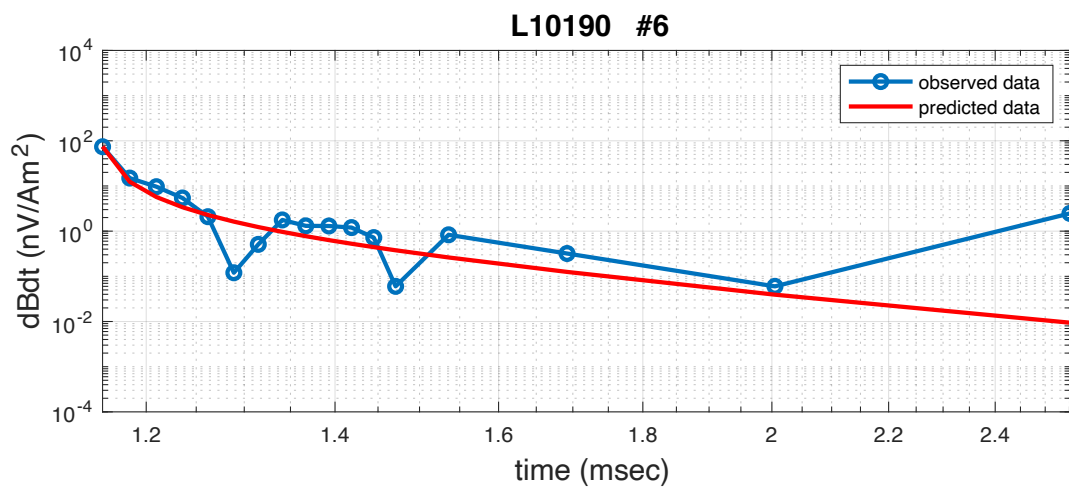
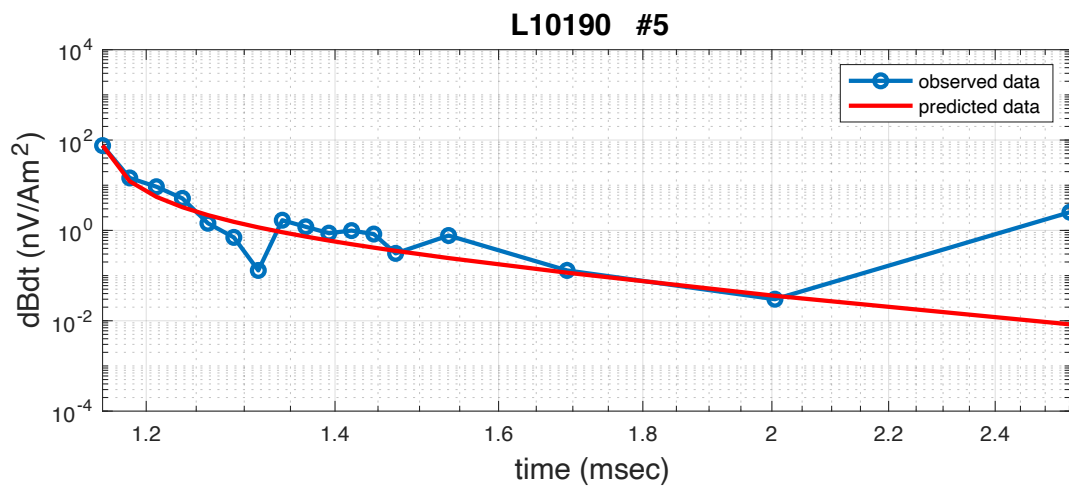
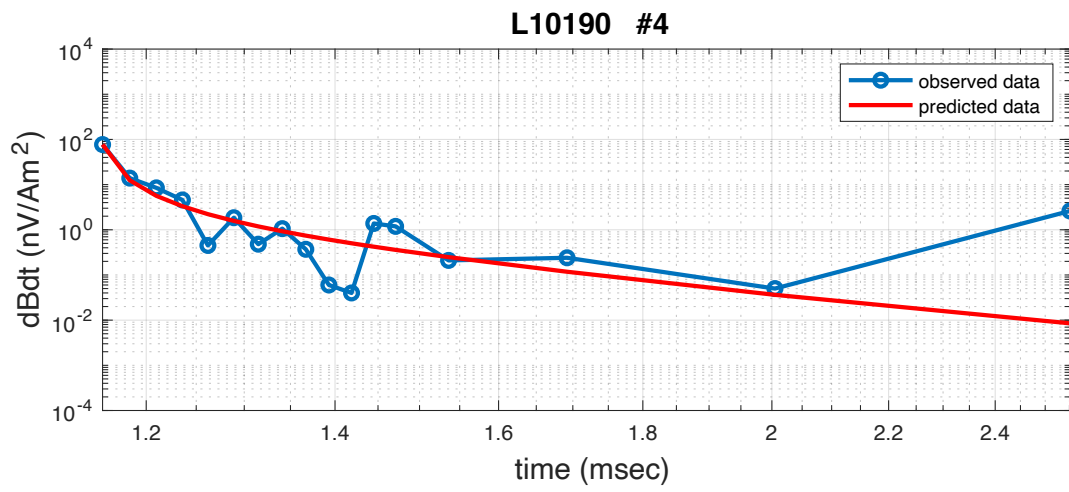


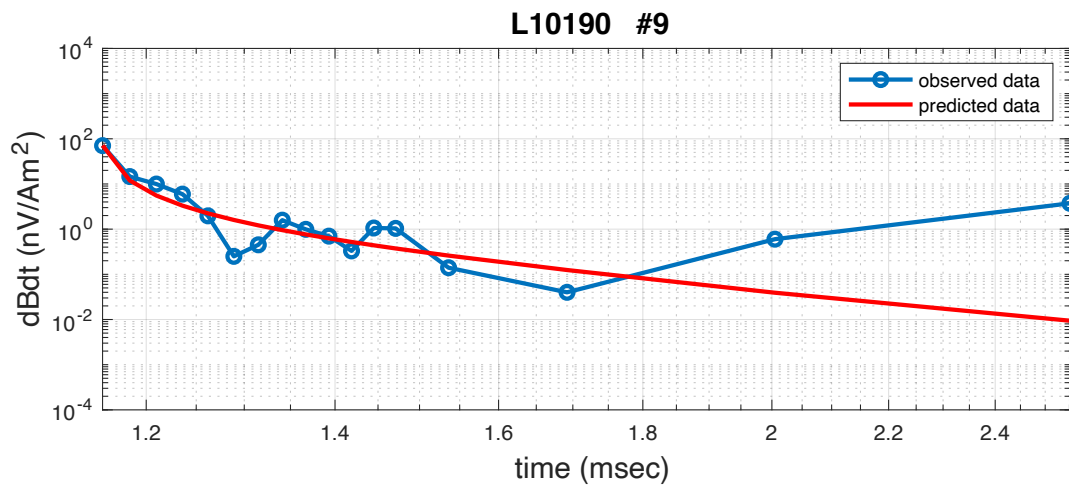
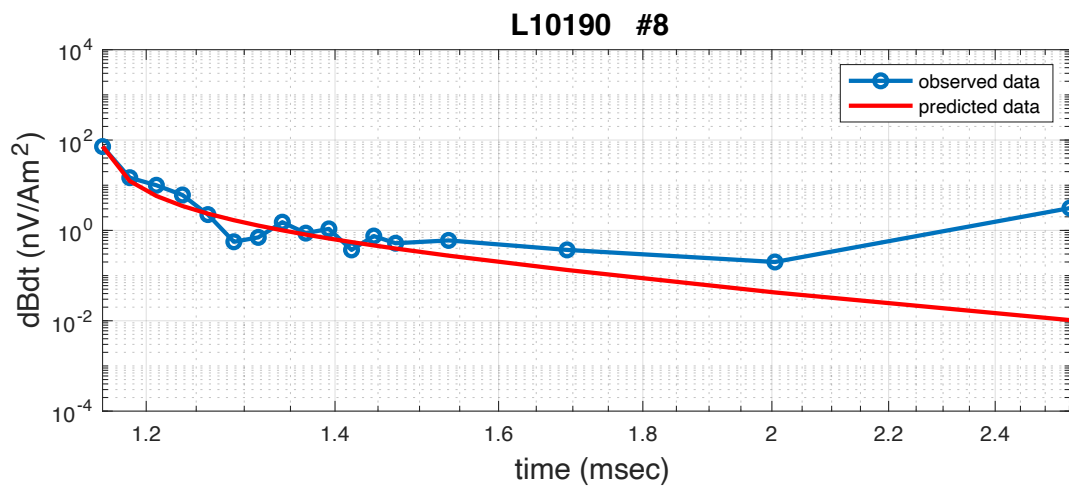
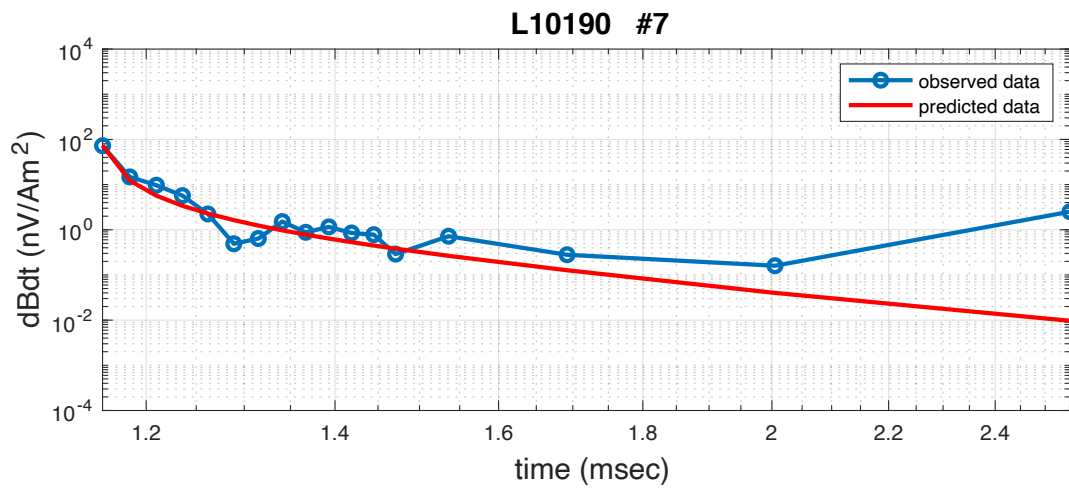
L10190

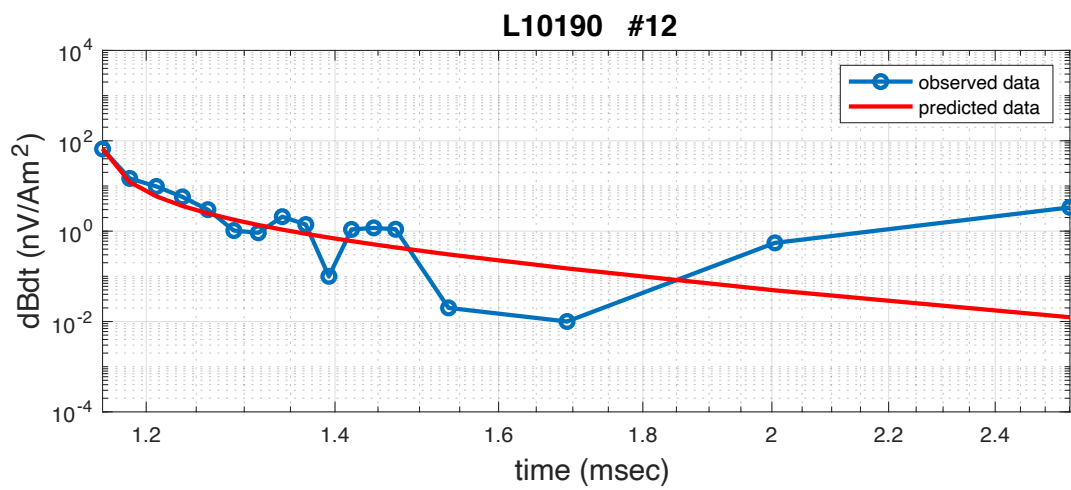
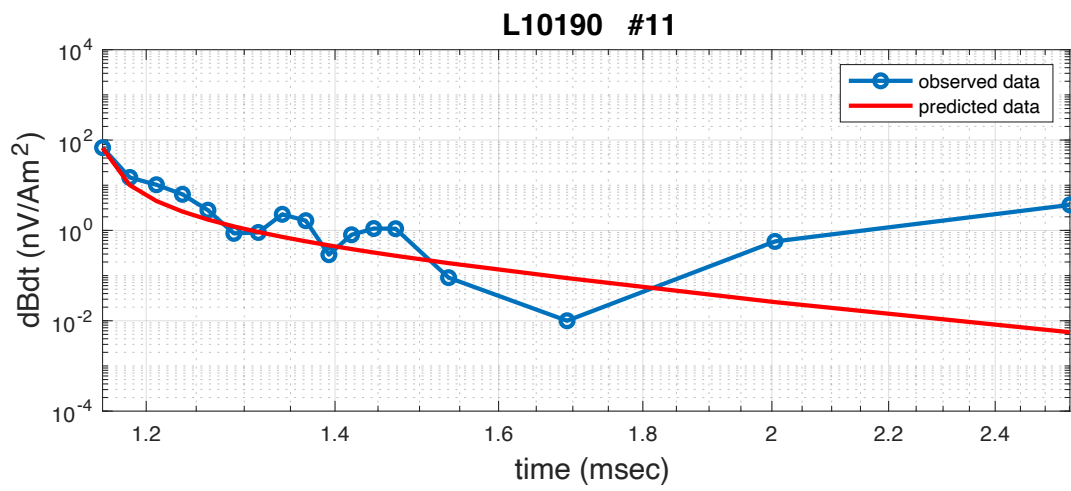
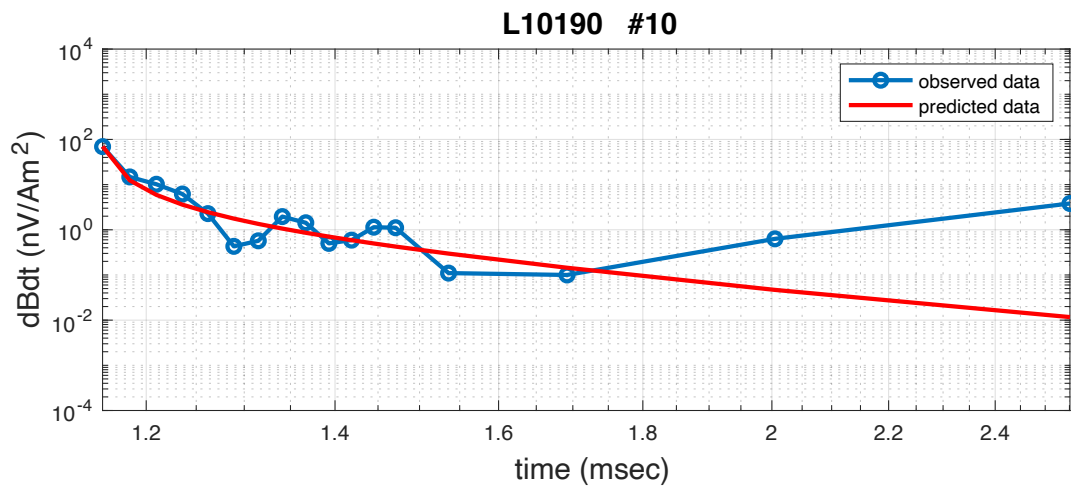


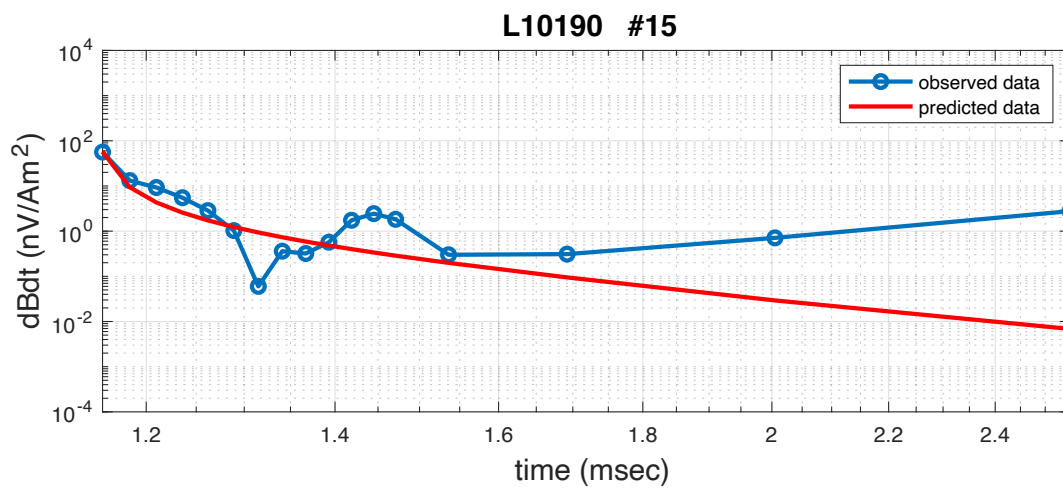
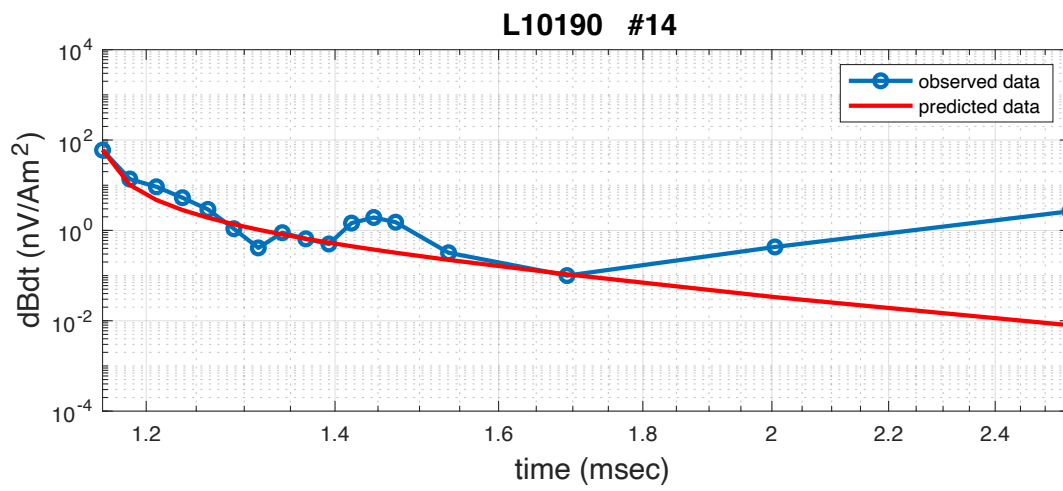
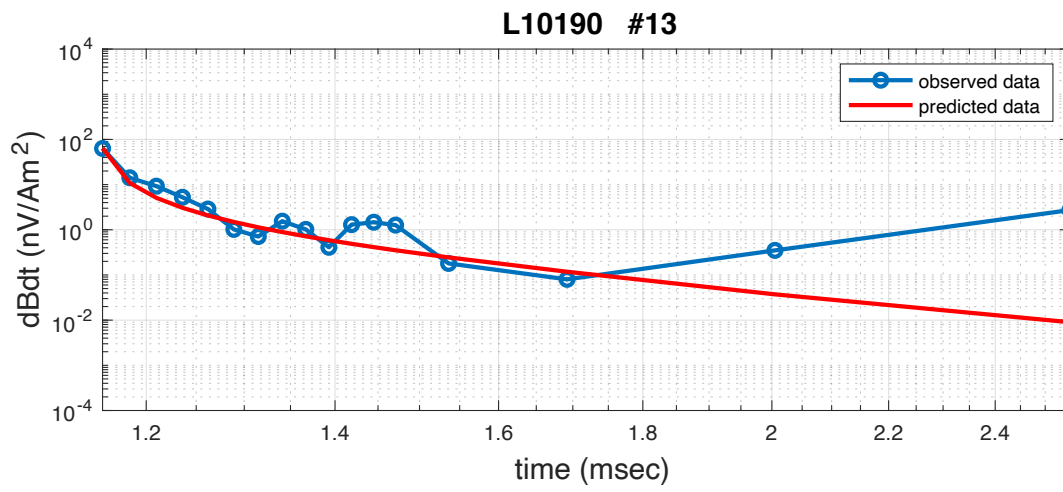
The observation points on L10190

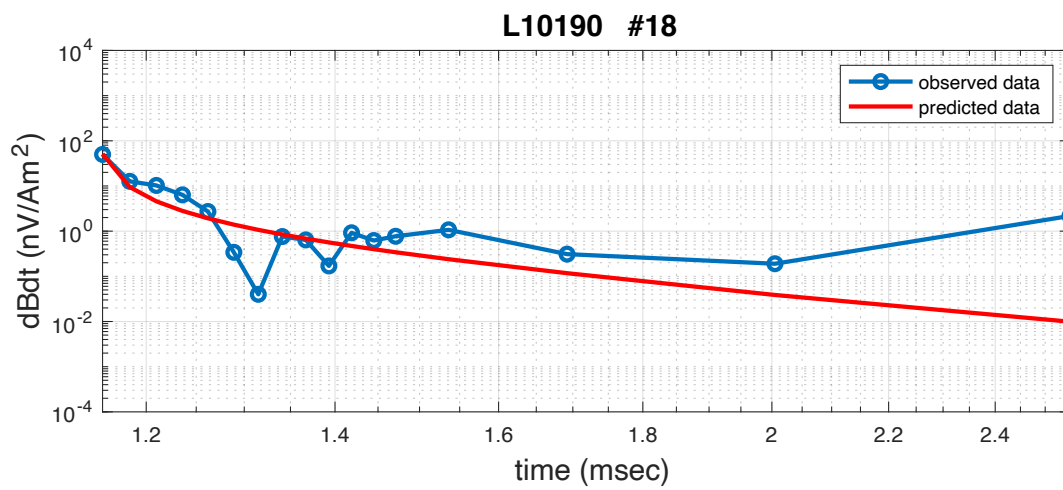
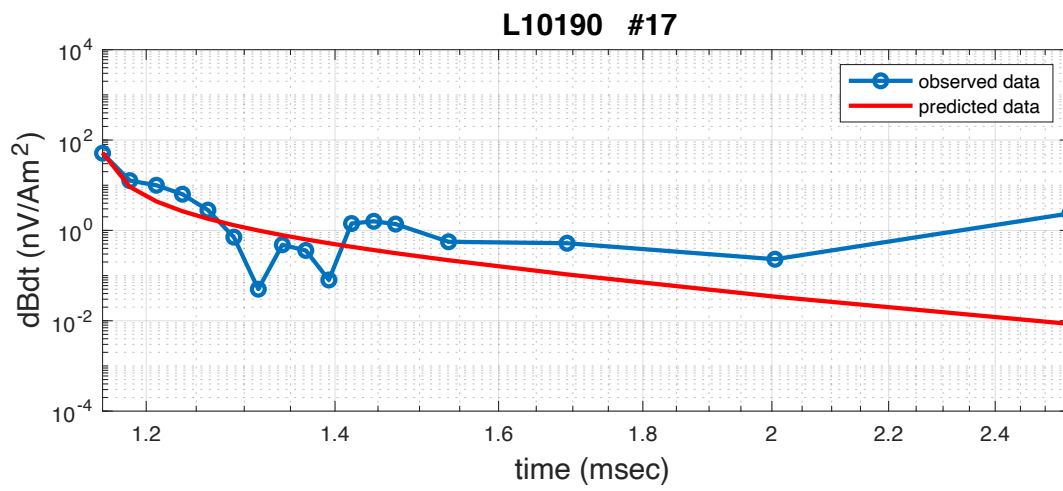
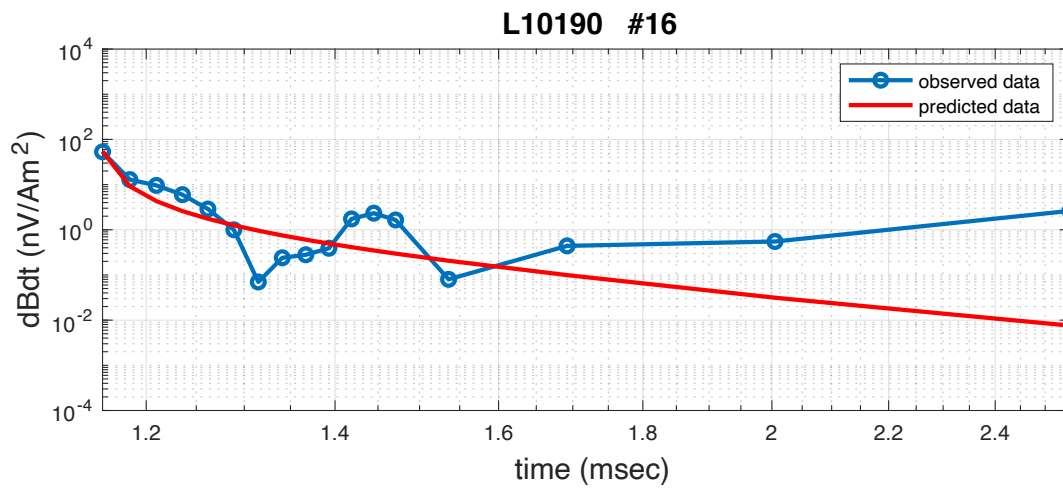


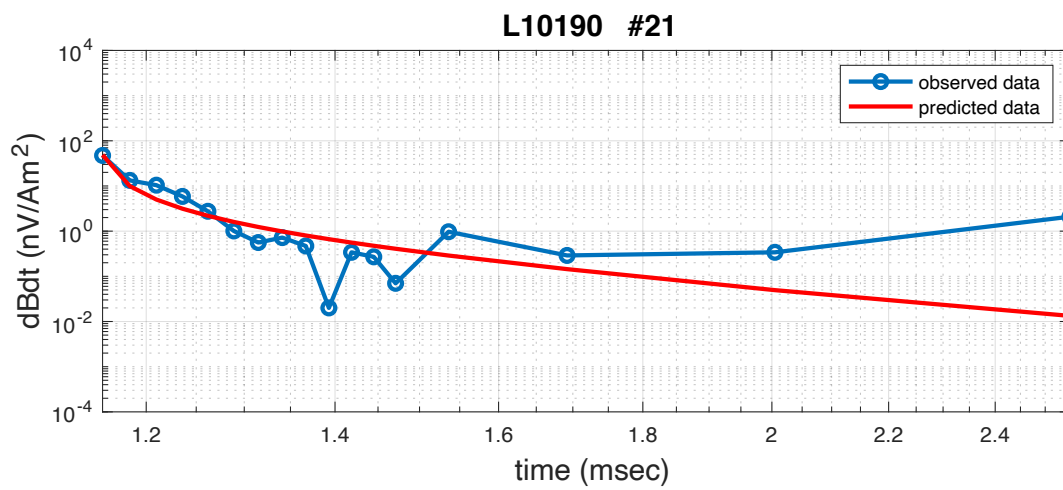
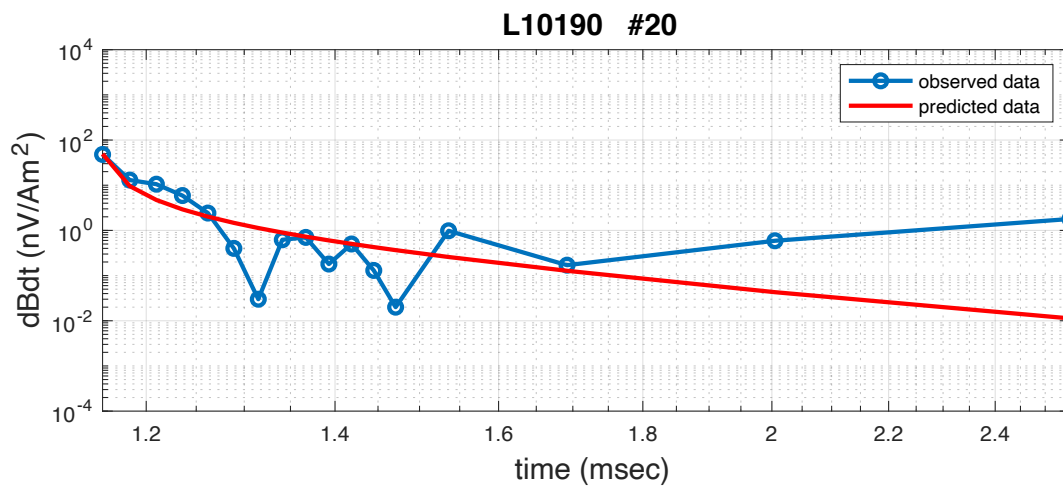
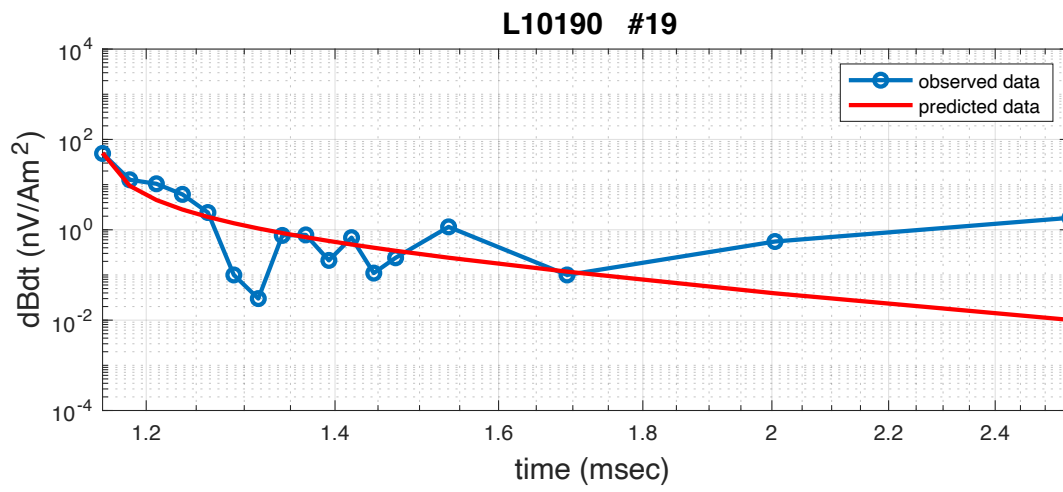


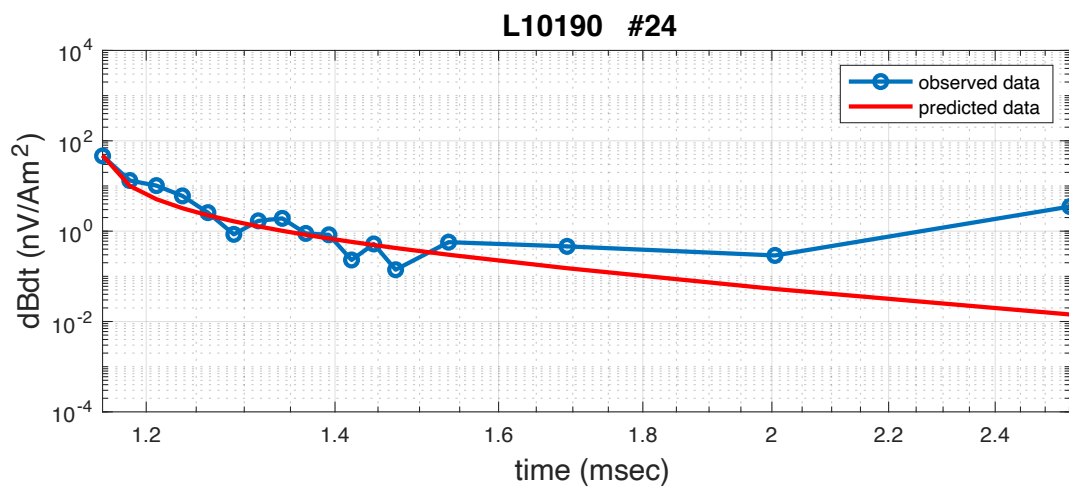
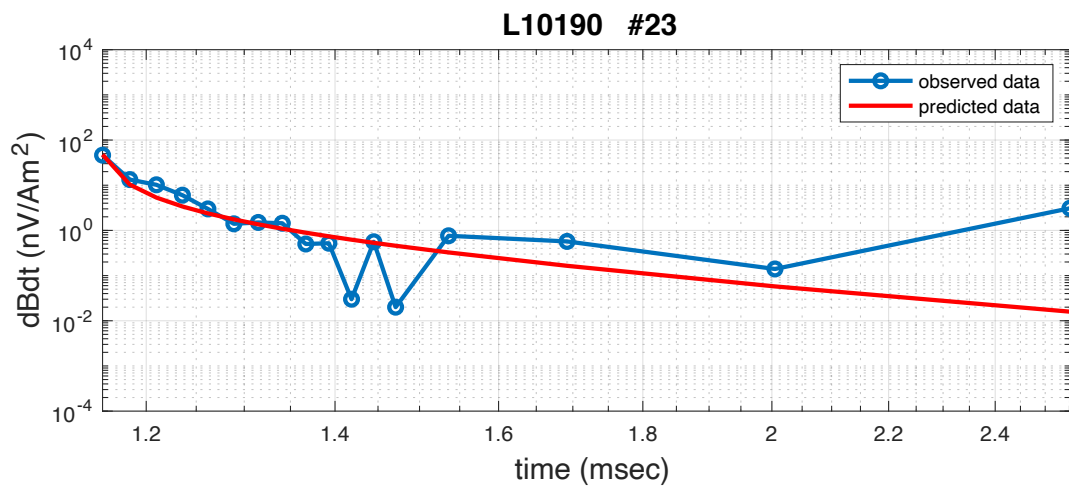
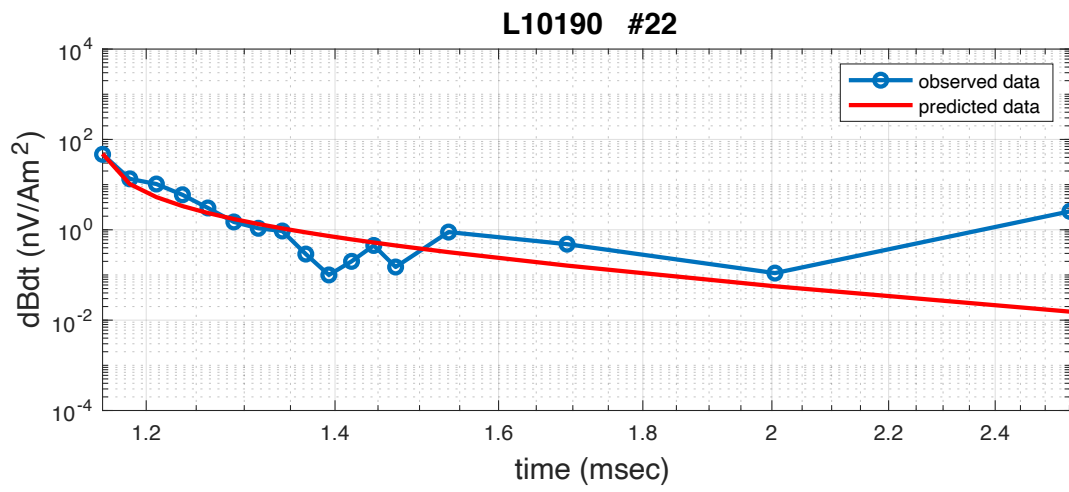


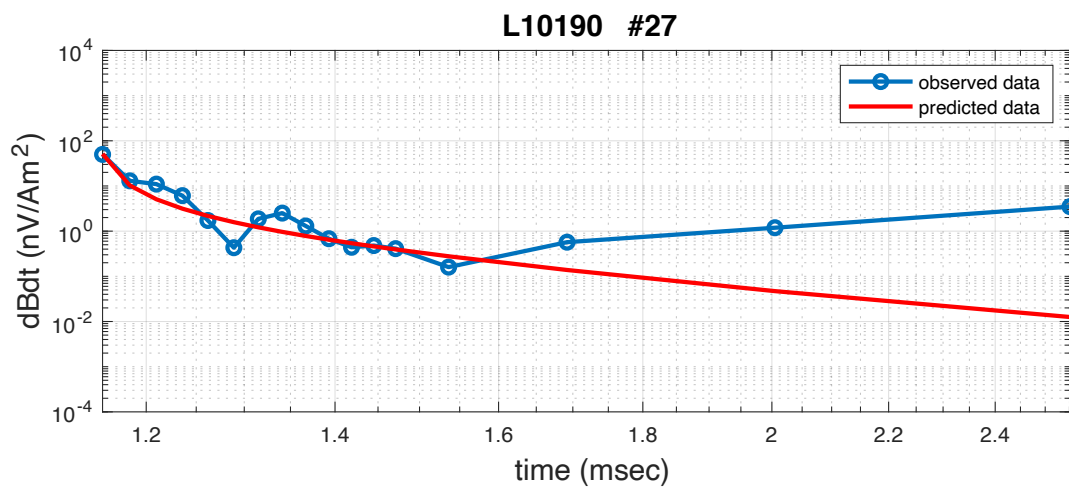
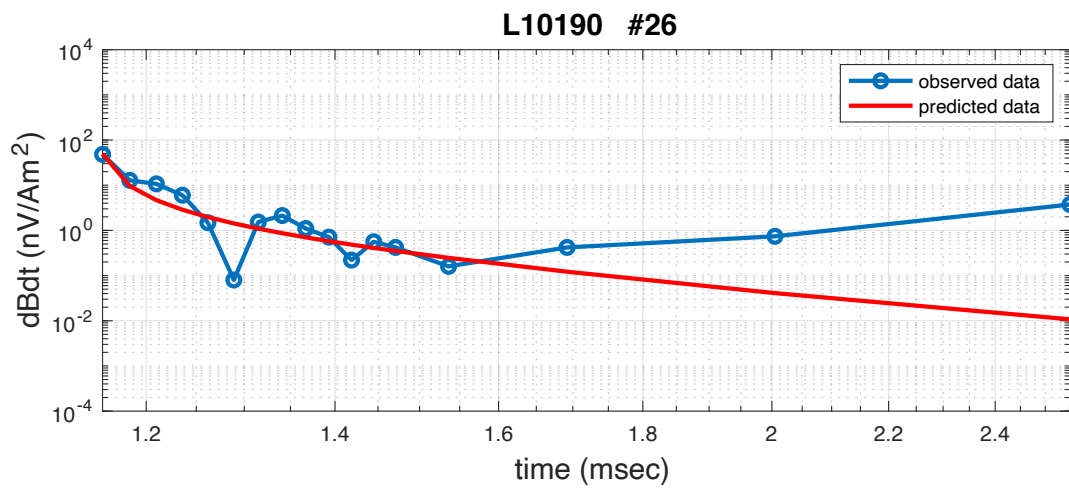
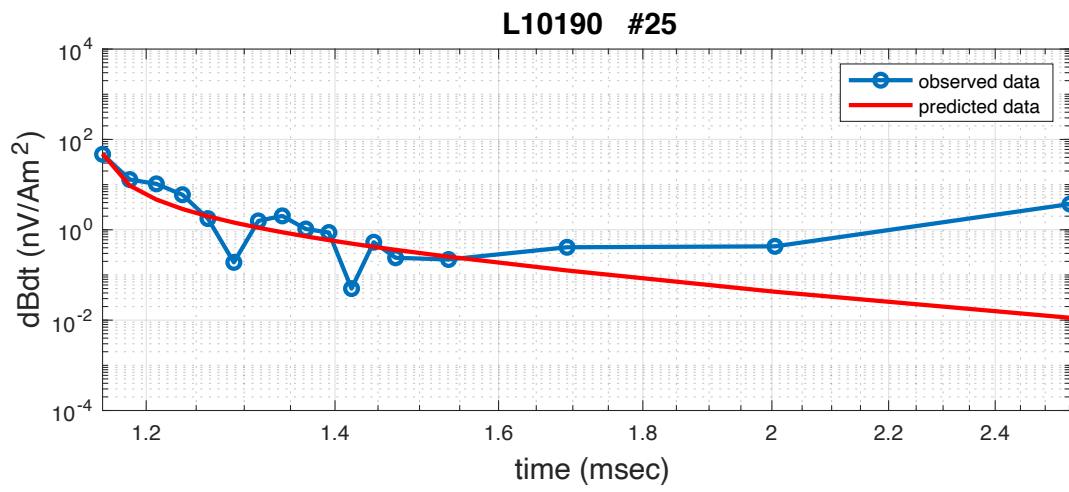


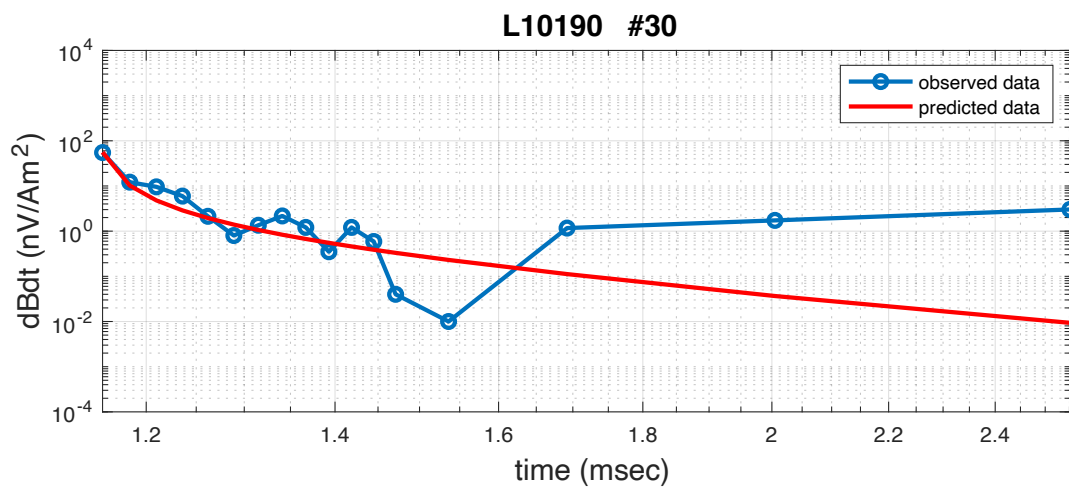
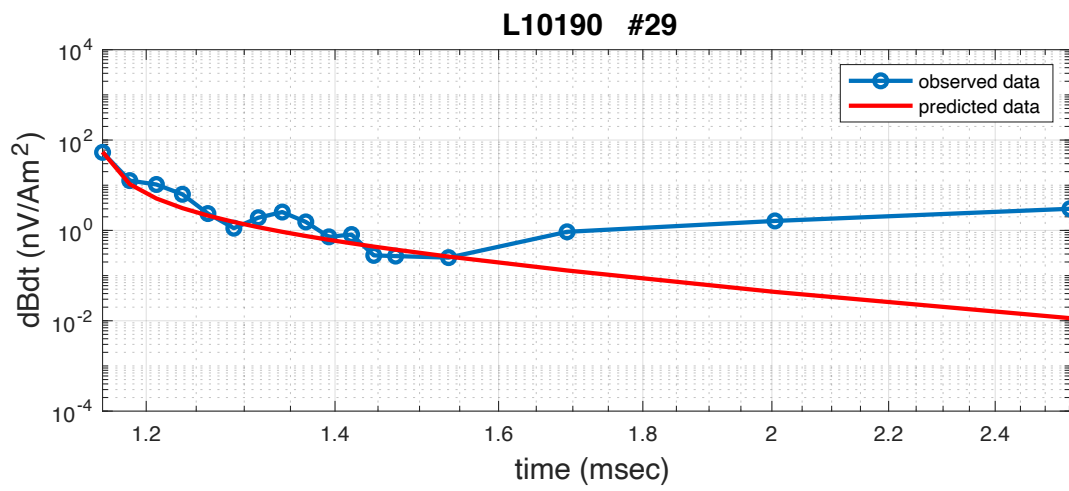
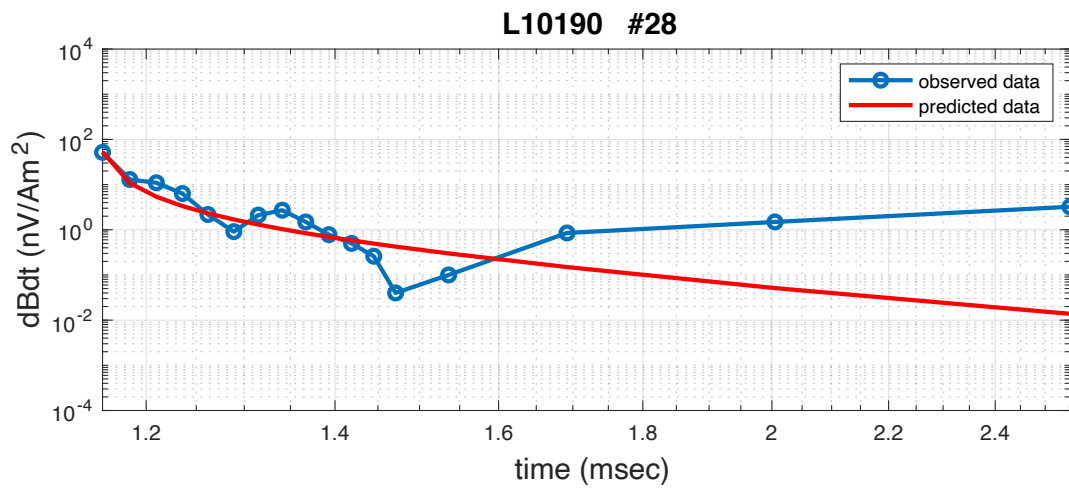


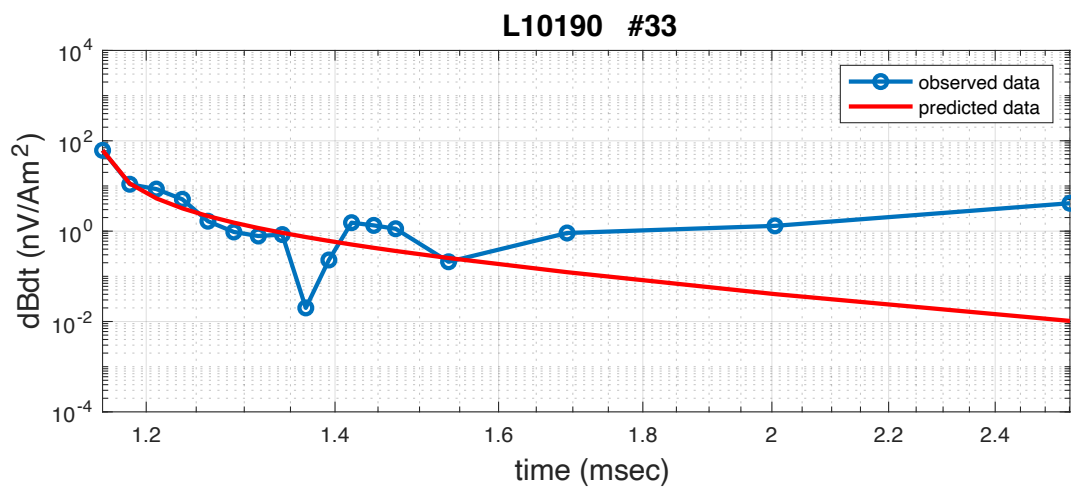
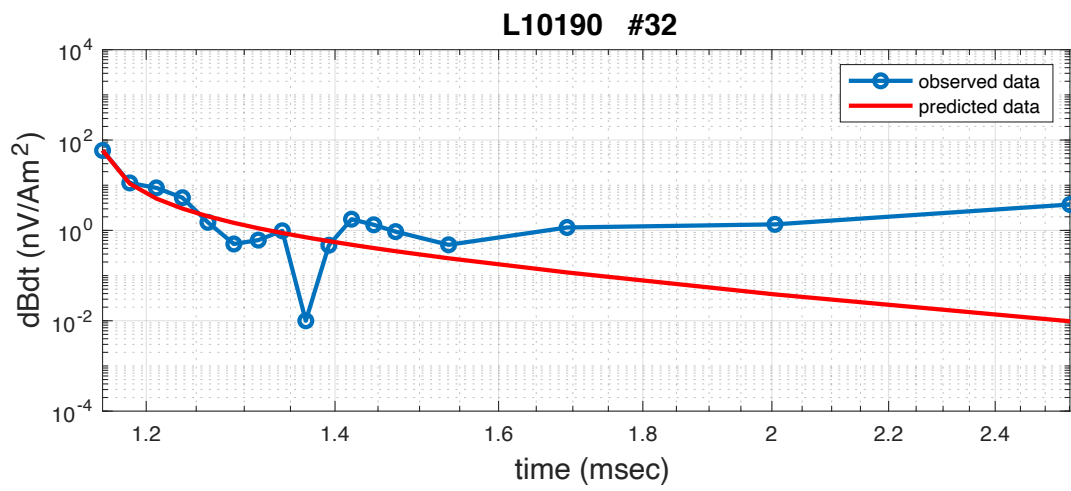
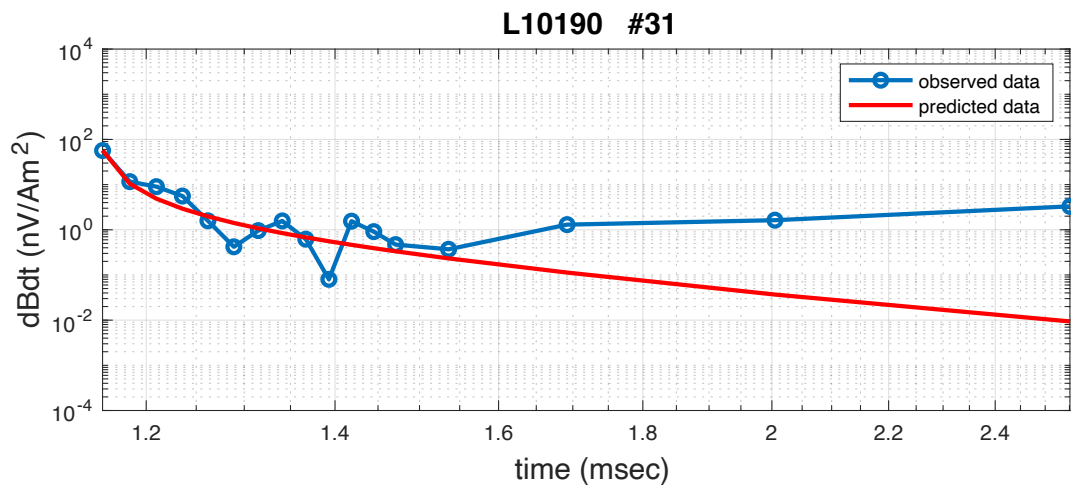


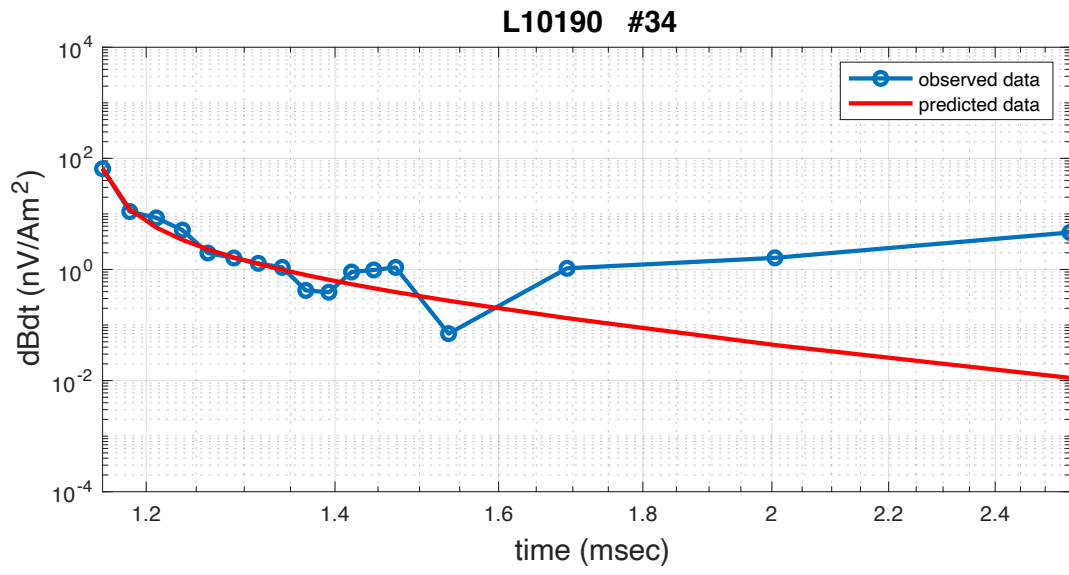




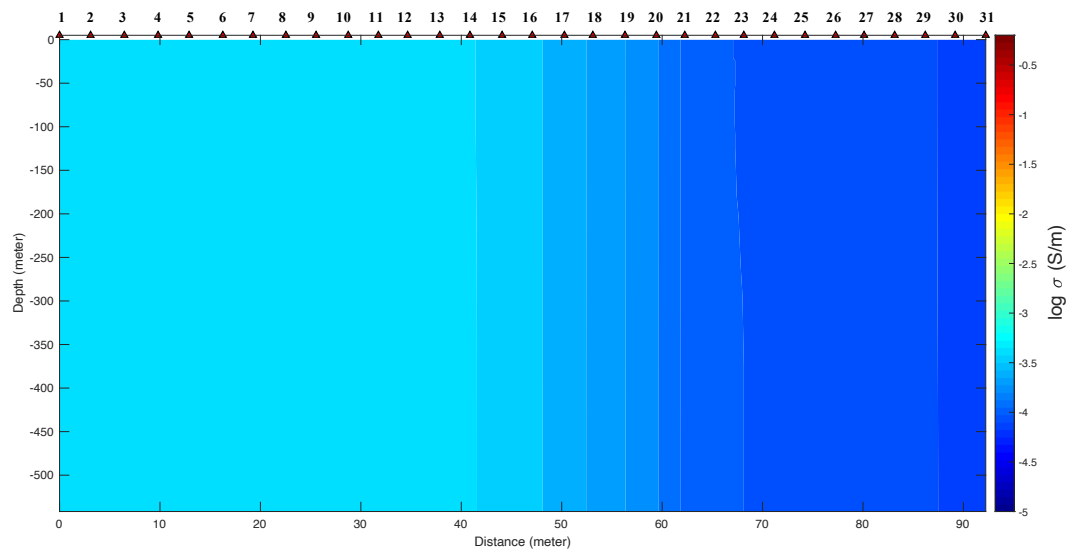




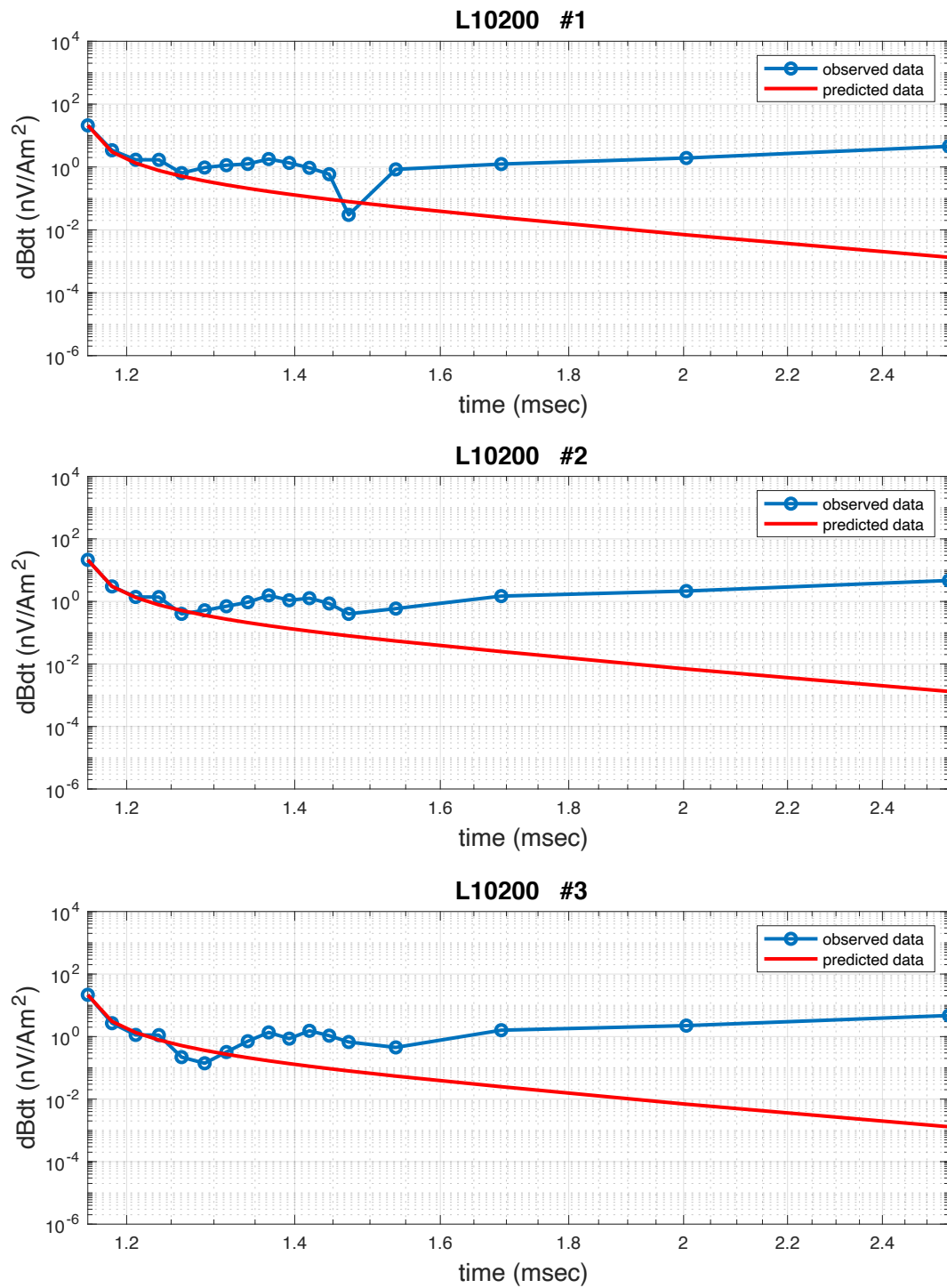


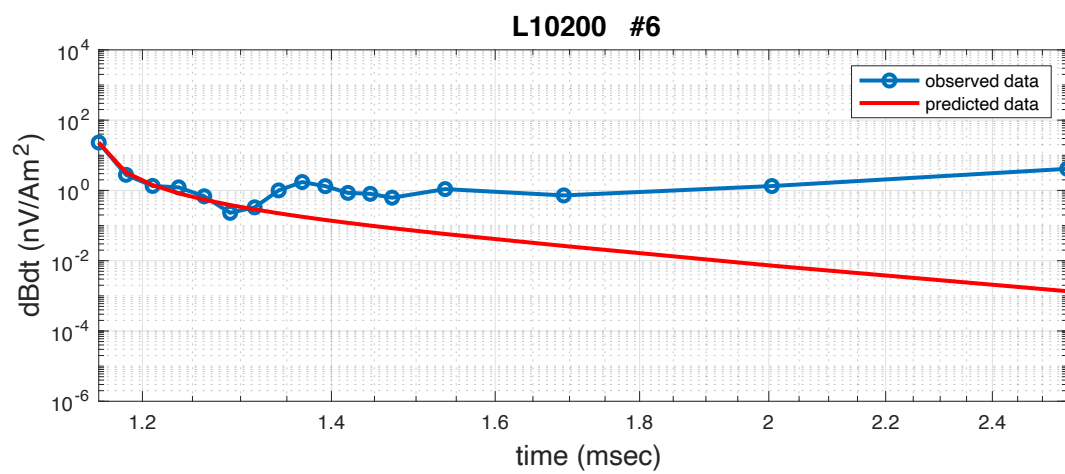
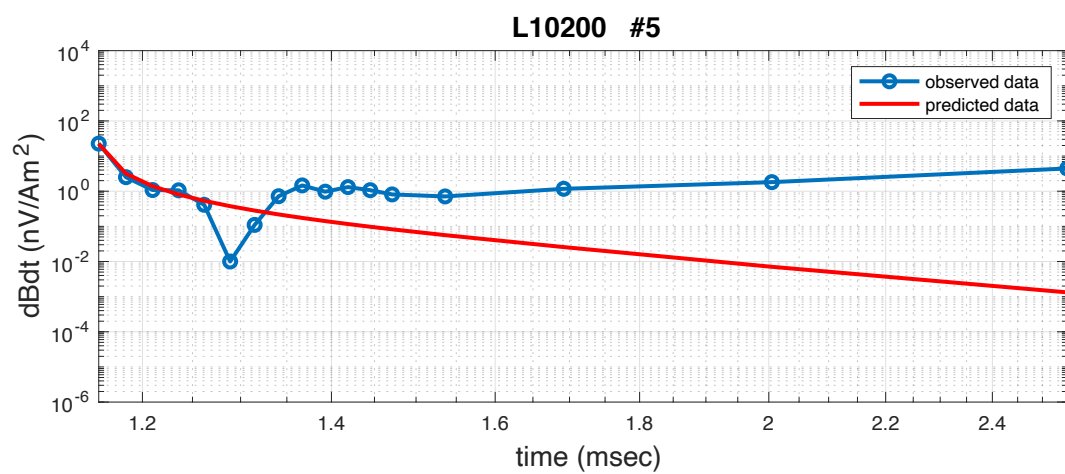
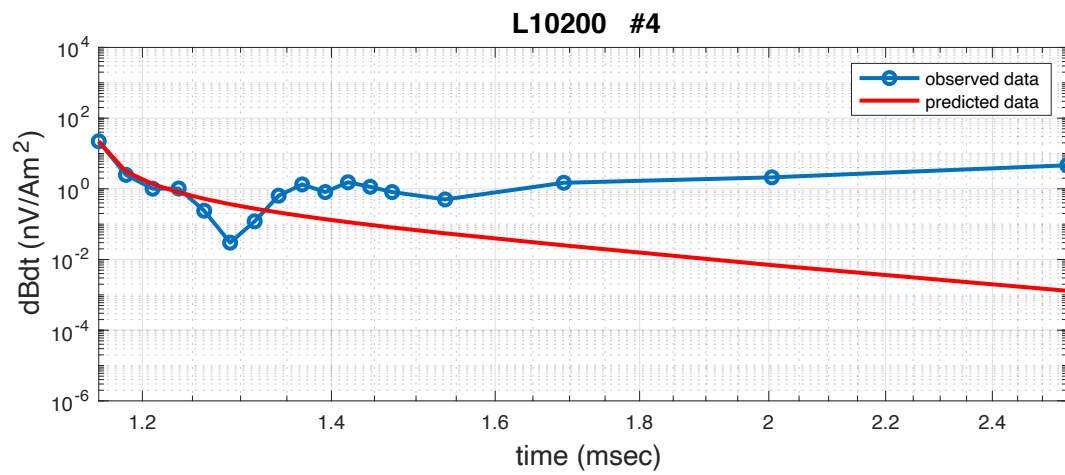


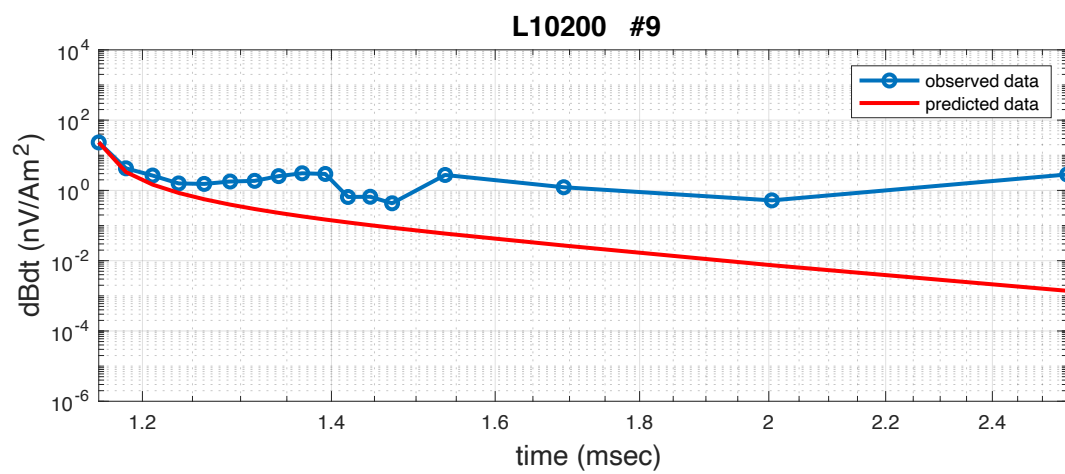
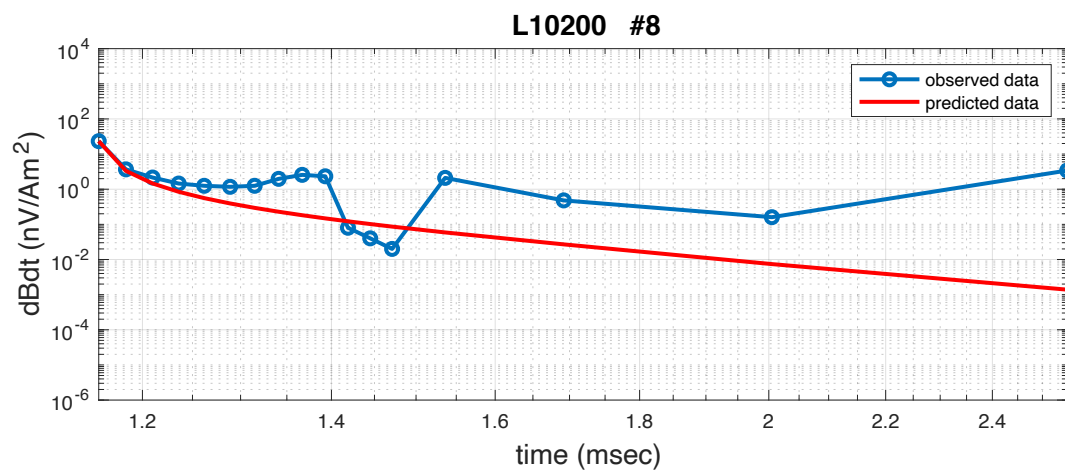
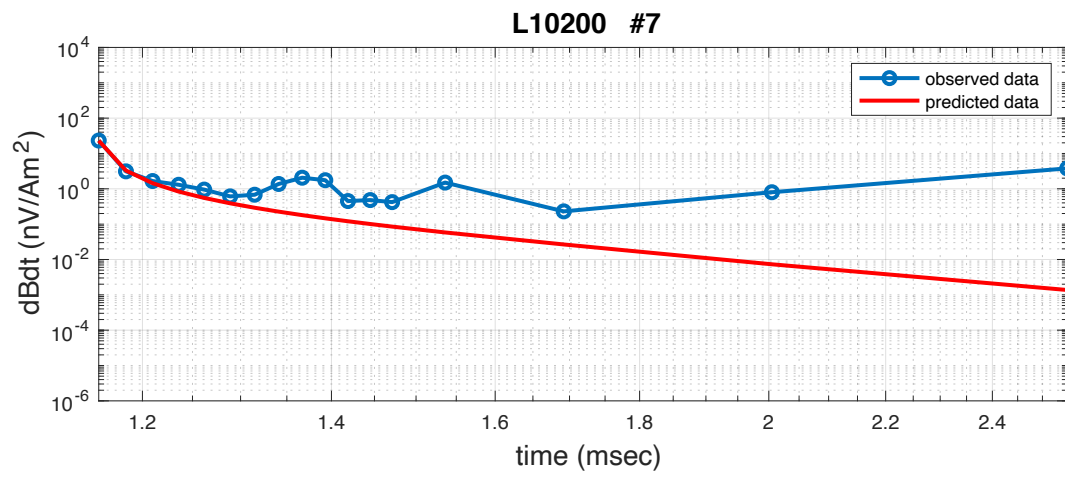
L10200

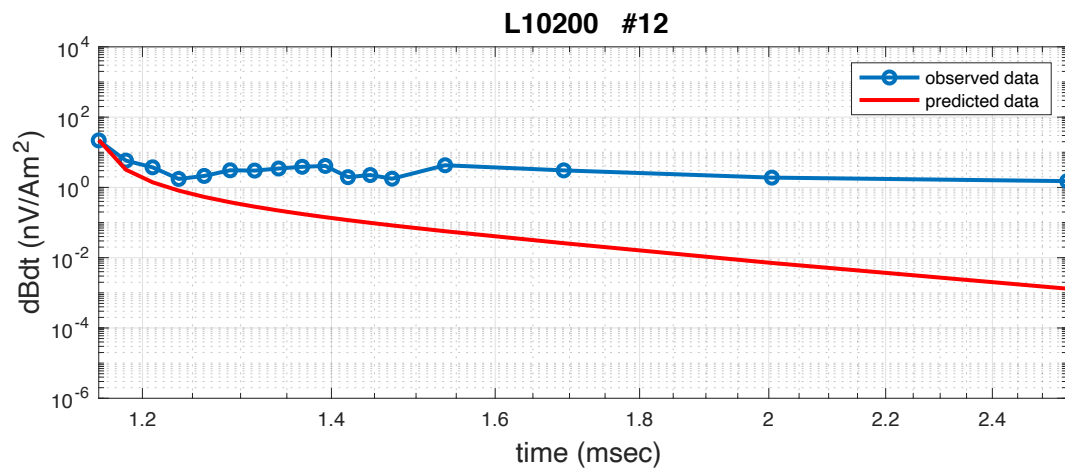
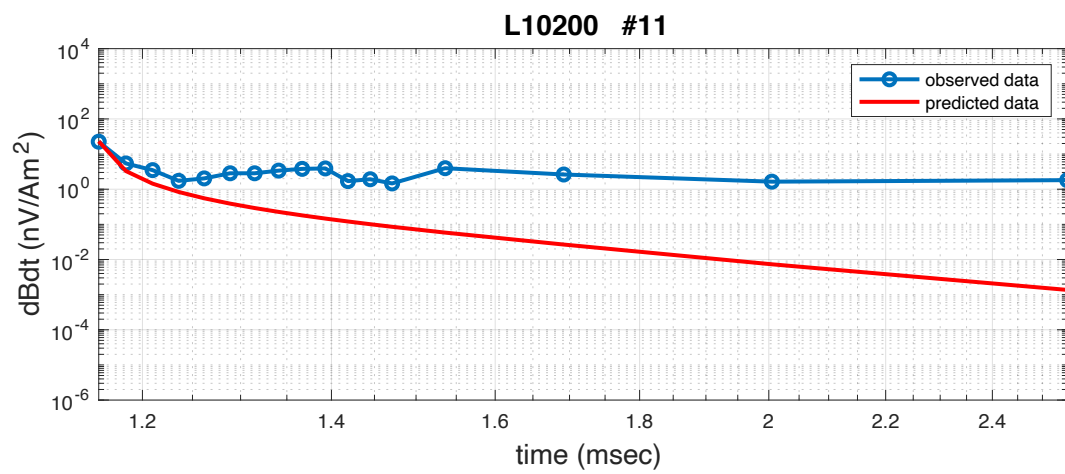
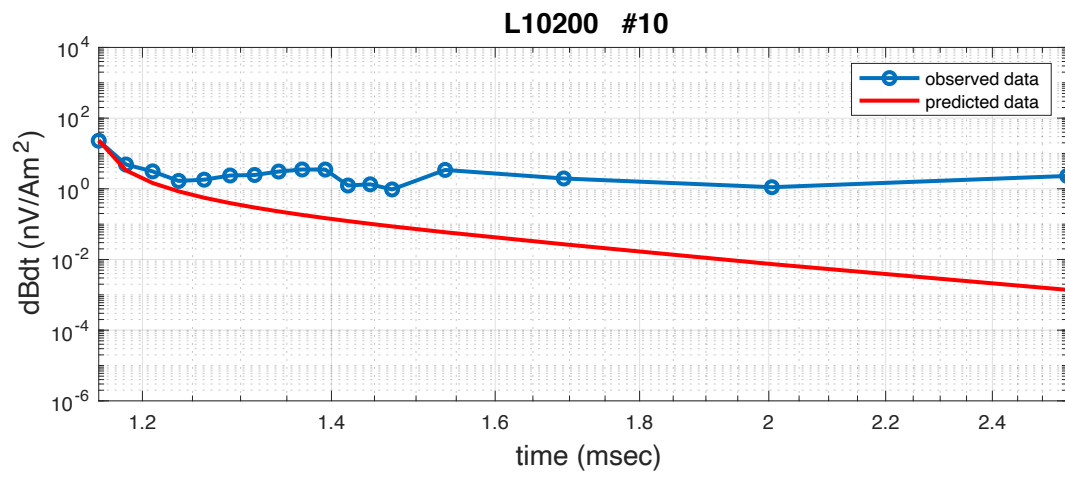


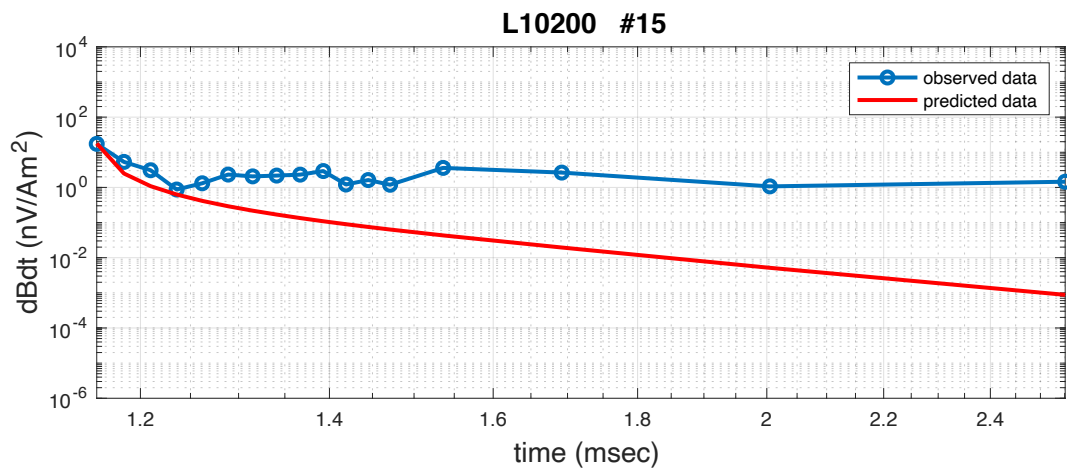
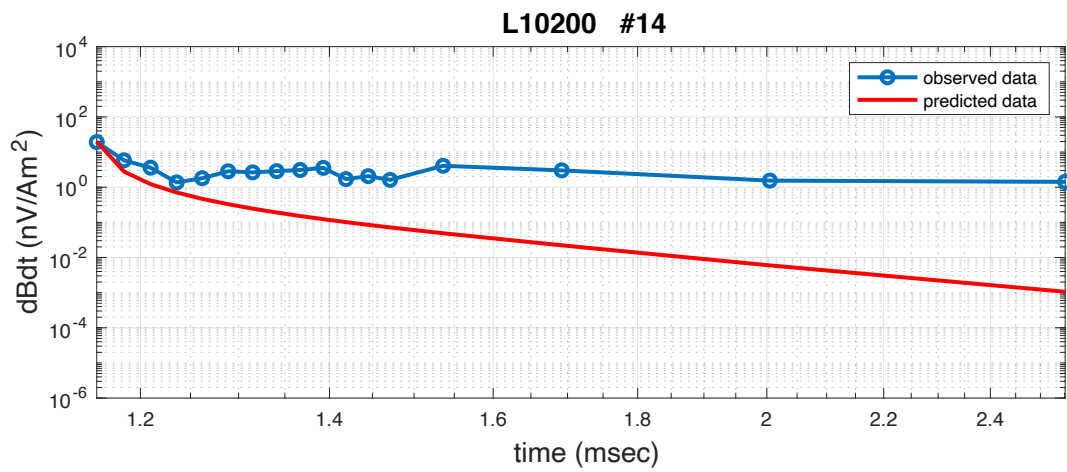
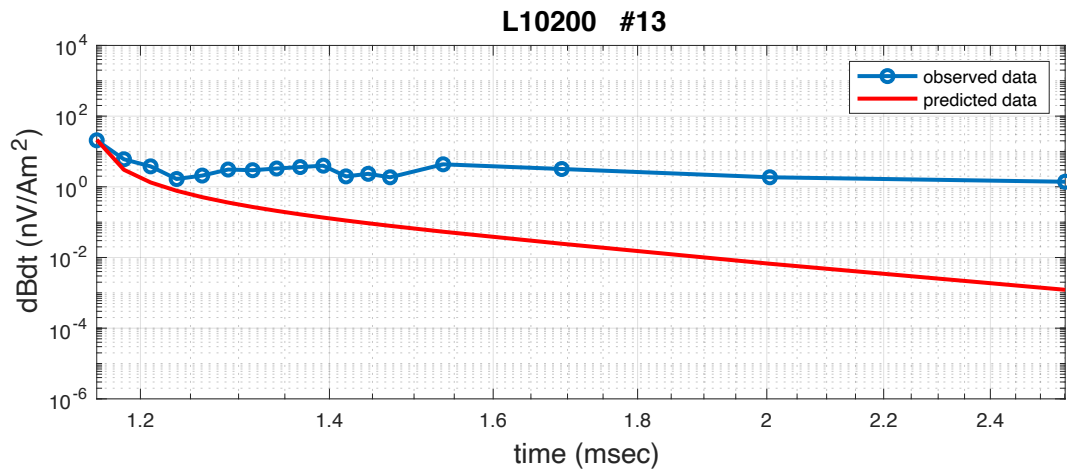
The observation points on L10200

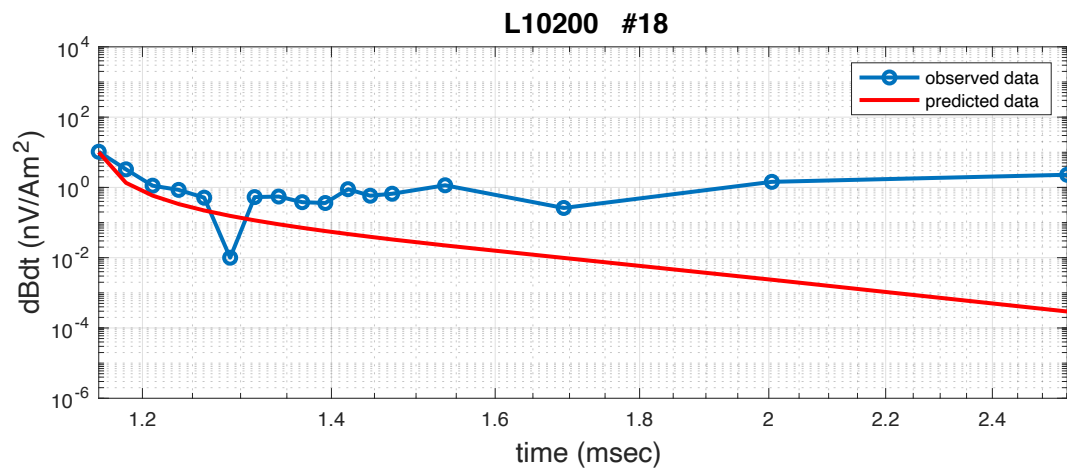
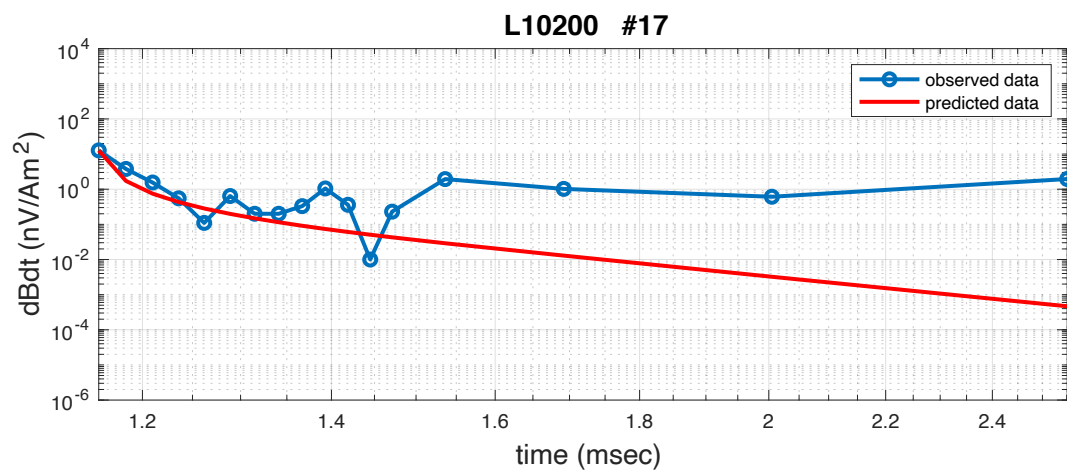
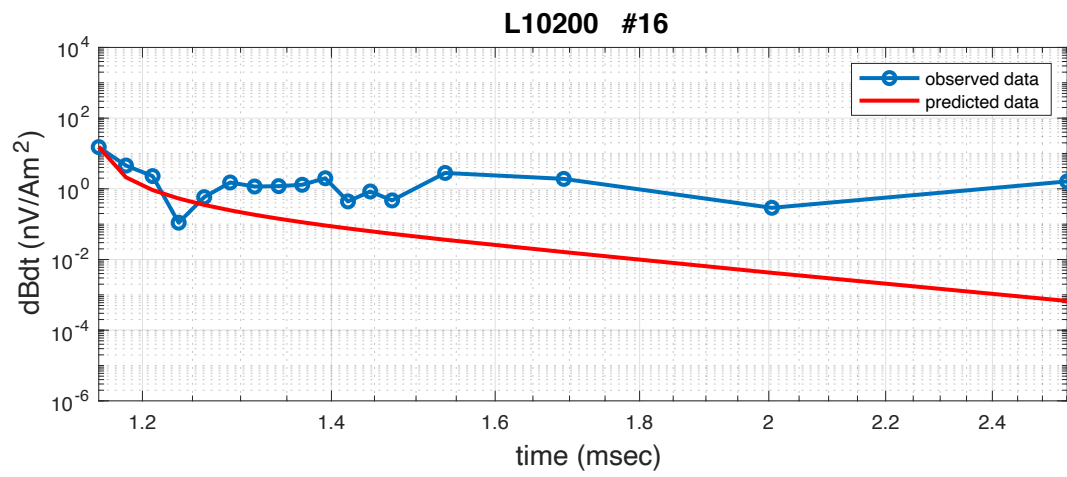


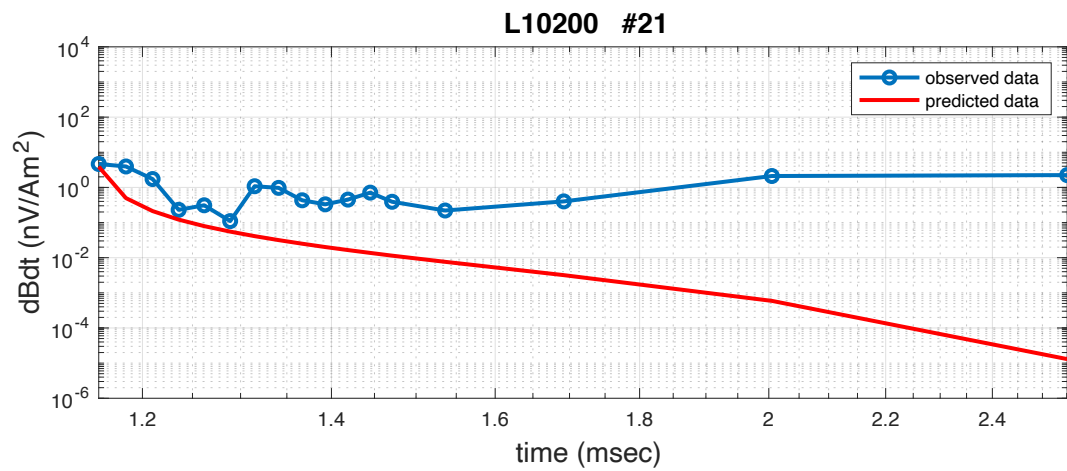
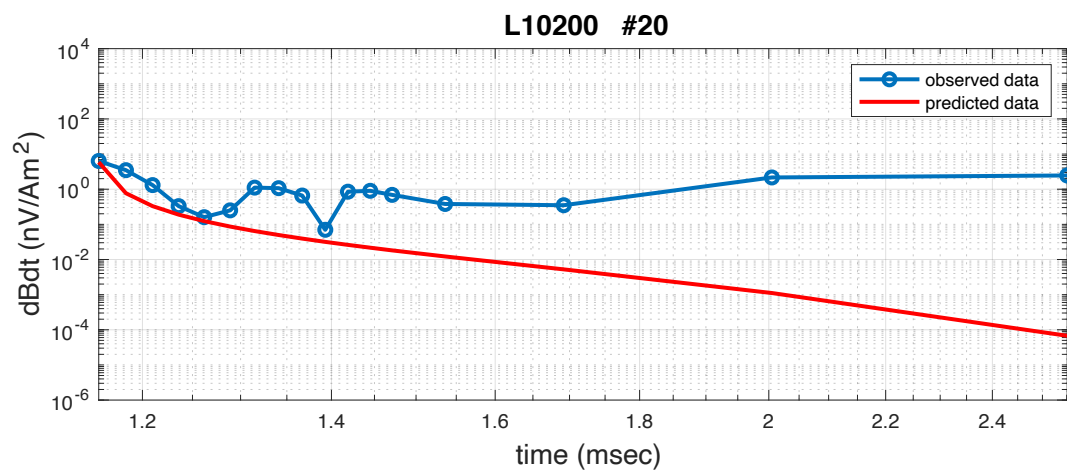
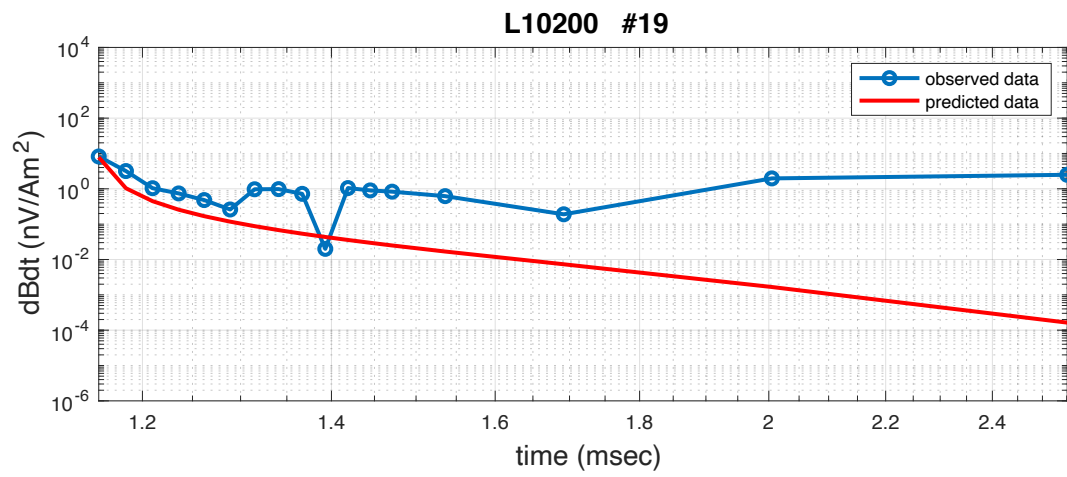


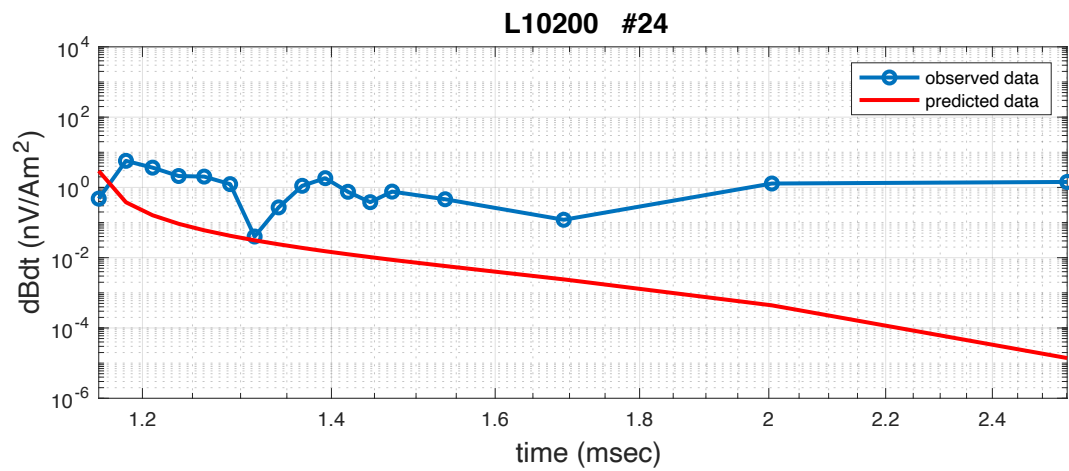
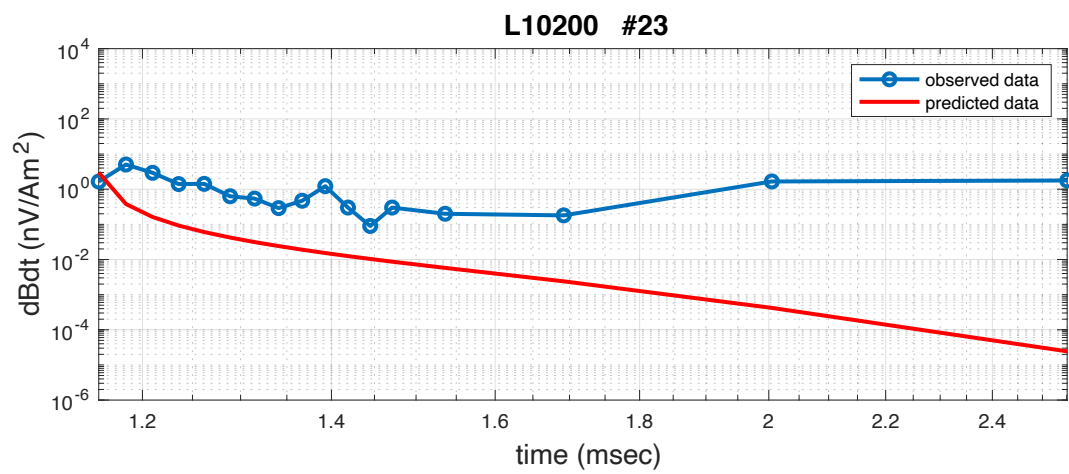
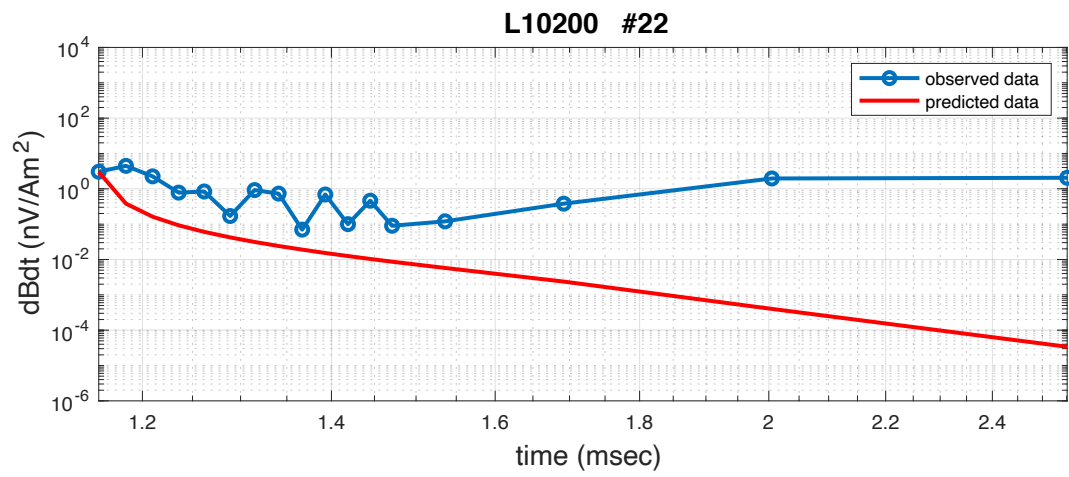


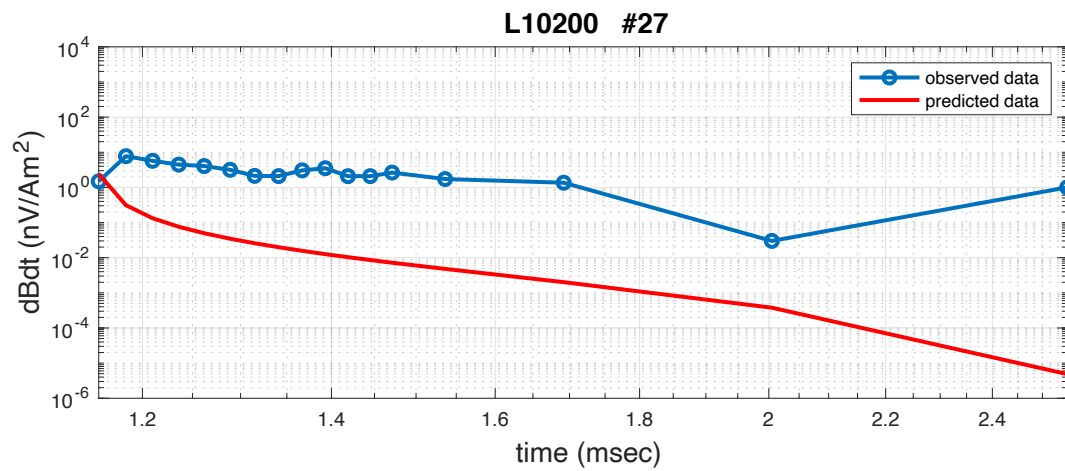
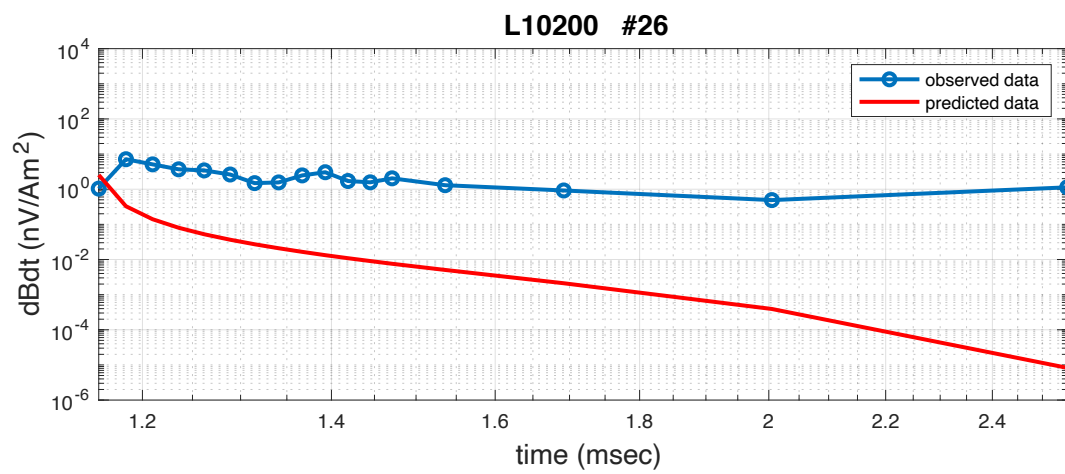
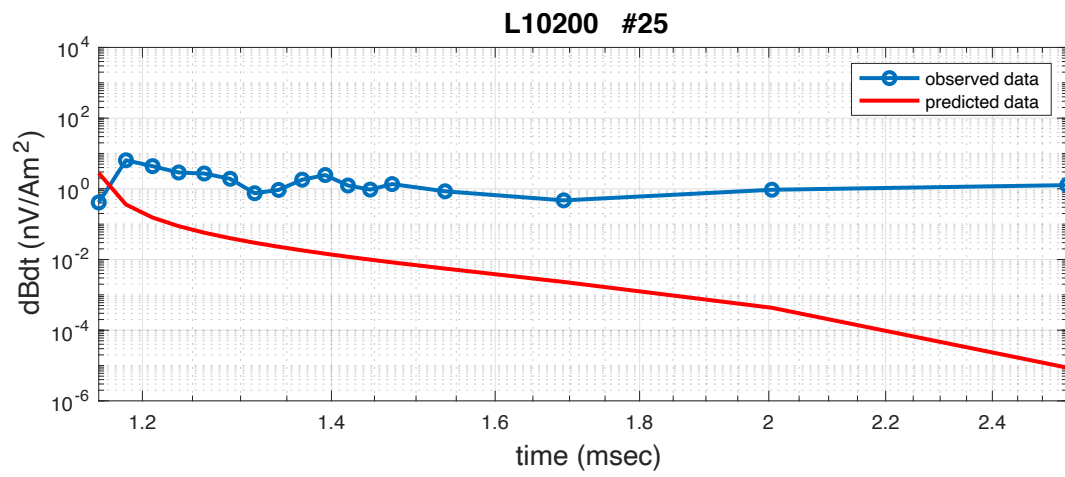


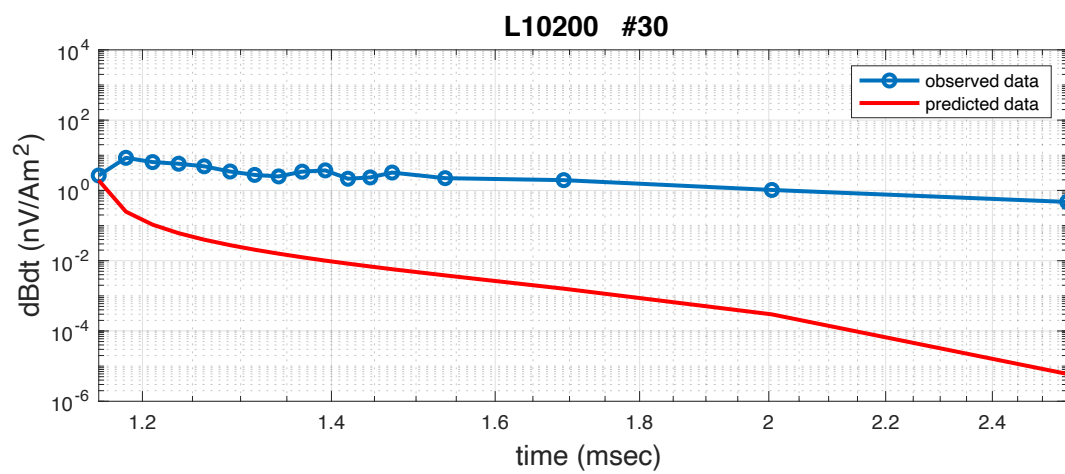
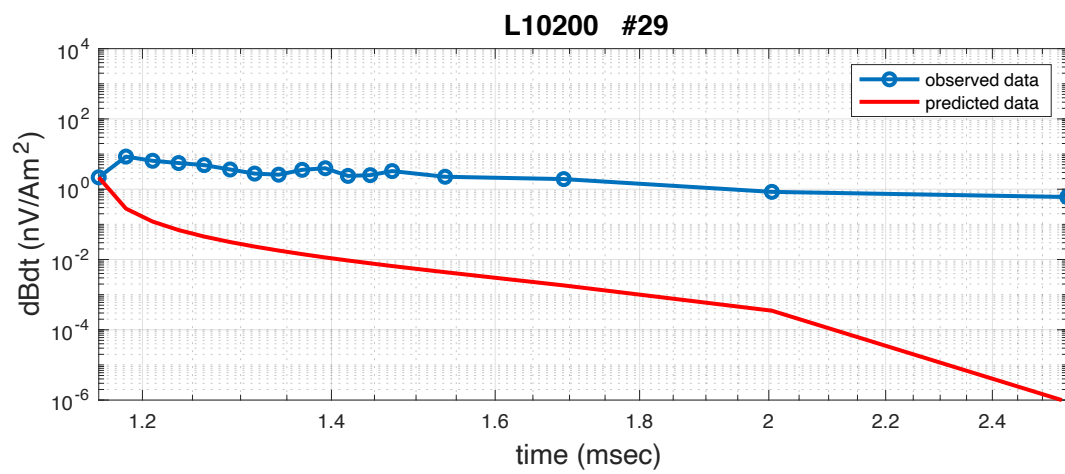
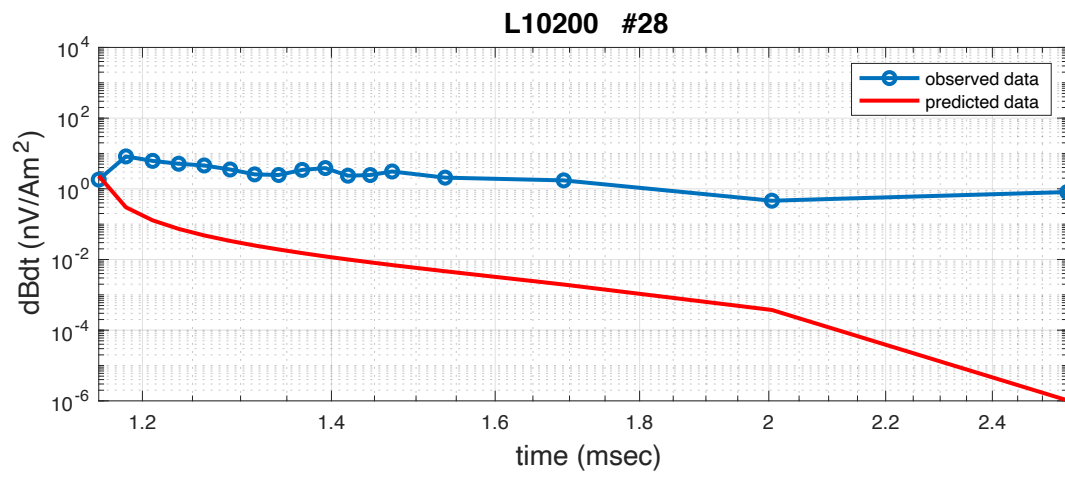


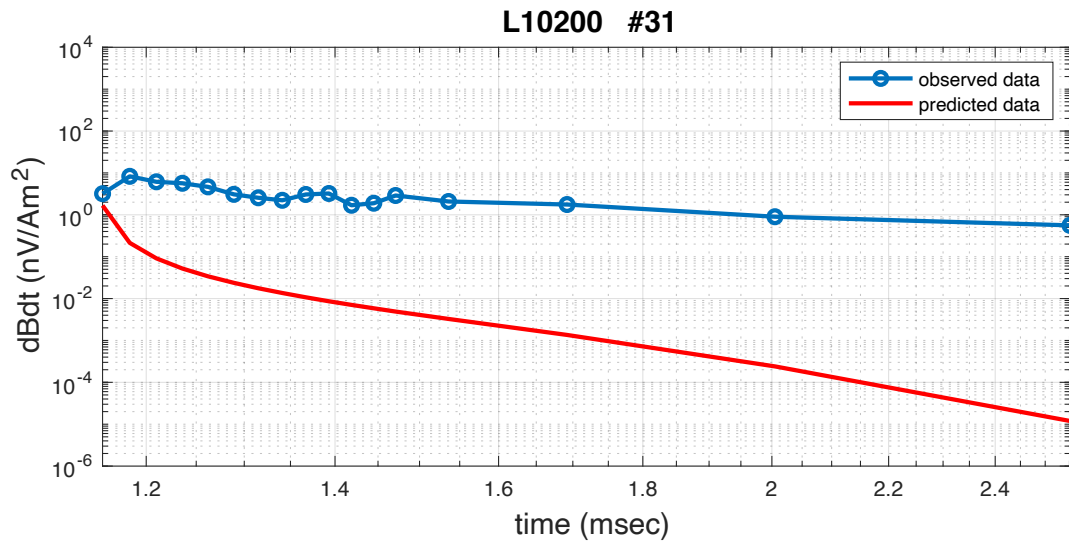




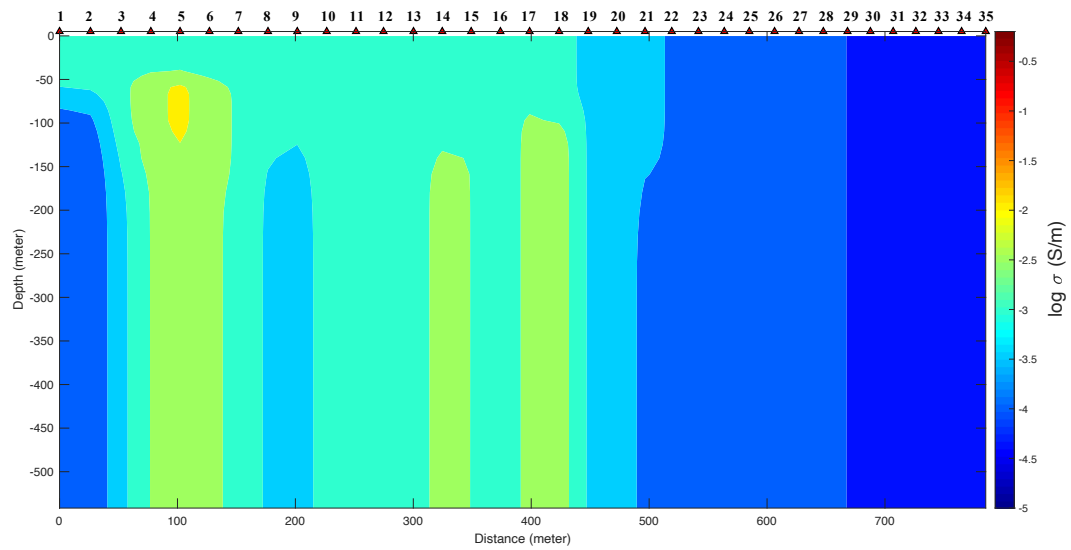




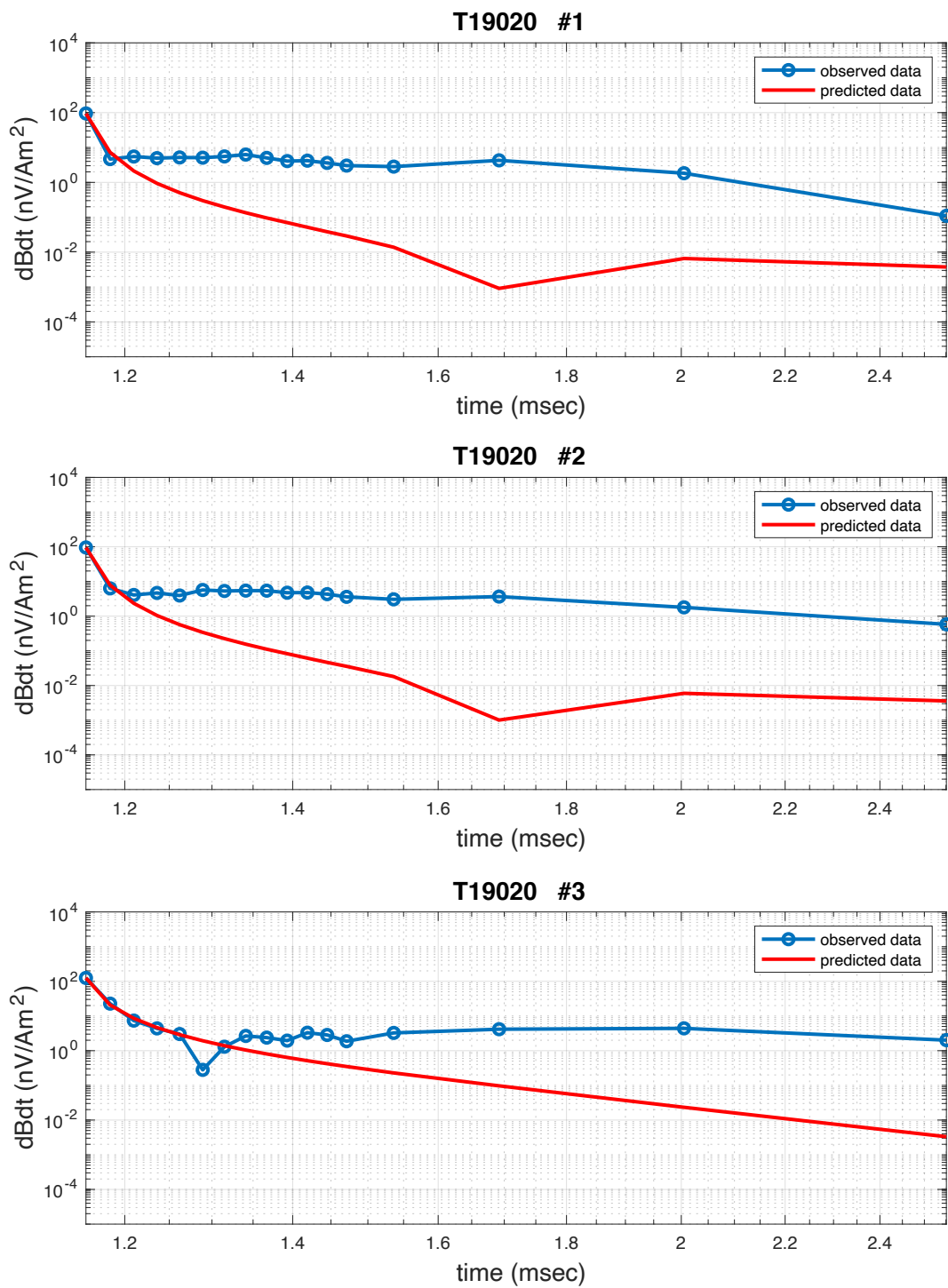


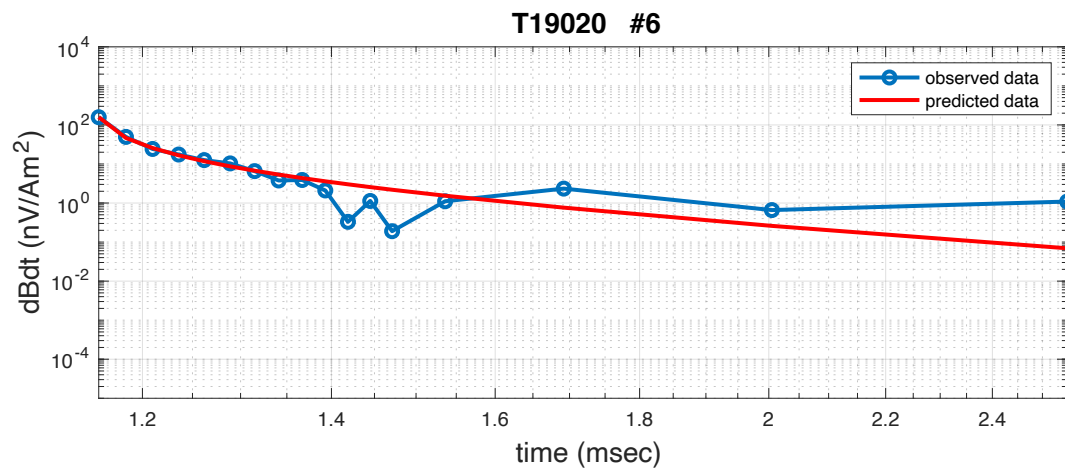
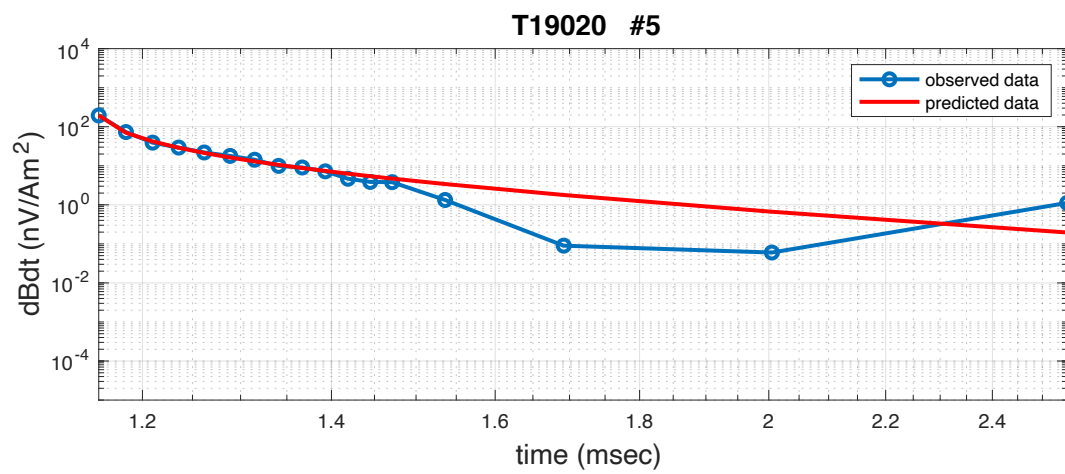
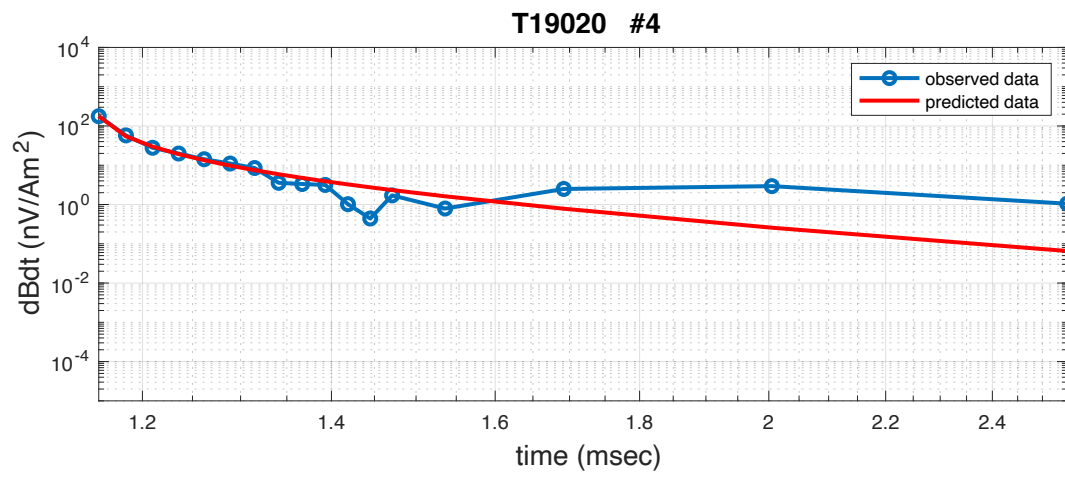


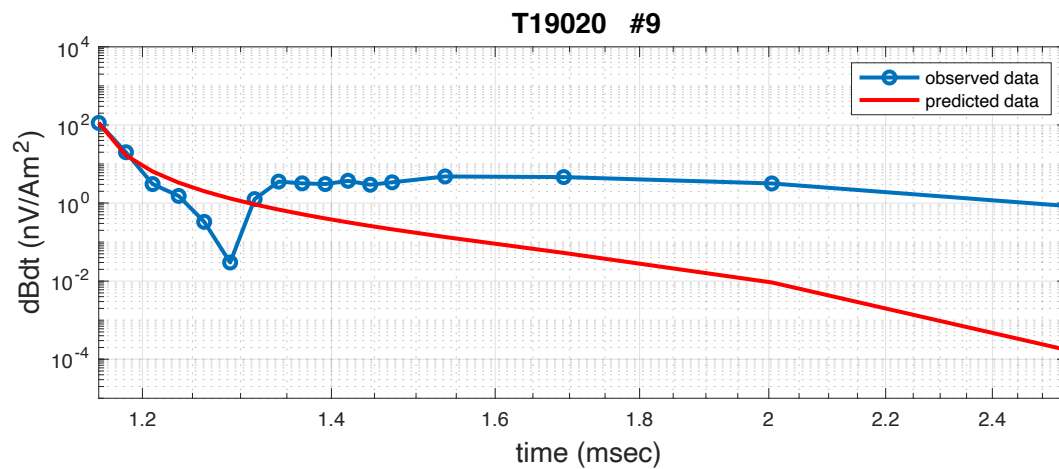
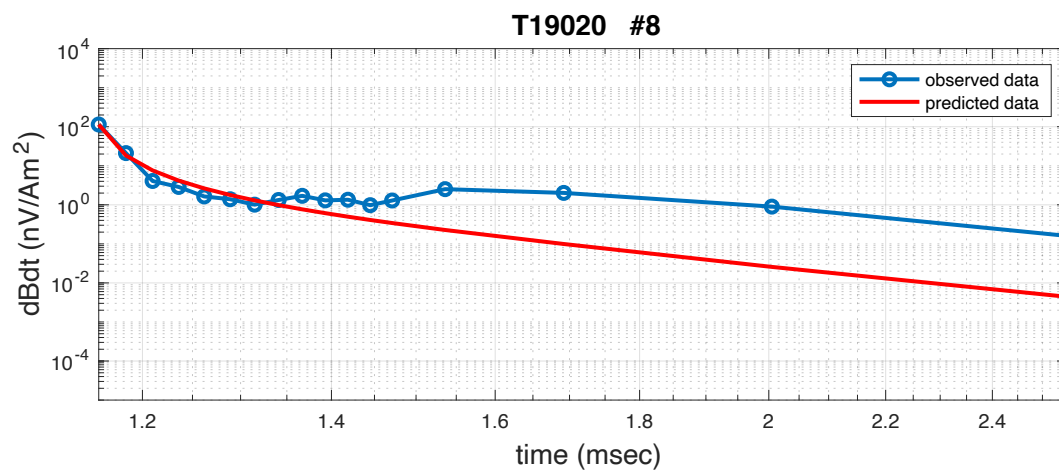
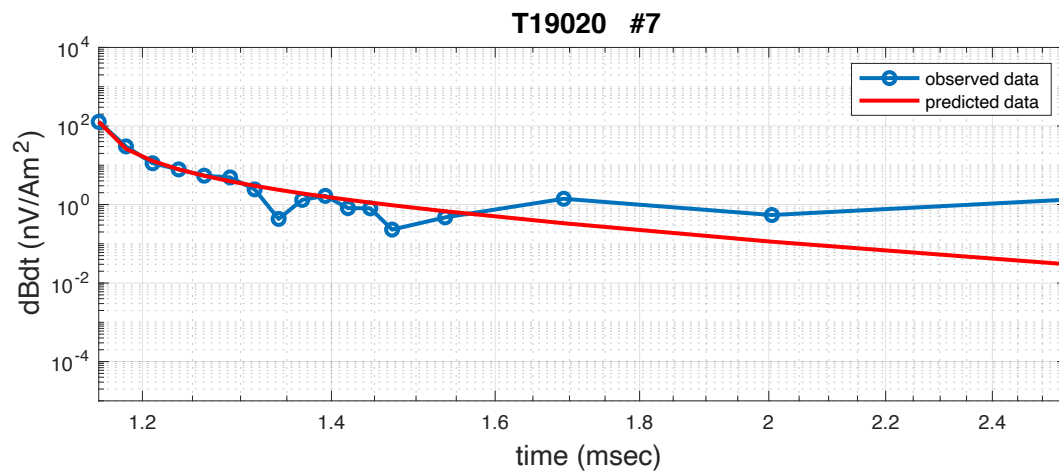
T19020

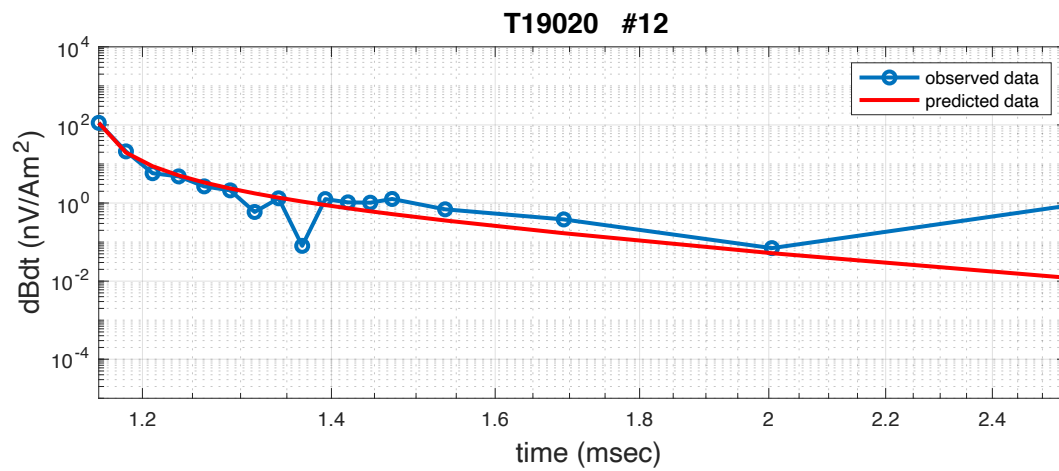
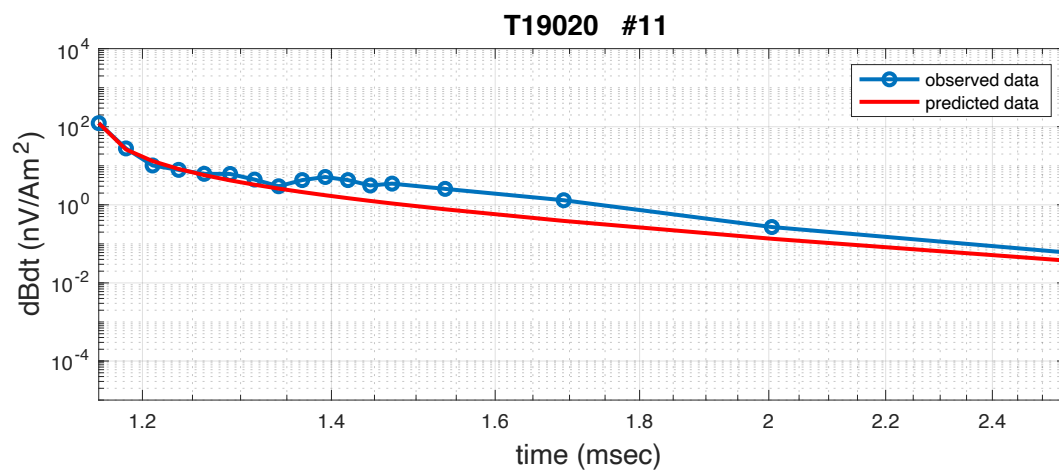
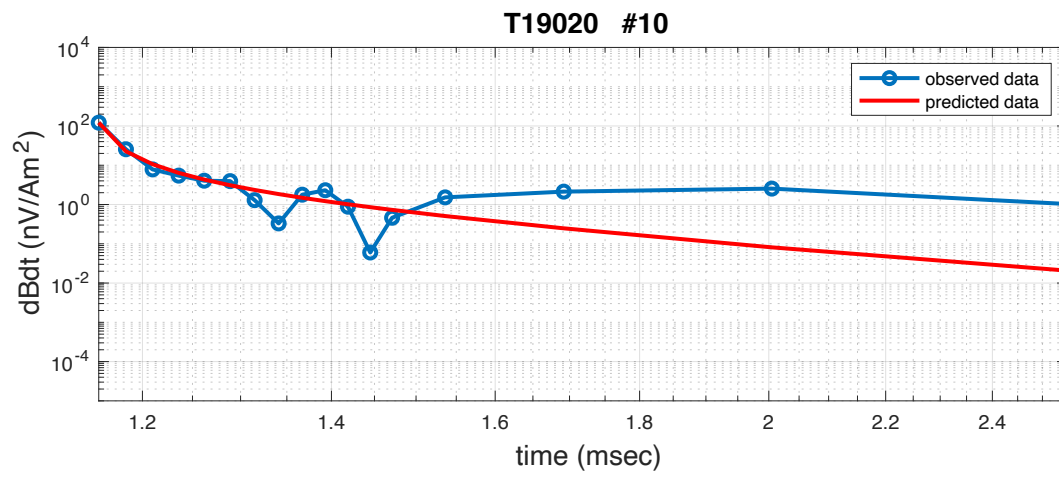


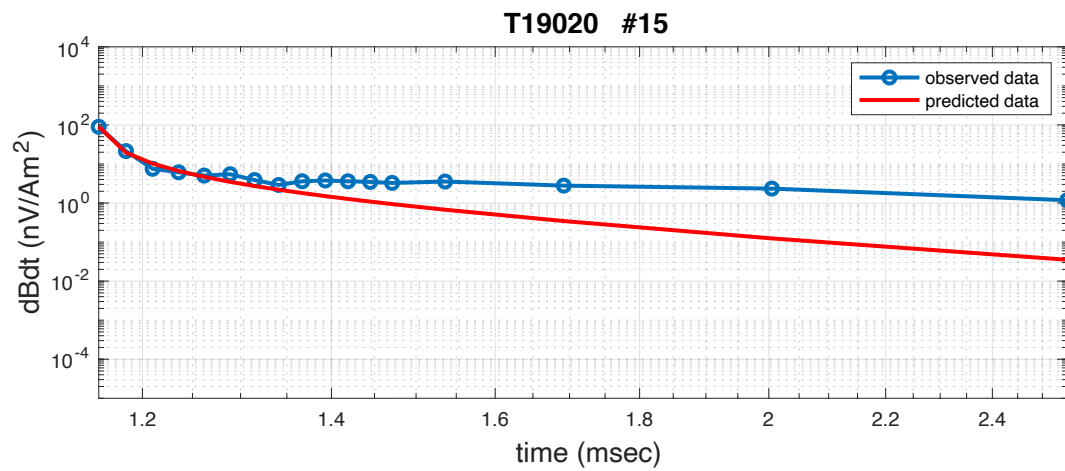
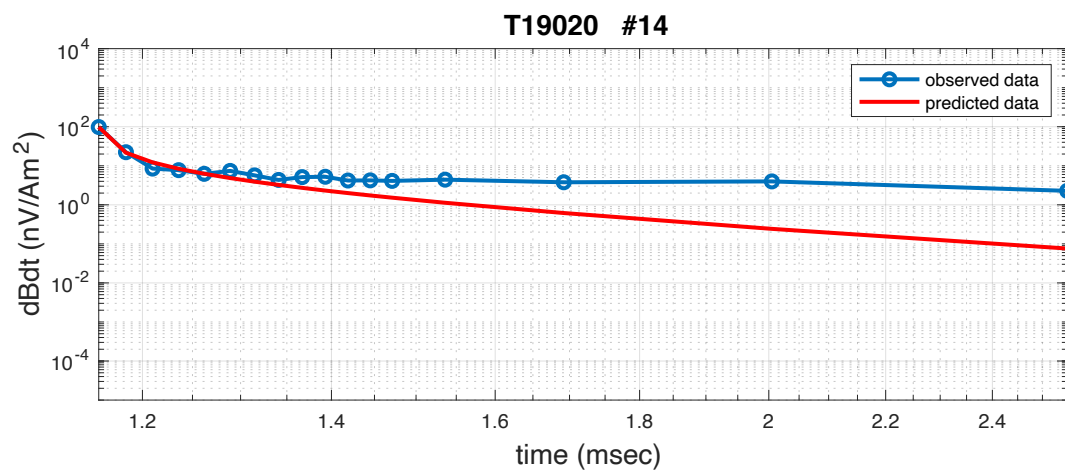
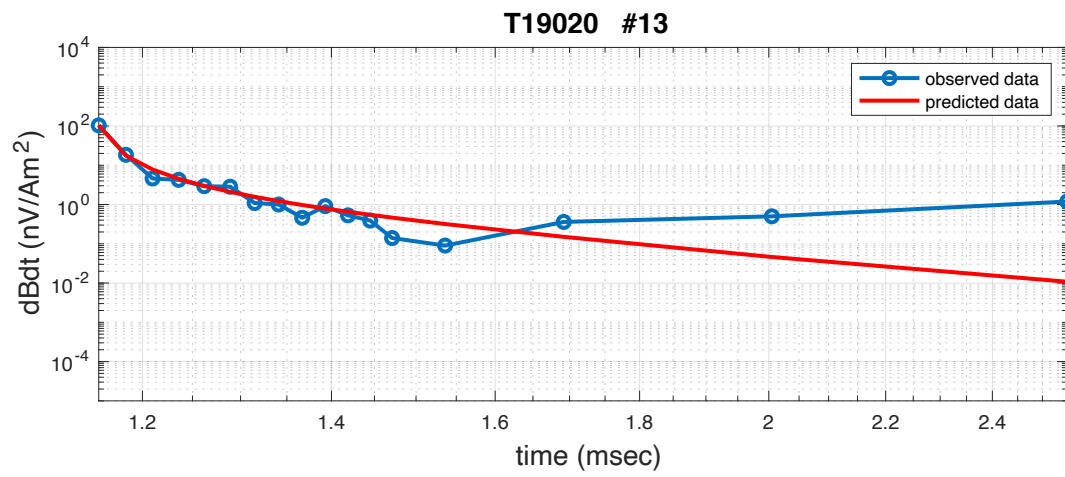
The observation points on T19020

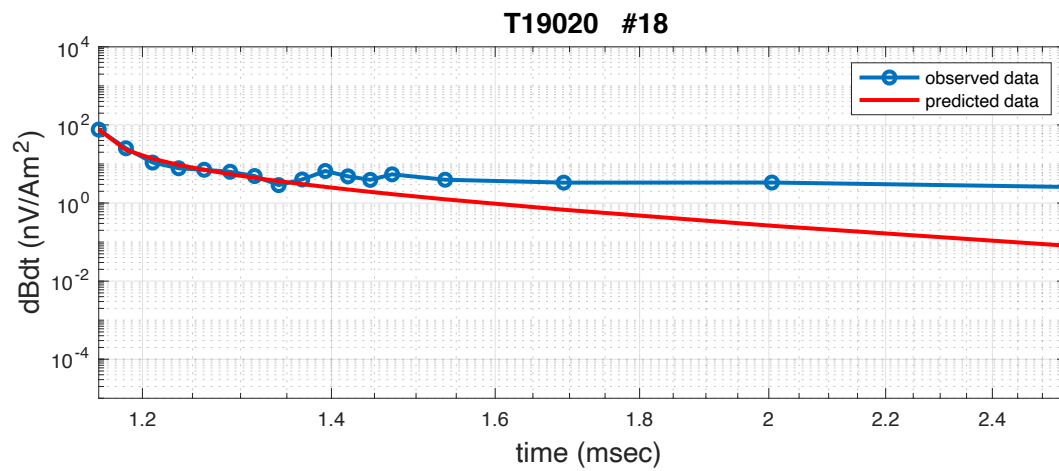
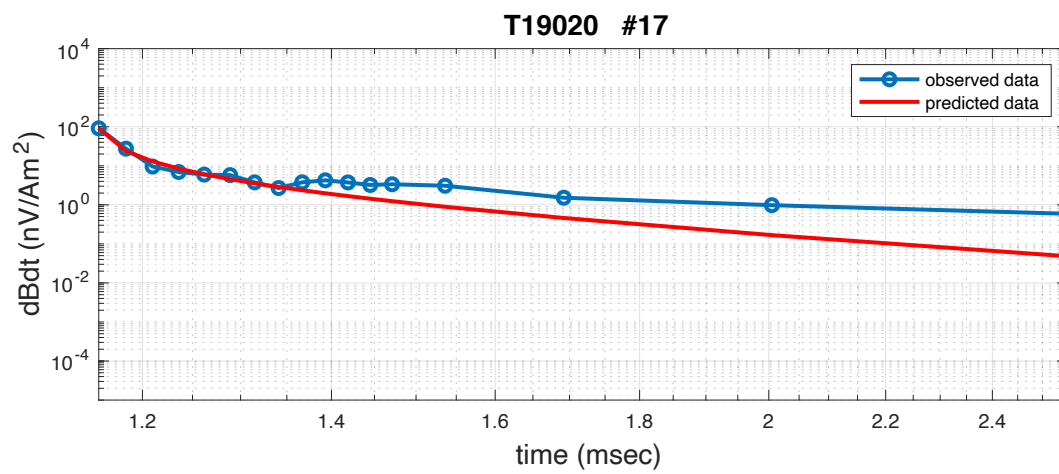
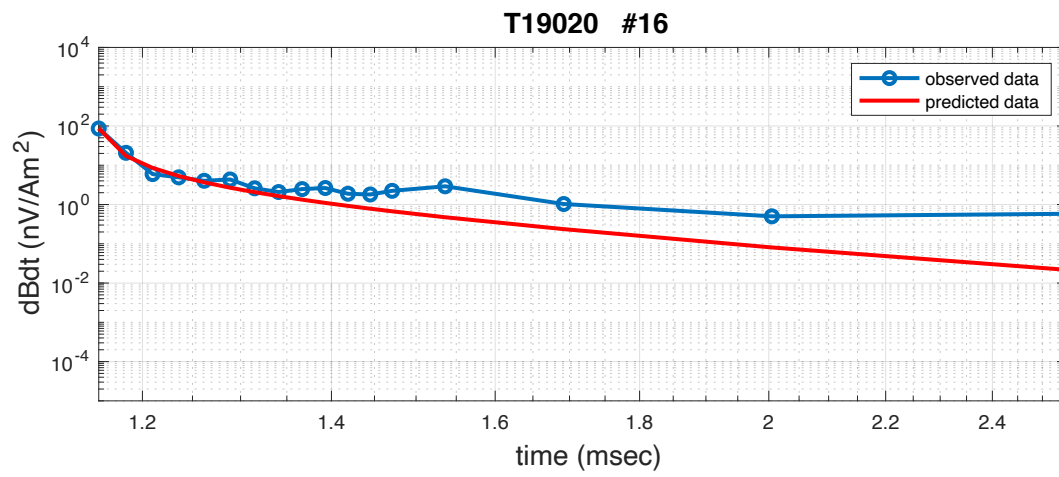


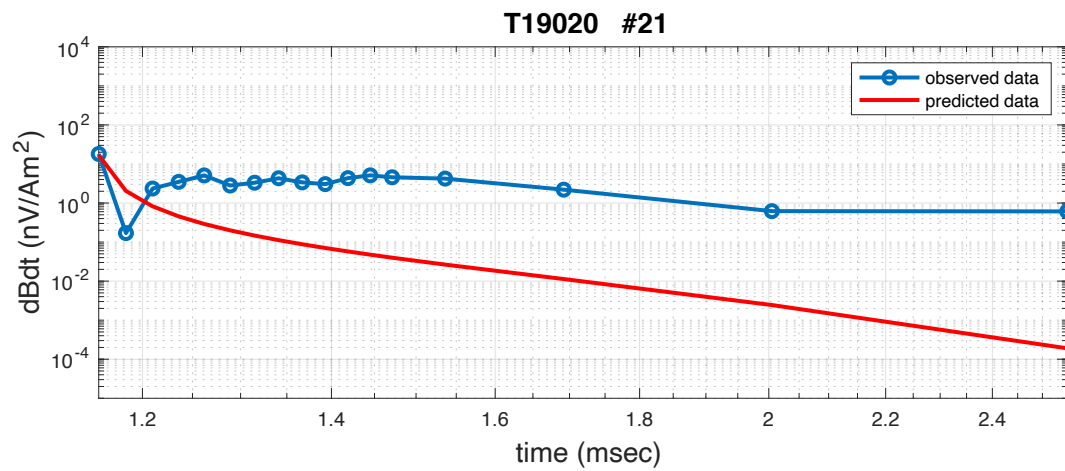
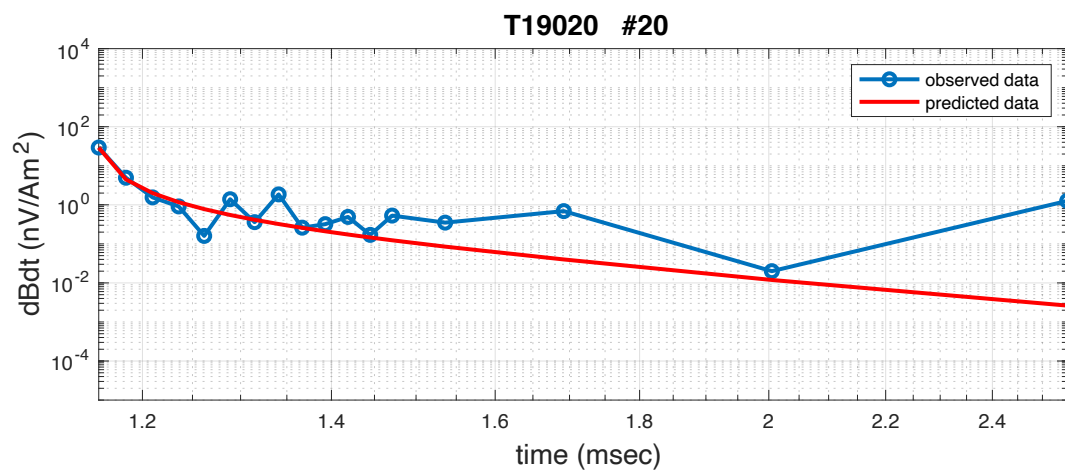
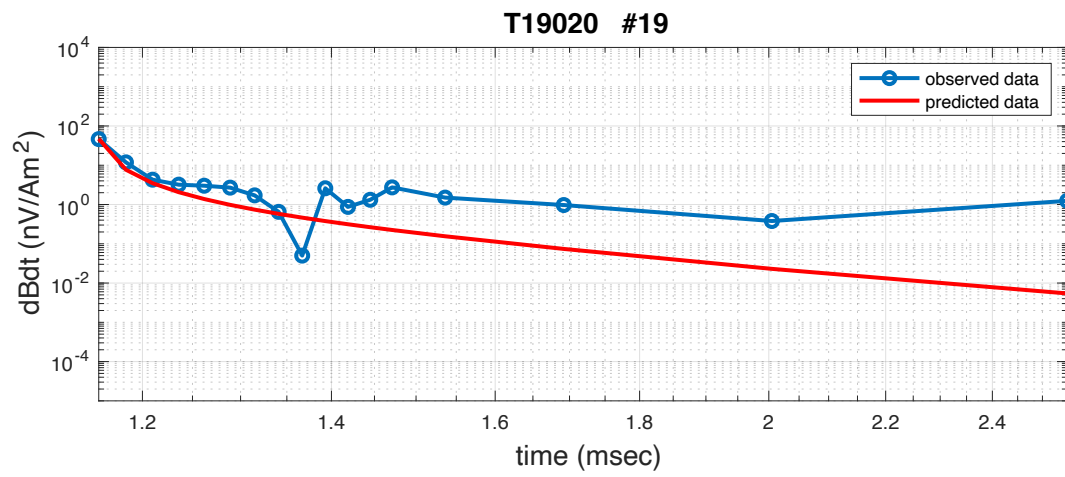


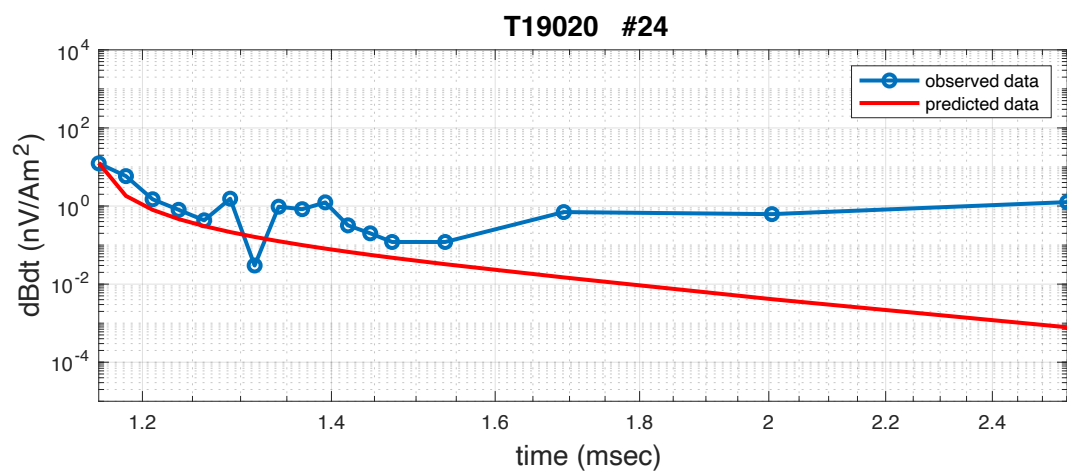
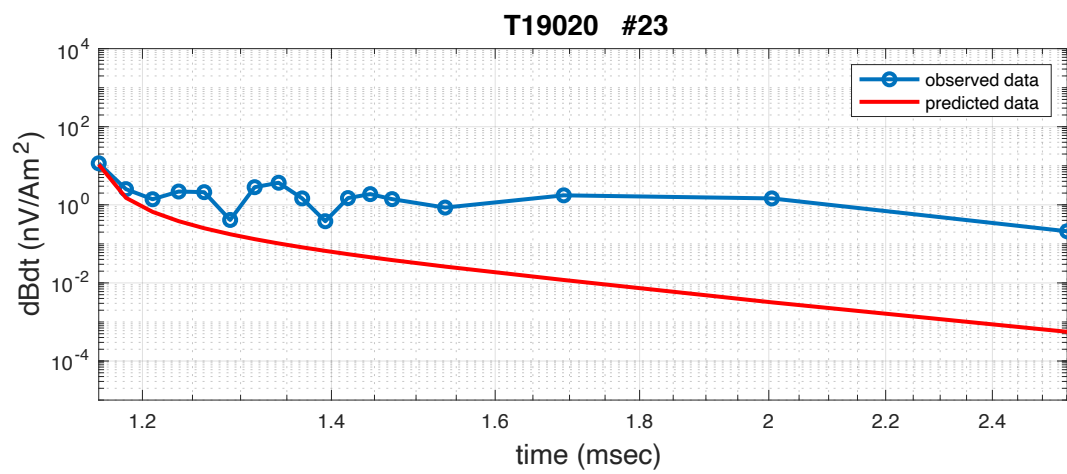
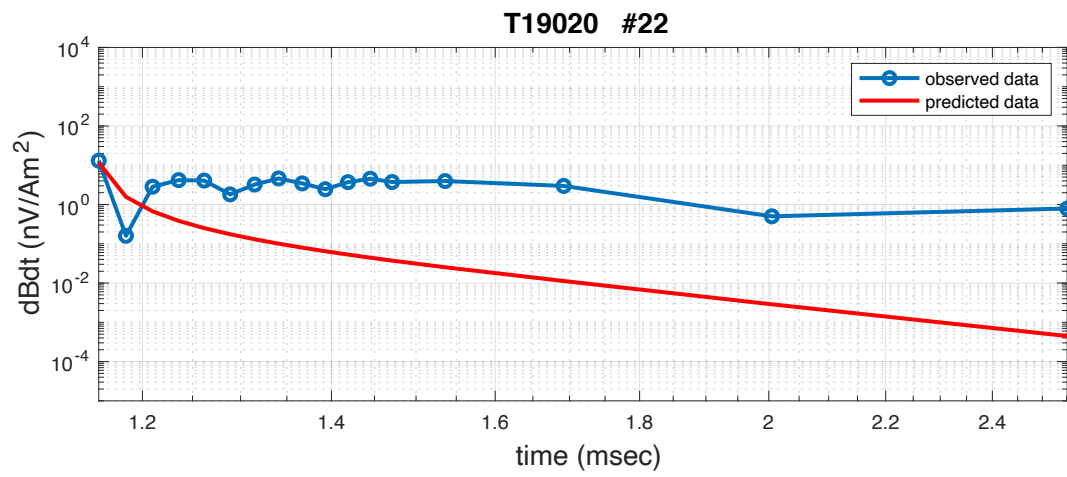


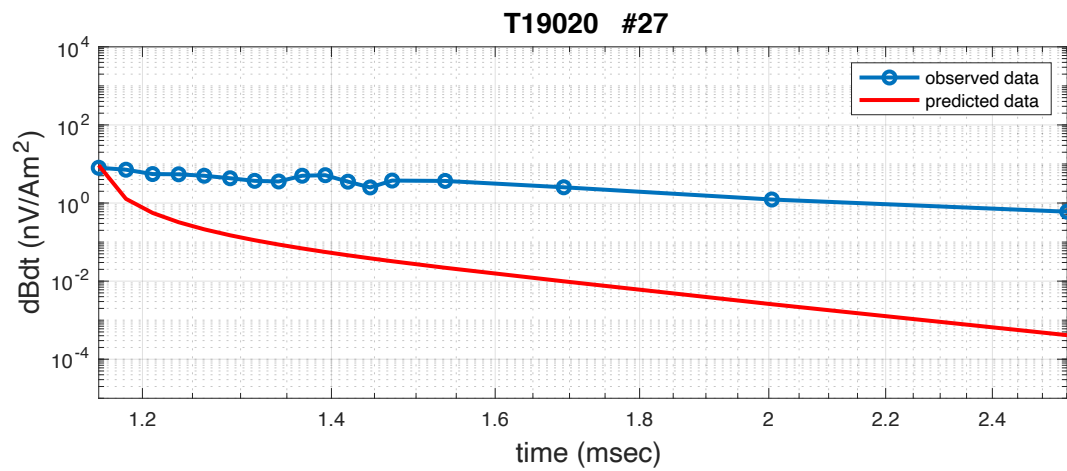
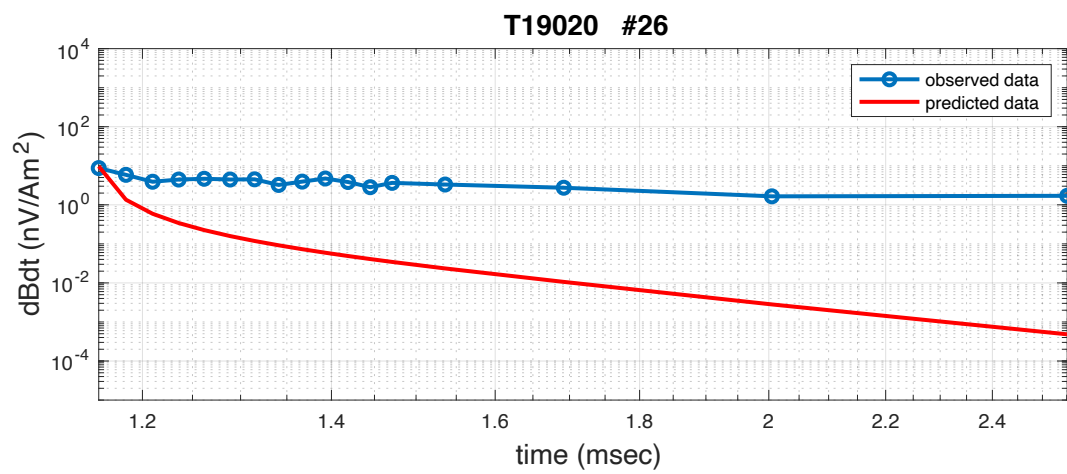
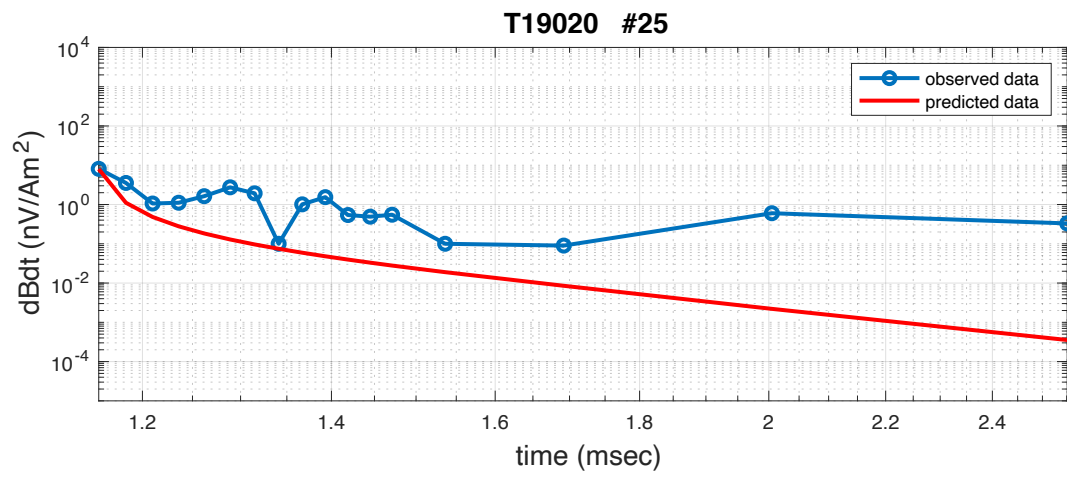


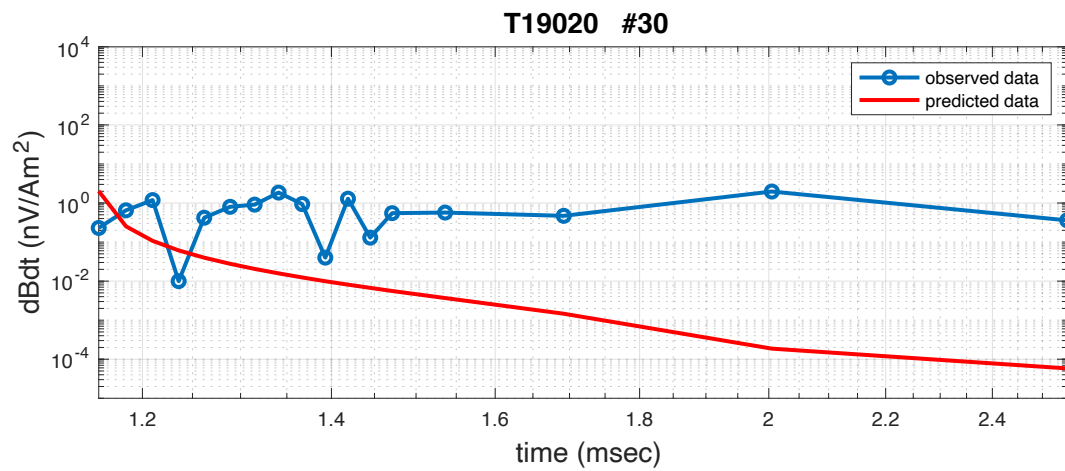
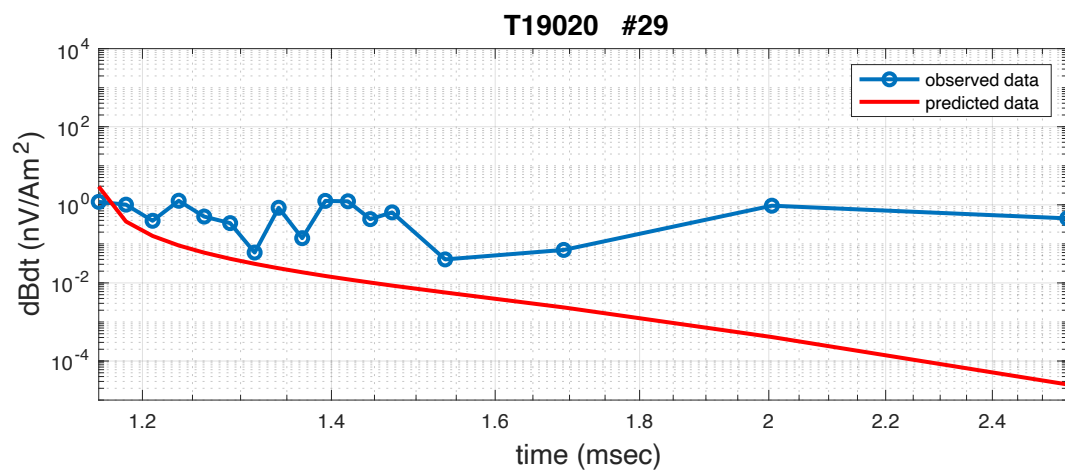
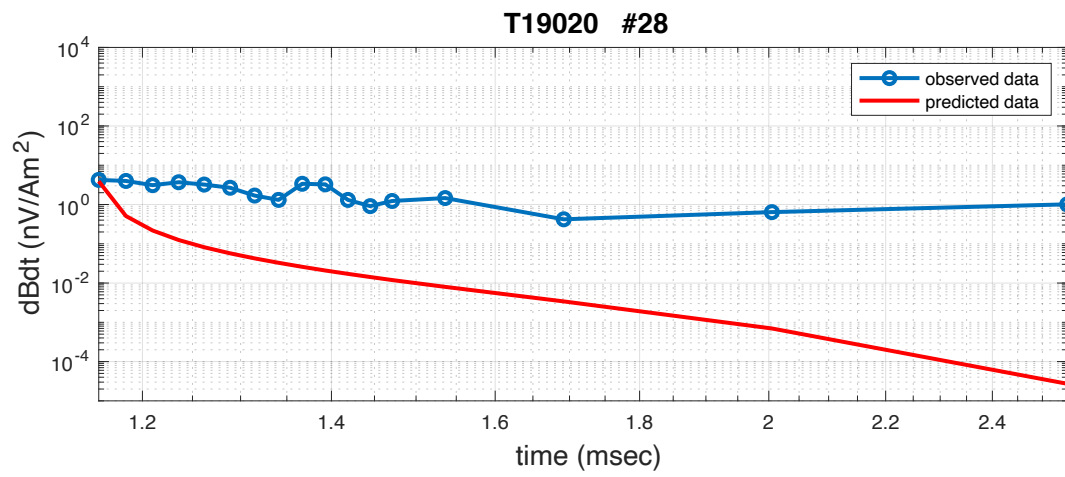


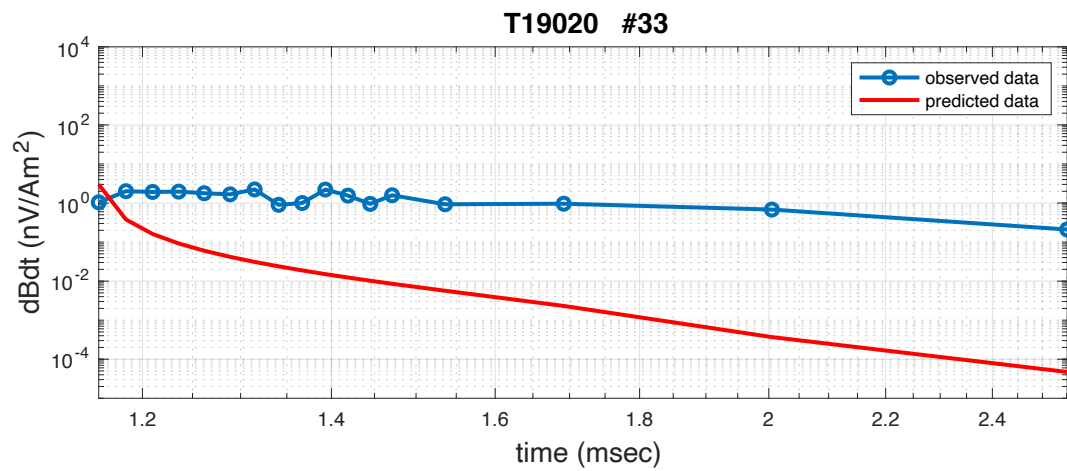
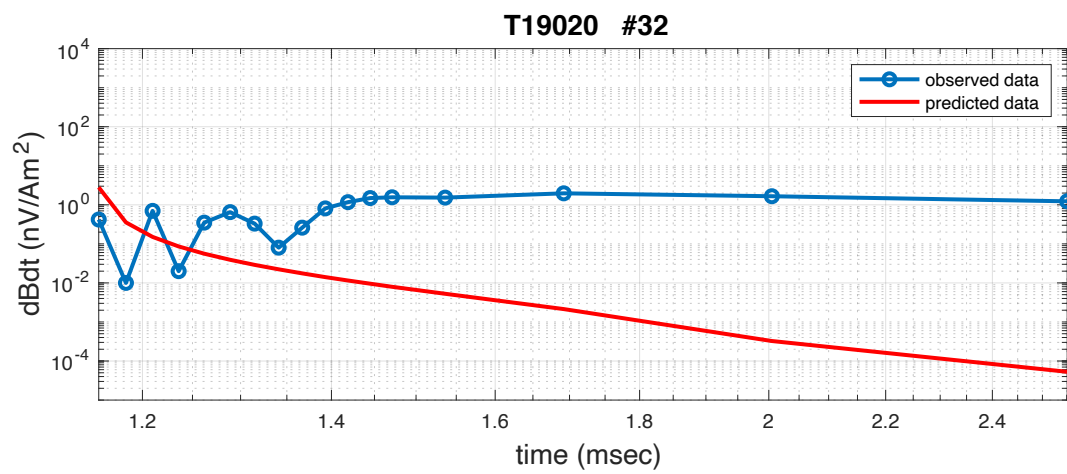
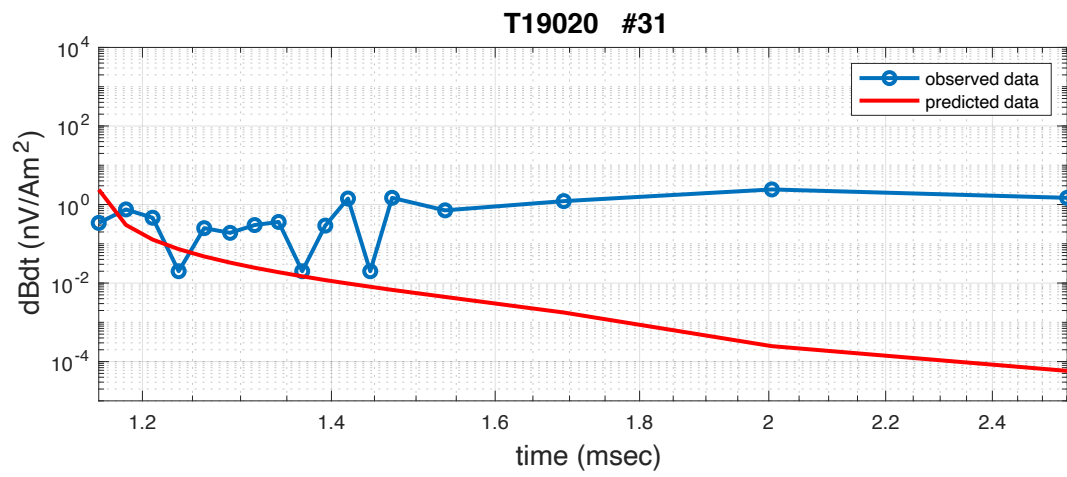


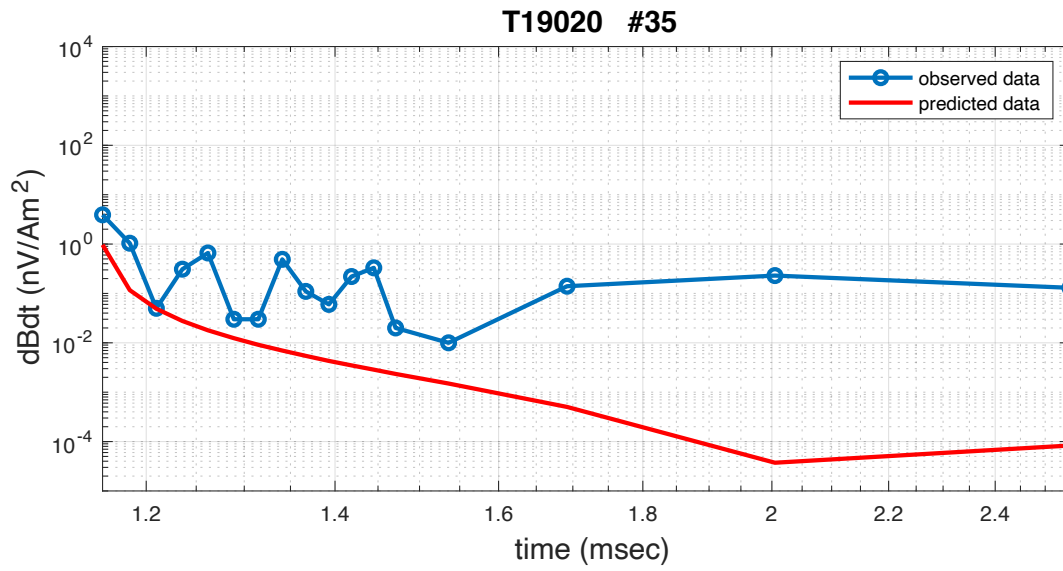
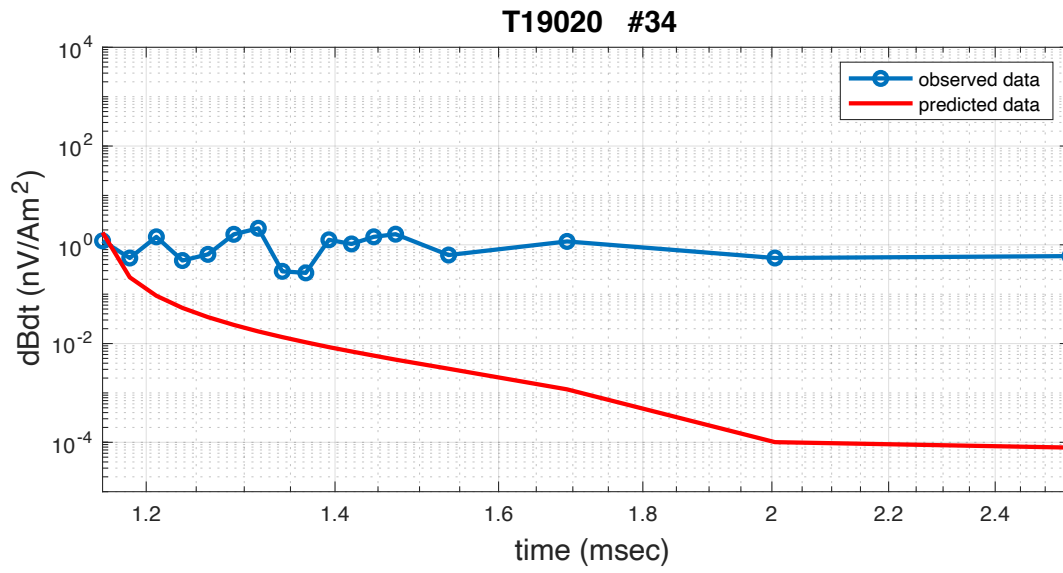






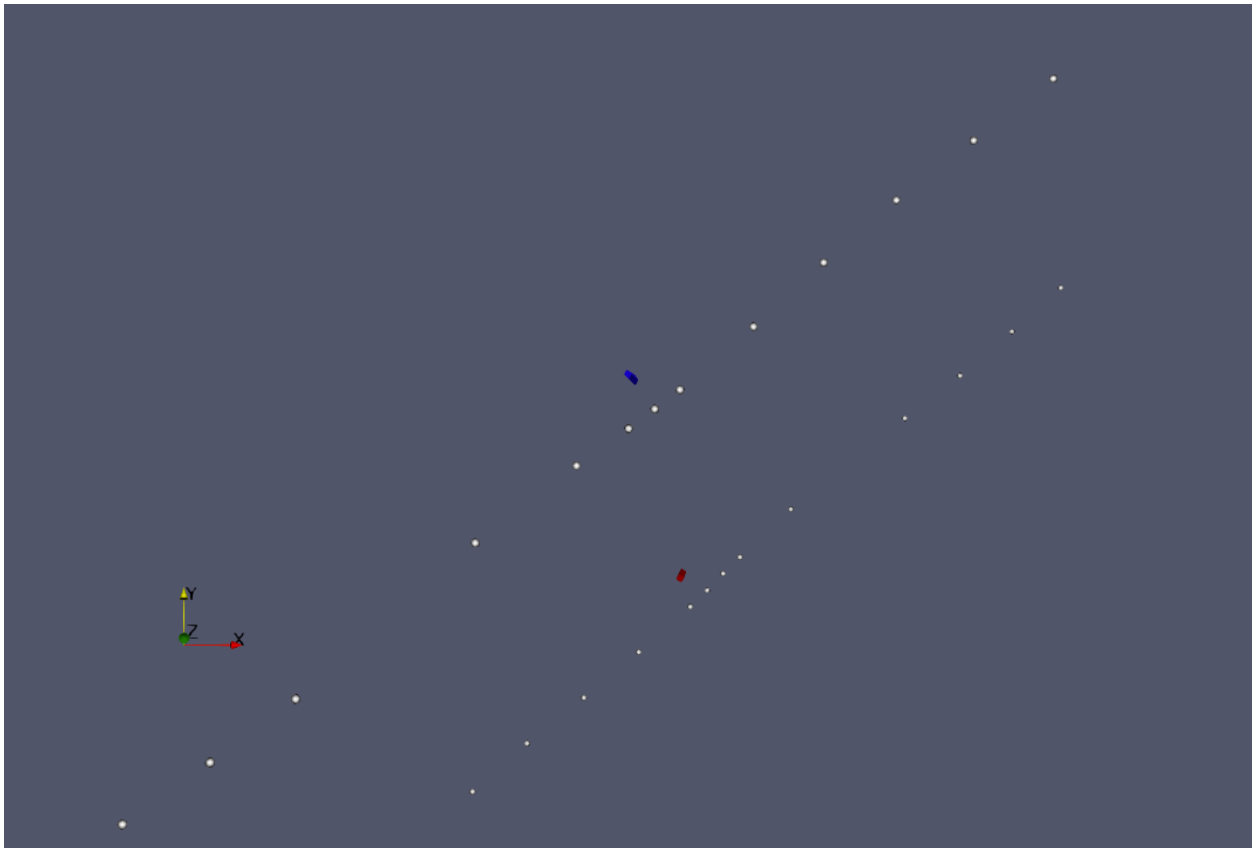


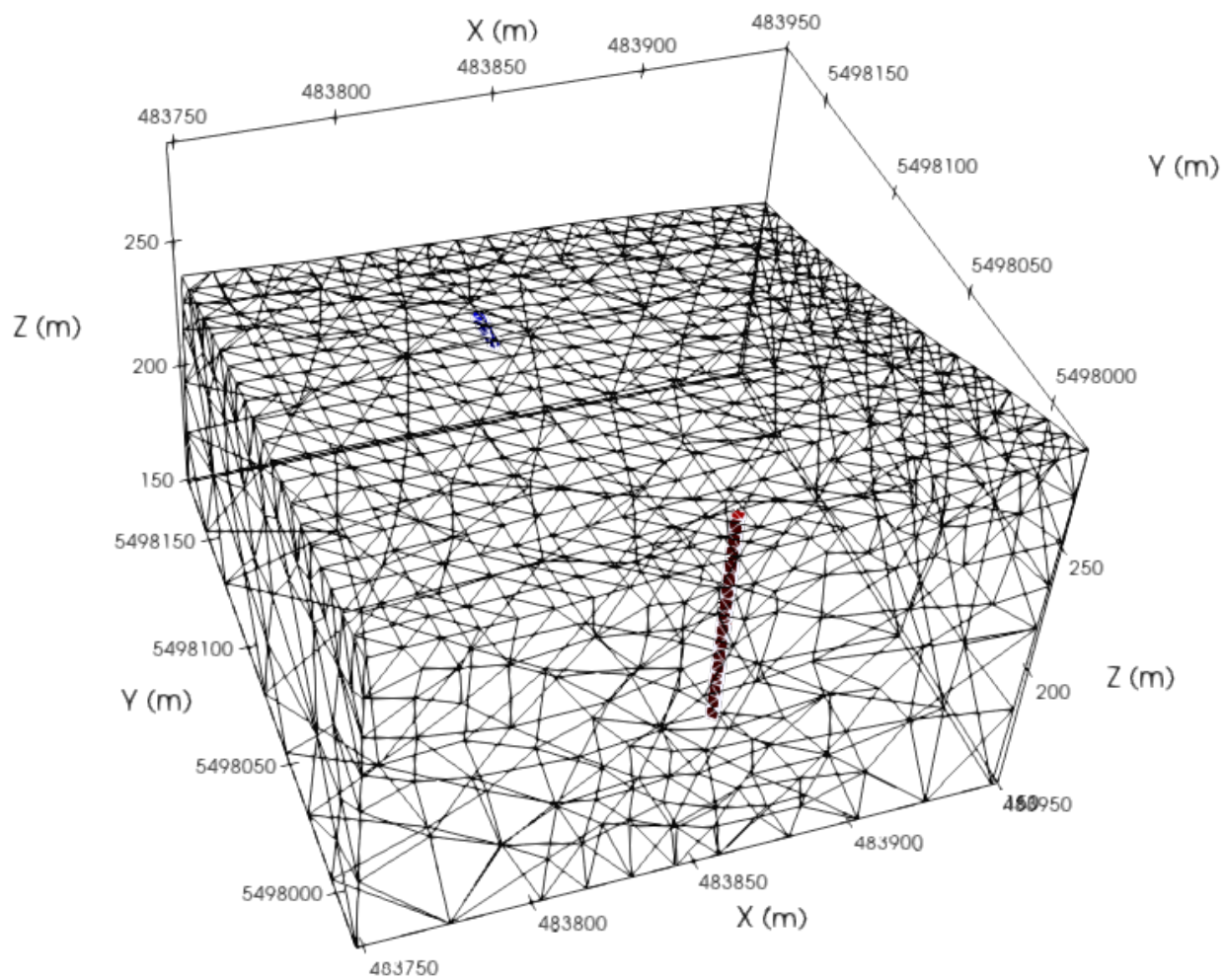




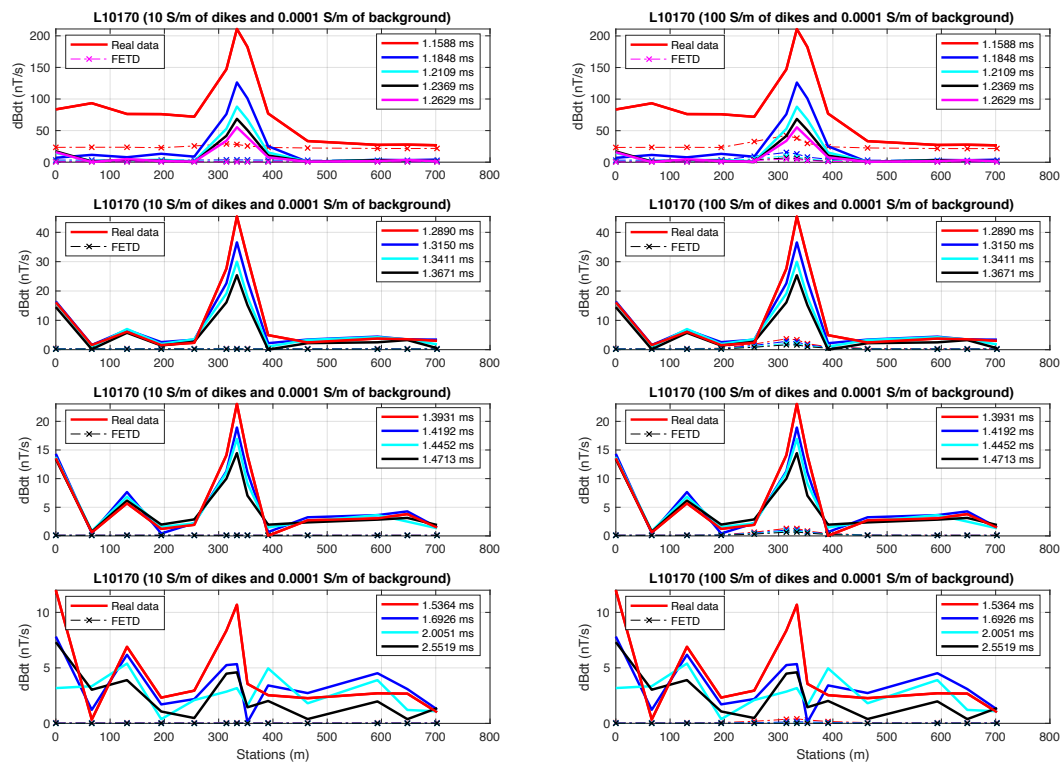
B. The FETD Responses of 3D Earth Models

Model 1

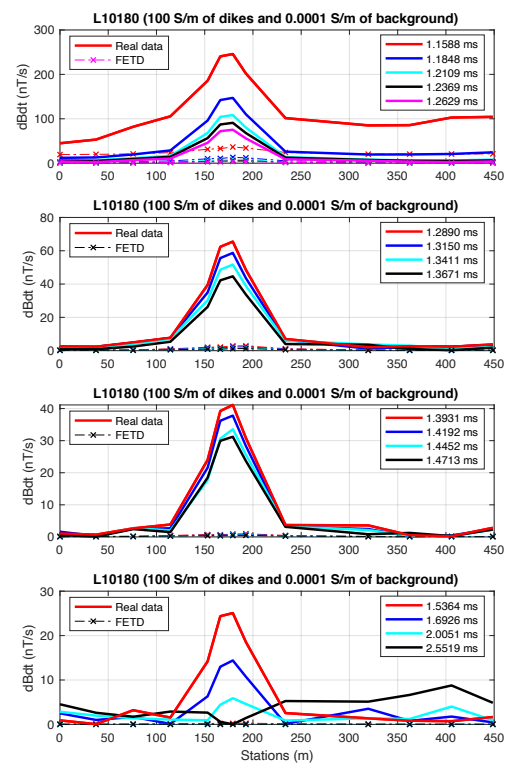
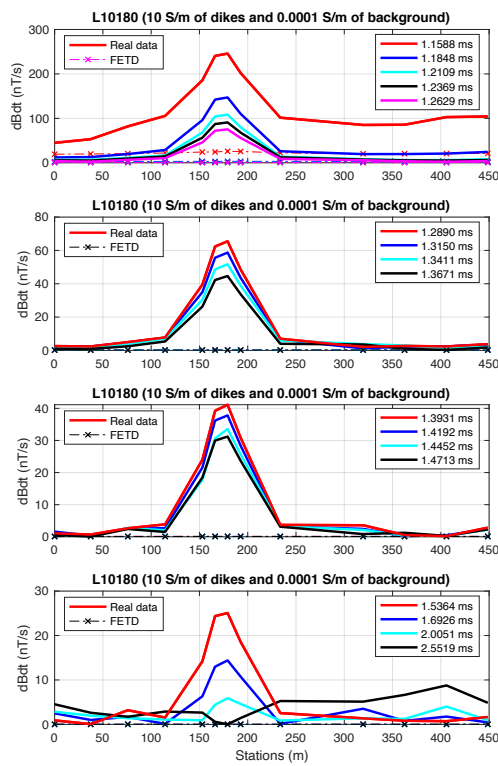




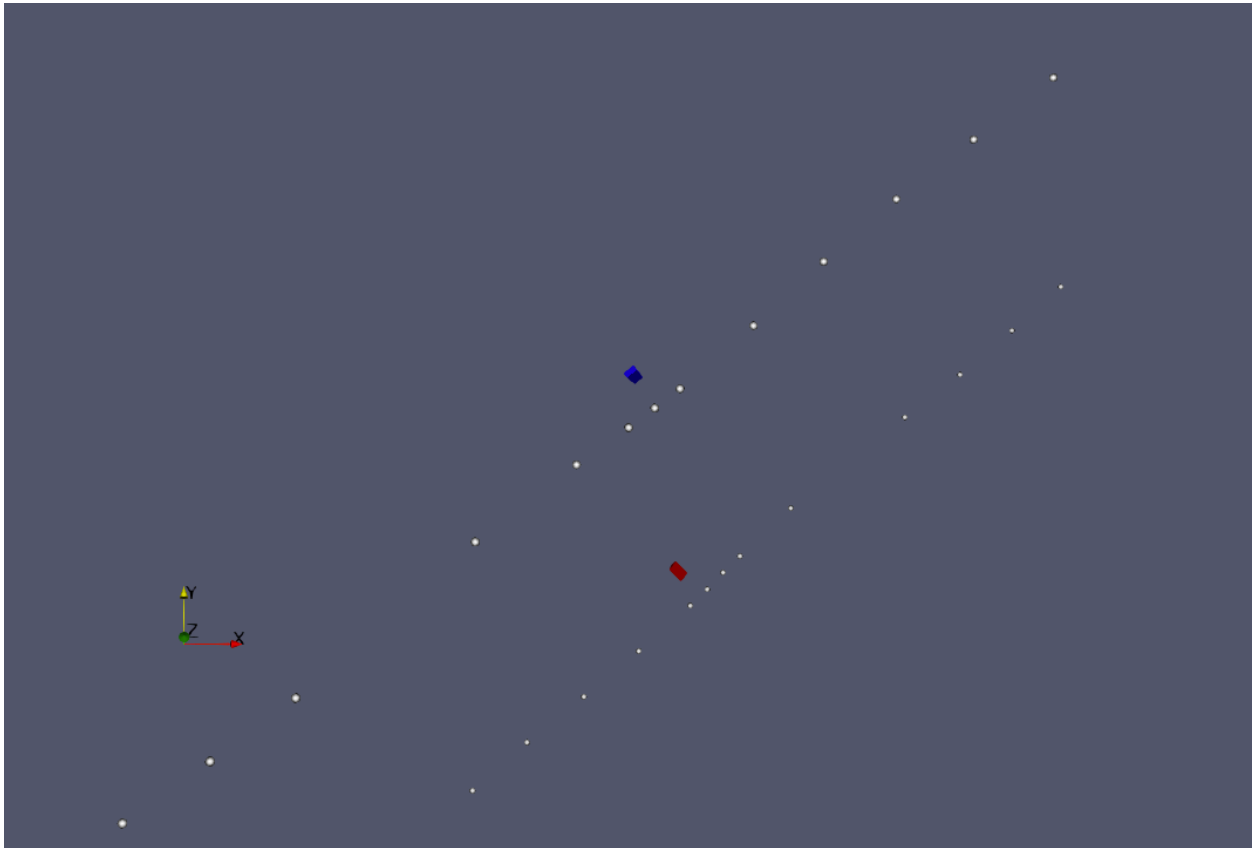
L10170

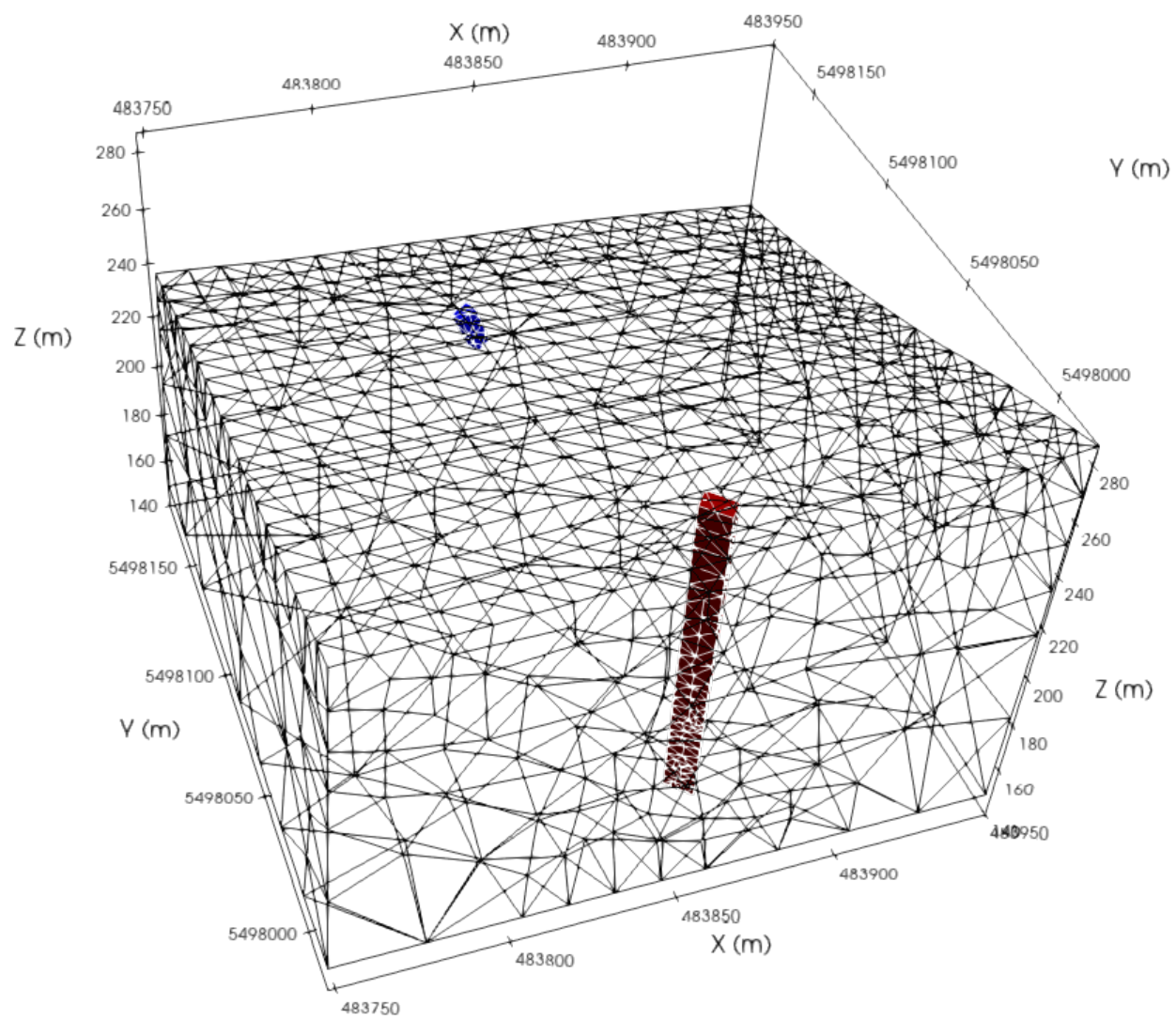


L10180

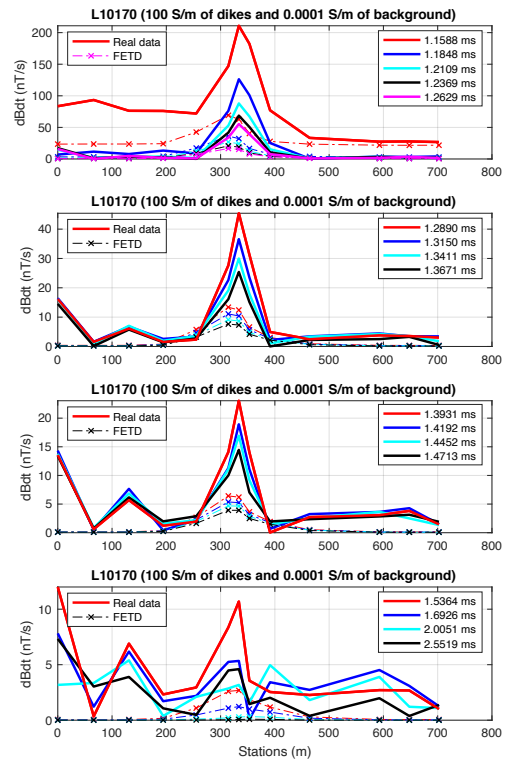
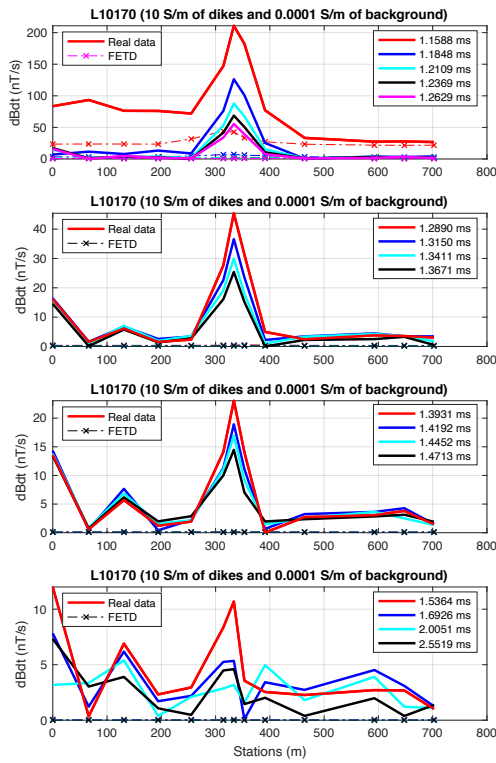


Model 2

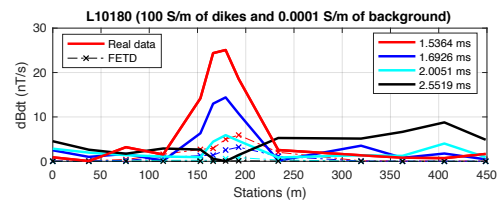
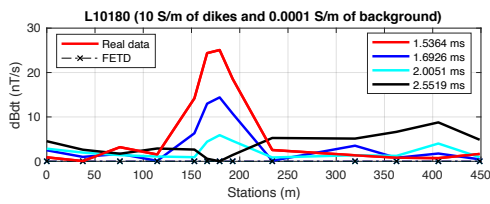
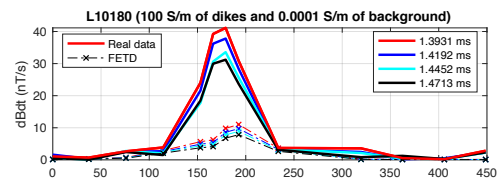
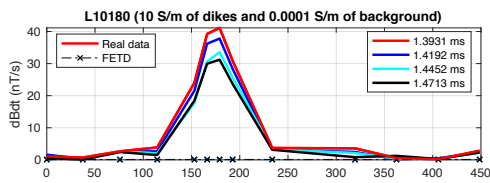
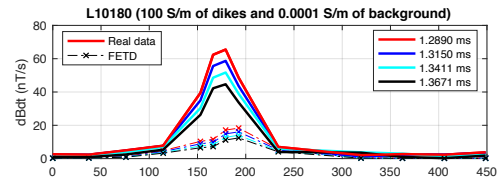
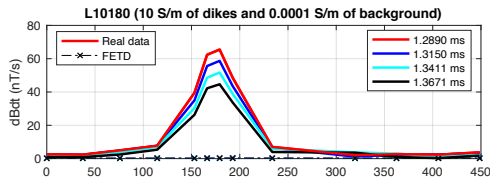
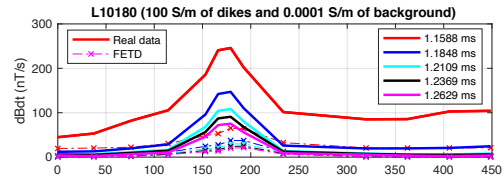
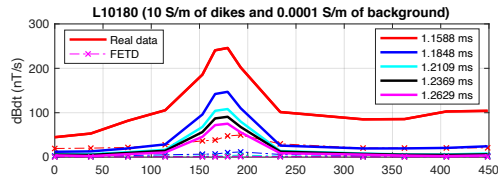




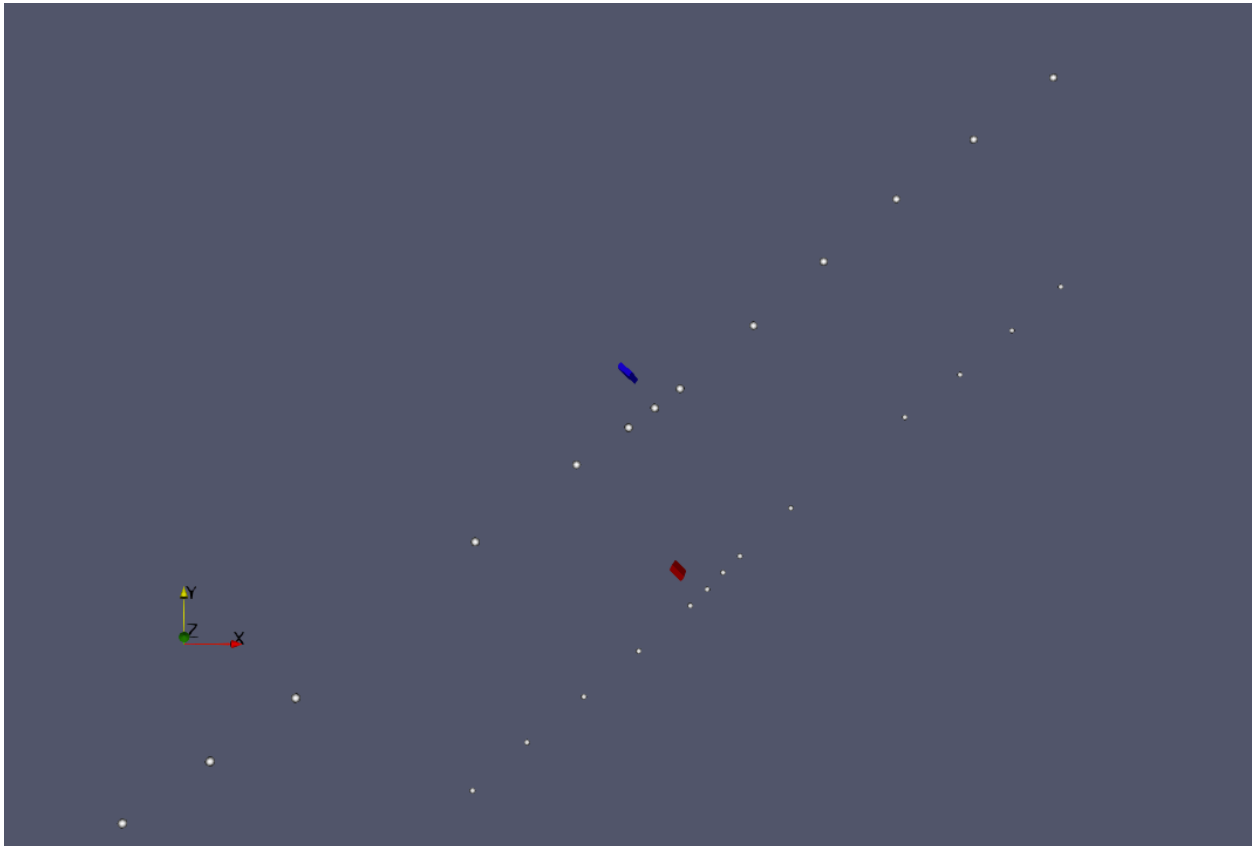
L10170

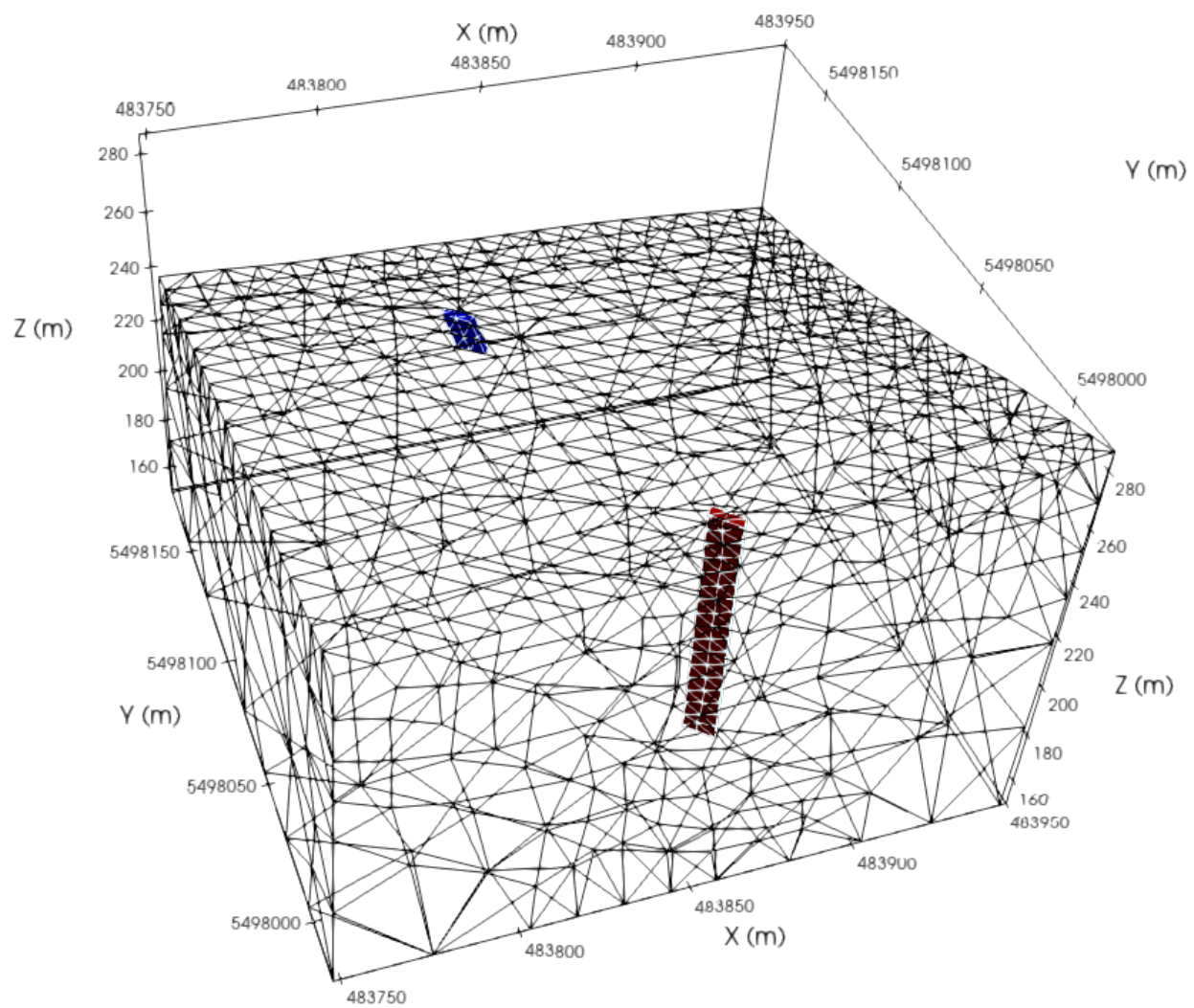


L10180

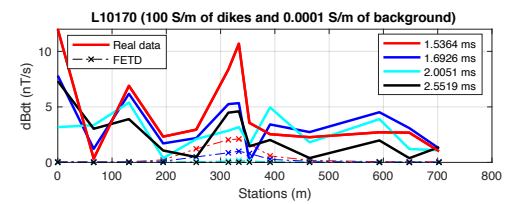
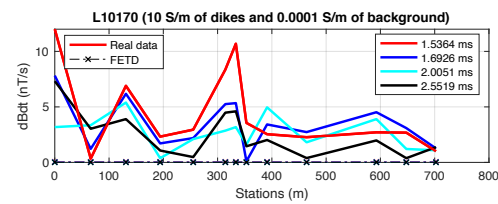
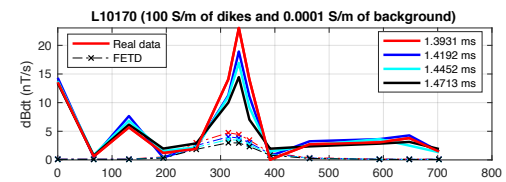
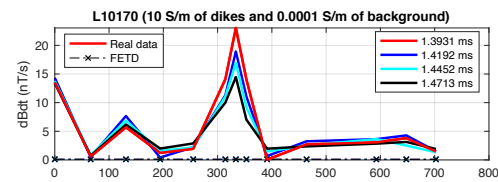
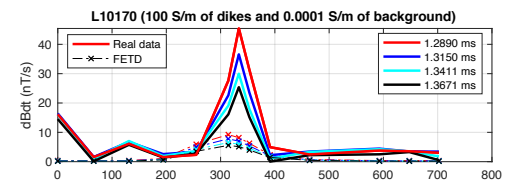
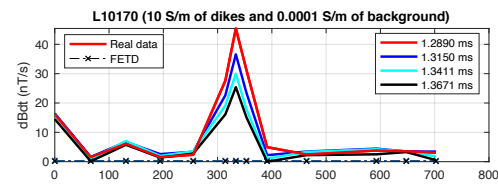
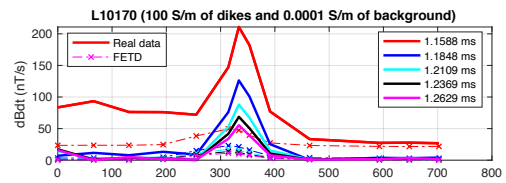
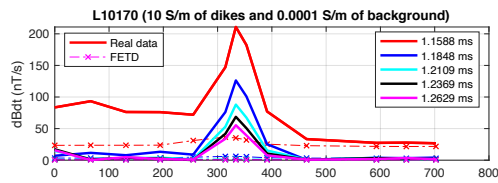


Model 3

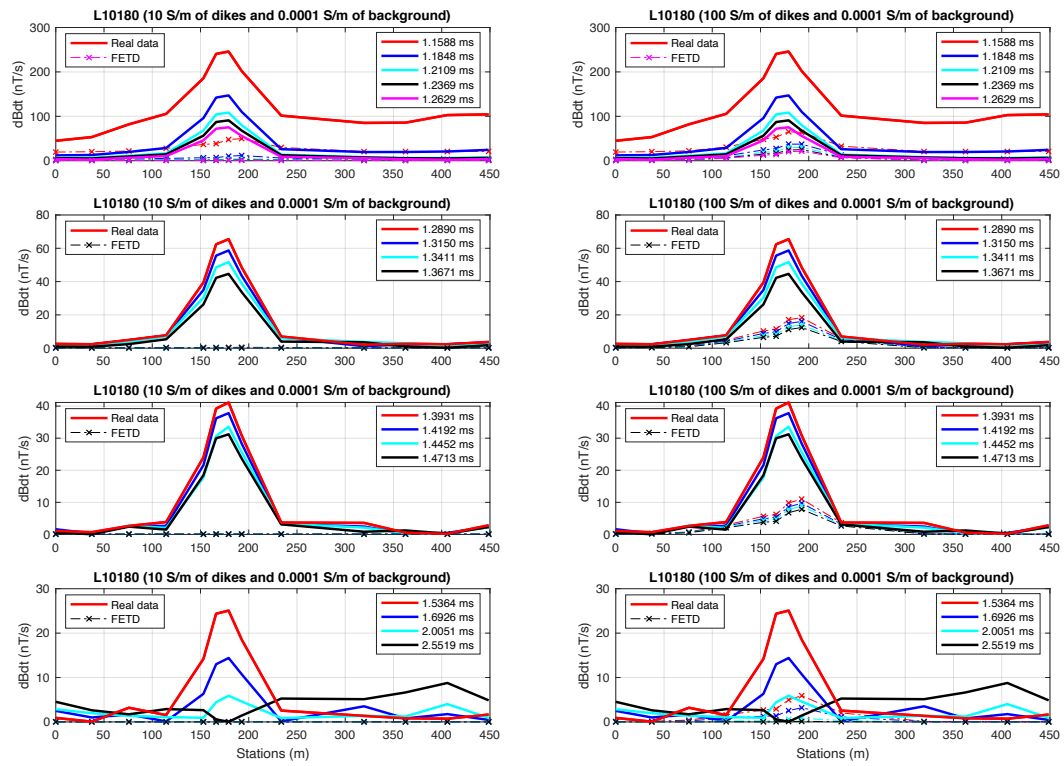




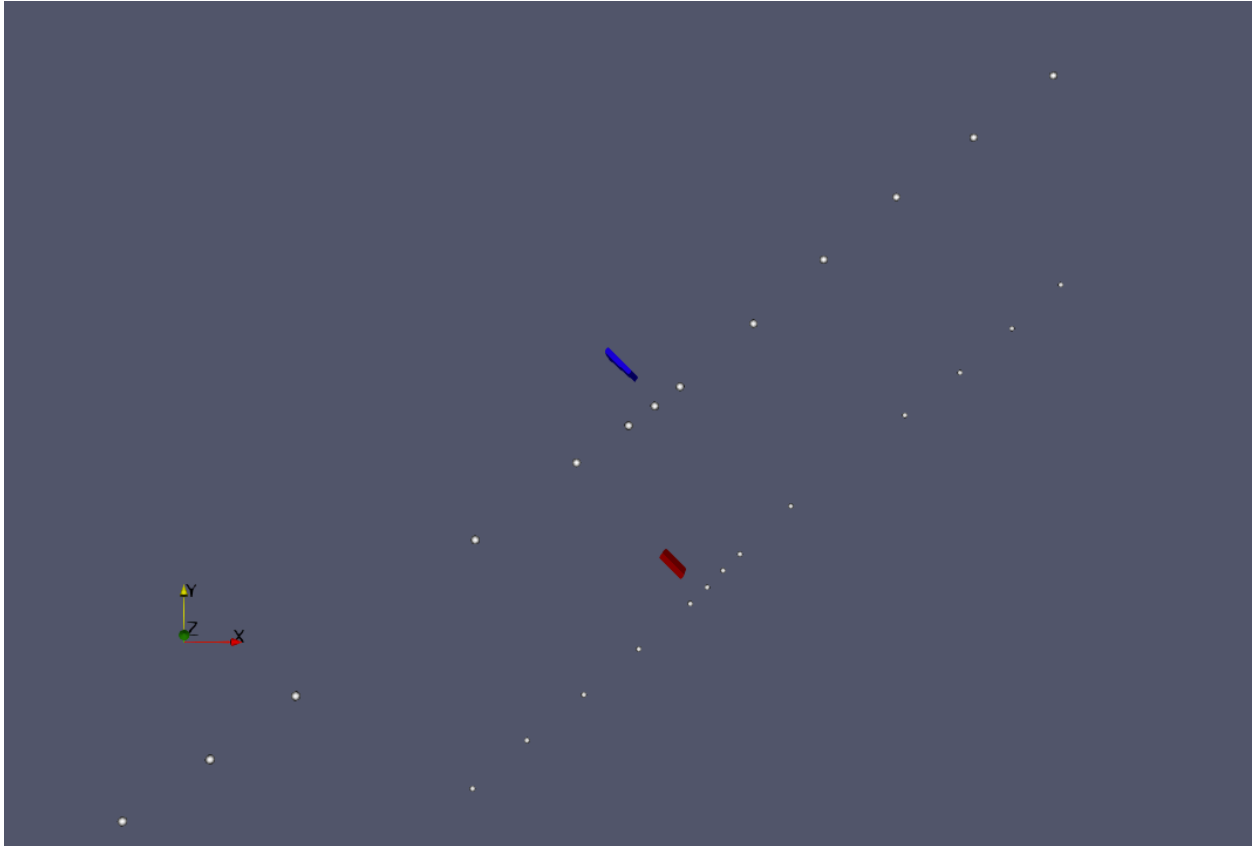
L10170

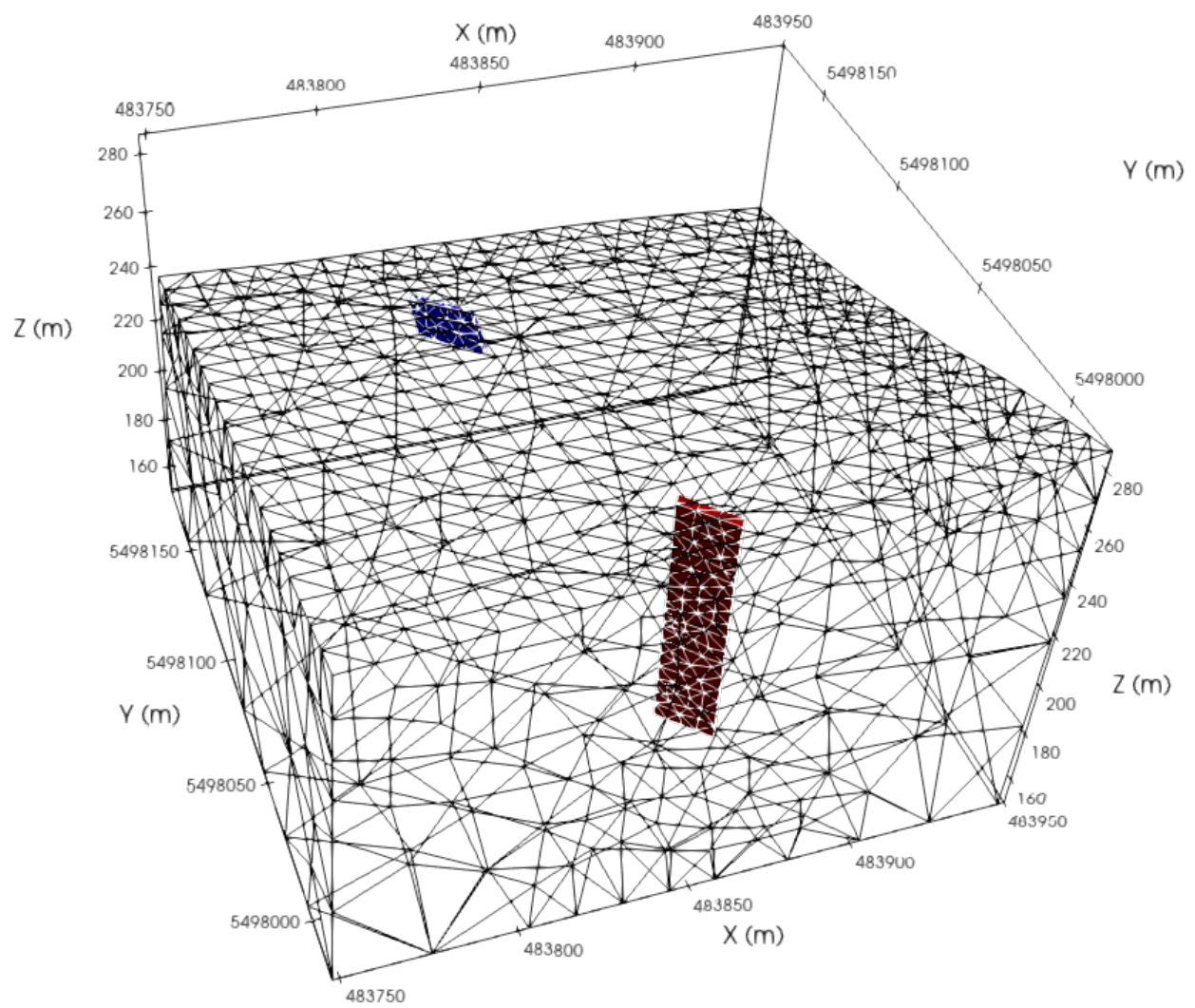


L10180

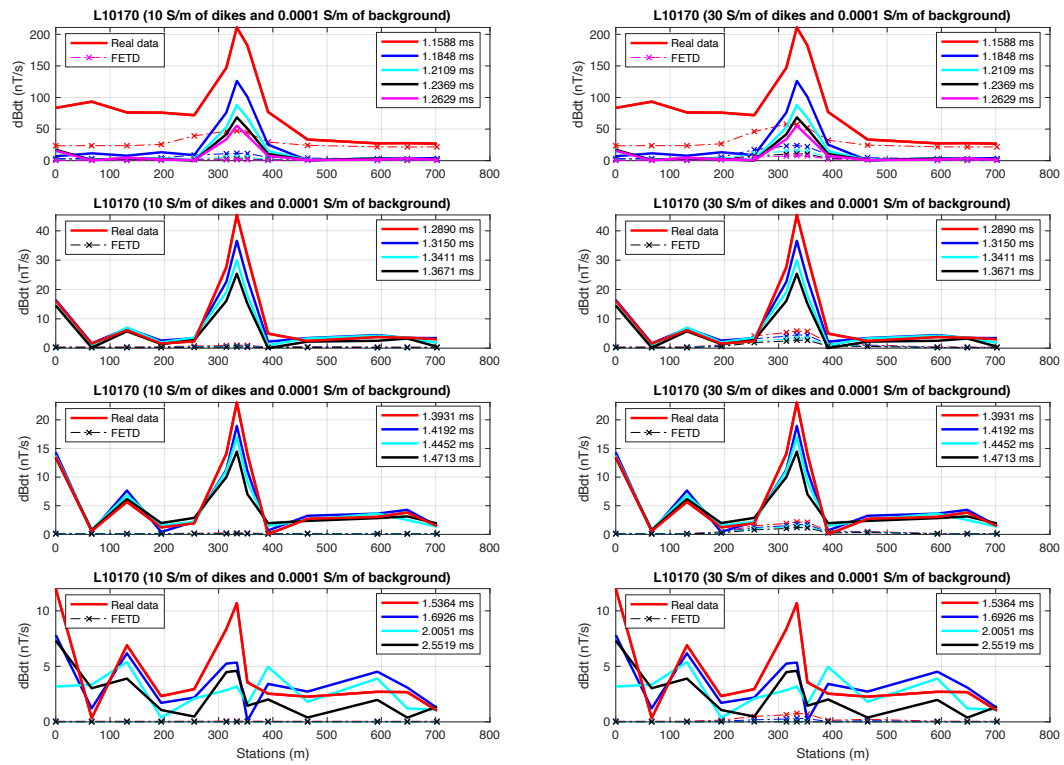


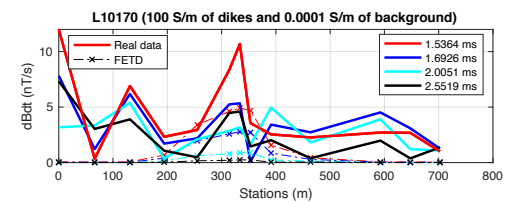
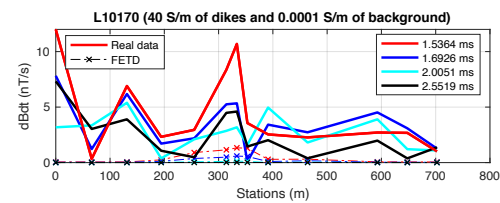
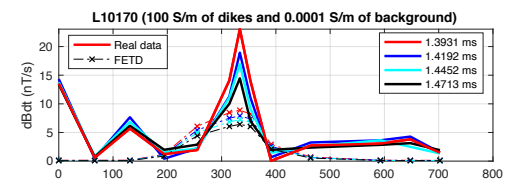
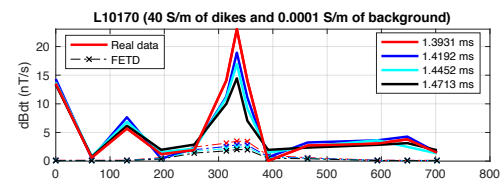
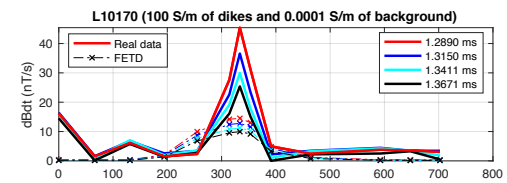
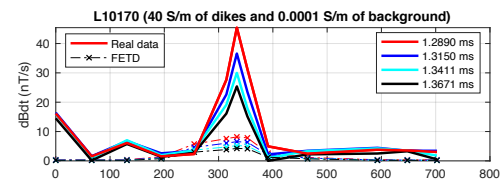
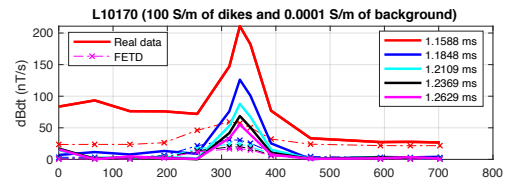
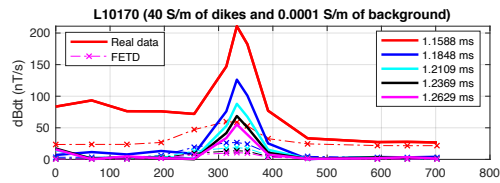
Model 4

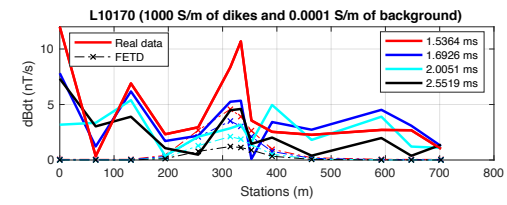
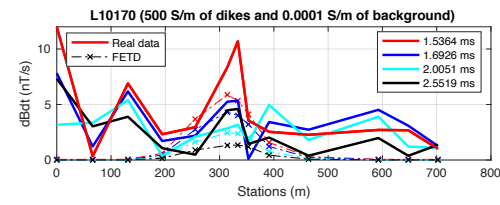
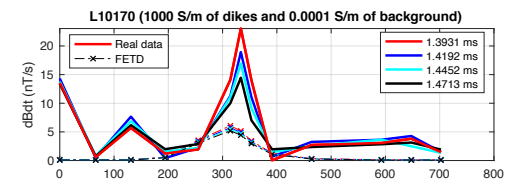
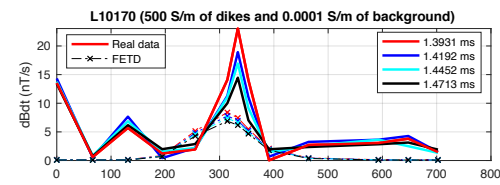
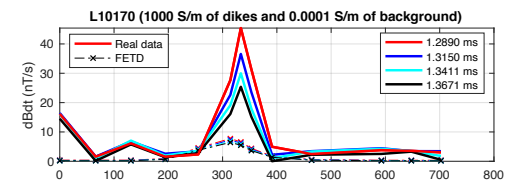
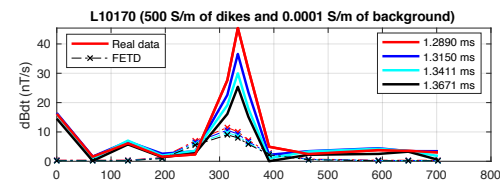
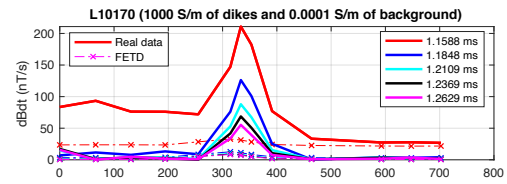
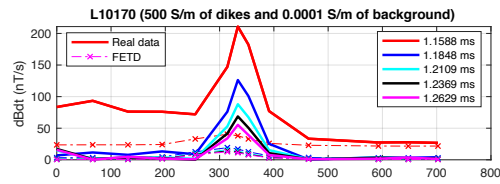




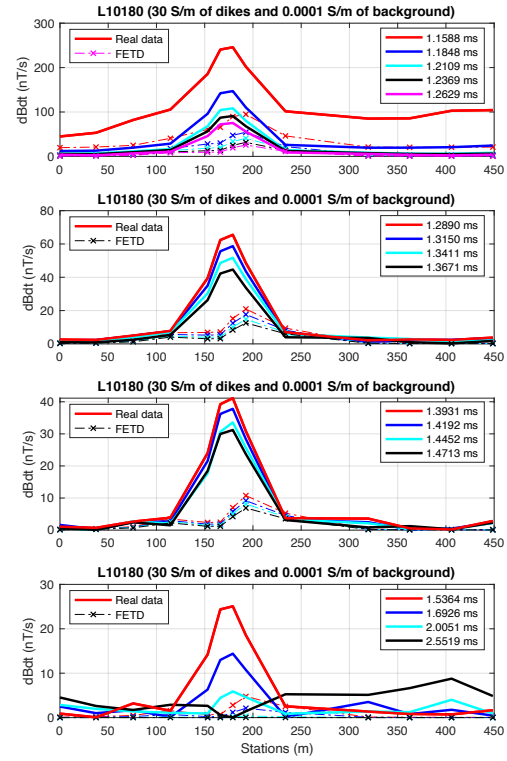
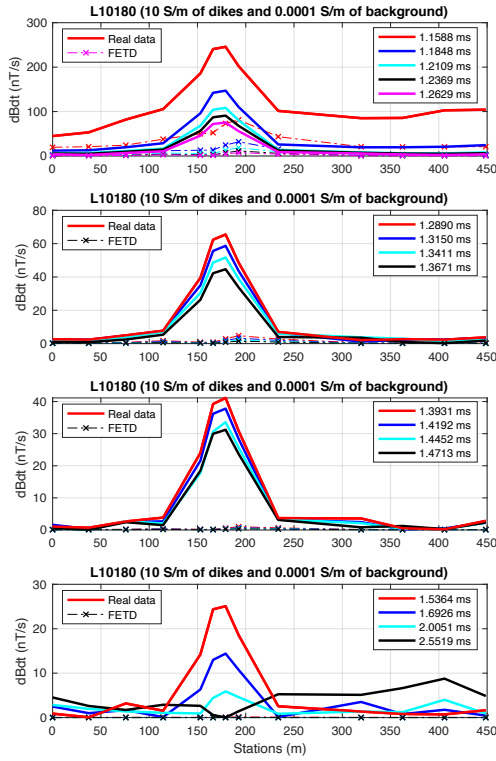
L10170

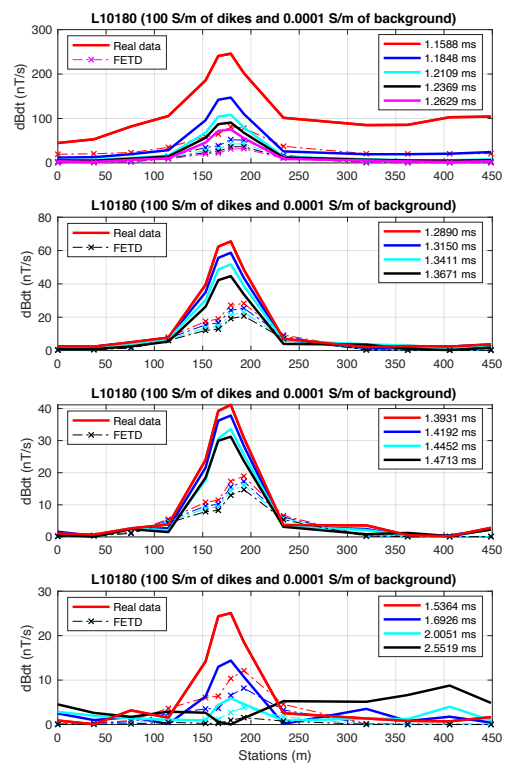
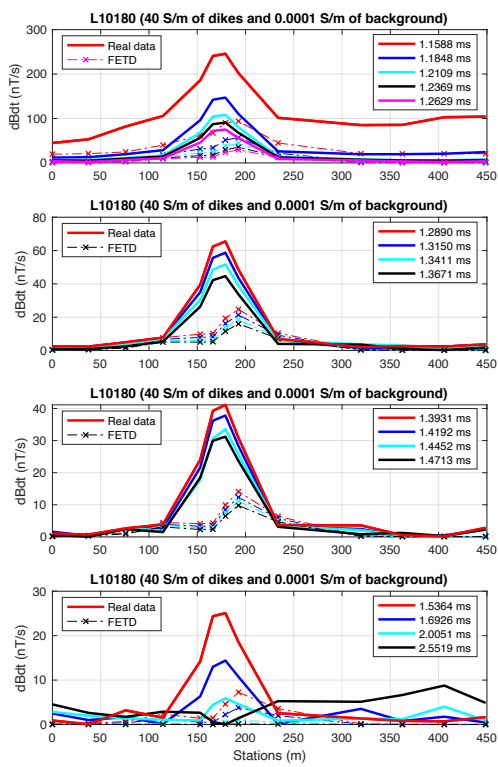


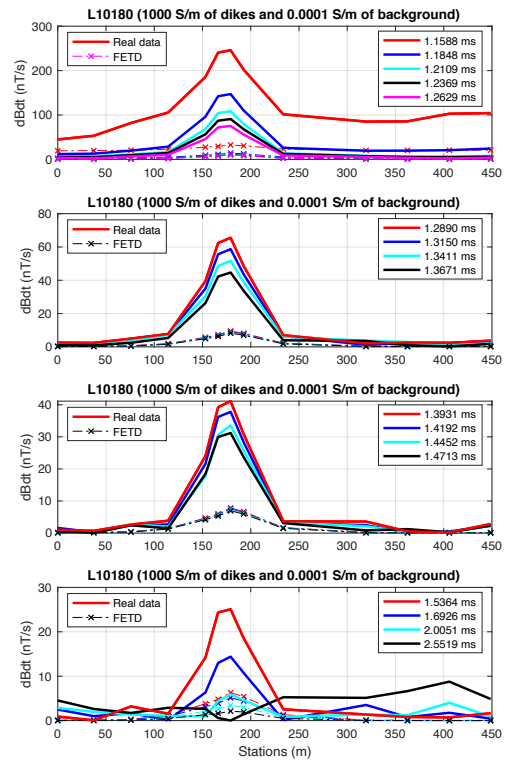
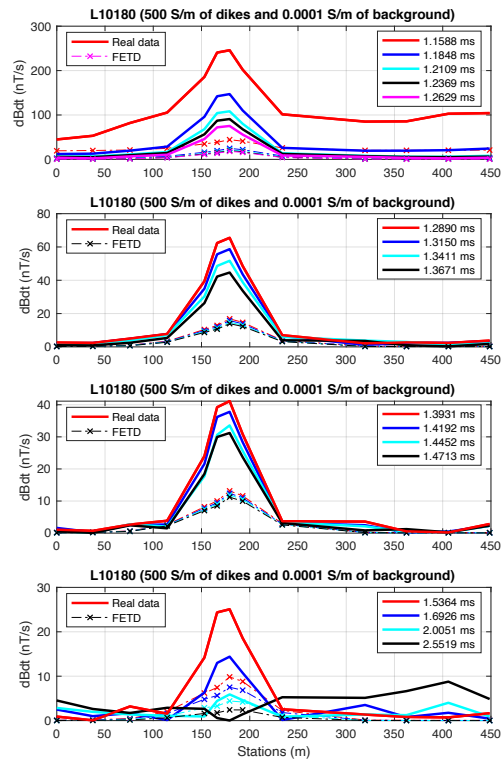




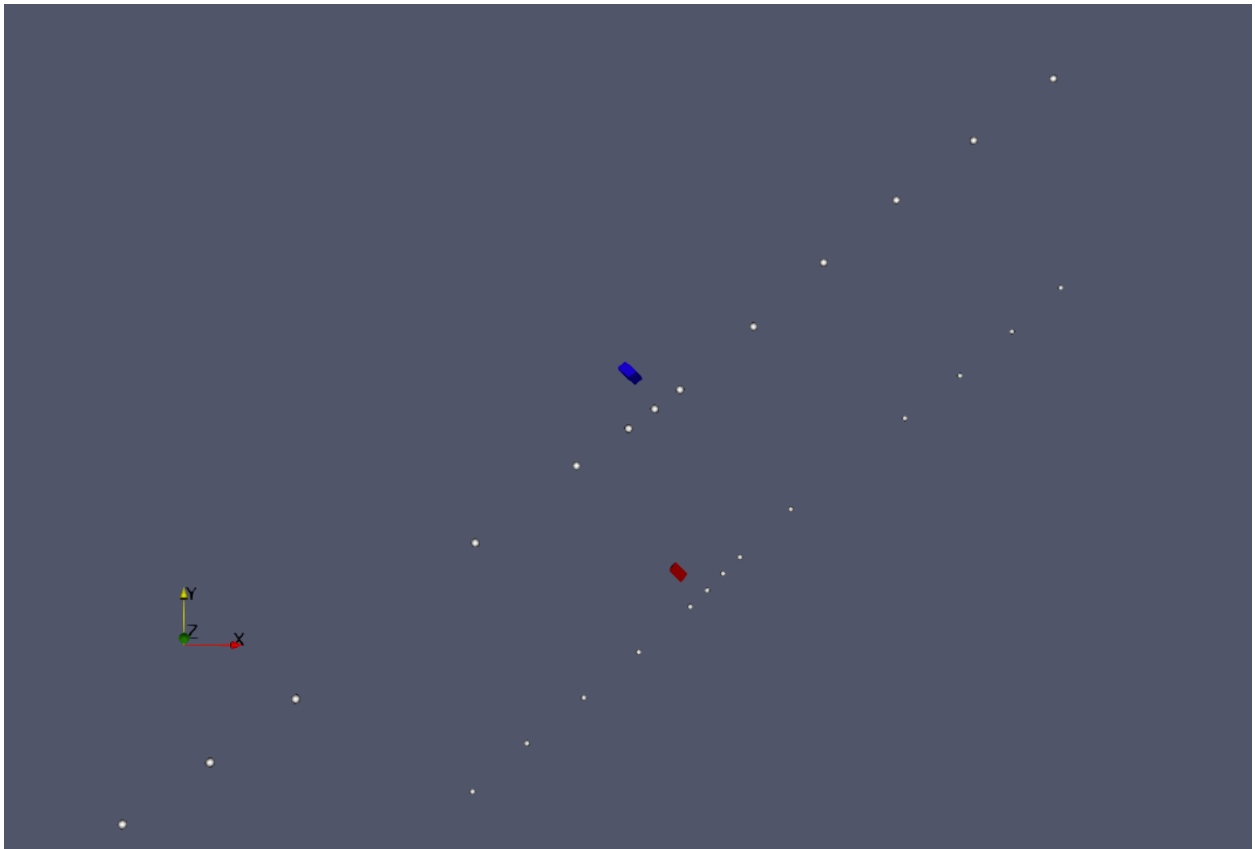
L10180

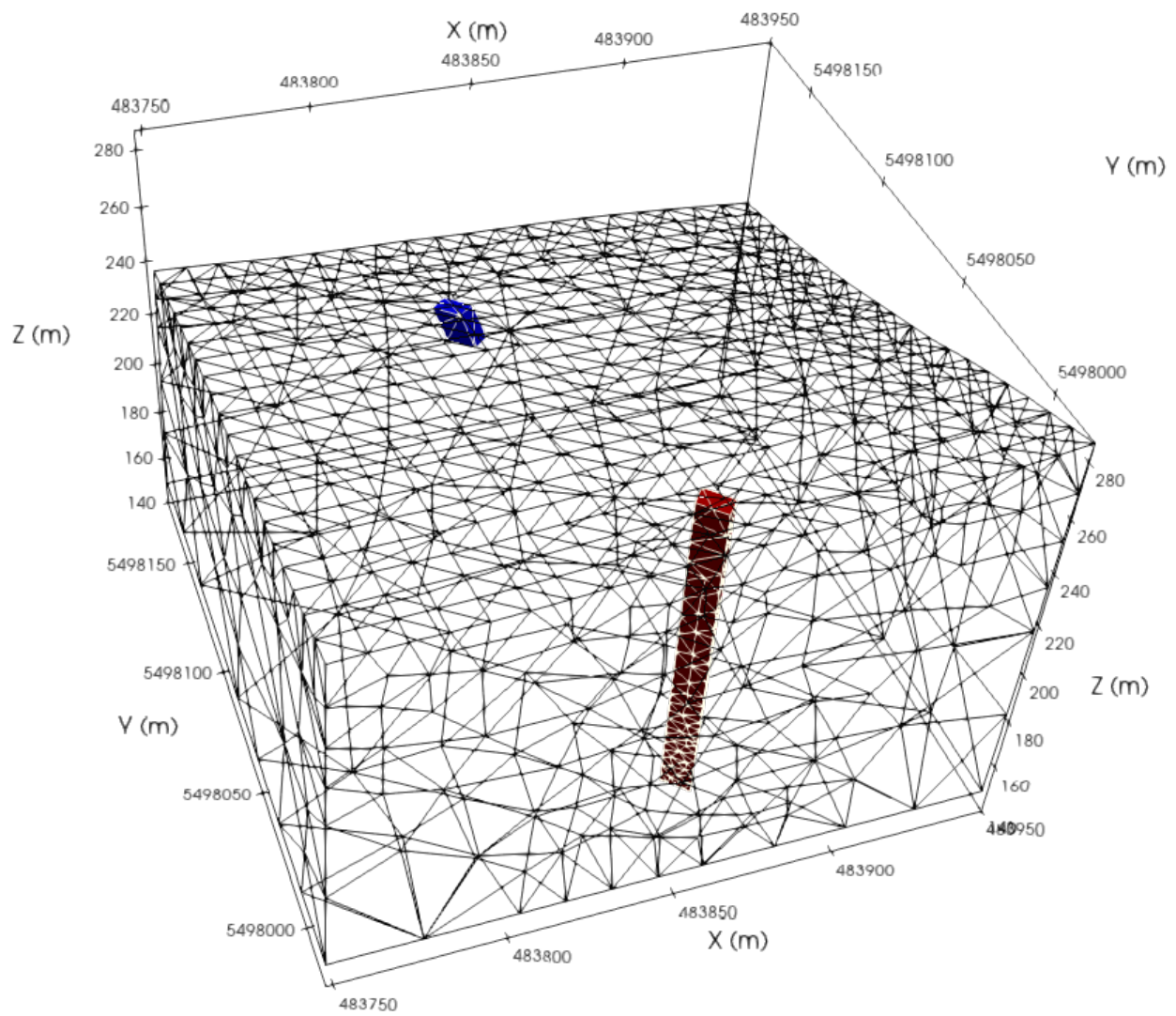




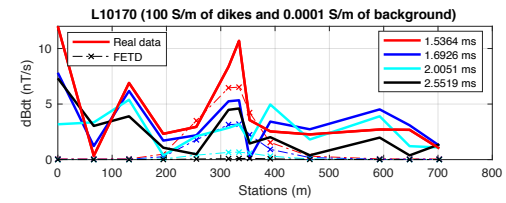
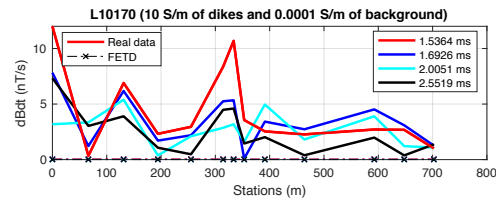
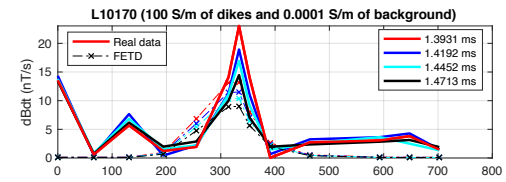
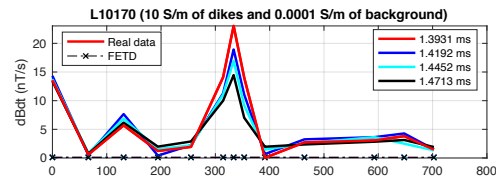
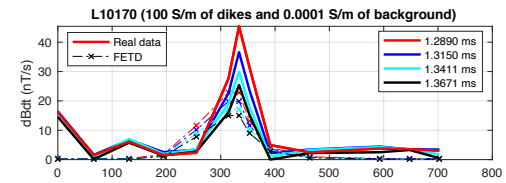
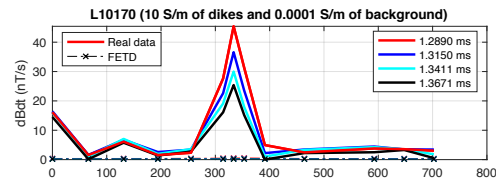
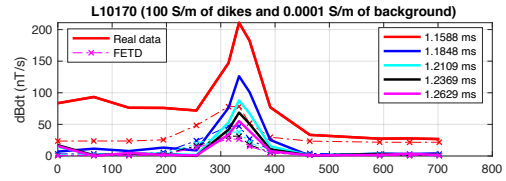
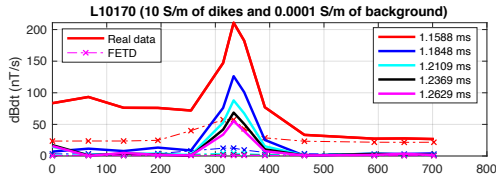


Model 6

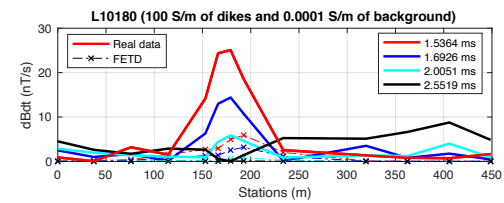
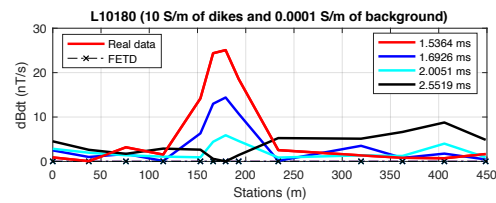
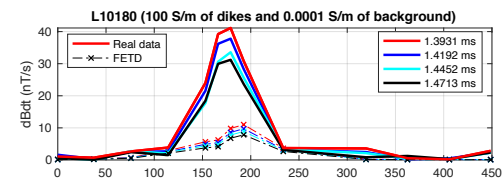
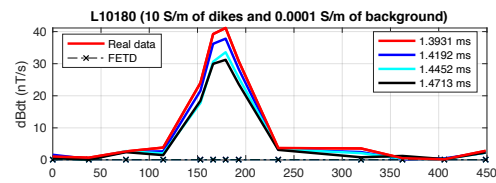
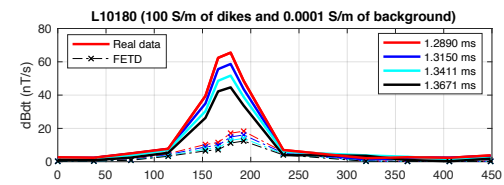
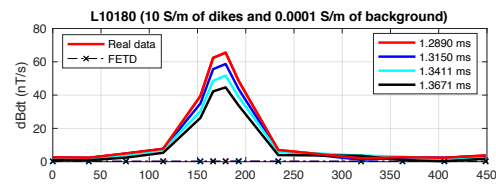
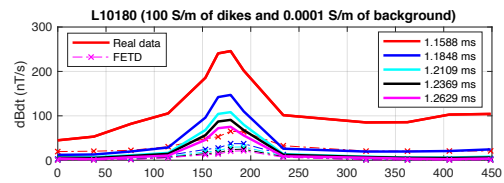
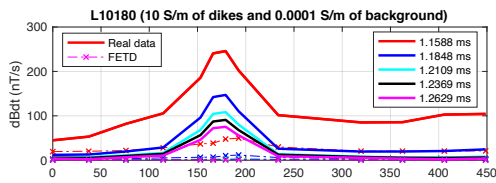




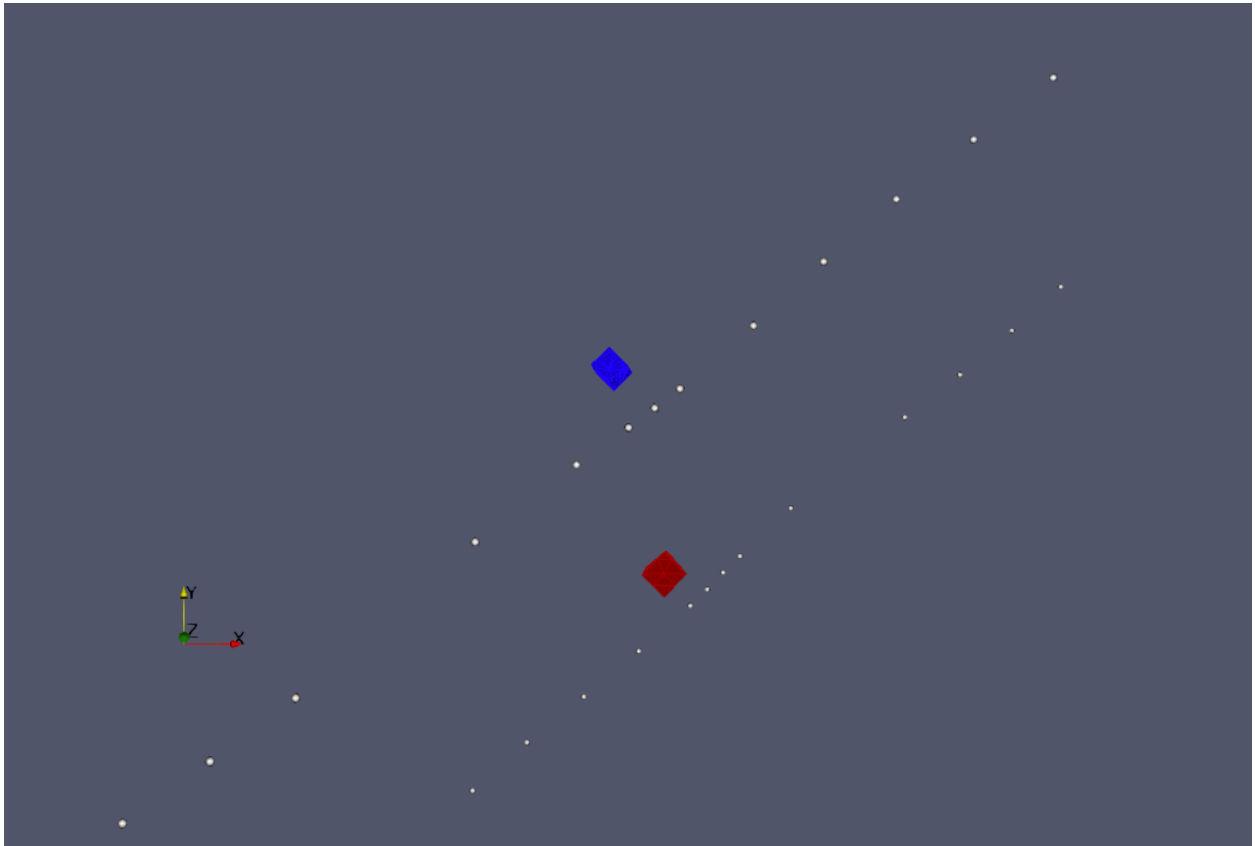
L10170

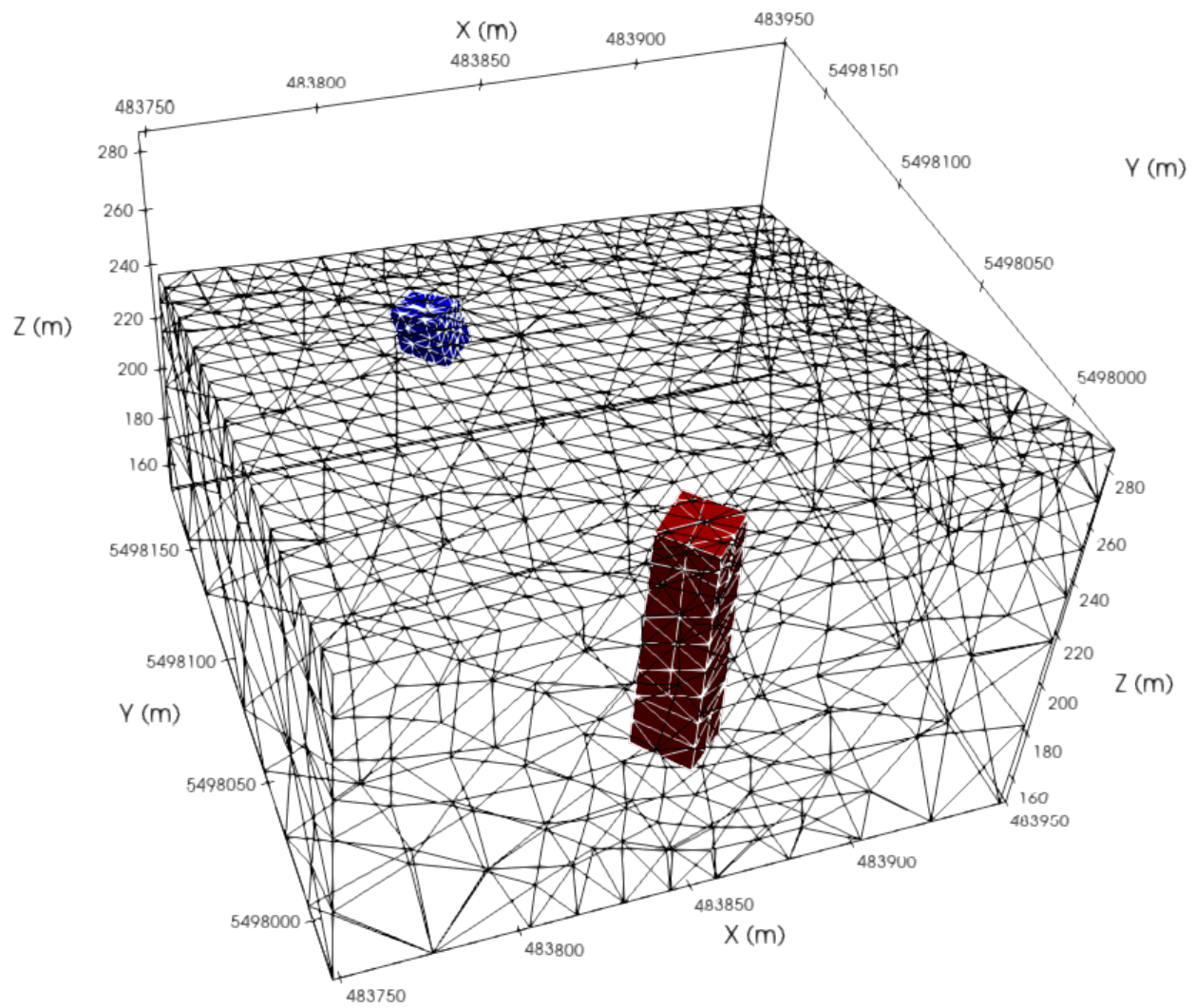


L10180

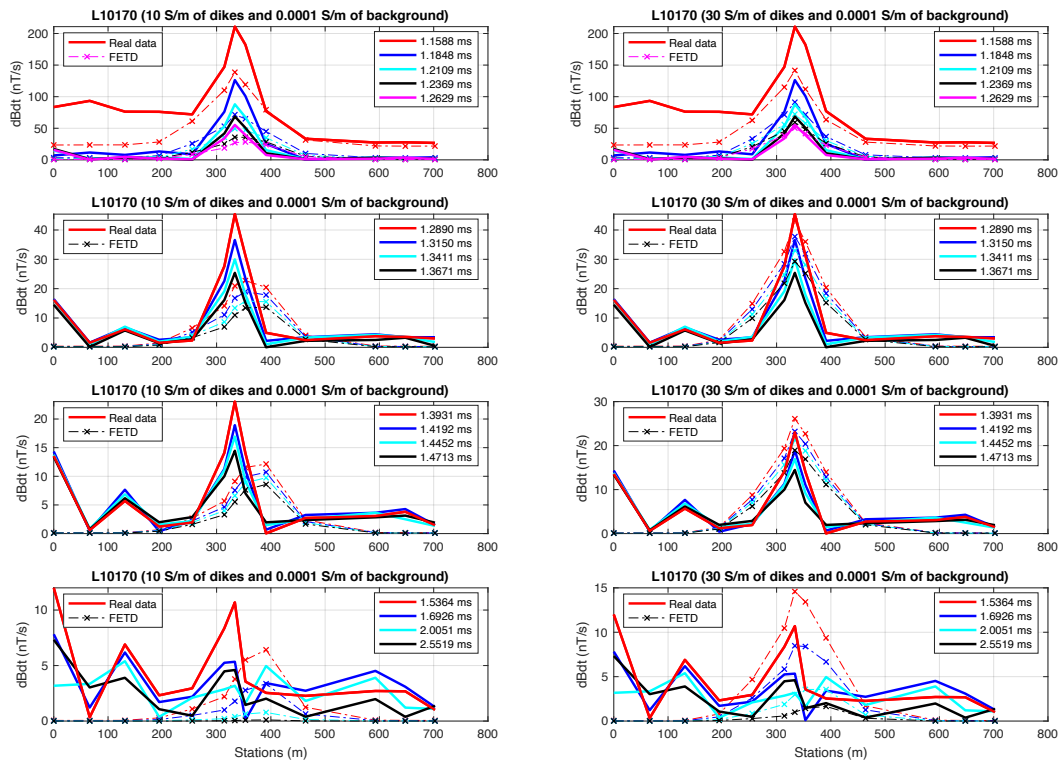


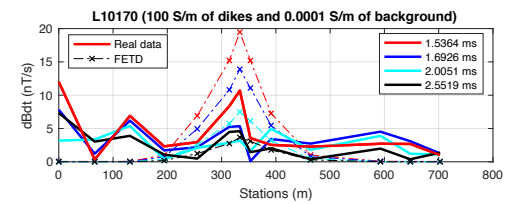
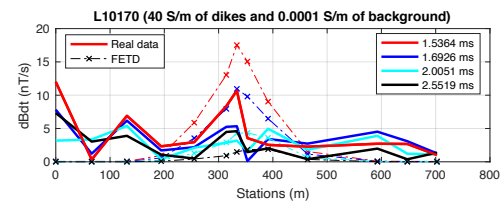
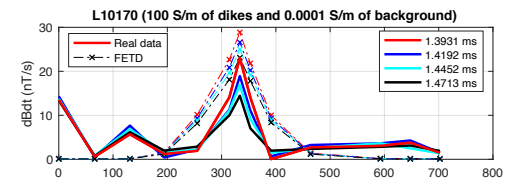
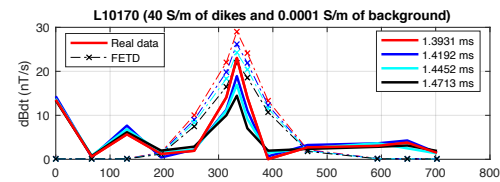
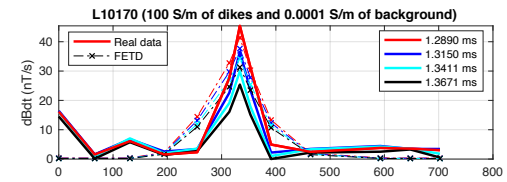
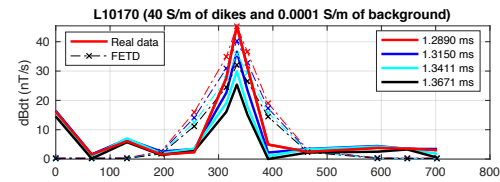
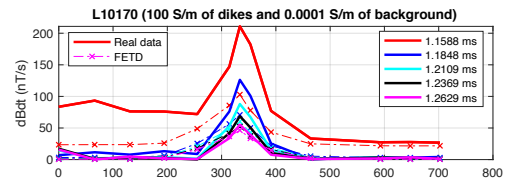
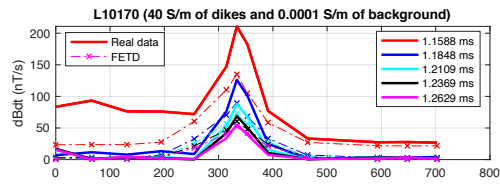
Model 7



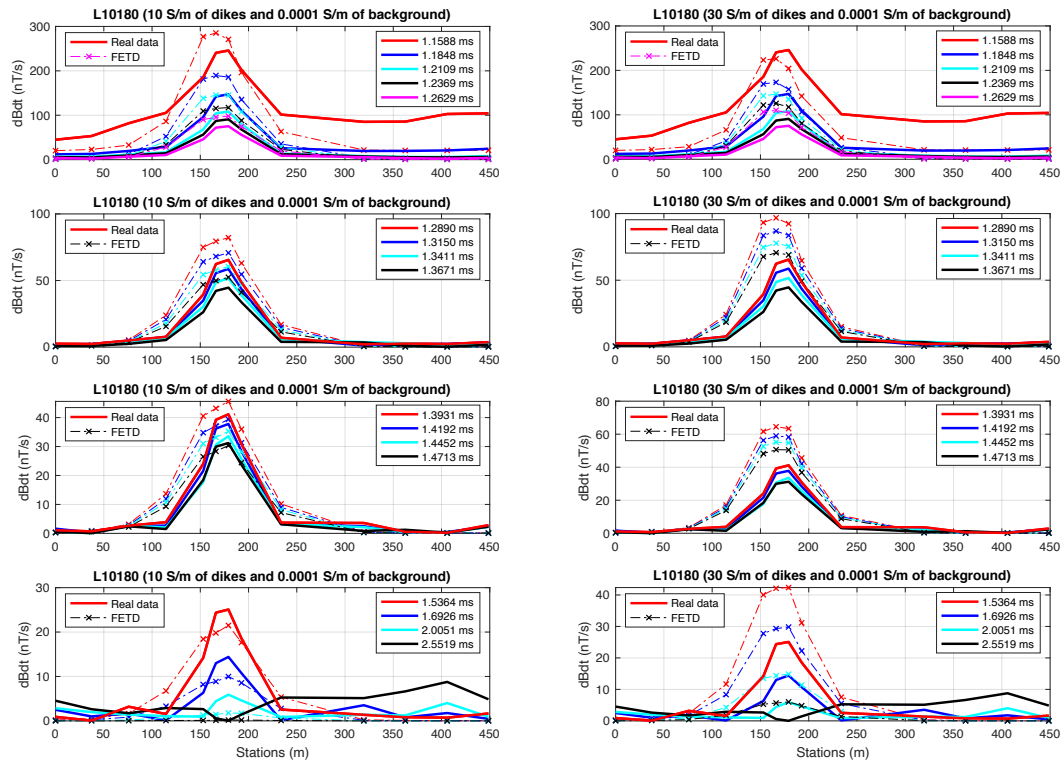


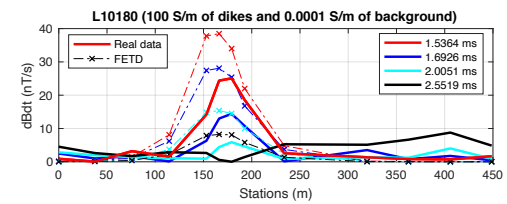
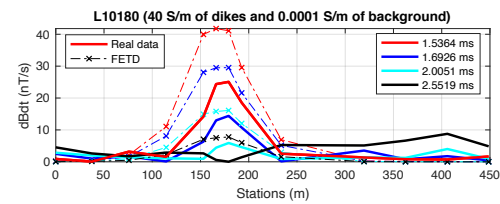
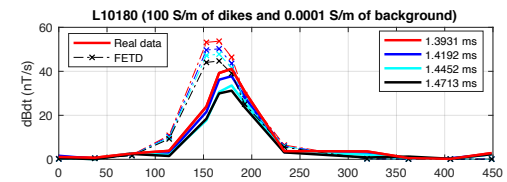
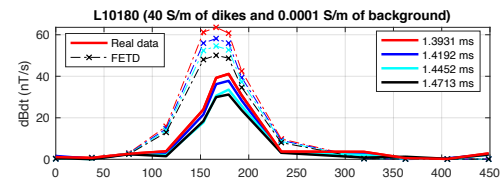
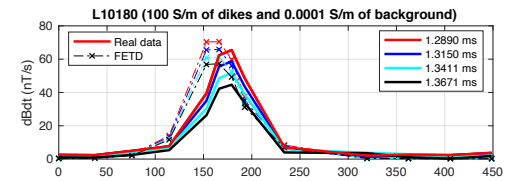
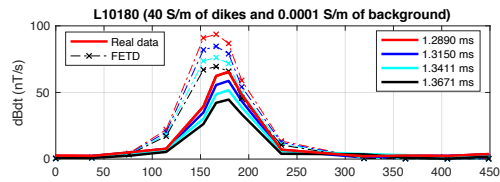
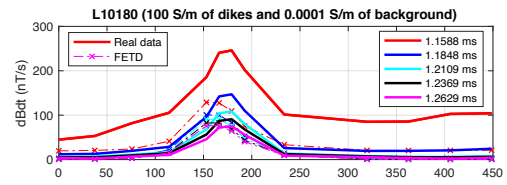
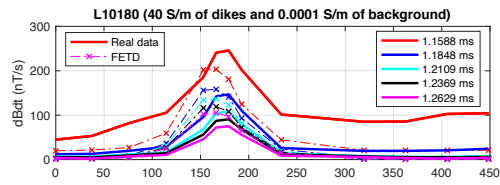
L10170



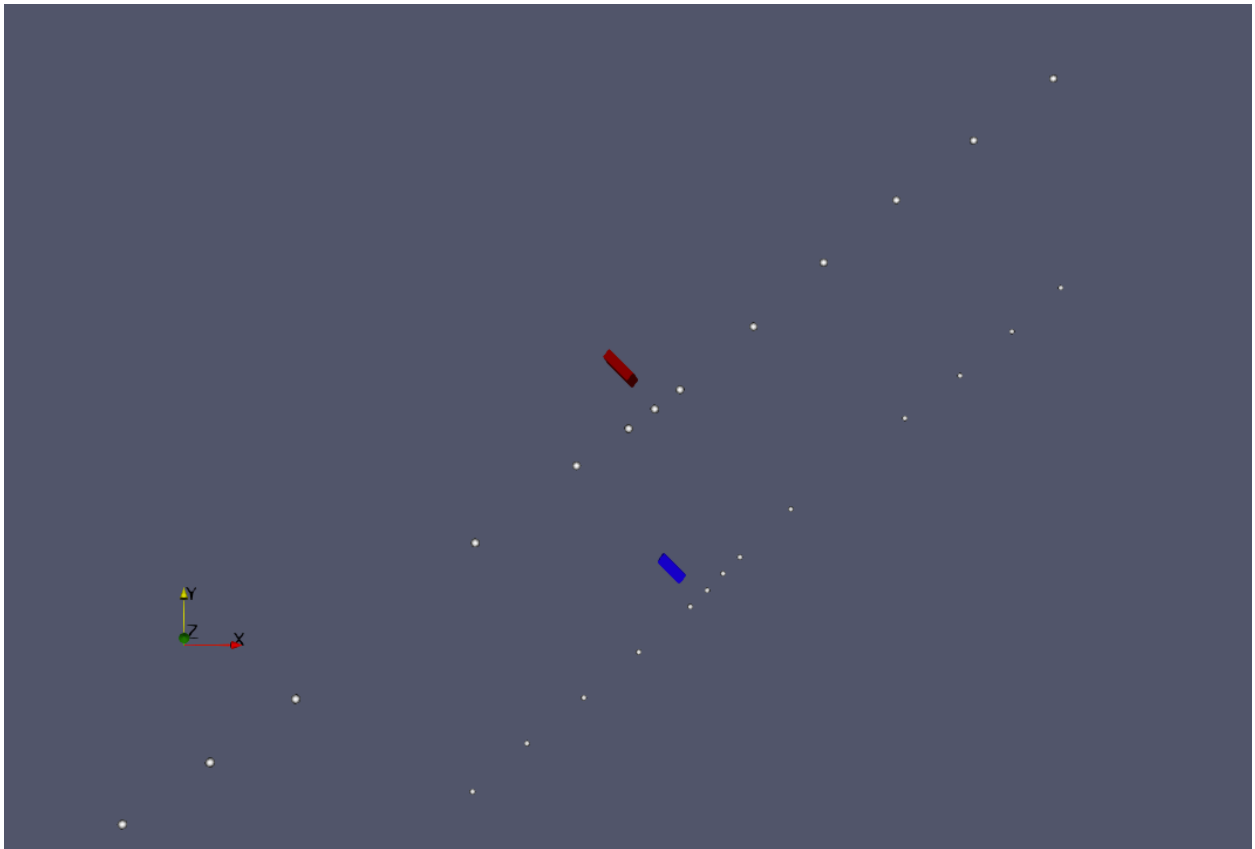


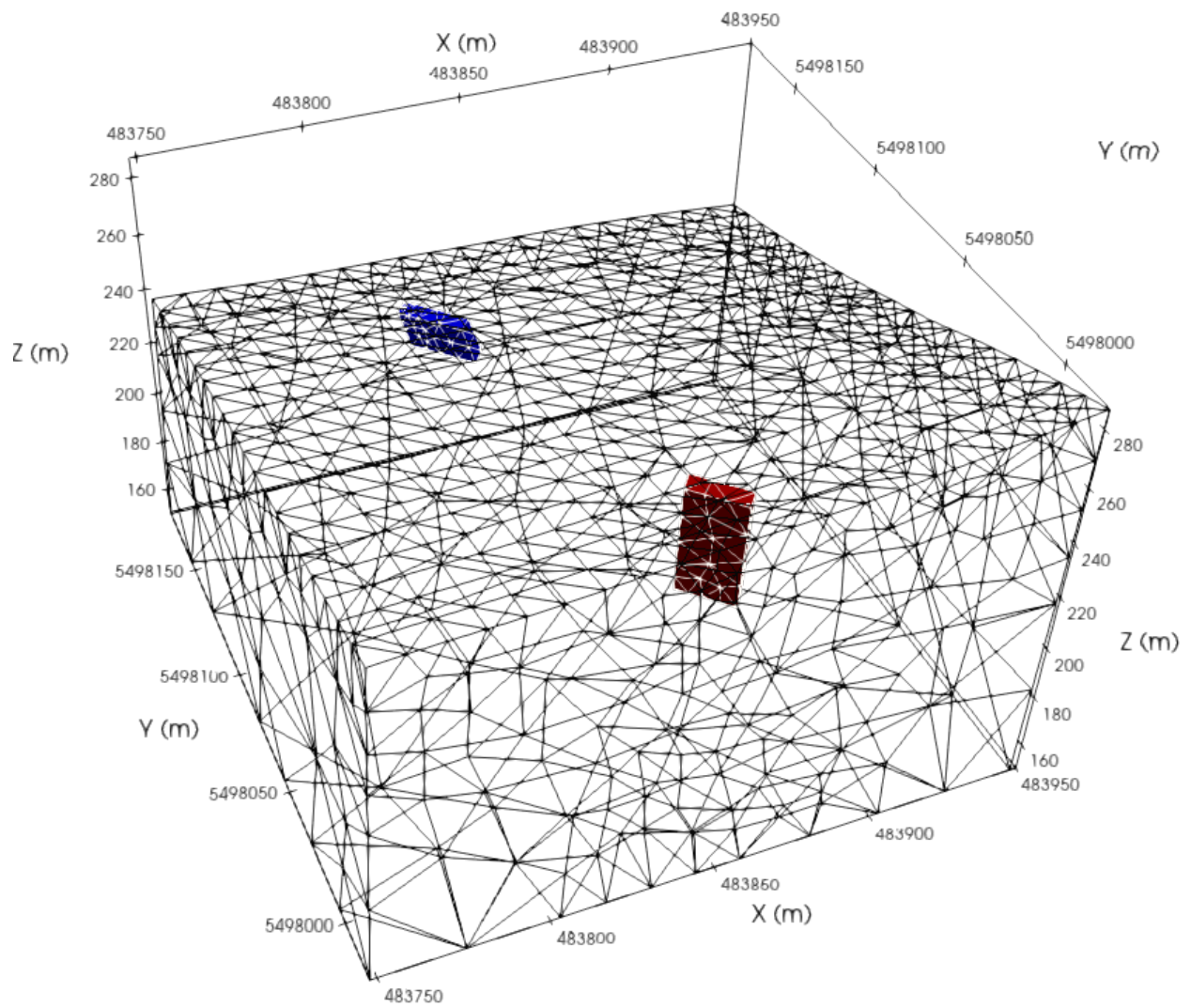
L10180



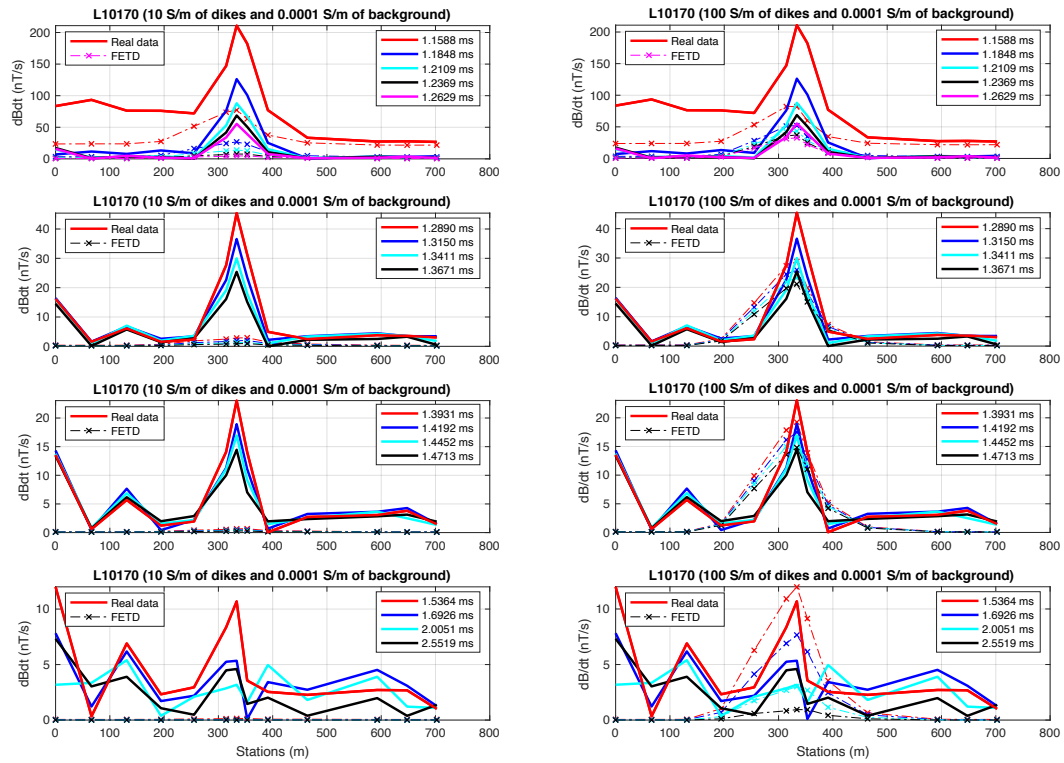


Model 9





L10170



L10180

